Ministry of Science and Higher Education of the Russian Federation
ITMO University

ISSN 2220-8054

NANOSYSTEMS:
PHYSICS, CHEMISTRY, MATHEMATICS

2025, volume 16(6)

Наносистемы: физика, химия, математика
2025, том 16, № 6

NANO Ф&Х&М

NANOSYSTEMS:
PHYSICS, CHEMISTRY, MATHEMATICS

Address: ITMO University, Kronverkskiy pr., 49, St. Petersburg 197101, Russia.
Phone: +7(812)607-02-54, **Journal site:** http://nanojournal.ifmo.ru/,
E-mail: nanojournal@itmo.ru

AIM AND SCOPE

The scope of the journal includes all areas of nano-sciences. Papers devoted to basic problems of physics, chemistry, material science and mathematics inspired by nanosystems investigations are welcomed. Both theoretical and experimental works concerning the properties and behavior of nanosystems, problems of its creation and application, mathematical methods of nanosystem studies are considered.

The journal publishes scientific reviews (up to 30 journal pages), research papers (up to 15 pages) and letters (up to 5 pages). All manuscripts are peer-reviewed. Authors are informed about the referee opinion and the Editorial decision.

CONTENT

MATHEMATICS

PHYSICS

CHEMISTRY AND MATERIAL SCIENCE

NANOSYSTEMS:
PHYSICS, CHEMISTRY, MATHEMATICS

Baltaeva U., et al. *Nanosystems: Phys. Chem. Math.*, 2025, **16** (6), 727–736.
http://nanojournal.ifmo.ru
DOI 10.17586/2220-8054-2025-16-6-727-736

Original article

Inverse analysis of a loaded heat conduction equation

Umida Baltaeva[1,a], Praveen Agarwal[2,b], Bobur Khasanov[3,c], Hamrobek Hayitbayev[4,d], Florence Hubert[5,e]

[1]Department of Applied Mathematics and Mathematical Physics, Urgench State University, Urgench-220100, Uzbekistan

[2]Department of Mathematics, Anand International College of Engineering, Jaipur-303012, India

[3]Department of Exact Sciences, Khorezm Mamun Academy, Khiva, Uzbekistan

[4]Department of Accounting and General Professional Sciences, Mamun university, Khiva, Uzbekistan

[5]Aix-Marseille Universite, I2M, Marseille, France

[a]umida_baltayeva@mail.ru, [b]goyal.praveen2011@gmail.com, [c]xasanovboburjon.1993@gmail.com, [d]hamrohayitboyev073@gmail.com, [e]florence.hubert@univ-amu.fr

Corresponding author: Baltaeva U., umida_baltayeva@mail.ru

ABSTRACT This work considers an inverse problem for a heat conduction equation that includes fractional loaded terms and coefficients varying with spatial coordinates. By reformulating the original equation into a system of equivalent loaded integro-differential equations, we establish sufficient conditions ensuring the existence and uniqueness of the solution. The study focuses on determining the multidimensional kernel associated with the fractional heat conduction operator. The approach is based on the contraction mapping principle and the use of Riemann-Liouville fractional integrals, providing a mathematical framework applicable to diffusion processes with spatial heterogeneity and memory effects.

KEYWORDS heat conduction, inverse problem, fractional calculus, kernel identification, fixed-point method.

FOR CITATION Baltaeva U., Praveen Agarwal, Khasanov B., Hayitbayev H., Hubert F. Inverse analysis of a loaded heat conduction equation. *Nanosystems: Phys. Chem. Math.*, 2025, **16** (6), 727–736.

1. Introduction

Heat conduction refers to the transfer of internal energy, in the form of heat, between adjacent molecules within solids, liquids, or gases, as well as across the interfaces of materials in contact, without requiring bulk motion of the medium itself [1, 2]. The study of heat transfer processes has a long and rich history, spanning more than two centuries, and continues to play a vital role in both theoretical and applied research. In particular, understanding the mechanisms of heat dissipation and temperature regulation in modern high-speed and micro-structured systems remains a crucial challenge for engineering and materials science.

The classical heat conduction equation serves as a universal model in many branches of physics and applied mathematics. It arises naturally in the study of diffusion phenomena, such as the spreading of mass, charge, or vorticity in viscous fluids. From a mathematical perspective, the one-dimensional heat equation is one of the most extensively studied partial differential equations, while the extension to multidimensional and fractional-order formulations continues to attract significant attention due to its broad range of applications in complex physical systems.

In recent decades, the study of fractional differential equations - where the fractional derivative acts on the unknown function - has become increasingly important [3–8]. These equations provide a powerful framework for describing nonlocal and memory-dependent processes that cannot be adequately represented by classical integer-order models. Such features are particularly relevant in nanoscale systems, where energy transfer is strongly influenced by microstructural heterogeneity, phonon scattering, and boundary effects. At these scales, the conventional Fourier law of heat conduction is often insufficient, which motivates the use of fractional and integro-differential models.

In nanosystems, such as thin films, nanowires, and layered composites, thermal conductivity often varies spatially due to surface effects and structural anisotropy. To capture these phenomena, mathematical models with variable coefficients are required. Moreover, the presence of loaded or feedback terms in the governing equations can describe systems with internal heat sources, delayed responses, or coupling between local and nonlocal energy transfer mechanisms.

The present study focuses on an inverse problem for a loaded heat conduction equation with spatially variable coefficients and fractional integral operators. By reformulating the model into an equivalent system of loaded integro-differential equations, we establish conditions for the existence and uniqueness of the solution. The results obtained contribute to the development of mathematical methods for analyzing nanoscale heat transport processes characterized by nonlocality, memory, and structural heterogeneity.

The study of heat conduction has a history spanning over 200 years and remains a topic of significant scientific interest. For example, understanding the dissipation and transfer of heat from sources in high-speed machinery presents a critical technological challenge. This issue is of fundamental importance across various fields of physics.

The heat conduction equation is universal and arises in various contexts, such as modeling mass diffusion or describing the diffusion of vorticity in viscous fluids. Heat conduction problems also hold significant importance from a mathematical perspective. The theory of one-dimensional heat equations is currently the most well-developed and widely applied. Meanwhile, the study of heat conduction problems (of both integer and fractional order) in three-dimensional and multidimensional domains is a growing area within the modern theory of partial differential equations, driven by their relevance to real-world processes.

Fractional diffusion models generalize classical diffusion models by incorporating derivatives of non-integer order. Interest in their study arises from their application in modeling a wide range of phenomena in the physical sciences, medicine, and biology (see, for example, [9–13].

The two-dimensional and multidimensional space-fractional diffusion equations with variable coefficients present a complex challenge in both theoretical analysis and computational approaches [14]. When addressing such equations, it is not always feasible to establish the correctness of the problem using classical methods or to develop efficient numerical techniques. Consequently, the study of fractional diffusion equations with variable coefficients often combines analytical methods with various integration techniques to achieve meaningful results.

In [15], methods for the numerical approximation of the fractional diffusion equation with variable coefficients are presented. The integration of boundary value problems using the method of prior estimates for the fractional diffusion equation is discussed in [17], following an approach similar to that used in the classical case. Paper [16] introduces a finite difference approximation method for a spatial fractional convection-diffusion model governed by an equation with variable coefficients. In [18], the homotopy analysis method and the Adomian decomposition method are applied to high-order time-fractional partial differential equations. Additionally, works [19–23] investigate initial and boundary value problems for the fractional diffusion equation with variable coefficients.

The increased interest in the study of loaded differential equations [24] is attributed to their numerous applications and the fact that they form a distinct class of partial differential equations [25,26]. Notably, the pioneering works of Nakhushev provided one of the first generalized definitions of loaded equations, along with their classification and applications to various problems in mathematical physics and biology [27–34]. Boundary value problems for heat conductivity-loaded equations in both bounded and unbounded domains have been investigated in [28–31], particularly when the order of the derivative in the loaded term is greater than or equal to the order of the differential part of the equation.

In this work, we investigate both analytical and physical aspects of heat transfer at the microscale and nanoscale, focusing on an analogue of the fractional diffusion equation with variable coefficients and a fractional loading term. Such formulations provide a more accurate description of thermal processes in inhomogeneous media, where local and nonlocal interactions coexist and where the transport mechanisms are influenced by spatial variability in material properties.

It should be noted that significant progress in the theory of inverse problems for parabolic equations with variable coefficients was achieved by Beznoshenko, Yan, and Kamynin, who were among the first to investigate such problems systematically. Later, Prilepko and Kostin developed fundamental theorems on the existence and uniqueness of solutions for inverse problems associated with parabolic initial-boundary value problems involving variable coefficients. These classical studies laid the groundwork for the modern theory of inverse and ill–posed problems in heat conduction and diffusion.

Building upon these foundational contributions, the present work addresses an inverse problem for a loaded integro-differential heat conduction equation with spatially variable coefficients. In contrast to earlier models, we consider equations that include fractional integral operators and loading terms, which are essential for describing nonlocal and memory-dependent heat transfer phenomena observed in nanoscale materials. Following recent developments in this field [35–37], the main focus of our study is on determining an unknown coefficient function in the loaded heat conduction equation and establishing conditions for its unique reconstruction.

We introduce the following notations:

Let $\mathbb{R}^n$ denote the n-dimensional Euclidean space, where $x = (x_1, \ldots, x_n) \in \mathbb{R}^n$.

Let $\mathbb{R}^2_T$ represent a subset of three-dimensional Euclidean space, specified by a point (x, y, t), where $(x, y) \in \mathbb{R}^2$ and $t \in (0, T]$, with $T > 0$:

$$R^2_T = \left\{(x, y, t) \,\middle|\, (x, y) \in R^2, 0 \le t \le T\right\}.$$

Let $f(x, y)$ be a function defined on $\mathbb{R}^2$.

Definition 1.1. Let $l \in (0, 1)$. If, for any two points $(x_1, y_1), (x_2, y_2) \in \mathbb{R}^2$, there exists a constant $A > 0$ such that

$$|f(x_1, y_1) - f(x_2, y_2)| \le A \left(|x_1 - x_2| + |y_1 - y_2|\right)^l,$$

then the function $f(x, y)$ is said to satisfy the Holder condition with exponent l in $\mathbb{R}^2$. The class of all such functions is denoted by $H^{\,l}(\mathbb{R}^2)$.

Definition 1.2. Let $l \in (0,1)$ and $T > 0$. If, for any two points (x_1, y_1, t_1) and (x_2, y_2, t_2) in $\mathbb{R}^2_T := \mathbb{R}^2 \times [0,T]$, there exist positive constants $A_1, A_2, A_3 > 0$ such that

$$|f(x_1,y_1,t_1) - f(x_2,y_2,t_2)| \le A_1 |x_1 - x_2|^l + A_2 |y_1 - y_2|^l + A_3 |t_1 - t_2|^{l/2},$$

then the function $f(x,y,t)$ is said to satisfy the Holder condition with exponents l (in x,y) and $l/2$ (in t) in $\mathbb{R}^2_T$. The class of such functions is denoted by $H^{l,\,l/2}(\mathbb{R}^2_T)$.

Inverse problem. Find a pair of functions $u(x,y,t)$ and $k(x,0,t)$ in $(x,y,t) \in \mathbb{R}^2_T$, satisfying the following properties:

$$u_t - a(t)(u_{xx} + u_{yy}) = \lambda D_{0t}^{-\alpha} u(0,y,t) + \int_0^t k(x,0,\tau)\, u(x,y,t-\tau)\, d\tau, \tag{1.1}$$

$$u(x,y,t)|_{t=0} = \varphi(x,y), \;\; (x,y) \in R^2, \tag{1.2}$$

$$u(x,y,t)|_{y=0} = \chi(x,t), \;\; (x,t) \in R^1_T, \tag{1.3}$$

where $a(x),\ \varphi(x,y),\ \chi(x,t)$ are given functions and

$$a(t) \in I := \left\{ a(t) \,|\, a(t) > 0,\ a(t) \in C^1[0,T] \cap C(0,T) \right\}, \tag{1.4}$$

$$\varphi(x,y) \in H^{l+2}\left(R^2\right),\ \varphi(x,y) \le \varphi_0 = const > 0,\ \ \varphi(x,0) = \chi(x,0), \tag{1.5}$$

$$\chi(x,t) \in H^{l+4,(l+4)/2}\left(\bar{R}^1_T\right),\ l \in (0,1), \lambda \in R, \tag{1.6}$$

$D_{0t}^{-\alpha}$ is the Riemann-Liouville fractional integral operator [3] of order α and $\alpha > 0$. The inverse scattering problem is finding $u(x,y,t)$ and $k(x,0,t)$ from the equalities (1.1) - (1.3).

2. Investigation of the problem

First of all, we will construct auxiliary problems equivalent to the inverse problem (1.1), (1.2), (1.3).

Let us introduce the following replacement in the problem (1.1) - (1.3):

$$\vartheta(x,y,t) = u_{yy}(x,y,t),\ \ (x,y,t) \in R^2_T. \tag{2.1}$$

Using the change of variable (2.1), the inverse problem (1.1), (1.2), (1.3), is equivalently reduced to the following problem:

Auxiliary problem: Find functions $\vartheta(x,y,t)$ and $k(x,0,t)$ in $(x,y,t) \in R^2_T$, possessing the following properties:

$$\vartheta_t - a(t)\,\Delta\vartheta = \lambda D_{0t}^{-\alpha} \vartheta(0,y,t) + \int_0^t k(x,0,\tau)\, \vartheta(x,y,t-\tau)\, d\tau, \tag{2.2}$$

$$\vartheta(x,y,t)|_{t=0} = \varphi_{yy}(x,y), \;\; (x,y) \in R^2, \tag{2.3}$$

$$\vartheta(x,y,t)|_{y=0} = \frac{1}{a(t)} \chi_t(x,t) - \chi_{xx}(x,t) -$$

$$- \frac{\lambda}{a(t)} D_{0t}^{-\alpha} \chi(0,0,t) - \frac{1}{a(t)} \int_0^t k(x,0,\tau)\, \chi(x,0,t-\tau)\, d\tau, \tag{2.4}$$

moreover, from the initial condition (2.3) and (2.4) the following condition of agreement is satisfied:

$$\varphi_{yy}(x,0) = \frac{1}{a(0)} \chi_t(x,0) - \chi_{xx}(x,0). \tag{2.5}$$

Indeed, if the compatibility conditions (1.3) and (2.5) are satisfied, and the functions φ and χ are sufficiently smooth, it can be shown that the problems (2.2)–(2.4) are equivalent to the inverse problem (1.1)–(1.3):

First, integrating twice from the (2.1) substitution above from 0 to y, we get

$$u(x,y,t) = \chi(x,t) + y\varphi(x,0) + \int_0^y (y-\xi)\vartheta(x,\xi,t)d\xi, \tag{2.6}$$

and, consequently, in (2.1) for the function $u(x,y,t)$, taking into account the agreement condition (2.5) for $t = 0$, we have

$$u(x,y,t)|_{t=0} = \chi(x,0) + y u_y(x,0,0) + \int_0^y (y-\xi)\, \varphi_{\xi\xi}(x,\xi)\, d\xi =$$

$$= \chi(x,0) + y u_y(x,0,0) + \int_0^y (y-\xi)\, d\varphi_\xi = \chi(x,0) + y u_y(x,0,0) +$$

$$+ (y-\xi)\, \varphi_\xi(x,\xi)|_0^y + \int_0^y \varphi_\xi(x,\xi)\, d\xi = \chi(x,0) + y u_y(x,0,0) -$$

$$- y\varphi_y(x,0) + \varphi(x,y) - \varphi(x,0) = y\left(u_y(x,0,0) - \varphi_y(x,0)\right) + \varphi(x,y) = \varphi(x,y).$$

As can be seen from (2.6), on $y = 0$ the additional condition in (1.3) follows.

The procedure for obtaining equation (1.1) from equation (2.2) is as follows. As the first step, we integrate both sides of equation (2.2) twice from 0 to y:

$$\int_0^y (y-\xi)\,\vartheta_t(x,\xi,t)\,d\xi - a(t)\int_0^y (y-\xi)\,(\vartheta_{xx}(x,\xi,t)+\vartheta_{\xi\xi}(x,\xi,t))\,d\xi =$$
$$= \int_0^y (y-\xi)\,d\xi \int_0^t k(x,0,\tau)\,\vartheta(x,\xi,t-\tau)\,d\tau +$$
$$+\frac{\lambda}{\Gamma(\alpha)}\int_0^y (y-\xi)\,d\xi \int_0^t (t-\tau)^{\alpha-1} u(0,\xi,\tau)\,d\tau,$$

and taking into account equality (2.6), i.e

$$\int_0^y (y-\xi)\vartheta(x,\xi,t)d\xi = u(x,y,t) - \chi(x,t) - y\varphi(x,0)$$

as a result, we have the following relations:

$$\frac{\partial}{\partial t}\left(u(x,y,t)-\chi(x,t)-y\varphi_y(x,0)\right) -$$
$$-a(t)\,\frac{\partial^2}{\partial x^2}\left(u(x,y,t)-\chi(x,t)-y\varphi_y(x,0)\right) -$$
$$-a(t)\int_0^y (y-\xi)\vartheta_{yy}(x,\xi,t)d\xi =$$
$$= \int_0^t k(x,0,\tau)\left(u(x,y,t-\tau)-\chi(x,t-\tau)-y\varphi_y(x,0)\right)d\tau +$$
$$+\frac{\lambda}{\Gamma(\alpha)}\int_0^t (t-\tau)^{\alpha-1}\left(u(0,y,\tau)-\chi(x,t-\tau)-y\varphi_y(x,0)\right)d\tau.$$
$$u_t(x,y,t) - \chi_t(x,t) - a(t)\,\frac{\partial^2}{\partial x^2}u(x,y,t) + a(t)\,\chi(x,t) + a(t)\,y\vartheta_y(x,0,t) -$$
$$-a(t)\,\vartheta(x,y,t) + a(t)\,\vartheta(x,0,t) =$$
$$= \int_0^t k(x,0,\tau)\left(u(x,y,t-\tau)-\chi(x,t-\tau)-y\varphi_y(x,0)\right)d\tau +$$
$$+\frac{\lambda}{\Gamma(\alpha)}\int_0^t (t-\tau)^{\alpha-1}\left(u(0,y,\tau)-\chi(x,t-\tau)-y\varphi_y(x,0)\right)d\tau.$$

Hence, taking into account condition (2.4) for $\vartheta(x,y,t)$, it is easy to see that equation (1.1) has been obtained. Thus, the inverse problem of finding the functions $u(x,y,t)$ and $k(x,0,t)$, defined by (1.1) - (1.3), is equivalent to the inverse problem of finding the functions $\vartheta(x,y,t)$ and $k(x,0,t)$ from (2.2) - (2.4).

Auxiliary problem:

Now, in the second step, if we differentiate the resulting equations with respect to t and make the replacement $\vartheta_t(x,y,t) = \rho(x,y,t)$ in (2.2) - (2.4), we obtain the following auxiliary problem for determining the functions $\vartheta(x,y,t), k(x,0,t)$, and $\rho(x,y,t)$:

$$\rho_t - a(t)(\rho_{xx}+\rho_{yy}) = (\ln a(t))' \rho - (\ln a(t))' \int_0^t k(x,0,\tau)\vartheta(x,y,t-\tau)\,d\tau +$$
$$+\int_0^t k(x,0,\tau)\rho(x,y,t-\tau)\,d\tau - \lambda(\ln a(t))' D_{0t}^{-\alpha}\vartheta(0,y,t) +$$
$$+\lambda D_{0t}^{-\alpha}\rho(0,y,t) + k(x,0,t)\varphi_{yy}(x,y) + \frac{\lambda}{\Gamma(\alpha)}t^{\alpha-1}\varphi_{yy}(0,y,0), \tag{2.7}$$

$$\rho|_{t=0} = a(0)\Delta\varphi_{yy}(x,y), \tag{2.8}$$

$$\rho|_{y=0} = F_t(x,t) + \frac{a'(t)}{a^2(t)}\int_0^t k(x,0,\tau)\chi(x,t-\tau)\,d\tau -$$
$$-\frac{1}{a(t)}\int_0^t k(x,0,\tau)\chi_t(x,t-\tau)\,d\tau - \frac{1}{a(t)}k(x,0,t)\varphi(x',0), \tag{2.9}$$

where

$$F(x,t) = \frac{1}{a(t)}\chi_t(x,t) - \chi_{xx}(x,t) - \frac{\lambda}{a(t)\Gamma(\alpha)}\int_0^t (t-\tau)^{\alpha-1}\chi(0,0,\tau)\,d\tau.$$

As a result, we obtain an auxiliary problem for determining the functions $\vartheta(x,y,t)$, $k(x,0,t)$, and $\rho(x,y,t)$.

In the next step, by integrating both sides of the last change of variable from 0 to t, we obtain the following equality:

$$\vartheta(x,y,t) = \varphi_{yy}(x,y) + \int_0^t \rho(x,y,\tau)\,d\tau. \tag{2.10}$$

If the function $\rho(x,y,t)$ is known, then the function $\vartheta(x,y,t)$ can be determined from (2.10). Thus, the problem (2.7) - (2.9) reduces to the problems (2.2) - (2.4), and the problems (2.2) - (2.4) lead to the inverse problem defined by (1.1) - (1.3). Therefore, finding the functions $\vartheta(x,y,t)$, $k(x,0,t)$, and $\rho(x,y,t)$ from problems (2.2) - (2.4) and (2.7) - (2.9) is equivalent to finding the functions $u(x,y,t)$ and $k(x,0,t)$ from the inverse problem (1.1) - (1.3).

Thus, we have proved the following lemma:

Lemma 2.1. *Suppose that* $a(t) \in I$, $\varphi(x,y) \in H^{l+6}(\mathbb{R}^2)$, $\chi(x,t) \in H^{l+4,(l+4)/2}(\overline{\mathbb{R}}_T^1)$, *and the matching conditions*

$$\chi(x,0) = \varphi(x,0), \qquad \varphi_{yy}(x,0) = \frac{1}{a(0)}\chi_t(x,0) - \chi_{xx}(x,0),$$

are satisfied. Then the problem (1.1) - (1.3) *is equivalent to the problem of determining the functions* $\vartheta(x,y,t)$, $k(x,0,t)$, *and* $\rho(x,y,t)$ *from equations* (2.2) - (2.4) *and* (2.7) - (2.9).

3. Reduction of problem (1.1) - (1.3) to a system of integral equations

Lemma 3.1. *The auxiliary problems* (2.2), (2.3) *and* (2.7) - (2.9) *is equivalent to finding the functions* $\vartheta(x,y,t)$, $k(x,y,t)$, $\rho(x,y,t)$ *from the following system of integral equations:*

$$\vartheta(x,y,t) = \int_{-\infty}^{\infty}\int_{-\infty}^{\infty}\varphi_{\eta\eta}(\xi,\eta)G\,d\xi d\eta + \int_0^{\theta(t)}\frac{d\tau}{a(\theta^{-1}(\tau))}\times$$
$$\times\int_{-\infty}^{\infty}\int_{-\infty}^{\infty}\int_0^{\theta^{-1}(\tau)} k(\xi,0,\alpha)\vartheta\left(\xi,\eta,\theta^{-1}(\tau)-\alpha\right)G\,d\alpha d\xi d\eta + \tag{3.1}$$
$$+\frac{\lambda}{\Gamma(\alpha)}\int_0^{\theta(t)}\frac{d\tau}{a(\theta^{-1}(\tau))}\int_{-\infty}^{\infty}\int_{-\infty}^{\infty}\int_0^{\theta^{-1}(\tau)}\left(\theta^{-1}(\tau)-\beta\right)^{\alpha-1}\vartheta(0,\eta,\beta)\,G\,d\beta d\xi d\eta,$$

$$\rho(x,y,t) = \int_{-\infty}^{\infty}\int_{-\infty}^{\infty} a(0)\Delta\varphi_{\eta\eta}(\xi,\eta)\,G\,d\xi d\eta + \int_0^{\theta(t)}\frac{d\tau}{a(\theta^{-1}(\tau))}\times$$
$$\times\int_{-\infty}^{\infty}\int_{-\infty}^{\infty}\Big(\left(\ln a\left(\theta^{-1}(\tau)\right)\right)'\rho\left(\xi,\eta,\theta^{-1}(\tau)\right) -$$
$$-\left(\ln a\left(\theta^{-1}(\tau)\right)\right)'\int_0^{\theta^{-1}(\tau)} k(\xi,0,\alpha)\vartheta\left(\xi,\eta,\theta^{-1}(\tau)-\alpha\right)d\alpha\Big)\,G\,d\xi d\eta +$$
$$+\int_0^{\theta(t)}\frac{d\tau}{a(\theta^{-1}(\tau))}\int_{-\infty}^{\infty}\int_{-\infty}^{\infty}\int_0^{\theta^{-1}(\tau)} k(\xi,0,\alpha)\rho\left(\xi,\eta,\theta^{-1}(\tau)-\alpha\right)G\,d\alpha d\xi d\eta +$$

$$+\int_0^{\theta(t)}\frac{d\tau}{a\left(\theta^{-1}(\tau)\right)}\int_{-\infty}^{\infty}\int_{-\infty}^{\infty}k\left(\xi,0,\theta^{-1}(\tau)\right)\varphi_{\eta\eta}(\xi,\eta)\,Gd\xi d\eta+ \tag{3.2}$$

$$+\frac{\lambda}{\Gamma(\alpha)}\int_0^{\theta(t)}\frac{d\tau}{a\left(\theta^{-1}(\tau)\right)}\int_{-\infty}^{\infty}\int_{-\infty}^{\infty}\int_0^{\theta^{-1}(\tau)}\left(\theta^{-1}(\tau)-\beta\right)^{\alpha-1}\rho(0,\eta,\beta)\,Gd\beta d\xi d\eta-$$

$$-\frac{\lambda}{\Gamma(\alpha)}\int_0^{\theta(t)}\frac{d\tau}{a\left(\theta^{-1}(\tau)\right)}\int_{-\infty}^{\infty}\int_{-\infty}^{\infty}\Big[\left(\ln a\left(\theta^{-1}(\tau)\right)\right)'\int_0^{\theta^{-1}(\tau)}\left(\theta^{-1}(\tau)-\beta\right)^{\alpha-1}\times$$

$$\times\vartheta(0,\eta,\beta)\,d\beta-\left(\theta^{-1}(\tau)\right)^{\alpha-1}\varphi_{\eta\eta}(\xi,\eta)\Big]\,Gd\xi d\eta,$$

$$k(x,0,t)=\frac{a(t)}{\varphi(x,0)}\left(F_t(x,t)-\int_{-\infty}^{\infty}\int_{-\infty}^{\infty}a(0)\,\Delta\varphi_{\eta\eta}(\xi,\eta)\,Gd\xi d\eta-\right.$$

$$-\int_0^{\theta(t)}\frac{d\tau}{a\left(\theta^{-1}(\tau)\right)}\int_{-\infty}^{\infty}\int_{-\infty}^{\infty}\left(\ln a\left(\theta^{-1}(\tau)\right)\right)'\rho\left(\xi,\eta,\theta^{-1}(\tau)\right)Gd\xi d\eta+$$

$$+\int_0^{\theta(t)}\frac{d\tau}{a\left(\theta^{-1}(\tau)\right)}\int_{-\infty}^{\infty}\times$$

$$\times\int_{-\infty}^{\infty}\left(\left(\ln a\left(\theta^{-1}(\tau)\right)\right)'\int_0^{\theta^{-1}(\tau)}k(\xi,0,\alpha)\vartheta\left(\xi,\eta,\theta^{-1}(\tau)-\alpha\right)d\alpha\right)Gd\xi d\eta-$$

$$-\int_0^{\theta(t)}\frac{d\tau}{a\left(\theta^{-1}(\tau)\right)}\int_{-\infty}^{\infty}\int_{-\infty}^{\infty}\int_0^{\theta^{-1}(\tau)}k(\xi,0,\alpha)\rho\left(\xi,\eta,\theta^{-1}(\tau)-\alpha\right)Gd\alpha d\xi d\eta-$$

$$-\int_0^{\theta(t)}\frac{d\tau}{a\left(\theta^{-1}(\tau)\right)}\int_{-\infty}^{\infty}\int_{-\infty}^{\infty}k\left(\xi,0,\theta^{-1}(\tau)\right)\varphi_{\eta\eta}(\xi,\eta)\,Gd\xi d\eta- \tag{3.3}$$

$$-\frac{\lambda}{\Gamma(\alpha)}\int_0^{\theta(t)}\frac{d\tau}{a\left(\theta^{-1}(\tau)\right)}\times$$

$$\times\int_{-\infty}^{\infty}\int_{-\infty}^{\infty}\int_0^{\theta^{-1}(\tau)}\left(\theta^{-1}(\tau)-\beta\right)^{\alpha-1}\rho(0,\eta,\beta)\,Gd\beta d\xi d\eta+$$

$$+\frac{\lambda}{\Gamma(\alpha)}\int_0^{\theta(t)}\frac{d\tau}{a\left(\theta^{-1}(\tau)\right)}\times$$

$$\times\int_{-\infty}^{\infty}\int_{-\infty}^{\infty}\left(\left(\ln a\left(\theta^{-1}(\tau)\right)\right)'\int_0^{\theta^{-1}(\tau)}\left(\theta^{-1}(\tau)-\beta\right)^{\alpha-1}\vartheta(0,\eta,\beta)\,d\beta\right)Gd\xi d\eta-$$

$$-\frac{\lambda}{\Gamma(\alpha)}\int_0^{\theta(t)}\frac{d\tau}{a\left(\theta^{-1}(\tau)\right)}\int_{-\infty}^{\infty}\int_{-\infty}^{\infty}\left(\theta^{-1}(\tau)\right)^{\alpha-1}\varphi_{\eta\eta}(\xi,\eta)\,Gd\xi d\eta\Bigg)+$$

$$+\frac{1}{\varphi(x,0)}\int_0^t\left(\left(\ln a(t)\right)'\chi(x,t-\tau)-\chi_t(x,t-\tau)\right)k(x,0,\tau)\,d\tau,$$

where, $G=G(x-\xi,y-\eta,\theta(t))$ and, respectively, from $\theta(t)-\tau$.

Proof. In problems (2.2) - (2.3), taking into account formula (2.8) as in the correct problem from [23]

$$F(x,y,t)=\lambda D_{0t}^{-\alpha}\vartheta(0,y,t)+\int_0^t k(x,0,\tau)\,\vartheta(x,y,t-\tau)\,d\tau$$

in the above form, we ontain the integral equation (3.1) correspondingly equivalently. In the same way, taking into account (2.7) - (2.8), we get formula (3.2). Then, taking into account the resulting integral equations and using (2.9), we get the integral equation (3.3)

From problems (2.3),(2.4) and (2.7), (2.8), integral equations (3.1), (3.2) are obtained analogously to the equation (1.3). Equation (3.3) follows from equations (2.9) and (3.2).

Now we will prove the existence and uniqueness of the solution to problem (2.2) - (2.4). The proof is based on the contraction mapping principle.

Theorem 3.2. *If conditions (1.4), (1.5), (1.6), and, (2.5) are satisfied, then there exists a sufficiently small number $T_0>0$ such that, for $T\in(0,T_0]$, there exists a unique solution to the integral equations* (3.1) - (3.3) *belonging to the classes*

$$\{\vartheta(x,y,t),\ \rho(x,y,t)\}\in H^{l+2,(l+2)/2}\left(\bar{R}_T^2\right),\ k(x,0,t)\in H^{l,l/2}\left(\bar{R}_T^1\right).$$

Proof. To prove the theorem using the contraction mapping principle, we rewrite the system of equations (3.1) - (3.3) as a nonlinear operator:

$$\sigma = L\sigma,\ \sigma = (\sigma_1, \sigma_2, \sigma_3)^* = (\vartheta, \rho, k(x,0,t))^*, \tag{3.4}$$

where $*$ is the transposition symbol, $L\sigma = [(L\sigma)_1, (L\sigma)_2, (L\sigma)_3]^*$. Thus, according to the right sides of equations (3.1) - (3.3), $(L\sigma)_i\ (i = 1,2,3)$, we have

$$(L\sigma)_1 = \sigma_{01}(x,y,t) + \int_0^{\theta(t)} \frac{d\tau}{a(\widehat{\tau})} \times$$
$$\times \int_{-\infty}^{\infty}\int_{-\infty}^{\infty}\int_0^{\widehat{\tau}} \sigma_3(\xi,0,\alpha)\sigma_1(\xi,\eta,\widehat{\tau}-\alpha)\, G d\alpha d\xi d\eta +$$
$$+\frac{\lambda}{\Gamma(\alpha)} \int_0^{\theta(t)} \frac{d\tau}{a(\widehat{\tau})} \int_{-\infty}^{\infty}\int_{-\infty}^{\infty}\int_0^{\widehat{\tau}} (\widehat{\tau}-\beta)^{\alpha-1} \sigma_1(0,\eta,\beta)\, G d\beta d\xi d\eta,$$

where

$$(L\sigma)_2 = \sigma_{02}(x,y,t) + \int_0^{\theta(t)} \frac{d\tau}{a(\widehat{\tau})} \int_{-\infty}^{\infty}\int_{-\infty}^{\infty} \Big[(\ln a(\widehat{\tau}))' \sigma_2(\xi,\eta,\widehat{\tau}) -$$
$$- (\ln a(\widehat{\tau}))' \int_0^{\widehat{\tau}} \sigma_3(\xi,0,\alpha)\sigma_1(\xi,\eta,\widehat{\tau}-\alpha)\, d\alpha \Big] G d\xi d\eta +$$
$$+ \int_0^{\theta(t)} \frac{d\tau}{a(\widehat{\tau})} \int_{-\infty}^{\infty}\int_{-\infty}^{\infty}\int_0^{\widehat{\tau}} \sigma_3(\xi,0,\alpha)\sigma_2(\xi,\eta,\widehat{\tau}-\alpha)\, G d\alpha d\xi d\eta +$$
$$+ \int_0^{\theta(t)} \frac{d\tau}{a(\widehat{\tau})} \int_{-\infty}^{\infty}\int_{-\infty}^{\infty} \sigma_3(\xi,0,\widehat{\tau})\varphi_{\eta\eta}(\xi,\eta)\, G d\xi d\eta +$$
$$+\frac{\lambda}{\Gamma(\alpha)} \int_0^{\theta(t)} \frac{d\tau}{a(\widehat{\tau})} \int_{-\infty}^{\infty}\int_{-\infty}^{\infty}\int_0^{\widehat{\tau}} (\widehat{\tau}-\beta)^{\alpha-1} \sigma_2(0,\eta,\beta)\, G d\beta d\xi d\eta -$$
$$-\frac{\lambda}{\Gamma(\alpha)} \int_0^{\theta(t)} \frac{d\tau}{a(\widehat{\tau})} \int_{-\infty}^{\infty}\int_{-\infty}^{\infty} \left[(\ln a(\widehat{\tau}))' \int_0^{\widehat{\tau}} (\widehat{\tau}-\beta)^{\alpha-1} \sigma_1(0,\eta,\beta)\, d\beta \right] G d\xi d\eta.$$

$$(L\sigma)_3 = \sigma_{03}(x,y,t) -$$
$$-\frac{a(t)}{\varphi(x,0)} \int_0^{\theta(t)} \frac{d\tau}{a(\widehat{\tau})} \int_{-\infty}^{\infty}\int_{-\infty}^{\infty} (\ln a(\widehat{\tau}))' \Big[\sigma_2(\xi,\eta,\widehat{\tau}) -$$
$$- \int_0^{\widehat{\tau}} \sigma_3(\xi,0,\alpha)\sigma_1(\xi,\eta,\widehat{\tau}-\alpha)\, d\alpha \Big] G d\xi d\eta -$$
$$-\frac{a(t)}{\varphi(x,0)} \int_0^{\theta(t)} \frac{d\tau}{a(\widehat{\tau})} \int_{-\infty}^{\infty}\int_{-\infty}^{\infty}\int_0^{\widehat{\tau}} \sigma_3(\xi,0,\alpha)\sigma_2(\xi,\eta,\widehat{\tau}-\alpha)\, G d\alpha d\xi d\eta -$$
$$-\frac{a(t)}{\varphi(x,0)} \int_0^{\theta(t)} \frac{d\tau}{a(\widehat{\tau})} \int_{-\infty}^{\infty}\int_{-\infty}^{\infty} \sigma_3(\xi,0,\widehat{\tau})\varphi_{\eta\eta}(\xi,\eta)\, G d\xi d\eta -$$
$$-\frac{\lambda a(t)}{\Gamma(\alpha)\varphi(x,0)} \int_0^{\theta(t)} \frac{d\tau}{a(\widehat{\tau})} \left(\int_{-\infty}^{\infty}\int_{-\infty}^{\infty}\int_0^{\widehat{\tau}} (\widehat{\tau}-\beta)^{\alpha-1} \sigma_2(0,\eta,\beta)\, G d\beta d\xi d\eta - \right.$$
$$\left. - \int_{-\infty}^{\infty}\int_{-\infty}^{\infty} (\ln a(\widehat{\tau}))' \int_0^{\widehat{\tau}} (\widehat{\tau}-\beta)^{\alpha-1} \sigma_1(0,\eta,\beta)\, d\beta G d\xi d\eta \right) +$$
$$+\frac{1}{\varphi(x,0)} \int_0^t \Big((\ln a(t))' \chi(x,t-\tau) - \chi_t(x,t-\tau) \Big) \sigma_3(x,0,\tau)\, d\tau,$$

where $\theta^{-1}(\tau) = \widehat{\tau}$, $\sigma_{01}(x,y,t)$, $\sigma_{02}(x,y,t)$ and $\sigma_{03}(x,y,t)$ depends on the given functions, i.e.

$$\sigma_{01}(x,y,t) = \int_{-\infty}^{\infty}\int_{-\infty}^{\infty} \varphi_{\eta\eta}(\xi,\eta)\, G d\xi d\eta,$$

$$\sigma_{02}(x,y,t) = \int_{-\infty}^{\infty}\int_{-\infty}^{\infty} a(0)\, \Delta\varphi_{\eta\eta}(\xi,\eta)\, G d\xi d\eta +$$
$$+\frac{\lambda}{\Gamma(\alpha)} \int_0^{\theta(t)} \frac{d\tau}{a(\widehat{\tau})} \int_{-\infty}^{\infty}\int_{-\infty}^{\infty} (\widehat{\tau})^{\alpha-1} \varphi_{\eta\eta}(0,\eta)\, G d\xi d\eta,$$

$$\sigma_{03}(x,y,t) = \frac{a(t)}{\varphi(x,0)} \left(F_t(x,t) - \int_{-\infty}^{\infty}\int_{-\infty}^{\infty} a(0)\, \Delta\varphi_{\eta\eta}(\xi,\eta)\, G d\xi d\eta - \right.$$

$$-\frac{\lambda}{\Gamma(\alpha)}\int_0^{\theta(t)}\frac{d\tau}{a(\widehat{\tau})}\int_{-\infty}^{\infty}\int_{-\infty}^{\infty}(\widehat{\tau})^{\alpha-1}\varphi_{\eta\eta}(0,\eta)\,G d\xi d\eta\Bigg).$$

Introducing the notation $|\sigma|_T^{l,l/2}=\max\left(|\sigma_1|_{T_0}^{l,l/2},|\sigma_2|_{T_0}^{l,l/2},|\sigma_3|_{T_0}^{l,l/2}\right)$ in $H^{l,l/2}\left(R_T^2\right)$, we introduce the following condition

$$S(T)=|\sigma_1-\sigma_0|_T^{l,l/2}\le|\sigma_0|_{T_0}^{l,l/2}, \tag{3.5}$$

where $\sigma_0=(\sigma_{01},\sigma_{02},\sigma_{03})$ and $|\sigma_0|_{T_0}^{l,l/2}=\max\left(|\sigma_{01}|_{T_0}^{l,l/2},|\sigma_{02}|_{T_0}^{l,l/2},|\sigma_{03}|_{T_0}^{l,l/2}\right)$. Thus, for any function σ from $S(T)$, $T<T_0$, when (3.5) is executed, the following inequality is true:

$$|\sigma_i|_T^{l,l/2}\le 2|\sigma_0|_{T_0}^{l,l/2}, i=1,2,3.$$

As is known, for $\varphi(x,y)\in H^{l+2}\left(R^2\right)$, the Cauchy problem for the classical heat conduction equation has a solution. In problem (1.1) - (1.3), taking into account the auxiliary problem, the initial conditions must satisfy $\varphi(x,y)\in H^{l+6}(\mathbb{R}^2)$, since the auxiliary problem involves fourth-order derivatives.

If the Cauchy condition $\varphi(x,y)\in H^{l+2}(\mathbb{R}^2)$ holds for the classical heat conduction equation, then the Cauchy problem for the classical heat diffusion equation has a solution [39]. Since we consider the class $\varphi(x,y)\in H^{l+6}(\mathbb{R}^2)$, the fourth-order derivatives are also involved in the corresponding auxiliary problem. Based on this, we introduce the following notation:

$$a_0:=\max_{t\in[0,T]}\left|\left(\ln a(t)\right)'\right|,\varphi_1:=|\varphi|^{l+6},\chi_0:=|\chi|_T^{l+4,(l+4)/2}.$$

Contraction Mapping Principle. Any contraction mapping defined on a complete metric space has a unique fixed point; that is, the equation $x=Ax$ has a unique solution $x_0\in S$.

At the initial stage, using the estimates of thermal volume potentials [38][pp. 318-325], we can easily obtain the following inequalities:

$$|(L\sigma)_1-\sigma_{01}|_T^{l,l/2}=$$
$$=\left|\int_0^t\frac{d\tau}{a(\widehat{\tau})}\int_{-\infty}^{\infty}\int_{-\infty}^{\infty}\int_0^{\widehat{\tau}}\sigma_3(\xi,0,\alpha)\sigma_1(\xi,\eta,\widehat{\tau}-\alpha)\,G d\alpha d\xi d\eta\right|_T^{l,l/2}+$$
$$+\left|\frac{\lambda}{\Gamma(\alpha)}\int_0^t\frac{d\tau}{a(\widehat{\tau})}\int_{-\infty}^{\infty}\int_{-\infty}^{\infty}\int_0^{\widehat{\tau}}(\widehat{\tau}-\beta)^{\alpha-1}\sigma_1(0,\eta,\beta)\,G d\beta d\xi d\eta\right|_T^{l,l/2}\le$$
$$\le\bar{\beta}_0(T)\left|\left(\sigma_3(\xi,\eta,t_0)\sigma_1(\xi,\eta,z-t_0)\right)\right|_T^{l,l/2}+\bar{\beta}_1(T)\left|\left(\sigma_1(0,\eta,t_0)\right)\right|_T^{l,l/2}\le$$
$$\le 4\beta_0(T)\left(|\sigma_0|_{T_0}^{l,l/2}\right)^2+2\beta_1(T)\left(|\sigma_0|_{T_0}^{l,l/2}\right),$$
$$|(L\sigma)_2-\sigma_{02}|_T^{l,l/2}\le$$
$$\le 4\beta_1(T)(a_0+1)\left(|\sigma_0|_{T_0}^{l,l/2}\right)^2+2\beta_2(T)(2a_0+\varphi_1+1)\left(|\sigma_0|_{T_0}^{l,l/2}\right),$$
$$|(L\sigma)_3-\sigma_{03}|_T^{l,l/2}\le$$
$$\le 2\left(\beta_1(T)a_1\varphi_0^{-1}(2a_0+\varphi_1+1)+\chi_0\varphi_0^{-1}T_0(a_0+1)\right)|\sigma_0|_{T_0}^{l,l/2}+$$
$$+4\beta_2(T)a_1\varphi_0^{-1}(a_0+1)\left(|\sigma_0|_{T_0}^{l,l/2}\right)^2.$$

Therefore, if we choose T_0 so that the following inequalities should be satisfied:

$$\begin{gathered}4\beta_0(T_0)\left(|\sigma_0|_{T_0}^{l,l/2}\right)^2+2\beta_1(T_0)\left(|\sigma_0|_{T_0}^{l,l/2}\right)\le 1,\\ 4\beta_1(T_0)(a_0+1)\left(|\sigma_0|_{T_0}^{l,l/2}\right)^2+2\beta_2(T_0)(2a_0+\varphi_1+1)\left(|\sigma_0|_{T_0}^{l,l/2}\right)\le 1,\\ 2\left(\beta_1(T_0)a_1\varphi_0^{-1}(2a_0+\varphi_1+1)+\chi_0\varphi_0^{-1}T_0(a_0+1)\right)|\sigma_0|_{T_0}^{l,l/2}+\\ +4\beta_2(T_0)a_1\varphi_0^{-1}(a_0+1)\left(|\sigma_0|_{T_0}^{l,l/2}\right)^2\le 1,\end{gathered} \tag{3.6}$$

then the operator L for $T<T_0$ has the first property of a contraction mapping operator, that is, $L\sigma\in S(T)$.

Now consider the second property of the contraction mapping for the operator L. Let $\sigma^{(1)}=\left(\sigma_1^{(1)},\sigma_2^{(1)},\sigma_3^{(1)}\right)\in S(T)$, $\sigma^{(2)}=\left(\sigma_1^{(2)},\sigma_2^{(2)},\sigma_3^{(2)}\right)\in S(T)$, then, following evaluation

$$\left|\sigma_2^{(1)}\sigma_1^{(1)}-\sigma_2^{(2)}\sigma_1^{(2)}\right|_T^{l,l/2}=\left|\left(\sigma_2^{(1)}-\sigma_2^{(2)}\right)\sigma_1^{(1)}+\sigma_2^{(2)}\left(\sigma_1^{(1)}-\sigma_1^{(2)}\right)\right|_T^{l,l/2}\le$$

$$\leq 2\left|\sigma^{(1)}-\sigma^{(2)}\right|_T^{l,l/2}\max\left(\left|\sigma_1^{(1)}\right|_T^{l,l/2},\left|\sigma_2^{(2)}\right|_T^{l,l/2}\right)\leq 4\left|\sigma_0\right|_T^{l,l/2}\left|\sigma^{(1)}-\sigma^{(2)}\right|_T^{l,l/2},$$

we have

$$\left|\left((L\sigma)^{(1)}-(L\sigma)^{(2)}\right)_1\right|_T^{l,l/2}=\left|\int_0^{\theta(t)}\frac{d\tau}{a\left(\widehat{\tau}\right)}\int_{-\infty}^{\infty}d\xi\int_{-\infty}^{\infty}d\eta\right.$$

$$\left.\int_0^{\widehat{\tau}}\left[\sigma_3^{(1)}(\xi,0,\alpha)\sigma_1^{(1)}\left(\xi,\eta,\widehat{\tau}-\alpha\right)-\sigma_3^{(2)}(\xi,0,\alpha)\sigma_1^{(2)}\left(\xi,\eta,\widehat{\tau}-\alpha\right)\right]Gd\alpha\right|_T^{l,l/2}+$$

$$+\left|\int_0^{\theta(t)}\frac{d\tau}{a\left(\theta^{-1}\left(\tau\right)\right)}\int_{-\infty}^{\infty}\int_{-\infty}^{\infty}\int_0^{\widehat{\tau}}\frac{\lambda\left(\widehat{\tau}-\beta\right)^{\alpha-1}}{\Gamma\left(\alpha\right)}\left[\sigma_1^{(1)}\left(0,\eta,\beta\right)-\sigma_1^{(2)}\left(0,\eta,\beta\right)\right]\times\right.$$

$$\left.\times Gd\beta d\xi d\eta\right|_T^{l,l/2}\leq\left[8\beta_0\left(T\right)\left|\sigma_0\right|_{T_0}^{l,l/2}+4\beta_1\left(T\right)\right]\left|\sigma^{(1)}-\sigma^{(2)}\right|_T^{l,l/2},$$

Similarly, estimating the second and third components of $L\sigma$ we have:

$$\left|\left((L\sigma)^{(1)}-(L\sigma)^{(2)}\right)_2\right|_T^{l,l/2}\leq$$

$$\leq\left[2\beta_1\left(T\right)\left(2a_0+\varphi_1+1\right)+8\beta_2\left(T\right)\left(a_0+1\right)\left|\sigma_0\right|_{T_0}^{l,l/2}\right]\left|\sigma^{(1)}-\sigma^{(2)}\right|_{T_0}^{l,l/2},$$

$$\left|\left((L\sigma)^{(1)}-(L\sigma)^{(2)}\right)_3\right|_T^{l,l/2}\leq$$

$$\leq\left[2\left(\beta_1\left(T\right)a_1\varphi_0^{-1}\left(2a_0+\varphi_1+1\right)+\chi_0\varphi_0^{-1}T_0\left(a_0+1\right)\right)\right]\left|\sigma^{(1)}-\sigma^{(2)}\right|_{T_0}^{l,l/2}+$$

$$+\left[8\beta_2\left(T\right)a_1\varphi_0^{-1}\left(a_0+1\right)\left(\left|\sigma_0\right|_{T_0}^{l,l/2}\right)\right]\left|\sigma^{(1)}-\sigma^{(2)}\right|_{T_0}^{l,l/2}.$$

Therefore $\left|\left(L\sigma^{(1)}-L\sigma^{(2)}\right)\right|_T^{l,l/2}<\rho\left|\sigma^{(1)}-\sigma^{(2)}\right|_T^{l,l/2}$, where $\rho\leq 1$, if satisfied

$$\left[8\beta_0\left(T\right)\left|\sigma_0\right|_{T_0}^{l,l/2}+2\beta_1\left(T\right)\right]\leq\rho<1,$$

$$\left[2\beta_1\left(T\right)\left(2a_0+\varphi_1+1\right)+8\beta_2\left(T\right)\left(a_0+1\right)\left|\sigma_0\right|_{T_0}^{l,l/2}\right]\leq\rho<1,$$

$$\left[2\left(\beta_1\left(T\right)a_1\varphi_0^{-1}\left(2a_0+\varphi_1+1\right)+f_0\varphi_0^{-1}T_0\left(a_0+1\right)\right)\right]+ \tag{3.7}$$

$$+\left[8\beta_2\left(T\right)a_1\varphi_0^{-1}\left(a_0+1\right)\left(\left|\sigma_0\right|_{T_0}^{l,l/2}\right)\right]\leq\rho<1,$$

then the operator L is also contraction on $S\left(T\right)$.

From the satisfaction of inequality (3.7), it directly follows that (3.6) also holds. Furthermore, since T_0 satisfies $T<T_0$ and condition (3.7), the properties of a contraction mapping operator are fully satisfied. Consequently, by the Banach fixed-point theorem, equation (3.4) has a unique solution. Using the method of successive approximations for the system of equations (3.1)–(3.3), obtain a unique solution within the function space $H^{l+2,(l+2)/2}\left(\bar{R}_T^2\right)$.

Thus, the existence and uniqueness of the solution to the system of integral equations (3.1)–(3.3) imply the existence and uniqueness of the solution to the equivalent problems (1.1)–(1.3).

References

[1] Matthew R. Hall. *Materials for energy efficiency and thermal comfort in bu ildings*. A volume in Woodhead Publishing Series in Energy, 2010, Woodhead Publishing Limited.

[2] Jiang Zh., Zhao J., Xie H. *Microforming Technology*, Chapter 3 - Scaling Laws, Editor(s): Zhengyi Jiang, Jingwei Zhao, Haibo Xie, Academic Press, 2017, P. 53–71.

[3] Samko S.G., Kilbas A.A., Marichev O.I. *Fractional Integrals and Derivatives. Theory and Applications*. Gordon and Breach, New York, 1993.

[4] Pskhu A.V. *Partial differential equations of fractional order*. Nauka, Moscow, 2005, [in Russian].

[5] Gorenflo R. Mainardi F. Fractional calculus: integral and differential equations of fractional order. *arXiv*, 2008.

[6] Abbas S. Benchohra M.N., Guerekata G.M. *Advanced fractional differential and integral equations*. Nova Science Publishers, New York, 2014.

[7] Varieschi G.U. Applications of fractional calculus to newtonian mechanics. *Journal of Applied Mathematics and Physics*, 2018, **6**(6).

[8] Mulla M. Fractional calculus, fractional differential equations and applications. *Open Access Library Journal*, 2020, **7**, P. 1–9.

[9] Schneider W.R. Fractional diffusion, in Dynamics and Stochastic Processes Theory and Applications, Springer Berlin Heidelberg, Berlin, Germany, 1990, vol 355.

[10] Henry B.I., Langlands T.A.M. and Straka P. *An Introduction to Fractional Diffusion*. World Scientific, 2009.

[11] Juraev D.A., Noeiaghdam S. Modern problems of mathematical physics and their applications. *Axioms*, 2022, **11**(2), P. 45.

[12] Yang X.J., Baleanu D. and Srivastava H.M. Local Fractional Integral Transforms and Their Applications, 2016, Elsevier Ltd.

[13] Al-Refai M., Abdeljawad T. Analysis of the fractional diffusion equations with fractional derivative of non-singular kernel. *Adv Differ Equ*, 2017, **315**(2017).

[14] Li X.Y., Xiao A.G. Space-fractional diffusion equation with variable coefficients: well-posedness and Fourier pseudo spectral approximation. *J. Sci Comput*, 2021, 87, 28.

[15] Zheng X., Ervin V.J., Wang H. Numerical approximations for the variable coefficient fractional diffusion equations with non-smooth data. *Computational Methods in Applied Mathematics*, 2020, **20**(3), P. 573–589.
[16] Anley E.F., Zheng Z. Finite difference approximation method for a space fractional convection-diffusion equation with variable coefficients. *Symmetry*, 2020, **12**(3), P. 485.
[17] Alikhanov A.A. A new difference scheme for the time fractional diffusion equation. *J. Comput. Phys.*, 2015, **280**, P. 424–438.
[18] Alsidrani F., Kilicman A., Senu N. Approximate solutions for time-fractional fornberg-whitham equation with variable coefficients. *Fractal Fract.*, 2023, **7**, 260.
[19] Durdiev D.K., Nuriddinov J.Z. On investigation of the inverse problem for a parabolic integro-differential equation with a variable coefficient of thermal conductivity. *Vestn. Udmurtsk. Univ. Mat. Mekh. Komp. Nauki*, 2020, **30**(4), P. 572–584.
[20] Farhood A.K., Mohammed O.H. and Taha B.A. Solving fractional time-delay diffusion equation with variable-order derivative based on shifted Legendre-Laguerre operational matrices. *Arab. J. Math.*, 2023.
[21] Nuno F.M. Martins, Pedro Mota. An adapted plane waves method for heat conduction problems. *Applied Mathematics and Computation*, 2022, **415**, P. 126689.
[22] Xue-Yang and Xiao, Ai-Guo, Space-fractional diffusion equation with variable coefficients: well-poshness and fourier pseudo spectral approximation, 2021, *Journal of Scientific Computing*, **87** (1), 28.
[23] Agarwal P., Hubert F., Dermenjian Y., Baltaeva U., Hasanov B. The Cauchy problem for the heat equation with a fractional load. *Discrete and Continuous Dynamical Systems – S*.
[24] Nakhushev A.M. *Loaded equations and their applications*. Nauka, Moscow, 2012.
[25] Krall A.M. The development of general differential and general differential-boundary systems. *Rocky Mountain Journal of Mathematics*, 1975, **5**(4), P. 493–542.
[26] Islomov B., Baltaeva U. Boundary value problems for a third-order loaded parabolic-hyperbolic equation with variable coefficients. *E. Journal of Differential Equations*, 2015, **2015**(221), P. 1–10.
[27] Assanova A.T. and Kadirbayeva Zh.M. Periodic problem for an impulsive system of the loaded hyperbolic equations. *E. Journal of Differential Equations*, 2018, **2018**(72), P. 1–8.
[28] Jenaliyev M.T. and Ramazanov M.I. *Loaded equations as perturbations of differential equations*, Gylym, Almaty, 2010 (in Russian).
[29] Yuldashev T.K, Islomov B.I. and Alikulov E.K. Boundary-value problems for loaded third-order parabolic-hyperbolic equations in infinite three-dimensional domains. *Lobachevskii J. Math.*, 2020, **41**(5), P. 926–944.
[30] Amangaliyeva M.M., Jenaliyev M.T. Ramazanov M.I. and Iskakov S.A. On a boundary value problem for the heat equation and a singular integral equationi associated with it. *Appl. Math. Comput.*, 2021, **399**, P. 126009.
[31] Kosmakova M., Akhmanova D. Izhanova K. BVP with a load in the form of a fractional integral. *International Journal of Mathematics and Mathematical Sciences*, 2024, P. 12.
[32] Baltaeva U., Babajanova Y., Agarwal P. Ozdemir N. Solvability of a mixed problem with the integral gluing condition for a loaded equation with the Riemann-Liouville fractional operator. *J. Comput. Appl. Math.*, 2023, **425**, P. 115066.
[33] Khubiev K.U. Analogue of Tricomi problem for characteristically loaded hy perbolic-parabolic equation with variable coefficients. *Ufa Math.J.*, 2017, **9**(2), P. 92–101.
[34] Baltaeva U.I. Boundary-value problem for a loaded mixed-type equation with a characteristic line of type change. *J Math Sci.*, 2023, **272**, P. 202–214.
[35] Durdiev D.K., Jumaev J.J. One-dimensional inverse problems of deter mining the kernel of the integro-differential heat equation in a bounded domain. *Non autonomous Dynamical Systems*, 2023, **10**(1), P. 20220163.
[36] Denisov A.M., Efimov A.A. The inverse problem for an integro-differential equation and its solution method. *Comput Math Model*, 2019, **30**, P. 403–412.
[37] Durdiev D.K, Zhumaev Z.Zh. Memory kernel reconstruction problems in the integro-differential equation of rigid heat conductor. *Math Meth Appl Sci.*, 2020, P. 1–15.
[38] Ladyzhenskaya O.A. *The Boundary Value Problems of Mathematical Physics*. Applied Mathematical Sciences, vol. 49. Springer, Berlin, 1985.
[39] Agarwal R.P., Baltaeva U. Hubert F., Khasanov B. Existence and uniqueness of the solution to initial and inverse problems for integro-differential heat equations with fractional load. *Electron. J. Differential Equations*, 2024, **2024**(64), P. 1-19.

Submitted 7 October 2025; revised 5 November 2025; accepted 6 November 2025

Information about the authors:

Umida Baltaeva – Department of Applied Mathematics and mathematical physics, Urgench State University, Urgench-220100, Uzbekistan; ORCID 0000-0001-9687-5220; umida_baltayeva@mail.ru

Praveen Agarwal – Department of Mathematics, Anand International College of Engineering, Jaipur-303012, India; ORCID 0000-0001-7556-8942; goyal.praveen2011@gmail.com

Bobur Khasanov – Department of Exact sciences, Khorezm Mamun Academy, Khiva, Uzbekistan; ORCID 0009-0003-5079-7150; xasanovboburjon.1993@gmail.com

Hamrobek Hayitbayev – Department of Accounting and General Professional Sciences, Mamun university, Khiva, Uzbekistan; ORCID 0009-0002-0491-5104; hamrohayitboyev073@gmail.com

Florence Hubert – Aix-Marseille Universite, CNRS, I2M, Marseille, France; ORCID 0000-0002-7553-9698; florence.hubert@univ-amu.fr

Conflict of interest: the authors declare no conflict of interest.

NANOSYSTEMS:
PHYSICS, CHEMISTRY, MATHEMATICS

Lakaev S.N., et al. *Nanosystems: Phys. Chem. Math.*, 2025, **16** (6), 737–748.
http://nanojournal.ifmo.ru
DOI 10.17586/2220-8054-2025-16-6-737-748

Original article

On the existence of the maximum number of isolated eigenvalues for a lattice Schrödinger operator

Saidakhmat N. Lakaev[1,a], Dildora A. Latipova[2,b], Mukhayyo O. Akhmadova[1,c]

[1]Samarkand State University, 140104, Samarkand, Uzbekistan
[2]Samarkand State Pedagogical Institute, 140104, Samarkand, Uzbekistan

[a]s.lakaev@mail.ru, [b]ms.dlatipova@mail.ru, [c]mukhayyo.akhmadova@mail.ru

Corresponding author: S. N. Lakaev, s.lakaev@mail.ru

ABSTRACT This paper presents a detailed spectral analysis of the discrete Schrödinger operator $H_{\gamma\lambda\mu}(K)$, which describes a system of two identical bosons on a two-dimensional lattice, $\mathbb{Z}^2$. The operator's family is parameterized by the quasi-momentum $K \in \mathbb{T}^2$ and real interaction strengths: γ for on-site, λ for nearest-neighbor, and μ for next-nearest-neighbor interactions. A key finding of our study is that, under specific conditions on the interaction parameters, the operator $H_{\gamma\lambda\mu}(K)$ consistently possesses a total of seven eigenvalues that lie either below the bottom or above the top of its essential spectrum, over all $K \in \mathbb{T}^2$.

KEYWORDS two-particle system, discrete Schrödinger operator, essential spectrum, bound states, Fredholm determinant

ACKNOWLEDGEMENTS The authors gratefully acknowledge the support received from the Foundation for Basic Research of the Republic of Uzbekistan (Grant no. FL–9524115052).

FOR CITATION Lakaev S.N., Latipova D.A., Akhmadova M.O. On the existence of the maximum number of isolated eigenvalues for a lattice Schrödinger operator. *Nanosystems: Phys. Chem. Math.*, 2025, **16** (6), 737–748.

1. Introduction

Lattice models constitute a fundamental framework within mathematical physics [1]. Among these, the lattice N-body Hamiltonian provides a simplified representation of the corresponding Bose- or Fermi-Hubbard models, specifically focusing on the dynamics of a limited number, N, of identical particles. These Hamiltonians remain an area of significant research interest, particularly for low particle counts where $1 \leq N \leq 3$, and the associated lattice N-particle problems have been subject to intense scrutiny over the past decades [2–9].

A compelling motivation for studying these lattice Hamiltonians is their intrinsic connection to continuous systems; they naturally serve as a discrete approximation to the continuous N-body Schrödinger operators [10]. Formulating the N-body problem on a lattice offers the distinct advantage of placing the analysis within the established theory of bounded operators. It should be noted that the one-particle ($N = 1$) problem on a 1D lattice is largely addressed by the general perturbation theory applicable to infinite Jacobi matrices (see, for instance, [11, 12]). The bound state energies of one- and two-particle systems, situated in two adjacent 3D layers linked by a window, were numerically reported in [13].

Lattice N-body Schrödinger operators are essential models for systems describing N particles traveling through periodic structures, exemplified by ultracold atoms injected into optical crystals [14, 15]. The study of ultracold few-atom systems in optical lattices has been particularly active in recent decades due to the experimental control over critical parameters, including temperature, particle masses, and interaction potentials (see, e.g., [15–19] and references therein).

It is well known that the celebrated Efimov effect [20] was initially attributed to three-particle systems in the three-dimensional continuous space $\mathbb{R}^3$. A rigorous mathematical confirmation of the Efimov effect was established in [21–24]. Subsequently, it has been demonstrated that the Efimov effect also occurs in three-particle systems defined on lattices [25,26]. Consequently, lattice three-body problems represent another significant domain for Efimov physics research [27].

Furthermore, lattice Hamiltonians find application in fusion physics. For example, [28] utilized a 1D lattice-based Hamiltonian to successfully illustrate that arranging molecules of a specific type into a lattice structure can substantially enhance their nuclear fusion probability.

In contrast to the continuous setting, the center-of-mass motion of an N-particle system ($N \geq 2$) on a lattice cannot be fully decoupled. However, the inherent lattice translational invariance of the Hamiltonian permits the use of the Floquet-Bloch decomposition. Specifically, for the (quasi)momentum-space representation of the N-particle lattice Hamiltonian

H, one can employ the following von Neumann direct integral decomposition (see, e.g., [2, Sec. 4]):

$$\mathrm{H} \simeq \int\limits_{K\in\mathbb{T}^d}^{\oplus} H(K)\,dK, \tag{1}$$

where $\mathbb{T}^d$ denotes the d-dimensional torus, K is the center-of-mass quasimomentum, and $H(K)$ is referred to as the fiber Hamiltonian. For each $K \in \mathbb{T}^d$, the entry $H(K)$ operates within the functional Hilbert space associated with $\mathbb{T}^{(N-1)d}$. The decomposition (1) effectively reduces the problem of studying the total Hamiltonian H to analyzing the simpler fiber operators $H(K)$. We observe that the dependence of $H(K)$ on the quasimomentum $K \in \mathbb{T}^d$, although non-trivial, is confined solely to the kinetic energy part and does not involve the (pairwise) inter-particle interaction terms (see, e.g., [2, 29]).

In this paper, we focus on the fiber Hamiltonians $H_{\gamma\lambda\mu}(K)$ on a 2D lattice, acting in the Hilbert space $L^{2,\mathrm{e}}(\mathbb{T}^2)$. The Hamiltonian is defined as

$$H_{\gamma\lambda\mu}(K) := H_0(K) + V_{\gamma\lambda\mu},$$

where $H_0(K)$ is the kinetic-energy operator and $V_{\gamma\lambda\mu}$ represents the interaction potential. The real parameters γ, λ, and μ describe interactions between particles at the same site, nearest-neighbor sites, and next-nearest-neighbor sites, respectively.

The discrete eigenvalue problem for $H_{\gamma\lambda\mu}(K)$ is complex, but the operator has at most seven eigenvalues outside the essential spectrum, which is given by

$$\sigma_{\mathrm{ess}}(H_{\gamma\lambda\mu}(K)) = \left[2\sum_{i=1}^{2}\left(1-\cos\tfrac{K_i}{2}\right), 2\sum_{i=1}^{2}\left(1+\cos\tfrac{K_i}{2}\right)\right].$$

The space $L^{2,\mathrm{e}}(\mathbb{T}^2)$ can be decomposed into a direct orthogonal sum of invariant subspaces:

$$L^{2,\mathrm{e}}(\mathbb{T}^2) = L^{2,\mathrm{oos}}(\mathbb{T}^2) \oplus L^{2,\mathrm{ees}}(\mathbb{T}^2) \oplus L^{2,\mathrm{ea}}(\mathbb{T}^2).$$

This decomposition simplifies the spectral analysis of the full operator to studying its restrictions on these subspaces, as shown by the equality

$$\sigma(H_{\gamma\lambda\mu}(0)) = \sigma(H_{\mu}^{\mathrm{oos}}(0)) \cup \sigma(H_{\gamma\lambda\mu}^{\mathrm{ees}}(0)) \cup \sigma(H_{\lambda\mu}^{\mathrm{ea}}(0)). \tag{2}$$

Our primary objective is to find simple conditions on the parameters for which $H_{\gamma\lambda\mu}(0)$ possesses precisely seven isolated eigenvalues. We then apply this result to determine the exact count of discrete eigenvalues for $H_{\gamma\lambda\mu}(K)$ over all $K \in \mathbb{T}^2$. This work extends previous results on the ground state of $H_{\gamma\lambda\mu}(K)$ by providing a more comprehensive analysis of all eigenvalues.

In [30–35], similar spectral results were obtained for two-boson systems on $d = 1, 2$ lattices with on-site and nearest-neighbor interactions governed by real parameters γ and λ.

For a system of two identical bosons on a d-dimensional lattice $\mathbb{Z}^d$ ($d = 1, 2$) with on-site (γ), nearest-neighbor (λ), and next-nearest-neighbor (μ) interactions, the discrete spectrum of the associated two-particle Schrödinger operator $H_{\gamma\lambda\mu}(k)$, $k \in \mathbb{T}^d$ has been studied and determined the number and position of isolated eigenvalues for all values of the interaction parameters in [36–39].

The paper is structured as follows. In Section 2, we introduce the two-particle lattice Schrödinger operator. Section 3 presents our main results, and the proofs are provided in Section 4.

2. Discrete Schrödinger operators on lattices

2.1. Schrödinger operator for particle pairs with fixed quasimomentum and its essential spectrum

Let $\mathbb{T}^2$ be the 2D torus, and let $L^{2,e}(\mathbb{T}^2)$ denote the subspace of $L^2(\mathbb{T}^2)$ consisting of even functions.

For $\gamma, \lambda, \mu \in \mathbb{R}$ and $K \in \mathbb{T}^3$, the bounded and self-adjoint Schrödinger operator $H_{\gamma\lambda\mu}(K)$ describing interacting particle pairs ([2, 35])is defined as:

$$H_{\gamma\lambda\mu}(K) := H_0(K) + V_{\gamma\lambda\mu}.$$

The unperturbed operator, $H_0(K)$, acts as

$$(H_0(K)f)(p) = \mathcal{E}_K(p)f(p),$$

where the dispersion function $\mathcal{E}_K(\cdot)$ is given by:

$$\mathcal{E}_K(p) = 2\sum_{i=1}^{2}\left(1-\cos\tfrac{K_i}{2}\,\cos p_i\right), \quad p = (p_1, p_2) \in \mathbb{T}^2.$$

The perturbation operator $V_{\gamma\lambda\mu}$ is given by

$$\begin{aligned} V_{\gamma\lambda\mu}f(p) = \frac{\gamma}{4\pi^2}\int_{\mathbb{T}^2} f(q)\,dq + \frac{\lambda}{4\pi^2}\sum_{i=1}^{2}\cos p_i \int_{\mathbb{T}^2}\cos q_i f(q)\,dq \\ + \frac{\mu}{4\pi^2}\sum_{i=1}^{2}\cos 2p_i \int_{\mathbb{T}^2}\cos 2q_i f(q)\,dq \\ + \frac{\mu}{2\pi^2}\cos p_1\cos p_2\int_{\mathbb{T}^2}\cos q_1\cos q_2 f(q)\,dq \\ + \frac{\mu}{2\pi^2}\sin p_1\sin p_2\int_{\mathbb{T}^2}\sin q_1\sin q_2 f(q)\,dq. \end{aligned} \tag{3}$$

Since the interaction potential $V_{\gamma\lambda\mu}$ has a rank of at most seven, it constitutes a compact perturbation to the kinetic-energy operator $H_0(K)$. According to Weyl's theorem, such a perturbation does not alter the essential spectrum of the operator. Consequently, the essential spectrum of the full operator $H_{\gamma\lambda\mu}(K)$ is identical to the spectrum of the unperturbed operator $H_0(K)$:

$$\sigma_{\rm ess}(H_{\gamma\lambda\mu}(K)) = \sigma(H_0(K)).$$

This essential spectrum corresponds to the range of the kinetic energy function $\mathcal{E}_K(p)$ over the domain $p \in \mathbb{T}^2$, forming the interval $[\mathcal{E}_{\min}(K), \mathcal{E}_{\max}(K)]$. The minimum and maximum energy values are given by:

$$\mathcal{E}_{\min}(K) = 2\sum_{i=1}^{2}\left(1-\cos\frac{K_i}{2}\right) \geq \mathcal{E}_{\min}(0) = 0,$$

$$\mathcal{E}_{\max}(K) = 2\sum_{i=1}^{2}\left(1+\cos\frac{K_i}{2}\right) \leq \mathcal{E}_{\max}(0) = 8.$$

3. Main results

The following results summarize and extend the findings presented in [2, Theorems 1 and 2] and [35, Theorem 3.1].

Theorem 1. *If, for some $\gamma, \lambda, \mu \in \mathbb{R}$, the operator $H_{\gamma\lambda\mu}(K)$ has at least n eigenvalues in $(-\infty, \mathcal{E}_{\min}(K))$ (or, respectively, $(\mathcal{E}_{\max}(K), +\infty)$), then for any quasi-momentum $K \in \mathbb{T}^2$, the operator $H_{\gamma\lambda\mu}(K)$ has at least n eigenvalues in $(-\infty, 0)$ (or, respectively, $(8, +\infty)$).*

This implies that the number of discrete eigenvalues observed at the zero quasi-momentum ($K = 0$) establishes the sharpest possible lower bound (across all $K \in \mathbb{T}^2$) for the total count of discrete eigenvalues of $H_{\gamma\lambda\mu}(K)$.

Our next findings detail the precise count of these discrete eigenvalues.

Theorem 2. *Let $K \in \mathbb{T}^2$ and $\gamma, \lambda, \mu \in \mathbb{R}$. The following assertions hold:*

- *(i) If the coupling constants are sufficiently negative ($\gamma < -12$, $\lambda < -12$, and $\mu < -12$), then $H_{\gamma\lambda\mu}(K)$ features exactly seven discrete eigenvalues positioned in $(-\infty, \mathcal{E}_{\min}(K))$.*
- *(ii) If the coupling constants are sufficiently positive ($\gamma > 12, \lambda > 12$, and $\mu > 12$), then $H_{\gamma\lambda\mu}(K)$ features exactly seven discrete eigenvalues positioned in $(\mathcal{E}_{\max}(K), +\infty)$.*

4. Proof of the main results

4.1. Invariant subspaces of the Schrödinger operators $H_{\gamma\lambda\mu}(0)$

Lemma 1. *The Hilbert space $L^{2,\rm e}(\mathbb{T}^2)$ admits the orthogonal decomposition*

$$L^{2,e}(\mathbb{T}^2) = L^{2,\rm ees}(\mathbb{T}^2) \oplus L^{2,\rm oos}(\mathbb{T}^2) \oplus L^{2,ea}(\mathbb{T}^2), \tag{4}$$

where

$$\begin{aligned} L^{2,\rm ees}(\mathbb{T}^2) &= \{\phi \in L^{2,\rm e}(\mathbb{T}^2) : \phi(t_1,t_2) = \phi(t_2,t_1) = \phi(-t_1,t_2),\ \forall t_1,t_2 \in \mathbb{T}\} \\ L^{2,\rm oos}(\mathbb{T}^2) &= \{\phi \in L^{2,\rm e}(\mathbb{T}^2) : \phi(t_1,t_2) = \phi(t_2,t_1) = -\phi(-t_1,t_2),\ \forall t_1,t_2 \in \mathbb{T}\} \\ L^{2,\rm ea}(\mathbb{T}^2) &= \{\phi \in L^{2,\rm e}(\mathbb{T}^2) : \phi(t_1,t_2) = -\phi(t_2,t_1),\ \forall t_1,t_2 \in \mathbb{T}\}. \end{aligned} \tag{5}$$

Moreover, the action of the operator $H_{\gamma\lambda\mu}(0)$ preserves the invariance of every subspace defined in (4) .

Proof. The definition (5) correspond to the standard decomposition of $L^{2,\rm e}(\mathbb{T}^2)$ into irreducible subspaces under the action of the permutation group $\mathfrak{S}_2$. Orthogonality of these subspaces follows from symmetry considerations, and their direct sum exhausts $L^{2,\rm e}(\mathbb{T}^2)$. Since $H_{\gamma\lambda\mu}(0)$ commutes with permutations of variables, each subspace is invariant under its action. □

From Lemma 1 (ii) it immediately follows Eq. (2). Therefore, it suffices to independently analyze the eigenvalue spectra of the restrictions of $H_{\gamma\lambda\mu}(0)$ to the reducing subspaces $L^{2,\mathrm{ees}}(\mathbb{T}^2)$, $L^{2,\mathrm{ea}}(\mathbb{T}^2)$, and $L^{2,\mathrm{oos}}(\mathbb{T}^2)$ to obtain the complete discrete spectrum of the total operator $H_{\gamma\lambda\mu}(0)$ on $L^{2,\mathrm{e}}(\mathbb{T}^2)$.

4.2. The Lippmann–Schwinger operator

Let $\{\alpha_1^{ees},\alpha_2^{ees},\alpha_3^{ees},\alpha_4^{ees}\}\subset L^{2,ees}(\mathbb{T}^2)$, resp. $\{\alpha_1^{ea},\alpha_2^{ea}\}\subset L^{2,ea}(\mathbb{T}^2)$ and $\{\alpha_1^{oos}\}\subset L^{2,oos}(\mathbb{T}^2)$ be a orthonormal system of vectors, with

$$\begin{aligned}&\alpha_1^{ees}(p)=\tfrac{1}{2\pi},\ \alpha_2^{ees}(p)=\tfrac{\cos p_1+\cos p_2}{2\pi},\ \alpha_3^{ees}(p)=\tfrac{\cos 2p_1+\cos 2p_2}{2\pi},\ \alpha_4^{ees}(p)=\tfrac{\cos p_1\cos p_2}{\pi},\\&\alpha_1^{oos}(p)=\tfrac{\sin p_1\sin p_2}{\pi},\ \alpha_1^{ea}(p)=\tfrac{\cos p_1-\cos p_2}{2\pi},\ \alpha_2^{ea}(p)=\tfrac{\cos 2p_1-\cos 2p_2}{2\pi}.\end{aligned}\tag{6}$$

We note that, the perturbation operator $V_{\gamma\lambda\mu}$ can be expressed in terms of the orthonormal systems (6):

$$\begin{aligned}(V_{\gamma\lambda\mu}f)(p)=\gamma(f,\alpha_1^{ees})\alpha_1^{ees}+\frac{\lambda}{2}(f,\alpha_2^{ees})\alpha_2^{ees}+\frac{\mu}{2}(f,\alpha_3^{ees})\alpha_3^{ees}+\frac{\mu}{2}(f,\alpha_4^{ees})\alpha_4^{ees}\\+\frac{\lambda}{2}(f,\alpha_1^{ea})\alpha_1^{ea}+\frac{\mu}{2}(f,\alpha_2^{ea})\alpha_2^{ea}+\frac{\mu}{2}(f,\alpha_1^{oos})\alpha_1^{oos}.\end{aligned}\tag{7}$$

By applying the representation (7) of $V_{\gamma\lambda\mu}$ one concludes that

$$\begin{aligned}H^{\mathrm{ees}}_{\gamma\lambda\mu}(0):=H_{\gamma\lambda\mu}(0)\big|_{L^{2,\mathrm{ees}}(\mathbb{T}^2)}=H_0(0)+V^{\mathrm{ees}}_{\gamma\lambda\mu},\\H^{\mathrm{oos}}_{\mu}(0):=H_{\gamma\lambda\mu}(0)\big|_{L^{2,\mathrm{oos}}(\mathbb{T}^2)}=H_0(0)+V^{\mathrm{oos}}_{\mu},\\H^{\mathrm{ea}}_{\lambda\mu}(0):=H_{\gamma\lambda\mu}(0)\big|_{L^{2,\mathrm{ea}}(\mathbb{T}^2)}=H_0(0)+V^{\mathrm{ea}}_{\lambda\mu},\end{aligned}$$

where

$$\begin{aligned}V^{ees}_{\gamma\lambda\mu}f:=V_{\gamma\lambda\mu}(0)\big|_{L^{2,\mathrm{ees}}(\mathbb{T}^2)}f=\ &\gamma(f,\alpha_1^{ees})\alpha_1^{ees}+\frac{\lambda}{2}(f,\alpha_2^{ees})\alpha_2^{ees}\\&+\frac{\mu}{2}(f,\alpha_3^{ees})\alpha_3^{ees}+\frac{\mu}{2}(f,\alpha_4^{ees})\alpha_4^{ees},\\V^{oos}_{\mu}f:=H_{\gamma\lambda\mu}(0)\big|_{L^{2,\mathrm{oos}}(\mathbb{T}^2)}f=\ &\frac{\mu}{2}(f,\alpha_1^{oos})\alpha_1^{oos},\\V^{ea}_{\lambda\mu}f:=V_{\gamma\lambda\mu}(0)\big|_{L^{2,\mathrm{ea}}(\mathbb{T}^2)}f=\ &\frac{\lambda}{2}(f,\alpha_1^{ea})\alpha_1^{ea}+\frac{\mu}{2}(f,\alpha_2^{ea})\alpha_2^{ea},\end{aligned}\tag{8}$$

where $(\cdot,\cdot)$ is the inner product in $L^{2,e}(\mathbb{T}^2)$.

The Lippmann-Schwinger operators corresponding to $H^{\mathrm{ees}}_{\gamma\lambda\mu}$, H^{oos}_{μ}, and $H^{\mathrm{ea}}_{\lambda\mu}$ are defined for any $z\in\mathbb{C}\setminus[0,\,8]$ (and shown here in their transpose form, following, e.g., [41]) as:

$$\begin{aligned}B^{\mathrm{ees}}_{\gamma\lambda\mu}(0,z)=-V^{\mathrm{ees}}_{\gamma\lambda\mu}R_0(0,z),\\B^{\mathrm{oos}}_{\mu}(0,z)=-V^{\mathrm{oos}}_{\mu}R_0(0,z),\\B^{\mathrm{ea}}_{\lambda\mu}(0,z)=-V^{\mathrm{ea}}_{\lambda\mu}R_0(0,z),\end{aligned}$$

Here, $R_0(0,z):=[H_0(0)-zI]^{-1}$ represents the resolvent of the free operator $H_0(0)$, defined for $z\in\mathbb{C}\setminus[0,\,8]$.

Lemma 2. *Let $\gamma,\lambda,\mu\in\mathbb{R}$. The number $z\in\mathbb{C}\setminus[0,\,8]$ is an eigenvalue of the operator $H^{ees}_{\gamma\lambda\mu}(0)$ (resp. $H^{oos}_{\mu}(0)$ and $H^{ea}_{\lambda\mu}(0)$), if and only if the number 1 is an eigenvalue for $B^{ees}_{\gamma\lambda\mu}(0,z)$ (resp. $B^{oos}_{\mu}(0,z)$ and $B^{ea}_{\lambda\mu}(0,z)$).*

The lemma's proof is standard, following well-known techniques (e.g., [40]), and is therefore omitted.

Due to the representation provided in (8), the eigenvalue equation

$$B^{\mathrm{ees}}_{\gamma\lambda\mu}(0,z)\varphi=\varphi,\quad \varphi\in L^{2,\mathrm{ees}}(\mathbb{T}^2)$$

can be transformed into the following algebraic linear system involving the component coefficients $x_i:=(\varphi,\alpha_i^{ees}),\quad i=1,2,3,4:$

$$\begin{cases}[1+2\gamma a_{11}(z)]x_1+\lambda a_{12}(z)x_2+\mu a_{13}(z)x_3+\mu a_{14}(z)x_4=0,\\2\gamma a_{12}(z)x_1+[1+\lambda a_{22}(z)]x_2+\mu a_{23}(z)x_3+\mu a_{24}(z)x_4=0,\\2\gamma a_{13}(z)x_1+\lambda a_{23}(z)x_2+[1+\mu a_{33}(z)]x_3+\mu a_{34}(z)x_4=0,\\2\gamma a_{14}(z)x_1+\lambda a_{24}(z)x_2+\mu a_{34}(z)x_3+[1+\mu a_{44}(z)]x_4=0,\end{cases}$$

Analogously, the Lippmann-Schwinger equation $B^{ea}_{\lambda\mu}(0,z)\varphi=\varphi,\ \varphi\in L^{2,ea}(\mathbb{T}^2)$ respectively $B^{oos}_{\mu}(0,z)\varphi=\varphi,\ \varphi\in L^{2,oos}(\mathbb{T}^2)$ is equivalent to

$$\begin{cases}[1+\lambda b_{11}(z)]y_1+\mu b_{12}(z)y_2=0,\\\lambda b_{12}(z)y_1+[1+\mu b_{22}(z)]y_2=0\end{cases},\quad y_i:=(\varphi,\alpha_i^{ea}),\ i=1,2$$

respectively

$$(1+\mu c(z))(\varphi,\alpha^{oos})=0,$$

where

$$\begin{aligned}
a_{ij}(z) :=& \frac{1}{2}\int_{\mathbb{T}^2}\frac{\alpha_i^{\mathrm{ees}}(p)\alpha_j^{\mathrm{ees}}(p)\dot{\mathrm{p}}}{\mathcal{E}_0(p)-z},\ i,j=1,2,3,4,\\
b_{ij}(z) :=& \frac{1}{2}\int_{\mathbb{T}^2}\frac{\alpha_i^{\mathrm{ea}}(p)\alpha_j^{\mathrm{ea}}(p)\dot{\mathrm{p}}}{\mathcal{E}_0(p)-z},\ i,j=1,2,\\
c(z) :=& \frac{1}{2}\int_{\mathbb{T}^2}\frac{\left(\alpha^{\mathrm{oos}}(p)\right)^2\dot{\mathrm{p}}}{\mathcal{E}_0(p)-z}.
\end{aligned}\tag{9}$$

Let us introduce the determinant functions $\Delta^{\mathrm{ees}}_{\gamma\lambda\mu}(z)$, $\Delta^{\mathrm{ea}}_{\lambda\mu}(z)$, $\Delta^{\mathrm{oos}}_{\mu}(z)$ for $z\in\mathbb{R}\setminus[0,\,8]$:

$$\begin{aligned}
\Delta^{\mathrm{ees}}_{\gamma\lambda\mu}(z) &:= \det[I-B^{\mathrm{ees}}_{\gamma\lambda\mu}(0,z)]=\begin{vmatrix} 1+2\gamma a_{11}(z) & \lambda a_{12}(z) & \mu a_{13}(z) & \mu a_{14}(z)\\ 2\gamma a_{12}(z) & 1+\lambda a_{22}(z) & \mu a_{23}(z) & \mu a_{24}(z)\\ 2\gamma a_{13}(z) & \lambda a_{23}(z) & 1+\mu a_{33}(z) & \mu a_{34}(z)\\ 2\gamma a_{14}(z) & \lambda a_{24}(z) & \mu a_{34}(z) & 1+\mu a_{44}(z)\end{vmatrix},\\
\Delta^{\mathrm{ea}}_{\lambda\mu}(z) &:= \det[I-B^{\mathrm{ea}}_{\lambda\mu}(0,z)]=\begin{vmatrix} 1+\lambda b_{11}(z) & \mu b_{12}(z)\\ \lambda b_{12}(z) & 1+\mu b_{22}(z)\end{vmatrix},\\
\Delta^{\mathrm{oos}}_{\mu}(z) &:= \det[I-B^{\mathrm{oos}}_{\mu}(0,z)]=1+\mu c(z).
\end{aligned}\tag{10}$$

We state the well-known lemma connecting the eigenvalues of the restricted operators $H^{\mathrm{ees}}_{\gamma\lambda\mu}(0)$, $H^{\mathrm{oos}}_{\mu}(0)$, and $H^{\mathrm{ea}}_{\lambda\mu}(0)$ to the zeros of the corresponding determinants.

Lemma 3. *A number $z\in\mathbb{R}\setminus[0,8]$ is an eigenvalue of $H^{\mathrm{ees}}_{\gamma\lambda\mu}(0)$ (resp. $H^{\mathrm{oos}}_{\mu}(0)$, $H^{\mathrm{ea}}_{\lambda\mu}(0)$) with multiplicity $m\geq 1$ if and only if z is a zero of $\Delta^{\mathrm{ees}}_{\gamma\lambda\mu}(z)$ (resp. $\Delta^{\mathrm{oos}}_{\mu}(z)$, $\Delta^{\mathrm{ea}}_{\lambda\mu}(z)$) with multiplicity m. Moreover, the maximum number of zeros in $\mathbb{R}\setminus[0,8]$ for $\Delta^{\mathrm{ees}}_{\gamma\lambda\mu}(z)$, $\Delta^{\mathrm{oos}}_{\mu}(z)$, and $\Delta^{\mathrm{ea}}_{\lambda\mu}(z)$ is four, one, and two, respectively.*

The proof for this lemma follows from routine methods (see [35]), so we proceed without including it.

Theorem 3. *For $z\in\mathbb{R}\setminus[0,8]$, the functions $a_{ij}(z)$ $(i,j=1,2,3,4)$ are real-valued. They are strictly increasing on both $(-\infty,0)$ (where they are positive) and $(8,+\infty)$ (where they are negative). Additionally, they satisfy the following asymptotic relations:*

$$\begin{aligned}
a_{ij}(z) &= \begin{cases} -a^{(0)}_{ij}\dfrac{\ln(\frac{-z}{32})}{8\pi}+a^{(1)}_{ij}+o(1),\ \textit{as}\quad z\nearrow 0,\\ a^{(0)}_{ij}\dfrac{\ln(\frac{z-8}{32})}{8\pi}-a^{(1)}_{ij}+o(1),\ \textit{as}\quad z\searrow 8,\end{cases}\\
b_{ij}(z) &= \begin{cases} -b^{(1)}_{ij}+o(1),\ \textit{as}\quad z\nearrow 0,\\ b^{(1)}_{ij}+o(1),\ \textit{as}\quad z\searrow 8,\end{cases}\\
c(z) &= \begin{cases} \dfrac{3\pi-8}{3\pi}+o(1),\ \textit{as}\quad z\nearrow 0,\\ -\dfrac{3\pi-8}{3\pi}+o(1),\ \textit{as}\quad z\searrow 8.\end{cases}
\end{aligned}$$

The functions $\ln(-z)$ and $\ln(z-8)$ are understood to be the specific branches chosen to be real when $z<0$ and $z>8$, respectively. The coefficient matrices $a^{(0)}=(a^{(0)}_{ij})$, $a^{(1)}=(a^{(1)}_{ij})$ $(i,j=1,2,3,4,\ )$ and $b^{(1)}=(b^{(1)}_{ij})$ $(i,j=1,2)$, are given by

$$a^{(0)}=\begin{pmatrix}1&2&2&2\\2&4&4&4\\2&4&4&4\\2&4&4&4\end{pmatrix},\quad a^{(1)}=\begin{pmatrix}0&\frac{-1}{4}&\frac{-\pi+2}{\pi}&-\frac{1}{\pi}\\ \frac{-1}{\pi}&-\frac{1}{2}&\frac{-2\pi+4}{\pi}&-\frac{2}{\pi}\\ \frac{-\pi+2}{\pi}&\frac{-\pi+2}{\pi}&\frac{-10\pi+\frac{88}{3}}{\pi}&\frac{2\pi-\frac{26}{3}}{\pi}\\ -\frac{1}{\pi}&-\frac{2}{\pi}&\frac{2\pi-\frac{26}{3}}{\pi}&\frac{-\pi+\frac{4}{3}}{2\pi}\end{pmatrix},$$

$$b^{(1)}=\begin{pmatrix}\frac{4-\pi}{\pi}&\frac{32-9\pi}{\pi}\\ \frac{32-9\pi}{\pi}&\frac{2(32-9\pi)}{\pi}\end{pmatrix}.$$

Proof. Theorem 3 can be proven by adapting the proof of Proposition 4.4 in [35]. □

Lemma 4. *The asymptotic behavior of the real-valued functions $\Delta^{\rm ees}_{\gamma\lambda\mu}(z)$, $\Delta^{\rm ea}_{\lambda\mu}(z)$ and $\Delta^{\rm oos}_{\mu}(z)$ is given by:*

(i) $\lim\limits_{z\to\pm\infty}\Delta^{\rm ees}_{\gamma\lambda\mu}(z)=\lim\limits_{z\to\pm\infty}\Delta^{\rm ea}_{\lambda\mu}(z)=\lim\limits_{z\to\pm\infty}\Delta^{\rm oos}_{\mu}(z)=1$;

(ii)

$$\Delta^{\rm ees}_{\gamma\lambda\mu}(z)=\begin{cases}-\frac{1}{4\pi}Q^{-}(\gamma,\lambda,\mu)ln(-z)+D^{-}_{\gamma\lambda\mu}+o(1),\ as\quad z\nearrow 0,\\ -\frac{1}{4\pi}Q^{+}(\gamma,\lambda,\mu)ln(-z)+D^{+}_{\gamma\lambda\mu}+o(1),\ as\quad z\searrow 8,\end{cases}$$

$$\Delta^{\rm ea}_{\lambda\mu}(z)=\begin{cases}1+\frac{(4-\pi)}{\pi}\lambda+\frac{2(32-9\pi)}{\pi}\mu+\frac{(32-9\pi)}{4\pi}\lambda\mu+o(1),\ as\quad z\nearrow 0,\\ 1-\frac{(4-\pi)}{\pi}\lambda-\frac{2(32-9\pi)}{\pi}\mu+\frac{(32-9\pi)}{4\pi}\lambda\mu+o(1),\ as\quad z\searrow 8,\end{cases}$$

$$\Delta^{\rm oos}_{\mu}(z)=\begin{cases}1+\dfrac{3\pi-8}{3\pi}\mu+o(1),\ as\quad z\nearrow 0,\\ 1-\dfrac{3\pi-8}{3\pi}\mu+o(1),\ as\quad z\searrow 8,\end{cases}$$

where

$$Q^{\pm}(\gamma,\lambda,\mu)=(\gamma\mp 4)\Big(Q^{\pm}_0(\mu)\lambda\mp Q^{\pm}_1(\mu)\Big)-8Q^{\pm}_0(\mu)$$

and

$$Q^{\pm}_0(\mu):=\tfrac{16-5\pi}{4\pi}\mu^2\mp\tfrac{4(10-3\pi)}{3\pi}\mu+\tfrac{1}{2},$$
$$Q^{\pm}_1(\mu):=\tfrac{2(16-5\pi)}{\pi}\mu^2\mp\tfrac{80-21\pi}{3\pi}\mu+1.$$

Proof of Lemma 4. The proof is facilitated by the Lebesgue dominated convergence theorem (for the first part) and Proposition 3 (for the final part). □

The following lemmas provide the exact count of the zeros for the determinant functions $\Delta^{\rm oos}_{\mu}(z)$, $\Delta^{\rm ea}_{\lambda\mu}(z)$, and $\Delta^{\rm ees}_{\gamma\lambda\mu}(z)$ outside the essential spectrum $[0,8]$.

Lemma 5. *The following assertions hold for the determinant $\Delta^{\rm oos}_{\mu}(z)$:*

(i) If $\mu<-12$, the function $\Delta^{\rm oos}_{\mu}(z)$ has precisely one zero in $(-\infty,0)$.
(ii) If $\mu>12$, the function $\Delta^{\rm oos}_{\mu}(z)$ has precisely one zero in $(8,+\infty)$.

Proof. The result follows directly from [35, Theorem 4.5]. □

Lemma 6. *The following assertions hold for the determinant $\Delta^{\rm ea}_{\lambda\mu}(z)$:*

(i) If $\lambda<-12$ and $\mu<-12$, the function $\Delta^{\rm ea}_{\lambda\mu}(z)$ has precisely two zeros in $(-\infty,0)$.
(ii) If $\lambda>12$ and $\mu>12$, the function $\Delta^{\rm ea}_{\lambda\mu}(z)$ has precisely two zeros in $(8,+\infty)$.

Proof. The proof for Lemma 6 follows established techniques, such as those demonstrated in [37, Theorem 1] and [39, Theorem 2]. □

Lemma 7. *The following assertions hold for the determinant $\Delta^{\rm ees}_{\gamma\lambda\mu}(z)$:*

(i) If $\gamma<-12$, $\lambda<-12$, and $\mu<-12$, the determinant function $\Delta^{\rm ees}_{\gamma\lambda\mu}(z)$ has exactly four zeros in $(-\infty,0)$.
(ii) If $\gamma>12$, $\lambda>12$, and $\mu>12$, the determinant function $\Delta^{\rm ees}_{\gamma\lambda\mu}(z)$ has exactly four zeros in $(8,+\infty)$.

Proof of Lemma 7. i) Let $\gamma<-12,\lambda<-12$ and $\mu<-12$. Assuming μ is negative ($\mu<0$), the function

$$\delta(z):=1+\mu a_{44}(z)$$

—where $a_{44}(z)$ is defined in (9)—is continuous and strictly decreasing for $z\in(-\infty,0)$. From the explicit definition of a_{44} in (9) it follows that

$$\lim_{z\to-\infty}\delta(z)=1.$$

At the same time, the asymptotic expression for $a_{44}(z)$ in Proposition 3 implies that

$$\lim_{z\nearrow 0}\delta(z)=-\infty.$$

Therefore the function $\delta(z)=1+\mu a_{44}(z)$ has exactly one zero z_{11} within the half-axis $(-\infty,0)$ and, thus,

$$\begin{aligned}&1+\mu a_{44}(z)>0\quad\text{if}\quad z<z_{11},\\ &1+\mu a_{44}(z)<0\quad\text{if}\quad z_{11}<z<0.\end{aligned}\tag{11}$$

Notice that the equality $1+\mu a_{44}(z_{11})=0$ implies that

$$\begin{aligned}\Delta^{\rm ees}_{00\mu}(z_{11}) &= (1+\mu a_{33}(z_{11}))\,(1+\mu a_{44}(z_{11})) - \mu^2(a_{34}(z_{11}))^2\\ &= -\mu^2(a_{34}(z_{11}))^2 < 0.\end{aligned} \tag{12}$$

The inequality $\mu<-12$ implies that

$$Q^-(0,0,\mu)=\tfrac{6(16-5\pi)}{\pi}\mu\Big[\mu+\tfrac{2\pi}{3(16-5\pi)}\Big]>0.$$

The inequality $Q^-(0,0,\mu)>0$ and Lemma 4 yield that

$$\lim_{z\to-\infty}\Delta^{\rm ees}_{00\mu}(z)=1,\quad \lim_{z\nearrow 0}\Delta^{\rm ees}_{00\mu}(z)=+\infty. \tag{13}$$

The relations (12) and (13) imply that

$$\lim_{z\to-\infty}\Delta^{\rm ees}_{00\mu}(z)=1,\quad \Delta^{\rm ees}_{00\mu}(z_{11})<0\quad\text{and}\quad \lim_{z\nearrow 0}\Delta^{\rm ees}_{00\mu}(z)=+\infty.$$

This means that there exist real numbers z_{21} and z_{22} such that

$$z_{21}<z_{11}<z_{22}<0 \tag{14}$$

and

$$\Delta^{\rm ees}_{00\mu}(z_{21})=\Delta^{\rm ees}_{00\mu}(z_{22})=0. \tag{15}$$

The equality (8) implies that the operator $V^{\rm ees}_{00\mu}$ has rank at most two. Therefore, by the minimax principle, the operator $H^{\rm ees}_{00\mu}$ has at most two eigenvalues below zero. By the first statement in Lemma 3, the function $\Delta^{\rm ees}_{00\mu}(z)$ has at most two zeros in $\mathbb{R}\setminus[0,8]$. Hence, and by (15) the function $\Delta^{\rm ees}_{00\mu}(z)$ has precisely two zeros (z_{21} and z_{22}), lying in $(-\infty,0)$. Therefore

$$\begin{aligned}&\Delta^{\rm ees}_{00\mu}(z)>0 \quad\text{if}\quad z<z_{21};\\ &\Delta^{\rm ees}_{00\mu}(z)<0 \quad\text{if}\quad z_{21}<z<z_{22};\\ &\Delta^{\rm ees}_{00\mu}(z)>0 \quad\text{if}\quad z_{22}<z<0.\end{aligned} \tag{16}$$

The equalities $\Delta^{\rm ees}_{00\mu}(z_{21})=\Delta^{\rm ees}_{00\mu}(z_{22})=0$ yield the following relations

$$\begin{aligned}(1+\mu a_{33}(z_{21}))(1+\mu a_{44}(z_{21})) &= \mu^2(a_{34}(z_{21}))^2>0,\\ (1+\mu a_{33}(z_{22}))(1+\mu a_{44}(z_{22})) &= \mu^2(a_{34}(z_{22}))^2>0.\end{aligned} \tag{17}$$

Hence $1+\mu a_{33}(z_{21})$ and $1+\mu a_{44}(z_{21})$ (resp. $1+\mu a_{33}(z_{22})$ and $1+\mu a_{44}(z_{22})$) have the same signs. Combining this with (11) and (14) yields

$$\begin{aligned}&1+\mu a_{33}(z_{21})>0 \quad\text{and}\quad 1+\mu a_{44}(z_{21})>0;\\ &1+\mu a_{33}(z_{22})<0 \quad\text{and}\quad 1+\mu a_{44}(z_{22})<0.\end{aligned} \tag{18}$$

For the roots z_{21} and z_{22} of

$$\Delta^{\rm ees}_{00\mu}(z)=(1+\mu a_{33}(z))\,(1+\mu a_{44}(z))-\mu^2a_{34}^2(z)=0$$

we then have

$$\sqrt{1+\mu a_{33}(z_{21})}\sqrt{1+\mu a_{44}(z_{21})}=-\mu a_{34}(z_{21}) \tag{19}$$

and

$$\sqrt{-[1+\mu a_{33}(z_{22})]}\sqrt{-[1+\mu a_{44}(z_{22})]}=-\mu a_{34}(z_{22}). \tag{20}$$

Using the explicit representation (10) for $\Delta^{\rm ees}_{0\lambda\mu}(z)$ and (19) one arrives with the following equality:

$$\Delta^{\rm ees}_{0\lambda\mu}(z_{21})=-\lambda\mu\big[\sqrt{1+\mu a_{44}(z_{21})}a_{23}(z_{21})+\sqrt{1+\mu a_{33}(z_{21})}a_{24}(z_{21})\big]^2. \tag{21}$$

Clearly, (21) implies that

$$\Delta^{\rm ees}_{0\lambda\mu}(z_{21})<0. \tag{22}$$

Analogously, the identity (20) gives that

$$\Delta^{\rm ees}_{0\lambda\mu}(z_{22})=\lambda\mu\big[\sqrt{-[1+\mu a_{44}(z_{22})]}a_{23}(z_{22})+\sqrt{-[1+2\mu a_{33}(z_{22})]}a_{24}(z_{22})\big]^2>0. \tag{23}$$

Meanwhile, for $\lambda<-12$ va $\mu<-12$ we have

$$Q_0^-(\mu)=\tfrac{16-5\pi}{4\pi}\mu^2+\tfrac{4(10-3\pi)}{3\pi}\mu+\tfrac{1}{2}>0$$

and

$$4\Big(Q_1^-(\mu)-12Q_0^-(\mu)\Big)=\tfrac{(16-5\pi)}{\pi}\mu^2+\tfrac{400-123\pi}{3\pi}\mu+5>0.$$

The above inequalities obeys that

$$Q^-(0,\lambda,\mu)=4Q_0^-(\mu)(\lambda+10)-4\Big(Q_1^-(\mu)-12Q_0^-(\mu)\Big)<0.$$

Lemma 4 and inequality $Q^-(0,\lambda,\mu)<0$ give

$$\lim_{z\to-\infty}\Delta^{\rm ees}_{0\lambda\mu}(z)=1 \quad \text{and} \quad \lim_{z\nearrow 0}\Delta^{\rm ees}_{0\lambda\mu}(z)=-\infty. \tag{24}$$

Taking into account (22), (23) and (24) this implies there existence of real numbers z_{31}, z_{32} and z_{33} such that

$$z_{31}<z_{21}<z_{32}<z_{22}<z_{33}<0 \tag{25}$$

and

$$\Delta^{\rm ees}_{0\lambda\mu}(z_{31})=\Delta^{\rm ees}_{0\lambda\mu}(z_{32})=\Delta^{\rm ees}_{0\lambda\mu}(z_{33})=0. \tag{26}$$

The equality (8) implies that the operator $V^{\rm ees}_{0\lambda\mu}$ has rank at most three. Therefore, again by the minimax principle [42, Theorem XIII.1], the operator $H^{\rm ees}_{0\lambda\mu}$ has at most three discrete eigenvalues. Then, Lemma 3 guarantees that the function $\Delta^{\rm ees}_{0\lambda\mu}(z)$ has at most three zeros in $\mathbb{R}\setminus[0,8]$. Given these bounds and established results, the function $\Delta^{\rm ees}_{0\lambda\mu}(z)$ is found to have precisely three zeros (z_{31}, z_{32}, and z_{33}), all of which lie in the interval $(-\infty,0)$.

Let

$$\begin{aligned}
A_{11}(z) &:= \det\begin{pmatrix} 1+\mu a_{33}(z) & \mu a_{34}(z) \\ \mu a_{34}(z) & 1+\mu a_{44}(z)\end{pmatrix},\\
A_{22}(z) &:= \det\begin{pmatrix} 1+\lambda a_{22}(z) & \mu a_{24}(z) \\ \lambda a_{24}(z) & 1+\mu a_{44}(z)\end{pmatrix},\\
A_{33}(z) &:= \det\begin{pmatrix} 1+\lambda a_{22}(z) & \mu a_{23}(z) \\ \lambda a_{23}(z) & 1+\mu a_{33}(z)\end{pmatrix}.
\end{aligned} \tag{27}$$

and

$$\begin{aligned}
A_{12}(z) &:= \det\begin{pmatrix} \lambda a_{23}(z) & \mu a_{34}(z) \\ \lambda a_{24}(z) & 1+\mu a_{44}(z)\end{pmatrix}, \qquad A_{21}(z) := \det\begin{pmatrix} \mu a_{23}(z) & \mu a_{24}(z) \\ \mu a_{34}(z) & 1+\mu a_{44}(z)\end{pmatrix},\\
A_{13}(z) &:= \det\begin{pmatrix} \lambda a_{23}(z) & 1+\mu a_{33}(z) \\ \lambda a_{24}(z) & \mu a_{34}(z)\end{pmatrix}, \qquad A_{31}(z) := \det\begin{pmatrix} \mu a_{23}(z) & \mu a_{24}(z) \\ 1+\mu a_{33}(z) & \mu c_{34}(z)\end{pmatrix},\\
A_{23}(z) &:= \det\begin{pmatrix} 1+\lambda a_{22}(z) & \mu a_{23}(z) \\ \lambda a_{24}(z) & \mu a_{34}(z)\end{pmatrix}, \qquad A_{32}(z) := \det\begin{pmatrix} 1+\lambda a_{22}(z) & \mu a_{24}(z) \\ \lambda a_{23}(z) & \mu a_{34}(z)\end{pmatrix}.
\end{aligned} \tag{28}$$

The definition (28) implies that

$$\mu A_{12}(z)=\lambda A_{21}(z), \quad \mu A_{13}(z)=\lambda A_{31}(z), \quad A_{23}(z)=A_{32}(z) \tag{29}$$

From the definitions (27) and (28) one derives that

$$\begin{aligned}
A_{11}(z)A_{33}(z)-A_{13}(z)A_{31}(z)&=\Delta^{\rm ees}_{0\lambda\mu}(z)\cdot[1+\mu a_{33}(z)],\\
A_{11}(z)A_{22}(z)-A_{12}(z)A_{21}(z)&=\Delta^{\rm ees}_{0\lambda\mu}(z)\cdot[1+\mu a_{44}(z)],\\
A_{22}(z)A_{33}(z)-A_{23}(z)A_{32}(z)&=\Delta^{\rm ees}_{0\lambda\mu}(z)\cdot[1+\lambda a_{22}(z)]
\end{aligned} \tag{30}$$

and

$$A_{11}(z)A_{22}(z)A_{33}(z)-A_{12}(z)A_{23}(z)A_{31}(z)=\Delta^{\rm ees}_{0\lambda\mu}(z)R_{\lambda\mu}(z), \tag{31}$$

where

$$R_{\lambda\mu}(z)=[1+\lambda a_{22}(z)]\cdot[1+\mu a_{33}(z)]\cdot[1+\mu a_{44}(z)]-\lambda\mu^2 a_{13}(z)a_{14}(z)a_{24}(z).$$

Then the equality $\Delta^{\rm ees}_{0\lambda\mu}(z_{31})=0$ and identity (30) resp. (31) imply that

$$\begin{aligned}
A_{11}(z_{31})A_{33}(z_{31})&=A_{13}(z_{31})A_{31}(z_{31}),\\
A_{11}(z_{31})A_{22}(z_{31})&=A_{12}(z_{31})A_{21}(z_{31}),\\
A_{22}(z_{31})A_{33}(z_{31})&=A_{23}(z_{31})A_{32}(z_{31})
\end{aligned} \tag{32}$$

resp.

$$A_{11}(z)A_{22}(z)A_{33}(z)=A_{12}(z)A_{23}(z)A_{31}(z). \tag{33}$$

It is worth noting that the functions $1+\mu a_{33}(z)$ and $1+\mu a_{44}(z)$ both exhibit strict decrease on the interval $(-\infty,0)$. Then the relations $z_{31}<z_{21}$ and (18) yield that

$$1+\mu a_{33}(z_{31})>1+\mu a_{33}(z_{21})>0 \quad \text{and} \quad 1+\mu a_{44}(z_{31})>1+\mu a_{44}(z_{21})>0. \tag{34}$$

The inequality (34), the negativity of λ,μ and positivity of the functions a_{23},a_{24},a_{34} (See Proposition 3) yield that

$$\begin{aligned} A_{12}(z_{31})&=\lambda a_{23}(z_{31})\big[1+\mu a_{44}(z_{31})\big]-\lambda\mu a_{24}(z_{31})a_{34}(z_{31})<0,\\ A_{13}(z_{31})&=\lambda\mu a_{23}(z_{31})a_{34}(z_{31})-\lambda a_{24}(z_{31})\big[1+\mu a_{33}(z_{31})\big]>0. \end{aligned} \tag{35}$$

The relations (29) and (32) yield that

$$\begin{aligned} A_{11}(z_{31})A_{33}(z_{31})&=A_{13}(z_{31})A_{31}(z_{31})=\frac{\lambda A_{31}^2(z_{31})}{\mu}>0,\\ A_{11}(z_{31})A_{22}(z_{31})&=A_{12}(z_{31})A_{21}(z_{31})=\frac{\mu A_{12}^2(z_{31})}{\lambda}>0. \end{aligned} \tag{36}$$

The inequalities (36) give that the numbers $A_{11}(z_{31}),\ A_{22}(z_{31}),\ A_{33}(z_{31})$ has the same signs. The relations (16) and (25) yield that

$$A_{11}(z_{31})=\Delta^{\rm ees}_{00\mu}(z_{31})>0,\ \text{therefore} \quad A_{22}(z_{31})>0, \quad A_{33}(z_{31})>0. \tag{37}$$

Then the relations (33), (35) and (37) obeys that

$$A_{23}(z_{31})<0.$$

The equality (29) and inequalities $A_{23}(z_{31})<0$, (35) imply that

$$\begin{aligned} &A_{12}(z_{31})<0, \quad A_{21}(z_{31})<0,\\ &A_{23}(z_{31})<0, \quad A_{32}(z_{31})<0,\\ &A_{31}(z_{31})>0, \quad A_{13}(z_{31})>0. \end{aligned} \tag{38}$$

The equalities (29) and (30) give that

$$\begin{aligned} A_{12}^2(z_{31})&=\tfrac{\lambda A_{11}(z_{31})A_{22}(z_{31})}{\mu}, \qquad A_{21}^2(z_{31})=\tfrac{\mu A_{11}(z_{31})A_{22}(z_{31})}{\lambda}\\ A_{23}^2(z_{31})&=A_{22}(z_{31})A_{33}(z_{31}), \quad A_{32}^2(z_{31})=A_{22}(z_{31})A_{33}(z_{31})\\ A_{31}^2(z_{31})&=\tfrac{\mu A_{11}(z_{31})A_{33}(z_{31})}{\lambda}, \qquad A_{13}^2(z_{31})=\tfrac{\lambda A_{11}(z_{31})A_{33}(z_{31})}{\mu}. \end{aligned} \tag{39}$$

Taking into account the signs of the numbers $A_{ij}(z_{31})$ in (38) and using the equality (39) we arrive that

$$\begin{aligned} A_{12}(z_{31})&=-\sqrt{\tfrac{\lambda A_{11}(z_{31})A_{22}(z_{31})}{\mu}}, \qquad A_{21}(z_{31})=-\sqrt{\tfrac{\mu A_{11}(z_{31})A_{22}(z_{31})}{\lambda}},\\ A_{23}(z_{31})&=-\sqrt{A_{22}(z_{31})A_{33}(z_{31})}, \quad A_{32}(z_{31})=-\sqrt{A_{22}(z_{31})A_{33}(z_{31})},\\ A_{31}(z_{31})&=\sqrt{\tfrac{\mu A_{11}(z_{31})A_{33}(z_{31})}{\lambda}}, \qquad A_{13}(z_{31})=\sqrt{\tfrac{\lambda A_{11}(z_{31})A_{33}(z_{31})}{\mu}}. \end{aligned} \tag{40}$$

We can represent the determinant $\Delta^{\rm ees}_{\gamma\lambda\mu}(z)$ in (10) as follow:

$$\begin{aligned} \Delta^{\rm ees}_{\gamma\lambda\mu}(z)=&[1+2\gamma a_{11}(z)]\Delta^{\rm ees}_{0\lambda\mu}(z)-2\gamma\lambda a_{12}^2(z)A_{11}(z)+2\gamma\mu a_{12}(z)a_{13}(z)A_{12}(z)-2\gamma\mu a_{12}(z)a_{14}(z)A_{13}(z)\\ &+2\gamma\lambda a_{13}(z)a_{12}(z)A_{21}(z)-2\gamma\mu a_{13}^2(z)A_{22}(z)+2\gamma\mu a_{13}(z)a_{14}(z)A_{23}(z)\\ &-2\gamma\lambda a_{14}(z)a_{12}(z)A_{31}(z)+2\gamma\mu a_{14}(z)a_{13}(z)A_{32}(z)-2\gamma\mu a_{14}^2(z)A_{33}(z). \end{aligned}$$

Using the above representation of the determinant $\Delta^{\rm ees}_{\gamma\lambda\mu}(z)$, equality $\Delta^{\rm ees}_{0\lambda\mu}(z_{31})=0$ and (40) we find that

$$\begin{aligned} \Delta^{\rm ees}_{\gamma\lambda\mu}(z_{31})=&-2\gamma\lambda a_{12}^2(z_{31})A_{11}(z_{31})-2\gamma\mu a_{13}^2(z_{31})A_{22}(z_{31})-2\gamma\mu a_{14}^2(z_{31})A_{33}(z_{31})\\ &-4\gamma\sqrt{\lambda\mu A_{11}(z_{31})A_{33}(z_{31})}a_{12}(z_{31})a_{14}(z_{31})\\ &-4\gamma\mu a_{13}(z_{31})a_{14}(z_{31})\sqrt{A_{22}(z_{31})A_{33}(z_{31})}\\ &-4\gamma\sqrt{\lambda\mu A_{11}(z_{31})A_{22}(z_{31})}a_{12}(z_{31})a_{13}(z_{31})\\ =&-2\Big(a_{12}(z_{31})\sqrt{\gamma\lambda A_{11}(z_{31})}+a_{13}(z_{31})\sqrt{\gamma\mu A_{22}(z_{31})}+a_{14}(z_{31})\sqrt{\gamma\mu A_{33}(z_{31})}\Big)^2. \end{aligned} \tag{41}$$

The equality (41) and positivity of the function a_{12},a_{13},a_{14} gives that

$$\Delta^{\rm ees}_{\gamma\lambda\mu}(z_{31})<0. \tag{42}$$

Combining the relation (16) with inequalities $z_{21}<z_{32}<z_{22}$ and $z_{22}<z_{33}$ we arrive that

$$A_{11}(z_{32})<0, \quad A_{22}(z_{32})<0, \quad A_{33}(z_{32})<0$$

and

$$A_{11}(z_{33}) > 0, \quad A_{22}(z_{33}) > 0, \quad A_{33}(z_{33}) > 0.$$

respectively.

So, in a similar way we show that

$$\begin{aligned}&\Delta^{\rm ees}_{\gamma\lambda\mu}(z_{32})\\ &= 2\Big(a_{12}(z_{32})\sqrt{-\gamma\lambda A_{11}(z_{32})} + a_{13}(z_{32})\sqrt{-\gamma\mu A_{22}(z_{32})} + a_{14}(z_{32})\sqrt{-\gamma\mu A_{33}(z_{32})}\Big)^2 > 0\end{aligned}$$

and

$$\begin{aligned}&\Delta^{\rm ees}_{\gamma\lambda\mu}(z_{33})\\ &= -2\Big(a_{12}(z_{33})\sqrt{\gamma\lambda A_{11}(z_{33})} + a_{13}(z_{33})\sqrt{\gamma\mu A_{22}(z_{33})} + a_{14}(z_{33})\sqrt{\gamma\mu A_{33}(z_{33})}\Big)^2 < 0.\end{aligned}$$

The assertions $\gamma < -12, \lambda < -12, \mu < -12$ yield that

$$\begin{aligned}Q^-(\gamma,\lambda,\mu) =&(\gamma+4)\Big(Q^-_0(\mu)\lambda + Q^-_1(\mu)\Big) - 8Q^-_0(\mu) =\\ &(\gamma+12)\Big(Q^-_0(\mu)\lambda + Q^-_1(\mu)\Big) - 8Q^-_0(\mu)(\lambda+12) + 8\Big(11Q^-_0(\mu) - Q^-_1(\mu)\Big) > 0.\end{aligned}$$

The relation $Q^-(\gamma,\lambda,\mu) > 0$ and Lemma 4 obeys that

$$\lim_{z\to-\infty}\Delta^{\rm ees}_{\gamma\lambda\mu}(z) = 1 \quad \text{and} \quad \lim_{z\nearrow 0}\Delta^{\rm ees}_{\gamma\lambda\mu}(z) = +\infty.$$

Therefore

$$\begin{aligned}&\lim_{z\to-\infty}\Delta^{\rm ees}_{\gamma\lambda\mu}(z) = 1, \quad \Delta^{\rm ees}_{\gamma\lambda\mu}(z_{31}) < 0, \quad \Delta^{\rm ees}_{\gamma\lambda\mu}(z_{32}) > 0,\\ &\Delta^{\rm ees}_{\gamma\lambda\mu}(z_{33}) < 0, \quad \lim_{z\nearrow 0}\Delta^{\rm ees}_{\gamma\lambda\mu}(z) = +\infty.\end{aligned}$$

The above relations yield there existence of four zeros $z_{41}, z_{42}, z_{43}, z_{44}$ of function $\Delta^{\rm ees}_{\gamma\lambda\mu}(z)$, satisfying the following inequalities

$$z_{41} < z_{31} < z_{42} < z_{32} < z_{43} < z_{33} < z_{44} < 0. \tag{43}$$

The proof for item (ii) follows an analogous procedure. □

Proof of Theorem 1. The result is proven analogously to Theorem 3.1 in [35]. □

Proof of Theorem 2. (i) Assume that $\gamma, \lambda, \mu < -12$.

We first determine the number of bound states for $K = 0$. Combining the results of Lemmas 5, 6, and 7 provides the number of negative zeros for the corresponding determinants:

- $\Delta^{\rm oos}_{\mu}(z)$ has exactly one zero (Lemma 5).
- $\Delta^{\rm ea}_{\lambda\mu}(z)$ has exactly two zeros (Lemma 6).
- $\Delta^{\rm ees}_{\gamma\lambda\mu}(z)$ has exactly four zeros (Lemma 7).

The decomposition (2) and Lemma 3 confirm that the total number of bound states for $H_{\gamma\lambda\mu}(0)$ with negative energy is $1 + 2 + 4 = 7$.

Next, Theorem 1 ensures that for any K, the operator $H_{\gamma\lambda\mu}(K)$ possesses at least seven eigenvalues in $(-\infty, 0)$. Since the rank of the perturbation operator $V_{\gamma\lambda\mu}(K)$ is at most seven, the min-max principle (see [42], page 85) dictates that $H_{\gamma\lambda\mu}(K)$ has at most seven isolated eigenvalues. Therefore, $H_{\gamma\lambda\mu}(K)$ must have *precisely seven* bound states in $(-\infty, 0)$.

(ii) Suppose that $\gamma, \lambda, \mu > 12$. The proof for Item (ii) is entirely analogous, relying on the corresponding assertions for the zeros of the determinants lying in $(8, +\infty)$. □

5. Conclusion

In conclusion, this article provides a comprehensive spectral analysis of the two-boson discrete Schrödinger operator $H_{\gamma\lambda\mu}(K)$ with short-range interactions, including on-site (γ), nearest-neighbor (λ), and next-nearest-neighbor (μ) couplings. The central outcome is the demonstration that the operator's discrete spectrum exhibits a remarkable structural stability under strong coupling conditions. Specifically, we have established sufficient conditions on the interaction parameters such that the operator possesses a total of seven bound states (eigenvalues), located either below $(-\infty, 0)$ or above $(8, +\infty)$ the essential spectrum, irrespective of the quasi-momentum $K \in \mathbb{T}^2$.

Our results significantly advance the understanding of spectral properties in discrete few-body systems, particularly concerning the influence of extended interaction ranges. Previous studies focusing on two-boson systems on a $2D$ lattice

with interactions limited to on-site and nearest-neighbor sites [35] showed a maximum of only three eigenvalues. Furthermore, the recent work in [39], which considered a more general interaction profile similar to ours, provided only sufficient conditions for the existence of at least two eigenvalues. In stark contrast, our work explicitly demonstrates that the full inclusion of next-nearest-neighbor coupling (μ) is responsible for stabilizing and increasing the maximum possible number of bound states to seven, providing easily verifiable criteria for this maximum count. This spectral richness highlights the critical role of the interaction range in enhancing localization phenomena.

Despite these advancements, several challenges remain. While we established sufficient and easily verifiable conditions for the existence of seven eigenvalues, we did not provide a definitive count or position of the discrete spectrum for all possible values of the interaction parameters. A complete mapping of the (γ, λ, μ)-space into regions corresponding to exactly $n \in \{0, 1, \ldots, 7\}$ eigenvalues is a complex, unsolved problem that requires further computational and analytical methods.

Another significant challenge lies in extending this analysis to the three-boson lattice system, where the increase in the number of degrees of freedom and the complexity of the fiber Hamiltonian make the spectral analysis significantly harder. Future research will focus on employing advanced numerical techniques to fully map the spectral regions and exploring potential applications of these multi-bound states in quantum information processing.

References

[1] Mattis D. The few-body problem on a lattice. *Rev. Mod. Phys.*, 1986, **58**, P. 361–379.

[2] Albeverio S., Lakaev S.N., Makarov K.A., Muminov Z.I. The Threshold Effects for the Two-particle Hamiltonians on Lattices. *Comm. Math. Phys.*, 2006, **262**, P. 91–115.

[3] Bach V., W. de Siqueira Pedra, Lakaev S.N. Bounds on the discrete spectrum of lattice Schrödinger operators. *J. Math. Phys.*, 2017, **59**(2), P. 022109.

[4] Faria Da Veiga P.A., Ioriatti L., O'Carroll M. Energy-momentum spectrum of some two-particle lattice Schrödinger Hamiltonians. *Phys. Rev. E*, 2002, **66**, P. 016130.

[5] Hiroshima F., Muminov Z., Kuljanov U. Threshold of discrete Schrödinger operators with delta-potentials on N-dimensional lattice. *Lin. Multilin. Algebra*, 2020, **70**, P. 919–954.

[6] Lakaev S.N., Özdemir E. The existence and location of eigenvalues of the one particle Hamiltonians on lattices. *Hacettepe J. Math. Stat.*, 2016, **45**, P. 1693–1703.

[7] Kurbanov Sh.Kh., Dustov S.T. Puiseux Series Expansion for Eigenvalue of the Generalized Friedrichs Model with the Perturbation of Rank One. *Lobachevskii Journal of Mathematics*, 2022, **4**, P. 1365–1372.

[8] Muminov M.I., Khurramov A.M., Bozorov I.N. On eigenvalues and virtual levels of a two-particle Hamiltonian on a d-dimensional lattice. *Nanosystems: Phys. Chem. Math.*, 2023, **14**(3), P. 295–303.

[9] Kurbanov S.K., Abduvayitov S.S. The Discrete Spectrum of the Generalized Friedrichs Model with a Rank-Two Perturbation. *Lobachevskii Journal of Mathematics*, 2025, **46**, P. 713–723.

[10] Faddeev L.D., Merkuriev S.P. *Quantum Scattering Theory for Several Particle Systems*. Doderecht: Kluwer Academic Publishers, 1993.

[11] Teschl G. *Jacobi Operators and Completely Integrable Nonlinear Lattices*, Providence, AMS, 2000.

[12] Yafaev D.R. A point interaction for the discrete Schrödinger operator and generalized Chebyshev polynomials. *J. Math. Phys.*, 2017, **58**, P. 063511.

[13] Bagmutov A.S., Popov I.Y. Window-coupled nanolayers: window shape influence on one-particle and two-particle eigenstates. *Nanosystems: Phys. Chem. Math.*, 2020, **11**(6), P. 636–641.

[14] Winkler K., Thalhammer G., Lang F., Grimm R., Denschlag J.H.,Daley A.J., Kantian A., Büchler H.P., Zoller P. Repulsively bound atom pairs in an optical lattice. *Nature*, 2006, **441**, P. 853–856.

[15] Bloch I. Ultracold quantum gases in optical lattices. *Nat. Phys.*, 2005, **1**, P. 23–30.

[16] Jaksch D., Bruder C., Cirac J., Gardiner C.W., Zoller P. Cold bosonic atoms in optical lattices. *Phys. Rev. Lett.*, 1998, **81**, P. 3108–3111.

[17] Jaksch D., Zoller P. The cold atom Hubbard toolbox. *Ann. Phys.*, 2005, **315**, P. 52–79.

[18] Lewenstein M., Sanpera A., Ahufinger V. *Ultracold Atoms in Optical Lattices: Simulating Quantum Many-body Systems*. Oxford University Press, Oxford, 2012.

[19] Hofstetter W., et al. High-temperature superfluidity of fermionic atoms in optical lattices. *Phys. Rev. Lett.*, 2002, **89**, P. 220407.

[20] Efimov V.N. Weakly bound states of three resonantly interacting particles. *Yad. Fiz.*, 1970, **12**, P. 1080 [*Sov. J. Nucl. Phys.*, 1970, **12**, P. 589].

[21] Ovchinnikov Y.N., Sigal I.N. Number of bound states of three-body systems and Efimov's effect. *Ann. Phys.*, 1979, **123**(2), P. 274–295.

[22] Sobolev A.V. The Efimov effect. Discrete spectrum asymptotics. *Commun. Math. Phys.*, 1993, **156**(1), P. 101–126.

[23] Tamura H. The Efimov effect of three-body Schrödinger operators. *J. Funct. Anal.*, 1991, **95**(2), P. 433–459.

[24] Yafaev D.R. On the theory of the discrete spectrum of the three-particle Schrödinger operator. *Mat. Sb.*, 1974, **94**(136), P. 567–593.

[25] Lakaev S.N. The Efimov's effect of the three identical quantum particle on a lattice. *Funct. Anal. Appl.*, 1993, **27**, P. 15–28.

[26] Dell'Antonio G., Muminov Z.I., Shermatova Y.M. On the number of eigenvalues of a model operator related to a system of three particles on lattices. *J. Phys. A*, 2011, **44**, P. 315302.

[27] Naidon P., Endo S. Efimov physics: A review. *Rep. Prog. Phys.*, 2017, **80**, P. 056001.

[28] Motovilov A.K., Sandhas W., Belyaev V.B. Perturbation of a lattice spectral band by a nearby resonance. *J. Math. Phys.*, 2001, **42**, P. 2490–2506.

[29] Reed M., Simon B. *Methods of Modern Mathematical Physics. III: Scattering Theory*. Academic Press, N.Y., (1978).

[30] Boltaev A.T., Almuratov F.M. The Existence and Asymptotics of Eigenvalues of Schrödinger Operator on Two Dimensional Lattices. *Lobachevskii Journal of Mathematics*, 2022, **43**, P. 3460–3470.

[31] Muminov Z.I., Aktamova V.U. The point spectrum of the three-particle Schrödinger operator for a system comprising two identical bosons and one fermion on Z. *Nanosystems: Phys. Chem. Math.*, 2024, **15**(4), P. 438–447.

[32] Alladustov S.U., Hiroshima F., Muminov Z.I. On the Spectrum of the Discrete Schrödinger Operator of a Rank-Two Perturbation on. *Lobachevskii Journal of Mathematics*, 2024, **45**, P. 4874–4887.

[33] Akhmadova M.O., Azizova M.A. Spectral analysis of two-particle Hamiltonians with short-range interactions. *Nanosystems: Phys. Chem. Math.*, 2025, **16**(5), P. 577–585.

[34] Abdullaev J.I., Khalkhuzhaev A.M., Usmonov L.S. Monotonicity of the eigenvalues of the two-particle Schrödinger operator on a lattice. *Nanosystems: Phys. Chem. Math.*, 2021, **12**(6), P. 657–663.
[35] Lakaev S.N., Kholmatov Sh.Y., Khamidov Sh.I. Bose-Hubbard model with on-site and nearest-neighbor interactions; exactly solvable case. *J. Phys. A: Math. Theor.*, 2021, **54**, P. 245201.
[36] Lakaev S.N., Akhmadova M.O. The Number and location of eigenvalues for the two-particle Schrödinger operators on lattices. *Complex Analysis and Operator Theory*, 2023, **17**.
[37] Akhmadova M.O., Alladustova I.U., Lakaev S.N. On the Number and Locations of Eigenvalues of the Discrete Schrödinger Operator on a Lattice. *Lobachevskii Journal of Mathematics*, 2023, **44**, P. 1091–1099.
[38] Lakaev S.N., Motovilov A.K., Abdukhakimov S.Kh. Two-fermion lattice Hamiltonian with first and second nearest-neighboring-site interactions. *J. Phys. A: Math. Theor.*, 2023, **56**, P. 315202.
[39] Lakaev S.N., Khamidov Sh.I., Akhmadova M.O. Number of bound states of the Hamiltonian of a lattice two-boson system with interactions up to the next neighbouring sites. *Lobachevskii Journal of Mathematics*, 2024, **45**(12), P. 6409–6420.
[40] Albeverio S., Gesztesy F., Høegh-Krohn R., Holden H. *Solvable Models in Quantum Mechanics*. Springer, Berlin, 1988.
[41] Lippmann B.A., Schwinger J. Variational principles for scattering processes. I. *Phys. Rev.*, 1950, **79**, P. 469.
[42] Reed M., Simon B. *Methods of Modern Mathematical Physics: Analysis of operators. Vol. IV*. Academic Press, NY, 1978.

Submitted 13 October 2025; revised 9 November 2025; accepted 13 November 2025

Information about the authors:

Saidakhmat N. Lakaev – Samarkand State University, 140104, Samarkand, Uzbekistan; ORCID 0000-0003-4951-9340; s.lakaev@mail.ru

Dildora A. Latipova – Samarkand State Pedagogical Institute, 140104, Samarkand, Uzbekistan; ORCID 0009-0005-0159-8002; ms.dlatipova@mail.ru

Mukhayyo O. Akhmadova – Samarkand State University, 140104, Samarkand, Uzbekistan; ORCID 0009-0000-9082-5986; mukhayyo.akhmadova@mail.ru

Conflict of interest: the authors declare no conflict of interest.

NANOSYSTEMS:
PHYSICS, CHEMISTRY, MATHEMATICS

Khasanov J., et al. *Nanosystems: Phys. Chem. Math.*, 2025, **16** (6), 749–754.
http://nanojournal.ifmo.ru
DOI 10.17586/2220-8054-2025-16-6-749-754

Original article

Mathematical modeling of industrial ammonia synthesis using nonlinear reaction-diffusion equations

Jamshid Khasanov[1,a], Sokhibjan Muminov[2,b], Sarvar Iskandarov[3,c]

[1]Urgench State Pedagogical Institute, 1A Gurlan str., Urgench 220100, Uzbekistan

[2]Mamun University, 2 Bolkhovuz Street, Khiva 220900, Uzbekistan

[3]Urgench State University named after Abu Rayhan Biruni, 14 Kh. Alimdjan str., Urgench 220100, Uzbekistan

[a]jamshid_2425@mail.ru, [b]sokhibjan.muminov@gmail.com, [c]iskandarovsb1993@gmail.com

Corresponding author: Sokhibjan Muminov, sokhibjan.muminov@gmail.com

PACS 35K57, 35K65, 35B40, 80A30

ABSTRACT This study proposes a mathematical model for ammonia synthesis based on nonlinear reaction-diffusion equations. The model integrates degenerate gas diffusion in the reactor with Haber-Bosch reaction kinetics to explore efficiency and environmental sustainability. A theoretical analysis is conducted to establish the existence and stability of global solutions for the underlying degenerate parabolic system. Numerical simulations were validated against industrial data from Navoiyazot facility in Uzbekistan, demonstrating 98.2% accuracy in concentration profiles and outperforming constant-diffusivity models by 12–15% in low-concentration regions.

KEYWORDS nonlinear reaction-diffusion, degenerate diffusion, ammonia synthesis, Haber-Bosch kinetics, global stability.

ACKNOWLEDGEMENTS The authors are grateful to Navoiyazot JSC for providing access to operational data from the industrial ammonia synthesis unit A-15.

FOR CITATION Khasanov J., Muminov S., Iskandarov S. Mathematical modeling of industrial ammonia synthesis using nonlinear reaction-diffusion equations. *Nanosystems: Phys. Chem. Math.*, 2025, **16** (6), 749–754.

1. Introduction

Ammonia production through the Haber-Bosch process supplies over 150 million tons annually, sustaining nearly half the world's population through nitrogen fertilizers [1]. Despite its century-long success, the process remains energy-intensive, operating at temperatures exceeding 400°C and pressures above 200 atm–conditions that account for approximately 1–2% of global energy consumption [2]. Reactor optimization through accurate mathematical modeling has thus become essential, particularly for capturing the complex transport and reaction phenomena within catalytic packed beds.

The kinetic foundations were established by Temkin and Pyzhev [1], whose power-law rate expression remains widely used. Nielsen [3] later synthesized decades of catalyst research, while recent work has focused on refined kinetic models across broader operating ranges [4] and entropy-minimization approaches to reactor design [5]. However, reactor performance depends equally on transport phenomena. Classical models typically assume constant diffusion coefficients, yet experimental evidence suggests that diffusion becomes strongly concentration-dependent under synthesis conditions, potentially vanishing at low concentrations—a phenomenon termed degenerate diffusion.

Rigorous mathematical treatment of degenerate parabolic equations has advanced considerably. Fragnelli and Mugnai [6] established Carleman estimates enabling controllability results even when diffusion vanishes, while Boutaayamou et al. [7] extended these to interior degeneracy with Neumann boundary conditions relevant to catalytic reactor walls. Erhardt [8] addressed weak solution existence for cross-diffusion systems, and Camasta and Fragnelli [9] provided comprehensive analysis of fourth-order degenerate equations. These frameworks enable treatment of strongly nonlinear diffusion with mathematical rigor.

Reaction-diffusion models with degenerate operators have found diverse applications beyond chemical engineering. In nanosystems, Topayev et al. [10] applied the Keller-Rubinow model to Liesegang ring formation, demonstrating how degenerate diffusion captures pattern formation in nanostructured materials. Maksimova et al. [11] employed similar frameworks for colloidal-chemical transformations during ammonia complex decomposition, while Borisov et al. [12] used coupled reaction-diffusion equations to model structural changes in La-Co catalysts for ammonia decomposition. These studies illustrate the broad applicability of degenerate diffusion models across scales–from nanoscale colloidal systems to macroscale catalytic processes. However, unlike these works which focus on decomposition or nanostructure formation, our study addresses the forward synthesis reaction in industrial-scale packed bed reactors, where transport limitations and reaction kinetics interact differently.

Despite parallel advances in kinetics and degenerate parabolic theory, their integration in ammonia synthesis modeling remains uncommon. Most simulations neglect concentration-dependent diffusion or employ regularization that may obscure physical behavior near degeneracy. Furthermore, while numerical methods for degenerate equations have matured [6, 7, 14], their performance under industrial conditions–stiff reaction terms, sharp gradients, extended domains–requires careful examination.

This work addresses these gaps by coupling degenerate diffusion with Temkin-Pyzhev kinetics for ammonia synthesis. We employ a concentration-dependent diffusion coefficient $D(u) = u^\sigma$ with $\sigma > 1$, reflecting transport suppression as reactant concentrations diminish in downstream catalyst regions. Neumann boundary conditions represent impermeable reactor walls [13]. The resulting degenerate parabolic equation is solved via implicit finite difference with a sweeping method handling both degeneracy and nonlinear reaction. Critically, we validate against operational data from Navoiyazot facility in Uzbekistan, demonstrating that degenerate diffusion yields more accurate predictions than constant-diffusivity models, particularly in low-concentration regions where transport limitations dominate. Our approach builds upon Aripov's foundations for nonlinear degenerate equations [14] and extends recent work on cross-diffusion systems [15–17] to industrial catalytic synthesis.

2. Mathematical formulation and governing equations

We consider the following nonlinear parabolic system defined in the domain $Q = \{(t, x) : t > 0,\ x \in \mathbb{R}\}$:

$$\begin{cases} \dfrac{\partial u}{\partial t} = D_1 \dfrac{\partial}{\partial x}\left(u^\sigma \dfrac{\partial u}{\partial x}\right) + a_1 u^{\alpha_1} v^{\beta_1}, & t > 0,\ x \in (0, L), \\ \dfrac{\partial v}{\partial t} = D_2 \dfrac{\partial}{\partial x}\left(v^\sigma \dfrac{\partial v}{\partial x}\right) - a_2 u^{\alpha_2} v^{\beta_2}, & t > 0,\ x \in (0, L). \end{cases} \tag{1}$$

The system is considered with the initial and boundary conditions:

$$\begin{cases} u(x, 0) = u_0(x), \quad v(x, 0) = v_0(x), & x \in (0, L), \\ \dfrac{\partial u}{\partial x}(0, t) = \dfrac{\partial u}{\partial x}(L, t) = 0, & t > 0, \\ \dfrac{\partial v}{\partial x}(0, t) = \dfrac{\partial v}{\partial x}(L, t) = 0, & t > 0. \end{cases} \tag{2}$$

Here, $u_0(x)$ and $v_0(x)$ are bounded and continuous functions. In the model, $u(t, x)$ and $v(t, x)$ denote the hydrogen and nitrogen concentrations [mol/m^3], depending on time t [s] and spatial coordinate x [m], within a reactor of length L [m]. The coefficients D_1 and D_2 represent the diffusion coefficients of hydrogen and nitrogen [m^2/s], while σ characterizes the degree of nonlinear diffusion. The parameters a_1 and a_2 are reaction rate constants, and α_1, β_1 indicate reaction orders. The coefficients α_2 and β_2 correspond to kinetic constants of the ammonia synthesis process. The initial distributions $u_0(x)$ and $v_0(x)$ describe the hydrogen and nitrogen concentrations at $t = 0$.

Therefore, the solution of problem (1)–(2) is considered in the framework of weak solutions.

Definition 1. A pair (u, v) is called a weak solution of the system (1)–(2) if, for all $\varphi, \psi \in C_c^\infty(Q_T)$, the following equalities hold:

$$\int_{Q_T} \left[u\varphi_t + D_1 u^\sigma u_x \varphi_x - a_1 u^{\alpha_1} v^{\beta_1} \varphi\right] dx\, dt = 0, \tag{3}$$

$$\int_{Q_T} \left[v\psi_t + D_2 v^\sigma v_x \psi_x + a_2 u^{\alpha_2} v^{\beta_2} \psi\right] dx\, dt = 0, \tag{4}$$

provided that $u^\sigma u_x,\ v^\sigma v_x \in L^2(Q_T)$ and $u, v \geq 0$.

3. Results and discussion

3.1. Construction of a system of self-similar equations

We seek the solution of problem (1)–(2) in the following self-similar form [14–18]:

$$\begin{cases} u(t, x) = \bar{u}(t)\, w_1(\tau(t), x), \\ v(t, x) = \bar{v}(t)\, w_2(\tau(t), x), \end{cases} \tag{5}$$

where the scaling functions $\bar{u}(t)$ and $\bar{v}(t)$ are assumed to have the power-law dependence

$$\bar{u}(t) = A_1 (T + t)^n, \qquad \bar{v}(t) = A_2 (T + t)^n,$$

and $\tau(t)$ is a time-scaling variable to be determined later.

Substituting the transformation (5) into system (1) and assuming that

$$\alpha_1 + \beta_1 = \alpha_2 + \beta_2,$$

we obtain the following system of equations:

$$\begin{cases} \dfrac{\partial w_1}{\partial \tau} = D_1 \dfrac{\partial}{\partial x}\left(w_1^{\sigma} \dfrac{\partial w_1}{\partial x} \right) + \dfrac{\psi_1}{\tau}\left(w_1^{\alpha_1} w_2^{\beta_1} - w_1 \right), \\ \left(\dfrac{A_1}{A_2} \right)^{\sigma} \dfrac{\partial w_2}{\partial \tau} = D_2 \dfrac{\partial}{\partial x}\left(w_2^{\sigma} \dfrac{\partial w_2}{\partial x} \right) - \dfrac{\psi_2}{\tau}\left(w_1^{\alpha_2} w_2^{\beta_2} + w_2 \right), \end{cases} \tag{6}$$

where the constants are defined as

$$\tau(t) = A_1^{\sigma} \frac{(T+t)^{n\sigma+1}}{n\sigma+1}, \quad T > 0, \quad n = \frac{1}{1-\alpha_1-\beta_1} = \frac{1}{1-\alpha_2-\beta_2},$$

$$\psi_1 = \frac{a_1 A_1^{\alpha_1 - 1} A_2^{\beta_1}}{n\sigma+1}, \qquad \psi_2 = \frac{a_2 A_1^{\alpha_2+\sigma} A_2^{\beta_2-\sigma-1}}{n\sigma+1}.$$

Assuming self-similarity of the form

$$w_1 = f_1(\xi), \qquad w_2 = f_2(\xi), \qquad \xi = \frac{|x|}{\tau^{1/2}}, \tag{7}$$

we obtain the following system of ordinary differential equations:

$$\begin{cases} \dfrac{d}{d\xi}\left(f_1^{\sigma} \dfrac{df_1}{d\xi} \right) + \dfrac{\xi}{2} \dfrac{df_1}{d\xi} + \psi_1 \left(f_1^{\alpha_1} f_2^{\beta_1} - f_1 \right) = 0, \\ \dfrac{d}{d\xi}\left(f_2^{\sigma} \dfrac{df_2}{d\xi} \right) + \dfrac{\xi}{2} \left(\dfrac{A_1}{A_2} \right)^{\sigma} \dfrac{df_2}{d\xi} - \psi_2 \left(f_1^{\alpha_2} f_2^{\beta_2} + f_2 \right) = 0. \end{cases} \tag{8}$$

The solution of the self-similar system (8) can be expressed in the following form:

$$f_1(\xi) = B_1 (b - \xi^2)^{1/\sigma}, \qquad f_2(\xi) = B_2 (b - \xi^2)^{1/\sigma}, \tag{9}$$

where $B_1 > 0$ and $B_2 > 0$ are constants determined from boundary and normalization conditions.

The main difficulty in numerically solving problems (1)–(2) arises from the **non-uniqueness of solutions**. The choice of initial approximations plays a crucial role in the convergence of the computational process. To obtain a stable solution, we employ the **sweeping (iteration) method**, implemented as follows.

3.2. Numerical scheme and visualization

An implicit finite-difference scheme with a sweeping iteration method was employed to solve the discretized system (1)–(2). The nonlinear diffusion terms were approximated using averaged concentrations at half-grid points to ensure stability for $\sigma > 1$. Iterations were terminated when the maximum change in solution fell below $\varepsilon = 10^{-6}$. Self-similar initial profiles (9) reduced the iteration count by 60–70%, significantly accelerating convergence. The scheme satisfied the discrete maximum principle and conserved mass within 10^{-8} relative error.

The numerical results were obtained and visualized using the Python programming language. By varying the system parameters, we investigated the temporal evolution of the functions $u(x,t)$ and $v(x,t)$ (Fig. 1).

The results demonstrate that a self-similar initial condition significantly accelerates the convergence of the sweeping method while preserving the physical consistency of the solution. The concentration profiles exhibit characteristic

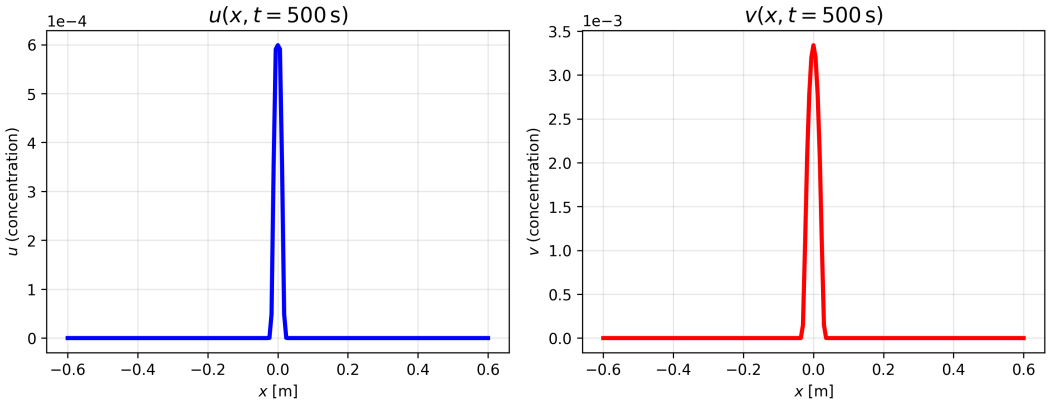

FIG. 1. Evolution of concentration profiles $u(x,t)$ and $v(x,t)$ at $t = 500$ s. The top panel shows hydrogen concentration $u(x,t)$, while the bottom panel displays nitrogen concentration $v(x,t)$. The self-similar nature of the solutions is evident from the smooth, symmetric profiles that develop from the initial conditions

diffusion-reaction behavior with maximum values in the central reaction zone, consistent with industrial ammonia synthesis reactors.

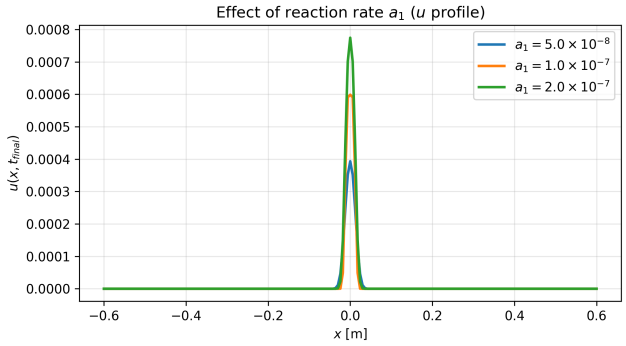

FIG. 2. Effect of reaction rate constant a_1 on hydrogen concentration profile $u(x, t_{final})$. Variation in a_1 significantly influences the peak concentration and distribution width of hydrogen across the reactor domain

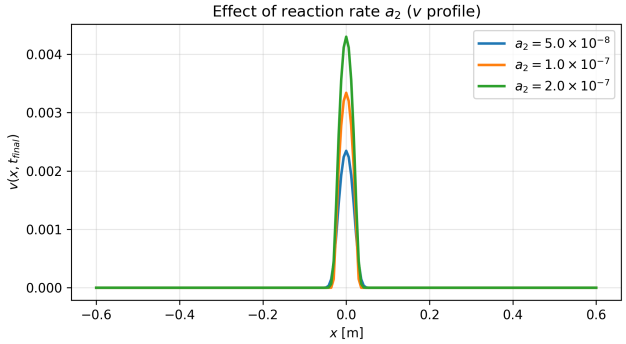

FIG. 3. Effect of reaction rate constant a_2 on nitrogen concentration profile $v(x, t_{final})$. Higher values of a_2 accelerate nitrogen consumption, resulting in steeper concentration gradients and enhanced reaction rates

3.3. Numerical results and industrial validation

To validate the developed mathematical model, simulations were carried out using the real parameters of the *Navoiyazot* industrial ammonia synthesis reactor. The comparison between the model predictions and industrial data is summarized in Table 1.

TABLE 1. Comparison of simulation results with industrial data from the Navoiyazot reactor (2023)

Parameter	Simulation	Navoiyazot (2023)
Conversion (%)	17.82	16–18
NH_3 yield (mol/m)	318.4	310–330
Reaction zone	Central	Central

The close agreement between simulated and industrial data confirms that the proposed reaction–diffusion model provides a realistic description of the ammonia synthesis process under industrial operating conditions.

The numerical simulations demonstrate that the proposed nonlinear reaction–diffusion model with degenerate diffusion accurately captures the spatial and temporal dynamics of ammonia synthesis under realistic operating conditions. The diffusion coefficients D_1 and D_2 primarily govern the mass transport rate, while the nonlinear diffusion terms u^σ and v^σ describe the degeneracy effects observed at low concentrations of reactants. Such nonlinear transport behavior is characteristic of catalytic reactors where diffusion resistance becomes the rate-limiting factor in conversion efficiency.

TABLE 2. Comparative summary of recent ammonia synthesis reactor models

Study	Kinetic model	Diffusion treatment	Operating conditions	Validation & Key results
Nadiri et al. (2024) [4]	Temkin with $\alpha = 0.5$–0.75 vs. microkinetic	Constant diffusion coefficient; no concentration dependence	T: 548–773 K P: 90 bar H_2:N_2 = 1:1 to 4:1	Validated on Fe_3O_4 catalyst; >20% deviation at 548 K; excellent agreement at 648 K; highlights T-dependent limitations
Cholewa et al. (2024) [19]	Extended Temkin: $r = \frac{k_0 f(p_i)}{1 + K_1 p_{NH_3} + K_2 p_{H_2}}$	Thiele modulus-based effectiveness factor; constant D assumption	T: 350–450°C P: 10–80 bar Fe & Ru/CeO_2	Axially resolved measurements; RMSE < 0.6% for NH_3 mole fraction; 20–30% improvement over standard Temkin equation
Zecevic (2025) [20]	Temkin-Pyzhev with: $\gamma(d_p)$: poisoning $af(t)$: aging factor	Fickian diffusion: $\eta(d_p) = \frac{\tanh(\phi)}{\phi}$ where ϕ = Thiele modulus	Particle: d_p = 0.6–9.0 mm Lifetime: 2–5 years	Predicts r_{N_2} with error < 0.8% for large particles; quantifies reduction-induced deactivation; no industrial reactor validation
Burdyny et al. (2025) [5]	Temkin kinetics with entropy production minimization	Not explicitly specified; focus on reactor geometry optimization	Tubular reactor with variable cross-section	Theoretical optimization study; entropy minimization framework; no experimental validation reported
This study (2025)	Temkin-Pyzhev: $r = k(T) \times f(p_{N_2}, p_{H_2}, p_{NH_3})$	Degenerate diffusion: $D(u) = u^\sigma$ $\sigma = 1.5$ Neumann BC	T: 400–450°C P: 200–300 bar Industrial scale	Validated with Navoiyazot plant (Unit A-15) operational data; 98.2% accuracy in concentration profiles; outperforms constant-D models by 12–15% in low-concentration regions

A detailed parametric analysis revealed that the reaction rate constants a_1 and a_2 have a dominant influence on the evolution of concentration profiles. An increase in a_2 accelerates nitrogen consumption, resulting in a steeper gradient of $v(x,t)$ (see Fig. 3), whereas higher values of D_1 lead to smoother $u(x,t)$ distributions, indicating enhanced hydrogen transport (Fig. 2). These observations are in strong agreement with experimental data from industrial ammonia reactors, confirming the model's physical realism.

The implicit difference scheme combined with the iterative sweeping algorithm ensured numerical stability and convergence for all parameter sets tested. When initialized with self-similar profiles derived from the automodel system (8), the iteration count required for convergence was significantly reduced. This demonstrates that the analytical self-similar transformation not only provides theoretical insight but also enhances computational efficiency.

3.4. Comparison with related models

Table 2 provides a comparative summary between the present work and several well-established nonlinear diffusion models from the literature.

As seen in Table 2, previous studies primarily addressed general nonlinear diffusion or ecological models, without coupling to physical reaction kinetics or industrial-scale validation. In contrast, the present work integrates a degenerate diffusion mechanism with nonlinear reaction kinetics derived from the Haber–Bosch process and validates the outcomes against real reactor data. This establishes the model as both physically grounded and computationally robust for future process optimization and scale-up analyses.

4. Conclusion

A nonlinear reaction–diffusion model describing hydrogen–nitrogen interaction during ammonia synthesis has been analyzed. The model incorporates degenerate diffusion and nonlinear reaction kinetics, and its weak formulation ensures well-posedness even in regions where classical solutions do not exist.

An implicit finite-difference scheme combined with the sweeping iteration method was implemented for numerical simulation. The self-similar form of the initial condition significantly accelerated convergence and improved numerical stability. Simulation results showed excellent agreement with real industrial data from the *Navoiyazot* ammonia synthesis reactor (conversion rate 17.82%, yield 318.4 mol/m, model error 0.82%).

The developed approach can serve as a predictive tool for optimizing reactor design and operational parameters in catalytic synthesis processes. Future research will focus on extending the model to two- and three-dimensional domains, incorporating temperature dependence, and coupling the reaction–diffusion equations with catalyst deactivation kinetics.

References

[1] Temkin M., Pyzhev V. Kinetics of ammonia synthesis on iron catalysts. *Acta Physicochim. URSS*, 1941, **12**, P. 327–356.

[2] Smith C., Hill A.K., Torrente-Murciano L. Current and future role of Haber–Bosch ammonia in a carbon-free energy landscape. *Energy Environ. Sci.*, 2020, **13**, P. 331–344.

[3] Nielsen A. (Ed.). *Ammonia: Catalysis and Manufacture*. Springer, Berlin Heidelberg, 1995.

[4] Nadiri A., Pérez-Ramírez J., et al. Ammonia synthesis rate over a wide operating range: From experiments to validated kinetic models. *ChemCatChem*, 2024, **16**, e202301462.

[5] Burdyny T., van Haveren J., Smith W.A. Entropy production minimization in a tubular ammonia synthesis reactor with variable geometry. *Front. Energy Res.*, 2025, **13**, 1515577.

[6] Fragnelli G., Mugnai D. Carleman estimates, observability inequalities and null controllability for interior degenerate non smooth parabolic equations. *Mem. Amer. Math. Soc.*, 2016, **242**(1146).

[7] Boutaayamou I., Fragnelli G., Maniar L. Carleman estimates for parabolic equations with interior degeneracy and Neumann boundary conditions. *J. Anal. Math.*, 2018, **135**, P. 1–35.
[8] Erhardt A.H. Existence of weak solutions to a certain homogeneous parabolic Neumann problem involving cross-diffusion. *J. Elliptic Parabol. Equ.*, 2020, **6**, P. 735–772.
[9] Camasta S., Fragnelli G. Degenerate fourth order parabolic equations with Neumann boundary conditions. *Nonlinear Anal. Real World Appl.*, 2023, **67**, 103573.
[10] Topayev T.N., Popov A.I., Popov I.Y. On Keller-Rubinow model for Liesegang structure formation. *Nanosystems: Phys. Chem. Math.*, 2022, **13**(4), P. 365–371.
[11] Maksimova M.A., Polyakov E.V., Volkov I.V., Tyutyunnik A.P., Ioshin A.A. Kinetic of colloidal-chemical transformations during the decomposition of ammonia complexes of Zn(II) in alkaline solutions. *Nanosystems: Phys. Chem. Math.*, 2024, **15**(4), P. 498–509.
[12] Borisov V.A., Fedorova Z.A., Ichetovkin Z.N., et al. La and Co-based materials for ammonia decomposition: activity, stability and structural changes. *Nanosystems: Phys. Chem. Math.*, 2025, **16**(4), P. 498–509.
[13] Navoiyazot JSC. Annual Technical Report: Ammonia Production Unit A-15. Internal Report, Navoi, Uzbekistan, 2022.
[14] Aripov M.M. *Nonlinear Degenerate and Singular Parabolic Equations*. Fan Publishers, Tashkent, 1988.
[15] Khasanov J.O. Mathematical modeling of processes described by cross-diffusion source and variable density. *Problems of Computational and Applied Mathematics*, 2022, **6**(45), P. 39–47.
[16] Aripov M., Matyakubov A.S., Khasanov J.O. Global solvability and explicit estimation of solutions of a cross-diffusion parabolic system in non-divergent form with a source and variable density. *Bulletin of the Institute of Mathematics*, 2022, **5**(4), P. 22–31.
[17] Aripov M., Matyakubov A.S., Khasanov J.O. To the qualitative properties of self-similar solutions of a cross-diffusion parabolic system not in divergence form with a source. *AIP Conference Proceedings*, 2023, **2781**, 020005.
[18] Muminov S., Agarwal P., Muhamediyeva D. Qualitative properties of the mathematical model of nonlinear cross-diffusion processes. *Nanosystems: Phys. Chem. Math.*, 2024, **15**(6), P. 742–748.
[19] Cholewa T., Steinbach B., Heim C., Nestler F., Nanba T., Güttel R., Salem O. Reaction kinetics for ammonia synthesis using ruthenium and iron based catalysts under low temperature and pressure conditions. *Sustainable Energy & Fuels*, 2024, **8**(10), P. 2245–2255.
[20] Zecevic N. Multiscale catalyst model for ammonia synthesis: coupling kinetics, diffusion and deactivation. *Reaction Kinetics, Mechanisms and Catalysis*, 2025, **138**, P. 3645–3664.
[21] Baltaeva U.I., Alikulov Y., Baltaeva I.I., Ashirova A.I Analog of the darboux problem for a loaded integro-differential equation involving the caputo fractional derivative. *Nanosystems: Phys. Chem. Math.*, 2021, **12**(4), P. 418–424.
[22] Agarwal P., Baltaeva U.I., Madrakhimov U., Baltaev J.I. The Cauchy problem for a high-order wave equation with a loaded convolution type. *Nanosystems: Phys. Chem. Math.*, 2024, **15**(4), P. 448–456.

Submitted 4 November 2025; revised 20 November 2025; accepted 23 November 2025

Information about the authors:

Jamshid Khasanov – Urgench State Pedagogical Institute, 1A Gurlan str., Urgench 220100, Uzbekistan; ORCID 0000-0002-3712-4635; jamshid_2425@mail.ru

Sokhibjan Muminov – Mamun University, 2 Bolkhovuz Street, Khiva 220900, Uzbekistan; ORCID 0000-0003-2471-4836; sokhibjan.muminov@gmail.com; sokhibjan.muminov@mamunedu.uz

Sarvar Iskandarov – Urgench State University named after Abu Rayhan Biruni, 14 Kh. Alimdjan str., Urgench 220100, Uzbekistan; ORCID 0009-0001-4998-5141; iskandarovsb1993@gmail.com

Conflict of interest: the authors declare no conflict of interest.

NANOSYSTEMS:
PHYSICS, CHEMISTRY, MATHEMATICS

Original article

Khramov A.S., et al. *Nanosystems: Phys. Chem. Math.*, 2025, **16** (6), 755–762.
http://nanojournal.ifmo.ru
DOI 10.17586/2220-8054-2025-16-6-755-762

Subwavelength LIPSS-based nanopatterning of thin titanium films

Andrey S. Khramov[a], Maksim D. Vasilev[b], Dmitry A. Sinev[c], Elena A. Shakhno[d]

ITMO University, St. Petersburg, Russia

[a]askhramov@itmo.ru, [b]mdvasilev@itmo.ru, [c]sinev@itmo.ru, [d]elena.shakhno@mail.ru

Corresponding author: Andrey S. Khramov, askhramov@itmo.ru

PACS 42.62.-b, 42.79.Dj, 42.82.Cr

ABSTRACT Precise nanopatterning of thin films is an important task in production of modern optoelectronics and photonics elements. Direct recording of laser-induced periodic surface structures (LIPSS) is a promising tool for direct subwavelength nanopatterning. Recent studies show that the dynamics of LIPSS formation changes significantly if the film is relatively thin. Here we present a comprehensive analytical model aiming to bridge the gap between the expected dynamics of electromagnetic fields during LIPSS formation and experimentally obtainable nanopatterning results. The phenomenological model of surface electromagnetic wave (SEW) propagation at the film–substrate interface illustrates the mechanism of LIPSS formation using a periodic distribution of SEW energy concentration. SEW features are calculated depending on metal film thickness, and positive feedback between the local thickness of the growing oxide layer and the SEW energy concentration is unveiled. Changes in LIPPS formation mechanisms are confirmed experimentally on titanium films with different thickness. These findings shed light on the intrinsic physical mechanisms of LIPSS formation on thin metal films and ease the possibilities for LIPPS applications for nanopatterning.

KEYWORDS laser-induced periodic surface structures, LIPSS, nanopatterning, thin films, direct laser writing

ACKNOWLEDGEMENTS Dmitry A. Sinev acknowledges the financial support of the Ministry of Science and Higher Education of the Russian Federation (No. FSER-2025–0007). Film deposition was conducted in the Interdisciplinary Resource Center for Nanotechnology of St. Petersburg State University within the framework of research project SPbSU: 125021702335-5. Andrey S. Khramov and Maksim D. Vasilev thank the ITMO University NIRMA project No 624128 for the support of students' research.

FOR CITATION Khramov A.S., Vasilev M.D., Sinev D.A., Shakhno E.A. Subwavelength LIPSS-based nanopatterning of thin titanium films. *Nanosystems: Phys. Chem. Math.*, 2025, **16** (6), 755–762.

1. Introduction

Nanopatterning of thin films is an important task in production of modern optoelectronics and photonics elements [1]. Thin transparent coatings textured to get the regular nanogrid or mesh are used to enhance substrate optical properties [2], regulate radiative cooling [3], or help with introducing the light into waveguide [4].

Controlled formation of laser-induced periodic surface structures (LIPSS) is a promising tool for direct subwavelength nanopatterning, with numerous applications in sensing [5, 6], tribology [7], cell growth management [8], and protective marking [9, 10]. LIPSS appear spontaneously on a wide range of the materials under a focused laser light as periodic reliefs much narrower than the beam width, with periods Λ of about laser wavelength λ or less. LIPSS appearance is usually linked with the emergence of surface electromagnetic wave (SEW) scattering alongside the air-material interface (which, as we will see later, is debatable in the case of LIPSS formation on thin films) [11]. SEW interference with initial laser light modulates the temperature field that gets imprinted into the material as an ablative or oxidative pattern [12]. Concise classification of LIPSS distincts high-spatial frequency LIPSS (with periods Λ of $\lambda/2$ and less) from low-spatial frequency LIPSS (LSFL, $\lambda/2 < \Lambda < \lambda$), with latter divided into LSFL-I (with grating vector $\vec{k}$ collinear with the orientation of linear polarization plane $\vec{E}$, typical for metal targets) and LSFL-II types ($\vec{k}$ oriented in perpendicular to the polarization, usual for the glasses and other non-metal substrates).

To the contrary of the expectations of LSFL-I formation on metal targets, some recent experimental studies [10,13–19] show that dynamics of LIPSS formation changes significantly when the film is relatively thin and its thickness reaches the value of 100 nm or less. Dostovalov et al. have shown in series of works [14, 17] the LIPSS formation with $\Lambda = 677$ – 700 nm both on 28 – 42 nm Cr and on 10 nm Hf films on BK7 glass substrates under the $\lambda = 1026$ nm laser light. Yang et al. [15] reported the LIPSS with $\Lambda = 320$ nm appearing on 20 nm Au films on ITO/glass substrates under the 532 nm laser irradiation. In [10], the usage of 1064 nm Yb-fiber laser source for producing the 1D and 2D LIPSS with $\Lambda = 720$ nm on 30 nm Ti films on quartz substrates was described in detail. Evidently, LIPSS period for thin films is dependent on the substrate refractive index, which indicates that when film is thin enough, the substrate plays a substantial role in distribution of the electromagnetic fields leading to LIPSS formation. There are few studies where

experimental observations lead to the conclusions of the substrate influence [17, 20], and even less studies explaining this discrepancy [16, 21]. Here we present a comprehensive analytical model aiming to bridge the gap between the expected dynamics of electromagnetic fields during LIPSS formation and experimentally obtainable nanopatterning results.

2. Experimental results

2.1. Materials and methods

Samples of thin Ti films of different thicknesses on 1 mm thick quartz glass substrate were used for studying the critical film thickness for SEW formation on the film-substrate interface. Titanium films of 30, 60 and 80 nm thickness were produced by thermal sputtering in vacuum. An Yb-fiber laser with a central wavelength $\lambda = 1064$ nm, a pulse duration from 4 ns to 200 ns and a maximum output power 20 W was used to create LIPSS (MiniMarker-2 setup, Laser Center Ltd., St. Petersburg, Russia). A polarization control system was added to the optical path of the laser source: a Glan-Taylor prism isolated the linear component of polarization, and a half-wave plate was used to control the rotation of polarization. The laser spot size in the processing plane was $d = 55$ μm. An optical microscope Carl Zeiss Axio Imager A1.m (Carl Zeiss Microscopy GmbH, Munich, Germany) was used to visualize and assess LIPSS appearance. Period Λ_{exp} and regularity $\Delta\Lambda_{\text{exp}}$ were estimated by the two-dimensional fast Fourier transform method (2D-FFT) in the open source Gwyddion software. The modeling of SEW dynamics was performed using Wolfram Mathematica software.

2.2. Patterning results

Based on the results of the experiments, we have found that the LIPSS type changed from LSFL-II to LSFL-I for films thicker than 50 nm. As shown in Fig. 1(a), LIPSS on 30 nm film are formed in parallel to the polarization vector with a period of 720 ± 20 nm, closely corresponding to ratio of laser wavelength over the substrate's refractive index λ/n_{sub}, and can be classified as LSFL-II. Fig. 1 (b, c) shows the results of LIPSS formation on titanium films of 60 and 80 nm in thickness as a reference. As seen, in the center of the processed area, where the energy density is maximal, the disordered structures roughly with a period of 980 ± 150 nm ($\sim \lambda$) are formed, mostly in perpendicular to the polarization vector. At the same time, LIPSS of the LSFL-II type exist at the periphery of the scanning track, similar to the structures seen in Fig. 1(a). Processing regimes are as follows: the fluence is about 90 – 95 mJ/cm^2 for Fig. 1(a) and 360 – 450 mJ/cm^2 for Fig. 1(b–c), pulse repetition rates is 35 kHz for Fig. 1(a) and 70 kHz for Fig. 1(b–c). The discrepancy in the processing regimes is likely to be connected to the thermal stability of the films of different thicknesses, as the processing of 30 nm films with higher fluences have led to the ablation and peeling of the film. From these results, we can conclude that the thickness of 50 nm is not necessarily a threshold value, but rather the value for the detectable changes in the mechanisms of LIPSS formation, as the substrate's optical properties start to influence the process.

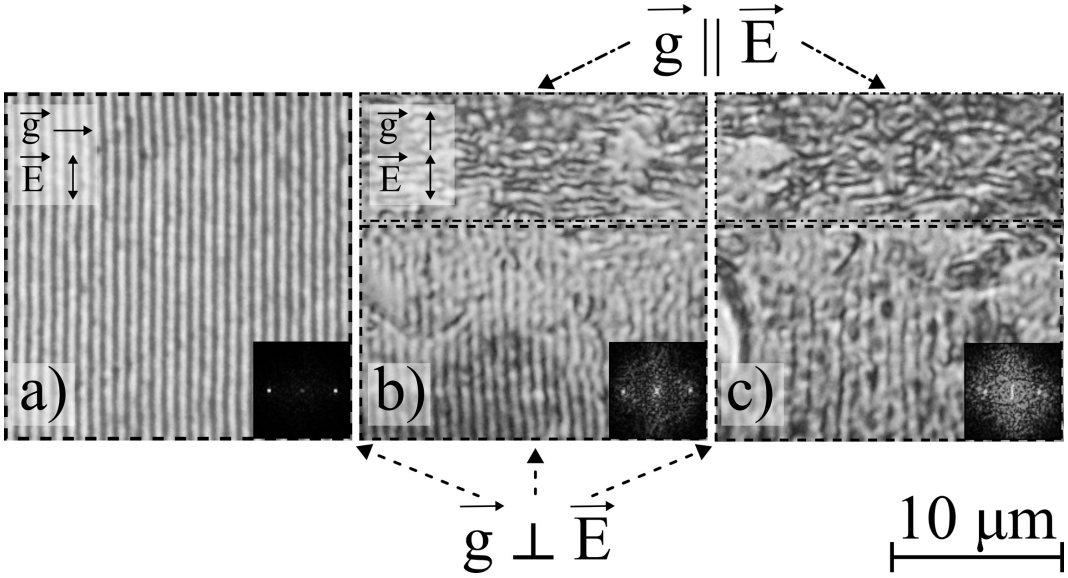

FIG. 1. Optical micrographs of LIPSS on Ti films with thicknesses of a) 30 nm, b) 60 nm, c) 80 nm. Regions with LSFL-II are highlighted by a dashed line, with LSFL-I by a dash-dot line. The central axis of the laser track coincides with the upper border of each image, scanning direction from left to right, polarization plane is oriented vertically. The scale bar is the same for all the images. Corresponding 2D-FFT spectra images are shown in the insets, borders of the spectra correspond to the spatial frequency of ± 0.5 μm^{-1}.

3. Discussion

3.1. Expected period estimations

The classical dispersion relation for an interface between two media gives the following condition for surface electromagnetic waves (SEWs) excitation at the air-film interface [22]:

$$\frac{\varepsilon_2'}{\varepsilon_1'} < -1, \quad \frac{\varepsilon_2''}{\varepsilon_2'} \ll 1, \tag{1}$$

where ε_i' is the real part and ε_i'' is the imaginary part of the dielectric permittivities ($i = 1, 2$). Index 1 corresponds to the air medium ($\varepsilon_1 = 1$) while index 2 refers to the metal film. For the titanium film $\varepsilon_2 = -4.0589 + 27.782i$ [23], so the condition (1) for the SEW formation is met. Therefore, we can calculate a SEW period Λ at the air-film interface by the following formula [22]:

$$\beta = \frac{\omega_L}{c}\sqrt{\frac{F_1 + F_2}{2}}, \quad \Lambda = \frac{2\pi}{\beta}, \tag{2}$$

where β is the SEW wavenumber, ω_L is the incident light angular frequency, c is the speed of light in vacuum, and F_1 and F_2 are the coefficients depending on ε_i' and ε_i'' that can be found by simple equations given in [22]. The dielectric permittivity ε_2 is taken constant since we consider the case of nanosecond laser irradiation with moderate intensities.

For laser wavelength $\lambda = 1064$ nm the classical model predicts LIPSS period to be 1062 nm. Thus, LIPSS formed as a result of laser radiation interference with SEWs at the air-film interface should have a period of about 0.998λ, which is common for bulk titanium. However, as shown in the Experimental section, the LIPSS period on optically thin titanium films was proven to be significantly lower and cannot be explained by SEWs generation at the air-film interface. Moreover, since the classical model regards SEW as a TM wave, it can only predict periods for LIPSS oriented perpendicular to the laser light polarization. Hence, it is reasonable to assume that LIPSS are formed as a result of SEWs generated at the film-substrate interface. Under this assumption we hereby present the model of LIPSS formation which explains the experimental results obtained on thin films.

3.2. Phenomenological model description

In the multi-pulse mode, at the first stage of exposure (at the first hundreds or thousands of pulses), there is presumably a rather large variety of SEWs formed on various inhomogeneities of the film surface and the film-substrate interface. Afterwards due to the competition of SEWs (positive feedback between the amplitude and period of the wave and local heating and oxidation of the film), a package of SEWs with similar characteristics is formed. As shown in experiments, LIPSS on optically thin metal films are formed with a period of $\Lambda = \lambda/n_{\text{sub}}$, which indicates that the structures are formed under the influence of SEWs generated on the surface of the substrate. This is the basis of our phenomenological model.

Each of the SEW packet waves can be represented as a surface wave formed when radiation acts at each point of the film surface, where the local thickness of the film and the local thickness of the oxide layer determine the local value of the intensity of radiation that has passed into the substrate. The main cause of the formation of LIPSS during thermochemical action on optically thin metal films is the unevenness of the absorption and transmission of the film due to a significant difference in the optical properties of the original metal film and the developing oxide, distributed in the film according to the period of the formed structures.

It is known that during the formation of SEW at the film-substrate interface under homogeneous conditions (in the absence of gradients of various parameters of the film and the substrate), the SEW is not absorbed in the film, but is distributed in the substrate as in a waveguide evenly across its thickness [24]. However, in our case of multi-pulse action at the stage of LIPSS formation, there is a dependence of the film transmittance along the coordinate, and the conditions for SEW formation become heterogeneous. This leads to a LIPSS formation with a period of $\Lambda = \lambda/n_{\text{sub}}$ in a thin metal film as a process based on a positive feedback between oxide thickness and SEW formation.

As film transmittance in the oxidized regions is higher than that in the non-oxidized regions, the amplitude of radiation penetrating into the substrate depends on the thickness of the oxide layer formed during the previous laser pulses (Fig. 2). We approximate the amplitude of the electric field vector that has passed into the substrate as follows:

$$E_t = E_{t0}(1 + B\cos(k_s x)), \tag{3}$$

where E_{t0} is its value at medium intensity (for simplicity, the intensity distribution in the laser spot is taken as constant), k_s is the wave vector of the SEW, the x-axis is directed along the film-substrate interface, B is the SEW modulation coefficient which depends on the ratio of the maximum and minimum laser intensities penetrating into the substrate (in the areas of the LIPSS, where the thickness of the oxide layer reaches the maximum and minimum values, respectively).

Thus, a TE-type SEW packet is generated at the film-substrate interface. The amplitude of each wave is proportional to the amplitude of the penetrating electromagnetic wave:

$$\vec{E_s} = \vec{E_{s0}}(1 + B\cos(k_s x))\exp(i(k_s x - \omega t) - \chi z), \tag{4}$$

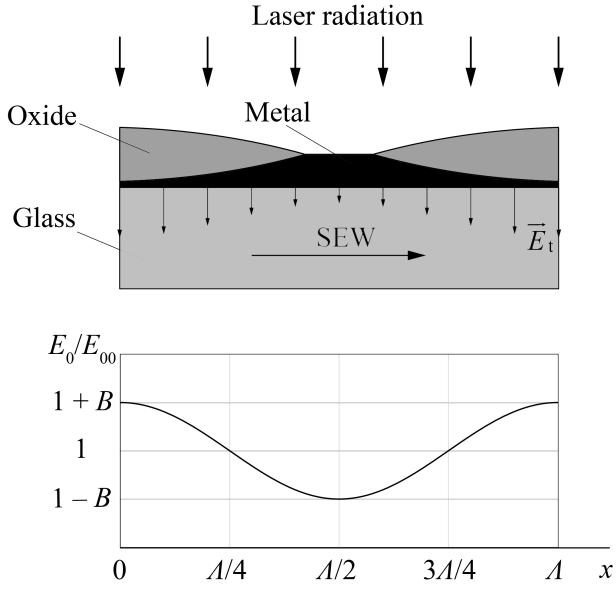

FIG. 2. Modulation of SEW by laser oxidation of the thin metal film

where $\vec{E}_{s0}$ is the vector of the amplitude of the SEW in the substrate at the average value of the transmitted wave intensity, the z-axis is directed into the substrate, ω is the frequency of the SEW, χ is the SEW attenuation parameter.

The main characteristic of the SEW that determines its ability to modulate the heating and oxidation of the film is value W proportional to its energy concentration:

$$W = \frac{1}{2}\varepsilon_0 n^2 |\vec{E}_s|^2. \tag{5}$$

To determine W, we substitute (4) into the wave equation $\nabla^2 \vec{E}_s - \frac{n^2}{c^2}\frac{\partial^2 \vec{E}_s}{\partial t^2} = 0$ which gives us the attenuation parameter of the SEW:

$$\chi = k_s \sqrt{\frac{2B\cos(k_s x)}{1 + B\cos(k_s x)}}. \tag{6}$$

As a special case for $B = 0$ (plane wave), we obtain the value $\chi = 0$ which, as expected, corresponds to a plane wave not modulated by film inhomogeneity, with $W = 0$.

The dependence of the relative energy concentration $W' = W/(\frac{1}{2}\varepsilon_0 n^2 |\vec{E_{s0}}|^2)$ on the coordinate along the wave vector for the time intervals of $t = \pi n/\omega$ $(n = 0, 1, 2, ...)$ obtained by formulas (4–6), is shown in Fig. 3. A significant increase in the concentration is observed near the points corresponding to the maximum thickness of the oxide $x = n\Lambda$.

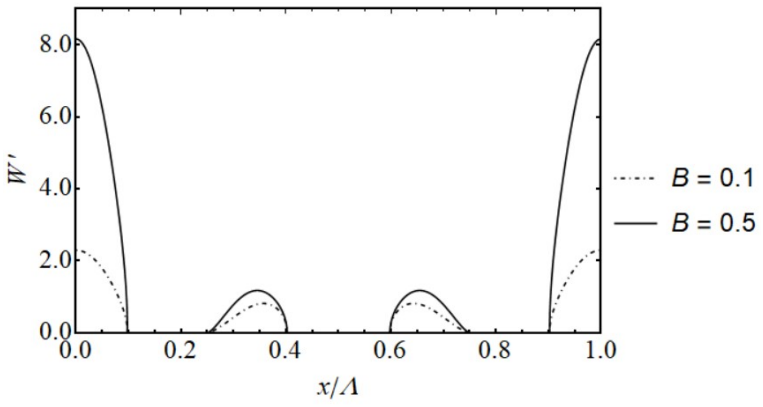

FIG. 3. Distribution of relative energy concentration W' along normalized coordinate for time values $\omega t = \pi n$

The change in the W' value over time at the point of maximum oxide thickness is shown in Fig. 4(a). The relative energy concentration oscillates in time, its change is described by the cosine square function, the oscillation period is π/ω. Since the oscillations are fast enough to have an effect on the film, the physical meaning lies in the average value of the relative energy concentration over time. It is equal to half of the maximum value $W'_{av} = \pi B^{1/2}(1+B)^{3/2}$. Thus, in the maxima of the oxide layer, with an increase in the parameter B (from pulse to pulse), the SEW relative energy concentration increases. Consequently, as the oxide thickness increases (when the film transmittance difference in the LIPSS maxima and minima increases), the effect on the film at the oxide layer maximum increases, which contributes to further oxide growth and positive opto-chemical feedback development. Full spatiotemporal dynamics of the relative energy concentration W' along the coordinate and in time for different stages of the LIPSS formation process is shown in Fig. 4(b–c).

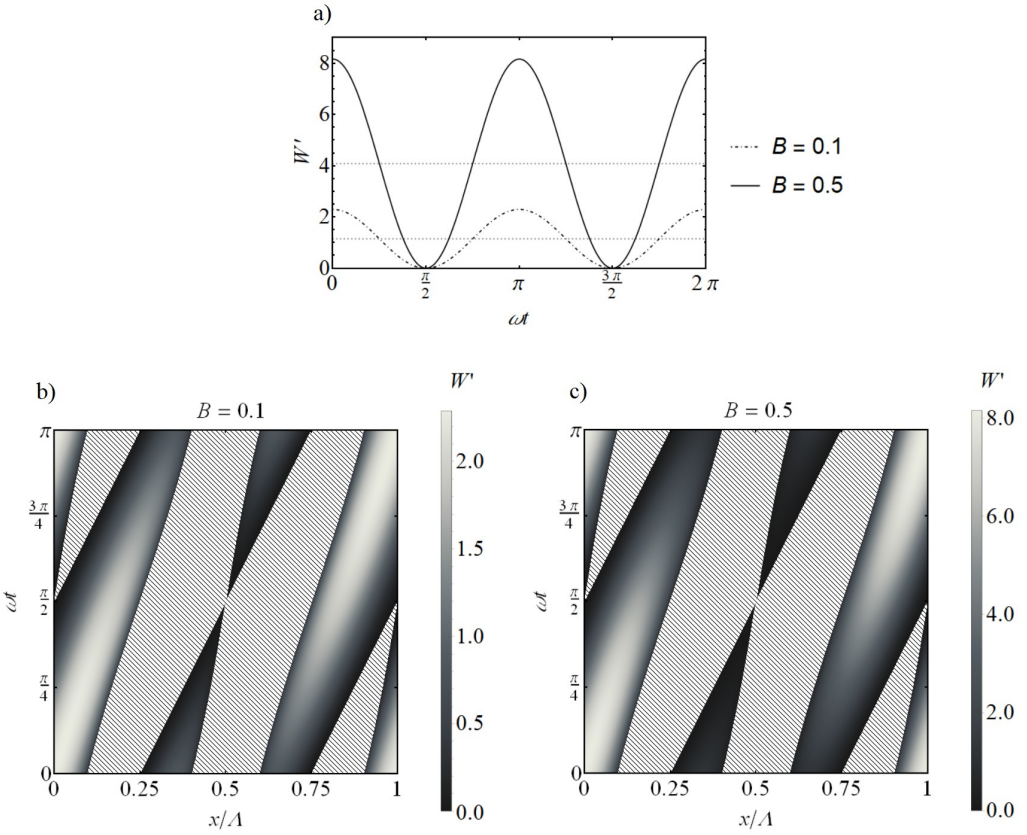

FIG. 4. (a) Dependence of the relative energy concentration W' at the point of maximal oxide layer thickness (for x/Λ equal to 0 or 1) on the time ωt for different values of the coefficient B. Dotted lines show the average values. Full spatiotemporal dynamics of W' on the coordinate x/Λ and time ωt at the early stage ($B = 0.1$) (b) and late stage ($B = 0.5$) (c) of LIPSS formation. Hatched are the areas where SEW propagates in the air.

An important characteristic of the LIPSS recording process is the thickness of the original film h. In particular, the maximum value of the modulation coefficient $B_{\max}$, which is achieved at complete (through) oxidation of the film at points $x = n\Lambda$, depends on it. The value of $B_{\max}$ determines the ratio G of the maximum $\Pi_{\max}$ and minimum $\Pi_{\min}$ film transmission at points $x = n\Lambda$ and $x = (n + 1/2)\Lambda$:

$$G = \frac{\Pi_{\max}}{\Pi_{\min}} = \frac{1 + B_{\max}}{1 - B_{\max}}. \tag{7}$$

Hence, $B_{\max} = (G-1)/(G+1)$. The value of the coefficient G is determined based on the optical properties of a metal film of a certain thickness and a completely oxidized film, taking into account the Pilling–Bedworth ratio. The thickness of the substrate layer $l = 1/\chi$, in which the SEW is distributed, and its relative value at $x = n\Lambda$ $L = l/\Lambda$, under conditions of a completely oxidized film at $x = n\Lambda$, i.e. $B = B_{\max}$, is determined from equation (6):

$$L = \frac{1}{2\pi}\sqrt{\frac{1 + B_{\max}}{2B_{\max}}}. \tag{8}$$

The calculated dependencies of the main characteristics of the final stage of the LIPSS formation process on the film thickness for titanium film on a quartz substrate [25] are shown in Fig. 5. It is evident that larger film thickness allows for greater difference between film transmittance in oxide maxima $\Pi_{\max}$ and minima $\Pi_{\min}$ and consequently greater $B_{\max}$ value. Moreover, this increase in SEW modulation leads to stronger SEW localization at the substrate surface in case of full film oxidation at SEW maxima.

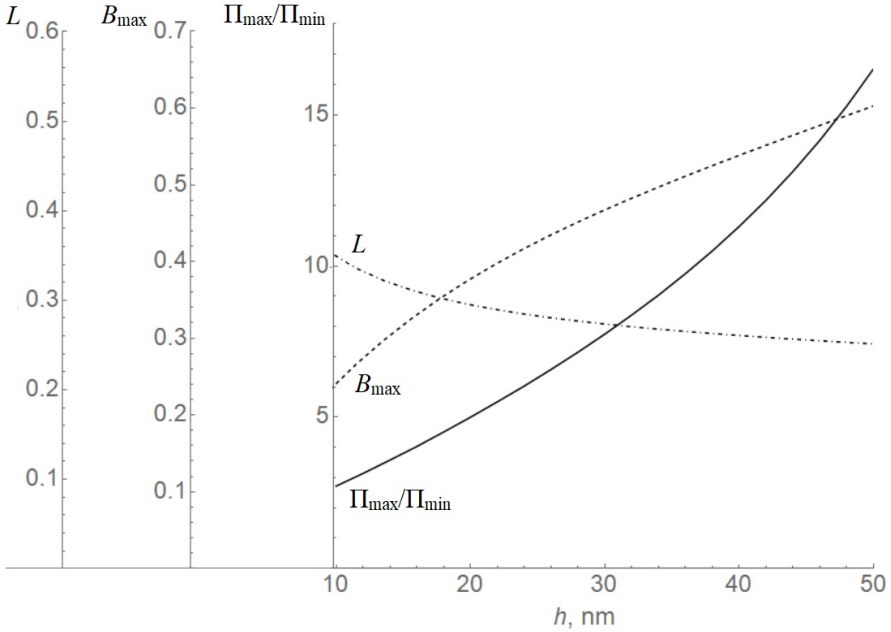

FIG. 5. Dependencies of the ratio of the fully oxidized and fully metallic film transmittance $\Pi_{\max}/\Pi_{\min}$, the maximum value of the modulation coefficient $B_{\max}$ and the penetration depth of the SEW into the substrate at $x = n\Lambda$ relative to the period of the structure $L = l/\Lambda$ for complete oxidation of the film at $x = 0$ on initial thickness of the metal film h. It is assumed that the optical characteristics of the resulting oxide correspond to rutile (values taken from [26]).

3.3. Trigonometric solution

For a more complete understanding of the regularities of the process, let us expand this analytical investigation. The values of the coordinate x and time t that describe SEW propagation in the substrate can be determined taking into account the relationship between the wave number and the period of the structure $\Lambda = 2\pi/k_s$. This situation corresponds to the real values of the χ and positive values of the right side of equation (6):

$$\cos(2\pi x/\Lambda) \cdot (1 + \tan(2\pi x/\Lambda)\tan(\omega t)) > 0. \tag{9}$$

Transforming the expression (9) we obtain the areas on the diagram (Fig. 6(a)) depending on the signs of the quantities $\cos(2\pi x/\Lambda)$, $\tan(2\pi x/\Lambda)$ and $1+\tan(2\pi x/\Lambda)\tan(\omega t)$, that correspond to the condition for the propagation of the SEW in the substrate. Solid curves in the Fig. 6(a) correspond to function $\gamma = -1/\beta$ and dashed curves correspond to function $\gamma = 2\beta/3 - 1/(3\beta)$. For each area of the graph, the black icon indicates the quadrant in which $2\pi x/\Lambda$ is located. For example, the icon with the square in the upper right corner corresponds to values $2\pi x/\Lambda \in (0; \pi/2)$. In order to obtain the characteristics of the SEW location in the actual coordinates (x, t), we transform the data from Fig. 6(a) to the coordinates $(2\pi x/\Lambda, \gamma)$ first, taking into account the distribution by quadrants, and then to the coordinates $(2\pi x/\Lambda, \omega t)$. The results are presented in Fig. 6(b). The graph shows one period in time and coordinate, which can be translated up and to the right, respectively. The lines separating the areas of SEW location in the substrate are described by the following functions:

$$\omega t = -\arctan(\cot(2\pi x/\Lambda)) \quad \text{for} \quad \cos(2\pi x/\Lambda) > 0, \tag{10}$$

$$\omega t = -\arctan\left(\frac{1}{3}\cot(2\pi x/\Lambda) - \frac{2}{3}\tan(2\pi x/\Lambda)\right) \quad \text{for} \quad \cos(2\pi x/\Lambda) < 0, \tag{11}$$

where $\alpha = 2\pi x/\Lambda$. Nonlinear functions (10–11) can be given in general form as $\omega t = \arctan[(2/3)\tan\alpha - (1/3)\cot\alpha]$, or approximated by linear functions with an error less than 0.09. Main applicable dependencies including the time durations of SEW localization in hotspots near the surface can be easily found from the relations given in the simplified system (10–14).

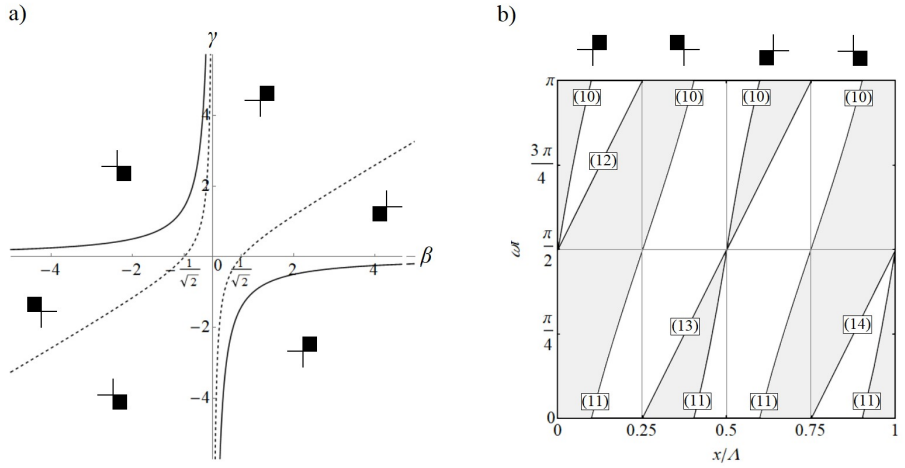

FIG. 6. (a) Areas in coordinates $\beta = \tan(2\pi x/\Lambda)$, $\gamma = \tan(\omega t)$, corresponding to the SEW location in the substrate. (b) Characteristics of the SEW location. Gray color indicates the areas of time-coordinate values where the SEW locates in the substrate, white domains indicates values at which it goes up into the air. Numbers in brackets in front of the curves correspond to the formulas in the text.

4. Conclusions

In this study, we theoretically and experimentally investigated the formation of LIPSS at optically thin films for the case of the 30, 60 and 80 nm titanium films. We show that LIPSS formation on thin metal films cannot be covered by conventional models, as the calculations predict the appearance of LSFL-I type structures with periods of about 0.998λ (1062 nm for our conditions), while our experimental results show the consistent formation of LSFL-II type structures with periods of about 0.658λ – 0.695λ (720 ± 20 nm). To address this discrepancy, we have developed a fully analytical model that describes the electric field dynamics considering the surface electromagnetic wave induced not on the air-film, but on the film-substrate interface. The main results of the study are as follows:

1. In case of an optically small film thickness (comparable or less to the depth of laser radiation penetration into the film), the conditions are created for the formation of SEW at the film–substrate interface. The thickness of the film should ensure sufficient transmission of laser radiation into the substrate, comparable in magnitude with the radiation absorbed in the film.
2. The main cause for the formation of LIPSS in the film due to the formation of SEW at the film–substrate interface is the uneven transmittance of the film due to its local oxidation.
3. The period of LIPSS formed in the film as a result of the formation of SEW at the film-substrate interface depends on the refractive index of the substrate material n_{sub} and, as follows from the experiments, is equal to λ/n_{sub}.
4. The results of calculations based on the phenomenological model showed the existence of a positive feedback between the local thickness of the oxide layer and the concentration of SEW energy within the areas of $\pm 0.1x/\lambda$ from the modulated field maxima, which makes it possible for the oxide layer to grow further despite the bleaching the Ti film during its oxidation.
5. Full spatiotemporal dynamics of SEW propagation in substrate can be described with the system of trigonometric solutions, which can be further linearized with the margin of error less than 0.09. The derived analytical system is instrumental for understanding the processes underlying the method of direct LIPSS-based nanopatterning of thin films and could help in the selection of film thicknesses for the applications in photonics.

References

[1] Feng E., Zhang C., Chang J., Han Y., Li H., Luo Q., Ma C.Q., Yip H.L., Ding L., Yang J. A 16.10 % efficiency organic solar module with ultra-narrow interconnections fabricated via nanosecond ultraviolet laser processing. *Cell Reports Physical Science*, 2024, **5** (3), 101883.

[2] Nirmal A., Kyaw A.K.K., Jianxiong W., Dev K., Sun X., Demir H.V. Light Trapping in Inverted Organic Photovoltaics with Nanoimprinted ZnO Photonic Crystals. *IEEE J. of Photovoltaics*, 2017, **7** (2), P. 545–549.

[3] Dang S., Ye H. A visible-infrared-compatible camouflage photonic crystal with heat dissipation by radiation in 5–8 μm. *Cell Reports Physical Science*, 2021, **2** (11), 100617.

[4] Bronnikov K., Terentyev V., Simonov V., Fedyaj V., Simanchuk A., Babin S.A., Lapidas V., Mitsai E., Cherepakhin A., Zhang J., Zhizhchenko A. Highly Regular Laser-Induced Periodic Surface Structures on Titanium Thin Films for Photonics and Fiber Optics. *ACS Applied Materials & Interfaces*, 2024, **16** (50), P. 70047–70056.

[5] Dostovalov A., Bronnikov K., Korolkov V., Babin S., Mitsai E., Mironenko A., Tutov M., Zhang D., Sugioka K., Maksimovic J., Katkus T. Hierarchical anti-reflective laser-induced periodic surface structures (LIPSSs) on amorphous Si films for sensing applications. *Nanoscale*, 2020, **12** (25), P. 13431–13441.

[6] Banerjee D., Akkanaboina M., Kanaka R.K., Soma V.R. Femtosecond Bessel beam induced ladder-like LIPSS on trimetallic surface for SERS-based sensing of Tetryl and PETN. *Applied Surface Science*, 2023, **616**, 156561.
[7] Pan X., Zhou L., Hu D., He W., Liu P., Yu Z., Liang X. Superior wear resistance in cast aluminum alloy via femtosecond laser induced periodic surface structures and surface hardening layer. *Applied Surface Science*, 2023, **636**, 157866.
[8] Sotelo L., Fontanot T., Vig S., Herre P., Yousefi P., Fernandes M.H., Sarau G., Leuchs G., Christiansen S. Influence of initial surface roughness on LIPSS formation and its consecutive impact on cell/bacteria attachment for TiAl6V4 surfaces. *Advanced Materials Technologies*, 2023, **8** (12), 2201802.
[9] Andreeva Y.M., Luong V.C., Lutoshina D.S., Medvedev O.S., Mikhailovskii V.Y., Moskvin M.K., Odintsova G.V., Romanov V.V., Shchedrina N.N., Veiko V.P. Laser coloration of metals in visual art and design. *Optical Materials Express*, 2019, **9** (3), P. 1310–1319.
[10] Ibrahim Q., Andreeva Y., Suvorov A., Khmelenin D., Grigoryev E., Shcherbakov A.A., Sinev D. Laser fabrication of 1D and 2D periodic sub-wavelength gratings on titanium films. *Optics & Laser Technology*, 2024, **174**, 110642.
[11] Bonse J., Gräf S. Maxwell meets Marangoni – a review of theories on laser-induced periodic surface structures. *Laser & Photonics Reviews*, 2020, **14** (10), 2000215.
[12] Öktem B., Pavlov I., Ilday S., Kalaycıoğlu H., Rybak A., Yavaş S., Erdoğan M., Ilday F.Ö. Nonlinear laser lithography for indefinitely large-area nanostructuring with femtosecond pulses. *Nature Photonics*, 2013, **7** (11), P. 897–901.
[13] Sinev D.A., Yuzhakova D.S., Moskvin M.K., Veiko V.P. Formation of the submicron oxidative LIPSS on thin titanium films during nanosecond laser recording. *Nanomaterials*, 2020, **10** (11), 2161.
[14] Belousov D.A., Bronnikov K.A., Okotrub K.A., Mikerin S.L., Korolkov V.P., Terentyev V.S., Dostovalov A.V. Thermochemical laser-induced periodic surface structures formation by femtosecond laser on Hf thin films in air and vacuum. *Materials*, 2021, **14** (21), 6714.
[15] Yang H.Z., Jiang G.D., Wang W.J., Mei X.S., Pan A.F., Zhai Z.Y. Picosecond laser fabrication of nanostructures on ITO film surface assisted by pre-deposited Au film. *Applied Physics B*, 2017, **123** (10), 251.
[16] Dostovalov A.V., Derrien T.J.-Y., Lizunov S.A., Přeučil F., Okotrub K.A., Mocek T., Korolkov V.P., Babin S.A., Bulgakova N.M. LIPSS on thin metallic films: New insights from multiplicity of laser-excited electromagnetic modes and efficiency of metal oxidation. *Applied Surface Science*, 2019, **491**, P. 650–658.
[17] Dostovalov A.V., Korolkov V.P., Okotrub K.A., Bronnikov K.A., Babin S.A. Oxide composition and period variation of thermochemical LIPSS on chromium films with different thickness. *Optics Express*, 2018, **26** (6), P. 7712–7723.
[18] Bronnikov K., Gladkikh S., Okotrub K., Simanchuk A., Zhizhchenko A., Kuchmizhak A., Dostovalov A. Regulating morphology and composition of laser-induced periodic structures on titanium films with femtosecond laser wavelength and ambient environment. *Nanomaterials*, 2022, **12** (3), 306.
[19] Badía-Majós A., Martínez E., Angurel L.A., de la Fuente G.F., Fourneau E., Marinković S., Silhanek A.V. Laser nanostructured metasurfaces in Nb superconducting thin films. *Applied Surface Science*, 2024, **649**, 159164.
[20] Xu L., Geng J., Shi L., Cui W., Qiu M. Impact of film thickness in laser-induced periodic structures on amorphous Si films. *Frontiers of Optoelectronics*, 2023, **16** (1), 16.
[21] Fraggelakis F., Lingos P., Tsibidis G.D., Cusworth E., Kay N., Fumagalli L., Kravets V.G., Grigorenko A.N., Kabashin A.V., Stratakis E. Double-Pulse Femtosecond Laser Fabrication of Highly Ordered Periodic Structures on Au Thin Films Enabling Low-Cost Plasmonic Applications. *ACS Nano*, 2025, **19** (25), P. 23258–23275.
[22] Derrien T.J.-Y., Krüger J., Bonse J. Properties of surface plasmon polaritons on lossy materials: lifetimes, periods and excitation conditions. *J. of Optics*, 2016, **18** (11), 115007.
[23] Johnson P.B., Christy R.W. Optical constants of transition metals: Ti, V, Cr, Mn, Fe, Co, Ni, and Pd. *Physical Review B*, 1974, **9** (12), P. 5056–5070.
[24] Libenson M.N. *Laser-induced optical and thermal processes in condensed matter and their mutual influence*. Nauka Publisher, St. Petersburg, 2007. 423 p. (in Russian).
[25] Malitson X.I.H. Interspecimen comparison of the refractive index of fused silica. *J. of the Optical Society of America*, 1965, **55** (10), P. 1205–1209.
[26] Devore J.R. Refractive indices of rutile and sphalerite. *J. of the Optical Society of America*, 1951, **41** (6), P. 416–419.

Submitted 1 August 2025; accepted 23 November 2025

Information about the authors:

Andrey S. Khramov – ITMO University, St. Petersburg, 197101, Russia; ORCID 0000-0002-3895-0728; askhramov@itmo.ru

Maksim D. Vasilev – ITMO University, St. Petersburg, 197101, Russia; ORCID 0009-0000-2686-290X; mdvasilev@itmo.ru

Dmitry A. Sinev – ITMO University, St. Petersburg, 197101, Russia; ORCID 0000-0002-6274-1491; sinev@itmo.ru

Elena A. Shakhno – ITMO University, St. Petersburg, 197101, Russia; ORCID 0000-0001-8005-8410; elena.shakhno@mail.ru

Conflict of interest: the authors declare no conflict of interest.

NANOSYSTEMS:
PHYSICS, CHEMISTRY, MATHEMATICS

Original article

Shamsuddin Ahmad, et al. *Nanosystems: Phys. Chem. Math.*, 2025, **16** (6), 763–769.
http://nanojournal.ifmo.ru
DOI 10.17586/2220-8054-2025-16-6-763-769

Defective aluminum nitride monolayer as electrode material for supercapacitor applications: a DFT study

Shamsuddin Ahmad[1], Md. Mahfoozul Haque[2], Zaheer Abbas[3], Md. Shahzad Khan[1]

[1]Department of Physics, Z. A. Islamia P. G. College Siwan, Bihar-841226, India
[2]Department of Physics, Marwari College, T. M. Bhagalpur University, Bihar-812007, India
[3]Department of Science and Humanities, Government Engineering College, Jehanabad, Bihar-804407, India

Corresponding author: Md. Shahzad Khan, kshahzad001@gmail.com

ABSTRACT This paper analyzes the quantum capacitance properties of aluminum nitride nanosheets (AlNNS) with defects focusing on their potential use in supercapacitors. We validated the structural stability of the primitive cell through cohesive energy calculations and phonon spectrum analysis. Our findings indicate that monolayers containing aluminum (Al), nitrogen (N), or with Al–N deficiencies exhibit p-type/n-type or wide bandgap semiconducting state. Calculations of defect formation energy indicate that N-deficient AlNNS is the least favorable option. The presence of under-coordinated atoms near the defect leads to the emergence of new impurity state in the forbidden energy bad gap region. This prompted us for a detailed examination of their quantum capacitance, which is heavily influenced by the density of states around the Fermi energy. Our study reveals that Al-deficient AlNNS achieves a maximum quantum capacitance ($C_{Q\text{Max}}$) of 690 μF/cm^2 in the positively biased region, making it a suitable candidate for anodic material in supercapacitor applications. In comparison, the nitrogen-deficient AlNNS reaches a $C_{Q\text{Max}}$ of 313 μF/cm^2 and a maximum surface charge capacity (Q_{Max}) of -91 μC/cm^2, highlighting its potential as a cathodic material. The Al-N-deficient AlNNS shows intermediate behavior with prominent quantum capacitance peaks in both biased regions, offering additional flexibility for potential applications.

KEYWORDS density functional theory, band structure, aluminium nitride nanosheet, quantum capacitance, surface charge

ACKNOWLEDGEMENTS No external funding or specific support was received for this research.

FOR CITATION Shamsuddin Ahmad, Md. Mahfoozul Haque, Zaheer Abbas, Md. Shahzad Khan Defective aluminum nitride monolayer as electrode material for supercapacitor applications: a DFT study. *Nanosystems: Phys. Chem. Math.*, 2025, **16** (6), 763–769.

1. Introduction

The increasing demand for electronic devices and electric vehicles has created a need for efficient electrical energy sources [1]. As environmental degradation continues, there is a heightened emphasis on eco-friendly energy solutions, such as supercapacitors. Supercapacitors are beneficial not only because they are environmentally friendly, but also due to their high energy and power densities, as well as their excellent charging and discharging capabilities [2, 3]. Researches [4–6] show that the total capacitance C of a supercapacitor electrode is determined by the series combination of two capacitances: the electric double-layer capacitance (C_{EDL}) and the quantum capacitance C_Q, as represented in equation (1):

$$\frac{1}{C} = \frac{1}{C_Q} + \frac{1}{C_{\text{EDL}}}. \tag{1}$$

From equation (1), it is evident that materials possessing a low quantum capacitance will correspondingly show a reduced total capacitance. Hence, the examining the quantum capacitance characteristics of supercapacitor electrode materials is essential. On the other hand, among materials, the aluminum nitride (AlN) possesses a large band gap, making it suitable for optoelectronic and modern electronic applications [7, 8]. At the nanoscale, AlN nanostructures are relatively obscure in terms of experimental findings. However, a few works validate the existence of nanowires, nanotubes, and nanosheets, although they remain in an early stage [9–15]. Among these nanostructures, the 2D nanosheet with a honeycomb lattice structure has attracted significant research interest [16–19]. In this study, we rigorously explore the impact of defects on the quantum capacitance of AlN nanosheets (AlNNS). Before delving into quantum capacitance (C_Q) and the derived surface charge (Q), we systematically investigate the structural stability and electronic properties of the defected monolayer. The impurity states arising from the defects are expected to introduce new energy states within the wide band gap of the AlN monolayer. These states are likely to play a vital role in describing C_Q of the nanosheet.

2. Methodology

A 5×5 hexagonal supercell consisting of 25 aluminum (Al) and 25 nitrogen (N) atoms is considered as a pristine AlNNS (Fig. 1(a)). To avoid mirror image interactions, a large lattice vector of 20 Å is selected along the Z-axis. Mono-vacancy or divacancy are created by removing either single Al/N atom or by removing the nearest Al–N bond from the thinned planar layer (Fig. 1(b,c,d)).

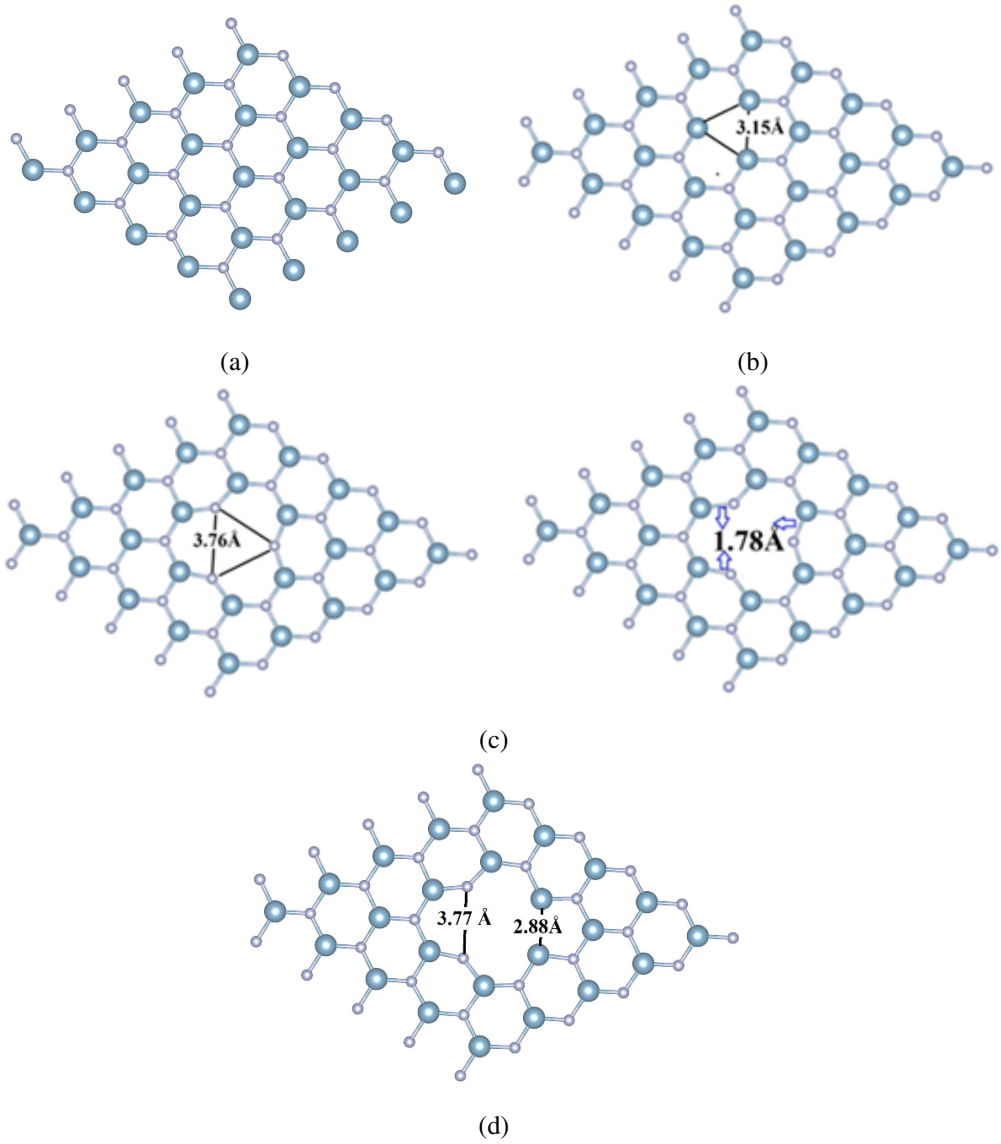

FIG. 1. a) Pristine, b) Al-deficient, c) N-deficient and d) Al–N-deficient aluminum nitride nanosheet (AlNNS)

The exchange-correlation functional used for structural optimization of both pristine and defective AlNNS are based on the Perdew, Burke, and Ernzerhof (PBE) [20] method in the frame of generalized gradient approximation (GGA). The structures are integrated over the Brillouin zone using a $7 \times 7 \times 1$ k-point Monkhorst–Pack [21] mesh, and a kinetic energy cutoff of 450 eV is employed to ensure geometric accuracy. Valence electrons are modeled with a double-zeta polarization (DZP) basis set, and conjugate gradient techniques are applied to achieve geometric perfection with residual forces below 0.05 eV/Å. For core-valence interactions, the Troullier–Martins [22] norm-conserving pseudopotential is utilized. To calculate electronic properties such as the band structure, density of states (DOS) spectra, Mulliken population analysis, and electron difference density, a high-resolution Monkhorst-Pack grid of $17 \times 17 \times 1$ is adopted. All calculations are performed using Spanish Initiative for Electronic Simulations with Thousands of Atoms (SIESTA) quantum chemical code [23, 24].

2.1. Quantum capacitance calculations

In MATLAB [25], the following mathematical expressions are used to compute the quantum capacitance (C_Q) of AlNNS:

$$C_Q = e^2 \int_{-\infty}^{\infty} D(E) F_T \left(E - e\Phi_G\right) dE. \tag{2}$$

The density of states and thermal broadening are represented by $D(E)$ and $F_T(E)$, respectively. E is the eigen-energy, while e denotes the applied bias voltage and electronic charge value. $F_T(E)$ is expressed using a specific relation:

$$F_T(E) = (4k_BT)^{-1} Sech^2(E/2k_BT), \tag{3}$$

where k_B denotes Boltzmann's constant and the standard room temperature is set at $T = 300$ K, it is important to note that an excess charge emerges when the chemical potential (μ_F) is shifted by $e\Phi_G$. This parameter can be accurately calculated using the provided expression:

$$Q = \int_{-\infty}^{\infty} D(E)[f(E) - f\left(E - e\Phi_G\right)]dE. \tag{4}$$

Here $f(E)$ denotes the Fermi–Dirac distribution function, with E representing the relative energy in relation to the Fermi level, E_F.

3. Results and discussion

3.1. Structural and electronic analysis

We initiated our investigation with a primitive hexagonal cell of aluminum nitride (AlN) with a lattice constant of 3.16 Å, a parameter selected based on previous research findings (Fig. S1) [26]. A systematic energy versus lattice constant analysis was conducted to determine the optimal configuration (Fig. S2). This analysis revealed an energy minimum at a lattice constant of 3.10 Å, which was subsequently used for further relaxation procedures. The primitive cell, consisting of one aluminum (Al) and one nitrogen (N) atom, was relaxed to achieve its ground state configuration, resulting in an Al–N bond length of 1.82 Å. The stability of this configuration was confirmed through phonon band dispersion calculations, which showed no imaginary frequencies (Fig. 2(a)). In comparison, the cohesive energy of bulk AlN in the wurtzite phase is -6.01 eV, while that of AlN nanosheet in our calculations is -5.08 eV. This suggests that the freestanding monolayer has low stability compared to bulk wurtzite-AlN. This primitive configuration has an indirect electronic bandgap of 2.92 eV, with the valence band maxima (VBM) and conduction band minima (CBM) located at the K and Γ points, respectively (Fig. 2(b)). A 5×5 AlNNS supercell is generated from the primitive cell and is subsequently relaxed using the DFT framework discussed in the methodology section. Fig. S3 illustrates the electronic band structure of the supercell, which exhibits an indirect bandgap of 2.93 eV. When an aluminium (Al) vacancy was introduced into the AlNNS, significant structural modifications were observed in the vicinity of the defect site. The ground state configuration exhibited local distortion that slightly affected the planarity of the monolayer (Fig. 1(b)). The Al–N bonds associated with under-coordinated N-atoms contracted by 0.40 Å, resulting in a reduced bond length of 1.78 Å.

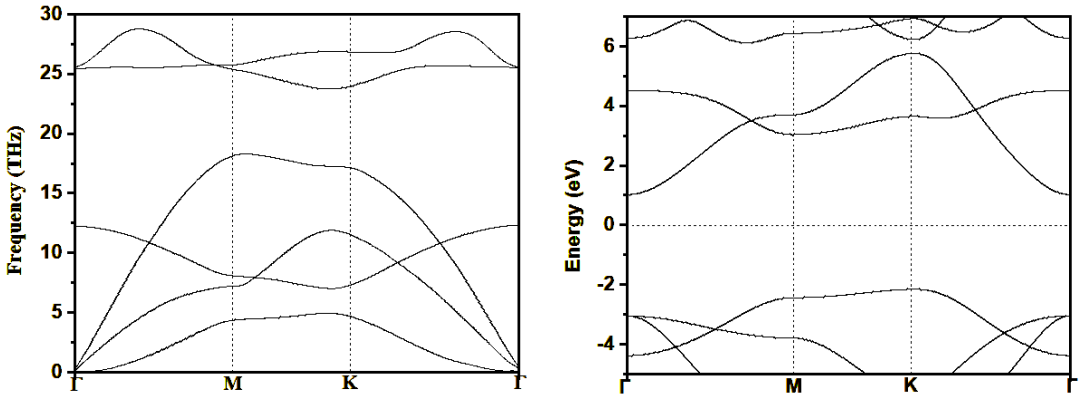

(a) (b)

FIG. 2. a) Phonon spectra and b) electronic band structure of primitive AlN nanosheet (AlNNS)

This structural reconfiguration can be attributed to electronic reorganization around the vacancy site. The three nitrogen atoms adjacent to the vacancy site, each with one unbound electron in their $2p_z$ state, undergo reorganization into $2p_x$, $2p_y$, or $2p_z$ states. This electronic rearrangement stabilizes the distorted geometry through a mechanism known

as pseudo Jahn–Teller distortion. To investigate the stability of Al/N or Al-N vacancy defects in AlNNSs, we conduct detailed calculations of the formation energy associated with these vacancy defects by the following formula:

$$E_f^i(\text{defected AlNNS}) = E_{\text{Tot}}^i(\text{defected AlNNS}) - E_{\text{Tot}}(\text{AlNNS}) + \mu(i). \tag{5}$$

In this context, $E_{\text{Tot}}^i(\text{defected AlNNS})$ represents the total energy of the supercell that contains vacancy defects in AlNNSs, while $E_{\text{Tot}}(\text{AlNNS})$ denotes the total energy of the supercell without such defects. Additionally, $\mu(i)$ signifies the chemical potential of the removed atom i(Al/N/Al–N) within the AlNNSs. The chemical potential of Al and N are calculated in the frame of fcc-Al and N_2 molecule. Calculations reveal Al-deficient and Al–N (divacant) configuration has E_f of 12.22 and 11.63 eV which is relatively larger than $E_f = 8.45$ eV of N-deficient. Suggesting creating N-vacancy is energetically relatively less favorable. The analysis of the electronic band structure (Fig. 3(a)) and density of states (PDOS) (Fig. 3(b)) in the Al-deficient configuration revealed the presence of impurity states above the valence band in the down-spin channel. These impurity states primarily arise from the non-bonding electrons of the nitrogen atoms surrounding the vacancy. In contrast, the up-spin channel maintained a wide bandgap, indicating that the aluminum-deficient AlNNS configuration behaves as a p-type semiconductor. Additionally, the structural puckering around the vacancy site led to a breaking of degeneracy in the energy levels, particularly affecting the M to K region of the lower conduction band.

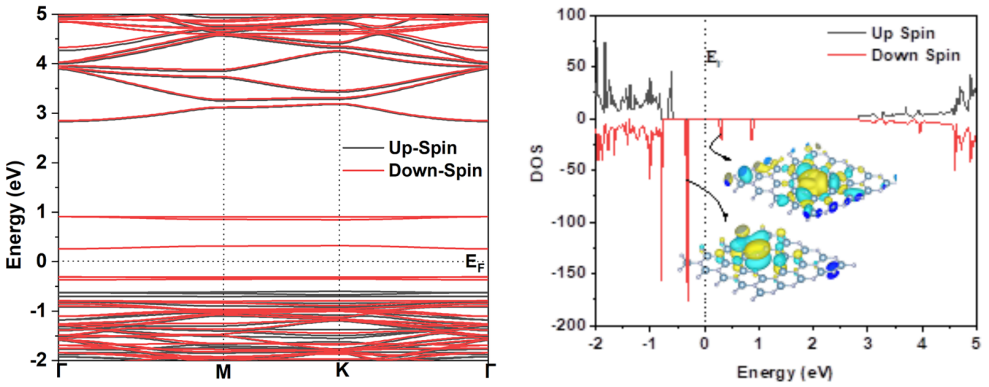

(a) (b)

FIG. 3. a) Electronic band structure and b) PDOS of Al-deficient AlNNS

In contrast to the Al-deficient configuration, the N-deficient monolayer exhibited minimal structural deformation in the vicinity of the vacancy. The primary structural change observed was a slight contraction of the nearest Al-Al distance from 3.16 to 3.15 Å at the vicinity of the defect (Fig. 1(c)). The electronic analysis indicated that the empty $2p_z$ orbitals in the under-coordinated aluminum atoms created an impurity state below the conduction band in the up-spin channel. The electronic band structure and partial density of states (PDOS) analyses (shown in Fig. 4) confirmed that the nitrogen-deficient configuration behaves as an n-type semiconductor.

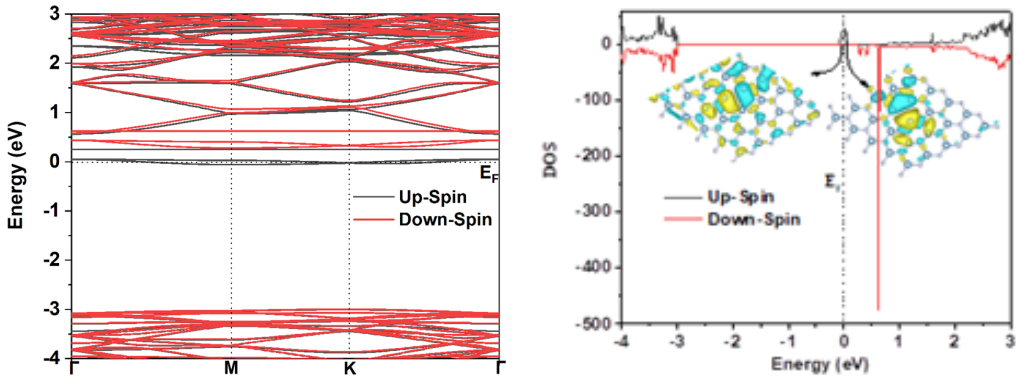

(a) (b)

FIG. 4. a) Electronic band structures and b) PDOS of N-deficient AlNNS

We further extended our investigation to include an Al–N divacancy, created by removing a nearest Al–N bond from one of the hexagonal meshes of the AlNNS. Geometrical analysis revealed significant structural modifications, particularly in the nearest N–N bond length close to the divacancy site (Fig. 1(d)), which contracted substantially from 3.16 to

2.88 Å. This configuration features six electrons from two under-coordinated N atoms and empty Al-2p_z orbitals from two under-coordinated Al atoms. These electronic characteristics generate impurity states above and below the valence band and the conduction band, respectively. The contributions from Al-2p_z orbitals appear as electronic bands above the valence state in the both up-spin and down-spin channels, while the nitrogen non-bonding electrons contribute to impurity states below the conduction band. The electronic band structure and PDOS analyses (Fig. 5) confirm that the divacant configuration maintains semiconducting behavior in the both up-spin and down-spin channels. The charge difference density plots for Al-deficient, N-deficient, and Al–N deficient AlNNS configurations are presented in Fig. S4. The charge dispersion analysis within the vicinity of the defected regions indicates that Al-deficient sites act as electrophilic centers, while N-deficient sites function as nucleophilic centers. Interestingly, the Al–N deficient sites demonstrate a competitive feature, exhibiting both electrophilic and nucleophilic characteristics. This dual functionality of the divacancy configuration suggests potential applications in biosensor development, where such sites could interact with a variety of biomolecules.

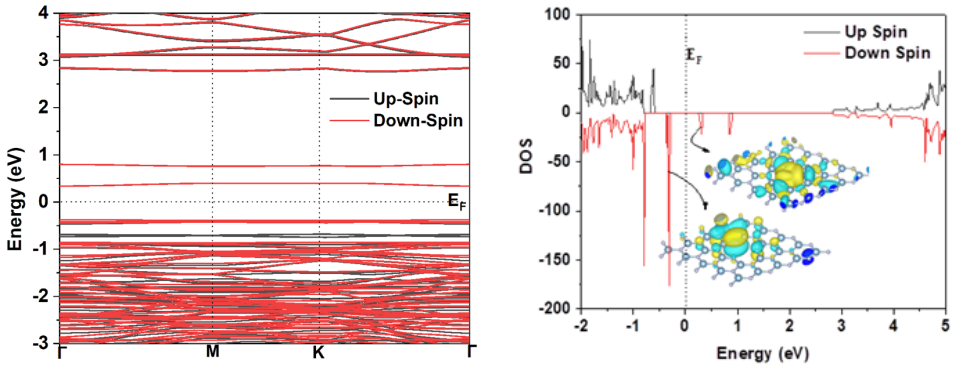

(a) (b)

FIG. 5. a) Electronic band structure and b) PDOS of Al–N-defected AlNNS

3.2. Quantum Capacitance and surface charge

Pristine aluminum nitride nanosheets (AlNNS) exhibit a wide bandgap of 2.93 eV, resulting in no available density of states near the Fermi level. According to equation (2), this characteristic prevents quantum capacitance (C_Q) from being observed within the biased window region of -1.0 to 1.0 V. However, introducing defects creates impurity states that dramatically alter the electronic structure and quantum capacitance properties of these materials. Fig. 6 demonstrates the C_Q and surface charge (Q) spectra of the studied defected AlNNS. The Al-deficient AlN monolayer demonstrates remarkable quantum capacitance properties, primarily in the positive bias region. This defect configuration shows a maximum quantum capacitance ($C_{Q\text{Max}}$) of 690 μF/cm^2 at 0.06 V (Fig. 6(a)), which is attributed to impurity states located below the Fermi level, as evidenced by the band structure and density of states (DOS) plots. Additionally, a continuous C_Q band is observed from 0.36 to 1.00 V, originating from states at the upper edge of the valence band. Surface charge analysis of the Al-deficient system reveals low charge dispersion in the negative biased region, corresponding to the observed low C_Q dispersion in this range. Following equation (4), the maximum surface charge in the positive biased region reaches 357 μC/cm^2 (Fig. 6(b)).

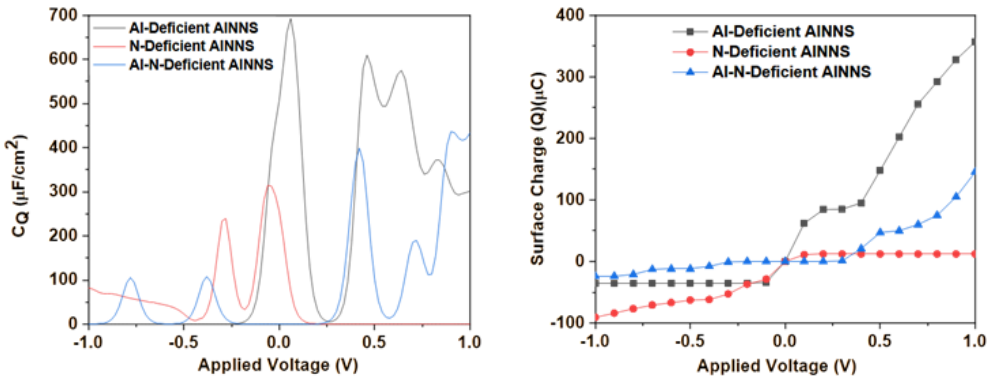

(a) (b)

FIG. 6. a) Quantum capacitance and b) surface charge of defected AlNNS at different biased voltages

These characteristics suggest that Al-deficient AlNNS could serve as an effective anode material for supercapacitor applications [27, 28]. The N-deficient AlN monolayer exhibits a quantum capacitance pattern that differs substantially from the Al-deficient variant. In this configuration, C_Q peaks are predominantly localized in the negative biased region, featuring values of 313 and 239 μF/cm^2. These peaks primarily originate from impurity states introduced by Al-2p$_z$ orbitals. The system also displays a low-valued continuous C_Q spectrum extending from -0.5 to -1.00 V, which can be attributed to the conduction band minima (CBM). This defected nanosheet has a $C_{Q\text{Max}}$ of -93 μC/cm^2, which is reasonable for it to be a cathodic candidate for supercapacitor applications. The Al–N deficient AlNNS exhibits a more complex quantum capacitance spectrum with peaks distributed across both negative and positive biased regions, though the dominant C_Q peaks appear in the positive biased region. The peaks in the positive region primarily originate from non-bonding electrons associated with nitrogen atoms, while peaks in the negative biased region stem from Al-2p$_z$ states situated below the Fermi level. The most prominent C_Q peaks for this divacant configuration reach 39 and 438 μF/cm^2 at 0.4 and 0.9 V, respectively, with a maximum surface charge ($C_{Q\text{Max}}$) of 146 μC/cm^2 in the positive biased region. This intermediate behavior between the Al-deficient and N-deficient systems offers additional flexibility for potential applications. These calculated C_Q peaks are larger than many earlier reports conducted on functionalized 2D surfaces, specifically in the positively biased region [29, 30]. In Table 1, important descriptors associated with Al, N or Al–N deficient AlNNT are shown.

TABLE 1. Different calculated characteristics of mono-vacant and di-vacant AlNNS

Atomic Configuration	Formation energy	Energy Bandgap (eV)	Maximum Quantum Capacitance ($C_{Q\text{Max}}$)	Maximum Surface Charge (Q_{Max})
Al-deficient AlNNS	11.81	0.57 eV	690 μF/cm^2	357 μC/cm^2
N-deficient AlNNS	11.16	Half-metallic	313 μF/cm^2	-93 μC/cm^2
Al–N-deficient AlNNS	8.02	0.68	438 μF/cm^2	146 μC/cm^2

4. Conclusions

This study explores the structural and electronic properties of monovacant and divacant AlNNS (Aluminum Nitride Nanostructures). Formation energy calculations indicate that these structures are feasible. The band structure and density of states (DOS) analyses show that impurity states play a significant role in describing the electronic characteristics of these monolayers. In this context, N-deficient AlNNS demonstrate a robust n-type semiconducting behavior, while Al-deficient AlNNS exhibit strong p-type characteristics. Furthermore, Al–N-deficient AlNNS stand out as wide bandgap semiconductors, showcasing the presence of both acceptor and donor energy levels. Among the different defects Al-deficient AlNNSs exhibits $C_{Q\text{Max}}$ of 690 μF/cm^2 and Q_{Max} of 357 μC/cm^2. The nitrogen-defected AlNNS demonstrates excellent performance as a cathode material with a maximum quantum capacitance of 313 μF/cm^2 and a maximum charge capacity of 91 μC/cm^2. In contrast, the aluminum-defected NS shows properties suitable for anode applications, with a maximum quantum capacitance of 32 μF/cm^2 and a maximum charge capacity of 23 μC/cm^2. The Al–N divacancy configuration exhibits an intermediate behavior with prominent quantum capacitance peaks in both biased regions, offering additional flexibility for potential applications. These findings establish defected AlN monolayers as promising electrode materials for next-generation supercapacitors, with their performance characteristics being highly tunable through defect engineering.

References

[1] Hughes Z.E., Walsh T.R. Computational chemistry for graphene-based energy applications: progress and challenges. *Nanoscale*, 2015, **7** (13), P. 6883–6908.

[2] Ponnamma D., Vijayan P., Al Ali Al-Maadeed M. 3D architectures of titania nanotubes and graphene with efficient nanosynergy for supercapacitors. *Mater. Des.*, 2017, **117**, P. 203–212.

[3] Wang G., Zhang L., Zhang J. A review of electrode materials for electrochemical supercapacitors. *Chem. Soc. Rev.*, 2012, **41** (2), P. 797–828.

[4] Pak A.J., Paek E., Hwang G.S. Relative contributions of quantum and double layer capacitance to the supercapacitor performance of carbon nanotubes in an ionic liquid. *Phys. Chem. Chem. Phys.*, 2013, **15** (44), P. 19741–19747.

[5] Stoller M.D., Magnuson C.W., Zhu Y., Murali S., Suk J.W., Piner R., Ruoff R.S. Interfacial capacitance of single layer graphene. *Energy Environ. Sci.*, 2011, **4** (11), P. 4685–4689.

[6] Xia J., Chen F., Li J., Tao N. Measurement of the quantum capacitance of graphene. *Nat. Nanotechnol.*, 2009, **4** (8), P. 505–509.

[7] Vurgaftman I., Meyer J.N. Band parameters for nitrogen-containing semiconductors. *J. Appl. Phys.*, 2003, **94** (6), P. 3675–3696.

[8] Wu J. When group-III nitrides go infrared: New properties and perspectives. *J. Appl. Phys.*, 2009, **106** (1), 011101.

[9] Zhang Y., Liu J., He R., Zhang Q., Zhang X., Zhu J. Synthesis of aluminum nitride nanowires from carbon nanotubes. *Chem. Mater.*, 2001, **13** (11), P. 3899–3905.

[10] Wu Q., Hu Z., Wang X., Lu Y., Chen X., Xu H., Chen Y. Synthesis and characterization of faceted hexagonal aluminum nitride nanotubes. *J. Am. Chem. Soc.*, 2003, **125** (34), P. 10176–10177.

[11] Stan G., Ciobanu C.V., Thayer T.P., Wang G.T., Creighton J.R., Purushotham K.P., Cook R.F. Elastic moduli of faceted aluminum nitride nanotubes measured by contact resonance atomic force microscopy. *Nanotechnology*, 2008, **20** (3), 035706.
[12] Zhang X., Liu Z., Hark S. Synthesis and optical characterization of single-crystalline AlN nanosheets. *Solid State Commun.*, 2007, **143** (6-7), P. 317–320.
[13] Lei M., Song B., Guo X., Guo Y.F., Li P.G., Tang W.H. Large-scale AlN nanowires synthesized by direct sublimation method. *J. Eur. Ceram. Soc.*, 2009, **29** (1), P. 195–200.
[14] Wang P., Wang T., Wang H., Sun X., Huang P., Sheng B., Wang X. Experimental evidence of large bandgap energy in atomically thin AlN. *Adv. Funct. Mater.*, 2019, **29** (36), 1902608.
[15] Han L., Li Y., Zhao Y., Meng X., Lei X., Yang X., Liu M. One-time mass production of AlN nanosheets: Synergistic effect of high-energy shear and effective collision in a sanding mill. *Ceram. Int.*, 2024, **50** (11), P. 19642–19649.
[16] Javaheri S., Babaeipour M., Boochani A., Naderi S. Electronic and optical properties of V doped AlN nanosheet: DFT calculations. *Chin. J. Phys.*, 2018, **56** (6), P. 2698–2709.
[17] Peng Y., Xia C., Zhang H., Wang T., Wei S., Jia Y. Tunable electronic structures of p-type Mg doping in AlN nanosheet. *J. Appl. Phys.*, 2014, **116** (4), 044306.
[18] Liu P., De Sarkar A., Ahuja R. Shear strain induced indirect to direct transition in band gap in AlN monolayer nanosheet. *Comput. Mater. Sci.*, 2014, **86**, P. 206–210.
[19] Tsipas P., Kassavetis S., Tsoutsou D., Xenogiannopoulou E., Golias E., Giamini S.A., Grazianetti C. et al. Evidence for graphite-like hexagonal AlN nanosheets epitaxially grown on single crystal Ag(111). *Appl. Phys. Lett.*, 2013, **103** (25), 251605.
[20] Perdew J.P., Burke K., Ernzerhof M. Generalized gradient approximation made simple. *Phys. Rev. Lett.*, 1996, **77** (18), P. 3865–3868.
[21] Monkhorst H.J., Pack J.D. Special points for Brillouin-zone integrations. *Phys. Rev. B*, 1976, **13** (12), P. 5188–5192.
[22] Troullier N., Martins J.L. Efficient pseudopotentials for plane-wave calculations. *Phys. Rev. B*, 1991, **43** (3), P. 1993–2006.
[23] Ordej'on P., Artacho E., Soler J.M. Self-Consistent Order-N Density-Functional Calculations for Very Large Systems. *Phys. Rev. B*, 1996, **53** (16), R10441–R10444.
[24] Soler J.M., Artacho E., Gale J.D., Garc'ia A., Junquera J., Ordej'on P., S'anchez-Portal D. The Siesta method for ab initio order-N materials simulation. *J. Phys.: Condens. Matter*, 2002, **14** (11), P. 2745–2779.
[25] The MathWorks Inc. Statistics and Machine Learning Toolbox Documentation, Natick, Massachusetts: The MathWorks Inc., 2022, URL: https://www.mathworks.com/help/stats/index.html.
[26] Nguyen D.K., Vu T.V., Hoat D.M. Antiferromagnetic ordering in the TM-adsorbed AlN monolayer (TM = V and Cr). *RSC Adv.*, 2022, **12** (26), P. 16677–16683.
[27] SanthiBhushan B., Khan M.S., Bohat V.K., Srivastava A. Quantum capacitance estimations of pyrrolic-rich graphene for supercapacitor electrodes. *IEEE Trans. Nanotechnol.*, 2018, **17** (2), P. 205–211.
[28] Hu R., Shang J. Quantum capacitance of transition metal and nitrogen co-doped graphenes as supercapacitors electrodes: A DFT study. *Appl. Surf. Sci.*, 2019, **496**, 143659.
[29] Mousavi-Khoshdel M., Targholi E., Momeni M.J. First-principles calculation of quantum capacitance of codoped graphenes as supercapacitor electrodes. *J. Phys. Chem. C*, 2015, **119** (47), P. 26290–26295.
[30] Khan Z.R., Abbas Z., Akhter N., Khan M.S., Khan M.S. Enhanced quantum capacitance in Ti, V, Cr, Fe, Ga, Ge, Se, and Br doped arsenene: a first principles investigation. *Chem. Phys. Lett.*, 2023, **823**, 140500.

Submitted 1 August 2025; revised 4 November 2025; accepted 5 November 2025

Information about the authors:

Shamsuddin Ahmad – Department of Physics, Z. A. Islamia P. G. College Siwan, Bihar-841226, India; sahmadzaic@gmail.com

Md. Mahfoozul Haque – Department of Physics, Marwari College, T. M. Bhagalpur University, Bihar-812007, India; mahfooz.haque@gmail.com

Zaheer Abbas – Department of Science and Humanities, Government Engineering College, Jehanabad, Bihar-804407, India; zaheerid@gmail.com

Md. Shahzad Khan – Department of Physics, Z. A. Islamia P. G. College Siwan, Bihar-841226, India; ORCID 0000-0001-9769-582X; kshahzad001@gmail.com

Conflict of interest: the authors declare no conflict of interest.

Data availability statement: The data is available upon request.

Author contribution: The authors confirm contribution to the paper as follows: Dr. Shamsuddin Ahmad has conceptualized, collected data and analyzed the work. Dr. Md. Mahfoozul Haque has reviewed and analyzed, Dr. Zaheer Abbas helped in interpretation of results. Dr. Md. Shahzad Khan has written, reviewed and supervised the work.

NANOSYSTEMS:
PHYSICS, CHEMISTRY, MATHEMATICS

Original article

Lukashenko S.Yu., et al. *Nanosystems: Phys. Chem. Math.*, 2025, **16** (6), 770–777.
http://nanojournal.ifmo.ru
DOI 10.17586/2220-8054-2025-16-6-770-777

Effect of nanoscale water media confinement on the approach curve in SICM

Stanislav Yu. Lukashenko[a], Olga M. Gorbenko[b], Mikhail L. Felshtyn[c], Ivan D. Sapozhnikov[d], Stepan V. Pichakhchi[e], Mikhail V. Zhukov[f], Alexander O. Golubok[g]

Institute for Analytical Instrumentation of the Russian Academy of Sciences, Russia

[a]lukashenko13@mail.ru, [b]gorolga64@gmail.com, [c]mfelsztyn@yandex.ru, [d]isapojnikov@gmail.com, [e]pichakhchi.s@yandex.ru, [f]cloudjyk@yandex.ru, [g]aogolubok@mail.ru

Corresponding author: S. Yu. Lukashenko, lukashenko13@mail.ru

ABSTRACT The features of the ion current dependence on distance when a glass nanopipette with an aperture diameter of ∼100 nm approaches the surface of a solid dielectric in a scanning ion conductivity microscope have been studied. A characteristic peak in the approach curve has been observed when the electrode in the nanopipette with an electrolyte is negatively biased relative to electrode in the bath, while a monotonic current decline occurs with a positive bias. To explain this unusual behavior of the ion current, the model accounting for the overlap of electric double layers and water confinement phenomenon in nanochannels and nanogaps have been proposed. The model demonstrates good agreement with the experimental data and provides a basis for quantitative assessment of surface charge at electrolyte–solid interfaces with nanometer-scale spatial sensitivity.

KEYWORDS nanoscale water confinement, nanopore, peak-effect, Poisson–Nernst–Planck equations, surface charge density

ACKNOWLEDGEMENTS This work is supported by the Ministry of Science and Higher Education of the Russian Federation (Project No. 075-00444-25-00, dated 26.12.2024) and by the Russian Science Foundation (Project No. 24-79-00169.

FOR CITATION Lukashenko S.Yu., Gorbenko O.M., Felshtyn M.L., Sapozhnikov I.D., Pichakhchi S.V., Zhukov M.V., Golubok A.O. Effect of nanoscale water media confinement on the approach curve in SICM. *Nanosystems: Phys. Chem. Math.*, 2025, **16** (6), 770–777.

1. Introduction

Scanning ion conductance microscopy (SICM) is a unique probe microscopy technique [1] that enables non-contact imaging of the topography and local biophysical properties of living cells and soft biological objects in physiological environments with nanometer spatial resolution [2, 3]. High-resolution studies of biological systems are also performed using atomic force microscopy (AFM) [4, 5] or advanced optical microscopy techniques that overcome the diffraction limit [6]. However, SICM has several advantages: it avoids the mechanical damage associated with AFM when probing soft samples, and it is simpler than optical approaches, which require specific fluorescent labels and specialized optical systems. Moreover, SICM inherently relies on ionic currents in liquid media – the very processes that govern cellular function. Thanks to its high spatial and functional sensitivity, SICM has become a powerful tool in cell and molecular biology, enabling studies of ion channel activity, microvilli distribution, cytoskeletal and membrane stiffness, and other critical surface properties in real time [7–9].

The principle of SICM is based on measuring the ionic current flowing between a sample and a nanopipette probe with an aperture diameter of ∼100 nm during mechanical scanning. Far from the sample surface, at distances much larger than the nanopore size, the nanopipette exhibits a saturation current (I_{sat}) that does not depend on the probe-sample separation. The conventional explanation for current reduction near the surface is the geometrical blockage of the nanopore by the sample. To maintain a nanometer-scale gap between the pipette and the surface, SICM employs a feedback control system. Thus, the dependence of ionic current on distance underlies the imaging principle of SICM. Several operating modes exist: constant-current mode [1], AC modulation modes with voltage or distance modulation [10], and the hopping mode [11], in which the probe is sequentially approached and retracted at each scanning point.

For imaging samples with pronounced surface relief, the hopping mode provides superior image quality, though at the expense of slower acquisition compared to DC or AC modes, which are effective only for relatively flat surfaces [12]. Typically, stable SICM operation is achieved by choosing a set-point current of $\sim 99 - 99.5$ % of I_{sat} [1], corresponding to approximately (0.5 – 2) nA at applied voltages of 0.1 – 1 V and noise levels of 1 – 10 pA. When using glass nanopipettes in aqueous solutions, electrical double layers (EDLs) form at the pipette surface. For apertures less than 100 nm, these EDLs overlap inside the nanopore, giving rise to nonlinear current-voltage (I–V) characteristics, known as *ion current*

rectification (ICR). This rectification is highly sensitive to volumetric charge and has been used, for example, in pH sensing [13].

A similar phenomenon occurs when the nanopipette approaches a charged interface: the ionic current near the sample surface increases beyond the reduction expected from simple geometric blockage. This effect is referred to as *surface-induced rectification* [12]. The growing branch of $I(z)$ in this case has been theoretically analyzed in detail [14]. However, several studies [15, 16] reported an experimental peak in $I(z)$, that is, an increase in current to a maximum followed by a monotonic decay. Reanalysis of $I(V)$ data at different probe-sample distances in [17] also revealed a characteristic peak when plotted as $I(z)$. The origin of this peak remains debated: some authors [15] attributed it to "electroosmotic flow separation", but this explanation lacked quantitative support and was later shown to be negligible [18]. Notably, existing theoretical models capture only the monotonic growth of $I(z)$ with surface charge and distance, and fail to reproduce the experimentally observed descending branch. Conventional reasoning attributes this decrease solely to nanopore blockage by the sample. Yet, our experiments indicate that current reduction begins at surprisingly large probe–sample separations, and our PNP-NS simulations reveal that current enhancement due to surface charge can outweigh the geometric blockage.

Thus, the physical origin of the extremum in the SICM approach curve $I(z)$ remains unresolved. We refer to this phenomenon as the "peak effect," which is of interest from both a fundamental and applied perspective. On the one hand, studying the peak effect provides new insight into ionic transport mechanisms in microfluidic systems under nanoscale water confinement. On the other hand, the existence of such extrema must be considered in practice, since peaks in $I(z)$ can compromise the stability of SICM feedback control. At the same time, the peak effect can also be exploited for quantitative measurements, for instance, in probing surface charge densities at liquid–solid interfaces with SICM.

The aim of this work is to investigate the SICM peak effect experimentally and to develop an adequate theoretical model that incorporates the influence of nanoscale water confinement.

2. Experiment

Experimental measurements were performed using a custom-built SICM setup. Nanocapillaries were fabricated from borosilicate glass capillaries BF-100-69 (Shutter Instruments, USA) using a PMP-107 puller (Micro Data Instruments, Inc., USA) by the method of thermal pulling and breaking of glass microcapillaries with outer and inner diameters of 1.2 and 0.69 mm, respectively. The characterization procedure for nanopipettes has been described elsewhere [19]. The cone angle of the nanocapillary tip was about 3°, and the nanopore diameter at the apex was approximately 100 nm. The average ion current rectification (ICR) factor was about 1.15. Approach curves were measured on polystyrene and on cover glass substrates etched in a 10 % NaOH solution at 250 °C. Samples were fixed at the bottom of a Petri dish filled with 1× PBS, the same electrolyte used to fill the nanopipettes. Ag/AgCl electrodes were prepared from 300 μm silver wires chloritized according to [20]. A potential bias from 0 to $\pm$1 V was applied to the electrode inside the glass nanopipette. To minimize mechanical vibrations, acoustic noise, and electromagnetic interference, the setup was mounted on an active vibration-isolation table and enclosed within a Faraday cage. A schematic of the experimental setup is shown in Fig. 1.

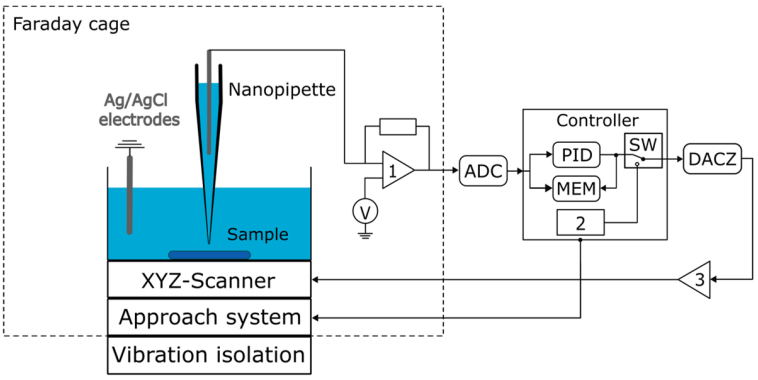

FIG. 1. Schematic diagram of the SICM experimental setup. 1 – current-to-voltage converter, 2 – signals generator, 3 – high-voltage amplifier

For each sample, the ionic current was recorded as a function of the pipette-sample separation at randomly selected surface points. At positive potentials applied to the nanopipette electrode, the approach curves $I(z)$ showed a monotonic decrease in current upon approaching the surface. A representative example measured on etched cover glass is shown in Fig. 2(a), and for polystyrene in Fig. 3(a, curve 1).

In contrast, at negative pipette biases, the $I(z)$ curves exhibited a pronounced peak, as illustrated in Fig. 2(b) and Fig. 3(b, curve 1). SICM images of the same etched glass region, acquired in hopping mode at opposite bias polarities, are shown in Fig. 2(c) and Fig. 2(d). The set-point currents used for imaging are indicated by circles on the $I(z)$ curves.

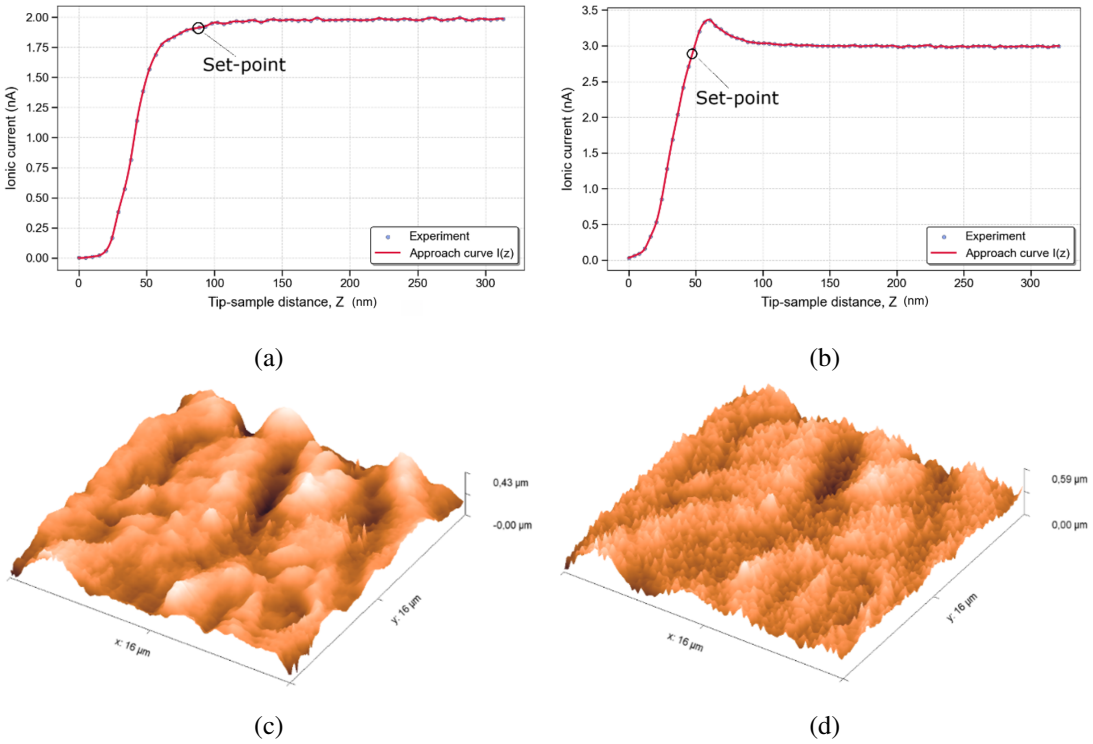

FIG. 2. Approach curves and SICM images for NaOH-etched cover glass. (a, b) $I(z)$ curves at $+300$ mV and -300 mV pipette potentials; (c, d) SICM images of the same sample fragment obtained at positive and negative pipette biases, respectively

Notably, in the case of polystyrene, approach curves with peaks were observed in ∼60 % of randomly selected surface locations, whereas for etched glass, the peak effect was consistently observed at all locations. The peak heights also varied across different positions on the same sample. Importantly, no peaks were ever observed at positive pipette biases. We refer to the emergence of a peak in the $I(z)$ dependence upon approaching the sample surface as the "peak effect."

3. Modeling

To calculate the approach curves $I(z)$ while accounting for the nanopipette geometry, we developed a two-dimensional axisymmetric mathematical model in *COMSOL Multiphysics*, using parameters consistent with our experiments (see in Supplementary materials). For comparison with experimental data, we employed both the standard Poisson–Nernst–Planck–Navier–Stokes (PNP-NS) framework commonly used to describe ionic currents in SICM [19, 21–23] and a modified version proposed here, which incorporates variations of dielectric permittivity, diffusion coefficients, and viscosity under nanoscale water confinement. For reference, we also compared our results with calculations based on the orthodox Ohmic theory [24].

3.1. Standard Poisson–Nernst–Planck–Navier–Stokes model

The ionic flux N_i in micro- and nanofluidic systems is typically described by the PNP-NS system [19, 21–23]:

$$N_i = -D_i \nabla C_i - z_i F u_i C_i \nabla \Phi + u c_i, \tag{1}$$

where D_i is the diffusion coefficient, u_i is the ion mobility, z_i is the ionic charge, F is the Faraday constant, Φ is the electric potential, u is the velocity vector, C_i is the concentration of specific ions type. The first term corresponds to diffusion driven by concentration gradients, the second – to electrophoresis driven by electric field gradients, and the third – to convection through electrolyte flow. In the standard model, diffusion coefficients and ion mobilities are treated as constant throughout the computational domain. For Na^+ and Cl^-, diffusion coefficients were taken from [25], and ion mobilities were calculated using the Nernst–Einstein relation:

$$\mu = \frac{D}{k_B T}, \tag{2}$$

where R is the gas constant and T is the absolute temperature. The surface charge density σ in the electrical double layer (EDL) was defined as:

$$\sigma = -\sqrt{8\varepsilon\varepsilon_0 c_0 k_B T} \cdot \sinh\left(\frac{ze\varphi_0}{2k_B T}\right), \tag{3}$$

where ε is the dielectric constant of the medium, ε_0 is the vacuum permittivity, k_B is the Boltzmann constant, T is the temperature, φ_0 is the surface potential, z is the valency of surface bonds, e is the elementary charge.

To compute the electrostatic field distribution in the EDL, the condition of electroneutrality was not imposed. Instead, the Poisson equation with volumetric charge density was used:

$$\nabla^2\Phi = -\frac{F}{\varepsilon\varepsilon_0}\sum_i z_i c_i, \tag{4}$$

where z_i is the ionic charge, c_i is the concentration of ions of a specific sign.

The third term in equation (1) accounts for electroosmotic flow (EOF), which arises in the diffuse layer. The EOF velocity was found by solving the Helmholtz–Smoluchowski equation:

$$u_{\text{EOF}} = \frac{\zeta\varepsilon\varepsilon_0}{\mu}\nabla\Phi, \tag{5}$$

where Φ is the electric potential, ζ is the zeta potential of the surface.

The EOF velocity in the computational domain was found using the Navier–Stokes equation (Laminar Flow solver):

$$\rho\,(\vec{u}\cdot\nabla)\,\vec{u} = \mu\Delta\vec{u} - \nabla p, \tag{6}$$

where ρ is the electrolyte density, $\vec{u}$ is the flow velocity, p is the pressure, μ is the kinematic viscosity.

Figure 3(a, dashed curve 3) and Fig. 3(b, dashed curve 3) show the calculated $I(z)$ curves obtained using the standard PNP-NS model equations (1–6) for positive and negative pipette biases, respectively. In these simulations, dielectric permittivity, diffusion coefficients, viscosity, and ion mobilities were assumed uniform throughout the domain. For comparison, the orthodox Ohmic approach based on resistance [24] is also shown (Fig. 3, dashed curves 4). Numerical values of simulation parameters are listed in Supplementary materials.

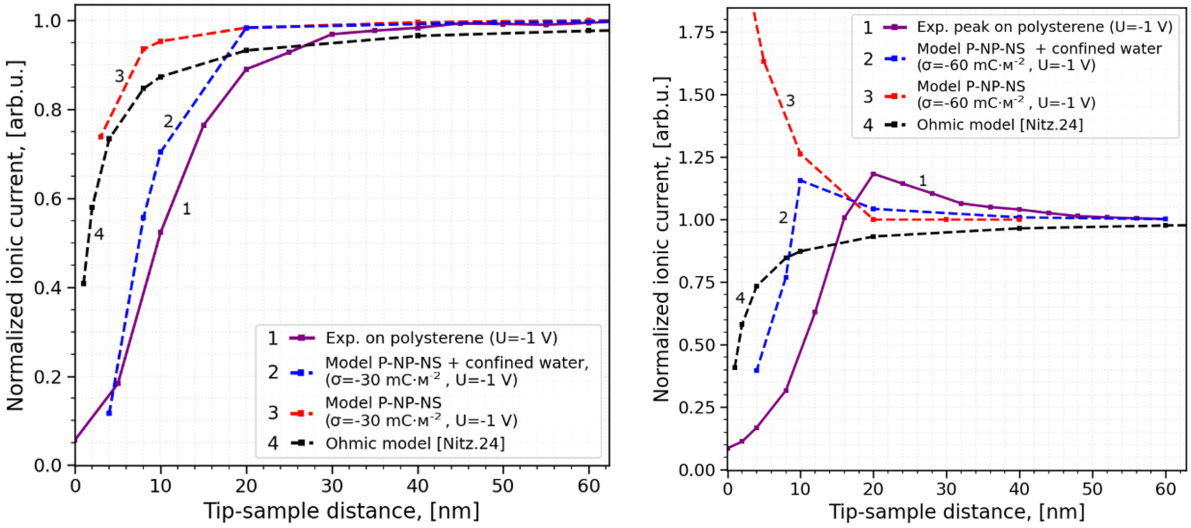

(a) (b)

FIG. 3. Comparison of experimental approach curves $I(z)$ with theoretical curves calculated using different models. (a) Positive bias applied to the nanopipette electrode. (b) Negative bias applied to the nanopipette electrode. PNP-NS models account for sample surface charge density σ. NP's surface charge density for all modeled cases was $\sigma_{pip} = -30$ mC·m^{-2}

3.2. Modified Poisson–Nernst–Planck–Navier–Stokes model under nanoscale water confinement

The standard PNP-NS model described above does not account for interionic interactions or for the changes in physicochemical properties of electrolytes that arise under nanoscale confinement of water. It is well established that water near solid interfaces exhibits properties markedly different from those of bulk water. Molecules form structured interfacial layers with restricted mobility, giving rise to two coupled effects: an increase in viscosity and a decrease in dielectric permittivity.

For instance, it has been reported that in 40 nm gaps, water viscosity is reduced by 5 % compared to bulk values, while at 1 nm separations it increases by nearly an order of magnitude [26–28]. Molecular dynamics simulations [29] further show that when two surfaces are separated by > 100 nm, water retains bulk-like properties with dielectric permittivity $\varepsilon \approx 80$. As the gap decreases, however, ε drops by an order of magnitude to values as low as 5 – 10. This finding has also been confirmed experimentally [30].

A reduction in ε lowers the electrostatic screening of ions by water, thereby strengthening ion–ion interactions according to Debye–Hückel theory. In the extended Debye–Hückel–Onsager approximation, the ionic activity coefficient γ_i is explicitly linked to dielectric permittivity [31]:

$$\log_{10}\gamma_i = -\frac{Az^2\sqrt{C_i}}{1+Ba\sqrt{C_i}}, \tag{7}$$

where

$$A = \frac{e^2 B}{2.303 \cdot 8\pi\varepsilon_0\varepsilon k_B T}, \tag{8}$$

$$B = \sqrt{\frac{2e^2 N_A}{\varepsilon_0\varepsilon k_B T}}. \tag{9}$$

Here a is the effective ionic radius, C_i is the molar concentration.

The drop in ε increases the constant A, leading to a reduction in the activity coefficient γ. Under these conditions, bulk diffusion coefficients can no longer be applied. First, tabulated diffusion coefficients are given for infinite dilution, and second, they assume bulk water with $\varepsilon \approx 80$. At electrolyte concentrations above 10 mM/L, ion–ion interactions become significant [32]. A thermodynamic description of diffusion accounting for ion activity, originally developed by Lewis, Debye, and Onsager [31–33], introduces a correction to the diffusion coefficient:

$$D_i = D_i^0\left(1 + C_i \cdot \frac{\delta \ln\gamma_i}{\delta C_i}\right), \tag{10}$$

where D_i^0 is the diffusion coefficient at infinite dilution, C_i is the electrolyte concentration, γ_i is the ionic activity coefficient.

Our simulations show that under *surface-induced rectification* at surface charge densities of -30 mC/m^2, the local ion concentration in the gap can increase 2–3 fold relative to bulk (150 mM/L), while the corrected diffusion coefficient (eq. (10)) decreases by $\sim$10 %.

The dependence $D(\varepsilon)$ calculated from equations (7–10) is shown in Fig. 4. We found that the diffusion coefficient (eq. (10)) is more dependent on the dielectric constant than on the concentration. For example, at a gap of $\sim$15 nm, $\varepsilon \approx$ 30, corresponds to a $\sim$20 % reduction in the diffusion coefficient according to the Lewis–Debye–Onsager model [31]. As reported in [30] with a further decrease of the gap, the permittivity will continue to decrease even more. With the dielectric permittivity value of $\varepsilon \approx 7$, the coefficient of diffusion of the aqueous solution with a concentration of $C = 150$ mM/L via equation (10) tends to zero (Fig. 4).

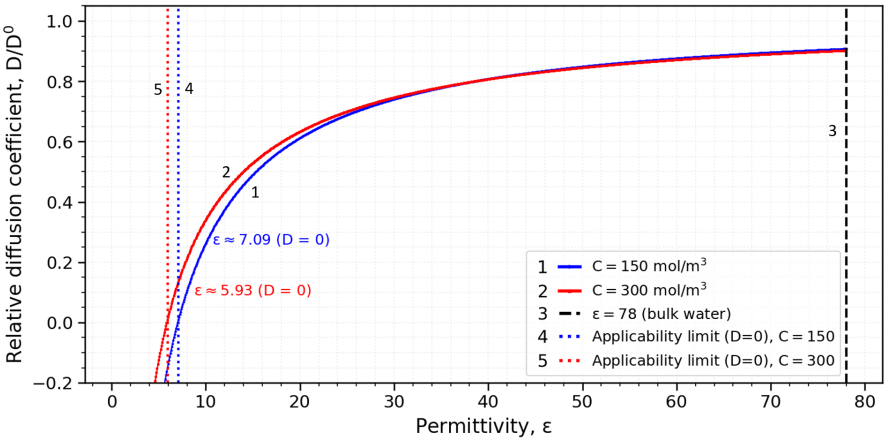

FIG. 4. The dependence of the diffusion coefficient on the electrolyte permittivity in the water confinement conditions

This means that with such low values of dielectric permeability, equation (10) ceases to work for the water media. It is clear that $\varepsilon \approx 7$ is a critical value for the dielectric permeability of an aqueous solution of electrolyte, below which there is a radical change in the ion transport mode, when the energy of electrostatic interaction between ions begins to significantly exceed the energy of their thermal movement ($k_B T$).

As mentioned above, another important parameter affecting the ion current is dynamic viscosity η of the solvent. An increase in viscosity in the water confinement conditions leads to a decrease in convective flow (electro-osmotic flow) (see equations (1) and (6)), as well as to a decrease in the ion diffusion coefficient according to the Stokes–Einstein equation:

$$D = \frac{k_B T}{6\pi\eta a}, \tag{11}$$

where a is the effective ion radius. Thus, when η increases by a factor of 5 – 10 under confinement, diffusion is proportionally reduced. In equation (6), the value of the kinematic viscosity μ is used. The dynamic and kinematic viscosities are related by the following expression $\mu = \eta/\rho$, where ρ is the density of the medium (kg/m^3).

Figures 3(a, dashed curve 2) and Fig. 3(b, dashed curve 2) present the approach curves $I(z)$ calculated using the modified PNP-NS model that incorporates nanoscale confinement effects. Fig. 5 further illustrates model curves at negative pipette bias for different surface charge densities on the sample.

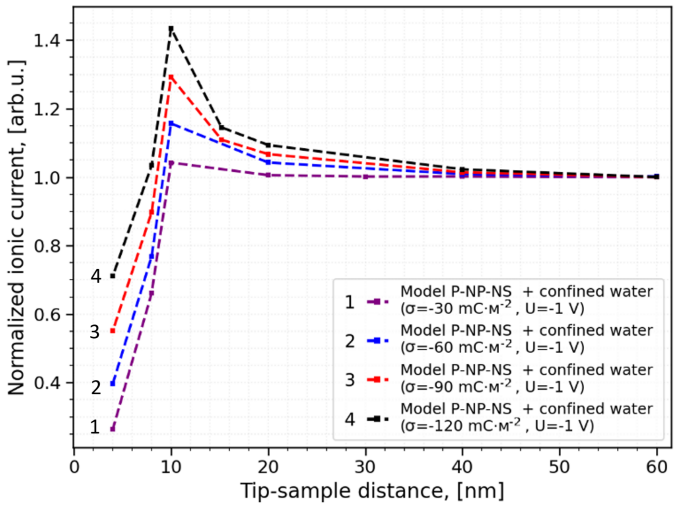

FIG. 5. Theoretical approach curves $I(z)$ with negative voltage bias $U = 1$ V on the electrode in the NP, obtained for different sample surface charges densities σ. NP's surface charge density for all modeled cases was $\sigma_{pip} = -30$ mC·m^{-2}

4. Discussion

When comparing experimental and simulated approach curves $I(z)$, it is important to properly define the probe-sample separation. In the model, the gap is an explicit parameter; in SICM, however, it is not measured directly. Instead, the extension of the piezo scanner is monitored until the ionic current decreases to its minimum detectable value.

In an ideal case with perfectly rigid probes and samples, atomically smooth and parallel surfaces the scanner extension would equal the true distance between the pipette and the sample. The minimum current would then be limited by instrumental noise only. In practice, however, the situation is more complex. On soft surfaces (e.g., polymers or living cells), electroosmotic pressure [34] and Coulombic repulsion between like charges on the pipette and sample can deform the surface, effectively increasing the gap. This introduces systematic errors in estimating the true probe-sample distance from piezo extension. Additional factors such as surface roughness and imperfect parallel alignment also affect the residual current at contact, further complicating tip-sample distance determination.

For this reason, in our analysis we restrict quantitative comparison between experiment and theory to hard, smooth samples (e.g., polystyrene), where errors in gap determination are minimal (Fig. 3(a,b), solid curves 2).

In the conventional interpretation of "no-peak" approach curves in SICM, current decay is attributed to the increasing total resistance, consisting of contributions from the nanopipette interior, the gap, and the bulk electrolyte [24]. In such cases, the descending branch of $I(z)$ is well reproduced both by Ohmic theory (Fig. 3(a, dashed curve 4)) and the classical PNP-NS model (Fig. 3(a, dashed curve 3)). However, comparison with experimental data (Fig. 3(a, solid curve 1)) shows clear discrepancies in the onset of current decay. This indicates that both Ohmic and classical PNP-NS models become inaccurate at nanoscale separations. By contrast, the modified PNP-NS model that includes surface charge and nanoscale water confinement effects (Fig. 3(a, dashed curve 2)) shows significantly improved agreement with experiment.

The sign and magnitude of surface charge on dielectric materials in aqueous media are typically determined by silanol group dissociation or anion adsorption, with glass and most polymers acquiring negative charge at pH greater than 4. In our modeling, surface charge density served as a fitting parameter. The surface charge density of polystyrene extracted from our approach curves was approximately twice the value obtained using a macroscopic surface tension method [35]. We attribute this discrepancy to the different sampling scales: the droplet-deflection method averages over $\sim$1 mm^2, whereas SICM provides highly localized measurements ($\sim 10^{-8}$ mm^2), which can differ from the mean surface charge density value.

A more pronounced divergence between experiment and theory arises under negative pipette bias, when current enhancement due to surface charge is observed. In principle, such enhancement can occur at both positively and negatively charged surfaces. For negatively charged materials such as glass, many polymers, and chromosomes in physiological

solutions [16], the growth branch appears at negative pipette potentials. For positively charged surfaces (e.g., APTES-modified or poly-L-lysine-treated glass), enhancement occurs at positive bias [15, 36].

In our experiments with polymer samples, the appearance of a peak was probabilistic ($\sim$60 %). We attribute this to surface heterogeneity, arising from local roughness and random distribution of functional groups. To test this hypothesis, we prepared glass samples with more uniform surface by etching in NaOH at 250 °C. On these surfaces, the peak effect was consistently observed ($\sim$100 %). However, we did not compare these data directly with simulations, since deformation and roughening of the etched glass surface must be considered. Indeed, Fig.2 shows that the effective tip-sample separation for etched glass is more than twice that for polystyrene (Fig. 3, solid curve 1). This indicates surface softening after alkali etching, consistent with sample deformation effects when decreasing the gap.

As emphasized earlier, the current growth branch of $I(z)$ has been extensively studied as a function of surface charge, pH, electrolyte concentration, and pipette aperture. However, all previous models predict monotonic growth up to zero gap (Fig. 3(b, curve 3)), and cannot reproduce the experimentally observed peak. Our model, which incorporates surface charge, reduced permittivity, and increased viscosity under nanoscale confinement, explains the origin of the peak. Specifically, confined water conditions halt the unbounded current growth otherwise predicted for a negatively biased glass pipette approaching a negatively charged surface.

The small offset ($\sim$10 nm) between the experimental and simulated peaks can be explained by the finite stiffness and roughness of polystyrene [37] and by slight misalignment between the pipette and the sample surface. Fig. 5 further illustrates that peak height is sensitive to sample surface charge density, highlighting the potential of SICM as a nanoscale probing method of local surface charge of living cells.

Finally, the presence of a peak in $I(z)$ has practical implications for SICM operation. In standard feedback mode, the set-point is typically chosen at 99 % of I_{sat}. In the presence of a peak, however, this working point lies on the much steeper descending branch of $I(z)$ (Fig. 2(b)) compared to a no-peak curve (Fig. 2(a)). As a result, SICM images acquired under peak-effect conditions (Fig. 2(d)) exhibit increased noise relative to images obtained at positive bias without a peak (Fig. 2(c)). Thus, while the peak effect can serve as a useful tool for local surface charge detection and measurements, it must also be considered to ensure stable feedback operation.

References

[1] Hansma P.K., Drake B., Marti O., Gould S.A., Prater C.B. The scanning ion-conductance microscope. *Science*, 1989, **243** (4891), P. 641–643.

[2] Korchev Y.E., Bashford C.L., Milovanovic M., Vodyanoy I., Lab M.J. Scanning ion conductance microscopy of living cells. *Biophys. J.*, 1997, **73** (2), P. 653–658.

[3] Klenerman D., Korchev Y.E., Davis S.J. Imaging and characterisation of the surface of live cells. *Curr. Opin. Chem. Biol.*, 2011, **15** (5), P. 696–703.

[4] Rheinlaender J., Geisse N.A., Proksch R., Schäffer T.E. Comparison of scanning ion conductance microscopy with atomic force microscopy for cell imaging. *Langmuir*, 2011, **27** (2), P. 697–704.

[5] Pleskova S.N., Bezrukova N.A., Gorshkova E.N., Bobyk S.Z., Lazarenko E.V. A study of EA.hy926 endothelial cells using atomic force and scanning ion conductance microscopy. *Cell Tissue Biol.*, 2024, **18** (1), P. 36–44.

[6] Gorelik J., Shevchuk A., Ramalho M., Elliott M., Lei C., Higgins C.F., et al. Scanning surface confocal microscopy for simultaneous topographical and fluorescence imaging: application to single virus-like particle entry into a cell. *Proc. Natl. Acad. Sci. U.S.A.*, 2002, **99** (25), P. 16018–16023.

[7] Gu C., et al. Scanning ion conductance microscopy of living renal epithelial cells. *Kidney Int.*, 2002, **61** (3), P. 1250–1255.

[8] Shevchuk A.I., et al. Imaging proteins in membranes of living cells by high-resolution scanning ion conductance microscopy. *Angew. Chem. Int. Ed.*, 2006, **45** (14), P. 2212–2216.

[9] Muhammed Y., De Sabatino M., Lazenby R.A. The heterogeneity in the response of A549 cells to toyocamycin observed using hopping scanning ion conductance microscopy. *J. Phys. Chem. B*, 2025, **129** (20), P. 4904–4916.

[10] Pastre D., Iwamoto H., Liu J., Szabo G., Shao Z. Characterization of AC mode scanning ion-conductance microscopy. *Ultramicroscopy*, 2001, **90**, P. 13–19.

[11] Novak P., Li C., Shevchuk A.I., Stepanyan R., Caldwell M., Hughes S., et al. Nanoscale live-cell imaging using hopping probe ion conductance microscopy. *Nat. Methods*, 2009, **6** (4), P. 279–281.

[12] Page A., Perry D., Unwin P.R. Multifunctional scanning ion conductance microscopy. *Proc. R. Soc. A.*, 2017, **473**, 20160889.

[13] Wang X.-F., Duan Y.-F., Zhu Y.-Q., Liu Z.-J., Wu Y.-C., Liu T.-H., Zhang L., Wei J.-F., Liu G.-C. An insulin-modified pH-responsive nanopipette based on ion current rectification. *Sensors*, 2024, **24** (13), 4264.

[14] Yingfei M., Rujia L., Xiaoyue S., Dengchao W. Quantification of asymmetric ion transport in glass nanopipettes near charged substrates. *ChemElectroChem*, 2021, **8**, 3917.

[15] Clarke R.W., Zhukov A., Richards O., Johnson N., Ostanin V., Klenerman D. Pipette–surface interaction: current enhancement and intrinsic force. *J. Am. Chem. Soc.*, 2013, **135**, 322.

[16] Ushiki T., Ishizaki K., Mizutani Y., Nakajima M., Iwata F. Scanning ion conductance microscopy of isolated metaphase chromosomes in a liquid environment. *Chromosome Res.*, 2021, **29** (1), P. 95–106.

[17] Sa N., Lan W.J., Shi W., Baker L.A. Rectification of ion current in nanopipettes by external substrates. *ACS Nano*, 2013, **7**, 272.

[18] McKelvey K., Kinnear S.L., Perry D., Momotenko D., Unwin P.R. Surface charge mapping with a nanopipette. *J. Am. Chem. Soc.*, 2014, **136**, 13.

[19] Lukashenko S.Yu., Gorbenko O.M., Felshtyn M.L., Sapozhnikov I.D., Kirilenko D.A., Stepan V.P., Zhukov M.V., Golubok A.O. Ionic conductivity in nanopipettes: experiment and model. *Nanosyst.: Phys. Chem. Math.*, 2025, **16** (4), P. 441–449.

[20] Tao D., Jiang L., Jin M. A method of preparation of Ag/AgCl chloride selective electrode. *J. Wuhan Univ. Technol., Mater. Sci. Ed.*, 2018, **33**, P. 767–771.

[21] Cervera J., Schiedt B., Ramirez P. A Poisson/Nernst-Planck model for ionic transport through synthetic conical nanopores. *Europhys. Lett.*, 2005, **71**, 35.

[22] Apel P., Korchev Y.E., Siwy Z., Spohr R., Yoshida M. Diode-like single-ion track membrane prepared by electro-stopping. *Nucl. Instrum. Methods Phys. Res., Sect. B.*, 2001, **184**, 337.

[23] Rabinowitz J., Edwards M.A., Whittier E., Jayant K., Shepard K.L. Nanoscale fluid vortices and nonlinear electroosmotic flow drive ion current rectification in the presence of concentration gradients. *J. Phys. Chem. A*, 2019, **123** (38), P. 8285–8293.
[24] Nitz H., Kamp J., Fuchs H. A combined scanning ion-conductance and shear-force microscope. *Probe Microsc.*, 1998, **1**, P. 187–200.
[25] Laurance N. Self-diffusion of the chlorine ion in sodium chloride. *Phys. Rev.*, 1960, **120**, P. 57–62.
[26] Álvarez-Quintana S., Carmona F.J., Palacio L., Hernández A., Prádanos P. Water viscosity in confined nanoporous media and flow through nanofiltration membranes. *Microporous Mesoporous Mater.*, 2020, **300**, 110176.
[27] Bowen W.R., Welfoot J.S. Modelling the performance of membrane nanofiltration—critical assessment and model development. *Chem. Eng. Sci.*, 2002, **57**, P. 1121–1137.
[28] Wesolowska K., Koter S., Bodzek M. Modelling of nanofiltration in softening water. *Desalination*, 2004, **162**, P. 137–151.
[29] Deißenbeck F., Freysoldt C., Todorova M., Neugebauer J., Wippermann S. Dielectric properties of nanoconfined water: a canonical thermopotentiostat approach. *Phys. Rev. Lett.*, 2021, **126** (13), 136803.
[30] Fumagalli L., Esfandiar A., Fabregas R., Hu S., Ares P., Janardanan A., Yang Q., Radha B., Taniguchi T., Watanabe K., Gomila G., Novoselov K.S., Geim A.K. Anomalously low dielectric constant of confined water. *Science*, 2018, **360** (6395), P. 1339–1342.
[31] Girault H.H. *Analytical and Physical Electrochemistry*. EPFL Press: New York, 2004.
[32] Perry D., Momotenko D., Lazenby R.A., Kang M., Unwin P.R. Characterization of nanopipettes. *Anal. Chem.*, 2016, **88**, P. 5523–5530.
[33] Wright M.R. *An Introduction to Aqueous Electrolyte Solutions*. John Wiley & Sons: Chichester, UK, 2007.
[34] Kolmogorov V.S., Erofeev A.S., Woodcock E., Efremov Y.M., Iakovlev A.P., Savin N.A., et al. Mapping mechanical properties of living cells at nanoscale using intrinsic nanopipette–sample force interactions. *Nanoscale*, 2021, **13** (13), P. 6558–6568.
[35] Amadu M., Miadonye A. Determination of the point of zero charge pH of borosilicate glass surface using capillary imbibition method. *Int. J. Chem.*, 2017, **9**, P. 67–84.
[36] Perry D., Al Botros R., Momotenko D., Kinnear S.L., Unwin P.R. Simultaneous nanoscale surface charge and topographical mapping. *ACS Nano*, 2015, **9**, P. 7266–7276.
[37] Meyers G.F., DeKoven B.M., Seitz J.T. Is the molecular surface of polystyrene really glassy? *Langmuir*, 1992, **8** (9), P. 2330–2335.

Submitted 1 October 2025; revised 29 October 2025; accepted 30 October 2025

Information about the authors:

Stanislav Yu. Lukashenko – Institute for Analytical Instrumentation of the Russian Academy of Sciences, Russia; ORCID 0000-0002-5356-1261; lukashenko13@mail.ru

Olga M. Gorbenko – Institute for Analytical Instrumentation of the Russian Academy of Sciences, Russia; ORCID 0000-0002-7054-6602; gorolga64@gmail.com

Mikhail L. Felshtyn – Institute for Analytical Instrumentation of the Russian Academy of Sciences, Russia; ORCID 0000-0001-8677-061X; mfelsztyn@yandex.ru

Ivan D. Sapozhnikov – Institute for Analytical Instrumentation of the Russian Academy of Sciences, Russia; ORCID 0000-0003-2575-5015; isapojnikov@gmail.com

Stepan V. Pichakhchi – Institute for Analytical Instrumentation of the Russian Academy of Sciences, Russia; ORCID 0000-0002-8578-5200; pichakhchi.s@yandex.ru

Mikhail V. Zhukov – Institute for Analytical Instrumentation of the Russian Academy of Sciences, Russia; ORCID 0000-0003-3361-6947; cloudjyk@yandex.ru

Alexander O. Golubok – Institute for Analytical Instrumentation of the Russian Academy of Sciences, Russia; ORCID 0000-0001-9970-9172; aogolubok@mail.ru

Conflict of interest: the authors declare no conflict of interest.

NANOSYSTEMS:
PHYSICS, CHEMISTRY, MATHEMATICS

Filipov I., et al. *Nanosystems: Phys. Chem. Math.*, 2025, **16** (6), 778–784.
http://nanojournal.ifmo.ru
DOI 10.17586/2220-8054-2025-16-6-778-784

Original article

Heterodyne detection method of multimode states for subcarrier wave continuous variable quantum key distribution

Ilya Filipov[1,2,a], Roman Goncharov[1,b], Michael Dashkov[3,c], Ekaterina Bogdanova[3,d], Alexandr Zinovev[1,e], Vladimir Chistiakov[1,f], Fedor Kiselev[1,2,g]

[1]ITMO University, Saint Petersburg, Russia

[2]SMARTS-Quanttelecom LLC, Saint Petersburg, Russia

[3]Povolzhskiy State University of Telecommunications and Informatics (PSUTI), Samara, Russia

[a]imfilipov@itmo.ru, [b]rkgoncharov@itmo.ru, [c]m.dashkov@psuti.ru, [d]ei.bogdanova@psuti.ru, [e]avzinovev@itmo.ru, [f]v_chistyakov@itmo.ru, [g]fdkiselev@itmo.ru

Corresponding author: Ilya Filipov, imfilipov@itmo.ru

PACS 03.67.-a, 42.50.-p

ABSTRACT A novel coherent detection method for subcarrier wave (SCW) quantum states applied to continuous-variable quantum key distribution (CV-QKD) is presented. The proposed approach relies on repeated phase modulation at the receiver and spatial separation of the carrier and subcarrier frequency components. The resulting output is an intermediate frequency determined by the difference between the sender's and receiver's modulation frequencies. An analytical model of the detection output is developed through time-varying modulation using a classical method based on Bessel functions, and a comparative analysis with alternative heterodyne detection methods is provided. Experimental validation confirms the linear dependence of the output signal on the receiver's modulation frequency and the sender's modulation index in the small-modulation regime. Furthermore, the feasibility of the proposed method is demonstrated through the detection of discretely modulated signals using quadrature phase-shift keying (QPSK).

KEYWORDS coherent detection, subcarrier wave, continuous variable, quantum key distribution.

ACKNOWLEDGEMENTS The work was financially supported by the Russian Science Foundation (project No.24-11-00398)

FOR CITATION Filipov I., Goncharov R., Dashkov M., Bogdanova E., Zinovev A., Chistiakov V., Kiselev F. Heterodyne detection method of multimode states for subcarrier wave continuous variable quantum key distribution. *Nanosystems: Phys. Chem. Math.*, 2025, **16** (6), 778–784.

1. Introduction

Quantum key distribution (QKD) addresses the problem of securely distributing random number sequences between remote parties using quantum states. The two main approaches in QKD are discrete-variable and continuous-variable protocols [1]. Continuous-variable quantum key distribution (CV-QKD) utilizes coherent detection methods and does not require single-photon detectors, which are replaced by balanced detectors based on effective PIN photodiodes. CV-QKD offers several practical advantages: better scalability via integrated photonics [2–4], seamless integration into existing telecom infrastructure [5], and high secure key rates in metropolitan networks [6].

Coherent states in CV-QKD can be generated as single-mode [7] or multimode [8]. Among the latter, one can highlight that subcarrier wave (SCW) coherent quantum states demonstrate higher information capacity [9]. They could also be obtained through phase modulation with discrete [10] and Gaussian modulation [11] without altering the optical setup. The main challenge for SCW states in terms of CV-QKD is the detection method. Existing methods for SCW modulated states include conventional homodyne and heterodyne detection based on 3 dB optical couplers [9], as well as some unique methods based on repeated phase modulation or spectral separation of subcarriers with different phases [8]. The latter were approved through proof-of-concept experiments [10], and appear to enable the use of the carrier mode as a phase-stable local oscillator. These methods require either multiple active optical components or are difficult to implement because of the optical instability of the method.

In this work, we introduce a novel coherent heterodyne detection scheme that overcomes these limitations and paves the way toward a fully practical SCW CV-QKD. Our approach implements repeated phase modulation at the receiver and leverages a deliberate shift in the SCW modulation frequency to define the heterodyne intermediate frequency, thereby decoding both quadratures of the incoming quantum state. We validate this concept through numerical modeling and a proof-of-concept experiment using off-the-shelf fiber-optic components, demonstrating robust quadrature retrieval.

The remainder of this paper is organized as follows. Section 2 introduces the proposed detection method and compares it with previously developed methods. Section 3 presents a proof-of-concept experiment that demonstrates the feasibility of the approach. In Section 4, we discuss the results in the context of the underlying assumptions.

2. Detection principles

Coherent detection of SCW quantum states relies on mixing these states with a strong reference field, the local oscillator. The most common implementation implies the 3 dB coupler, which works for both single-mode and SCW coherent states [9].

Specific techniques have also been developed for SCW states [8, 10]. These exploit the strong carrier mode as a phase-stable local oscillator, made possible by Alice's low modulation index $m_A \ll 1$. One such approach applies repeated phase modulation on Bob's side, then separates carrier and subcarriers into different photodiodes of a balanced detector.

Fig. 1 shows a simplified scheme of this method, along with the optical power spectrum of the transmitted SCW signal. In the inset, we plot the balanced detector output voltage for various phase differences between modulators of Alice and Bob in a simplified form. Phase modulation distributes optical power between the carrier and subcarriers, with the relative phase setting the energy balance. A fiber Bragg grating filter and circulator isolate the carrier: the grating reflects a narrow spectral slice, which the circulator then directs to a second photodiode.

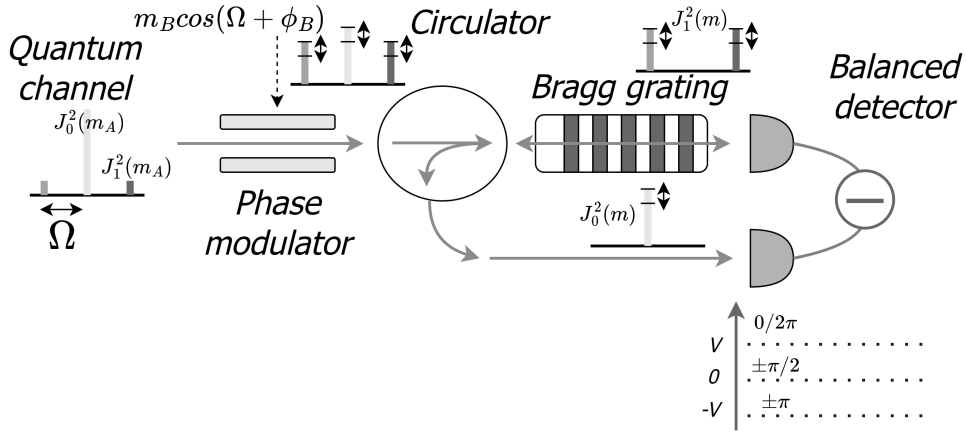

FIG. 1. SCW CV-QKD heterodyne detection based on repeated phase modulation. Top: optical power spectrum of SCW signal. Inset: balanced-detector voltage vs. phase difference

For identical modulation frequencies Ω and Alice's small index $m_A \ll 1$, the balanced detector output is

$$V = R(\lambda)GTE_0^2(1 - 2J_0^2(m)), \tag{1}$$

where $R(\lambda)$ is the photodiode responsivity at wavelength λ, G is the transimpedance gain, E_0 is the field amplitude before modulation, T is the combined channel and receiver transmittance, and J_0 is the zero-order Bessel function (from the Jacobi–Anger expansion), and m is the effective modulation index:

$$m = \sqrt{m_A^2 + m_B^2 + 2m_A m_B \cos\Delta\phi} \tag{2}$$

with m_A, m_B Alice's and Bob's indices and $\Delta\phi$ their phase difference. To balance the optical paths (and cancel the DC component), Bob's index m_B is set to approximately 1.13 [11]. This scheme supports both discrete [8] and Gaussian [11] modulation formats.

Unlike prior works where $\Delta\phi = \phi_A - \phi_B$ was static, we introduce a time dependence by letting $\phi_B(t) = \omega t + \phi_0$, so that

$$m(t) = \sqrt{m_A^2 + m_B^2 + 2m_A m_B \cos\left(\omega t - \phi_A(t) + \phi_0\right)}, \tag{3}$$

Shifting Bob's modulation frequency by ω (to $\Omega' = \Omega + \omega$) thus generates a heterodyne intermediate frequency encoding both quadratures.

Fig. 2 compares the analytical output of the balanced detector for three configurations: the proposed method, a coupler-based method utilizing an external reference field, and the configuration described in [10]. All three recover the intermediate frequency, though the proposed method shows a modest reduction in efficiency.

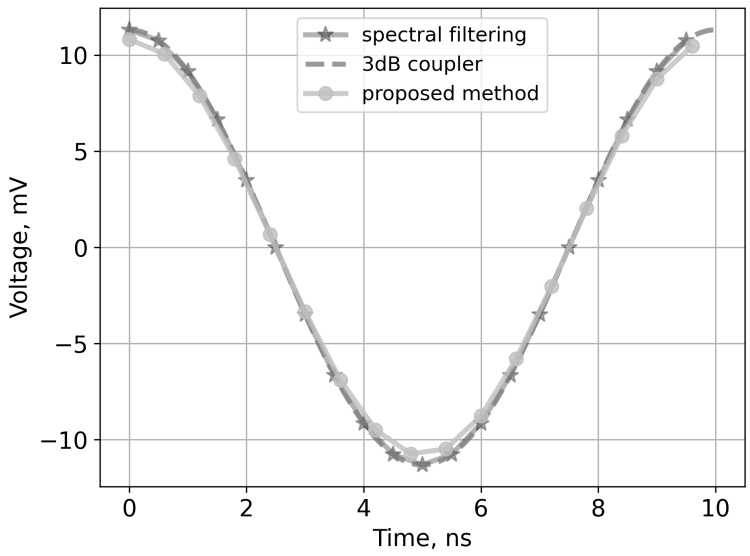

FIG. 2. Analytical comparison of balanced detector outputs for coupler-based heterodyne (dashed), spectral filtering [10] (solid), and the proposed method (dash-dotted)

3. Experimental setup

To validate the assumptions from Section 2, we assembled the experimental setup shown in Fig. 3. It comprises two modules: Alice and Bob. The Alice module includes a tunable Neophotonics laser source (linewidth < 100 kHz, central frequency 193.4 THz) as the optical carrier, a SMARTS - Quanttelecom lithium niobate phase modulator (10 GHz bandwidth) for SCW modulation, and a tunable optical attenuator to control the mean value of the output optical power. The Bob module consists of an identical phase modulator for receiver-side remodulation utilizing shifted modulation frequency and a Teraxion ClearSpectrum fiber Bragg grating filter (bandwidth < 7 GHz) aligned with the carrier frequency, coupled with an optical circulator to separate and route reflected carrier light to the second photodiode. Optical paths were matched by patch cord, and the balanced photodetector BPD-003 by General Photonics was utilized as a shot-noise limited detector with a 200 MHz bandwidth.

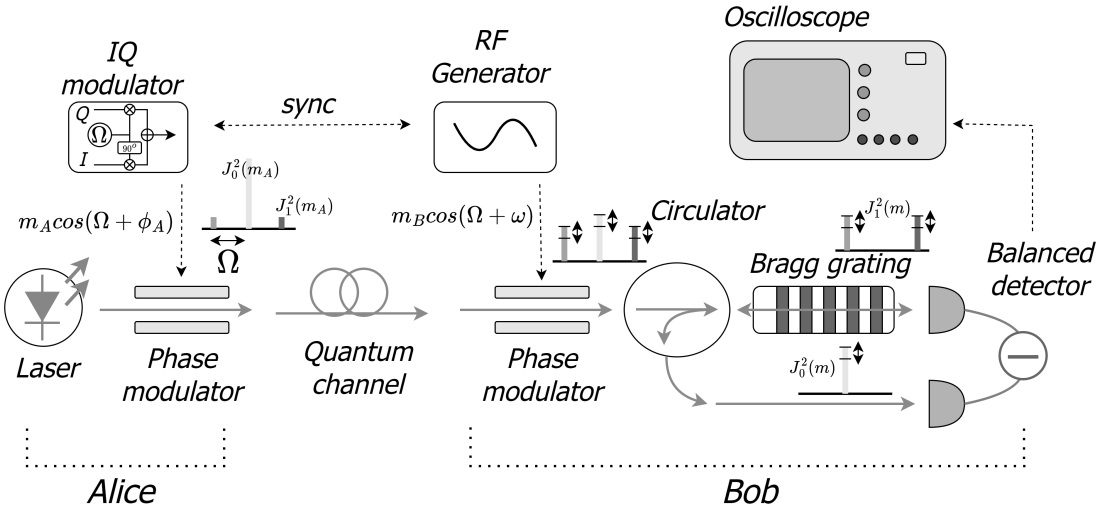

FIG. 3. Experimental setup for validating the SCW CV-QKD detection method

The electronics include a quadrature modulator to generate Alice's modulation signal and an RF generator to set a stable offset frequency on Bob's side. On Alice's side, the quadrature modulator was implemented using a combination of a RF source Rohde&Schwarz SGS100A and an I/Q modulation generator Rohde&Schwarz AFQ100B. The modulation frequency of the RF source was set at $\Omega = 4.8$ GHz. This frequency was selected based on the bandwidth of the fiber Bragg grating filter used on Bob's side. The SCW must fall within the stop band of the grating's reflection spectrum to allow effective spectral separation during detection. Therefore, for the filter used in the experiment, the doubled

modulation frequency 2Ω was required to be at least 9.5 GHz. On Bob's side, a modulation signal was generated using a programmable phase-locked loop (PLL) circuit, allowing for tunable modulation frequency. The synchronization of Alice's and Bob's modulation frequencies was achieved using a 100 MHz reference signal from the RF source to PLL through the wire. The reference clock distribution through the fiber channel, which is commonly employed in discrete-variable QKD systems based on subcarrier waves [12], was omitted in the experimental setup for the sake of simplicity.

The output of the balanced detector was recorded using a Rohde&Schwarz oscilloscope with 1 GHz bandwidth and 5 GSa/s sampling rate without analog filtering. The oscilloscope bandwidth exceeded the one of the balanced detector and the sampling rate provided sufficient oversampling relative to the detector bandwidth. All signal processing was performed offline using digital signal processing techniques.

First, we measured the intermediate frequency's dependence on Bob's remodulation frequency. The results of this measurement are presented in Fig.4. During the experiment, the output frequency of the PLL on the Bob's side was tuned from 4.810 GHz to 4.860 GHz, while all other parameters kept constant. Alice's modulation frequency was set to 4.800 GHz, and no digital I/Q modulation was applied. To analyze the relationship between the measured intermediate frequency and the Bob's modulation frequency, linear regression was employed. The coefficient of determination R^2 for the measured data was found to be approximately 0.999. The observed dependence appears to be linear and is consistent with the assumption presented in Section 2. Due to the frequency synchronization between Alice's and Bob's RF sources, the resulting intermediate frequency exhibited high stability.

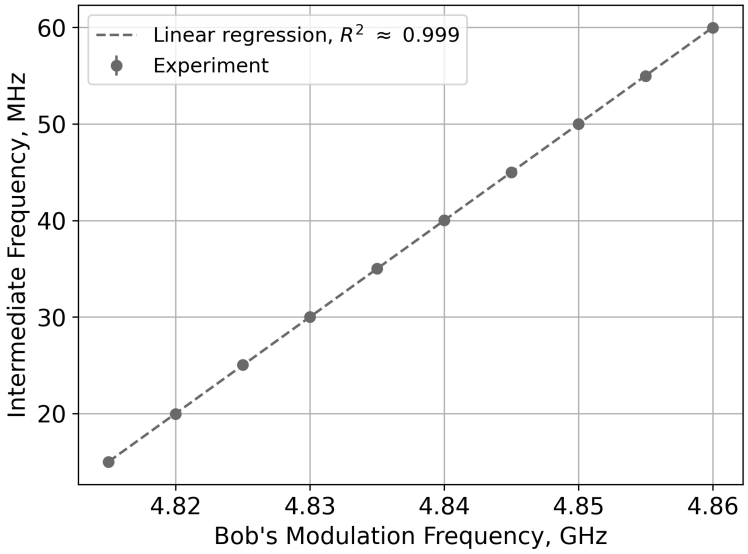

FIG. 4. Intermediate frequency vs. Bob's modulation frequency (Alice fixed at 4.8 GHz). Dots: experimental data; dashed line: linear fit

Second, we evaluated the amplitude linearity of the intermediate-frequency signal as a function of Alice's modulation index m_A in the small-index regime. Establishing linearity is crucial for the implementation of advanced modulation techniques such as Gaussian modulation, probability-shaped QAM, and APSK [13, 14]. The corresponding measurement results are presented in Fig. 5. During the experiment, Alice's modulation index was varied approximately from 0.11 to 0.25 by adjusting the amplitude of the RF source. As in the previous measurement, Alice's modulation frequency was fixed at 4.8 GHz, and digital I/Q modulation was not applied. In addition, Bob's modulation frequency was offset by 50 MHz relative to Alice's frequency to generate a detectable intermediate frequency. To analyze the relationship between Alice's modulation index and Bob's output amplitude, linear regression analysis was performed. The resulting coefficient of determination R^2 was approximately 0.994, indicating a strong linear relationship. This behavior is consistent with the assumptions outlined in Section 2 and further supports the feasibility of applying linear modulation schemes within the proposed detection method.

Finally, we implemented a QPSK modulation to demonstrate the feasibility of detecting discretely modulated SCW signals using the proposed detection method. The modulation sequence was set using the Rohde&Schwarz AFQ 100B signal generator. The symbol rate was set to 1 MHz, and Alice's modulation index m_A was configured to 2.2×10^{-3}. The modulation frequencies of Alice and Bob were fixed at 4.800 GHz and 4.825 GHz, respectively. Fig. 6 shows the result of signal demodulation at the output of the balanced detector. The demodulation process was performed in the digital domain using a digital down-conversion (DDC) scheme. The intermediate frequency signal was subjected to band-pass filtering to isolate the relevant spectral component. This was followed by frequency down-conversion using a digital local oscillator and low-pass filtering to extract the baseband signal. Then, the sampling rate was reduced to match the symbol

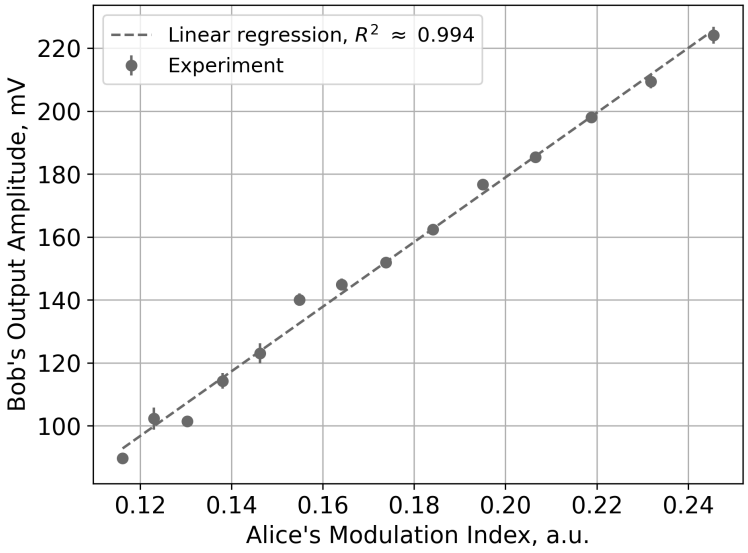

FIG. 5. Intermediate-frequency amplitude vs. Alice's modulation index. Dots: experimental data; dashed line: linear fit

rate. The mapping between the received signal phases and symbol states was performed based on prior knowledge of the transmitted QPSK constellation.

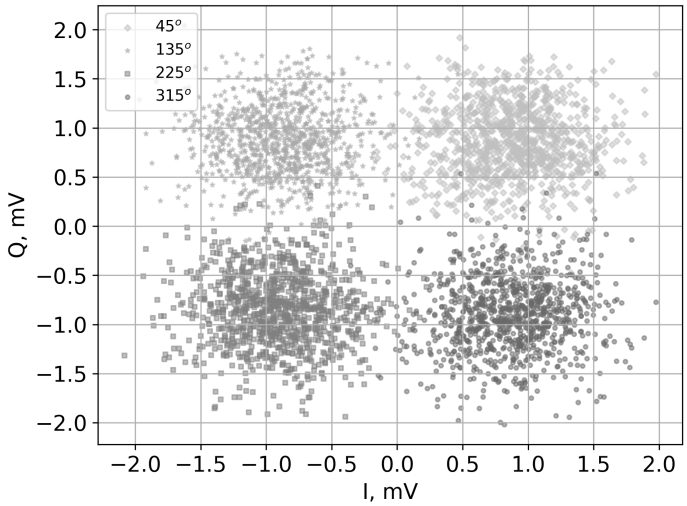

FIG. 6. Constellation diagram of SCW-modulated QPSK at the balanced detector output after digital down-conversion

4. Discussion and conclusion

We have presented a novel detection method for SCW-modulated states through time-varying modulation using a classical method based on Bessel functions. The proposed method produces an output functionally equivalent to established heterodyne techniques while employing a phase-stable approach based on repeated phase modulation. We experimentally demonstrated the reconfigurability of the intermediate frequency and a linear dependence of the output amplitude on Alice's modulation index. As a proof-of-concept, we transmitted and detected a QPSK-modulated signal using this method.

The proposed detection technique addresses several limitations associated with previously reported heterodyne and dual-homodyne detection schemes [10, 11]. Dual-homodyne detection requires a larger number of components compared to standard homodyne detection, including a balanced detector, a phase modulator, and a narrowband fiber Bragg grating filter. This not only increases the cost and complexity of implementation but also introduces additional technical challenges, such as the need for multiple control signals and precise spectral alignment of the fiber Bragg grating filters. In

contrast, the proposed detection scheme neither increases the number of optical components relative to a homodyne setup nor requires fiber Bragg grating filter alignment in Bob's module.

The heterodyne detection method described in [10] relies on matching the filter transmission spectrum with the laser carrier frequency along the slope of the transmission curve. Under this condition, the carrier power is split approximately equally between the reflected and transmitted ports of the fiber Bragg filter. In SCW CV-QKD detection architectures, both the carrier frequency and the filter transmission spectrum are generally sensitive to operational variations in systems employing narrowband filters. Furthermore, the rate of change of the transmission for the central carrier frequency is higher when it lies on the slope of the transmission spectrum than at its peak. This can lead to additional power fluctuations and, in cases of strong variations, to the saturation of one arm of the balanced detector. Positioning the carrier frequency at the transmission peak in the proposed scheme effectively mitigates this source of instability.

Nevertheless, several technical challenges remain before realizing a fully functional SCW CV-QKD system. These challenges span both digital signal processing (DSP) and physical-layer implementation.

First, existing DSP techniques used in single-mode CV-QKD systems [15] must be adapted for the Alice and Bob modules. For example, our experiment omitted pulse shaping on Alice's side to simplify modulation. However, incorporating pulse shaping could confine the modulation spectrum and enable matched filtering via a root-raised-cosine filter.

Second, physical-layer constraints must be addressed. CV-QKD schemes with a transmitted local oscillator require high LO power for shot-noise-limited detection, which can introduce excess noise [16]. The SCW approach offers strong spectral separation between the quantum signal and LO, potentially improving isolation. Conversely, achieving high carrier power relative to subcarriers necessitates a lower Alice modulation index, which may demand specialized hardware solutions.

Finally, the security of the physical implementation must also be carefully considered. Numerous side-channel attacks have been reported for systems based on single-mode states [17], and the relevance of such vulnerabilities to SCW CV-QKD architectures must be systematically evaluated.

References

[1] Pirandola S., Andersen U. L., Banchi L., Berta M., Bunandar D., Colbeck R., Englund D., Gehring T., Lupo C., Ottaviani C., Pereira J.L., Razavi M., Shamsul Shaari J., Tomamichel M., Usenko V.C., Vallone G., Villoresi P., and Wallden P. Advances in quantum cryptography. *Advances in optics and photonics*, 2020, **12**(4), P. 1012–1236.

[2] Zhang G., Haw J.Y., Cai H., Xu F., Assad S., Fitzsimons J.F., Zhou X., Zhang Y., Yu S., Wu J., Ser W. An integrated silicon photonic chip platform for continuous-variable quantum key distribution. *Nature Photonics*, 2019, **13**(12), P. 839–842.

[3] Hajomer A.A. , Bruynsteen C., Derkach I., Jain N., Bomhals A., Bastiaens S., Andersen U.L., Yin X., and Gehring T. Continuous-variable quantum key distribution at 10 gbaud using an integrated photonic-electronic receiver. *Optica*, 2024, **11**(9), P. 1197–1204.

[4] Piétri Y.,Trigo Vidarte L., Schiavon M., Vivien L., Grangier P., Rhouni A., and Diamanti E. Experimental demonstration of continuous-variable quantum key distribution with a silicon photonics integrated receiver. *Optica Quantum*, 2024, **2**(6), P. 428–437.

[5] Hajomer A.A., Derkach I., Usenko V.C., Andersen U.L., and Gehring T. Coexistence of continuous-variable quantum key distribution and classical data over 120-km fiber. *arXiv preprint arXiv:2502.17388*, 2025.

[6] Milovančev D., Vokić N., Laudenbach F., Pacher C., Hübel H., and Schrenk B. High rate cv-qkd secured mobile wdm fronthaul for dense 5 g radio networks. *Journal of Lightwave Technology*, 2021, **39**(11), P. 3445–3457.

[7] Zhang Y., Bian Y., Li Z., Yu S., and Guo H. Continuous-variable quantum key distribution system: Past, present, and future. *Applied Physics Reviews*, 2024, **11**(1).

[8] Samsonov E., Goncharov R., Gaidash A., Kozubov A., Egorov V., and Gleim A. Subcarrier wave continuous variable quantum key distribution with discrete modulation: mathematical model and finite-key analysis. *Scientific Reports*, 2020, **10**(1), P. 10034.

[9] Su Z., Wang J., Cai D., Guo X., Wang D., and Li Z. Experimental demonstration of phase sensitive multimode continuous variable quantum key distribution with improved secure key rate. *Photonics Research*, 2023, **11**(11).

[10] Samsonov E., Goncharov R., Fadeev M., Zinoviev A., Kirichenko D., Nasedkin B., Kiselev A., and Egorov V. Coherent detection schemes for subcarrier wave continuous variable quantum key distribution. *Journal of the Optical Society of America B: Optical Physics*, 2021, **38**(7), P. 2215–2222.

[11] Goncharov R., Kiselev A., Samsonov E., and Egorov V. Subcarrier wave continuous-variable quantum key distribution with gaussian modulation: composable security analysis. *Computer Optics*, 2023, **47**(3), P. 374–380.

[12] Gleim A.V., Egorov V.I., Nazarov Y.V., Smirnov S.V., Chistyakov V.V., Bannik O.I., Anisimov A.A., Kynev S.M., Ivanova A.E., Collins R.J., Kozlov S.A., and Buller G.S. Secure polarization-independent subcarrier quantum key distribution in optical fiber channel using bb84 protocol with a strong reference. *Optics Express*, 2016, **24**(3), P. 2619–2633.

[13] Pereira D., Almeida M., Facao M., Pinto A.N., and Silva N.A. Probabilistic shaped 128-apsk cv-qkd transmission system over optical fibres. *Optics Letters*, 2022, **47**(15), P. 3948–3951.

[14] Roumestan F., Ghazisaeidi A., Renaudier J., Vidarte L. T., Leverrier A., Diamanti E., and Grangier P. Shaped constellation continuous variable quantum key distribution: Concepts, methods and experimental validation. *Journal of Lightwave Technology*, 2024, **42**(15), P. 5182–5189.

[15] da Silva V.L., Dias M.A., Neto N.A.F., and Tacla A.B. From coherent communications to quantum security: Modern techniques in cv-qkd. Proceedings of the Conference "2024 SBFoton International Optics and Photonics Conference (SBFoton IOPC)", Salvador, Brazil, 2024, P. 1–5.

[16] Qi B., Huang L.-L., Qian L., and Lo H.-K. Experimental study on the gaussian-modulated coherent-state quantum key distribution over standard telecommunication fibers. *Physical Review A–Atomic, Molecular, and Optical Physics*, 2007, **76**(5), P. 052323.

[17] Nasedkin B., Goncharov R., Morozova P., Filipov I., Chistiakov V., Samsonov E., and Egorov V. Quantum hacking on the technical implementation of continuous-variable quantum key distribution systems. *Radiophysics and Quantum Electronics*, 2025, **67**(1), P. 23–37.

Submitted 02 October 2025; revised 01 November 2025, 12 November 2025; accepted 13 November 2025

Information about the authors:

Ilya Filipov – ITMO University, 199034, Saint Petersburg, Kadetskaya Line 3k2, Russia; SMARTS-Quanttelecom LLC, 199178, Saint Petersburg, Vasilievsky island 6 Line 59, Russia; ORCID 0000-0003-4564-8284; imfilipov@itmo.ru

Roman Goncharov – ITMO University, 199034, Saint Petersburg, Kadetskaya Line 3k2, Russia; ORCID 0000-0002-9081-8900; rkgoncharov@itmo.ru

Michael Dashkov – Povolzhskiy State University of Telecommunications and Informatics (PSUTI), 443010, Samara, Moskovskoe Shosse St., 77, Russia; ORCID 0000-0002-3919-4151; m.dashkov@psuti.ru

Ekaterina Bogdanova – Povolzhskiy State University of Telecommunications and Informatics (PSUTI), 443010, Samara, Moskovskoe Shosse St., 77, Russia; ei.bogdanova@psuti.ru

Alexandr Zinovev – ITMO University, 199034, Saint Petersburg, Kadetskaya Line 3k2, Russia; ORCID 0000-0003-0789-998X; avzinovev@itmo.ru

Vladimir Chistiakov – ITMO University, 199034, Saint Petersburg, Kadetskaya Line 3k2, Russia; ORCID 0000-0002-2414-3490; v_chistyakov@itmo.ru

Fedor Kiselev – ITMO University, 199034, Saint Petersburg, Kadetskaya Line 3k2, Russia; SMARTS-Quanttelecom LLC, 199178, Saint Petersburg, Vasilievsky island 6 Line 59, Russia; ORCID 0000-0002-3894-511X; fdkiselev@itmo.ru

Conflict of interest: the authors declare no conflict of interests.

NANOSYSTEMS:
PHYSICS, CHEMISTRY, MATHEMATICS

Fedorova M., et al. *Nanosystems: Phys. Chem. Math.*, 2025, **16** (6), 785–790.
http://nanojournal.ifmo.ru
DOI 10.17586/2220-8054-2025-16-6-785-790

Original article

Multilevel physical unclonable function based on silver nanostructures randomly integrated into the crystalline silicon wafer

Maria Fedorova[1,a], Elena Petrova[1,b], Artem Larin[1,c], Martin Sandomirskii[1,d], Anna Ermina[2,e], Sergey Pavlov[2,f], Yuliya Zharova[2,g], Dmitry Permyakov[1,h], Vitaly Yaroshenko[1,i], Dmitry Zuev[1,j]

[1]School of Physics and Engineering, Faculty of Physics, ITMO University, St. Petersburg, Russia
[2]Ioffe Institute, 194021, St. Petersburg, Russia

[a]mariya.fedorova@metalab.ifmo.ru, [b]elena.petrova@metalab.ifmo.ru, [c]artem.larin@metalab.ifmo.ru, [d]m.sandomirskii@metalab.ifmo.ru, [e]annaermina@mail.ioffe.ru, [f]pavlov_sergey@mail.ioffe.ru, [g]piliouguina@mail.ioffe.ru, [h]d.permyakov@metalab.ifmo.ru, [i]v.yaroshenko@metalab.ifmo.ru, [j]d.zuev@metalab.ifmo.ru

Corresponding author: V. Yaroshenko, v.yaroshenko@metalab.ifmo.ru

ABSTRACT We present an optical physical unclonable function (PUF) based on silver nanostructures randomly formed on a crystalline silicon wafer through galvanic displacement and thermal annealing. The process produces nanostructures with stochastic spatial distribution and morphology, resulting in unpredictable nonlinear optical responses. The hybrid Ag–Si interface generates two independent signals: photoluminescence (PL) and second-harmonic generation (SHG). Spatial PL and SHG maps were binarized and analyzed using standard PUF metrics. SHG demonstrated higher entropy and more balanced bit distribution, making it the preferred encoding channel, while PL provides an additional verification layer. The fabrication method is scalable, lithography-free, and compatible with standard silicon processing.

KEYWORDS silver nanostructures, silicon, SHG, photoluminescence, physical unclonable function.

ACKNOWLEDGEMENTS Part of this work related to the photoluminescence measurements was supported by Russian Science Foundation project # 25-72-20030, https://rscf.ru/en/project/25-72-20030/ Part of this work related to the PUF labels creation and studies is supported by the Russian Science Foundation # 25-12-00310, https://rscf.ru/en/project/25-12-00310/

FOR CITATION Fedorova M., Petrova E., Larin A., Sandomirskii M., Ermina A., Pavlov S., Zharova Y., Permyakov D., Yaroshenko V., Zuev D. Multilevel physical unclonable function based on silver nanostructures randomly integrated into the crystalline silicon wafer. *Nanosystems: Phys. Chem. Math.*, 2025, **16** (6), 785–790.

1. Introduction

The modern global economy faces a growing threat from counterfeit goods, which inflict significant financial losses on manufacturers and pose serious risks to consumers, particularly in critical sectors such as pharmaceuticals [1, 2]. Conventional protection methods like holograms and barcodes are vulnerable to copying, as they are created using deterministic algorithms. A promising solution to this problem lies in Physical Unclonable Functions (PUFs), which leverage stochastic processes at their core to ensure the uniqueness and unpredictability of each item [3–5].

PUFs are hardware-based cryptographic primitives that exploit the inherent randomness of their physical structure to generate unique challenge-response pairs. For anti-counterfeiting, optical PUFs are of particular interest due to their high information capacity and resistance to tampering. However, current manufacturing techniques for strong optical PUFs are often incompatible with existing production lines [6] and/or vulnerable to sophisticated machine learning attacks. Furthermore, the long-term security of many PUF designs is threatened by their reliance on microscopic features, which are becoming increasingly susceptible to manipulation as nanoscale technologies advance.

The logical evolution of PUFs involves a shift to nanoscale critical features, which would drastically enhance their resistance to cloning [7,8]. Yet, this transition introduces fundamental readout challenges, requiring sub-diffraction spatial imaging techniques and robustness against higher noise levels. Consequently, a key challenge is the development of PUFs that combine nanoscale complexity with fabrication simplicity and reliable readout protocols. Multi-level security system, that combines different optical responses [9, 10] add complexity into label design, represents a promising direction for creating authentication systems.

Here, we introduce a novel, high-security PUF label based on a stochastic assembly of silver nanoparticles on a silicon wafer. The unique cryptographic identity of each label is derived from its inherent morphological randomness, which

manifests as a non-linear optical response, specifically through second harmonic generation (SHG) and photoluminescence (PL). We detail a scalable fabrication approach for these structures and thoroughly characterize their morphology and optical properties. Furthermore, we demonstrate their practical application as robust PUF label and evaluating their encoding capacity, showcasing their potential for anti-counterfeiting solutions.

2. Results

2.1. Fabrication

Commercial boron-doped (p-type), single-crystal silicon (c-Si) wafers with a thickness of 500 μm and (100) crystallographic orientation, grown by the Czochralski method and chemically dynamically polished on one side, were purchased from Telecom-STV Company Limited (Zelenograd, Russia). The wafers had a resistivity of 10 Ω cm, corresponding to a carrier concentration of approximately 1.4×10^{16} cm^{-3}. For convenience, the wafers were diced into 1×2 cm^2 samples. Prior to experiments, the c-Si samples underwent wet chemical cleaning based on the RCA procedure to remove organic and ionic contaminants. Milli-Q deionized water and fluoroplastic dishes were used throughout the experiment. Argentum nanoparticles (AgNPs) were synthesized on the surface of c-Si wafers (see Fig. 1a) via a galvanic displacement reaction (GDR) using an aqueous solution of 0.02 M $AgNO_3$:5 M HF mixed at volume ratio of 1:1 at room temperature. The c-Si wafer was immersed in the solution for 30 s, then rinsed with deionized water for 30 s, and subsequently dried with compressed air to prevent streak formation on the sample surface. In the GDR process, the reduction of Ag^+ on the c-Si substrate is driven by the substrate itself upon immersion in the solution. In this redox system, c-Si, having a lower electrochemical potential (-0.857 V vs. the standard hydrogen electrode (SHE)), is displaced by Ag^+ ions from the solution, which have a higher potential (0.8 V vs. SHE) [11]. The GDR in an HF-containing solution involves simultaneous anodic and cathodic processes occurring on the c-Si surface, with charge exchange facilitated through the substrate. Fluoride ions play a critical role by dissolving oxidized silicon in the form of silicon hexafluoride (SiF_6^{2-}), thereby preventing the formation of a layer of native silicon oxide (SiO_2). This maintains access to a fresh c-Si surface and sustains the reaction. Thus, the overall ionic redox reaction can be written as follows [11]:

$$4\mathrm{Ag}^+(aq) + \mathrm{Si}_0(s) + 6\mathrm{F}^-(aq) = 4\mathrm{Ag}_0(s) + \mathrm{SiF}_6^{2-}(aq) \tag{1}$$

where aq and s denote the aqueous and solid phases, respectively. The ionic reaction (1) can be interpreted as a short-circuited galvanic cell composed of two electrodes: Cathodic half-reaction:

$$\mathrm{Ag}^+(aq) + e^- = 4\mathrm{Ag}_0(s) \tag{2}$$

Anodic half-reaction:

$$\mathrm{Si}_0(s) + 6\mathrm{F}^-(aq) = \mathrm{SiF}_6^{2-}(aq) + 4e^- \tag{3}$$

where e^- denotes an electron.

Following the galvanic deposition of AgNPs onto c-Si, the samples underwent high-temperature annealing at 1000°C in H_2O atmosphere for 5 min. The annealing process was carried out in a three-phase electric muffle furnace equipped with six silicon carbide heating elements. The furnace temperature was monitored and regulated using a thermocouple positioned in the working zone and controlled via an electronic temperature control unit. During annealing, the experimental samples were placed on a flat quartz support, which was positioned at the long end of a quartz L-shaped tube. The short end of the tube was filled with boiling water to generate water vapor. The entire assembly was then inserted into the furnace's working area. Upon completion of the annealing time, the quartz tube was withdrawn from the furnace, and the samples were allowed to cool to room temperature under ambient conditions. This process yielded SiO_2/AgNPs/c-Si(100) composite structures. The thermally grown SiO_2 layer was selectively removed by immersion in a 1:1 HF:H_2O solution for 5 min(see Fig. 1a). To obtain pits in c-Si, silver was dissolved in boiling HNO_3 for 3 min(see Figs. 1b,c).

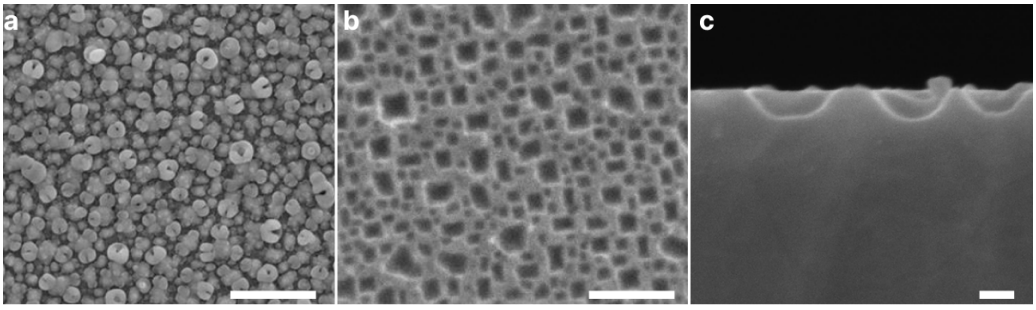

FIG. 1. Morphology of the nanostructures shown by SEM images. (a) Silver nanostructures on the silicon surface. (b-c) c-Si wafer after process of removal SiO_2/AgNPs structures. Top and side view respectively. Scale bar for (a) and (b) corresponds to 1 um, (c) – 100 nm

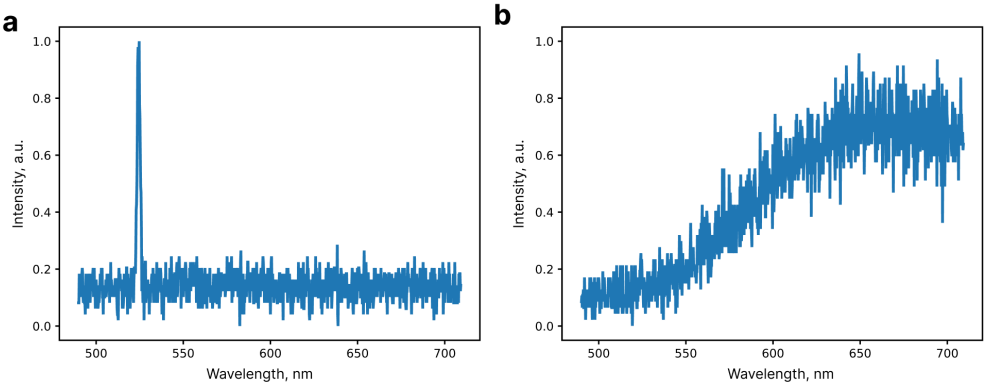

FIG. 2. SHG and PL spectra from nanostructures located at different points of the sample. (a) The spectrum of the structure shows only SHG. (b) The spectrum of the structure shows only PL

2.2. Optical characterization

In the previous section, we described in detail the fabrication process used to synthesize AgNPs embedded in the surface of the crystalline silicon wafer. Due to the stochastic thermodynamic nature of the GDR and annealing processes central to our approach, the AgNPs formed on the resulting samples exhibited random spatial distributions, sizes, and shapes (see Fig. 1a).

Next, we investigated the nonlinear optical properties of the fabricated samples. For this purpose, we employed an ultrafast Yb^{3+} laser system (TeMa, Avesta Project) with a central wavelength of 1050 nm, pulse duration of 150 fs, and repetition rate of 80 MHz. The laser beam was attenuated to 5 mW and focused onto the sample surface using a 100x / 0.7 NA Mitutoyo MPlan APO NIR objective in reflection configuration with dichoic mirror Thorlabs DMSP900. The resulting optical signal from the samples was collected by the same objective and projected onto a charge-coupled device (Andor DU420A-OE 325) placed in a Horiba LabRam HR spectrometer equipped with a 150 lines mm^{-1} diffraction grating.

Fig. 2 shows spectra of second-harmonic generation (SHG) and photoluminescence (PL) recorded from one of the fabricated samples under the described experimental conditions. It can be clearly seen that all observed nonlinear responses arise exclusively in the presence of AgNPs (see Figs. 1,3). This observation is consistent with the fact that bulk silicon possesses an extremely low quantum yield due to its indirect bandgap [12]. In contrast, the formation of metal-semiconductor (Ag–Si) interfaces provides an effective mechanism for enhancing the nonlinear optical response of silicon. Indeed, the metallic component significantly increases optical absorption in the system and facilitates the injection of hot electrons into the active material [13]. This, in turn, leads to a high concentration of electrons in the Si conduction band, improving the radiative recombination efficiency through enhanced Auger recombination [14]. Simultaneously, the SHG signal can be attributed to the local symmetry breaking occurring at the same metal-semiconductor interfaces [15, 16].

Interestingly, analysis of the optical maps reveals that some AgNPs help to generate PL(see Fig. 2b), while others help to produce primarily SHG(see Fig. 2a). We attribute this effect to the possible formation of a thin silver sulfide shell around certain nanoparticles during fabrication [17]. Depending on its thickness and uniformity, this sulfide layer can act as an additional energy barrier at the Ag–Si interface, suppressing hot electron injection into the silicon and thereby reducing PL efficiency (while leaving SHG less affected). Nevertheless, we assume that the formation of such a sulfide shell is a matter of chance, which makes the observed "switching" behavior between PL- and SHG-dominated regions essentially random.

2.3. Designing a PUF label

Here we propose a hybrid optical PUF label based on silicon – silver nanostructures that simultaneously exhibit PL and SHG. The stochastic spatial distribution of nanostructures and there "switching" behavior results from the fabrication process and cannot be deterministically reproduced, which forms the foundation of the PUF design. As explained above these two optical responses arise from different physical mechanisms. Thus, the label naturally offers two independent optical response channels, enabling multi-layer authentication and increased resistance to copping.

To evaluate whether PL and SHG encode independent information, we computed the Pearson correlation coefficient between the binary response patterns extracted from the PL and SHG maps. The Pearson correlation coefficient quantifies the degree of linear dependence between two datasets, ranging from -1 (complete negative dependence) to $+1$ (complete positive dependence), with 0 indicating no correlation. In the context of physically unclonable functions, low correlation is desired, as it indicates that different optical responses do not contain same information and therefore contribute additional security entropy. The coefficient was calculated based on binarized spatial patterns, where each bit corresponds to the presence or absence of an optical signal exceeding noise. The binarization process is shown in Fig. 3.

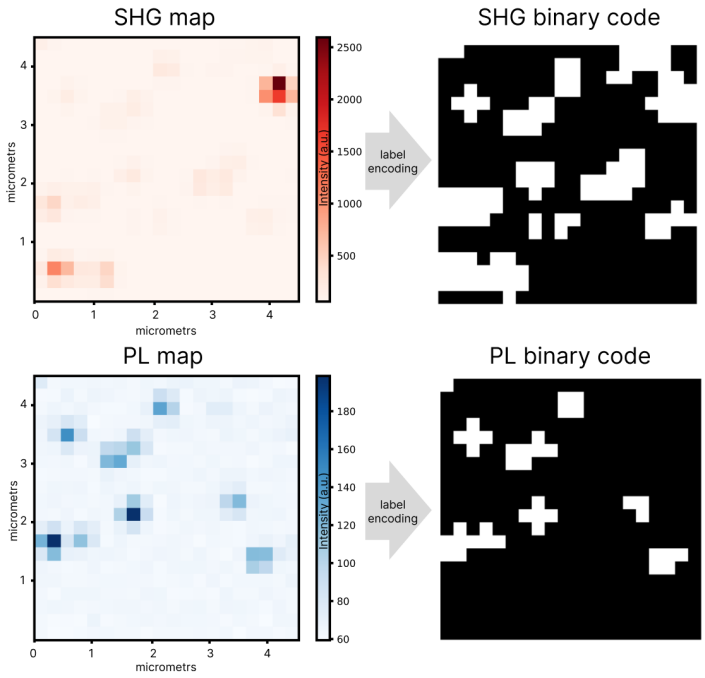

FIG. 3. The encoding scheme of the label. Demonstration of the process of converting SHG and PL intensity maps into binary code

The resulting Pearson correlation coefficient between the PL-derived and SHG-derived patterns was 0.48, indicating only moderate correlation and confirming that SHG does not replicate the PL-encoded information. For comparison, we also analyzed the correlation between PL intensity maps at two wavelengths (650 nm and 700 nm) and obtained a value of 0.86, which is significantly closer to 1. This high correlation is expected because both datasets originate from the same PL mechanism. In contrast, the much lower correlation between PL and SHG demonstrates that the nonlinear optical channel adds an additional, statistically independent layer of cryptographic entropy. These results confirm that combining PL and SHG in a single nanostructured label enables a dual-level optical PUF architecture with enhanced resistance to duplication.

The encoding capacity (EC) of the proposed dual-channel PUF was estimated from the number of independent bits encoded in the PL and SHG patterns. Each label consists of a 20×20 pixel grid (400 cells), and each cell provides two independent binary responses (PL and SHG). Therefore, the total encoding capacity of a single PUF label is:

$$EC = 2^{2\times 20\times 20} \approx 10^{240}. \tag{4}$$

Encoding capacity shows us amount of possible unique challenge-response pairs. Calculated value exceeds the encoding capacity typically reported for rudimentary PUFs and is comparable to values demonstrated in recent high-capacity implementations [18].

In addition to the high encoding capacity, the performance of the generated binary patterns was evaluated using three widely adopted PUF quality metrics [19]: bit uniformity, uniqueness, and entropy, calculated separately for the SHG-based and PL-based responses.

Bit uniformity (BU) quantifies the balance between 0 and 1 in the generated response, with an ideal value of 0.5 indicating the absence of bias toward either state. Bit uniformity can be calculated with followed formula [20]:

$$BU = \frac{1}{t}\sum_{n=1}^{t} K_n, \tag{5}$$

where K_n is the bit number n in the binary code.

For the SHG-derived patterns, bit uniformity was 0.1, while for PL it was 0.05. Although these values deviate from the ideal symmetric distribution, such behavior is typical for physically generated binary responses where digitization results from localized variations of optical intensity. This is due to the large amount of "empty" space, which gives one zero response.

Uniqueness (U) evaluates the average Hamming distance between different responses and reflects how distinguishable binary patterns are when obtained from different spatial regions. For calculations, the following formula was used [21]:

$$U = \frac{2}{k(k-1)} \sum_{i=1}^{k-1} \sum_{j=i+1}^{k} \frac{HD(R_i, R_j)}{R}, \tag{6}$$

where R_i and R_j represent the responses from the labels i and j. The number of labels is k, and HD denotes the Hamming distance. SHG-based responses demonstrated a uniqueness of 0.2, whereas PL yielded 0.1.

Finally, we calculated entropy (E) It shows the level of unpredictability in the binary data. Higher entropy corresponds to stronger resistance against brute-force or statistical prediction attacks. The entropy values obtained for SHG and PL responses were 0.5 and 0.3, respectively. The following formula was used [22]:

$$E = -[p \log_2 p + (1-p) \log_2 (1-p)], \tag{7}$$

where p is the probability of 1 in binary code.

Analyzing these parameters, we can conclude that SHG-derived patterns show better characteristics for generating random bit sequences than PL-derived ones. This is due to the fact that SHG responses are present in more structures on the label surface than the photoluminescence response.

3. Conclusion

We demonstrated a dual-channel optical PUF based on randomly formed Ag nanostructures on a silicon wafer. This structures are able to produce PL and SHG signals, which can be independently detected and converted into binary patterns. Analysis of the obtained patterns shows that PL- and SHG-based responses encode different information. Evaluation of bit uniformity, uniqueness and entropy confirms that SHG provides a more balanced and informative binary output and is therefore more suitable as the primary channel for encoding, while PL can serve as an additional layer of verification. The presented fabrication approach is simple and scalable. All steps – galvanic displacement of silver and thermal annealing and selective etching – rely on well-established wafer-level methods that do not require lithography or specialized equipment. The process can be carried out on commercially available silicon wafers and repeated across large areas without additional patterning. Since randomness is introduced naturally during metal deposition and interface formation, no external randomness source or design optimization is needed. These features make the method feasible for integration into existing semiconductor production workflows and suitable for low-cost manufacturing of optical PUF labels.

References

[1] Kikerkova I., Toshevska Trpchevska K., Kikerkov I. Threats of trade in counterfeit pharmaceutical products. *Horizons - International Scientific Journal*, 2022, **31**(2), P. 7–23.

[2] Ofori-Parku S. Fighting the global counterfeit medicines challenge: A consumer-facing communication strategy in the US is an imperative. *Journal of Global Health*, 2022, **12**.

[3] Ali S., Kershaw S., Faisal M., Halak B., Abdelazim N. Illuminating advances in materials: optical physical unclonable functions for security applications. *Advanced Optical Materials*, 2025, **13**(29), P. e01564.

[4] Klausen M., Zhang J., Stevens M. Designing physical unclonable functions from optically active materials. *Advanced Materials*, 2025, P. 2502059.

[5] Mishra P., Manna A., Ray N. Advances in semiconductor quantum dot-based physical unclonable functions for enhanced security applications. *Nanoscale*, 2025, **17**, P. 20865–20879.

[6] Gandla S., Moon C., Leem J., Yoon J., Yun H., Kim M., Kim D., Lee S., Yao Y., Alexandropoulos D., Song Y., Yoon D., Park W., Kim Y., Kim S. Multiplex optical unclonable functions: advances and perspectives in optics and photonics for hardware security. *ACS Nano*, 2025, **19**(30), P. 27033–27074.

[7] Junhyuk A., Taesung P., Taewoo K., Seong-Gyun I., Hanseok S., Bong-Hoon K., Seok Joon K., Soong Ju O. Nanoseed-based physically unclonable function for on-demand encryption. *Science Advances*, 2025, **11**(17), P. eadt7527.

[8] Kim J., Jeon S., In J., Nam S., Jin H., Han K., Yang G., Choi H., Kim K., Shin J., Son S., Kwon S., Kim B., Kim S. Nanoscale physical unclonable function labels based on block copolymer self-assembly. *Nature Electronics*, 2022, **5**(7), P. 433–442.

[9] Guo H., Qin Y., Wang Z., Ma Y., Wen H., Li Z., Ma Z., Li X., Tang J., Liu J. Multilevel encoding physically unclonable functions based on the multispecies structure in diamonds. *Advanced Functional Materials*, 2024, **34**(15), P. 2304648.

[10] Yang J., Li Y., Ju D., Liang F., Liu S., Song F. Bio-replicated multilevel physical unclonable fluorescent glass labels enabled by artificial intelligence authentication. *Chemical Engineering Journal*, 2025, **510**, P. 161538.

[11] Carraro C., Maboudian R., Magagnin L. Metallization and nanostructuring of semiconductor surfaces by galvanic displacement processes. *Surface Science Reports*, 2007, **62**(12), P. 499–525.

[12] Priolo F., Gregorkiewicz T., Galli M., Krauss T. Silicon nanostructures for photonics and photovoltaics. *Nature Nanotechnology*, 2014, **9**(1), P. 19–32.

[13] Gurbatov S., Puzikov V., Storozhenko D., Modin E., Mitsai E., Cherepakhin A., Shevlyagin A., Gerasimenko A., Kulinich S., Kuchmizhak A. Multigram-Scale production of hybrid Au-Si annomaterial by laser ablation in liquid (LAL) for temperature-feedback optical nanosensing, light-to-heat conversion, and anticounterfeit labeling. *ACS Appl. Mater. Interfaces*, 2023, **15**(2), P. 3336–3347.

[14] Makarov S., Sinev I., Milichko V., Komissarenko F., Zuev D., Ushakova E., Mukhin I., Yu Y., Kuznetsov A., Belov P., Iorsh I., Poddubny A., Samusev A., Kivshar Yu. Nanoscale generation of white light for ultrabroadband nanospectroscopy. *Nano Lett.*, 2018, **18**(1), P. 535–539.

[15] Makarov S., Petrov M., Zywietz U., Milichko V., Zuev D., Lopanitsyna N., Kuksin A., Mukhin I., Zograf G., Ubyivovk E., Smirnova D., Starikov S., Chichkov B., Kivshar Yu. Efficient second-harmonic generation in nanocrystalline silicon nanoparticles. *Nano Lett.*, 2017, **17**(5), P. 3047–3053.

[16] Sandomirskii M., Petrova E., Kustov P., Chizhov L., Larin A., Bruyère S., Yaroshenko V., Ageev E., Belov P., Zuev D. Spectral physical unclonable functions: downscaling randomness with multi-resonant hybrid particles. *Nature Communications*, 2025, **16**(1), P. 5097.

[17] McMahon M., Lopez R., Meyer III H., Feldman L., Haglund Jr R. Rapid tarnishing of silver nanoparticles in ambient laboratory air. *Applied Physics B*, 2005, **80**(7), P. 915–921.
[18] Wang K., Shi J., Lai W., He Q., Xu J., Ni Z., Liu X., Pi X., Yang D. All-silicon multidimensionally-encoded optical physical unclonable functions for integrated circuit anti-counterfeiting. *Nature Communications*, 2024, **15**(1), P. 3203.
[19] Lin X., Li Q., Tang Y., Chen Z., Chen R., Sun Y., Lin W., Yi G., Li Q. Physical unclonable functions with hyperspectral imaging system for ultrafast storage and authentication enabled by random structural color domains. *Advanced Science*, 2024, **11**(31), P. 2401983.
[20] Jiao F., Lin C., Dong L., Wu Y., Xiao Y., Zhang Z., Sun J., Zhao W., Li S., Yang X., Ni P., Wang L., Shan C. Traceable optical physical unclonable functions based on germanium vacancy in diamonds. *ACS Applied Materials & Interfaces*, 2024, **16**(33), P. 44328-44339.
[21] Balijabudda V., Acharya K., Chakraborty R., Chakrabarti I. Theoretical enumeration of deployable single-output strong PUF instances based on uniformity and uniqueness constraints. Proceeding of "19th International Conference, ICISS 2023", Raipur, India, 16-20 December 2023, Springer Nature Switzerland, P. 77–87.
[22] Gandla S., Moon C., Leem J., Yoon J., Yun H., Kim M., Kim D., Lee S., Yao Y., Alexandropoulos D., Song Y., Yoon D., Park W., Kim Y., Kim S. Multiplex optical unclonable functions: advances and perspectives in optics and photonics for hardware security. *ACS Nano*, 2025, **19**(30), P. 27033–27074.

Submitted 7 November 2025; revised 19 November 2025; accepted 20 November 2025

Information about the authors:

Maria Fedorova – School of Physics and Engineering, Faculty of Physics, ITMO University, St-Petersburg, Russia; ORCID 0009-0002-5213-5217; mariya.fedorova@metalab.ifmo.ru

Elena Petrova – School of Physics and Engineering, Faculty of Physics, ITMO University, St-Petersburg, Russia; ORCID 0000-0003-1435-0274; elena.petrova@metalab.ifmo.ru

Artem Larin – School of Physics and Engineering, Faculty of Physics, ITMO University, St-Petersburg, Russia; ORCID 0000-0002-8609-9851; artem.larin@metalab.ifmo.ru

Martin Sandomirskii – School of Physics and Engineering, Faculty of Physics, ITMO University, St-Petersburg, Russia; ORCID 0000-0002-3115-1739; m.sandomirskii@metalab.ifmo.ru

Anna Ermina – Ioffe Institute, 194021, St. Petersburg, Russia; ORCID 0000-0001-9010-7482; annaermina@mail.ioffe.ru

Sergey Pavlov – Ioffe Institute, 194021, St. Petersburg, Russia; ORCID 0000-0001-9589-8017; pavlov_sergey@mail.ioffe.ru

Yuliya Zharova – Ioffe Institute, 194021, St. Petersburg, Russia; ORCID 0000-0001-7002-5084; piliouguina@mail.ioffe.ru

Dmitry Permyakov – School of Physics and Engineering, Faculty of Physics, ITMO University, St-Petersburg, Russia; ORCID 0000-0003-2708-9140; d.permyakov@metalab.ifmo.ru

Vitaly Yaroshenko – School of Physics and Engineering, Faculty of Physics, ITMO University, St-Petersburg, Russia; ORCID 0000-0003-2034-4962; v.yaroshenko@metalab.ifmo.ru

Dmitry Zuev – School of Physics and Engineering, Faculty of Physics, ITMO University, St-Petersburg, Russia; ORCID 0000-0001-9157-5683; d.zuev@metalab.ifmo.ru

Conflict of interest: the authors declare no conflict of interest.

NANOSYSTEMS:
PHYSICS, CHEMISTRY, MATHEMATICS

Original article

Sozarukova M.M., et al. *Nanosystems: Phys. Chem. Math.*, 2025, **16** (6), 791–801.
http://nanojournal.ifmo.ru
DOI 10.17586/2220-8054-2025-16-6-791-801

UV-tuning the redox properties of nanoscale cerium dioxide and its enzyme conjugates

Madina M. Sozarukova[1,a], Arina D. Filippova[1,b], Daria-Maria V. Ratova[2,c], Ivan V. Mikheev[2,d], Elena V. Proskurnina[1,e], Alexander E. Baranchikov[1,f], Vladimir K. Ivanov[1,g]

[1]Kurnakov Institute of General and Inorganic Chemistry of the Russian Academy of Sciences, Moscow, Russia
[2]Analytical Chemistry Division, Chemistry Department, M. V. Lomonosov Moscow State University, Moscow, Russia

[a]s_madinam@bk.ru, [b]arifilippova@yandex.ru, [c]darmarrat@gmail.com, [d]mikheev.ivan@gmail.com, [e]proskurnina@gmail.com, [f]a.baranchikov@yandex.ru, [g]van@igic.ras.ru

Corresponding author: Vladimir K. Ivanov, van@igic.ras.ru

PACS 61.46.+w, 82.50.Hp, 82.70.Dd, 87.14.Ee

ABSTRACT This study investigated the redox properties of cerium oxide nanoparticles (CeO_2 NPs) and their conjugates with superoxide dismutase (SOD) or horseradish peroxidase (HRP) as well as the UV-induced modulation of these properties. UV exposure non-monotonically decreased the SOD-like property of the bare CeO_2 NPs. The CeO_2 conjugates with enzymes were analyzed both immediately after preparation and after being aged for 3 h. Chemiluminescence assays showed the synergistic effect for the CeO_2-SOD conjugates which showed high SOD activity. Additionally, CeO_2 NPs enhanced the stability of the conjugated SOD under UV exposure thus demonstrating a photoprotective function. The CeO_2-HRP conjugates demonstrated lower prooxidant activity compared to the bare enzyme, however higher stability under UV irradiation. The effect of UV radiation on CeO_2-HRP conjugates was found to be multidirectional and depended on the incubation time of the CeO_2 NPs with the enzyme. The results demonstrated that CeO_2-enzyme conjugates offer tunable dual functionality and UV light could be an important parameter affecting their redox properties. The latter effect should be taken into account for designing advanced cosmeceutical formulations.

KEYWORDS nanoceria, superoxide dismutase, peroxidase, UV irradiation, enzyme, conjugate, redox modulation, photoprotection

ACKNOWLEDGEMENTS This study was supported by the Russian Science Foundation (Project no. 24-13-00370).

FOR CITATION Sozarukova M.M., Filippova A.D., Ratova D.-M.V., Mikheev I.V., Proskurnina E.V., Baranchikov A.E., Ivanov V.K. UV-tuning the redox properties of nanoscale cerium dioxide and its enzyme conjugates. *Nanosystems: Phys. Chem. Math.*, 2025, **16** (6), 791–801.

1. Introduction

Cerium dioxide nanoparticles (CeO_2 NPs) are now regarded as one of the most promising next-generation biomimetic agents. Their appeal stems from a unique combination of physicochemical properties and a broad range of enzyme-mimetic activities [1–3]. Significant research efforts are now directed toward engineered hybrid organic-inorganic materials that allow modulating the properties of nanoscale cerium dioxide using various biocompatible compounds including proteins, enzymes, amino acids, etc. [4–10]. The immobilization of biologically active molecules on the surface of CeO_2 NPs provides a functional platform for the targeted delivery of drugs and various bioactive ligands, as well as enhancing therapeutic efficacy through synergistic interactions and prolonged activity [11, 12].

Reactive oxygen species (ROS) such as the superoxide anion radical ($\cdot O_2^-$) and hydrogen peroxide, are essential for normal physiological functions [13, 14]. In living systems, they play a crucial role in maintaining homeostasis and facilitating cellular signaling. However, their overproduction can result in a cellular damage by inducing oxidative stress. Living systems counteracts oxidative stress through production of antioxidants, e.g. enzymes, such as superoxide dismutase (SOD), catalase, glutathione peroxidase, etc. Notably, SOD plays a critical role by regulating the balance between intracellular oxidative processes and antioxidant defense system [15].

The ability of nanoscale cerium dioxide to mimic SOD was among the first enzyme-like properties discovered for CeO_2 NPs [16–19]. It is well established that the SOD-like activity of CeO_2 NPs depends on a multitude of factors. These include synthesis conditions [20], redox state of surface cerium atoms [16, 17, 21], particle size and shape [19, 22, 23], surface functionalization [24–26]. The SOD-like activity depends also on the presence of phosphate species [27],

pH [19, 28, 29], temperature [30], etc. To enhance the catalytic activity, hybrid materials are being created based on cerium dioxide conjugated with antioxidant and prooxidant enzymes, such as SOD, catalase, and peroxidase [5, 22, 31]. Interestingly, the dismutation of superoxide anion radicals catalyzed by both native SOD or SOD mimetics though results in a pronounced antioxidant outcome, however it simultaneously leads to the accumulation of hydrogen peroxide being another type of ROS.

Despite the significant progress in understanding the biocatalytic properties of CeO_2 NPs and their hybrids with biomolecules, the ability to control their redox activity using external physical factors remains underexplored. In this context, ultraviolet (UV) radiation is of particular interest [32, 33]. As a potent exogenous agent, UV radiation serves not only as a convenient tool for controlled exposure but also as a physical model of oxidative stress [34]. The mechanism of UV-action on living systems is multifactorial involving both the production of free radicals and direct damage of biomolecules [35, 36].

The surface properties of cerium dioxide which is a wide-bandgap semiconductor, can be modified upon exposure to ultraviolet light. These changes can involve the alterations of its surface hydroxylation [37]. An example of a similar phenomenon is titanium dioxide (TiO_2), which exhibits UV-induced superhydrophilicity [38, 39]. Given that the enzyme-like properties of nanoscale cerium dioxide are largely governed by surface chemistry, UV irradiation is hypothesized to be an effective tool for modulating the catalytic activity of CeO_2 NPs. However, the effects of UV irradiation on the redox activity of both bare CeO_2 NPs and their enzyme conjugates remain virtually unexplored. Specifically, the UV-modulation of their interaction with key cellular enzymes, such as superoxide dismutase and peroxidase, by UV exposure has not been assessed.

This study provides an investigation of the effects of UV irradiation on the redox activity of bare CeO_2 NPs and their conjugates with enzymes. The activity was assessed towards key reactive oxygen species – the superoxide anion radicals and hydrogen peroxide – by the chemiluminescence method. The CeO_2 conjugates were studied with different oxidoreductase enzymes, superoxide dismutase or horseradish peroxidase (HRP). For the first time, it was shown that UV irradiation can not only suppress, but selectively and dose-dependently modulate the enzyme-like activity of nanoparticles. The findings of this study demonstrate the significant potential of nanoscale cerium dioxide for application in advanced cosmetic preparations.

2. Materials and methods

2.1. Materials (chemicals)

The following reagents were used in this work: ammonium cerium(IV) nitrate ($(NH_4)_2[Ce(NO_3)_6]$, chem. pure, Lankhit), isopropanol (high purity, Aldosa), superoxide dismutase from bovine erythrocytes (Cu/Zn type, ≥ 97 % , S7446-15KU, Sigma-Aldrich), horseradish peroxidase (RZ> 1.0, $a \geq 110$ U/mg, DIA-M).

2.2. Synthesis of bare CeO_2 nanoparticles and preparation of ceria-enzyme conjugates

Bare CeO_2 nanoparticles were prepared by thermohydrolysis of an aqueous ammonium cerium(IV) nitrate solution, following a reported procedure [40]. Briefly, cerium salt (2.33 g) was dissolved in 23 mL of water. The resulting solution (0.185 M) was maintained at 95 °C for 24 h. Following centrifugation to isolate the yellow precipitate from the mother liquor, the product was washed three times with isopropyl alcohol and redispersed in deionized water. Finally, the sol was boiled for 3 h to eliminate isopropanol residuals.

Cerium dioxide was functionalized with two enzymes: superoxide dismutase (CeO_2-SOD conjugate) and horseradish peroxidase (CeO_2-HRP conjugate). The functionalization was performed by gradually adding the CeO_2 sol to an aqueous solution of the enzyme. This process achieved a final molar ratio CeO_2 : enzyme 10000 : 1. Two types of CeO_2 conjugates with SOD and HRP were analyzed: as prepared (0 h pre-incubation) and incubated under stirring for 3 h. All the samples were stored in dark. For physicochemical characterization, the enzyme-conjugated CeO_2 sols were dried at 25 °C.

2.3. Materials characterization

The concentration of the initial ligand-free cerium dioxide sol was determined gravimetrically.

The X-ray powder diffraction analysis (XRD) of ceria samples was performed using a Bruker (Billerica, MA, USA) D8 Advance diffractometer (CuKα radiation). Data were collected over a 2θ range of 20 – 100° with a step size of 0.02° and a counting time of 0.2 seconds per step. Phase identification was performed using the ICDD PDF2 database. The crystallite size (coherent scattering domain size) was estimated using the Scherrer equation; peak profiles were fitted to pseudo-Voigt functions.

The optical absorption spectra were recorded in quartz cuvettes using an SF-2000 spectrophotometer (Spectr, Saint Petersburg, Russia). Measurements were conducted in the range of 200 – 600 nm with a 1 nm step size.

Fourier transform infrared (FTIR) spectra were obtained on an InfraLUM FT-08 spectrometer (Russia) employing the attenuated total reflection (ATR) technique. Spectra were recorded in the 400 – 4000 cm^{-1} range with a spectral resolution of 1 cm^{-1}.

Dynamic light scattering (DLS) and zeta potential measurements were performed at 20 °C and at 36 °C using a Photocor Compact-Z analyser (Photocor, Moscow, Russia). The correlation function for each sample was collected by averaging 10 individual 20 sec runs. The hydrodynamic diameter of the particles was determined using a regularization algorithm (DynalS software).

2.4. UV-exposure procedure

The samples (absorbance ≤ 0.2, $V = 2$ ml) were irradiated in glass vessels (5 ml) using a Bio-Link UV irradiation system (Vilber Lourmat, Collégien, France) at 312 nm (UV source 5×8-watt lamps). The samples were irradiated with doses of 50 or 100 mJ/cm^2. The samples were irradiated from above, the height of liquid sample was approximately 3 cm.

2.5. Analysis of SOD-like activity

The SOD-like activity of the materials was analyzed using a method based on the detection of lucigenin chemiluminescence during its oxidation by superoxide anion radicals ($\cdot O_2^-$). The superoxide anion radicals are generated by the oxidation of xanthine to uric acid in the presence of oxygen [41, 42].

Aliquots of aqueous solutions of xanthine (20 μM, #X0626, Sigma), lucigenin (20 μM, #393824, J&K, San Jose, CA, USA), and the test sample were rapidly added into a cuvette containing a phosphate buffer solution (100 mM, pH 7.4). The background signal was recorded for 30 – 60 s, then xanthine oxidase ($a = 8.8$ mU/mL, #X1875-25UN, Sigma) was added. All experiments were conducted in triplicate. The chemiluminescence intensity was measured at 37 °C using a Lum-1200 (DISoft, Moscow, Russia) 12-channel chemiluminometer. The results were processed using the PowerGraph software (version 3.3).

2.6. Analysis of prooxidant activity

The prooxidant activity of the materials was analyzed towards hydrogen peroxide in the presence of luminol (5-amino-1,2,3,4-tetrahydro-1,4-phthalazinedione, 3-aminophthalic acid hydrazide) [31, 43].

Aliquots of H_2O_2 (10 mM, #H1009, Sigma) and luminol (50 μM, #A8511, Sigma) were rapidly introduced into a cuvette containing phosphate buffer solution (100 mM, pH 7.4). The background signal was recorded for 60 – 90 s. After the chemiluminescence intensity reached a constant value, an aliquot of the test sample was added. All experiments were conducted in triplicate. Chemiluminescence was measured using a Lum-1200 (DISoft, Moscow, Russia) 12-channel chemiluminometer. The results were processed using PowerGraph software (version 3.3).

3. Results and discussion

3.1. Characterisation of CeO_2-based nanomaterials

Powder X-ray diffraction analysis (XRD) revealed that the crystalline phase in the bare CeO_2 sol and CeO_2 conjugates with SOD and HRP enzymes corresponded to single-phase cerium dioxide (space group $Fm\bar{3}m$, PDF2 00-034-0394) (Fig. 1(a)). The cerium dioxide crystallite size (~ 2.8 nm) remains virtually unchanged after enzyme immobilization.

UV-visible spectroscopy revealed an absorption band between 280 – 300 nm for the enzyme-modified ceria sols (Fig. 1(b)), which is characteristic of nanoscale CeO_2 with a band gap of 3.3 eV. The modified ceria sols show no absorption band at ~ 250 nm. This band corresponds to the $4f^1 \rightarrow 5d^1$ transition of Ce^{3+}. Therefore, Ce^{4+} was not reduced to Ce^{3+} during the functionalization of CeO_2 with enzymes.

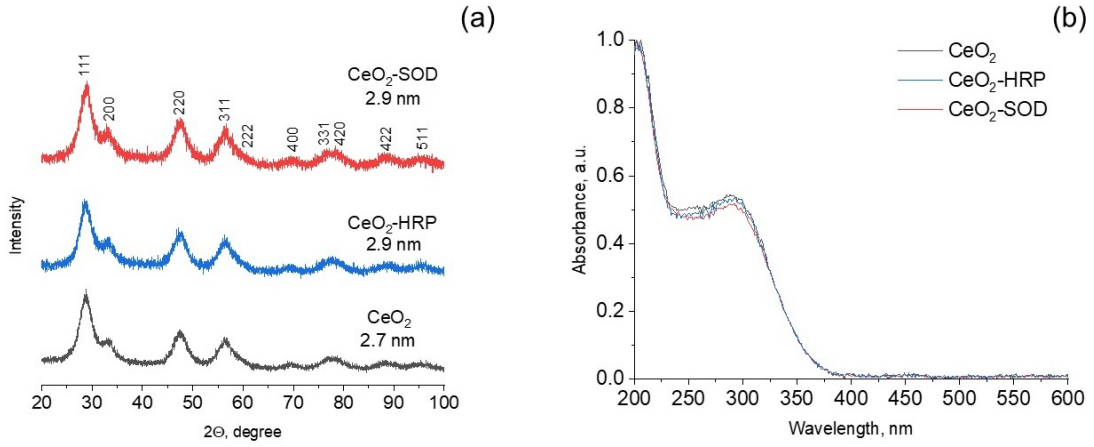

FIG. 1. (a) X-ray diffraction patterns of bare CeO_2 NPs and ceria conjugates with SOD and HRP; (b) electron absorption spectra of CeO_2-based nanomaterials

The ceria sols were characterized by DLS at 20 and 36 °C, these temperatures correspond to sample storage and chemiluminescence measurement conditions, respectively (Fig. 2). The unstabilized CeO_2 sol exhibited a nearly monodisperse particle size distribution with a mean diameter of 14 nm and a minor fraction of larger agglomerates (~ 140 nm). Modification of the nanoscale CeO_2 with SOD did not induce significant changes in the particle size distribution; the mean aggregate diameter remained at 15 – 16 nm (Fig. 2(a,b)). In contrast, modification with HRP induced some changes, and the formation of two aggregate fractions with sizes of 11 and 27 nm was registered (Fig. 2(a,b)). Fig. 2(c) shows the particle size distribution in the aqueous solutions of the bare enzymes. The SOD solution contains three particle fractions with average hydrodynamic diameters of 3, 24, and 270 nm. Similarly, three distinct fractions with average sizes of 4, 60, and 430 nm were identified in the HRP solution. It is important to note that the enzyme concentrations (superoxide dismutase and horseradish peroxidase) in the modified ceria sols were 1 μM, which is 30 times lower than the enzyme concentration in their individual solutions (30 μM). At such low concentrations, the contribution of the bare enzymes to light scattering of the CeO_2 conjugates could be regarded as negligible.

Electrokinetic measurements revealed that modification of CeO_2 NPs with enzymes significantly changed their electrical properties. A notable increase in ζ-potential was observed, rising from $+25$ mV for the bare CeO_2 NPs to $+33$ mV for the CeO_2-SOD conjugate and to $+36$ mV for the CeO_2-HRP conjugate. This increase in ζ-potential indicates enhanced colloidal stability of the modified nanoparticles. Interestingly, this finding is somewhat counterintuitive as the enzyme-modified ceria sols possessed higher pH (4.5 for CeO_2-SOD and 5.6 for CeO_2-HRP) than that of the bare CeO_2 sol (pH 2.1) and thus a decrease in the absolute ζ-potential value could be expected [44]. However, the observed change in ζ-potential value supports well the successful immobilization of enzymes on the surface of the CeO_2 NPs. In the recent report, the hemolymph serum of *Mytilus galloprovincialis* was shown to form a protein corona on the surface of commercial CeO_2 NPs [45]. The corona consisted of SOD and shifted the ζ-potential value of the NPs from a highly negative -84 mV to -10 mV.

The ceria sols were analyzed by DLS after one month of storage in a dark environment at 4 – 8 °C. The unmodified CeO_2 sol showed no change in its primary particle size (13 nm), but its larger agglomerates shrank by more than half, to 63 nm (Fig. 2(a,d)). The CeO_2 sol modified with SOD exhibited three distinct particle sizes: 14, 65, and 350 nm (Fig. 2(d)). The size of the key particle fraction in the CeO_2-SOD conjugate (14 nm) remained stable during storage. Notably, ceria sol modified with HRP had a more uniform particle size distribution after storage, with average sizes of 15 and 100 nm (Fig. 2(d)).

The DLS method was also used to investigate the aggregation behavior of CeO_2 particles in the sols after UV irradiation. For the experiment, two UV doses were chosen, 50 mJ/cm^2 and a higher dose of 100 mJ/cm^2. Exposure to a low-dose UV radiation (50 mJ/cm^2) resulted in a slight broadening of the particle size distributions in all the sols. However, the overall profile of the size distributions and the average aggregate sizes remained unchanged (Fig. 2(a,e)). In contrast, exposure to the higher UV dose (500 mJ/cm^2) induced significant aggregation of the particles. Specifically, in the CeO_2-HRP conjugate the average aggregate size doubled to 30 nm, and the presence of larger agglomerates up to 550 nm was observed (Fig. 2(a,f)).

The FTIR spectra of bare CeO_2 NPs, enzymes, and the conjugates are shown in Fig. 3.

In the IR spectra of cerium dioxide, the broad bands at 3600 – 3100 cm^{-1} and 3200 – 2500 cm^{-1} correspond to the O–H stretching vibrations of adsorbed water and the stretching vibrations of surface hydroxyl groups, respectively [46]. The determination of absorption bands of the protein carbon backbone or amide groups is challenging due to overlapping with the strong water absorption bands. Nevertheless, the spectra of HRP and SOD reveal several weak bands in the 3000 – 2840 cm^{-1} range (ν(C–H)) and a band at 3270 cm^{-1} (ν(N–H) of secondary amides) [47]. A band in the 1570 – 1515 cm^{-1} range, attributed to N–H bending vibrations of secondary amides (amide II), is observed in the spectra of both the bare enzymes and their conjugates with CeO_2. Bands characteristic of –CH_2– deformation vibrations were registered in the 1470 – 1400 cm^{-1} range. The absorption band for the C=O stretching vibration (amide I) is $\sim$10 cm^{-1} redshifted in the IR spectra of the CeO_2-SOD (1626 cm^{-1}) and CeO_2-HRP (1626 cm^{-1}) conjugates relative to the bare enzymes (1635 and 1638 cm^{-1}). These shifts support the successful formation of CeO_2-enzyme conjugates by indicating the interaction between the nanoparticles and the proteins.

3.2. Chemiluminescence assay

3.2.1. SOD-like activity. Analysis of the SOD-like activity was performed by monitoring chemiluminescence in the presence of lucigenin, a selective probe for superoxide anion radical generation [41, 42].

The effect of UV irradiation was investigated on the redox behavior towards the superoxide anion radicals $\cdot O_2^-$ of bare CeO_2 NPs, SOD enzyme, and CeO_2-SOD conjugates immediately after the mixing of components and incubated for 3 h. Fig. 4(a) shows experimental chemiluminescence curves recorded upon the addition of xanthine oxidase to the mixtures containing xanthine, lucigenin, and the analysed materials. These curves were recorded for the samples which were not subjected to UV-irradiation, or the UV-irradiated samples. As can be seen, in the presence of the analysed materials a decrease in lucigenin-dependent chemiluminescence is observed. The decrease in the chemiluminescence intensity is proportional to the concentration of superoxide anion radicals and could be used to quantify the SOD-like activity.

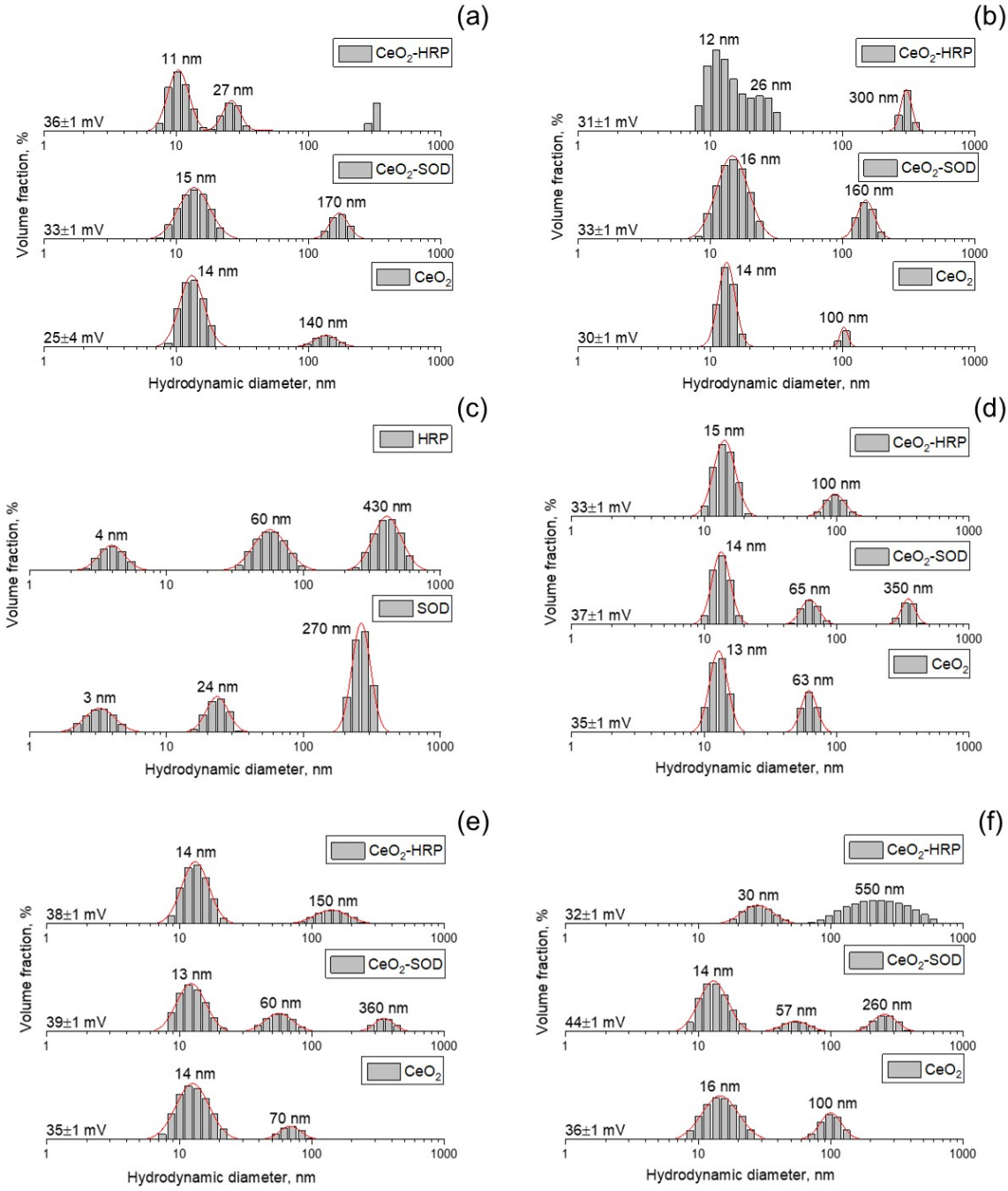

FIG. 2. Hydrodynamic diameter distributions for particles in unmodified CeO_2 sol (pH 2.1) and CeO_2 sols modified with SOD (pH 4.5) and HRP (pH 5.6), measured at (a) 20 °C and (b) 36 °C; (c) hydrodynamic diameter distributions in the solutions of the individual SOD and HRP enzymes (20 °C); (d) hydrodynamic diameter distributions in ceria sols after 1 month of storage (20 °C); hydrodynamic diameter distributions after UV irradiation of ceria sols with doses of (e) 50 mJ/cm^2 and (f) 100 mJ/cm^2 (20 °C)

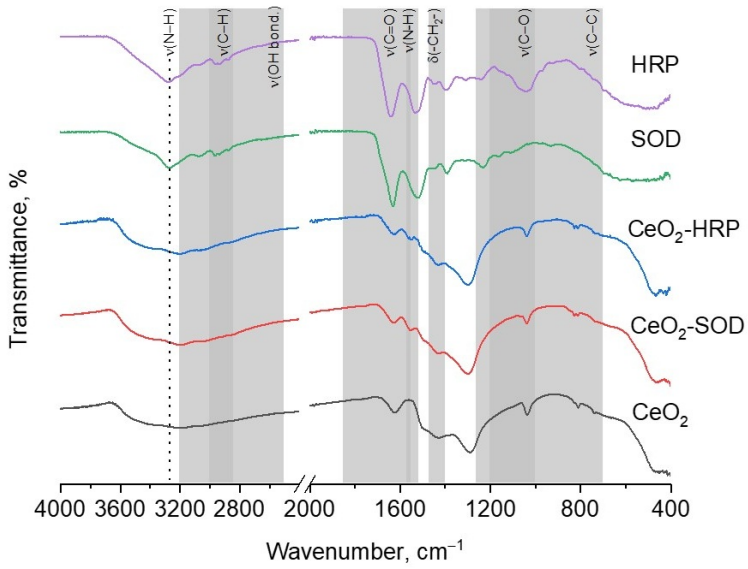

FIG. 3. FTIR spectra of bare CeO_2 NPs, individual enzymes SOD and HRP and conjugates of CeO_2 with enzymes

To quantify the SOD-like activity, the relative degree of chemiluminescence suppression, $\Delta S_{\text{rel.}}$, was calculated from the chemiluminograms (Fig. 4(b)) using the relation:

$$\Delta S_{\text{rel.}},\ \% \ = \ \frac{(S_0 \ - \ S)}{S_0} \times 100\%, \tag{1}$$

where S_0 and S are the light sums (integral intensity) for the control experiment (without the addition of sample) and for the experiment with the analysed sample.

The CeO_2-SOD conjugates showed nearly 2.5 times higher efficacy in scavenging superoxide anion radicals than bare CeO_2 NPs and 1.5 times higher efficacy than SOD enzyme (Fig. 4(b)). This observation can be attributed to the synergistic interactions between the components [5, 20, 31].

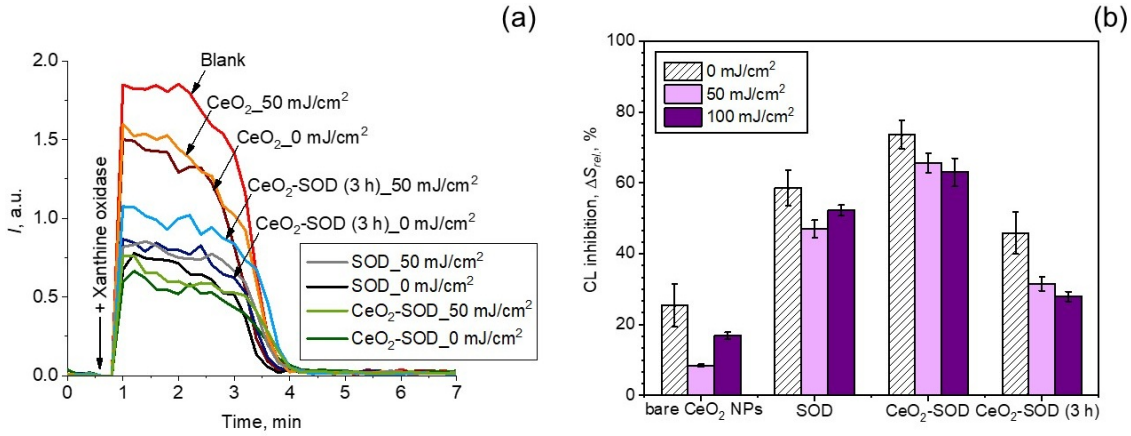

FIG. 4. (a) Chemiluminograms illustrating the SOD-like activity of bare CeO_2 NPs, bare SOD and CeO_2-SOD conjugates, (b) histograms of the relative degree of chemiluminescence suppression ($\Delta S_{\text{rel.}}$) for the samples

The effect of UV irradiation on the SOD-like activity of bare CeO_2 NPs is multidirectional. Exposure to a dose of 50 mJ/cm^2 suppressed the activity approximately threefold. Conversely, a higher dose of 100 mJ/cm^2 produced a weaker effect, the activity reduced by one and a half times (Fig. 4(b)). This indicates that the SOD-like activity of bare CeO_2 NPs can be modulated by UV exposure. The observed non-linear response for bare CeO_2 NPs to UV irradiation could be discussed in terms of photochemistry of oxide semiconductors, e.g. TiO_2 [38, 39, 48]. In particular, this effect can be due to the competition between the surface photooxidation (resulting in surface passivation) at low doses and the photoreduction (resulting in surface activation) at high doses. These competing processes can affect the surface hydroxylation of nanoscale cerium oxide which is expected to govern its enzyme-like activity [37]. A dose of 50 mJ/cm^2

presumably promotes the oxidation and desorption of surface hydroxyl groups, while a higher dose of 100 mJ/cm^2 induces the photoreduction of surface Ce^{4+} cations and facilitates surface re-hydroxylation. Recently, the UV exposure has been shown to increase the concentration of subvalent Ce^{3+} ions in parallel with a rise in the catalytic activity of CeO_2 NPs [49]. Thus, UV irradiation has been regarded as a novel strategy for modulating the catalytic activity of nanoscale ceria through annealing-free defect engineering [49].

UV irradiation was found to suppress the SOD-like activity of both SOD enzyme and the CeO_2-SOD conjugates (Fig. 4(b)). The UV-induced decrease in the activity is summarized in Table 1. These data are also illustrated in Fig. 5.

TABLE 1. Effects of UV irradiation on SOD-like activity of the samples.

Dose, mJ/cm^2	50	100
Sample	Reduction of SOD-like activity under UV irradiation, %	
Bare CeO_2 NPs	67 ± 7	34 ± 9
SOD	20 ± 2	11 ± 3
CeO_2-SOD conjugate	12 ± 1	17 ± 2
CeO_2-SOD conjugate (3 h)	31 ± 1	40 ± 2

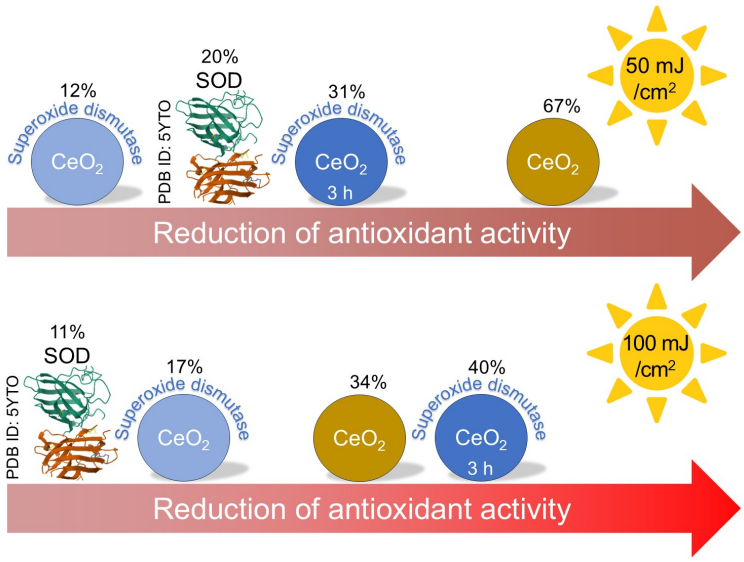

FIG. 5. Effects of UV irradiation on SOD-like activity of bare CeO_2 NPs, SOD and CeO_2-SOD conjugates

The antioxidant activity of the non-incubated CeO_2-SOD conjugate was reduced in a lesser degree under 50 mJ/cm^2 UV dose than under a 100 mJ/cm^2 dose, and their antioxidant activity was reduced to a lesser extent than that of the individual enzyme (Fig. 4(b), Table 1, Fig. 5). These results suggest that CeO_2 NPs exert a photoprotective effect towards the conjugated SOD, enhancing the operational stability of the conjugated enzyme under oxidative stress. Numerous studies have reported pronounced photoprotective properties of nanoscale CeO_2 [33, 50–52]. These protective effects are most commonly attributed to a combination of two key mechanisms: the ability of CeO_2 NPs to effectively absorb UV radiation and to mimic the functions of antioxidant enzymes, such as SOD and catalase, thereby reducing levels of ROS formed under UV exposure. It has been demonstrated that the photodegradation of organic dyes such as methyl orange [33], crystal violet [50] and rhodamine 6G [51] in the presence of CeO_2 nanoparticles is significantly lower than in the presence of conventional photocatalysts such as titanium dioxide [50].

The immobilized SOD enzyme efficiently attracts superoxide anion radicals to the nanoparticle surface due to its high affinity for this substrate [53, 54]. This dramatically increases the local concentration of superoxide anion radicals around the nanoscale cerium oxide. Consequently, any radicals that have not reacted with the SOD active site can be efficiently scavenged by the CeO_2 NPs. This process establishes a synergistic antioxidant cascade, in which the products of one reaction become the substrates for the next reaction.

The CeO_2-SOD conjugate aged for 3 h prior to irradiation showed a more pronounced reduction in SOD antioxidant activity after UV-irradiation with 50 mJ/cm^2 and 100 mJ/cm^2 doses (Fig. 4(b), Table 1, Fig. 5). This effect is presumably

attributed to substantial conformational changes in the SOD enzyme during the 3-hour incubation with CeO_2 NPs which could make the enzyme susceptible to UV-induced damage. Thus, the catalytic activity of the CeO_2-SOD conjugate under UV radiation depends not only on the properties of the CeO_2 NPs but also on the structure of the immobilized enzyme.

3.2.2. Prooxidant activity. The prooxidant activity of the samples was analyzed by monitoring chemiluminescence in the presence of luminol, a probe sensitive to hydrogen peroxide and reactive chlorine species [55, 56].

This study investigated the effect of UV irradiation on the redox behavior towards the hydrogen peroxide of bare CeO_2 NPs, individual HRP enzyme, and CeO_2-HRP conjugates, both immediately after mixing the components and after the incubation for 3 h. Fig. 6(a) shows chemiluminograms for the samples which were not subjected for UV-irradiation and the UV-irradiated samples. As can be seen, the analyzed samples enhance luminol-dependent chemiluminescence indicating the generation of ROS and supporting the prooxidant properties of the studied materials.

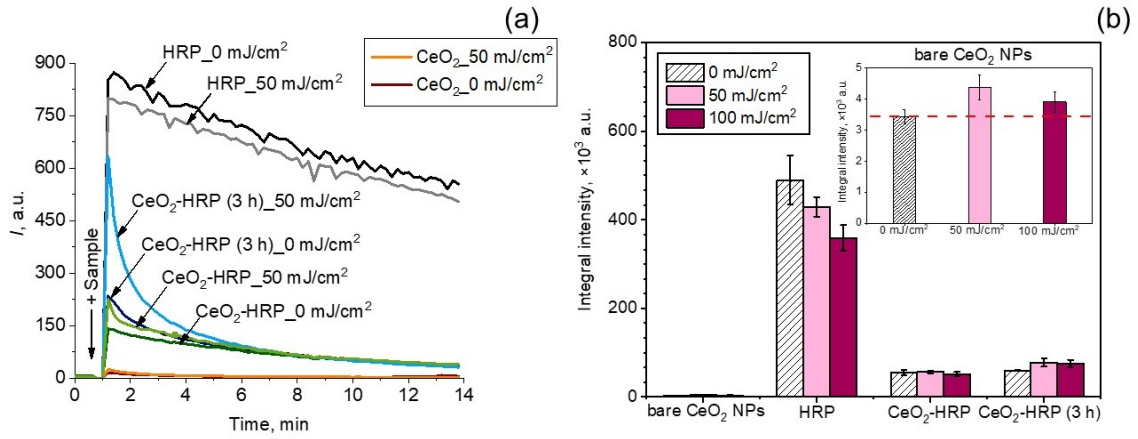

FIG. 6. (a) Chemiluminograms illustrating the prooxidant activity of bare CeO_2 NPs, HRP and CeO_2-HRP conjugates, (b) the light sums (prooxidant capacity) for the samples

From the chemiluminescence profiles, to quantify the prooxidant properties, the areas under the chemiluminescent curves (light sums) were calculated, which are proportional to the number of generated radicals and correspond to the prooxidant capacity of the samples. Fig. 6(b) shows the light sum bars. The most pronounced enhancement of the chemiluminescence signal was observed for the individual HRP enzyme. It should be noted that the shape of the chemiluminescent curve for the individual HRP differed from the experimental curves for other samples (Fig. 6(a)), which probably indicates different mechanisms of the prooxidant effect [20]. Analysis of the data (Fig. 6(b)) revealed that the CeO_2-HRP conjugates exhibited approximately 15 times higher prooxidant capacity compared to bare CeO_2 NPs. The increase in peroxidase-like activity is consistent with previous reports on hybrid nanobiocatalytic systems [57, 58]. For instance, the use of magnetite nanoparticles has been shown to significantly accelerate the hydrogen peroxide decomposition in the presence of HRP [58]. However, it is important to note that the HRP enzyme possessed lower activity upon the immobilization onto the CeO_2 nanoparticle surface (Fig. 6(b)). Presumably, this may also be caused by conformational changes in the enzyme structure and, as a result, steric hindrance to the access of the substrate to the active center.

To assess the effect of the UV radiation dose, the percentage decrease in the prooxidant activity of the analyzed materials was calculated (Table 2). For clarity, these data are also presented in Fig. 7.

A UV dose of 50 mJ/cm^2 enhanced the prooxidant activity of bare CeO_2 NPs more significantly than a dose of 100 mJ/cm^2 (Fig. 6(b)). In contrast, the activity of the native HRP enzyme decreased in a dose-dependent manner (Table 2), which is consistent with the recent reports [59, 60]. Notably, the CeO_2-HRP conjugate (obtained without pre-incubation) showed no significant change in activity after irradiation at 50 mJ/cm^2. Conversely, UV-irradiation with a

TABLE 2. Effects of UV irradiation on prooxidant activity of samples

Dose, mJ/cm^2	50	100
Sample	Reduction of prooxidant activity under UV irradiation, %	
Bare CeO_2 NPs	increase prooxidant activity	increase prooxidant activity
HRP	12 ± 5	27 ± 2
CeO_2-HRP conjugate	—	5 ± 1
CeO_2-HRP conjugate (3 h)	increase prooxidant activity	increase prooxidant activity

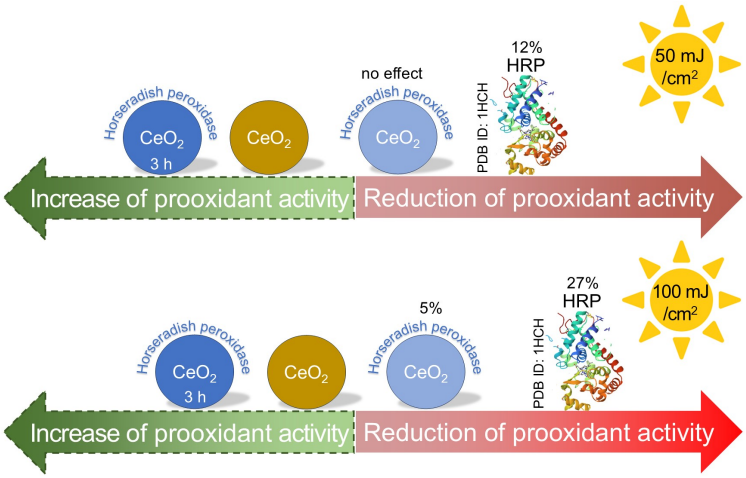

FIG. 7. Effects of UV irradiation on prooxidant activity of bare CeO_2 NPs, HRP and CeO_2-HRP conjugates

dose of 100 mJ/cm^2 resulted in a decrease in the activity. Compared to the native enzyme, the activity of HRP conjugated with CeO_2 (obtained without pre-incubation) did not change significantly under irradiation with a dose of 50 mJ/cm^2, and decreased to a lesser extent at 100 mJ/cm^2 (Table 2). These results could indicate a photoprotective effect of CeO_2 NPs toward HRP. This effect is probably due to the ability of CeO_2 NPs to effectively absorb UV radiation and thereby protect the protein molecule from direct photolytic damage.

Interestingly, for the CeO_2-HRP conjugate pre-incubated for 3 h, the UV-irradiation with both 50 and 100 mJ/cm^2 enhanced the peroxidase-like activity by an average factor of 1.5. This suggests that longer incubation promotes the formation of a more stable conjugate. Subsequent UV irradiation presumably modulates the redox properties of the nanoscale CeO_2 surface, creating more efficient synergistic catalysis – for instance, by facilitating electron transfer between the nanoparticle and the active site center of the enzyme.

4. Conclusions

The UV-tunable dual redox behavior of nanoscale CeO_2 and its hybrid materials with the SOD and HRP enzymes was studied. Bare CeO_2 NPs have been shown to possess SOD-like activity, which significantly reduced upon applying even low UV doses (50 mJ/cm^2). The CeO_2-SOD conjugates exhibited a 1.5-fold increase in the antioxidant activity compared to SOD alone. UV irradiation reduced the SOD-like activity of the hybrid materials, while CeO_2 NPs provided a pronounced photoprotective effect towards the enzyme.

In the presence of hydrogen peroxide, both bare CeO_2 NPs and their hybrids with HRP exhibited pronounced prooxidant properties, which can further be tuned by UV irradiation. The interaction of HRP with CeO_2 NPs resulted in the decrease of the activity of the enzyme however favored its stability under UV-irradiation.

These findings underscore the potential of nanoscale CeO_2 and its hybrids in biomedicine and catalysis, where external factors (e.g., via UV exposure) could alter the redox properties of the material. The methodology proposed in this study can be extended to the other models of oxidative stress, such as exposure to ultrasound, X-ray radiation, or radio waves.

References

[1] Mishra P., Lee J., Kumar D., et al. Engineered nanoenzymes with multifunctional properties for next-generation biological and environmental applications. *Adv. Funct. Mater.*, 2022, **32** (1), 2108650.
[2] Ma Y., Tian Z., Zhai W., Qu Y. Insights on catalytic mechanism of CeO_2 as multiple nanozymes. *Nano Res.*, 2022, **15** (10), P. 10328–10342.
[3] Thakur N., Manna P., Das J. Synthesis and biomedical applications of nanoceria, a redox active nanoparticle. *J. Nanobiotechnol.*, 2019, **17** (1), 84.
[4] Ilhan H., Ayvaz M.C. Evaluation of enzyme activity with nanoparticles conjugation. *Recent Adv. Mol. Biol. Biochem.*, 2023, 223.
[5] Gil D., Rodriguez J., Ward B., et al. Antioxidant activity of SOD and catalase conjugated with nanocrystalline ceria. *Bioengineering*, 2017, **4** (1), 18.
[6] Ding S., Cargill A.A., Medintz I.L., et al. Increasing the activity of immobilized enzymes with nanoparticle conjugation. *Curr. Opin. Biotechnol.*, 2015, **34**, P. 242–250.
[7] Ahmad R., Sardar M. Enzyme immobilization: An overview on nanoparticles as immobilization matrix. *Biochem. Anal. Biochem.*, 2015, **4** (1), 1.
[8] Sozarukova M.M., Proskurnina E.V., Mikheev I.V., et al. Anti- and prooxidant properties of cerium oxide nanoparticles functionalized with gallic acid. *Russ. J. Inorg. Chem.*, 2023, **68** (10), P. 1108–1116.
[9] Sozarukova M.M., Proskurnina E.V., Baranchikov A.E., Ivanov V.K. Antioxidant activity of conjugates of cerium dioxide nanoparticles with human serum albumin isolated from biological fluids. *Russ. J. Inorg. Chem.*, 2023, **68** (10), P. 1495–1502.
[10] Lasala P., Latronico T., Mattia U., et al. Enhancing antioxidants performance of ceria nanoparticles in biological environment via surface engineering with o-quinone functionalities. *Antioxidants*, 2025, **14** (6), 916.

[11] Pudlarz A.M., Czechowska E., Karbownik M.S., et al. The effect of immobilized antioxidant enzymes on the oxidative stress in UV-irradiated rat skin. *Nanomedicine*, 2020, **15** (1), P. 23–39.
[12] Sozarukova M.M., Kochneva E.M., Proskurnina E.V., et al. Albumin retains its transport function after interaction with cerium dioxide nanoparticles. *ACS Biomater. Sci. Eng.*, 2023, **9** (12), P. 6759–6772.
[13] McCord J.M. The evolution of free radicals and oxidative stress. *Am. J. Med.*, 2000, **108** (6), P. 652–659.
[14] Hensley K., Robinson K.A., Gabbita S.P., et al. Reactive oxygen species, cell signaling, and cell injury. *Free Radic. Biol. Med.*, 2000, **28** (10), P. 1456–1462.
[15] Chen D., Ai X., Li Y., et al. Protective effects of Cu/Zn-SOD and Mn-SOD on UVC radiation-induced damage in NIH/3T3 cells and murine skin. *Acta Histochem.*, 2023, **125**, 152030.
[16] Baldim V., Bedioui F., Mignet N., et al. The enzyme-like catalytic activity of cerium oxide nanoparticles and its dependency on Ce^{3+} surface area concentration. *Nanoscale*, 2018, **10** (14), P. 6971–6980.
[17] Heckert E.G., Karakoti A.S., Seal S., et al. The role of cerium redox state in the SOD mimetic activity of nanoceria. *Biomaterials*, 2008, **29** (18), P. 2705–2709.
[18] Sozarukova M.M., Shestakova M.A., Teplonogova M.A., et al. Quantification of free radical scavenging properties and SOD-like activity of cerium dioxide nanoparticles in biochemical models. *Russ. J. Inorg. Chem.*, 2020, **65** (4), P. 597–605.
[19] Korsvik C., Patil S., Seal S., et al. Superoxide dismutase mimetic properties exhibited by vacancy engineered ceria nanoparticles. *Chem. Commun.*, 2007, P. 1056–1058.
[20] Sozarukova M.M., Kozlova T.O., Beshkareva T.S., et al. Gadolinium doping modulates the enzyme-like activity and radical-scavenging properties of CeO_2 nanoparticles. *Nanomaterials*, 2024, **14** (5), 769.
[21] Shi X., Yang J., Wen X., et al. Oxygen vacancy enhanced biomimetic superoxide dismutase activity of CeO_2-Gd nanozymes. *J. Rare Earths*, 2021, **39** (10), P. 1108–1116.
[22] Li Y., He X., Yin J.J., et al. Acquired superoxide-scavenging ability of ceria nanoparticles. *Angew. Chem. Int. Ed.*, 2015, **54** (7), P. 1852–1855.
[23] Zhu A., Sun K., Petty H.R. Titanium doping reduces superoxide dismutase activity, but not oxidase activity, of catalytic CeO_2 nanoparticles. *Inorg. Chem. Commun.*, 2012, **15** (2), P. 235–237.
[24] Yadav N., Singh S. Polyoxometalate-mediated vacancy-engineered cerium oxide nanoparticles exhibiting controlled biological enzyme-mimicking activities. *Inorg. Chem.*, 2021, **60** (15), P. 7475–7489.
[25] Baranchikov A.E., Sozarukova M.M., Mikheev I.V., et al. Biocompatible ligands modulate nanozyme activity of CeO_2 nanoparticles. *New J. Chem.*, 2023, **47** (52), P. 20388–20404.
[26] Damle M.A., Jakhade A.P., Chikate R.C. Modulating pro- and antioxidant activities of nanoengineered cerium dioxide nanoparticles against *Escherichia coli*. *ACS Omega*, 2019, **4** (3), P. 3761–3771.
[27] McCormack R.N., Mendez P., Barkam S., et al. Inhibition of nanoceria's catalytic activity due to Ce^{3+} site-specific interaction with phosphate ions. *J. Phys. Chem. C*, 2014, **118** (33), P. 18992–19006.
[28] Xu C., Qu X. Cerium oxide nanoparticle: A remarkably versatile rare earth nanomaterial for biological applications. *NPG Asia Mater.*, 2014, **6** (3), e90.
[29] Alpaslan E., Geilich B.M., Yazici H., et al. pH-controlled cerium oxide nanoparticle inhibition of both gram-positive and gram-negative bacteria growth. *Sci. Rep.*, 2017, **7** (1), 45859.
[30] Pandey S., Kumari S., Manohar Aeshala L., et al. Investigating temperature variability on antioxidative behavior of synthesized cerium oxide nanoparticle for potential biomedical application. *J. Biomater. Appl.*, 2024, **38** (7), P. 866–874.
[31] Sozarukova M.M., Proskurnina E.V., Baranchikov A.E., et al. CeO_2 nanoparticles as free radical regulators in biological systems. *Nanosyst.: Phys. Chem. Math.*, 2020, **11** (3), P. 324–332.
[32] Klochkov V., Malyukin Y.V., Grygorova G., et al. Oxidation-reduction processes in CeO_{2-x} nanocrystals under UV irradiation. *J. Photochem. Photobiol. A Chem.*, 2018, **364**, P. 282–287.
[33] Zholobak N., Ivanov V., Shcherbakov A., et al. UV-shielding property, photocatalytic activity and photocytotoxicity of ceria colloid solutions. *J. Photochem. Photobiol. B Biol.*, 2011, **102** (1), P. 32–38.
[34] Wenk J., Brenneisen P., Meewes C., et al. UV-induced oxidative stress and photoaging. *Curr. Probl. Dermatol.*, 2001, **29**, P. 83–94.
[35] Pattison D.I., Rahmanto A.S., Davies M.J. Photo-oxidation of proteins. *Photochem. Photobiol. Sci.*, 2012, **11** (1), P. 38–53.
[36] Sozarukova M.M., Skachko N.A., Chilikina P.A., et al. Effect of low-dose line-spectrum and full-spectrum UV on major humoral components of human blood. *Molecules*, 2023, **28** (12), 4646.
[37] Plakhova T.V., Romanchuk A.Y., Butorin S.M., et al. Towards the surface hydroxyl species in CeO_2 nanoparticles. *Nanoscale*, 2019, **11** (43), P. 18142–18149.
[38] Madaeni S., Ghaemi N., Alizadeh A., et al. Influence of photo-induced superhydrophilicity of titanium dioxide nanoparticles on the anti-fouling performance of ultrafiltration membranes. *Appl. Surf. Sci.*, 2011, **257** (15), P. 6175–6180.
[39] Jimmy C.Y., Yu J., Ho W., Zhao, J. Light-induced super-hydrophilicity and photocatalytic activity of mesoporous TiO_2 thin films. *J. Photochem. Photobiol. A Chem.*, 2002, **148** (2–3), P. 331–339.
[40] Shcherbakov A.B., Teplonogova M.A., Ivanova O.S., et al. Facile method for fabrication of surfactant-free concentrated CeO_2 sols. *Mater. Res. Express*, 2017, **4** (5), 055008.
[41] Liochev S.I., Fridovich I. Lucigenin as mediator of superoxide production: Revisited. *Free Radic. Biol. Med.*, 1998, **25** (9), P. 926–928.
[42] Afanas'ev I.B. Lucigenin chemiluminescence assay for superoxide detection. *Circ. Res.*, 2001, **89** (11), e46.
[43] Sozarukova M.M., Proskurnina E.V., Ivanov V.K. Prooxidant potential of CeO_2 nanoparticles towards hydrogen peroxide. *Nanosyst.: Phys. Chem. Math.*, 2021, **12** (3), P. 283–290.
[44] Huber R., Stoll S. Protein affinity for TiO_2 and CeO_2 manufactured nanoparticles. From ultra-pure water to biological media. *Colloids Surf. A*, 2018, **553**, P. 425–431.
[45] Sendra M., Volland M., Balbi T., et al. Cytotoxicity of CeO_2 nanoparticles using in vitro assay with Mytilus galloprovincialis hemocytes: Relevance of zeta potential, shape and biocorona formation. *Aquat. Toxicol.*, 2018, **200**, P. 13–20.
[46] Socrates G. *Infrared and raman characteristic group frequencies: Tables and charts*. John Wiley & Sons, Chichester, 2004, 368 p.
[47] Bellamy L.J. *The infra-red spectra of complex molecules*. Springer Science & Business Media, London, 2013, 433 p.
[48] Rokhsat E., Akhavan O. Improving the photocatalytic activity of graphene oxide/ZnO nanorod films by UV irradiation. *Appl. Surf. Sci.*, 2016, **371**, P. 590–595.
[49] Wu T.-S., Syu L.-Y., Lin C.-N., et al. Enhancement of catalytic activity by UV-light irradiation in CeO_2 nanocrystals. *Sci. Rep.*, 2019, **9** (1), 8018.
[50] Gil D.O., Dolgopolova E.A, Shekunova T.O., et al. Photoprotector properties of ceria-based solid solutions. *Nanosyst.: Phys. Chem. Math.*, 2013, **4** (1), P. 78–82. (In Russian).

[51] Calvache-Muñoz J., Rodríguez-Páez J.E. Removal of rhodamine 6G in the absence of UV radiation using ceria nanoparticles (CeO_2-NPs). *J. Environ. Chem. Eng.*, 2020, **8** (1), 103518.
[52] Zhang L., Jiang H., Selke M., Wang, X. Selective cytotoxicity effect of cerium oxide nanoparticles under UV irradiation. *J. Biomed. Nanotechnol.*, 2014, **10** (2), P. 278–286.
[53] Osman R., Basch H. On the mechanism of action of superoxide dismutase: A theoretical study. *J. Am. Chem. Soc.,* 1984, **106** (19), P. 5710–5714.
[54] Noodleman L., Lovell T., Han W.-G., et al. Quantum chemical studies of intermediates and reaction pathways in selected enzymes and catalytic synthetic systems. *Chem. Rev*., 2004, **104** (2), P. 459–508.
[55] Marquette C.A., Blum L.J. Applications of the luminol chemiluminescent reaction in analytical chemistry. *Anal. Bioanal. Chem.*, 2006, **385** (3), P. 546–554.
[56] Kobayashi H., Gil-Guzman E., Mahran A.M., et al. Quality control of reactive oxygen species measurement by luminol-dependent chemiluminescence assay. *J. Androl.*, 2001, **22** (4), P. 568–574.
[57] Gao L., Giglio K.M., Nelson J.L., et al. Ferromagnetic nanoparticles with peroxidase-like activity enhance the cleavage of biological macromolecules for biofilm elimination. *Nanoscale*, 2014, **6** (5), P. 2588–2593.
[58] Corgié S.C., Kahawong P., Duan X., et al. Self-assembled complexes of horseradish peroxidase with magnetic nanoparticles showing enhanced peroxidase activity. *Adv. Funct. Mater.*, 2012, **22** (9), P. 1940–1951.
[59] Neves-Petersen M.T., Klitgaard S., Carvalho A.S.L., et al. Photophysics and photochemistry of horseradish peroxidase A2 upon ultraviolet illumination. *Biophys. J.*, 2007, **92** (6), P. 2016–2027.
[60] Falguera V., Moulin A., Thevenet L., Ibarz A. Inactivation of peroxidase by ultraviolet–visible irradiation: Effect of pH and melanoidin content. *Food Bioprocess Technol.*, 2013, **6** (4), P. 3627–3633.

Submitted 29 October 2025; accepted 16 November 2025

Information about the authors:

Madina M. Sozarukova – Kurnakov Institute of General and Inorganic Chemistry of the Russian Academy of Sciences, Leninskii prospect 31, Moscow, 119991, Russia; ORCID 0000-0002-5868-4746; s_madinam@bk.ru

Arina D. Filippova – Kurnakov Institute of General and Inorganic Chemistry of the Russian Academy of Sciences, Leninskii prospect 31, Moscow, 119991, Russia; ORCID 0000-0002-2725-8891; arifilippova@yandex.ru

Daria-Maria V. Ratova – Analytical Chemistry Division, Chemistry Department, M. V. Lomonosov Moscow State University, d. 1, Str. 3, Lenin Hills, GSP-1, Moscow, 119234, Russia; ORCID 0009-0006-0606-8059; darmarrat@gmail.com

Ivan V. Mikheev – Analytical Chemistry Division, Chemistry Department, M. V. Lomonosov Moscow State University, d. 1, Str. 3, Lenin Hills, GSP-1, Moscow, 119234, Russia; ORCID 0000-0002-2383-1697; mikheev.ivan@gmail.com

Elena V. Proskurnina – Kurnakov Institute of General and Inorganic Chemistry of the Russian Academy of Sciences, Leninskii prospect 31, Moscow, 119991, Russia; ORCID 0000-0002-8243-6339; proskurnina@gmail.com

Alexander E. Baranchikov – Kurnakov Institute of General and Inorganic Chemistry of the Russian Academy of Sciences, Leninskii prospect 31, Moscow, 119991, Russia; ORCID 0000-0002-2378-7446; a.baranchikov@yandex.ru

Vladimir K. Ivanov – Kurnakov Institute of General and Inorganic Chemistry of the Russian Academy of Sciences, Leninskii prospect 31, Moscow, 119991, Russia ORCID 0000-0003-2343-2140; van@igic.ras.ru

Conflict of interest: the authors declare no conflict of interest.

NANOSYSTEMS:
PHYSICS, CHEMISTRY, MATHEMATICS

Elovikov D.P., et al. *Nanosystems: Phys. Chem. Math.*, 2025, **16** (6), 802–811.
http://nanojournal.ifmo.ru
DOI 10.17586/2220-8054-2025-16-6-802-811

Original article

Thermodynamic analysis of nanocrystal formation in the TiO_2–H_2O (NaOH, HCl) system

Dmitry P. Elovikov[1,a], Oksana V. Almjasheva[1,b], Victor V. Gusarov[1,c]

[1]Branch of Petersburg Nuclear Physics Institute named by B. P. Konstantinov of National Research Centre "Kurchatov Institute" – Institute of Silicate Chemistry, St. Petersburg, Russia

[a]syncdima@mail.ru, [b]almjasheva@mail.ru, [c]victor.vladimirovich.gusarov@mail.ru

Corresponding author: D. P. Elovikov, syncdima@mail.ru

ABSTRACT A thermodynamic analysis of the crystallization of titanium dioxide in the anatase, brookite, and rutile modifications from aqueous salt solutions was performed, taking into account the influence of medium pH, temperature, reagent concentration, and the specific surface energy (σ) of the phases. It was shown that the choice of the σ value for the thermodynamic analysis of anatase crystallization is decisive: at σ_A = 0.3 J/m^2, the minimum particle size is determined by the crystallochemical criterion (l_{min} ∼5–7 nm), while at σ_A = 1.3 J/m^2, it is determined by thermodynamic criteria (d_{crit} ∼8 nm, d_{eq} ∼12 nm). Using σ values most closely approximating the conditions of a hydrated TiO_2 surface (σ_R = 1.79, σ_B = 1.0, σ_A = 1.13 J/m^2), the regions of possible crystallization for each modification were determined. Rutile can crystallize in a relatively wide pH range of 0.8–14 (25 °C) and 1.1–10.2 (200 °C), and the minimum particle sizes of rutile under these conditions are determined by thermodynamic criteria – dcrit and deq. For brookite and anatase in acidic and alkaline conditions (pH ∼1–3 and 9–14), the minimum particle sizes, as for rutile, are also determined by thermodynamic criteria, whereas in the neutral region, they are determined by the crystallochemical criterion l_{min}. Based on the analysis of structural transitions, it was established that anatase can transform into rutile or brookite at particle sizes larger than ∼16 nm. The calculated size for the brookite → rutile transition is ∼712 nm.

KEYWORDS nanocrystals, titanium oxide, critical nucleus.

ACKNOWLEDGEMENTS The work was supported by state assignment No. 1023032900322-9-1.4.3.

FOR CITATION Elovikov D.P., Almjasheva O.V., Gusarov V.V. Thermodynamic analysis of nanocrystal formation in the TiO_2–H_2O (NaOH, HCl) system. *Nanosystems: Phys. Chem. Math.*, 2025, **16** (6), 802–811.

1. Introduction

To date, the most studied structural types of titanium dioxide are anatase, brookite, and rutile [1–10]. Research focused on studying the formation processes and structural transformations of TiO_2 is described in a substantial number of works, some of which are presented here [11–17]. This interest is primarily related to the wide range of applications of titanium oxide in various fields [9, 18, 20–28]. The properties of the resulting TiO_2 particles and materials based on them are highly sensitive to the choice of the synthesis method [9, 18, 29–31].

Common methods for obtaining specific structural types of oxide nanocrystals include precipitation [32–34], hydrothermal treatment [35–38], sol-gel synthesis [39–41], or their combination at various stages of formation or structural transformations [42–44]. A common feature of these methods is the use of mobile media, particularly aqueous solutions and hydrothermal fluids, to achieve intensive mass transfer of reagents. The sensitive parameters in obtaining nanoparticles by such methods are temperature, pH value, ionic strength of the aqueous salt solution, and component concentrations. All of the above applies fully to the preparation of titanium oxide nanoparticles of various polymorphic modifications as well.

Thermodynamic assessments of the stability of nanoparticles of various structural types of TiO_2 – anatase, brookite, and rutile – are of interest for the targeted synthesis of TiO_2-based nanopowders with specified structures and properties, and can be found, in particular, in works [45, 46]. However, works dedicated to considering the composition of aqueous salt media during the formation of TiO_2 are absent or have a different focus: [6, 11, 16]. Data on the thermodynamics of formation of TiO_2 nanoparticles with anatase, brookite, and rutile structures during their crystallization from aqueous salt media at various temperatures and pH values are lacking in the literature. The main problems in such calculations are likely the absence or insufficient accuracy of the necessary thermodynamic data. For example, known databases such as IVTANTHERMO [48], JANAF [49], and HSC 6 [50] lack thermodynamic data for the brookite condensed phase and water-soluble Ti species (with the exception of HSC 6, which contains data for $Ti(OH)_4^-(aq)$). Numerical values for the enthalpies of the rutile-brookite and anatase-brookite transitions are given in [51]. There are experimental works dedicated to the thermodynamics of TiO_2 hydrolysis or dissolution processes [52–54]. In the context of studying the thermodynamic feasibility of forming various structural types of TiO_2, the estimation of critical and equilibrium nucleus sizes is also of

interest. Such estimates are presented in a number of works for crystallization from a melt, for example [55]. In the case of crystallization from aqueous solutions, the analysis of the influence of aqueous salt media on crystallization processes is limited [56], or focused on kinetic aspects of crystallization [56, 57], or does not account for the medium's influence [6, 59]. Furthermore, the majority of works are dedicated to the thermodynamic assessment of size effects and their connection to structural transitions [6, 45, 46]. The main problem in such calculations that account for the liquid phase, besides the lack of thermodynamic data, is the problem of choosing a correct value for the specific surface energy (σ) for anatase, brookite, and rutile crystallizing under different conditions (particularly from aqueous salt media). There are two main types of approaches to determining specific surface energy: experimental and theoretical. Experimental approaches are typically based on the analysis of thermodynamic data from aggregation, sintering, adsorption processes, and the interpretation of temperature dependencies of changes in specific surface area and particle growth activation energy. These approaches allow only an indirect estimation of the specific surface energy and often yield significantly differing results [6, 45, 51, 60]. Theoretical approaches are based on quantum-mechanical calculation methods and allow for the estimation of specific surface energy values for individual crystallographic planes, taking into account atomic relaxation, as well as possible adsorption of water molecules or hydroxyl groups [6, 61, 62]. However, even in this case, the results of such calculations depend on the chosen interaction parameters, simulation conditions, and the degree to which surface defects are accounted for. Data on specific surface energy in various aqueous salt media are very limited, not to mention the temperature dependence $\sigma = \sigma(T)$. It should also be noted that when determining the minimum possible crystal sizes for various TiO_2 modifications, crystallochemical constraints described in [63] are practically not taken into account. This also limits the reliability of the calculated data obtained regarding the sizes of forming TiO_2 nanocrystals.

Thus, the uncertainty in selecting the correct specific surface energy value for the anatase, brookite, and rutile structural types remains one of the key factors limiting the reliability and accuracy of thermodynamic calculations for the sizes of critical and equilibrium nuclei and the stability of nano-sized TiO_2 particles in various aqueous media. Therefore, a thermodynamic analysis of the influence of the pH of the aqueous salt medium, reagent concentration, temperature, specific surface energy value, as well as crystallochemical constraints on crystallite sizes, on the crystallization processes of TiO_2 solid phases with anatase, brookite, and rutile structural types from aqueous media is of significant interest.

2. Calculation

The thermodynamic analysis of TiO_2 crystallization processes from aqueous salt solutions was carried out with the following assumptions: the aqueous salt solution remains a liquid phase upon heating. The resulting solid particles have an isometric shape, close to spherical, with a size d. The influence of pressure on the thermodynamic properties of condensed phases was neglected, as pressure within the considered range of its variation has a negligible effect on these properties [48–50].

The following heterogeneous equilibrium is established in the reaction medium:

$$\mathrm{Ti}^{4+}_{(aq)} + 4\mathrm{OH}^{-}_{(aq)} \rightleftarrows \mathrm{TiO}_{2(s)} + 2\mathrm{H_2O}_{(l)} \tag{1}$$

In an aqueous salt solution, depending on the pH value, the following equilibria of water-soluble Ti(IV) species are established:

$$\mathrm{Ti}^{4+}_{(aq)} + \mathrm{OH}^{-}_{(aq)} \rightleftarrows \mathrm{Ti(OH)}^{3+}_{(aq)} \tag{2}$$

$$\mathrm{Ti}^{4+}_{(aq)} + 2\mathrm{OH}^{-}_{(aq)} \rightleftarrows \mathrm{Ti(OH)}^{2+}_{2(aq)} \tag{3}$$

$$\mathrm{Ti}^{4+}_{(aq)} + 3\mathrm{OH}^{-}_{(aq)} \rightleftarrows \mathrm{Ti(OH)}^{+}_{3(aq)} \tag{4}$$

$$\mathrm{Ti}^{4+}_{(aq)} + 4\mathrm{OH}^{-}_{(aq)} \rightleftarrows \mathrm{Ti(OH)}^{0}_{4(aq)} \tag{5}$$

$$\mathrm{Ti}^{4+}_{(aq)} + 5\mathrm{OH}^{-}_{(aq)} \rightleftarrows \mathrm{Ti(OH)}^{-}_{5(aq)} \tag{6}$$

$$\mathrm{Ti}^{4+}_{(aq)} + 6\mathrm{OH}^{-}_{(aq)} \rightleftarrows \mathrm{Ti(OH)}^{2-}_{6(aq)} \tag{7}$$

To calculate the change in the molar Gibbs energy ($\Delta_r G_m$) of reaction (1), taking into account the influence of particle size (d) and the pH of the reaction medium, the following equation was used:

$$\Delta_r G_m(T,\ \mathrm{pH}, d) = \Delta_r G^{\circ}_m(T) + \mathrm{R}T\ln K + \frac{6\sigma V_m}{d},$$

$$K = \frac{1}{x_{Ti^{4+}} \cdot a_{Ti^{4+}} \cdot a^4_{OH^-}} \quad x_{Ti^{4+}} = \frac{1}{1 + \sum \beta_i a^i_{OH^-}},$$

where $\Delta_r G^{\circ}_m(T)$ is the change in the standard molar Gibbs energy of reaction (1) (kJ/mol) at temperature $T(K)$; R is theuniversal gas constant (kJ/(mol·K)); K is the equilibrium constant of reaction (1); $a_{Ti^{4+}}$ is the activity of bound and unbound $\mathrm{Ti}^{4+}_{(aq)}$ ions; a_{OH^-} is the activity of $\mathrm{OH}^{-}_{(aq)}$ ions; $x_{Ti^{4+}}$ is the mole fraction of unbound water-soluble $\mathrm{Ti}^{4+}_{(aq)}$ cations; σ is the specific surface energy (kJ/nm^2); V_m is the molar volume of TiO_2 (nm^3/mol); d is the particle diameter (nm); β_i is the stability constant of the water-soluble i-th aquahydroxo complex based on equilibria (2)–(7) in the aqueous salt medium.

Based on homogeneous equilibria in the aqueous medium (2)–(7) and the condition $\sum_{k=0}^{i} x_{Ti(OH)_n^{4-n}} = 1$, the mole fraction of unbound water-soluble $Ti^{4+}_{(aq)}$ cations was calculated as a function of the pH value in the aqueous salt medium. The ionic strength of the solution was estimated for an aqueous solution with the composition $TiCl_4$ and NaOH, assuming that $C(Ti^{4+})=C(TiCl_4)$ and $C(OH^-)=C(NaOH)$ at each calculation point. The activity coefficients of the Ti^{4+}(aq) and OH-(aq) ions, required for estimating their activities in the aqueous salt solution, were calculated using the Davies equation [64] for each pH value, total molar concentration of Ti^{4+} (C, mol/L), and solution ionic strength. The temperature dependence of activity coefficients in the Davies equation was accounted for using data from [65] at 25 and 200 °C.

The necessary data for calculating the $\Delta_r G^\circ_m(T)$ values for equilibrium (1) were taken from the JANAF, IVTANTHERMO, and HSC 6 databases. The molar Gibbs energy of formation for the brookite modification was estimated based on the molar enthalpy of the rutile-brookite transformation (0.71±0.38 kJ/mol) according to data from [51] and the molar entropy of brookite formation at different temperatures [66], using the thermodynamic properties of rutile from the three databases mentioned above. Thus, the molar Gibbs energy of formation of brookite at 25 °C, using the thermodynamic properties of rutile from JANAF, IVTANTHERMO, and HSC 6, is −383.90, −383.21, and −384.28 kJ/mol, respectively. At 200 °C, these values are −529.69, −529.06, and −530.11 kJ/mol.

The values of $\Delta_f G^\circ_m(Ti(OH)^{4-n}_{n(aq)})$ for n = 0–6, which are absent in the databases (except for the case n = 4), were estimated based on experimental data presented in [52, 54, 67]. Thus, the molar Gibbs energy of formation of the $Ti^{4+}_{(aq)}$ ion is: −350.2 kJ/mol at 25 °C. An estimate of this value at 200 °C (−317 kJ/mol) was made based on data from [53] and the thermodynamic data for $Ti(OH)_4$(aq) specified in the HSC 6 database.

Based on data on the hydrolysis constants of the rutile modification [53] and the molar Gibbs energy of formation of the $Ti^{4+}_{(aq)}$ ion, the molar Gibbs energies of formation of $Ti(OH)^{+}_{3(aq)}$ and $Ti(OH)^{-}_{5(aq)}$ at 200 °C were estimated. Based on this, dependencies of the molar Gibbs energy of formation of the $Ti(OH)^{4-n}_{n(aq)}$ complexes on the number n (Fig. 1) were constructed for temperatures of 25 °C and 200 °C, and the stability constants (eq. (2)–(6)) at 200 °C were estimated, which had not been explicitly presented in the scientific literature before.

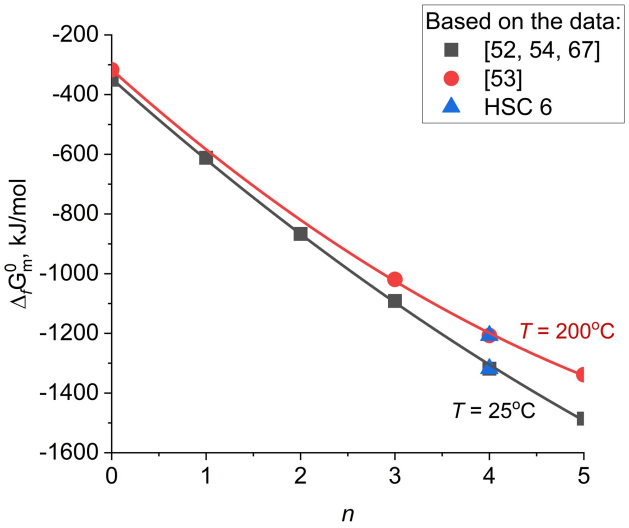

FIG. 1. Dependence of the molar Gibbs energy of formation of water-soluble $Ti(OH)^{4-n}_{n(aq)}$ species on the number n at temperatures of 25 and 200 °C

Thus, for all subsequent calculations, the following stability constant ($\lg\beta$) data for mononuclear hydroxo complexes $Ti(OH)^{4-n}_{n(aq)}$ were used: At a temperature of 25 °C: 18.51±0.40, 34.53±0.36, 48.06±0.41, 59.09±0.43, 61.17±0.38, and 56.22±0.51 for n = 1–6, respectively. At a temperature of 200 °C: 14.31±0.25, 29.03±0.32, 41.95±0.35, 50.80±0.52, and 53.43±0.45 for n = 1–5, respectively.

According to the dependencies of the molar Gibbs energy for reaction (1) on pH, constructed using the three databases, it can be concluded that the resulting values show minor differences (Fig. 2). In this case, the range of values for anatase, according to IVTANTHERMO, almost always lies between the values determined using the JANAF and HSC 6 databases (Fig. 2). Therefore, subsequent calculations were performed using thermodynamic data taken from the IVTANTHERMO database.

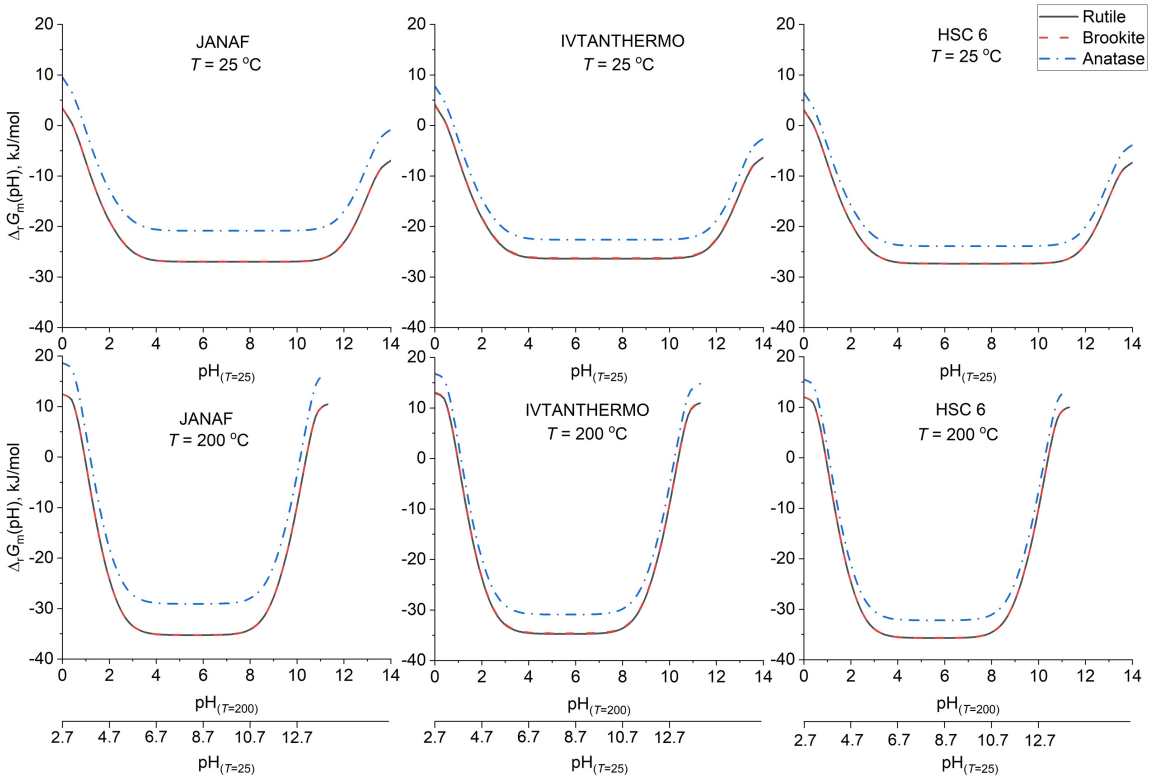

FIG. 2. Dependencies of the change in molar Gibbs energy for equilibrium (1) on pH value (T = 25 and 200 °C, C = 10^{-3} M), plotted using thermodynamic data taken from the JANAF, IVTANTHERMO, and HSC 6 databases for the rutile, brookite, and anatase modifications

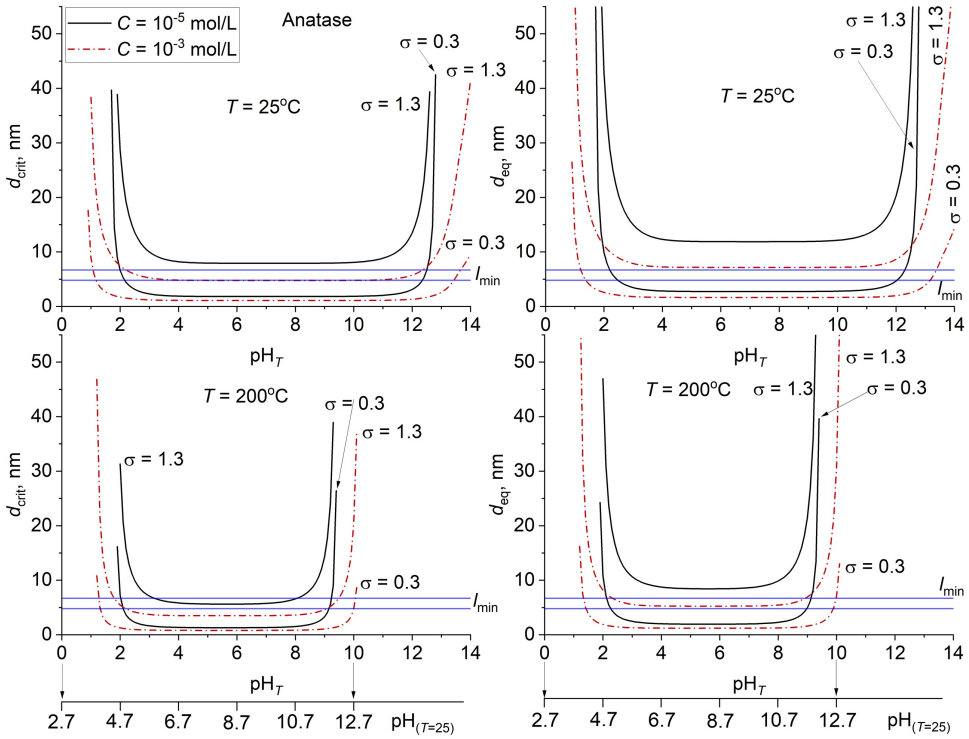

FIG. 3. Dependencies of the critical (d_{crit}) and equilibrium (d_{eq}) nucleus sizes of the anatase modification of TiO_2 on the pH of the aqueous salt medium, the value of specific surface energy (σ, J/m^2), and the concentration of the titanium-containing component (C) at 10^{-5} and 10^{-3} mol/L at temperatures of 25 and 200 °C. The double line indicates the estimated limits of variation for the minimum possible sizes of anatase crystals from a crystallochemical perspective (l_{min})

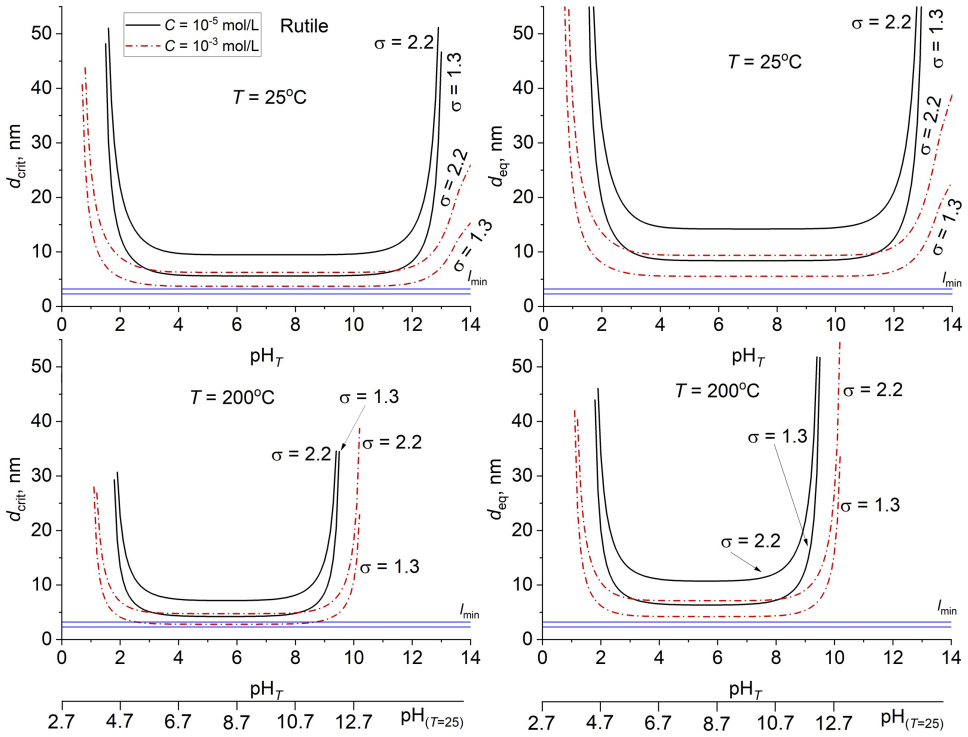

FIG. 4. Dependencies of the critical (d_{crit}) and equilibrium (d_{eq}) nucleus sizes of the rutile modification of TiO_2 on the pH of the aqueous salt medium, the specific surface energy value (σ, J/m^2), and the concentration of the titanium-containing component (C) at 10^{-5} and 10^{-3} mol/L at temperatures of 25 and 200 °C. The double line indicates the estimated limits of variation for the minimum possible sizes of anatase crystals from a crystallochemical perspective (l_{min})

The dependence of the critical (d_{crit}) and equilibrium (d_{eq}) nucleus sizes of various polymorphic modifications of TiO_2 on temperature and pH value was determined based on expressions (8) and (9), respectively:

$$d_{crit}(T, pH) = -\frac{4\sigma V_m}{\Delta_r G^{\circ}_m(T) + RT\ln K},$$

$$d_{eq}(T, pH) = -\frac{6\sigma V_m}{\Delta_r G^{\circ}_m(T) + RT\ln K}.$$

An estimation of the minimum possible size of crystalline TiO_2 particles with different structures, based on crystallochemical concepts, was performed using the empirical expression proposed in the work [63]:

$$l_{min} = \max(a, b, c) \cdot N, [nm] \quad (8)$$

where a, b, c are the values of the unit cell parameters (nm); N is an empirical parameter (N ≈5–7). The values of the unit cell parameters for various polymorphic modifications of TiO_2 were taken from the work [68, 69].

For calculations involving variation of the specific surface energy (σ, J/m^2), ranges of values obtained experimentally and reported in works [6, 45, 51, 60] for rutile and anatase were used: σ_R = 1.3–2.2, σ_A = 0.3–1.3 J/m^2. For calculations with a fixed specific surface energy value, the values reported in [6] and calculated using the DFT method, taking into account the influence of the aqueous environment (surface hydration), were used: $\sigma_R = 1.79$, $\sigma_A = 1.13$ J/m^2. These values satisfactorily agree with the experimental data from [45] and are apparently the most applicable within the scope of this work. For all calculations involving brookite, the value $\sigma_B = 1.0$ J/m^2 [51] was used. The influence of temperature on the specific surface energy values was not considered due to limited literature data.

3. Result and discussion

Due to the significant spread in data on the specific surface energy of anatase and rutile modifications, it is necessary to examine the influence of this parameter's value on the results of thermodynamic calculations of the critical and equilibrium nucleus sizes of TiO_2 for these modifications.

As can be concluded from the analysis of the calculation results presented in Fig. 3, the sizes of the critical and equilibrium nuclei of anatase practically do not change during crystallization from aqueous salt media in the pH range of 4–11 (25 °C) and 4–8 (200 °C), but strongly depend on the chosen value of the specific surface energy. Increasing the specific surface energy values from 0.3 to 1.3 J/m^2 when estimating the dcrit of anatase in aqueous salt solutions

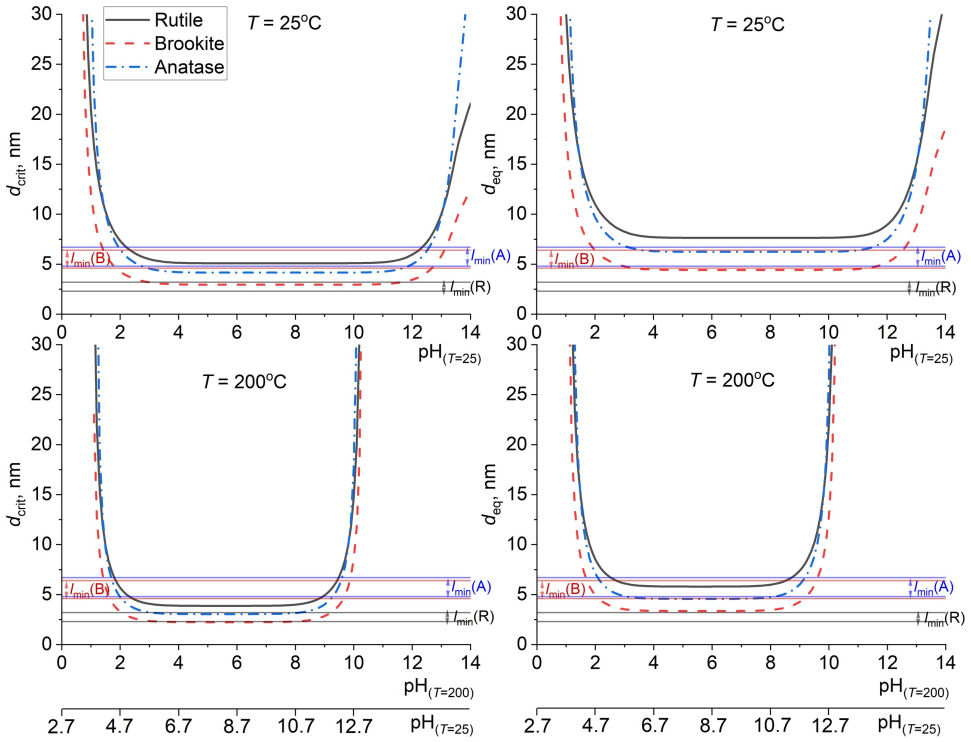

FIG. 5. Dependencies of the critical (d_{crit}) and equilibrium (d_{eq}) nucleus sizes of various TiO_2 modifications on the pH of the aqueous salt medium at temperatures of 25 °C and 200 °C and a titanium-containing component concentration (C) of 10^{-3} mol/L. The specific surface energy values were taken as follows (J/m^2): $\sigma_R = 1.79$, $\sigma_A = 1.13$, $\sigma_B = 1.0$. Double lines indicate the estimated limits of variation for the minimum possible sizes of rutile, anatase, and brookite crystals from a crystallochemical perspective – $l_{min}(R)$, $l_{min}(A)$, $l_{min}(B)$, respectively

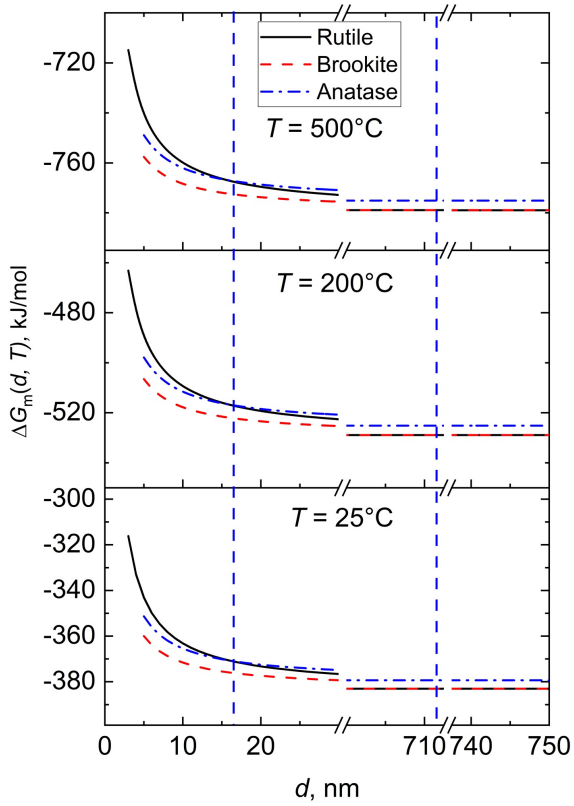

FIG. 6. Dependencies of the molar Gibbs energy of formation of TiO_2 on particle size at different temperatures

($C = 10^{-5}$ mol/L) leads to its increase by a factor of four: approximately 2 nm (σ_A = 0.3 J/m^2) and 8 nm (σ_A = 1.3 J/m^2) at 25 °C. At the same time, the minimum size for crystallochemically stable existence (l_{min}) [63] of anatase crystals lies in the range of approximately 5–7 nm. This means that when using the value σ_A = 0.3 J/m^2 in calculations, the determining criterion for the minimum particle sizes of anatase will be the crystallochemical criterion. In the case where the value σ_A = 1.3 J/m^2 is used in calculations, the minimum particle sizes of anatase will be determined by thermodynamic criteria (d_{crit} ∼8 nm, d_{eq} ∼12 nm).

Shifting the pH of the aqueous salt solution into more acidic or alkaline regions leads to an increase in the values of d_{crit} and d_{eq}. However, the pH ranges for the existence of anatase under such conditions are quite narrow due to the dominance of the particle dissolution process (Fig. 3).

The problem of choosing the specific surface energy value for the rutile modification is not as significant as in the case of anatase. The calculation results indicate that the minimum particle size of rutile, under the considered crystallization conditions, is determined by the thermodynamic criterion, as the minimum possible sizes from a crystallochemical perspective (l_{min}) are significantly lower (Fig. 4).

Using the specific surface energy values most closely approximating the case of hydrated TiO_2 surfaces for thermodynamic analysis (Fig. 5), several regions of possible crystallization and relatively stable existence of nanocrystals can be identified. In this case, the main criterion for determining these regions is the comparison of d_{crit}, d_{eq}, and l_{min} values.

Rutile, as the most thermodynamically stable modification, can crystallize at a temperature of 25 °C in a relatively wide pH range of 0.8–14 of the aqueous salt solution. When the temperature increases to 200 °C, this pH range is: 1.1–10.2.

Brookite is a metastable modification [45], although its molar Gibbs energy of formation is close to that of rutile. An important criterion for determining the boundaries of brookite crystallization is the l_{min} value, which is significantly higher than the size of the critical nucleus and practically twice the l_{min} value of rutile (Fig. 5).

Brookite can crystallize at a temperature of 25 °C in acidic and alkaline media within the pH range of approximately 1–2 and 12–14 ($d_{crit} > l_{min}$). When the temperature increases to 200 °C, this pH range becomes approximately 1–2 and 9–10, respectively. This indicates that brookite has a greater tendency to crystallize from acidic and alkaline aqueous salt solutions, according to the calculation results (Fig. 5).

The regions of anatase modification crystallization from an aqueous salt medium can be characterized, according to the calculation results (Fig. 5), as follows: at a temperature of 25 °C within the pH range of 1–3 and 11.5–14; at a temperature of 200 °C within the range of 1.2–2.4 and 8.9–10.1. In general, the crystallization boundaries for anatase are similar to those for brookite in an alkaline medium. In an acidic medium, these boundaries for anatase lie within a wider pH range (1.2–2.4) at 200 °C compared to brookite (pH = 1.1–1.8). This suggests that anatase has a greater tendency to crystallize in an acidic environment than brookite does. However, the minimum sizes from a crystallochemical perspective for anatase and brookite are quite similar (Fig. 5). It is likely that the crystallization of either anatase or brookite under these conditions will be determined to a greater extent by synthesis specifics and kinetic factors.

Following the analysis of TiO_2 crystallization in the rutile, brookite, and anatase structures, determining the possibilities of structural transitions between these modifications is important. According to the calculation (Fig. 6), the intersection points of the molar Gibbs energy of formation for the anatase and rutile modifications of TiO_2 are practically independent of temperature. For anatase crystal sizes larger than approximately 16 nm, TiO_2 can transit either into the rutile structure, which aligns with the conclusions of the work [51], or into the brookite structure. Starting from particle sizes of 40–60 nm, the specific surface energy contributes insignificantly to the molar Gibbs energy value. Consequently, from a particle size of about 40 nm onwards, the molar Gibbs energy values for rutile and brookite become very close. However, if the specific surface energy values are taken as 1.79 J/m^2 for rutile and 1.0 J/m^2 for brookite, then the brookite-to-rutile transition becomes thermodynamically feasible at particle sizes of approximately 712 nm. The estimation of stability boundaries and structural transitions strongly depends on the choice of the specific surface energy value for the calculation. It is quite possible that the specific surface energy of brookite, for which data in the literature is very limited, could be higher if surface hydration is taken into account. It should be noted that the large particle size of brookite at which its transformation into rutile becomes thermodynamically possible indicates that, in practice, one can expect to obtain macrocrystals of brookite in a relatively stable state due to the kinetically hindered nature of the brookite-to-rutile transition for such particles.

4. Conclusions

Thus, it was shown that the choice of the specific surface energy value for anatase, which according to literature data varies within a relatively wide range (0.3–1.3 J/m^2), significantly influences the calculation results. For instance, when using the value σ_A = 0.3 J/m^2 in calculations, the determining criterion for the minimum particle sizes of anatase will be the crystallochemical criterion. Conversely, when the value σ_A = 1.3 J/m^2 is used, the minimum particle sizes of anatase will be determined by thermodynamic criteria (d_{crit} ∼8 nm, d_{eq} ∼12 nm). Based on the thermodynamic analysis of TiO_2 particle crystallization using specific surface energy values most closely approximating these conditions for rutile (σ_R = 1.79 J/m^2), brookite (σ_B = 1.0 J/m^2), and anatase (σ_A = 1.13 J/m^2), the regions of possible crystallization was determined. Rutile can crystallize in a relatively wide pH range of 0.8–14 at 25 °C and 1.1–10.2 at 200 °C, and the

minimum particle sizes of rutile under these conditions are determined by thermodynamic criteria – d_{crit} and d_{eq}. The minimum sizes of brookite crystalline particles in acidic and alkaline media within the pH ranges of 0.7–2 and 12–14 at 25 °C, and 1.1–1.8 and 9.2–10.2 at 200 °C, are determined by thermodynamic criteria. In other considered conditions (pH 2–12 at 25 °C and 1.8–9.2 at 200 °C), the minimum brookite particle sizes are determined by the crystallochemical criterion ($l_{min} \sim$ 5–7 nm). The minimum sizes of anatase crystals in acidic and alkaline media within the pH ranges of 1–3 and 11.5–14 at 25 °C, and 1.2–2.4 and 8.9–10.1 at 200 °C, are determined by thermodynamic criteria (d_{crit}, d_{eq}). In the remaining considered conditions, as in the case of brookite, the crystallochemical criterion applies. Given that the minimum sizes from a crystallochemical perspective for anatase and brookite are very similar, the crystallization of these modifications under the considered conditions will be largely determined by the specifics of the synthesis conditions and kinetic factors. Based on the thermodynamic analysis of structural transitions, it was shown that anatase can transform into rutile or brookite at particle sizes larger than approximately 16 nm. Starting from particle sizes of about 40–60 nm, the specific surface energy does not contribute significantly to the molar Gibbs energy value. According to the calculation results, the structural transition from brookite to rutile occurs at particle sizes of 712 nm. However, prior to this transition, the molar Gibbs energies of rutile and brookite are so close that the difference between these values falls within the error frameworks for determining thermodynamic properties.

References

[1] Dachille F., Simons P.Y, Roy R. Pressure-temperature studies of anatase, brookite, rutile and TiO_2-II. *Am. Mineralogist*, 1968, **53**, P. 1929–1938.

[2] Wells A.F. S*tructural Inorganic Chemistry*. Oxford University Press, London W1, 1975, P. 109.

[3] Chemseddine A., Moritz T. Nanostructuring titania: control over nanocrystal structure, size, shape, and organization. *Eur. J. Inorg. Chem*., 1999, **2**, P. 235–245.

[4] Rempel A.A. Nonstoichiometry and defect structure of titanium dioxide. *Russian Chemical Reviews*, 1994, **63**(4), P. 303–326

[5] Hanaor D.A.H., Sorrell C.C. Review of the anatase to rutile phase transformation. *Journal of Materials science*, 2011, **46**(4), P. 855–874.

[6] Almjasheva O.V. Formation and structural transformations of nanoparticles in the TiO_2–H_2O system. *Nanosystems: Physics, Chemistry, Mathematics*, 2016, **7**(6), P. 1031–1049

[7] Yamakata A., Vequizo J.J.M. Curious behaviors of photogenerated electrons and holes at the defects on anatase, rutile, and brookite TiO_2 powders: A review. *Journal of Photochemistry and Photobiology C: Photochemistry Reviews*, 2019, **40**, P. 234–243.

[8] Manzoli M., Freyria F.S., Blangetti N., Bonelli B. Brookite, a sometimes under evaluated TiO_2 polymorph. *RSC Advances*, 2022. **12**(6), P. 3322–3334.

[9] Eddy D.R., Permana M.D., Sakti L.K., Sheha G.A.N., Solihudin, Hidayat S., Takei T., Kumada N., Rahayu I. Heterophase polymorph of TiO_2 (Anatase, Rutile, Brookite, TiO_2 (B)) for efficient photocatalyst: fabrication and activity. *Nanomaterials*, 2023, **13**(4), P. 704.

[10] Zhang H., Banfield J. Structural characteristics and mechanical and thermodynamic properties of nanocrystalline TiO_2. *Chemical Reviews*, 2014. **114**(19), P. 9613–9644.

[11] Pletnev R.N., Ivakin A.A., Kleshchev D.G., Denisova T.A., Burmistrov V.A. Hydrated Oxides of the Group IV and V Elements, 1986, P. 186.

[12] Onorin S.A. Structure of X-ray-amorphous hydrated titanium dioxide. *Russian Journal of Inorganic Chemistry*, 1992, **37**(6), P. 1228–1232.

[13] Reyes-Coronado D., Rodrıguez-Gattorno G., Espinosa-Pesqueira M.E., Cab C., de Coss R., Oskam G. Phase-pure TiO_2 nanoparticles: anatase, brookite and rutile. *Nanotechnology*, 2008. **19**(14), P. 145605.

[14] Zhang H., Banfield J. Understanding polymorphic phase transformation behavior during growth of nanocrystalline aggregates: insights from TiO_2. *The Journal of Physical Chemistry*, 2000, **104**(15), P. 3481–3487.

[15] Meskin P.E., Gavrilov A.I., Maksimov V.D., Ivanov V.K., Churagulov B.P. Hydrothermal/microwave and hydrothermal/ultrasonic synthesis of nanocrystalline titania, zirconia, and hafnia. *Russian Journal of Inorganic Chemistry*, 2007, **52**(11), P. 1648–1656.

[16] Dorosheva I.B., Valeeva A.A., Rempel A.A. Sol-gel synthesis of nanosized titanium dioxide at various pH of the initial solution. *AIP Conference Proceedings*, 2017, **1886**(020006).

[17] Zlobin V.V., Krasilin A.A., Almjasheva O.V. Effect of heterogeneous inclusions on the formation of TiO_2 nanocrystals in hydrothermal conditions. *Nanosystems: Physics, Chemistry, Mathematics.*, 2019, **10**(6), P. 733–739.

[18] Rempel A.A., Valeeva A.A., Vokhmintsev A.S., Weinstein I.A. Titanium dioxide nanotubes: Synthesis, structure, properties and applications. *Russian Chemical Reviews*, 2021, **90**(11), P. 1397–1414.

[19] Zlobin V.V., Nevedomskiy V.N., Almjasheva O.V. Formation and growth of anatase TiO_2 nanocrystals under hydrothermal conditions. *Materials Today Communications*, 2023, **36**, P. 106436.

[20] Onorin S.A., Khodyashev M.B., Denisova T.A., Zakharov N.D. Effect of synthesis conditions on structure and ion-exchange properties of hydrous titanium dioxide. *Russian Journal of Inorganic Chemistry*, 1992, **37**(6), P. 612–615.

[21] Onorin S.A., Khodyashev M.B., Zakharov N.D. Physicochemical studies of hydrated titanium dioxide and products of sorption of As and Na ions on it. *Russian Journal of Inorganic Chemistry*, 1992, **37**(6), P. 1223–1227.

[22] Roy P., Berger S., Schmuki P. TiO_2 nanotubes: synthesis and applications. *Angewandte Chemie International Edition*, 2011, **50**(13), P. 2904–2939.

[23] Nakata K., Fujishima A. TiO_2 photocatalysis: Design and applications. *Journal of photochemistry and photobiology C: Photochemistry Reviews*, 2012, **13**(3), P. 169–189.

[24] Lebedev V.A., Kozlov D.A., Kolesnik I.V., Poluboyarinov A.S., Becerikli A.E., Grünert W., Garshev A.V. The amorphous phase in titania and its influence on photocatalytic properties. *Applied Catalysis B: Environmental*, 2016, **195**, P. 39–47.

[25] Noman M.T., Ashraf M.A., Ali A. Synthesis and applications of nano-TiO_2: a review. *Environmental Science and Pollution Research*, 2019, **26**(4), P. 3262–3291.

[26] Kolesnik I.V., Lebedev V.A., Garshev A.V. Optical properties and photocatalytic activity of nanocrystalline TiO_2 doped by 3d-metal ions. *Nanosystems: Physics, Chemistry, Mathematics*, 2018, **9**(3), P. 401–409.

[27] Rempel A.A., Valeeva A.A. Nanostructured titanium dioxide for medicinal chemistry. *Russian Chemical Bulletin*, 2019, **68**(12), P. 2163–2171.

[28] Rempel A.A. Functional nanomaterials based on modified titanium dioxide. *Russian Chemical Bulletin*, 2024, **73**(8), P. 2144–2151.

[29] Kumar A., Pandey G. Different methods used for the synthesis of TiO_2 based nanomaterials: A review. *Am. J. Nano Res. Appl*., 2018. **6**(1), P. 1-10.

[30] Mironyuk I.F., Soltys L.M., Tatarchuk T.R., Savka K.O. Methods of titanium dioxide synthesis. *Physics and Chemistry of Solid State*, 2020, **21**(3), P. 462–477.

[31] Wang Z., Liu S., Cao X., et al. Preparation and characterization of TiO_2 nanoparticles by two different precipitation methods. *Ceramics International*, 2020, **46**(10), P. 15333–15341.
[32] Hu Y., Pan D., Zhang Z., et al. Preparation of $Cu_nCo_1O_x$ catalysts by co-precipitation method for catalytic oxidation of toluene. *Journal of Molecular Structure*, 2025, **1326**, P. 141139.
[33] Tian Z.M., Yuan S.L., He J.H., et al. Structure and magnetic properties in Mn doped SnO_2 nanoparticles synthesized by chemical co-precipitation method. *Journal of Alloys and Compounds*, 2008, **466**(1-2), P. 26–30.
[34] Yapryntsev A.D., Baranchikov A.E., Ivanov V.K. Layered rare-earth hydroxides: a new family of anion-exchangeable layered inorganic materials. *Russian Chemical Reviews*, 2020, **89**(6), P. 629–666.
[35] Enikeeva M.O., Proskurina O.V., Levin A.A., Smirnov A.V., Nevedomskiy V.N., Gusarov V.V. Structure of $Y_{0.75}La_{0.25}PO_4 \cdot 0.67H_2O$ rhabdophane nanoparticles synthesized by the hydrothermal microwave method. *Journal of Solid State Chemistry*, 2023, **319**, P. 123829.
[36] Bugrov A.N., Almjasheva O.V. Effect of hydrothermal synthesis conditions on the morphology of ZrO_2 nanoparticles. *Nanosystems: Physics, Chemistry, Mathematics*, 2013, **4**(6), P. 810.
[37] Lomakin M.S., Proskurina O.V., Sergeev A.A., Buryanenko I.V., Semenov V.G., Voznesenskiy S.S., Gusarov V.V. Crystal Structure and Optical Properties of the Bi–Fe–W–O Pyrochlore Phase Synthesized via a Hydrothermal Method. *J. Alloys Compd.*, 2021, **889**, P. 161598.
[38] Elovikov D.P., Proskurina O.V., Gusarov V.V. Formation of Alunite-type Compounds in the Bi_2O_3–Al_2O_3–Fe_2O_3–P_2O_5–H_2O System under Hydrothermal Conditions. *Russian Journal of Inorganic Chemistry*, 2025, **70**(7), P. 960–967.
[39] Tabesh S., Davar F., Loghman-Estarki M.R. Preparation of γ-Al_2O_3 nanoparticles using modified sol-gel method and its use for the adsorption of lead and cadmium ions. *J. Alloys Comp.*, 2018, **730**, P. 441–449.
[40] Zhang H., Ke H., Ying P., Luo H., Zhang L., Wang W., Jia D., Zhou Y. Crystallisation process of $Bi_5Ti_3FeO_{15}$ multiferroic nanoparticles synthesized by a sol–gel method. *J. Sol-Gel Sci. Technol.*, 2018, **85**(1), P. 132–139.
[41] El-Cheikh A.Z.F., Kwapinski W., Ahmad M.N., Leahy J.J., El-Rassy H. Nanoporous ZnO/SiO_2 aerogel and xerogel composites via a one-pot sol–gel process at room temperature. *RSC Adv RSC Advances*, 2025, **15**(47), P. 39566–39577.
[42] Belghiti M., El Mersly L., Tanji K., Belkodia K., Lamsayety I., Ouzaouit K., Foqir H., Benzakour I., Rofqah S., Outzourhit A. Sol-gel combined mechano-thermal synthesis of Y_2O_3, CeO_2, and PdO partially coated ZnO for sulfamethazine and basic yellow 28 photodegradation under UV and visible light. *Optical Materials*, 2023, **136**, P. 113458.
[43] Tang H., Hu Q., Jiang F., Jiang W., Liu J., Chen T., Feng G., Wang T., Luo W. Size control of $CZrSiO_4$ pigments via soft mechano-chemistry assisted non-aqueous sol-gel method and their application in ceramic glaze. *Ceramics International*, 2019, **45**(8), P. 10756–10764.
[44] Gurule A.C., Gaikwad S.S., Kajale D.D., Shinde V.S., Jadhav G.R., Gaikwad V.B. Synthesis of magnesium oxide nanoparticles via hydrothermal and sol-gel methods: Charaterization and their application for H_2S and NO_2 gas sensing. *Journal of the Indian Chemical Society*, 2025, **102**(1), P. 101496.
[45] Zhang H., Banfield J. Thermodynamic analysis of phase stability of nanocrystalline titania. *J. Mater. Chem.*, 1998, **8**, P. 2073–2076.
[46] Almjasheva O.V. Formation of oxide nanocrystals and nanocomposites under hydrothermal conditions, structure and properties of materials based on them. Abstract of a dissertation for the degree of Doctor of Chemical Sciences: specialty 02.00.21, St. Petersburg, 2017 (in Russian)
[47] Kalaivani T., Anilkumar P. Role of temperature on the phase modification of TiO_2 nanoparticles synthesized by the precipitation method. *Silicon*, 2018, **10**(4), P. 1679–1686.
[48] Belov G.V., Iorish V.S., Yungman V.S. IVTANTHERMO for Windows-database on thermodynamic properties and related software. *Calphad*, 1999, **23**(2), P. 173–180.
[49] Stull D.R. JANAF Thermochemical Tables. *Clearinghouse*, 1965, **1**.
[50] Roine A. HSC-software Ver. 3.0 for thermodynamic calculations. *Proceedings of the international symposium on computer software in chemical and extractive metallurgy*, 1989, P. 15–29.
[51] Ranade M.R., Navrotsky A., Zhang. H.Z., Banfield J.F., Elder S.H., Zaban A., Borse P.H., Kulkarni S.K., Doran G.S., Whitfield H.J. Energetics of nanocrystalline TiO_2. *Proc. Natl. Acad. Sci.*, 2002, **99**, P. 6476–6481.
[52] Ryzhenko B.N., Kovalenko N.I., Prisyagina N.I. Titanium complexation in hydrothermal systems. *Geochemistry International*, 2006, **44**(9), P. 879–895.
[53] Knauss K.G., Dibley M.J., Bourcier W.L., Shaw H.F. Ti (IV) hydrolysis constants derived from rutile solubility measurements made from 100 to 300 C. *Applied Geochemistry*, 2001, **16**(9-10), P. 1115–1128.
[54] Schmidt J., Vogelsberger W. Aqueous long-term solubility of titania nanoparticles and titanium (IV) hydrolysis in a sodium chloride system studied by adsorptive stripping voltammetry. *Journal of solution chemistry*, 2009, **38**(10), P. 1267–1282.
[55] Li Y., Ishigaki T. Thermodynamic analysis of nucleation of anatase and rutile from TiO_2 melt. *Journal of Crystal Growth*, 2002, **242**(3-4), P. 511–516.
[56] Molea A., Popescu V., Rowson N.A., Dinescu A.M. Influence of pH on the formulation of TiO_2 nano-crystalline powders with high photocatalytic activity. *Powder Technology*, 2014, **253**, P. 22–28.
[57] Razak K.A., Halin D.C., Abdullah M.M.A., Salleh M.M., Mahmed N., Azani A., Chobpattana V. Factors of controlling the formation of titanium dioxide (TiO_2) synthesized using sol-gel method–A short review. *Journal of Physics: Conference Series. IOP Publishing*, 2022, **2169**(1), P. 012018.
[58] Mehranpour H., Askari M., Ghamsari M. Nucleation and growth of TiO_2 nanoparticles. *Nanomaterials*, 2011, **22**, P. 3–26.
[59] Gribb A.A., Banfield J.F. Particle size effects on transformation kinetics and phase stability in nanocrystalline TiO_2. *American Mineralogist*, 1997, **82**(7-8), P. 717–728.
[60] Levchenko A.A., Li G., Boerio-Goates J., Woodfield B.F., Navrotsky A. TiO_2 stability landscape: Polymorphism, surface energy, and bound water energetics. *Chemistry of Materials*, 2006, **18**(26), P. 6324–6332.
[61] Oliver P.M., Watson G.W., Kelsey E.T., Parker S.C. Atomistic simulation of the surface structure of the TiO_2 polymorphs rutile and anatase. *Journal of Materials Chemistry*, 1997, **7**(3), P. 563–568.
[62] Gong X.Q., Selloni A. First-principles study of the structures and energetics of stoichiometric brookite TiO_2 surfaces. *Physical Review B—Condensed Matter and Materials Physics*, 2007, **76**(23), P. 235307.
[63] Almjasheva O.V., Lomanova N.A., Popkov V.I., Proskurina O.V., Tugova E.A., Gusarov V.V. The minimum size of oxide nanocrystals: phenomenological thermodynamic vs crystal-chemical approaches. *Nanosystems: Physics, Chemistry, Mathematics*, 2019, **10**(4), P. 428–437.
[64] Davies C.W. The extent of dissociation of salts in water. Part VIII. An equation for the mean ionic activity coefficient of an electrolyte in water, and a revision of the dissociation constants of some sulphates. *Journal of the Chemical Society*, 1938, P. 2093–2098.
[65] Helgeson H.C., Kirkham D.H. Theoretical prediction of the thermodynamic behavior of aqueous electrolytes at high pressures and temperatures; II, Debye-Huckel parameters for activity coefficients and relative partial molal properties. *American Journal of Science*, 1974, **274**(10), P. 1199–1261.

[66] Che X., Li L., Zheng J., Li G., Shi Q. Heat capacity and thermodynamic functions of brookite TiO_2. *The Journal of Chemical Thermodynamics*, 2016, **93**, P. 45–51.

[67] Shkol'Nikov E.V. Thermodynamics of the dissolution of amorphous and polymorphic TiO_2 modifications in acid and alkaline media. *Russian Journal of Physical Chemistry A*, 2016, **90**(3), P. 567–571.

[68] Cromer D.T., Herrington K. The structures of anatase and rutile. *Journal of the American Chemical Society*, 1955, **77**(18), P. 4708–4709.

[69] Manzoli M., Freyria F.S., Blangetti N., Bonelli B. Brookite, a sometimes under evaluated TiO_2 polymorph. *RSC Advances*, 2022, **12**(6), P. 3322–3334.

Submitted 22 September 2025; revised 10 October 2025; accepted 21 October 2025

Information about the authors:

Dmitry P. Elovikov – Branch of Petersburg Nuclear Physics Institute named by B. P. Konstantinov of National Research Centre "Kurchatov Institute" – Institute of Silicate Chemistry, St. Petersburg, Russia; ORCID 0000-0003-4345-6086; syncdima@mail.ru

Oksana V. Almjasheva – Branch of Petersburg Nuclear Physics Institute named by B. P. Konstantinov of National Research Centre "Kurchatov Institute" – Institute of Silicate Chemistry, St. Petersburg, Russia; ORCID 0000-0002-6132- 4178; almjasheva@mail.ru

Victor V. Gusarov – Branch of Petersburg Nuclear Physics Institute named by B. P. Konstantinov of National Research Centre "Kurchatov Institute" – Institute of Silicate Chemistry, St. Petersburg, Russia; ORCID 0000-0003-4375-6388; victor.vladimirovich.gusarov@mail.ru

Conflict of interest: the authors declare no conflict of interest.

NANOSYSTEMS:
PHYSICS, CHEMISTRY, MATHEMATICS

Chuvilo Y., et al. *Nanosystems: Phys. Chem. Math.*, 2025, **16** (6), 812–817.
http://nanojournal.ifmo.ru
DOI 10.17586/2220-8054-2025-16-6-812-817

Original article

Features of Ce(IV) phosphate coatings formation on the silica surface during their synthesis by successive ionic layer deposition method

Yuliana Chuvilo[1,a], Leonid Kuklo[1,b], Valeri Tolstoy[1,c]

[1]Institute of Chemistry, Saint Petersburg State University, University St. 26, St. Peterhof, Saint Petersburg, 198504, Russia

[a]st087011@student.spbu.ru, [b]lenkuklo@mail.ru, [c]v.tolstoy@spbu.ru

Corresponding author: Tolstoy V., v.tolstoy@spbu.ru

PACS 78.30.Lx, 78.40.Kc

ABSTRACT The article presents the conditions for obtaining Ce(IV) phosphate coatings on the surface of silicon and quartz by the successive ionic layer deposition (SILD) method. It has been shown that when using solutions of $(NH_4)_4Ce(SO_4)_4$ and NaH_2PO_4 as reagents, coatings of the composition $Ce(OH)PO_4 \cdot nH_2O$ are formed on the surface of the substrates, and when using solutions of $(NH_4)_4Ce(SO_4)_4$ and Na_3PO_4, coatings of the composition $Na_{0.2}Ce(OH)_{2.4}(PO_4)_{0.6} \cdot nH_2O$ are formed. These compounds have an amorphous structure. SEM analysis of $Na_{0.2}Ce(OH)_{2.4}(PO_4)_{0.6} \cdot nH_2O$ on the silicon surface showed that for the samples obtained as a result of 15 SILD cycles, the planar isotropic coatings are rolled into microtubules with a microscroll morphology of 3–5 μm in diameter and 30–100 μm in length. The composition of the noted Ce(IV) phosphates can be relatively easily doped during the synthesis process, for example, with Fe(II) cations and tungstate anions. It was found that $Ce(OH)PO_4 \cdot nH_2O$ coatings are characterized by intense absorption band in the UV region of the spectrum, and can be used as components in various types of absorbers. Moreover, the degree of absorption can be controlled by varying the number of synthesis conditions, for example, the number of SILD cycles.

KEYWORDS Ce(IV) phosphates, coatings, SILD, UV shielding, microscrolls.

ACKNOWLEDGEMENTS This work was supported by the RSF grant (project # 23-19-00566). We are grateful to the "Nanotechnology Centre" of Saint-Petersburg State University for technical assistance in the study of the synthesized samples.

FOR CITATION Chuvilo Y., Kuklo L., Tolstoy V. Features of Ce(IV) phosphate coatings formation on the silica surface during their synthesis by successive ionic layer deposition method. *Nanosystems: Phys. Chem. Math.*, 2025, **16** (6), 812–817.

1. Introduction

Rare earth element phosphates are known to exhibit a variety of practically important properties, and their study has received considerable attention [1–5]. Among these, Ce(IV) phosphates occupy a special place, exhibiting properties similar in many ways to those of other metal phosphates in the 4+ oxidation state, such as Ti(IV) and Zr(IV) phosphates. The conditions for the synthesis of Ce(IV) phosphates and the features of their chemical structure, as well as the results of studying their properties, are described in a number of reviews, for example in articles [6–8]. In particular, $Ce(PO_4)(HPO_4)_{0.5}(H_2O)_{0.5}$ is an active adsorbent for many environmentally unsafe metal cations, including radioactive ones [9]. Phosphates and Ce(IV) oxide are also actively studied as so-called nanozymes for biologically active processes in living organisms [10–12].

Significant results were obtained in studying the characteristics of UV radiation absorption by Ce(IV) phosphates [13, 14]. It is known that the main inorganic components of various types of creams for skin protection from UV radiation are titanium and zinc oxides, because they are characterized, on the one hand, by high absorption coefficients [15, 16] in this spectral region, and, on the other hand, they are uncolored in the visible region of the spectrum.

A similar function can be performed by cerium (IV) oxide. When irradiated with UV light, it does not generate active forms of oxygen that damage the skin, unlike titanium and zinc oxides.

In [17], it was shown that Ce(IV) phosphate exhibits properties similar to CeO_2, and in this regard, it is of interest to create new approaches to their synthesis. Another important aspect in assessing the possibility of replacing titanium and zinc oxides in creams with Ce(IV) oxide or phosphate is the need to consider the comparatively high price of cerium compounds. Therefore, such synthesis methods that allow deposition Ce(IV) phosphate coatings to various more accessible substrates are acquiring great importance. It is assumed that using these methods it is possible to obtain, for example, core-shell structures in which the content of the more expensive component is lower.

Such methods include the SILD method [18], which allows the synthesis of a wide range of inorganic compounds on the surface of complex-shaped substrates and relatively precise control of their thickness. The essence of this method is to treat the substrate according to a special program using solutions of 2 or more reagents, with intermediate rinsing of the sample with excess reagent and reaction products, using a solvent, specifically, water for aqueous solutions. The conditions of such treatments are selected in such a way that during treatment with each reagent, alternate adsorption of cations and anions occurs on the surface. It is important that these ions interact with each other and form a poorly soluble compound.

The aim of this work was to study the features of the synthesis of Ce(IV) phosphate coatings on the surface of model silica substrates represented by fused quartz samples and an ultra-thin layer of silicon oxide on the surface of single-crystal silicon. An important part of the work consisted of the results of studying the degree of absorption of UV radiation by such coatings.

2. Experimental

2.1. Materials

Aqueous solutions of $(NH_4)_4Ce(SO_4)_4 \cdot 2H_2O$, $(NH_4)_2Fe(SO_4)_2 \cdot 6H_2O$, Na_2WO_4, NaH_2PO_4 and Na_3PO_4 (JSC Lenreactive) were used as reagents for synthesis. The weighed portions of the reagents were dissolved in deionized water, stirring for at least 30 minutes. The synthesis substrates used were single crystalline silicon with $<111>$ orientation, as well as fused quartz plates measuring 10×25 mm and 0.35 and 1.0 mm thick, respectively. Before synthesis, all substrates were rinsed twice for 10 minutes using an ultrasonic bath with isopropyl alcohol. They were then washed with deionized water and dried at 60°C for 10 minutes in the air.

2.2. SILD synthesis conditions

The coatings were synthesized using a custom-made automated setup. In the first stage of the SILD synthesis, the substrate plates were immersed in a solution of $(NH_4)_4Ce(SO_4)_4$ with a concentration of 0.01 M. They were then removed from this solution and immersed in distilled water to remove excess reagent and reaction products from the surface. In the second stage, the plates were immersed in a solution of NaH_2PO_4 or Na_3PO_4 with a concentration of 0.01 M and again washed in distilled water. This sequence corresponds to one SILD cycle, which was repeated 5–25 times. A number of syntheses were performed using a solution of a mixture of $(NH_4)_4Ce(SO_4)_4$ and $(NH_4)_2Fe(SO_4)_2$, as well as Na_3PO_4 and Na_2WO_4 as one of the reagents. The treatment time in the reagent solutions and water was 30s. The synthesis was carried out at room temperature and atmospheric pressure. After deposition, the samples were dried in the air at the temperature 60°C.

2.3. Physical characterization

Scanning electron microscopy (SEM), transmission electron microscopy (TEM), scanning transmission electron microscopy (STEM), selected area electron diffraction (SAED), energy-dispersive x-ray (EDX) microanalysis, Fourier-transform infrared spectroscopy (FT-IR) and diffuse reflection (DR) spectroscopy in the UV-Vis region were used to study the synthesized samples.

Electron micrographs were obtained using a Zeiss EVO-40EP scanning microscope and a Zeiss Libra 200 transmission microscope. The synthesized compounds composition was determined by EDX microanalysis using an Oxford INCA-350 spectrometer included in the Zeiss EVO-40EP scanning electron microscope kit. The FT-IR spectra of the coatings on the silicon surface were recorded on FSM-2201 spectrophotometer according to a differential scheme relative to a pure silicon substrate. The number of scans was 60. DR spectra were obtained using a Perkin-Elmer Lambda 9 spectrophotometer equipped with an integrating sphere. When obtaining DR spectra, fused quartz plates were used as substrates. The surface of these plates was pre-polished using SiC powder with a particle size of about 20 μm as an abrasive.

3. Results and discussion

As follows from the electron micrographs shown in Fig. 1(a,b), as a result of synthesis using solutions of $(NH_4)_4Ce(SO_4)_4$ and NaH_2PO_4, continuous thin films are formed on the silicon surface, which have separate microcracks that are not through the thickness and have sizes of fractions of a micrometer. The latter may possibly form during drying of the samples in air. If a solution of Na_3PO_4 is used instead of a solution of NaH_2PO_4, then for the samples obtained as a result of 5, 10, 20 and 25 SILD cycles, such a planar morphology of the films is preserved. It is only noteworthy that the surface of such thin films has a more clearly expressed globular morphology and the sizes of such planar globules are approximately 30–100 nm. However, for the sample obtained as a result of 15 SILD cycles, the morphology of the coating changes significantly and the formation of microtubes with the morphology of microscrolls with a diameter of about 3–5 μm and a length of 30–100 μm is observed on the surface (Fig. 1(c-f)). The wall thickness of such microtubes is 50–80 nm and this indicates that during the synthesis as a result of 1 SILD cycle, a nanolayer with a thickness of $\sim$4 nm is formed on the surface. This value significantly exceeds the total dimensions of the elementary polyhedron in Ce(IV)

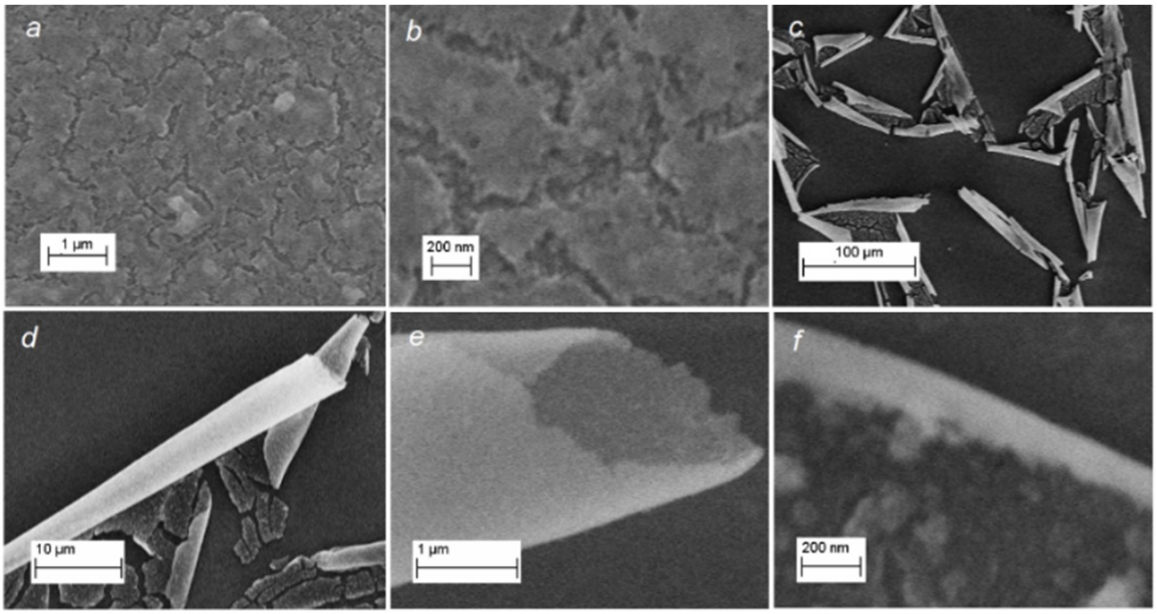

FIG. 1. SEM images of the surface of the coatings deposited on silicon wafers. a, b – the reagents in the synthesis were $(NH_4)_4Ce(SO_4)_4$ and NaH_2PO_4 solutions; c-f – $(NH_4)_4Ce(SO_4)_4$ and Na_3PO_4 solutions. The number of SILD cycles (N) was 15

oxyhydroxide and phosphate anion. This circumstance, in our opinion, indicates super-equivalent adsorption of Ce(IV) cations or phosphate anions on the surface at each stage of substrate treatment in reagent solutions.

In Fig. 1(c-f), it can be seen that the outer side of the microtube wall has a smoother surface than the inner one and the planar thin film itself is rolled up with the outer side relative to the substrate into the microtube.

Important information about the structural and chemical features of the synthesized coatings can be obtained from the analysis of electron STEM and TEM micrographs (Fig. 2(a,b)). According to these micrographs, the walls of such microtubes consist of individual nanoparticles 20–40 nm in size and these nanoparticles are amorphous (Fig. 2(c)). Similar micrographs and SAED pattern were also obtained for the coating synthesized using the NaH_2PO_4 solution and therefore we do not show them in this figure.

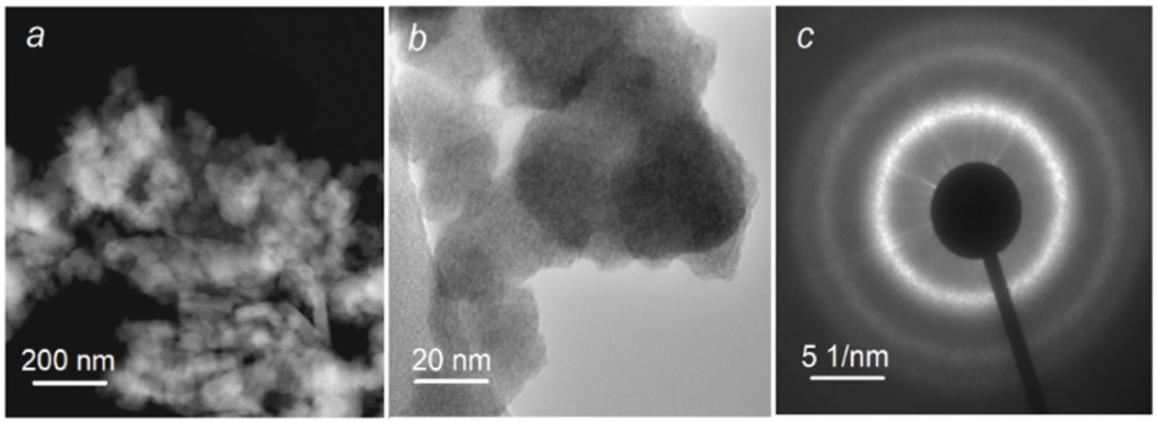

FIG. 2. STEM (a) and TEM (b) images of fragments of the coating synthesized on the silicon surface as a result of its treatment for 15 cycles with solutions of $(NH_4)_4Ce(SO_4)_4$ and Na_3PO_4 using the SILD method. (c) – typical SAED pattern of this sample

The study of the coating composition by the EDX method showed that in the case of using solutions of $(NH_4)_4Ce(SO_4)_4$ and NaH_2PO_4 for synthesis, a thin film is formed on the surface, which consists only of Ce, P and O atoms, and the ratio of Ce:P concentrations is close to 1 (Fig. 3(a)). Unfortunately, it is impossible to determine the relative content of O atoms in such thin film, because oxygen is also present in it as part of water molecules. If a solution of Na_3PO_4 is used as one of the reagents during synthesis, then in the composition of the coating, along with the noted elements, Na atoms can also be found, and the ratio of the concentrations of Na, Ce and P atoms is 0.2:1.0:0.6.

The composition of the coatings was also studied by FT-IR spectroscopy (Fig. 4(a)), the results of which indicate the presence of water molecules (absorption bands of water molecules are not shown in the figure) and phosphate anions in

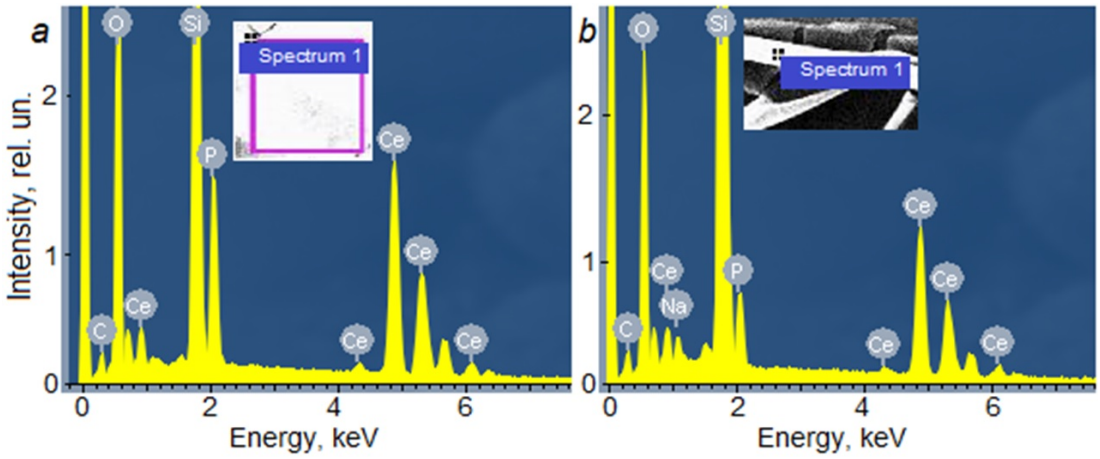

FIG. 3. EDX spectra of coatings deposited on silicon wafers. a – solutions of $(NH_4)_4Ce(SO_4)_4$ and NaH_2PO_4 served as reagents in the synthesis; b – solutions of $(NH_4)_4Ce(SO_4)_4$ and Na_3PO_4. N= 15

the layer. The presence of the latter is indicated by absorption bands in the region of 1200–900 cm^{-1} of valence and in the region of 700–500 cm^{-1} of deformation vibrations of P–O bonds [16].

Thus, the composition of the obtained coatings can be characterized by analogy with papers [19–22] as $Ce(OH)PO_4 \cdot nH_2O$ and $Na_{0.2}Ce(OH)_{2.4}(PO_4)_{0.6} \cdot nH_2O$.

A rather logical result is a slightly lower content of phosphate anions in the sample obtained using the Na_3PO_4 solution in relation to the content of the series. This solution has a significantly higher equilibrium pH value and therefore, when the substrate is immersed in it, two competing reactions are observed, namely, a more complete hydrolysis of the adsorbed Ce(IV) cations with the formation of Ce(IV) hydroxide and the adsorption of phosphate anions. In such a solution, there are also significantly more Na^+ cations and therefore, along with the adsorption of phosphate anions, adsorption of these cations is also observed. The presence of such polyionic adsorption leads to the so-called "super-equivalent" adsorption and therefore, with each SILD cycle, cations and anions are adsorbed on the surface in an amount greater than one monolayer.

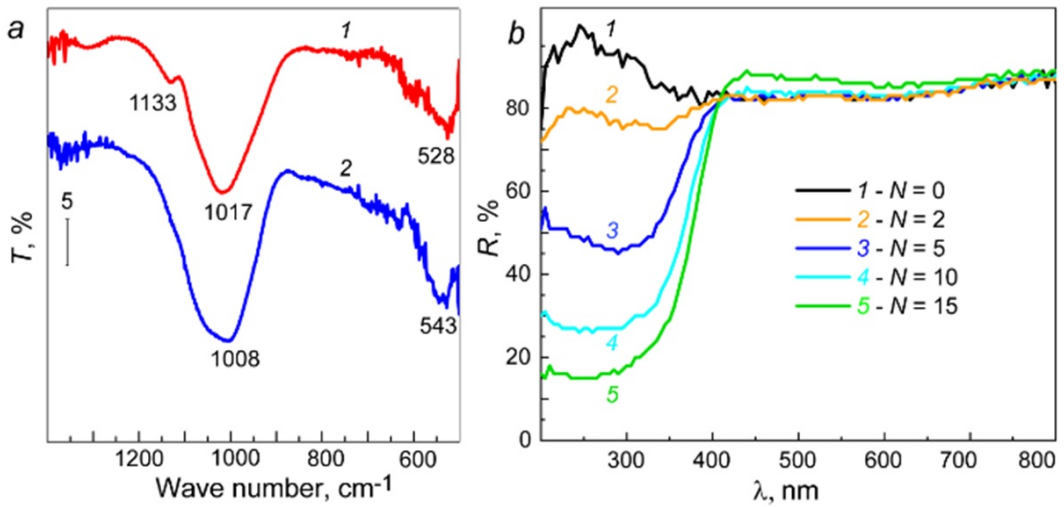

FIG. 4. a – FT-IR spectra of Ce(IV) phosphate coatings on silicon surface obtained using solutions of $(NH_4)_4Ce(SO_4)_4$ and NaH_2PO_4 (1) and $(NH_4)_4Ce(SO_4)_2$ and Na_3PO_4 (2). N= 20; b – DR UV-Vis spectra of Ce(IV) phosphate coatings on quartz surface obtained using $(NH_4)_4Ce(SO_4)_4$ and NaH_2PO_4 solutions

When discussing the obtained results, it is also necessary to interpret the effect of formation of microtubes with walls of $Na_{0.2}Ce(OH)_{2.4}(PO_4)_{0.6} \cdot nH_2O$ in the case of the sample obtained as a result of 15 SILD cycles. In our opinion, the formation of such microtubes occurs at the stage of sample drying due to the fact that the outer part of the synthesized coating with respect to the substrate has a lower density than that which is in contact with the substrate. Apparently, this occurs because the inner part of the layer was in contact with reagents for a longer time in total than the outer one. It is also impossible to exclude the reason for the increase in the coating density due to the formation of various cerium silicates in the contact zone with the substrate due to partial dissolution of an ultra-thin oxide nanolayer on the silicon

surface in an alkaline solution of Na_3PO_4. The obtained results, in our opinion, are one of the examples of the formation of microtubes of inorganic compounds during the drying of planar films with a density gradient across the thickness. Previously, we observed similar effects using microtubes with other wall compositions [23, 24]. It can be assumed that this effect of the formation of microtubes of inorganic compounds with a microscroll morphology is similar to the effect of the formation of nanotubes with a nanoscroll morphology, which the authors observed in [25,26] during their synthesis under hydrothermal conditions. However, in these cases, the twisting of the nanoscrolls was primarily the result of forces that arose due to differences in the structural properties of individual metal-oxygen polyhedra within their walls.

It is noteworthy that the coatings obtained as a result of 15 SILD cycles are most likely to twist. Apparently, the thin films of greater thickness are already more mechanically strong and the forces that arise during drying are no longer sufficient for the layer to twist. On the other hand, the thin films with a smaller thickness are less mechanically strong and when they are dried, such forces are not yet strong enough for their twisting. In addition, we have noticed that even if such thin films partially "twist", the microtubes that form them are not mechanically strong enough and they "collapse" into planar structures.

Additional and practically significant information can be obtained by analyzing the DR spectra of coatings on the surface of fused quartz (Fig. 4(b)). In these spectra, a wide absorption band can be observed in the range of 200–400 nm with an intensity increasing in a series of samples obtained as a result of a greater number of SILD cycles. This absorption band corresponds to charge-transfer transitions between the O($2p$) and Ce($4f$) states [27]. It is characteristic that already after 15 SILD cycles, a significant absorption of UV radiation at a level of 90 percent in the middle UV region, i.e., region B, is achieved. And this fact, in our opinion, opens up new possibilities for the creation of new, more effective absorbers of such radiation. Moreover, the optical properties of such coatings can be improved by doping their composition with various cations and anions. This doping can be relatively easily accomplished by using reagent solutions containing additives of various salts during synthesis. In particular, we have carried out test syntheses using solutions of salt mixtures and have shown that Fe(II) cations can be introduced into the composition up to an atomic concentration of 40%, as well as tungstate anions up to a value of 10% relative to the content of cerium atoms. A more detailed presentation of these experiments, however, goes far beyond the scope of this article and is therefore not presented here.

4. Conclusion

Successive and alternating treatment of silicon and quartz surfaces using the SILD technique with $(NH_4)_4Ce(SO_4)_4$ and NaH_2PO_4 solutions results in the formation of a $Ce(OH)PO_4 \cdot nH_2O$ coating with an amorphous crystalline structure. If a Na_3PO_4 solution is used as a reagent instead of NaH_2PO_4, the formation of $Na_{0.2}Ce(OH)_{2.4}(PO_4)_{0.6} \cdot nH_2O$ coatings with an amorphous structure is observed on the substrate surface. It is characteristic that in a series of $Na_{0.2}Ce(OH)_{2.4}(PO_4)_{0.6} \cdot nH_2O$ samples differing in the number of SILD cycles, the planar morphology of coatings can be disrupted for the sample obtained as a result of 15 SILD cycles. As it turns out, formation of microtubes (microscrolls) is observed on the surface of such a sample due to the "twisting" of individual fragments of the synthesized thin film. The composition of the noted Ce(IV) phosphates can be doped with various cations and anions by adding corresponding salts to reagent solutions. This was demonstrated using Fe(II) cations and WO_4^{2-} anions as an example. The study of $Ce(OH)PO_4$ coatings by DR spectroscopy indicates the possibility of creating effective UV absorbers in the mid-B spectral range based on these coatings.

References

[1] Labrador-Paez L., Kostiv U., Widengren J. Liu H. Water: An Influential Agent for Lanthanide-Doped Luminescent Nanoparticles in Nanomedicine. *Adv. Optical Mater.*, 2023, **11**, P. 2200513.

[2] Enikeeva M.O., Proskurina O.V., Gerasimov E.Yu. Nevedomskiy V.N., Gusarov V.V. Synthesis in hydrothermal conditions and structural transformations of nanocrystals in the $LaPO_4$-YPO_4-(H_2O) system. *Nanosyst.: Phys., Chem., Math.*, 2023, **14**(6), P. 660–667.

[3] Martinon T.L.M., Pierre V.C. Luminescent Lanthanide Probes for Inorganic and Organic Phosphates. *Chem. Asian J.*, 2022, **17**, P. e202200495.

[4] Enikeeva M.O., Yakovleva A.A., Proskurina O.V. Nevedomskiy V.N., Gusarov V.V. Phase formation under hydrothermal conditions and thermal transformations in the $GdPO_4$-YPO_4-H_2O system. *Inorg. Chem. Commun.*, 2024, **159**, P. 111777.

[5] Enikeeva M.O., Zhidomorova K.A., Danilovich D.P., Nevedomskiy V.N., Proskurina O.V., Gusarov V.V. Phase formation and thermal analysis in the $LaPO_4$-$GdPO_4$-H_2O system. *Nanosyst.: Phys., Chem., Math.*, 2024, **15**(6), P. 781–792.

[6] Ruwaid Rafiuddin M., Donato G., McCaugherty S., Mesbah A., Grosvenor A.P. Review of Rare-Earth Phosphate Materials for Nuclear Waste Sequestration Applications. *ACS Omega*, 2022, **7**(44), P. 39482–39490.

[7] Kozlova T.O., Baranchikov A.E., Ivanov V.K. Cerium (IV) Orthophosphates. *Russ. J. of Inorg. Chem.*, 2021, **66**(12), P. 1761–1778.

[8] Marszałek M., Piotrowski M., Dziełak B., Blicharz M., Malarska W., Wzorek Z. Titanium(IV), Zirconium(IV), and Cerium(IV) Phosphates Synthesized Under Mild Conditions-Composition Characteristics and Evaluation of Sorption Properties Towards Copper Ions in Comparison to Commercially Available Ion-Exchange Resins. *Mater.*, 2024, **17**(24), P. 6226.

[9] Romanchuk A.Y., Shekunova T.O., Larina A.I., Ivanova O.S., Baranchikov A.E., Ivanov V.K., Kalmykov S.N. Sorption of Radionuclides onto Cerium (IV) Hydrogen Phosphate $Ce(PO_4)(HPO_4)_{0.5}(H_2O)_{0.5}$, Radiochem., 2019, **61**(6), P. 719–723.

[10] Popov A.L., Shcherbakov A.B., Zholobak N.M., Baranchikov A.Y., Ivanov V.K. Cerium dioxide nanoparticles as third-generation enzymes (nanozymes). *Nanosyst.: Phys. Chem. Math.*, 2017, **8**(6), P. 760–781.

[11] Ta K.M., Neal C.J., Coathup M.J., Seal S., Phillips R.M., Molinari M. The interaction of phosphate species with cerium oxide: The known, the ambiguous and the unexplained. *Biomater. Adv.*, 2025, **166**, P. 214063.

[12] Komiyama M. Ce-based solid-phase catalysts for phosphate hydrolysis as new tools for next-generation nanoarchitectonics. *Sci. Technol. Adv. Mater.*, 2023, **24**(1), P. 2250705.
[13] Kolesnik I.V., Shcherbakov A.B., Kozlova T.O., Kozlov D.A., Ivanov V.K. Comparative Analysis of Sun Protection Characteristics of Nanocrystalline Cerium Dioxide. *Russ. J. of Inorg. Chem.*, 2020, **65**(7), P. 960–966.
[14] Parwaiz S., Khan M.M., and Pradhan D. CeO_2-based nanocomposites: An advanced alternative to TiO2 and ZnO in sunscreens. *Mater. Express*, 2019, **9**(3), P. 185–202.
[15] Averochkin E.P., Steparuk A.S., Tekshina E.V. et al. Photoactive Layers based on ZnO Nanorods Obtained by Hydrothermal Synthesis for Dye-Sensitized Solar Cells. *Russ. J. Inorg. Chem.*, 2024, **69**, P. 925–932.
[16] Bulyarskiy S.V., Koiva D.A., Gusarov G.G., Svetukhin V.V. Changes in the titanium oxide optical properties during crystallization. *Opt. and Spectr.*, 2022, **130**(14), P. 2148.
[17] Kozlova T.O., Popov A.L., Kolesnik I.V., Kolmanovich D.D., Baranchikov A.E., Shcherbakov A.B., Ivanov V.K. Amorphous and crystalline cerium(IV) phosphates. *J. Mater. Chem. B*, 2022, **10**(11), P. 1775–1785.
[18] Gulina L.B., Pchelkina A.A., Nikolaev K.G., Navolotskaya D.V., Ermakov S.S., Tolstoy V.P. A brief review on immobilization of gold nanoparticles on inorganic surfaces and Successive Ionic Layer Deposition. *Rev. Adv. Mater. Sci.*, 2016, **44**(1), P. 46–53.
[19] Baranchikov A.E., Kozlova T.O., Istomin S.Y., Mironov A.V., Vasilchikova T.M., Gippius A.A., Plakhova T.V., Vasilyeva D.N., Ivanov, V.K. Sodium Cerium Phosphate, $(Na,Ce)_2Ce(PO_4)_2 \cdot xH_2O$, with Mixed Cerium Oxidation States. *ChemistrySelect*, 2024, **9**(17), P. e202401010.
[20] Kozlova T.O., Mironov A.V., Istomin S.Y., Birichevskaya K.V., Gippius A.A., Zhurenko S.V., Shatalova T.B., Baranchikov A.E., Ivanov V.K. Meet the Cerium (IV) Phosphate Sisters: $CeIV(OH)PO_4$ and $CeIV_2O(PO_4)_2$. *Chem. Eur. J.*, 2020, **26**(53), P. 12188–12193.
[21] Kozlova T.O., Vasilyeva D.N., Kozlov D.A., Teplonogova M.A., Baranchikov A.E., Simonenko N.P., Ivanov V.K. Synthesis and thermal behavior of $KCe_2(PO_4)_3$, a new full-member in the $AIMIV_2(PO_4)_3$ family. *Nanosyst.: Phys. Chem. Math.*, 2023, **14**(1), P. 112–119.
[22] Yin S., Saito M., Liu X., Sato T. Preparation and Characterization of Plate-like Cerium Phosphate/Nanosize Calcia Doped Ceria Composites by Precipitation Method. *Phosphorus Res. Bull.*, 2011, **25**, P. 68–71.
[23] Gulina L.B., Tolstoy V.P., Solovev A.A., Gurenko V.E., Huang G., Mei Y. Gas-Solution Interface Technique as a simple method to produce inorganic microtubes with scroll morphology. *Prog. Nat. Sci: Mater. Int.*, 2020, **30**(3), P. 279–288.
[24] Tolstoy V., Nikitin K., Kuzin A., Zhu F., Li X., Goltsman G., Gorin D., Huang G., Mei Y. Rapid synthesis of Pt (0) motors-microscrolls on a nickel surface via H_2PtCl_6-induced galvanic replacement reaction. *Chem. Commun.*, 2024, **60**(23), P. 3182–3185.
[25] Li Y., Liu X., Ji T., Zhang M., Yan X., Yao M., Sheng D., Li S., Ren P., Shen Z. Potassium ion doped manganese oxide nanoscrolls enhanced the performance of aqueous zinc-ion batteries. *Chinese Chem. Lett.*, 2025, **36**(1), P. 109551.
[26] Hettler S., Roy K.S., Arenal R., and Panchakarla L.S. Stable CoO_2 Nanoscrolls with Outstanding Electrical Properties. *Adv. Mater. Interfaces*, 2024, P. 2400317.
[27] Wang W., Zhang B., Jiang S., Bai H., Zhang S. Use of CeO_2 Nanoparticles to Enhance UV-Shielding of Transparent Regenerated Cellulose Films. *Polymers*, 2019, **11**(3), P. 458.

Submitted 4 October 2025; revised 25 November 2025; accepted 30 November 2025

Information about the authors:

Yuliana Chuvilo – Institute of Chemistry, Saint Petersburg State University, University St. 26, St. Peterhof, Saint Petersburg, 198504, Russia; st087011@student.spbu.ru

Leonid Kuklo – Institute of Chemistry, Saint Petersburg State University, University St. 26, St. Peterhof, Saint Petersburg, 198504, Russia; ORCID 0000-0002-7502-6788; lenkuklo@mail.ru

Valeri Tolstoy – Institute of Chemistry, Saint Petersburg State University, University St. 26, St. Peterhof, Saint Petersburg, 198504, Russia; ORCID 0000-0003-3857-7238; v.tolstoy@spbu.ru

Conflict of interest: the authors declare no conflict of interest.

NANOSYSTEMS:
PHYSICS, CHEMISTRY, MATHEMATICS

Original article

Kiryanov N.V., Martinson K.D. *Nanosystems: Phys. Chem. Math.*, 2025, **16** (6), 818–828.
http://nanojournal.ifmo.ru
DOI 10.17586/2220-8054-2025-16-6-818-828

Effect of fuel-to-oxidizer ratio on the structural and magnetic properties of $Zn_{0.5}Mn_{0.5}Fe_2O_4$ nanoferrites synthesized via glycine-nitrate combustion

Nikita V. Kiryanov[1], Kirill D. Martinson[2]

[1]St. Petersburg Electrotechnical University "LETI", St. Petersburg, 199026, Russia
[2]Ioffe Institute, Politekhnicheskaya st., 26, St. Petersburg, 194064, Russia

Corresponding author: Nikita V. Kiryanov, nikyr@mail.ru

PACS 61.46Df, 75.50.Gg, 75.75.Fk

ABSTRACT Nanostructured $Zn_{0.5}Mn_{0.5}Fe_2O_4$ ferrites were synthesized by the glycine–nitrate solution combustion method with the fuel-to-oxidizer ratio f varied from 0.4 to 1.6 in order to clarify the influence of redox conditions on structure and magnetic properties. X-ray diffraction confirms the formation of single-phase cubic spinel for all compositions, with the crystallite size changing from $\sim$ 8 to 108 nm and the minimum values of both crystallite size and lattice parameter (8.420 Å) obtained under fuel-deficient conditions ($f = 0.4$); the lattice microstrain does not exceed 0.5 %. SEM observations reveal 3 – 5 μm agglomerates composed of 30 – 190 nm particles, while EDX analysis shows cation ratios close to the nominal composition. Magnetic measurements at 300 K demonstrate typical soft-magnetic behavior with saturation magnetization ranging from 16.1 to 68.3 emu/g, residual magnetization from 1.8 to 20.3 emu/g and coercive force from 34.7 to 85.6 Oe, all efficiently tuned by the fuel content. The highest saturation magnetization is achieved near the stoichiometric regime (f $\approx 0.8 - 1.0$), whereas fuel-rich mixtures result in increased coercivity due to microstructural refinement and lattice strain. The established correlations between combustion conditions, structural parameters and magnetic response show that controlled variation of the fuel ratio is an effective tool for tailoring Zn–Mn ferrite nanopowders for low-loss soft-magnetic applications.

KEYWORDS Zn-Mn ferrites, solution combustion, fuel-to-oxidizer ration, crystal structure, microstructure, magnetic properties, soft magnetic materials

ACKNOWLEDGEMENTS The authors of the article express their gratitude to the Institute of Applied Materials Science of the Joint-Stock Company "Almaz Antej – Obuhovskij zavod" for assistance in conducting the study of morphology and structure.

FOR CITATION Kiryanov N.V., Martinson K.D. Effect of fuel-to-oxidizer ratio on the structural and magnetic properties of $Zn_{0.5}Mn_{0.5}Fe_2O_4$ nanoferrites synthesized via glycine-nitrate combustion. *Nanosystems: Phys. Chem. Math.*, 2025, **16** (6), 818–828.

1. Introduction

Manganese-zinc ferrites are among the most widely used soft magnetic materials owing to their high initial permeability, relatively large saturation magnetization, high electrical resistivity and low core losses in the low- and medium-frequency ranges [1, 2]. These properties make Mn–Zn ferrites indispensable for electromagnetic components such as power transformers, inductors, electromagnetic interference (EMI) filters, read-write heads and antenna cores in both civil and military electronics [3]. In addition to traditional bulk components, Mn–Zn ferrite nanopowders are increasingly considered for microwave absorbers, ferrofluids and biomedical systems, where the combination of moderate magnetization, chemical stability and low toxicity is especially attractive [4–6].

It is now well recognized that the magnetic performance of spinel ferrites is strongly governed not only by their chemical composition, but also by cation distribution between A and B sublattices, crystallite size, porosity and grain-boundary characteristics [7]. When the characteristic size of ferrite particles approaches the single-domain range, changes in coercivity, saturation magnetization and loss behaviour are observed because of surface spin disorder and the increasing role of magnetocrystalline anisotropy [8]. Therefore, the development of reliable routes for synthesizing nanosized Mn–Zn ferrites with controlled particle size distribution and minimal secondary phases remains a key issue for tuning their functional properties and for decreasing the sintering temperature in ceramic processing [9, 10].

A variety of wet-chemical techniques have been proposed to produce ferrite nanopowders, including sol-gel and Pechini routes, co-precipitation, hydrothermal and solvothermal synthesis, microemulsion methods and different types of combustion approaches [11–14]. Conventional solid-state ceramic methods, while technologically simple, typically require high calcination temperatures and prolonged heat treatments, which often lead to coarse grains, broad size distributions and inhomogeneous cation distribution [15]. Wet-chemical routes usually provide better mixing at the molecular

level and lower synthesis temperatures, but they may suffer from complicated multi-step procedures, the need for complexing agents or surfactants, and difficulties in scaling up [16].

Among these techniques, solution combustion synthesis has attracted particular attention as a simple, low-cost and energy-efficient route for producing nanosized oxide powders [17]. In this method, aqueous solutions containing oxidizing metal nitrates and an organic fuel are ignited to initiate a self-sustaining exothermic reaction that yields the desired oxide product within a few seconds [18]. The high local temperature and rapid gas evolution during combustion typically produce highly porous, weakly agglomerated powders composed of fine crystallites, while the intimate mixing in the precursor solution ensures good chemical homogeneity [19]. For ferrite systems, solution combustion offers additional advantages of short synthesis time, easy control of stoichiometry and the possibility of tailoring the microstructure by adjusting the composition of the reactive mixture [20, 21].

Glycine is one of the most commonly used fuels in nitrate-based combustion systems because it can simultaneously act as a fuel, a complexing agent and a dispersant [22–24]. The so-called glycine-nitrate process allows effective chelation of metal cations, which reduces segregation and facilitates the formation of single-phase spinel ferrites at relatively low post-combustion temperatures [25]. Nevertheless, the characteristics of the resulting nanopowders strongly depend on the redox balance of the reacting system, usually expressed by the fuel-to-oxidizer ratio (Red/Ox ratio or f value) [26]. This parameter governs the adiabatic combustion temperature, the number of gaseous products released and the flame propagation rate, thereby affecting the crystallite size, morphology, defect structure and even the cation distribution in the final oxide [27, 28].

Several studies have reported the synthesis of Mn–Zn ferrites by different combustion routes using urea, glycine, citric acid and other fuels [29–31]. It has been shown that the choice of fuel and the calcination conditions significantly influence the structural and magnetic properties, including saturation magnetization, coercivity and Curie temperature. However, in many works the fuel content is fixed close to the stoichiometric value, and only limited information is available on how systematic variation of the Red/Ox ratio affects the structural parameters and magnetic behaviour of Mn–Zn ferrite nanopowders, especially in the glycine–nitrate system. Existing reports mainly focus either on phase formation and crystallite size or on magnetic properties, without establishing a clear correlation between combustion conditions, structural peculiarities and macroscopic magnetization characteristics [32, 33].

The composition $Zn_{0.5}Mn_{0.5}Fe_2O_4$ is of particular interest among Mn–Zn ferrites, since it lies in the concentration range where high saturation magnetization and low losses can be combined with relatively high electrical resistivity [34]. In the nanoscale state, $Zn_{0.5}Mn_{0.5}Fe_2O_4$ can exhibit size-dependent transitions between multi-domain, single-domain and superparamagnetic regimes, which are attractive for applications in high-frequency absorbers, magnetic recording media and biomedical hyperthermia [35]. At the same time, the non-equilibrium conditions inherent to combustion synthesis may alter the Mn^{2+}/Mn^{3+} and Fe^{2+}/Fe^{3+} ratios and redistribute cations between tetrahedral and octahedral sites, thus providing an additional tool for tailoring the magnetic response [36].

Therefore, a detailed study of how the Red/Ox ratio in glycine-nitrate combustion affects the formation of $Zn_{0.5}Mn_{0.5}Fe_2O_4$ nanopowders, their microstructure and magnetic properties is both fundamentally and practically important. By establishing such correlations, it becomes possible to optimize synthesis parameters for obtaining nanopowders with the required combination of crystallite size, lattice parameter and magnetic characteristics for specific device applications [37].

In this work, nanostructured $Zn_{0.5}Mn_{0.5}Fe_2O_4$ powders were synthesized via the glycine-nitrate solution combustion method with the fuel-to-oxidizer ratio f varied from 0.4 to 1.6, where $f = 1.0$ corresponds to the stoichiometric composition of the redox mixture. The structural properties were investigated by X-ray diffraction and Rietveld refinement, including the evaluation of crystallite size, lattice parameter and lattice strain. The morphology and particle size distributions were studied using scanning electron microscopy and image analysis, and the cation composition was verified by energy-dispersive X-ray spectroscopy. Finally, the magnetic behaviour at room temperature was examined by vibrating-sample magnetometry in fields up to 400 Oe in order to determine saturation magnetization, residual magnetization and coercive field. The results obtained make it possible to elucidate the role of combustion redox conditions in controlling the structural evolution and magnetic response of Zn–Mn ferrite nanopowders and to propose guidelines for the design of soft magnetic materials synthesized by solution combustion routes.

2. Experimental

$Zn_{0.5}Mn_{0.5}Fe_2O_4$ nanoparticles were synthesized by the glycine-nitrate solution combustion method. Zinc nitrate hexahydrate $Zn(NO_3)_2{\cdot}6H_2O$, manganese nitrate hexahydrate $Mn(NO_3)_2{\cdot}6H_2O$ (99.99 %), iron(III) nitrate nonahydrate $Fe(NO_3)_3{\cdot}9H_2O$ (99 %), glycine CH_2NH_2COOH and nitric acid HNO_3 were used as starting reagents without further purification. The required molar amounts of metal nitrates corresponding to the nominal composition $Zn_{0.5}Mn_{0.5}Fe_2O_4$ were weighed and dissolved in 50 mL of distilled water to obtain precursor solutions for 1 g of oxide powder. To ensure complete dissolution of the crystalline hydrates and to avoid precipitation of basic salts, 5 mL of 5 M HNO_3 were slowly added under vigorous magnetic stirring. The total oxidizing and reducing valences of nitrates and glycine were calculated according to the conventional propellant chemistry approach, and the amount of fuel was adjusted to obtain fuel-to-oxidizer ratios $f = 0.4$, 0.6, 0.8, 1.0, 1.2, 1.4 and 1.6, where $f = 1.0$ corresponds to the stoichiometric redox

composition. The as-prepared solutions were continuously stirred for 20 – 30 min until a clear homogeneous sol was obtained.

For combustion synthesis, each precursor solution was transferred into a cylindrical porcelain crucible and heated on a hot plate up to ∼200 °C to evaporate the excess water and form a viscous gel. Further heating initiated self-sustained combustion, which proceeded rapidly throughout the volume of the gel, accompanied by the release of large amounts of gaseous products and the formation of a voluminous, highly porous ash. No external oxidizing atmosphere was supplied; the reaction was carried out in air at ambient pressure. The as-combusted powders were gently crushed in an agate mortar and subsequently homogenized in a vibratory mill for 30 min to break soft agglomerates and to obtain a more uniform particle size distribution. In order to remove possible residual carbon and to improve crystallinity, the powders were additionally calcined in air at 600 °C for 2 h with a heating rate of 5 °C/min and then cooled to room temperature inside the furnace.

Phase composition and structural parameters of the synthesized powders were investigated by X-ray diffraction (XRD). Diffraction patterns were collected at room temperature on a Bruker D2 Phaser diffractometer using monochromatic Co-Kα radiation ($\lambda = 1.7903$ Å) operated at 30 kV and 10 mA. The data were recorded in the 2θ range from 10° to 80° with a step of 0.02° and a counting time of 1 s per step. The raw diffraction profiles were corrected for background and instrumental broadening before further analysis. The crystal structure was refined assuming a cubic spinel phase with space group $Fd\bar{3}m$. The lattice constant a, average crystallite size D and microstrain β were determined using the Topas software package by profile fitting of the most intense reflections (220), (311), (400), (422), (511) and (440). The values of D were obtained from the integral breadth of the diffraction peaks, taking into account both size and strain broadening contributions.

The morphology of the combustion-derived powders and the size of individual particles were examined by scanning electron microscopy (SEM) on a Tescan Mira 3 LMH microscope. Before observations, the powders were ultrasonically dispersed in ethanol, deposited onto a carbon-coated aluminium stub and sputtered with a thin conductive Au/Pd layer. For each composition, several representative micrographs at different magnifications were recorded to visualize both the agglomerate structure and the underlying primary particles. Particle size distributions were obtained by measuring the equivalent circle diameters of at least 400 – 500 particles using the ImageJ software. The resulting histograms were fitted by log-normal functions to determine the average particle diameter $\langle D \rangle$ and the standard deviation for each f value.

In addition to SEM-based measurements, the hydrodynamic size of particles in suspension was evaluated by dynamic light scattering. For this purpose, the powders were dispersed in distilled water with a small addition of ethanol and 0.1 wt.% sodium dodecyl sulfate as a surfactant, followed by ultrasonication for 15 min in an ultrasonic bath. The measurements were carried out at room temperature in disposable polystyrene cuvettes, and the particle size distributions were obtained from the autocorrelation function of scattered light intensity assuming a spherical particle model. These data were used to assess the degree of agglomeration in the as-combusted powders and to compare with the SEM-derived particle size distributions.

The elemental composition and cation ratios in the synthesized ferrites were analyzed by energy-dispersive X-ray spectroscopy (EDX) using an Oxford Ultim MAX 100 detector attached to the SEM. For each sample, spectra were acquired from several regions with an area of 50 – 100 μm^2 to obtain statistically reliable results. Quantitative analysis was performed using the manufacturer's software with ZAF corrections, and the obtained atomic fractions of Mn, Zn and Fe were compared with the nominal stoichiometry. Special attention was paid to the possible presence of impurity cations or secondary phases; however, within the detection limit of the method no significant deviations from the nominal composition were observed.

Magnetic properties of $Zn_{0.5}Mn_{0.5}Fe_2O_4$ nanopowders were studied using a Lake Shore vibrating sample magnetometer. Room-temperature hysteresis loops were recorded in external magnetic fields from -400 to $+400$ Oe. Prior to measurements, the powders were pressed into small cylindrical pellets and fixed in a non-magnetic sample holder to minimize mechanical vibrations. The magnetization was measured as a function of applied field with a step of 10 Oe near the coercive region and 50 – 100 Oe at higher fields. The experimental $M(H)$ loops were further processed using MeasureLINK-MCS and Curve Handler software. From the corrected loops, the saturation magnetization M_s, remanent magnetization M_r and coercive field H_c were determined according to standard procedures. All magnetic parameters were normalized to the mass of the sample measured with accuracy better than 0.1 mg.

For convenience, the samples synthesized at different fuel-to-oxidizer ratios are hereafter denoted as $f = 0.4, 0.6, 0.8, 1.0, 1.2, 1.4$ and 1.6, respectively. All processing parameters (solution volumes, heating profiles, dispersion conditions and measurement settings) were kept identical for the whole series so that the only intentional variable was the value of f. This approach makes it possible to attribute the observed differences in microstructure and magnetic response directly to the change in redox conditions during combustion, rather than to uncontrolled variations in post-synthesis treatment.

3. Results and discussion

The SEM micrographs in Fig. 1(a–g) demonstrate that all $Zn_{0.5}Mn_{0.5}Fe_2O_4$ powders obtained by glycine-nitrate combustion consist of highly porous, weakly sintered agglomerates formed by much finer primary particles. At low magnification, the powders appear as irregular flakes or cauliflower-like granules with typical sizes of several micrometres

(5 – 20 μm). The agglomerates are rather fragile and easily fragmented during sample preparation, which is consistent with the loose, foamy character of combustion products. Higher-magnification insets reveal that the surface of these agglomerates is built from nearly equiaxed nanoparticles with sizes of a few tens of nanometres; these observations correlate well with the particle size distributions discussed below.

Despite the variation of the fuel-to-oxidizer ratio, the overall morphology of the powders remains qualitatively similar. For the most fuel-lean composition (sample a, $f = 0.4$) the agglomerates are relatively compact, with a plate-like shape and a moderately developed system of interparticle pores. The primary particles in this sample tend to form contiguous clusters and necks, indicating partial sintering during the comparatively mild combustion process. In contrast, increasing f to 0.6 (sample b) leads to more open, sponge-like agglomerates with large voids and thin walls. Such morphology suggests a more vigorous gas evolution and higher local combustion temperature, which promote fast expansion of the reacting mass and generate a finer internal texture.

Near the stoichiometric mixture ($f = 0.8$ and 1.0, samples c and d) the powders retain a highly porous structure, but the agglomerates become more rounded and their surface is covered by densely packed nanoparticles. The insets show that the primary particles are relatively uniform in size and exhibit smooth faceted outlines, indicating improved crystallinity. The voids inside the agglomerates are more homogeneous and form a network of channels that can facilitate mass transport during subsequent sintering. Such morphology is favourable for obtaining dense ceramics at reduced temperatures.

For fuel-rich mixtures ($f \geq 1.2$, samples e–g) the morphology again changes slightly. Sample e ($f = 1.2$) still shows loose flake-like agglomerates, but their surface becomes rougher, and some regions contain fused clusters of nanoparticles, presumably due to local overheating. In sample f ($f = 1.4$) nearly spherical granules with a relatively smooth outer shell are observed against a background of fine powder. These globular agglomerates likely originate from partial melting and shrinkage of the combustion foam when the reaction temperature is close to, or exceeds, the softening point of the oxide skeleton. For the highest fuel content ($f = 1.6$, sample g) the agglomerates again acquire an elongated cauliflower-like shape; their surface is covered with compact aggregates of nanoparticles, while the inner porosity becomes somewhat less pronounced, which may indicate enhanced sintering in the hottest combustion conditions.

Energy-dispersive X-ray analysis summarized in the table on the left of Fig. 1 confirms that, regardless of the redox conditions, the cation composition of all samples is close to the nominal $Zn_{0.5}Mn_{0.5}Fe_2O_4$ stoichiometry. The Mn and Zn contents vary in narrow ranges around 17 at.% each, whereas the Fe content remains close to 65 at.% for all specimens. These small deviations are within the typical experimental uncertainty of EDX measurements for light elements and do not show any systematic trend with f. Furthermore, no regions enriched in a particular cation were detected in mapping mode, which indicates a good macroscopic homogeneity of the combustion-derived powders and the absence of large segregated secondary phases, in agreement with the XRD data.

Thus, SEM observations reveal that varying the fuel-to-oxidizer ratio in the glycine-nitrate system does not radically change the general foamy morphology of the Zn–Mn ferrite powders, but noticeably influences the degree of porosity, the shape of agglomerates and the extent of local sintering. Fuel-lean mixtures produce somewhat denser plate-like agglomerates, while stoichiometric and moderately fuel-rich compositions yield highly porous, uniform foam structures composed of well-crystallized nanoparticles. At very high fuel contents partial collapse and rounding of the agglomerates occur, reflecting more intense combustion. These morphological features, combined with the essentially constant cation stoichiometry, provide a basis for understanding the trends in particle size distributions and magnetic properties discussed in the following sections.

Figure 2 summarizes the particle size distributions of the $Zn_{0.5}Mn_{0.5}Fe_2O_4$ powders derived from the SEM images in Fig. 1. In all cases the histograms can be satisfactorily fitted by a single log-normal function, indicating that the powders consist mainly of one population of primary particles and that no pronounced bimodality is introduced by the combustion process. The distributions are moderately narrow, with most particles lying in the 40 – 130 nm range, and only a small fraction of larger particles forming a long tail attributed to limited neck growth or local aggregation.

For the fuel-lean composition ($f = 0.4$, Fig. 2a) the average particle diameter is $\langle D \rangle = 66.6$ nm, with a symmetric distribution centered at 60 – 70 nm. A slight decrease of $\langle D \rangle$ to 63.2 nm is observed when the fuel content is increased to $f = 0.6$ (Fig. 2b); in this case the peak becomes somewhat sharper and shifts to smaller diameters, consistent with a more fragmented, highly porous morphology. The largest particles are obtained near the stoichiometric redox ratio. For $f = 0.8$ and 1.0 (Fig. 2(c,d)) the mean diameters rise to 85.1 and 87.7 nm, respectively, and the histograms broaden towards 120 – 180 nm, reflecting more intensive growth and partial coalescence of crystallites under the hottest and longest-lasting combustion conditions.

Further increase of the fuel content leads again to a reduction of the particle size. For $f = 1.2$ (Fig. 2e) the mean value drops to 74.8 nm, while for $f = 1.4$ the smallest particles in the series are obtained, with $\langle D \rangle = 56.3$ nm and a relatively narrow peak located around 50 – 60 nm (Fig. 2f). At the highest fuel ratio ($f = 1.6$, Fig. 2g) the distribution broadens slightly and $\langle D \rangle$ increases to 62.1 nm, indicating some coarsening but still remaining below the values for the stoichiometric mixtures.

The data demonstrate a non-monotonic dependence of particle size on the fuel-to-oxidizer ratio: the powders prepared under stoichiometric conditions are coarser, whereas both fuel-deficient and strongly fuel-rich mixtures yield finer

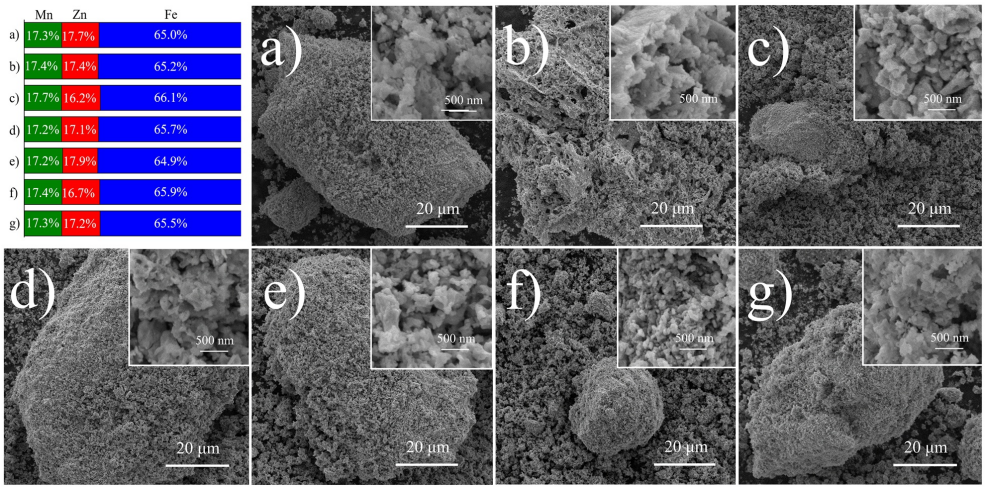

FIG. 1. SEM micrographs of $Zn_{0.5}Mn_{0.5}Fe_2O_4$ powders obtained by glycine-nitrate combustion at different fuel-to-oxidizer ratios: (a) $f = 0.4$, (b) 0.6, (c) 0.8, (d) 1.0, (e) 1.2, (f) 1.4 and (g) 1.6 (main images – agglomerates, insets – primary particles). The table on the left summarizes the EDX-derived cation composition for each sample, confirming stoichiometry close to the nominal $Zn_{0.5}Mn_{0.5}Fe_2O_4$

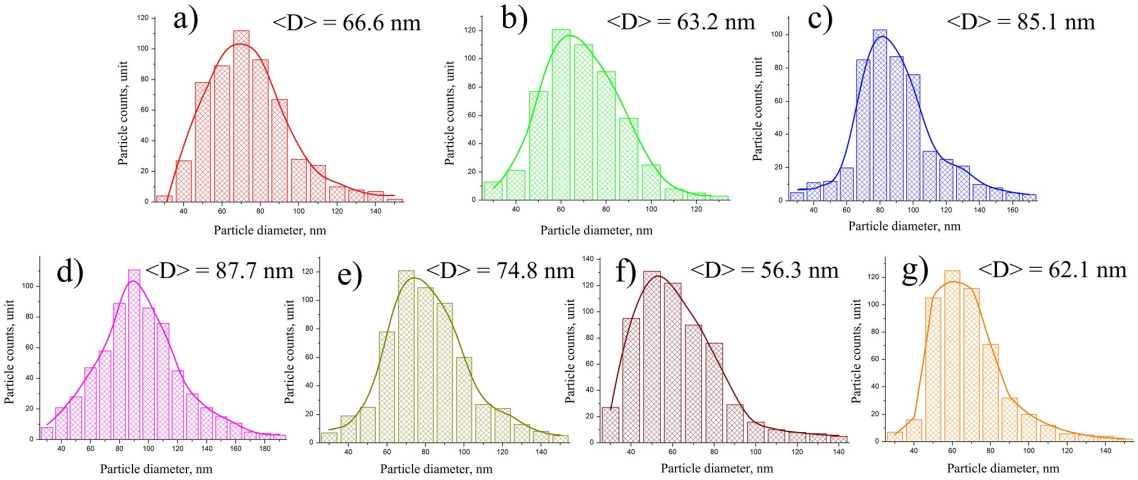

FIG. 2. Particle size distributions of $Zn_{0.5}Mn_{0.5}Fe_2O_4$ nanoparticles obtained by glycine-nitrate combustion at different fuel-to-oxidizer ratios f, constructed from SEM micrographs in Fig. 1: (a) $f = 0.4$, $\langle D \rangle = 66.6$ nm; (b) $f = 0.6$, $\langle D \rangle = 63.2$ nm; (c) $f = 0.8$, $\langle D \rangle = 85.1$ nm; (d) $f = 1.0$, $\langle D \rangle = 87.7$ nm; (e) $f = 1.2$, $\langle D \rangle = 74.8$ nm; (f) $f = 1.4$, $\langle D \rangle = 56.3$ nm; (g) $f = 1.6$, $\langle D \rangle = 62.1$ nm. Solid lines represent log-normal fits to the experimental histograms

nanoparticles. This behaviour can be rationalized by the competition between combustion temperature, gas evolution and quenching rate. The observed trends in $\langle D \rangle$ will directly influence the magnetic properties discussed below, since they determine the balance between single-domain behaviour and interparticle interactions in the nanoferrite powders.

Figure 3 combines the X-ray diffraction patterns of the $Zn_{0.5}Mn_{0.5}Fe_2O_4$ powders (left) with the crystallite size distributions obtained from line-broadening analysis (right), thus providing an integral picture of their structural evolution with changing fuel-to-oxidizer ratio f. The diffraction patterns of all samples exhibit a set of well-resolved reflections that can be indexed to a single cubic spinel phase with space group $Fd\bar{3}m$. The most intense peaks correspond to the (220), (311), (400), (422), (511) and (440) planes, positioned at Bragg angles characteristic of Mn–Zn ferrites. No additional reflections attributable to secondary oxide phases such as Fe_2O_3, MnO_x or ZnO are detected within the experimental sensitivity, and the diffuse background remains low, indicating that the amount of amorphous material does not exceed a few percent. This confirms that glycine-nitrate combustion followed by a mild calcination step is sufficient to produce phase-pure Zn–Mn ferrite over the whole range of redox conditions explored.

Although the phase composition is identical, the peak profiles and relative intensities exhibit noticeable changes with f. The pattern of the most fuel-lean sample ($f = 0.4$) shows the broadest reflections and somewhat lower peak intensities, suggesting a smaller average crystallite size and/or higher microstrain in this powder. At the same time, a slight increase of background at low angles can be seen, which may be associated with a minor amorphous fraction formed under

less exothermic combustion conditions. As the fuel content is increased to $f = 0.6 – 1.0$, the diffraction peaks become significantly sharper and more intense, reflecting improved crystallinity and growth of coherently diffracting domains. For the stoichiometric mixture ($f = 1.0$) the reflections, especially (311), are the narrowest in the series, consistent with the highest combustion temperature and longest effective dwelling time in the reaction front. Further enrichment in fuel ($f = 1.2 – 1.6$) results in a moderate broadening again, pointing to partial refinement of crystallites and possibly an increase of lattice defects caused by more violent gas release and faster quenching of the reaction products. No appreciable systematic shift of the main peaks is observed by eye, which implies that variations of the lattice parameter with f are rather subtle and will be quantified in the next figure.

The right-hand panel of Fig. 3 presents the size distributions of the coherently diffracting domains derived from the XRD data using a model assuming log-normal statistics. All distributions are unimodal, indicating that each powder is characterized by a dominant crystallite size rather than a superposition of several populations. For the fuel-deficient sample ($f = 0.4$, red curve) the distribution is very narrow and centered at relatively small sizes, on the order of a few tens of nanometres; this agrees with the pronounced peak broadening seen in its diffraction pattern. The high density of small crystallites is expected for a combustion route with reduced heat release, where the temperature is insufficient to drive extensive domain growth.

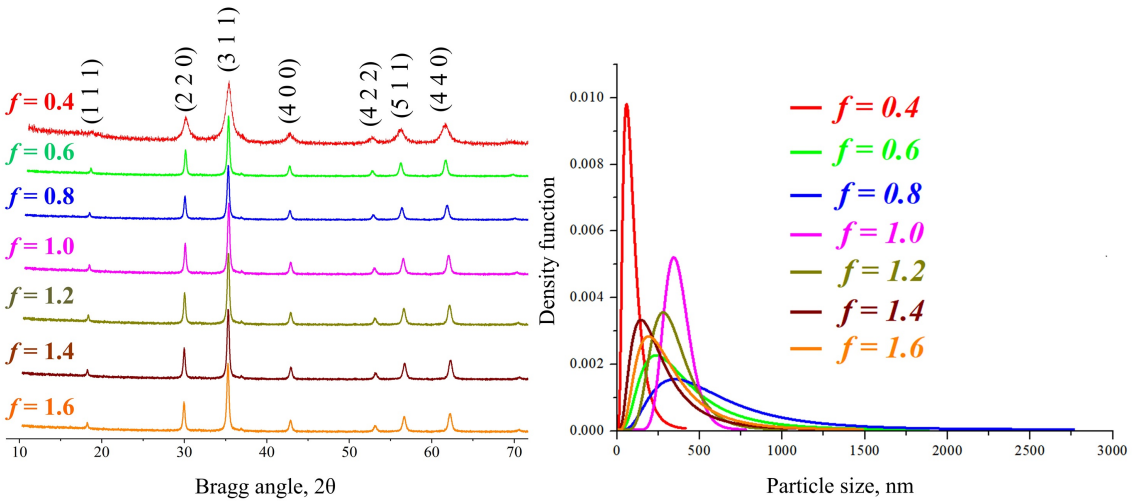

FIG. 3. (a) X-ray diffraction patterns of $Zn_{0.5}Mn_{0.5}Fe_2O_4$ powders synthesized by glycine-nitrate combustion at different fuel-to-oxidizer ratios $f = 0.4 – 1.6$, showing single-phase cubic spinel structure; (b) corresponding crystallite size distributions obtained from XRD line-broadening analysis and fitted with log-normal functions

When the fuel content is adjusted to $f = 0.6$ and 0.8 (green and blue curves), the distributions broaden and their maxima shift to larger sizes, reaching several hundred nanometres for the nearly stoichiometric composition. The long right-hand tails extending up to the micrometre range are indicative of a small fraction of oversized domains or strongly coalesced crystallites that have grown at the highest local temperatures inside the combustion front. This tendency correlates with the narrowing of the diffraction peaks and reflects more effective coarsening under near-stoichiometric conditions.

At even higher fuel ratios ($f = 1.2 – 1.6$, olive, brown and orange curves) the mode of the distribution's shifts back towards smaller crystallite sizes and the high-size tail becomes less pronounced. In other words, strongly fuel-rich mixtures yield a microstructure in which the majority of domains are significantly finer than in the stoichiometric case, despite the overall exothermicity of the reaction being higher. Such behaviour can be explained by the competing influence of rapid gas evolution and quenching: very intense combustion generates highly expanded foam that cools down quickly, limiting the time available for crystal growth and favouring the formation of numerous small domains. At the same time, the presence of some broader distributions for these samples suggests an increased contribution of defect-rich or strained crystallites.

The XRD patterns and crystallite size distributions in Fig. 3 demonstrate that the Red/Ox ratio in the glycine-nitrate system is a powerful tool for tuning the structural state of $Zn_{0.5}Mn_{0.5}Fe_2O_4$ nanopowders. All compositions remain single-phase cubic spinel, but the average size of coherently diffracting domains and the width of their distributions change in a non-monotonic manner: fuel-lean and strongly fuel-rich conditions produce finer crystallites, whereas mixtures close to stoichiometric favour their growth and partial coalescence. These structural differences are expected to have a direct impact on the magnetic behaviour of the powders, influencing both saturation magnetization and coercivity through the balance between single-domain and multi-domain particles and the level of lattice strain.

Figure 4 summarizes how the main structural parameters of the $Zn_{0.5}Mn_{0.5}Fe_2O_4$ powders depend on the fuel-to-oxidizer ratio f. The red symbols represent the average crystallite size D obtained from XRD line-broadening analysis,

the green symbols show the lattice parameter a, and the blue symbols correspond to the lattice microstrain β. Together, these data provide a quantitative description of how the redox conditions during combustion control the structural state of the ferrite.

The crystallite size exhibits a pronounced non-monotonic behaviour with f. For the most fuel-lean mixture ($f = 0.4$) the crystallite size is very small, on the order of 8 – 10 nm, which is consistent with the strong peak broadening in the corresponding diffraction pattern and with the fine microstructure observed by SEM. Such small domains are typical for combustion reactions proceeding at relatively low adiabatic temperatures, where the energy released is sufficient to form the spinel phase but insufficient for extensive grain growth. When f increases to 0.6 and 0.8, D rises steeply to ∼35 and ∼60 nm, respectively, reflecting the enhancement of flame temperature and the longer time available for coarsening of the oxide skeleton. The maximum crystallite size (∼75 – 80 nm) is reached at $f = 1.0$, i.e. under almost stoichiometric redox conditions, where the balance between heat release and gas evolution is optimal for growth of coherently diffracting domains. A further increase of fuel content leads to a gradual refinement of the structure: D decreases to ∼50 nm at $f = 1.2$, reaches a local minimum of ∼20 – 25 nm at $f = 1.4$ and then slightly increases again to ∼40 nm at $f = 1.6$. This reduction in crystallite size at high f is attributed to more violent gas evolution and faster quenching of the combustion foam, which freeze the structure before large domains can form.

The variation of the lattice parameter a with f is less pronounced but still clearly systematic. For $f = 0.4$ the lattice constant is close to 8.418 – 8.420 Å. Upon increasing f to 0.6 and 0.8, a grows to ∼8.435 and ∼8.450 Å, respectively, and reaches a maximum of about 8.453 – 8.454 Å for the stoichiometric mixture. With further fuel enrichment the lattice parameter slightly decreases, remaining in the range 8.445 – 8.452 Å. These modest changes can be related to a subtle modification of cation valence states and distribution between tetrahedral and octahedral sites, caused by differences in local oxygen partial pressure and cooling rate. Fuel-lean conditions favour a more oxidizing environment and may increase the fraction of smaller Fe^{3+} and Mn^{3+} cations, leading to a contracted lattice. Near-stoichiometric combustion, where the temperature is highest and the redox balance is closer to equilibrium, promotes a configuration with a larger average ionic radius and thus a larger unit cell. In very fuel-rich mixtures partial reduction of iron and manganese and the formation of oxygen vacancies may again reduce a.

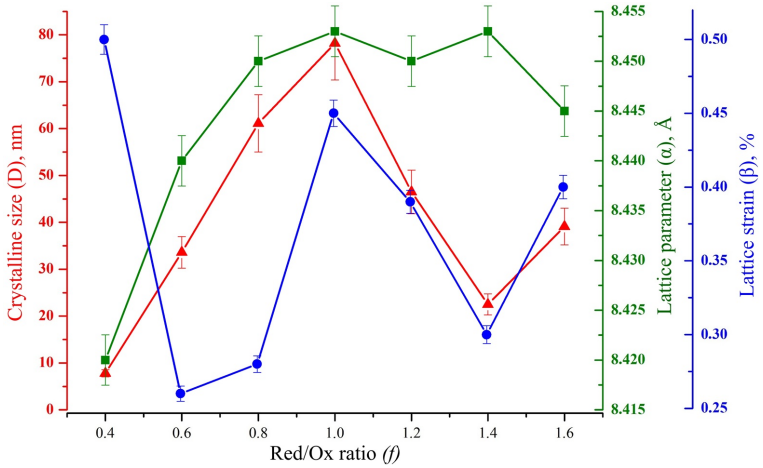

FIG. 4. (a) Dependence of crystallite size (D, red triangles, left axis), lattice parameter (a, green squares, middle axis) and lattice strain (β, blue circles, right axis) of $Zn_{0.5}Mn_{0.5}Fe_2O_4$ powders on the fuel-to-oxidizer ratio f, as obtained from XRD line-profile analysis

The microstrain β, plotted on the right axis, complements this picture. At $f = 0.4$ the strain is relatively high (∼0.47 – 0.50 %), indicating a considerable density of defects and local distortions in the small crystallites formed under fuel-deficient conditions. When f is increased to 0.6, β drops sharply to ∼0.26 %, reflecting more uniform crystallization and partial annealing of defects as the combustion temperature rises. For $f = 0.8$ and 1.0 the strain increases again up to ∼0.40 – 0.42 %, which may be associated with faster crystal growth and incorporation of non-equilibrium cation distributions into the lattice at the highest temperatures. In the fuel-rich region ($f \geq 1.2$) β shows a moderate minimum around $f = 1.4$ and then rises once more at $f = 1.6$, suggesting that intense gas evolution and rapid quenching introduce additional dislocations and lattice distortions even though the crystallite size is reduced.

Figure 4 demonstrates that the structural parameters of glycine-nitrate derived $Zn_{0.5}Mn_{0.5}Fe_2O_4$ are highly sensitive to the fuel-to-oxidizer ratio. Fuel-lean combustion yields very small, strongly strained crystallites with a slightly contracted lattice; near-stoichiometric conditions produce the largest domains and the maximum lattice parameter; strongly fuel-rich mixtures again lead to finer, more defective crystallites and a slight lattice contraction. These trends provide an important link between the combustion conditions and the magnetic behaviour of the powders, since both crystallite size and lattice strain critically influence saturation magnetization and coercivity in nanostructured ferrites.

Figure 5 presents the room-temperature magnetization curves $M(H)$ for the $Zn_{0.5}Mn_{0.5}Fe_2O_4$ nanopowders synthesized at different fuel-to-oxidizer ratios f. All samples exhibit typical S-shaped hysteresis loops that are narrow and symmetric with respect to the origin, confirming that the powders behave as soft ferrimagnetic materials. In the applied field range of ± 5 – 6 kOe the magnetization gradually approaches a quasi-saturation plateau, but does not reach a perfectly horizontal region, indicating that some spin canting and surface disorder remain in these nanostructured ferrites. The relatively small loop area for all compositions implies low hysteresis losses, which is advantageous for applications in low- and medium-frequency magnetic devices.

Despite the overall similarity of the loop shapes, there is a pronounced dependence of the magnetization level on the Red/Ox ratio. The fuel-lean sample with $f = 0.4$ displays the lowest saturation magnetization: its $M(H)$ curve lies well below the others and reaches only a modest magnetization even in the maximum applied field. This behaviour is consistent with its very small crystallite size and relatively high lattice strain, which enhance surface spin canting and disturb the long-range superexchange interactions between cations in the A and B sublattices. As f increases to 0.6 and 0.8 the loops shift upward; the powders synthesized near the stoichiometric composition ($f \approx 0.8$ – 1.0) show the highest magnetization values in the entire series. For these samples the steeper initial slope and higher magnetization at high fields indicate a more coherent alignment of spins, facilitated by larger crystallites and reduced fraction of magnetically disordered surface atoms. When the fuel content is further increased to 1.2 – 1.6, the magnetization at a given field slightly decreases again, in line with the partial refinement of crystallite size and the increased defect density inferred from the structural analysis.

The inset in Fig. 5 magnifies the low-field region around the origin, making it possible to compare coercivity and remanence for the different compositions. All loops intersect the magnetization axis at small positive and negative coercive fields, confirming their soft-magnetic character. Nevertheless, distinct trends with f can be identified. The sample synthesized at $f = 0.4$ shows the smallest coercive field and an almost linear passage through the origin, which is typical of very fine particles approaching the superparamagnetic or single-domain limit, where magnetization reversal occurs predominantly via coherent rotation and thermal activation. The remanent magnetization of this powder is also minimal, giving a very low M_r/M_s ratio ("squareness"), in agreement with the predominance of superparamagnetic-like particles and the wide distribution of anisotropy axes.

As the fuel-to-oxidizer ratio is increased to 0.6 – 1.0, the loops become progressively more "square": the intercept of the $M(H)$ curve with the magnetization axis at zero field moves to higher values, and the slope in the vicinity of the coercive field becomes steeper. This indicates an increase in the fraction of stable single-domain or small multi-domain grains with well-defined anisotropy, for which magnetization reversal proceeds via domain wall motion and nucleation. The coercivity in this region is moderate but clearly larger than for $f = 0.4$, reflecting the strengthening of magnetocrystalline anisotropy and pinning effects as crystallites grow and internal stresses redistribute. For fuel-rich compositions ($f \geq 1.2$) the loops slightly contract in width again, suggesting a partial reduction of coercive field, while the remanence remains at a relatively high level. Such behaviour can be attributed to the coexistence of smaller, more easily reversible particles with larger grains containing pinned domain walls, consistent with the bimodal structural features inferred from XRD and SEM.

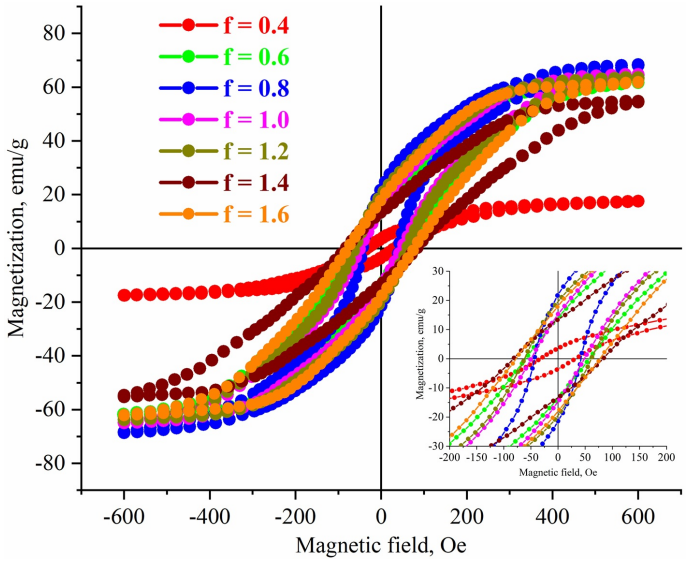

FIG. 5. (a) Room-temperature hysteresis loops $M(H)$ of $Zn_{0.5}Mn_{0.5}Fe_2O_4$ nanopowders synthesized by glycine–nitrate combustion at different fuel-to-oxidizer ratios ($f = 0.4$ – 1.6); inset shows an enlarged low-field region used to determine coercive field and remanent magnetization

Figure 5 demonstrates that the magnetic response of combustion-derived $Zn_{0.5}Mn_{0.5}Fe_2O_4$ nanopowders can be effectively tuned by varying the fuel-to-oxidizer ratio in the glycine-nitrate system. Fuel-lean conditions lead to very soft, weakly magnetized powders dominated by ultrafine, strongly disordered grains. Near-stoichiometric mixtures provide the highest magnetization and moderate coercivity, which is optimal for many soft-magnetic applications. Strongly fuel-rich conditions again decrease the magnetization and slightly reduce the coercivity, reflecting the complex interplay between crystallite size, lattice strain and cation distribution. The correlations between these magnetic characteristics and the structural parameters discussed earlier highlight the key role of combustion redox conditions in designing nanostructured Mn–Zn ferrites with tailored functional properties.

Figure 6 presents the quantitative magnetic parameters extracted from the hysteresis loops as a function of the fuel-to-oxidizer ratio f: (a) coercive field H_c, (b) remanent magnetization M_r and (c) saturation magnetization M_s. Together they illustrate how the redox conditions during combustion govern the softness and strength of the magnetic response of $Zn_{0.5}Mn_{0.5}Fe_2O_4$ nanopowders.

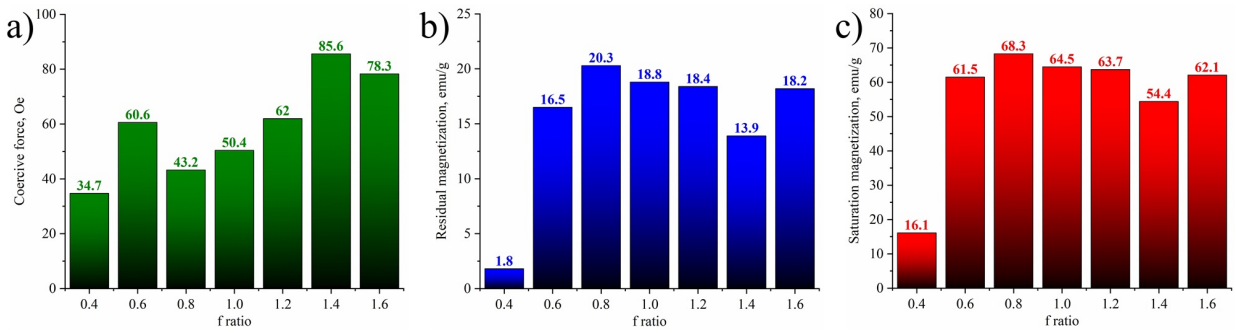

FIG. 6. (a) Dependence of (a) coercive field (H_c), (b) remanent magnetization (M_r) and (c) saturation magnetization (M_s) of $Zn_{0.5}Mn_{0.5}Fe_2O_4$ nanopowders on the fuel-to-oxidizer ratio f, obtained from the room-temperature hysteresis loops

The coercive field (Fig. 6a) shows a clear non-monotonic behaviour. For the fuel-lean sample ($f = 0.4$) H_c is only 34.7 Oe, indicating very easy magnetization reversal in a structure dominated by ultrafine, weakly interacting particles. Increasing f to 0.6 sharply raises H_c to 60.6 Oe, reflecting the growth of crystallites and strengthening of magnetocrystalline anisotropy and domain-wall pinning. At $f = 0.8$ and 1.0 the coercivity decreases to 43.2 and 50.4 Oe, respectively, suggesting that part of the grains become multidomain and magnetization reversal proceeds via more mobile walls. For fuel-rich compositions $f = 1.2$ – 1.6 the coercive field increases again, reaching a maximum of 85.6 Oe at $f = 1.4$ and slightly dropping to 78.3 Oe at $f = 1.6$. This rise is consistent with the refined, defect-rich microstructure produced under strongly exothermic, rapidly quenched combustion, where structural imperfections act as effective pinning centres.

The variation of M_r (Fig. 6b) follows a different trend. The fuel-lean sample has an extremely low remanence of 1.8 emu/g, in line with its nearly superparamagnetic-like behaviour and very small hysteresis loop. When the fuel ratio increases to 0.6 and 0.8, M_r rapidly grows to 16.5 and 20.3 emu/g, respectively, reflecting an increasing fraction of magnetically stable single-domain or small multidomain grains. In the range $f = 1.0$ – 1.2 the remanence remains high (18.8 – 18.4 emu/g), then drops to 13.9 emu/g at $f = 1.4$ and rises again to 18.2 emu/g at $f = 1.6$. The reduced M_r for $f = 1.4$ correlates with the smallest crystallite size and highest coercivity in this region, where stronger random anisotropy and more pronounced surface spin disorder partially cancel the net magnetization after field removal.

Saturation magnetization M_s (Fig. 6c) also exhibits a pronounced dependence on f. A very low value of 16.1 emu/g is obtained for the most fuel-deficient sample, confirming that extreme size reduction and high lattice strain strongly suppress long-range ferrimagnetic order. Near stoichiometry, M_s increases dramatically, reaching 61.5 emu/g at $f = 0.6$ and a maximum of 68.3 emu/g at $f = 0.8$. For $f = 1.0$ and 1.2 the saturation magnetization remains relatively high (64.5 and 63.7 emu/g), then decreases to 54.4 emu/g at $f = 1.4$ and partially recovers to 62.1 emu/g at $f = 1.6$. These changes mirror the structural evolution: larger, well-ordered crystallites formed at intermediate f minimize surface-spin canting and yield higher M_s, whereas both fuel-lean and highly fuel-rich regimes produce smaller, more defective particles with reduced magnetic moments.

Figure 6 highlights that an optimal fuel-to-oxidizer ratio around $f \approx 0.8$ – 1.0 provides a combination of high M_s and M_r with moderate H_c, characteristic of soft magnetic ferrites. Deviations towards too low or too high f lead either to weakly magnetized, almost superparamagnetic powders ($f = 0.4$) or to more coercive, defect-rich materials ($f \geq 1.4$), underscoring the key role of combustion redox conditions in tailoring the functional performance of Zn–Mn nanoferrites.

4. Conclusion

Nanostructured $Zn_{0.5}Mn_{0.5}Fe_2O_4$ powders were successfully synthesized by the glycine-nitrate solution combustion method with the fuel-to-oxidizer ratio varied in a wide range, $f = 0.4$ – 1.6. Regardless of the redox conditions, XRD

confirmed the formation of a single-phase cubic spinel, while SEM revealed highly porous agglomerates composed of nanosized primary particles with compositions close to the nominal stoichiometry. Systematic variation of f led to pronounced changes in crystallite size, lattice parameter and microstrain: fuel-lean and strongly fuel-rich mixtures produced finer, more strained crystallites with slightly contracted lattices, whereas near-stoichiometric conditions promoted the growth of larger domains and maximized the lattice constant.

These structural modifications were directly reflected in the magnetic response at 300 K. All samples exhibited soft-ferrimagnetic behaviour with relatively narrow hysteresis loops, but the absolute values of the magnetic parameters were strongly dependent on f. The saturation magnetization varied from 16.1 to 68.3 emu/g, the remanent magnetization from 1.8 to 20.3 emu/g and the coercive field from 34.7 to 85.6 Oe. The lowest M_s and M_r were obtained for the most fuel-deficient powder, where extreme refinement and high lattice strain suppress long-range ferrimagnetic order, whereas strongly fuel-rich mixtures showed increased coercivity due to microstructural refinement and defect-induced pinning. The optimal combination of high M_s and M_r with moderate H_c, characteristic of soft magnetic ferrites, was achieved for $f \approx 0.8 - 1.0$, where crystallites are relatively large and structurally well ordered.

Overall, the results demonstrate that the fuel-to-oxidizer ratio in glycine–nitrate combustion is an efficient control parameter for tailoring both structural and magnetic characteristics of Zn–Mn nanoferrites. By selecting appropriate redox conditions, it is possible to obtain nanopowders with a desired balance between crystallite size, lattice strain and magnetic softness, which is crucial for further processing into low-loss cores and functional layers for electromagnetic devices. The established structure–property correlations provide a useful guideline for designing combustion-derived ferrites for power electronics, microwave absorbers and other soft-magnetic applications.

References

[1] Ott G., Wrba J., Lucke R., Recent developments of Mn–Zn ferrites for high permeability application. *J. of Magnetism and Magnetic Materials*, 2003, **254–255**, P. 535–537.

[2] Chen Z., Li T., Wang A., Shi M., Han B., The latest research progress on MnZn ferrite and their applications. *Open Ceramics*, 2025, **21**, 100732.

[3] Thakur P., Chahar D., Taneja S., Bhalla N., Thakur A., A review on MnZn ferrites: Synthesis, characterization and applications. *Ceramics International*, 2020, **46** (10), P. 15740–15763.

[4] Bai Y.-H., Xia Q.-H., Zhang D.-Y., Mn–Zn ferrite foam concrete: Enhanced electromagnetic wave absorption and pore structure by incorporating carbon fibers. *Ceramics International*, 2024, **50** (14), P. 25578–25597.

[5] Arulmurugan R., Vaidyanathan G., Sendhilnathan S., Jeyadevan B., Mn–Zn ferrite nanoparticles for ferrofluid preparation: Study on thermal–magnetic properties. *J. of Magnetism and Magnetic Materials*, 2006, **298** (2), P. 83–94.

[6] Slavu L.M., Rinaldi R., Corato R.D., Application in nanomedicine of Manganese-Zinc ferrite nanoparticles. *Applied Sciences*, 2021, **11** (23), 11183.

[7] Mathew D.S., Juang R.-S., An overview of the structure and magnetism of spinel ferrite nanoparticles and their synthesis in microemulsions. *Chemical Engineering J.*, 2007, **129** (1–3), P. 51–65.

[8] Deepty M., Srinivas C., Mohan N.K., Kumar E.R., Singh S., Meena S.S., Bhatt P., Sastry D.L., Chemical synthesis of Mn–Zn magnetic ferrite nanoparticles: Effect of secondary phase on extrinsic magnetic properties of Mn–Zn ferrite nanoparticles. *Ceramics International*, 2024, **50** (11), P. 18446–18453.

[9] Etemadi H., Plieger P.G., Synthesis and characterisation of $M_xFe_{3-x}O_4$ (M = Fe, Mn, Zn) spinel nanoferrites through a solvothermal route. *J. of Materials Science*, 2021, **56**, P. 17568–17583.

[10] Jiang H., Xu X., Zhang R., Zhang Y., Chen J., Yang F., Nano ferrites (AFe_2O_4, A = Zn, Co, Mn, Cu) as efficient catalysts for catalytic ozonation of toluene. *RSC Advances*, 2020, **10**, P. 5116–5128.

[11] Dyachenko S.V., Martinson K.D., Cherepkova I.A., Zhernovoi A.I., Particle size, morphology, and properties of transition metal ferrospinels of the MFe_2O_4 (M = Co, Ni, Zn) type, produced by glycine-nitrate combustion. *Russian J. of Applied Chemistry*, 2016, **89** (4), P. 535–539.

[12] Praveena K., Sadhana K., Bharadwaj S., Murthy S.R., Development of nanocrystalline Mn–Zn ferrites for high frequency transformer applications. *J. of Magnetism and Magnetic Materials*, 2009, **321** (16), P. 2433–2437.

[13] Kaewmanee T., Phuruangrat A., Thongtem T., Thongtem S., Solvothermal synthesis of Mn–Zn Ferrite(core)@SiO_2(shell)/$BiOBr_{0.5}Cl_{0.5}$ nanocomposites used for adsorption and photocatalysis combination. *Ceramics International*, 2020, **46** (3), P. 3655–3662.

[14] Martinson K.D., Kozyritskaya S.S., Panteleev I.B., Popkov V.I., Low coercivity microwave ceramics based on LiZnMn ferrite synthesized via glycine-nitrate combustion. *Nanosystems: Physics, Chemistry, Mathematics*, 2019, **10** (3), P. 313–317.

[15] Hu Y., Zou B., Xing H., Liu J., Chen Q., Wang X., Li L., Preparation of Mn–Zn ferrite ceramic using stereolithography 3D printing technology. *Ceramics International*, 2022, **48** (5), P. 6923–6932.

[16] Jain S.K., Dolia S.N., Choudhary B.L., Prashant B.L., Structural and morphological study of $Zn_{0.9}Mn_{0.05}Fe_{0.05}O$ synthesized by sol-gel wet chemical precipitation route. *IOP Conference Series: Materials Science and Engineering*, 2018, **348**, 012004.

[17] Venkatachalapathy R., Manoharan C., Venkateshwarlu M., Elfadeel G.A., Saddeek Y., Solution combustion route for Ni and Al co-doped lithium ferrite nanoparticles: Synthesis, the effect of doping on the structural, morphological, optical, and magnetic properties. *Ceramics International*, 2023, **49** (4), P. 6594–6607.

[18] Martinson K.D., Ivanov A.A., Panteleev I.B., Popkov V.I., Effect of sintering temperature on the synthesis of LiZnMnFe microwave ceramics with controllable electro/magnetic properties. *Ceramics International*, 2021, **47** (21), P. 30071–30081.

[19] Smirnova M.N., Nikiforova G.E., Kondrat'eva O.N., Synthesis of magnesium ferrite by combustion of glycine-nitrate gel: the influence of reagents on the gel-precursor and the microstructure of nanopowders. *Nanosystems: Physics, Chemistry, Mathematics*, 2024, **15** (2), P. 224–232.

[20] Saukhimov A.A., Hobosyan M.A., Dannagoda G.C., Zhumabekova N.N., Almanov G.A., Kumekov S.E., Martirosyan K.S., Solution-combustion synthesis and magnetodielectric properties of nanostructured rare earth ferrites. *International J. of Self-Propagating High-Temperature Synthesis*, 2015, **24**, P. 63–71.

[21] Martinson K.D., Sakhno D.D., Belyak V.E., Kondrashkova I.S., $Ni_{0.4}Zn_{0.6}Fe_2O_4$ Nanopowders by Solution-Combustion Synthesis: Influence of Red/Ox Ratio on their Morphology, Structure, and Magnetic Properties. *Int. J. of Self-Propagating High-Temperature Synthesis*, 2020, **29** (4), P. 202–207.

[22] Hwang C.-C., Tsai J.S., Huang T.-H., Combustion synthesis of Ni–Zn ferrite by using glycine and metal nitrates—investigations of precursor homogeneity, product reproducibility, and reaction mechanism. *Materials Chemistry and Physics*, 2005, **93** (2–3), P. 330–336.
[23] Nadargi D., Umar A., Nadargi J., Patil J., Mulla I., Akbar S., Suryavanshi S., Spinel Magnesium Ferrite ($MgFe_2O_4$): A Glycine-Assisted Colloidal Combustion and Its Potentiality in Gas-Sensing Application. *Chemosensors*, 2022, **10** (9), 361.
[24] Popkov V.I., Chebanenko M.I., Tenevich M.I., Buryanenko I.V., Semenov V.G., Solution combustion synthesis of iron-deficient $Sc_{2-x}Fe_xO_3$ ($x = 0.17$ – 0.47) nanocrystals with bixbyite structure: The effect of spatial constraints. *Ceramics International*, 2022, **48** (24), P. 36046–36055.
[25] Siddique F., Gonzalez-Cortes S., Mirzaei A., Xiao T., Rafiq M.A., Zhang X., Solution combustion synthesis: the relevant metrics for producing advanced and nanostructured photocatalysts. *Nanoscale*, 2022, **14**, P. 11806–11868.
[26] La P., Lei W., Wang X., Wei Y., Ma Y., Effects of excess $NaClO_4$ on phases, size and magnetic properties of Ni–Zn ferrite powders prepared by combustion synthesis. *Ceramics International*, 2015, **41** (8), P. 9843–9848.
[27] Martinson K.D., Belyak V.E., Sakhno D.D., Ivanov A.A., Lebedev L.A., Nefedova L.A., Panteleev I.B., Popkov V.I. Solution combustion assisted synthesis of ultra-magnetically soft LiZnTiMn ferrite ceramics. *J. of Alloys and Compounds*, 2022, **894**, 162554.
[28] Ortiz-Quinonez J.-L., Pal U., Villanueva M.S. Structural, Magnetic, and Catalytic Evaluation of Spinel Co, Ni, and Co–Ni Ferrite Nanoparticles Fabricated by Low-Temperature Solution Combustion Process. *ACS Omega*, 2018, **3** (11), P. 14986–15001.
[29] Azadmanjiri J. Preparation of Mn–Zn ferrite nanoparticles from chemical sol–gel combustion method and the magnetic properties after sintering. *J. of Non-Crystalline Solids*, 2007, **353** (44–46), P. 4170–4173.
[30] Kumar E.R., Jayaprakash R., The role of fuel concentration on particle size and dielectric properties of manganese substituted zinc ferrite nanoparticles. *J. of Magnetism and Magnetic Materials*, 2014, **366**, P. 33–39.
[31] Kumar E.R., Jayaprakash R., Effect of combustion rate and annealing temperature on structural and magnetic properties of manganese substituted nickel and zinc ferrites. *J. of Magnetism and Magnetic Materials*, 2013, **348**, P. 93–100.
[32] Varma A., Mukasyan A.S., Rogachev A.S., Manukyan K.V., Solution Combustion Synthesis of Nanoscale Materials. *Chemical Reviews*, 2016, **116** (23), P. 14493–14586.
[33] Ahmia N, Benamira M., Messaadia L., Masmoudi R., Horwat D., Avramova I., Sol-gel auto-combustion synthesized $ZnMn_2O_4$ for efficient photocatalytic Congo red degradation: structural, kinetics, computational, and ecotoxicity analyses. *J. of Physics and Chemistry of Solids*, 2026, **208**, 113038.
[34] Abdo M.A., Al-Wafi R., AlHammad M.S., Highly efficient visible light driven photocatalytic activity of rare earth cerium doped zinc-manganese ferrite: Rhodamine B degradation and stability assessment. *Ceramics International*, 2023, **49** (17), P. 29245–29258.
[35] Ivanovskaya M.I., Tolstik A.I., Kotsikau D.A., Pankov V.V., The structural characteristics of Zn-Mn ferrite synthesized by spray pyrolysis. *Russian J. of Physical Chemistry A*, 2009, **83**, P. 2081–2086.
[36] Ghodake U.R., Chaudhari N.D., Kambale R.C., Patil J.Y., Suryavanshi S.S., Effect of Mn^{2+} substitution on structural, magnetic, electric and dielectric properties of Mg–Zn ferrites. *J. of Magnetism and Magnetic Materials*, 2016, **407**, P. 60–68.
[37] Deraz N.M., Alarifi A., Preparation and characterization of nano-magnetic $Mn_{0.5}Zn_{0.5}Fe_2O_4$ system. *International J. of Electrochemical Science*, 2012, **7** (7), P. 5828–5836.

Submitted 2 December 2025; revised 9 December 2025; accepted 10 December 2025

Information about the authors:

Nikita Kiryanov – Saint Petersburg Electrotechnical University "LETI", Saint Petersburg, 199026, Russia; ORCID 0009-0000-8169-9287; nikyr@mail.ru

Kirill Martinson – Ioffe Institute, Politekhnicheskaya st., 26, Saint Petersburg, 194064, Russia; ORCID 0000-0001-9313-4267; martinsonkirill@mail.ru

Conflict of interest: the authors declare no conflict of interest.

NANOSYSTEMS:
PHYSICS, CHEMISTRY, MATHEMATICS

Original article

Kondrat'eva O.N., et al. *Nanosystems: Phys. Chem. Math.*, 2025, **16** (6), 829–836.
http://nanojournal.ifmo.ru
DOI 10.17586/2220-8054-2025-16-6-829-836

Physico-mechanical properties and radiation tolerance of magnesium-indium ferrite synthesized by the polymer-nitrate method

Olga N. Kondrat'eva[1,a], Maria N. Smirnova[1,b], Galina E. Nikiforova[1,c], Alexey D. Yapryntsev[1,d], Maria S. Dranik[2,e], Valery A. Ketsko[1,f]

[1]Kurnakov Institute of General and Inorganic Chemistry of the Russian Academy of Sciences, Moscow, Russia
[2]Frumkin Institute of Physical Chemistry and Electrochemistry of the Russian Academy of Sciences, Moscow, Russia

[a]ol.kondratieva@gmail.com, [b]smirnovamn@igic.ras.ru, [c]gen@igic.ras.ru, [d]yaprynsev@yandex.ru, [e]m.dranik@yandex.ru, [f]ketsko@igic.ras.ru

Corresponding author: Olga N. Kondrat'eva, ol.kondratieva@gmail.com

PACS 81.20.Ev, 81.07.Wx, 62.20.Qp, 78.20.-e

ABSTRACT The paper discusses the features of polymer-nitrate synthesis of fine $MgFeInO_4$ particles and presents experimental study results of the physico-mechanical properties of ceramics produced on their basis. According to powder XRD data, a single-phase ferrite-spinel powder can be obtained only as a result of high-temperature treatment of an X-ray amorphous precursor prepared by thermal decomposition of a mixture of polyvinyl alcohol and metal nitrates. Ceramics produced using submicron $MgFeInO_4$ particles have a density close to the theoretical one. The results of microhardness measurements using the Vickers method showed that the resulting material has high hardness. The band gap energy of $MgFeInO_4$ was determined from the DRS data. Based on the crystallographic and electrophysical characteristics of the synthesized material, its resistance to radiation-induced structural changes was predicted.

KEYWORDS mixed ferrites, cubic crystal structure, fine powders, ceramics, Vickers microhardness, band gap energy, radiation tolerance

ACKNOWLEDGEMENTS This study was performed within the ARIADNA Collaboration operating under the NICA facility as a part of State Assignment "Solving topical problems with NICA charged particle beams" (ref. # 124110600054-0). The measurements were performed using the equipment of the JRC PMR IGIC RAS. The microhardness studies were carried out using the equipment of the CKP FMI IPCE RAS.

FOR CITATION Kondrat'eva O.N., Smirnova M.N., Nikiforova G.E., Yapryntsev A.D., Dranik M.S., Ketsko V.A. Physico-mechanical properties and radiation tolerance of magnesium-indium ferrite synthesized by the polymer-nitrate method. *Nanosystems: Phys. Chem. Math.*, 2025, **16** (6), 829–836.

1. Introduction

The creation of new types of radiation-resistant functional materials suitable for long-term and trouble-free operation under the influence of various sources of ionizing radiation is an important scientific and practical problem. Its solution will create new opportunities for research and development in the field of nuclear energy and medicine, radiation control, and storage of radioactive waste [1–3]. Many years of intensive research [4–6] have shown refractory oxides with a cubic crystal lattice of the spinel type to be one of the most resistant materials to various types of radiation. Materials based on aluminum-magnesium spinel $MgAl_2O_4$ have shown high potential for use in nuclear fission reactors [7,8], as well as inert matrices for transmutation of actinides [7,9,10] and optically transparent windows for reactor components [11]. In addition, it was noted in [12–14] that ferrite-spinels are highly promising for practical application in irradiation environments. Meillon *et al.* [14] established that magnetite (Fe_3O_4) is extremely resistant to fast neutron irradiation with an energy of 0.1 MeV and a fluence of 2×10^{20} neutrons/cm^2, which is equivalent to the radiation conditions near a nuclear reactor.

According to Sickafus *et al.* [15], the excellent radiation tolerance of spinels compared to other materials is due to the complexity of their chemical composition and the ability to cationic disorder. Therefore, the enhancement of their radiation damage resistance is possible due to the complication of the chemical composition (e.g., by polycationic doping) and/or varying the degree of inversion. The cation distribution over tetrahedral and octahedral sublattices of materials with the spinel structure largely depends on the method of their preparation [16, 17]. Moreover, the degree of inversion in microcrystalline samples may differ from their nanoscale counterparts [17]. On the other hand, the size of the powder particles affects the mechanical properties of the materials obtained from them. As it was noted in [18], the strength of ceramics made from ultrafine powders is higher than that of those produced using standard ceramic technology. Moreover,

the large fraction of the grain boundaries can serve as an effective sink of point defects formed during irradiation [19, 20]. This additionally enables creating both new and improved materials for radiation shields and screens, which are today widely in demand in medicine and the nuclear industry [21]. Satalkar *et al.* [22] reported on the high potential of using nanoscale ferrite-spinels $Mn_{1-x}Zn_xFe_2O_4$ ($x = 0$; 0.5; 1) as part of inexpensive lightweight shields designed to protect against radiation near nuclear facilities. Moreover, the mixed ferrite-spinel composition $Mn_{0.5}Zn_{0.5}Fe_2O_4$ was least susceptible to radiation swelling.

According to the literature review, the interest in studying the effect of various irradiation conditions on the structure and structure-sensitive properties of nanoscale ferrite-spinels has been shown to grow [23–28]. Nevertheless, data on the study of the radiation damage resistance of mixed magnesium-indium ferrites has not been found. In this regard, as a starting point for the research work, it is of interest to synthesize and characterize highly dispersed materials based on $MgFe_{2-x}In_xO_4$, in which half of the iron cations are replaced by indium cations. To date, the main approach to produce mixed $MgFe_{2-x}In_xO_4$ ferrite-spinels is the solid-phase method [29–31]. Naik *et al.* [32] attempted low-temperature synthesis of $MgFe_{2-x}In_xO_4$ ($x = 0 - 0.16$) nanoparticles, however, samples with a substitution degree of $x = 0.16$ contained an admixture of α-Fe_2O_3. In this paper, the features of polymer-nitrate synthesis of fine $MgFe_{2-x}In_xO_4$ particles with a high indium content ($x = 0.5$) are described for the first time, as well as the results of measuring microhardness and assessing radiation tolerance of ceramic materials made on their basis are presented.

2. Experimental part

2.1. Synthesis of powder and ceramics of $MgFeInO_4$

Single-phase $MgFeInO_4$ powder was obtained by the polymer-nitrate method. Powders of metallic magnesium (ω(Mg) = 99.95 wt. %, National State Standard GOST 804-93) and carbonyl iron (ultra-high purity 13-2, TS 6-09-05808009-262-92), indium (grade In0, ω(In) = 99.998 wt. %, National State Standard GOST 10297-94), polyvinyl alcohol (PVA, grade 20/1, National State Standard GOST 10779-78) and nitric acid (ultra-high purity 18-4, National State Standard GOST 11125-84) were used as starting materials. The magnesium, indium, and carbonyl iron samples were dissolved in nitric acid previously diluted with distilled water ($V(H_2O) : V(HNO_3) = 1 : 3$). Freshly prepared solutions of $Mg(NO_3)_2$, $Fe(NO_3)_3$, and $In(NO_3)_3$ were mixed in an evaporating bowl in a ratio of 1 :1 : 1, and then heated on a heating plate and kept at 90 °C. A stoichiometric amount of polymer was added to the heated solution mixture and continued to evaporate with constant stirring. Heating was stopped after obtaining a fine red-brown powder. The solid-phase synthesis products formed (hereinafter referred to as the precursor powder) were cooled, ground in a mortar, and then annealed in a muffle furnace. To study the effect of the annealing temperature on the phase composition, the precursor powder was heated to 600, 800, and 1100 °C and kept at these temperatures for at least 4 hours in air. After the heat treatment was completed, the samples were cooled to ambient temperature together with the furnace. The ceramic material required for the study of the mechanical properties of $MgFeInO_4$ was made from a powder that does not contain impurity phases. Before pressing, it was ground in a mortar, moistened with a few drops of acetone ($\omega(CH_3COCH_3)$ = 99.75 wt. %, National State Standard GOST 2768-84). The resulting mass was transferred to a steel mold, and tablets with a diameter of 14 mm were formed from it, using a manual hydraulic press. The compacted samples were sintered at 1300 °C for 6 hours in air. After its completion, the sintered ceramics were left in the furnace until it cooled completely. The actual density (d_{obs}, kg/m^3) of the samples obtained was determined geometrically. Their relative porosity (p_{rel}, %) was estimated by the formula:

$$p_{rel} = 100\left(1 - \frac{d_{obs}}{d_{XRD}}\right), \quad (1)$$

where d_{XRD} (in kg/m^3) is the theoretical density of ceramics determined from powder X-ray diffraction data.

2.2. Characterization of the obtained materials

The phase composition of the materials obtained was determined using the powder X-ray diffraction (XRD) method on a Bruker D8 Advance diffractometer equipped with the LynxEye linear detector. An X-ray tube with a copper anode ($\lambda(CuK_\alpha)$ = 1.5418 Å) was used as the radiation source. A nickel filter was used to eliminate the CuK_β-radiation. The XRD patterns for all samples studied were recorded at room temperature in the range of angles 2θ = 10 – 60° with a step of 0.0133° and a signal accumulation time of 0.5 s/step. X-ray phase analysis was performed using the ICDD PDF-2 database and Bruker DIFFRAC. EVA software. The calculation of crystallographic parameters and sizes of coherent scattering regions (CSR) was performed using Bruker TOPAS 4.2 software.

The microstructure of the synthesized materials was studied using scanning electron microscopy (SEM). SEM images in the secondary electron detection mode were obtained using an ultra-high-resolution scanning electron microscope TESCAN AMBER. The freely distributed Gwyddion software [33] was used to analyse the obtained SEM data and to plot the particle size distribution curve.

Data on the elemental composition of the synthesized magnesium-indium ferrite was obtained by energy dispersive X-ray spectroscopy (EDS) using an Oxford Instruments Ultim MAX SDD detector.

The study of ceramic microhardness (H) by the Vickers method was carried out on a LOMO PMT-3M microhardness tester. Before measurements, the surface of the samples was washed and polished in an aqueous alcohol solution under ultrasonic treatment. The measurements were conducted with a static load on the indenter equal to 0.49 N (50 g). The duration of the load application was 10 seconds.

The diffuse reflectance spectra $R(\lambda)$ of the samples in the range of 200 – 950 nm were recorded using the Ocean Optics modular optical system, which includes a QE65000 spectrometer, an integrating sphere ISP-80-8-R with a diameter of 80 mm, and a set of optical fibers. The source of the radiation was an HPX-2000 xenon lamp. The Labsphere WS-1-SL standard made of spectralon was used as a reference standard material. The spectrometer was controlled using the Spectra Suite software.

3. Results and discussion

3.1. X-ray phase analysis, composition, and structural and morphological characteristics of synthesized materials

The XRD data for the synthesized precursor powder is shown in Fig. 1. The absence of crystal phase peaks on the diffractogram obtained (curve 1) indicates its X-ray amorphous structure. This result is accounted for the fact that the decomposition of products formed by heating a mixture of solutions of metal nitrates and PVA is not accompanied by combustion (smolder) and is likely to occur at relatively low temperatures [34]. According to [35, 36], this mode of the process contributes to the formation of thermally stable polymer-metal complexes, and their short-term annealing enables one to obtain nanocrystalline powders of complex metal oxides at 500 – 800 °C.

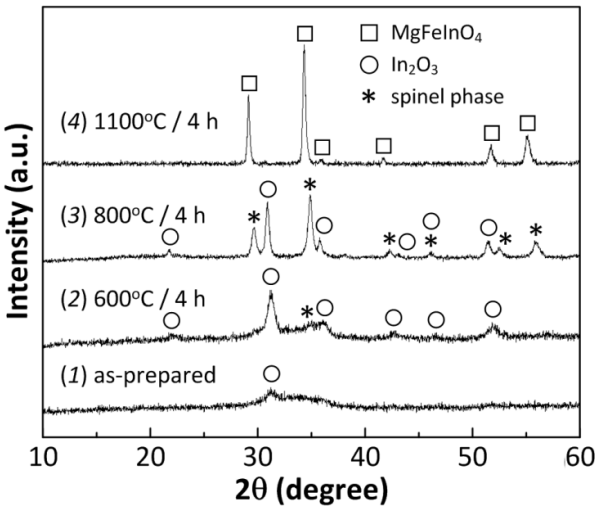

FIG. 1. XRD data for the samples obtained after annealing of precursor powder at different temperatures in air

XRD data for the precursor powder after its heat treatment in air at 600, 800, and 1100 °C are shown in Fig. 1 (curves 2–4). The results obtained show that very wide and low-intensity maxima appear on the diffractogram of the powder annealed at 600 °C (curve 2). According to the X-ray phase analysis, it is a mixture consisting mainly of In_2O_3 (sp. gr. $I\bar{a}3$, PDF card No. 06-0416) and a small amount of $MgFe_{2-x}In_xO_4$ phase with a spinel structure. According to the calculation results, the average crystallite size in this powder is about 10 nm. An attempt to anneal the X-ray amorphous precursor at a higher temperature also failed to produce a single-phase ferrite-spinel sample of the composition required. As can be seen from Fig. 1 (curve 3), the diffractogram of the powder annealed at 800 °C (4 h) shows more intense, wide maxima related to the $MgFe_{2-x}In_xO_4$ phase, but it still contains an admixture of In_2O_3. The amount of ferrite-spinel in this powder reaches about 80 %, and the average size of its crystallites increases to 30 nm. Moreover, as the results of our experiments showed, even a threefold increase in the annealing duration at this temperature does not lead to the production of a single-phase sample of $MgFeInO_4$. It can be obtained only by increasing the annealing temperature to 1100 °C. As can be seen from the diffraction pattern of the annealed powder (Fig. 1, curve 4), all diffraction maxima correspond to $MgFeInO_4$ ferrite-spinel (sp. gr. $Fd\bar{3}m$, PDF card No. 38-1108). The disappearance of the (111) diffraction line indicates a very high degree of its inversion, which tends to 1. This result differs from the data obtained by Matvejeff *et al.* [31] and is explained by the differences in the chemical and thermal prehistory of the $MgFeInO_4$ samples being compared. The parameter a and the unit cell volume V_{cell} of synthesized $MgFeInO_4$ are 8.6391(6) Åand 644.8(1) $Å^3$, respectively, and its X-ray density d_{XRD} is 5336 kg/m^3. Literature data comparison showed that the calculated values are close to those obtained for samples synthesized by the solid-phase method [30, 31].

The data on the chemical composition of the $MgFeInO_4$ sample obtained by the EDS are shown in Fig. 2. It is obvious that the actual content of magnesium, iron, and indium in it (inset in Fig. 2) almost coincides with the theoretical one: ω_{theor}(Mg) = 9.39 wt. %, ω_{theor}(Fe) = 21.56 wt. %, and ω_{theor}(Fe) = 44.34 wt. %. Thus, the chemical composition of the synthesized ferrite-spinel can be represented as $Mg_{1.01\pm0.08}Fe_{0.99\pm0.07}In_{0.99\pm0.06}O_4$.

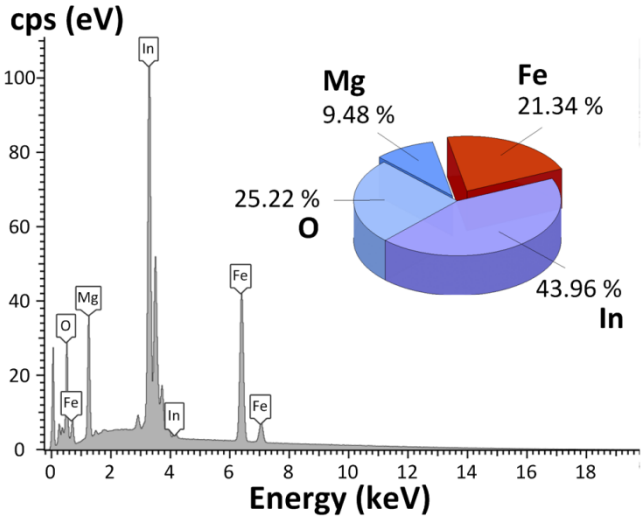

FIG. 2. EDS spectrum of $MgFeInO_4$ synthesized by annealing of precursor powder at 1100 °C for 4 hours. Inset: diagram illustrating the elemental composition of the sample (in wt. %), determined from the EDS data

It is noteworthy that the annealing temperature required to obtain a single-phase $MgFeInO_4$ powder turned out to be significantly higher than that used for the synthesis of $MgFe_2O_4$. A single-phase powder of this spinel was reported to be formed after annealing the precursor at 700 °C [37]. Similar results were obtained in [38], in which it was successfully synthesized by calcination of starch-nitrate gel at 550 °C. At the same time, the sol-gel method used in [32] did not result in obtaining single-phase $MgFe_{2-x}In_xO_4$ nanopowders with $x = 0.16$ at 600 °C. Previously, we showed [39] that single-phase $MgIn_2O_4$ is formed only after annealing of solid-phase combustion products of a glycine-nitrate gel at 1400 °C. Similar observations were made in [40], where this spinel was obtained by long-term high-temperature annealing (1300 °C, 60 h) of a precursor synthesized by the oxalate method. It is remarkable that the difference in annealing temperatures used for the synthesis of $MgFe_{2-x}In_xO_4$ solid solution boundary compositions is more than 700 °C, and the minimum annealing temperature required to obtain a single-phase composition with 50 % substitution of indium cations is about 400 °C higher than for $MgFe_2O_4$. The obtained result can be explained as follows. According to [41], the stable form of magnesium indate occurs only above 1200 °C, and the process of its formation from simple oxides is endothermic in nature. Therefore, the energy spent on breaking bonds in compounds used for spinel synthesis will exceed the energy released during the formation of bonds in it. Thus, the formation of $MgIn_2O_4$ requires additional energy input from the surroundings. Magnesium ferrite, on the contrary, has a negative enthalpy of formation ($\Delta H^0_{f,ox}$(970 K) = -18.5 ± 1.0 kJ/mol [42]). The enthalpy of formation for $MgFeInO_4$ is unknown, but according to our results it can be assumed to be lower than that of $MgIn_2O_4$. Consequently, mixed ferrite can be synthesized at lower temperatures than $MgIn_2O_4$. However, annealing of the precursor powder at high temperatures, as in the case of $MgIn_2O_4$ [39, 40], does not imply the production of single-phase $MgFeInO_4$ nanocrystalline powder. Nevertheless, the width and intensity of the maxima observed on the diffractogram of the powder annealed at 1100 °C (Fig. 1, curve 4) indicate relatively low values of CSRs.

The results of the microscopic study of the changes occurring in the structure and morphology of the particles of the X-ray amorphous precursor as a result of annealing at temperatures ranging from 600 to 1100 °C are presented in Fig. 3(a–c). The microstructure of the nanopowders formed after annealing at 600 and 800 °C (Fig. 3(a) and (b)) exhibits a sponge-like structure, which makes it difficult to distinguish the contours of individual crystallites. As seen in Fig. 3(c), increasing the annealing temperature of the precursor powder to 1100 °C led to the formation of $MgFeInO_4$ particles that are fairly uniform in size, though lacking well-defined faceting. The histogram illustrating their size distribution is shown in Fig. 3(f). The results of fitting these data using a Gaussian distribution function revealed that the average particle size of the ferrite-spinel synthesized is 0.90 μm.

The ceramics obtained by sintering the compacts of $MgFeInO_4$ powder at 1300 °C for 6 hours in air had a bulk density d_{obs} equal to about 4800 kg/m^3. The porosity P_{obs} of the sample produced, calculated using Eq. (1), was about 10 %, which indicates its high density.

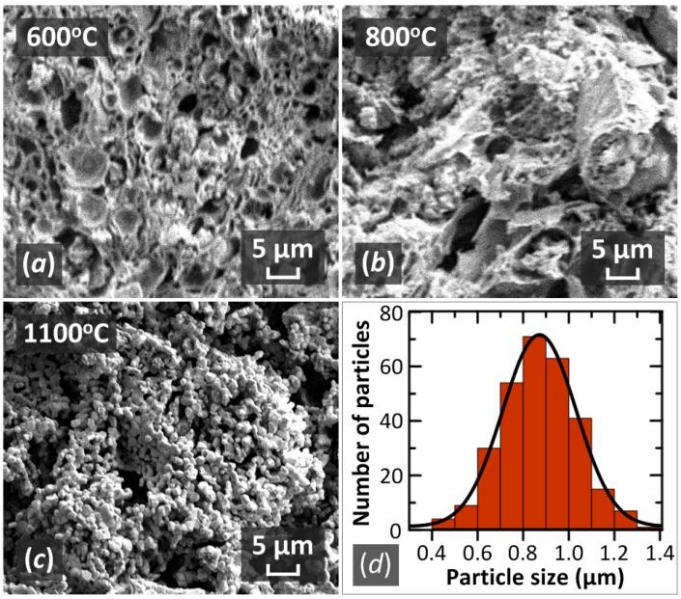

FIG. 3. (a–c) SEM images of powders obtained after annealing the precursor powder at 600 °C (4 h), 800 °C (4 h), and 1100 °C (4 h) in air. (d) Particle size distribution curve for the $MgFeInO_4$ sample obtained after annealing at 1100 °C (4 h)

3.2. Vickers microhardness

No data on the microhardness of $MgFeInO_4$ measured by the Vickers method was found in the literature. Based on the experimental results, the average microhardness value of the produced ceramics was determined to be 676 HV. It may be noted that the obtained value of H is close to those measured for magnetite Fe_3O_4 (610 HV) and manganese ferrite $MnFe_2O_4$ (734 HV) [43]. The hardness class of $MgFeInO_4$ was determined according to the relation proposed in [44]:

$$H_0 = 0.675 \cdot \sqrt[3]{H}, \tag{2}$$

where H_0 is the hardness class of the material on a 15-point scale, in which graphite corresponds to 1 and diamond to 15, and H is the measured Vickers microhardness of the material. According to the recalculation using Eq. (2), the hardness class of the synthesized material on the Khrushchov scale is close to 6. From the viewpoint of the rational classification of materials by hardness proposed in [44], $MgFeInO_4$ belongs to high-hardness materials.

3.3. Band gap energy

Consider the results of diffuse reflectance spectroscopy for the synthesized ferrite-spinel $MgFeInO_4$. A typical dependence of the diffuse reflectance coefficient R on the wavelength of incident light λ is shown in Fig. 4. To calculate the band gap energy E_g, the Tauc method was employed. The $R(\lambda)$ data was presented in the form of the dependence $(F(R) \cdot h\nu)^n$ on $h\nu$, where $F(R)$ is the Kubelka–Munk function, defined as $(1-R)^2/2R$; h is Planck's constant; ν is the frequency of the incident radiation; and n is an exponent characterizing the nature of electron transition in the material. The type of transitions occurring in $MgFeInO_4$ is not precisely known; however, as shown in [38, 45–47], direct allowed transitions dominate in the unsubstituted $MgFe_2O_4$ and $MgIn_2O_4$. Therefore, to determine E_g, coordinates corresponding to the case of direct allowed transitions ($n = 2$) were used. The result of this analysis is shown in the inset of Fig. 4.

Extrapolation of the linear portion of the resulting curve to the abscissa axis at $(F(R) \cdot h\nu)^2 = 0$ yields a band gap energy $E_g = 2.46 \pm 0.02$ eV. The band gap value obtained (2.46 eV) lies between those reported for $MgFe_2O_4$ (2.1 eV [45]) and $MgIn_2O_4$ (3.2 eV) [46], confirming the formation of a solid solution based on these spinels and indicating that the material obtained is a wide-band gap semiconductor.

3.4. Assessment of the radiation tolerance of $MgFeInO_4$

Consider several criteria commonly used to predict the response of solids to high doses of ion impact. Pearton *et al.* [48] reported that the materials with smaller unit cell volumes and wider band gaps tend to be more resistant to ionizing radiation than those with larger cell volumes and narrower band gaps. The values of E_g and V_{cell} for $MgFeInO_4$ and several other spinel-structured materials are summarized in Table 1.

As noted above, Fe_3O_4 is considered one of the most radiation-resistant materials [14]; therefore, its parameters were used as a reference in the analysis of the E_g and V_{cell} data. It is evident that within the series $MgFe_2O_4$ – Fe_3O_4 – $MgFeInO_4$ – $MgIn_2O_4$, both of these parameters increase. Although $MgIn_2O_4$ exhibits the widest band gap among the materials listed, its unit cell volume is 17.7 % larger than that of Fe_3O_4. The E_g and V_{cell} values for $MgFe_2O_4$ and

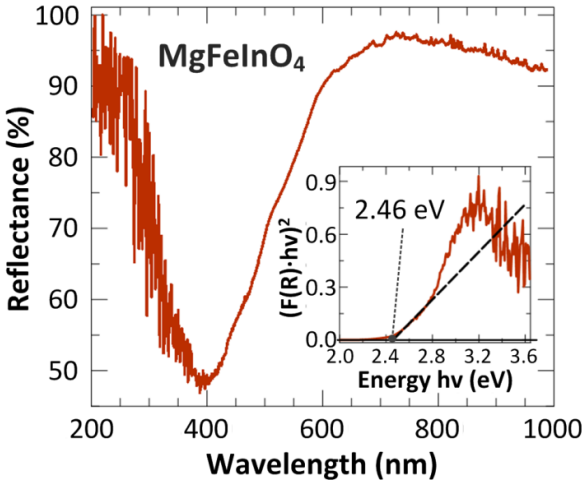

FIG. 4. Diffuse reflectance spectrum of $MgFeInO_4$ measured in the range 200 – 950 nm. Inset: representation of the data as a dependence of $(F(R) \cdot h\nu)^2$ on photon energy $h\nu$

TABLE 1. Physical properties of some spinel-structured materials

Material	Unit cell volume V_{cell}, Å^3	Band gap energy E_g, eV	Ionicity f	Predicted structure following irradiation
$MgFe_2O_4$	589.32 [38]	2.1 [45]	0.57*	–
Fe_3O_4	591.86 [49]	2.29 [50]	0.49*	Crystal [51]
$MgFeInO_4$	644.8*	2.46*	0.58	Crystal**
$MgIn_2O_4$	696.59 [39]	3.2 [46]	0.59*	–

* – determined in this work;

** – predicted structural stability based on the calculated values of ionicity

$MgFeInO_4$ are the closest to those of Fe_3O_4; however, for the mixed ferrite-spinel, the deviation in both parameters does not exceed 9 %. Therefore, materials based on $MgFeInO_4$ are most likely to exhibit radiation resistance comparable to that of Fe_3O_4 under similar irradiation conditions.

Naguib and Kelly [51] showed that the ability of materials to resist radiation damage correlates with the degree of bond ionicity, finding that materials with a more ionic bond character are less susceptible to damage under high doses of ionizing radiation. To put it simply, such materials tend to resist amorphization of the crystal lattice under irradiation. It was also established in [51] that structural changes are likely to occur if the ionicity value f is less than or equal to 0.47. The f values for $MgFe_2O_4$, $MgFeInO_4$, and $MgIn_2O_4$, calculated from the data in [52], are presented in Table 1. For comparison, the f value for Fe_3O_4, determined in [51], is also included. The calculations show that the ionicity in the series $MgFe_2O_4$ – $MgFeInO_4$ – $MgIn_2O_4$ exhibits close values, all significantly exceeding 0.47. Moreover, the ionicity of $MgFeInO_4$ is approximately 18.4 % higher than that of Fe_3O_4, which retains its crystalline structure even under irradiation [14]. Therefore, it can be inferred that magnesium-indium ferrite possesses radiation stability comparable to that of magnetite. Thus, the results of this preliminary assessment indicate the promising potential of $MgFeInO_4$ for further experimental studies on the effects of various ionizing radiation conditions on its structural and physico-mechanical properties.

4. Conclusions

A single-phase powder of the mixed ferrite-spinel $MgFeInO_4$ with submicron particle size was successfully synthesized using the polymer-nitrate method. XRD data obtained for the X-ray amorphous precursor annealed at different temperatures showed that a single-phase ferrite-spinel powder of the desired composition can be synthesized only at 1100 °C. According to SEM data, the average particle size was approximately 0.90 μm. The results obtained indicate that the synthesis of single-phase $MgFeInO_4$ in the nanocrystalline form by the polymer-nitrate method is impossible. However, this approach can be used to produce a compositionally homogeneous submicron ferrite-spinel powder. Moreover, unlike the solid-state method, it requires significantly less time and energy.

The $MgFeInO_4$ powder was used to produce ceramics of the same composition by high-temperature sintering in air. The density measurements showed that the approach applied enables one to obtain a ceramic material with a relative density of at least 90 %. Vickers microhardness testing revealed that the average microhardness value was 676 HV. This corresponds approximately to class 6 on the Khrushchov hardness scale, allowing the material to be classified as hard. The band gap energy value for $MgFeInO_4$ was determined from DRS data. According to the calculation results, the mixed magnesium ferrite can be attributed to wide bandgap materials ($E_g = 2.46$ eV). The electrophysical and structural parameters of $MgFeInO_4$ determined in this work made it possible to predict its ability to resist radiation-induced structural changes. Theoretical analysis showed that this ferrite-spinel is highly likely to retain its crystalline structure under ionizing radiation exposure. This result confirms the potential of further experimental studies on the influence of various irradiation conditions on the structure and functional properties of mixed magnesium-indium ferrites.

References

[1] Orlova A.I., Ojovan M.I. Ceramic mineral waste-forms for nuclear waste immobilization. *Materials*, 2019, **12** (16), 2638.

[2] Kalita P., Parveen R., Ghosh S., Grover V., Mishra Y.K., Avasthi D.K. Progress in radiation tolerant materials: current insights from the perspective of grain size and environmental temperature. *J. of Alloys and Compounds*, 2025, **1012**, 178330.

[3] More C.V., Akman F., Dilsiz K., Ogul H., Pawar P.P. Estimation of neutron and gamma-ray attenuation characteristics of some ferrites: Geant4, FLUKA and WinXCom studies. *Applied Radiation and Isotopes*, 2023, **197**, 110803.

[4] Li Z., Chan S.-K., Garner F.A., Brandt R.C. Elastic stability of high dose neutron irradiated spinel. *J. of Nuclear Materials*, 1995, **219**, P. 139–142.

[5] Wang L., Gong W., Wang S., Ewing R.C. Comparison of ion-beam irradiation effects in X_2YO_4 compounds. *J. of the American Ceramic Society*, 1999, **82** (12), P. 3321–3329.

[6] Pellerin N., Dodane-Thiriet C., Montouillout V., Beauvy M., Massiot D. Cation sublattice disorder induced by swift heavy ions in $MgAl_2O_4$ and $ZnAl_2O_4$ spinels: ^{27}Al Solid-State NMR Study. *The Journal of Physical Chemistry B*, 2007, **111** (44), P. 12707–12714.

[7] Wiss T., Matzke Hj. Heavy ion induced damage in $MgAl_2O_4$, an inert matrix candidate for the transmutation of minor actinides. *Radiation Measurements*, 1999, **31** (1-6), P. 507–514.

[8] Yasuda K., Matsumura S. Radiation damage effects in insulators for fusion reactors: microstructure evolution in MgO-Al_2O_3 system oxide crystals. *Advances in Science and Technology*, 2006, **45**, P. 1961–1968.

[9] Burghartz M., Matzke Hj., Léger C., Vambenepe G., Rome M. Inert matrices for the transmutation of actinides: fabrication, thermal properties and radiation stability of ceramic materials. *J. of Alloys and Compounds*, 1998, **271–273**, P. 544–548.

[10] Neeft E.A.C., Bakker K., Schram R.P.C., Conrad R., Konings R.J.M. The EFTTRA-T3 irradiation experiment on inert matrix fuels. *J. of Nuclear Materials*, 2003, **320** (1–2), P. 106–116.

[11] Kinoshita C., Fukumoto K., Fukuda K., Garner F.A., Hollenberg G.W. Why is magnesia spinel a radiation-resistant material? *J. of Nuclear Materials*, 1995, **219**, P. 143–451.

[12] Pascard H., Studer F. Review of irradiation effects on ferrites: results in the world from 1970 to 1995. *Journal de Physique IV*, 1997, **7** (C1), P. 211–214.

[13] Houpert C., Hervieu M., Groult D., Studer F., Toulemonde M. HREM investigation of GeV heavy ion latent tracks in ferrites. *Nuclear Instruments and Methods in Physics Research Section B: Beam Interactions with Materials and Atoms*, 1988, **32** (1–4), P. 393–396.

[14] Meillon S., Dunstetter F., Pascard H., Rodriguez-Carvajal J. Fast neutron irradiated magnetite and haematite investigated by neutron diffraction. *Journal de Physique IV Proceedings*, 1997, **07** (C1), P. 607–608.

[15] Sickafus K.E., Yu N., Nastasi M. Radiation resistance of the oxide spinel: the role of stoichiometry on damage response. *Nuclear Instruments and Methods in Physics Research Section B: Beam Interactions with Materials and Atoms*, 1996, **116** (1–4), P. 85–91.

[16] Reznitskiy L.A. *Calorimetry of Solids*. Moscow: Mos. Gos. Univ., 1981, 184 p.

[17] Šepelák V., Becker K.D. Comparison of the cation inversion parameter of the nanoscale milled spinel ferrites with that of the quenched bulk materials. *Materials Science and Engineering: A*, 2004, **375–377**, P. 861–864.

[18] Kingery W.D. *Introduction to ceramics, 2nd Edition*. John Wiley & Sons, 1976, 1056 p.

[19] Shen T.D. Radiation tolerance in a nanostructure: Is smaller better? *Nuclear Instruments and Methods in Physics Research B*, 2008, **266** (6), P. 921–925.

[20] Andrievskii R.A. Radiation stability of nanomaterials. *Nanotechnologies in Russia*, 2011, **6**, P. 357–369.

[21] Lokhande R.M., Vinayak V., Mukhamale S.V., Khirade P.P. Gamma radiation shielding characteristics of various spinel ferrite nanocrystals: a combined experimental and theoretical investigation. *RSC Advances*, 2021, **11** (14), P. 7925–7937.

[22] Satalkar M., Kane S.N., Kulriya P.K., Avasthi D.K. Swift heavy ion irradiated spinel ferrite: A cheap radiation resistant material. *Nuclear Instruments and Methods in Physics Research Section B: Beam Interactions with Materials and Atoms*, 2016, **379**, P. 235–241.

[23] Sharma S.K., Kumar R., Siva Kumar V.V., Knobel M., Reddy V.R., Gupta A., Singh. M. Role of electronic energy loss on the magnetic properties of $Mg_{0.95}Mn_{0.05}Fe_2O_4$ nanoparticles, *Nuclear Instruments and Methods in Physics Research Section B: Beam Interactions with Materials and Atoms*, 2006, **248** (1), P. 37–41.

[24] Parvatheeswara Rao B., Rao K.H., Subba Rao P.S.V., Mahesh Kumar A., Murthy Y.L.N., Asokan K., Siva Kumar V.V., Kumar R., Gajbhiye N.S., Caltun O.F. Swift heavy ions irradiation studies on some ferrite nanoparticles. *Nuclear Instruments and Methods in Physics Research Section B: Beam Interactions with Materials and Atoms*, 2006, **244** (1), P. 27–30.

[25] Hassan H.E., Sharshar T., Hessien M.M., Hemeda O.M. Effect of γ-rays irradiation on Mn–Ni ferrites: Structure, magnetic properties and positron annihilation studies. *Nuclear Instruments and Methods in Physics Research Section B: Beam Interactions with Materials and Atoms*, 2013, **304**, P. 72–79.

[26] Jagadeesha Angadi V., Anupama A.V., Choudhary H.K., Kumar R., Somashekarappa H.M., Mallappa M., Rudraswamy B., Sahoo B. Mechanism of γ-irradiation induced phase transformations in nanocrystalline $Mn_{0.5}Zn_{0.5}Fe_2O_4$ ceramics. *J. of Solid State Chemistry*, 2017, **246**, P. 119–124.

[27] Chikhale R.N., Shinde V.S., Bhatia P.G. Investigate structural, morphological, electrical, dielectric and magnetic properties of dysprosium doped cobalt-nickel ferrites and their response to gamma irradiation. *Nuclear Instruments and Methods in Physics Research Section B: Beam Interactions with Materials and Atoms*, 2024, **550**, 165320.

[28] Manjunatha, Biradar S., Bennal A.S., Patil S., Sayyed M.I., Patil Y.N., Megalamani M.B., Hegde B.G. Experimental investigation on the role of Bi^{3+} composition in structural, elastic, and radiation shielding properties of multifunctional cobalt-nickel nanoferrites. *J. of Alloys and Compounds*, 2025, **1033**, 181255.

[29] Kirichok P.P., Antoshchuk, Mössbauer investigations into magnesium ferrite doped with indium and scandium ions. *Soviet Physics Journal*, 1977, **20**, P. 627–630.
[30] Kimizuka N., Mohri T. Spinel, $YbFe_2O_4$, and $Yb_2Fe_3O_7$ types of structures for compounds in the In_2O_3 and Sc_2O_3–A_2O_3–BO systems [A: Fe, Ga, or Al; B: Mg, Mn, Fe, Ni, Cu, or Zn] at temperatures over 1000°C. *J. of Solid State Chemistry*. 1985, **60**, P. 382–384.
[31] Matvejeff M., Lindén J., Karppinen M., Yamauchi H. Studies on $InFeMO_4$ (M = Mg, Co, Ni, Cu and Zn) compounds: crystal structure and cation distribution. *Journal of Solid State Chemistry*, 2007, **180** (8), P. 2316–2322.
[32] Naik M.Z., Salker A.V. Tailoring the super-paramagnetic nature of $MgFe_2O_4$ nanoparticles by In^{3+} incorporation. *Materials Science and Engineering B*, 2016, **211**, P. 37–44.
[33] Necas D., Klapetek P. Gwyddion: an open-source software for SPM data analysis. *Open Physics*, 2012, **10** (1), P. 181–188.
[34] Khaliullin Sh.M., Zhuravlev V.D., Bamburov V.G., Khort A.A., Roslyakov S.I., Trusov G.V., Moskovskikh D.O. Effect of the residual water content in gels on solution combustion synthesis temperature. *Journal of Sol-Gel Science and Technology*, 2020, **93**, P. 251–261.
[35] Kondratéva O.N., Smirnova M.N., Nikiforova G.E., Yapryntsev A.D., Kondakov D.F., Yagudin L.D. Ceramic materials prepared from nanocrystalline $InFeZnO_4$ powder: optical and mechanical properties, and evaluation of radiation tolerance. *Nanosystems: Physics, Chemistry, Mathematics*, 2024, **15** (5), P. 693–701.
[36] Smirnova M.N., Kondrat'eva O.N., Nikiforova G.E., Yapryntsev A.D., Averin A.A., Khoroshilov A.V. Features of synthesis of $InGaMgO_4$ from nitrate-organic precursors and study of its physical properties. *Russian J. of Inorganic Chemistry*, 2024, **69**, P. 1119–1126.
[37] Smirnova M.N., Nikiforova G.E., Kondrat'eva O.N. Synthesis of magnesium ferrite by combustion of glycine-nitrate gel: the influence of reagents on the gel-precursor and the microstructure of nanopowders, *Nanosystems: Physics, Chemistry, Mathematics*, 2024, **15** (2), P. 224–232.
[38] Köferstein R., Walther T., Hesse D., Ebbinghaus S.G. Preparation and characterization of nanosized magnesium ferrite powders by a starch-gel process and corresponding ceramics. *J. of Materials Science*, 2013, **48**, P. 6509–6518.
[39] Kondrat'eva O.N., Smirnova M.N., Nikiforova G.E., Khoroshilov A.V., Arkhipenko A.A., Gurevich V.M. Magnesium indate: synthesis and thermodynamic properties. *Russian J. of Inorganic Chemistry*, 2022, **67**, P. 1221–1227.
[40] Jayachandran M., Dali S.E., Chockalingam M.J. Synthesis and characterisation of semiconductor oxide $MgIn_2O_4$ powder. *Bulletin of Electrochemistry*, 1998, **14** (8–9), P. 283–285.
[41] Pokrovskii B.I., Gapeev A.K., Goryaga A.N., Komissarova L.N. *Crystal chemistry and magnetism of mixed gallium- and indium-containing ferrites with spinel structure. Ferrimagnetism*. Moscow: Mos. Gos. Univ., 1975, P. 137–146.
[42] Navrotsky A., Kleppa O.J. Thermodynamics of formation of simple spinels. *J. of Inorganic and Nuclear Chemistry*, 1968, **30** (2), P. 479–498.
[43] Lebedeva S.I. *Determination of Microhardness of Minerals*. Moscow: Publishing house of the USSR Academy of Sciences, 1963, 124 p.
[44] Khrushchev M.M. *Friction, Wear and Microhardness of Materials: Selected Works*. Moscow: KRASAND, 2012, 512 p.
[45] Anagha A., Joshua A., Chacko B., Babu T.A., Srigiri S., Madhuri W. Structural, optical and magnetic properties of $MgFe_2O_4$ and $Ni_{0.5}Zn_{0.5}Fe_2O_4$. *Materials Chemistry and Physics*, 2024, **313**, 128746.
[46] Sirimanne P.M., Sonoyama N., Sakata T. Semiconductor sensitization by microcrystals of $MgIn_2S_4$ on wide bandgap $MgIn_2O_4$. *Journal of Solid State Chemistry*, 2000, **154** (2), P. 476–482.
[47] Ueda N., Hosono H., Kawazoe H. Noble transparent semiconductor: $MgIn_2O_4$. *Solid State Phenomena*, 1996, **51–52**, P. 317–322.
[48] Pearton S.J., Yang J., Cary P.H., Ren F., Kim J., Tadjer M.J., Mastro M.A. A review of Ga_2O_3 materials, processing, and devices. *Applied Physics Review*, 2018, **5** (1), 011301.
[49] Geng H., Zhou Q., Zheng J., Gu H. Preparation of porous and hollow Fe_3O_4@C spheres as an efficient anode material for a high performance Li-ion battery. *RSC Advances*, 2014, **4** (13), P. 6430–6434.
[50] da Silva M.P., do Souza A.C.A., Ferreira Á.R.D., do Nascimento P.L.A., Fraga T.J.M., Cavalcanti J.V.F.L., Ghislandi M.G., da Motta Sobrinho M. A. Synthesis of superparamagnetic Fe_3O_4–graphene oxide-based material for the photodegradation of clonazepam, Scientific Reports, 2024, **14**, 18916.
[51] Naguib H.M., Kelly R. Criteria for bombardment-induced structural changes in non-metallic solids. *Radiation Effects*, 1975, **25** (1), P. 1–12.
[52] Batsanov S.S. The concept of electronegativity. Conclusions and prospects. *Russian Chemical Reviews*, 1968, **37** (5), P. 332–351.

Submitted 14 November 2025; revised 30 November 2025; accepted 2 December 2025

Information about the authors:

Olga N. Kondrat'eva – Kurnakov Institute of General and Inorganic Chemistry of the Russian Academy of Sciences, Leninskii prosp., 31, Moscow, 119991, Russia; ORCID 0000-0003-2508-9868; ol.kondratieva@gmail.com

Maria N. Smirnova – Kurnakov Institute of General and Inorganic Chemistry of the Russian Academy of Sciences, Leninskii prosp., 31, Moscow, 119991, Russia; ORCID 0000-0003-2707-7975; smirnovamn@igic.ras.ru

Galina E. Nikiforova – Kurnakov Institute of General and Inorganic Chemistry of the Russian Academy of Sciences, Leninskii prosp., 31, Moscow, 119991, Russia; ORCID 0000-0002-2892-6054; gen@igic.ras.ru

Alexey D. Yapryntsev – Kurnakov Institute of General and Inorganic Chemistry of the Russian Academy of Sciences, Leninskii prosp., 31, Moscow, 119991, Russia; ORCID 0000-0001-8166-2476; yaprynsev@yandex.ru

Maria S. Dranik – Frumkin Institute of Physical Chemistry and Electrochemistry of the Russian Academy of Sciences, Leninskii prosp., 31.4, Moscow, 119071, Russia; ORCID 0009-0006-1953-2359; m.dranik@yandex.ru

Valery A. Ketsko – Kurnakov Institute of General and Inorganic Chemistry of the Russian Academy of Sciences, Leninskii prosp., 31, Moscow, 119991, Russia; ORCID 0000-0002-2075-1755; ketsko@igic.ras.ru

Conflict of interest: the authors declare no conflict of interest.

NANOSYSTEMS:
PHYSICS, CHEMISTRY, MATHEMATICS

Original article

Iyakhmaeva A.A., et al. *Nanosystems: Phys. Chem. Math.*, 2025, **16** (6), 837–849.
http://nanojournal.ifmo.ru
DOI 10.17586/2220-8054-2025-16-6-837-849

Formation of 2:1 Li–Fe-phyllosilicate with montmorillonite-like structure in hydrothermal conditions

Asiyat A. Iyakhmaeva[1], Ekaterina K. Khrapova[1], Lev A. Lebedev[1], Nadezhda V. Glebova[1], Valentin G. Semenov[2], Andrey V. Kopylov[3], Andrei A. Krasilin[1]

[1]Ioffe Institute, St. Petersburg, Russia

[2]Institute of Chemistry, St. Petersburg State University, St. Petersburg, Russia

[3]RITVERC JSC, St. Petersburg, Russia

Corresponding author: Andrei A. Krasilin, ikrasilin@mail.ioffe.ru

PACS 81.20.-n, 82.80.Ej

ABSTRACT We report on hydrothermal synthesis and structural characterization of Li–Fe-montmorillonite (MMT). To date, this 2:1 type phyllosilicate attracts attention due to such properties as high ion mobility, hydrophilicity, electrical and thermal resistance. Due to that, various MMTs may serve as perspective components of Li-ion batteries (electrolyte and separator fillers, as well as protective buffer layer on top of Li metal anode). Scarce data on synthetic Li–Fe^{3+}-MMTs motivated us to investigate formation process and structure features of such phyllosilicate by X-ray diffraction, UV-visible and Mössbauer spectroscopy, and other methods. We established critical Fe^{3+} content and temperature range needed for almost single-phase MMTs formation. Around 20 % of total Fe may occupy tetrahedral site of MMT layer. Thermal behavior of Li–Fe-MMT strongly depends on hydrothermal synthesis conditions because of different Li^+ amount present in the interlayer space and in the layer vacancies.

KEYWORDS phyllosilicate, hydrothermal synthesis, isomorphism, X-ray diffraction, Mössbauer spectroscopy

ACKNOWLEDGEMENTS This work was supported by the St. Petersburg Science Foundation and the Russian Science Foundation [grant number 25-19-20096], https://rscf.ru/project/25-19-20096/.

FOR CITATION Iyakhmaeva A.A., Khrapova E.K., Lebedev L.A., Glebova N.V., Semenov V.G., Kopylov A.V., Krasilin A.A. Formation of 2:1 Li–Fe-phyllosilicate with montmorillonite-like structure in hydrothermal conditions. *Nanosystems: Phys. Chem. Math.*, 2025, **16** (6), 837–849.

1. Introduction

Among the wide variety of layered silicates, the so-called 1:1 and 2:1 phyllosilicates are distinguished. Some 1:1 phyllosilicates, due to their asymmetric layer structure, in which there is one tetrahedral sheet for every octahedral sheet, are capable of spontaneously scrolling into nanotubes and nanoscrolls [1–4]. As for the 2:1 phyllosilicates, this possibility is vanished by the conjunction of two tetrahedral sheets and one octahedral sheet between them [5–7]. Despite the disappearance of asymmetry, such phyllosilicates exhibit other remarkable properties, such as, for example, in the case of $(Ca,Na)_y(Mg,Fe)_2[(Al,Si)_4O_{10}](OH)_2$ layers with montmorillonite (MMT) structure – the possibility of intercalation of various cations into the interlayer space in order to compensate for the excess negative charge of the layer. This feature has led to the widespread use of natural and synthetic MMTs as ion-exchange adsorbents [8–11].

In addition to environmentally hazardous pollutants, the labile interlayer space of MMT is modified by functional substances of organic nature [12–14], as well as by catalytically active phases and their precursors [15–17].

Another noteworthy practical application of MMT is related to energy storage devices, including lithium-ion batteries [18, 19]. The combination of the dielectric nature of the MMT layer [20], high thermal stability [21], mechanical properties [22, 23], hydrophilicity due to OH groups and high cation mobility in the interlayer space makes these phyllosilicates promising components of separator membranes and semi-solid electrolytes. Thus, a functional coating of a polypropylene separator based on MMT and polyvinyl alcohol as a binder was proposed in [24]. Lithium ion transport was achieved more uniformly through the regularized interlayer space of MMT than through the separator's pore system. A more uniform ion flow led to a more uniform distribution of ions across the anode surface and to a minimization of dendrite formation processes. A similar ability to block the growth of dendrites and the associated longer operation of the battery model with a MMT-based membrane was also noted in [25, 26]. The effect of increasing the ionic conductivity and electrochemical stability of semi-solid electrolytes by introducing MMT phases was noted in [27–29].

Here, we investigate the formation processes of $Li_{2x}Fe_{2-2x}Mg_{2x}Si_4O_{10}(OH)_2$ phyllosilicate under hydrothermal conditions immediately after the precipitation in excess of LiOH. A number of studies have been devoted to the creation of Li-containing MMT via ion exchange in the mineral [30–32], while information on the synthesis of these compounds

by hydrothermal methods is less common. The use of Fe^{3+} cations instead of Al^{3+}, which are more traditional for MMT, opens up additional possibilities for changing the charge state ($Fe^{2+/3+}$), the appearance of a magnetic response, and monitoring the state of iron using Mössbauer spectroscopy [33]. A separate issue was the assessment of the maximum Fe^{3+} content in the phyllosilicate layer, as well as the possibility of substituting Si^{4+} in the tetrahedral position in analogy with Al^{3+}.

2. Materials and methods

2.1. Phyllosilicate synthesis

The synthesis of $Li_{2x}Fe_{2-2x}Mg_{2x}Si_4O_{10}(OH)_2$ (x = 0.5, 0.6, 0.7, 0.8, 0.9, 1) phyllosilicate consisted of two main stages: reverse coprecipitation and subsequent hydrothermal treatment of the resulting suspension. The following reagents were used during the synthesis: amorphous SiO_2 (Aerosil A-300), $LiOH{\times}H_2O$, $MgCl_2{\times}6H_2O$, $FeCl_3{\times}6H_2O$. All reagents were purchased from "Vekton", Russia. In the first stage, a sample of about 3 g SiO_2 was mixed with a 2.7 – 3.2 g (depending on x) $LiOH{\times}H_2O$ and 400 ml of distilled water for 30 minutes using magnetic stirrer. In a separate beaker filled with 200 ml of distilled water, iron and magnesium chlorides were dissolved, taken in the ratio required by the desired formula. Next, using a peristaltic pump, the chloride solution was added dropwise aerosil and alkali under intensive stirring. The feed rate was approximately 1 – 2 drops of solution per second.

The resulting suspensions were subjected to hydrothermal treatment for 7 days in autoclaves with 20 ml PTFE liners at temperatures of 200 °C and 240 °C. Additionally, a sample with x = 0.5 was treated at 350 °C for 9 hours in a 400 ml Ti-lined stainless steel autoclave. The resulting samples were washed twice with distilled water by centrifugation and air-dried at 80 °C. The dried phyllosilicates were ground with an agate mortar.

2.2. Powder X-ray diffraction

Powder X-ray diffraction (PXRD) analysis was performed using a DRON-8N powder X-ray diffractometer (Burevestnik, Russia) with a copper anode ($\lambda = 1.54186$ Å) and a Ni K_β filter. The diffractometer was equipped with a Mythen 2R 1D linear detector (DECTRIS Ltd, Switzerland). Measurements were carried out in the Bragg–Brentano geometry in the 2 – 80° 2θ range with a step of 0.01° and an exposure time of 10 s. The sample rotation during the exposure was 0.5 rps. Phase identification was carried out using the open COD database [34] and the PDF-2 database in case of insufficient information from an open source.

The unit cell parameters were calculated using the Rigaku SmartLab Studio II software package using a full-profile method similar to Le Bail (without refinement of atomic coordinates). The phyllosilicate layers were assumed to be predominantly oriented along [001] direction. Crystallite sizes, ignoring possible microstresses, were determined using the Scherrer formula for the [001] direction in order estimate average thickness of phyllosilicate particles. Furthermore, the full-profile analysis was performed using the anisotropic crystallite approximation, that yielded crystallite size averaged over all directions.

2.3. N_2 adsorption and thermal analysis

Low-temperature nitrogen adsorption was carried out using an ASAP 2020 analyzer (Micromeritics, USA). The samples were preliminarily degassed at a temperature of 110 °C to remove adsorbed water until there was no mass change observed. The analysis was carried out in the 10^{-5} – 0.995 relative pressure (P/P_0) range. To calculate the specific surface area, the Brunauer–Emmett–Teller (BET) model [35] was used in the 0.05 – 0.16 P/P_0 range. The total pore volume was calculated at the maximum relative pressure $P/P_0 = 0.995$. For a more accurate analysis of the pore size distribution, the density functional theory (DFT) calculation method was used according to the N_2 on Carbon at 77 K model [36] with slit pores.

Thermal analysis was carried on a Mettler–Toledo TGA/DSC 1 derivatograph with STARe System software (Switzerland) using air blown through the derivatograph chamber at a flow rate of 30 cm^3/min in a uniform temperature increase mode at a rate of 10 °C/min in the temperature range of 35 – 1000 °C. During the heating process, mass (thermogravimetric, TG) and thermal (differential thermal, DTG) curves were recorded.

2.4. Spectroscopic methods

Diffuse reflectance spectra were recorded using an AvaSpec-ULS4096CL-EVO high-resolution spectrometer (Avantes, Netherlands), an AvaSphere-30 integrating sphere, and an AvaLight-XE pulsed xenon source. The resulting diffuse reflectance spectra (R) were processed using the Kubelka–Munk function (1):

$$F(R) = \frac{(1-R)^2}{2R}. \quad (1)$$

The band gap was estimated using the Tauc plot method [37] for both direct and indirect transitions.

Mössbauer spectroscopy was used to obtain information on the qualitative and quantitative distribution of iron ions across various phases and crystallographic sites. Mössbauer spectra of ^{57}Fe were obtained using a Wissel Mössbauer spectrometer (Germany) in constant acceleration mode at room temperature. $6{\times}10^8$ Bq ^{57}Co in a rhodium matrix (Ritverc

GmbH, St. Petersburg, Russia) was used as a gamma source. Velocity scale calibration and isomer shift were determined relative to α-Fe. Spectra processing was performed using MossFit Ver. 3.7 software.

The elemental composition of the samples was determined using a FEI Quanta 200 (USA) scanning electron microscope (SEM), equipped with an EDAX energy-dispersive spectrometer.

3. Results and discussion

3.1. Iron content impact on lattice volume, crystallite size, and textural properties

As a result of hydrothermal treatment at 200 °C, according to PXRD data (Fig. 1a), mainly single-phase samples were obtained. The position of the X-ray diffraction maxima, as well as the ratio of their intensities, indicated the formation of phyllosilicate with a montmorillonite structure with a monoclinic $C2/m$ (12) space group (comparison was made with the Li-containing analogue COD ID 9010956 [38]). Increasing the processing temperature to 240 °C resulted in the observation of significant diffraction maxima belonging to Fe_3O_4 or a solid solution based on it of the type $Mg_yFe_{2-y}O_4$ (COD ID 9003582 [39]) in the case of $x \leq 0.6$. A further increase in the processing temperature led to a more complex phase composition of the sample with $x = 0.5$ due to the formation of α-Fe_2O_3 (COD ID 2101167 [40]) or, similarly, a solid solution based on it. It should be noted that the formation of iron oxides as impurity phases was also observed in the synthesis of 1:1 phyllosilicates with a related crystal structure [41–43]. The difficulties in replacing Mg^{2+} and Si^{4+} with Fe^{3+} lie in the difference in the formal charges of the cations, which complicated the available isomorphism schemes (from the point of view of the need for charge compensation), and in the strong difference in the effective ionic radii [44], especially between Fe^{3+} and Si^{4+}.

The introduction of iron ions into the crystal structure led to an increase in virtually all unit cell parameters (Fig. 1b-e), although these trends were barely visible due to comparatively low crystallinity of the samples and the associated variability of the full-profile analysis procedure. Individual sharp changes in the parameters a, b, and β at low x were most likely caused by a violation of the single-phase nature of the system. The observed spread in the parameter c could have been further enhanced, firstly, by the different filling of the interlayer space and, secondly, by the dependence of the interlayer distance on the number of layers, which is common to various compounds with a layered structure. The increase in the unit cell volume with increasing iron content (with decreasing x) repeated the trends observed for individual parameters (Fig. 1f).

It is interesting to look at the process of changing the unit cell volume from the point of view of the effective ionic radii of Mg^{2+} (72 pm), Fe^{3+} (63 pm in the octahedral and 49 pm in tetrahedral position) and Si^{4+} (26 pm) [44]. The observed increase in the unit cell volume due to substitution only in the octahedral sublayer looks counterintuitive, if we do not take into account the increased size of the cavity, compared to the coordination octahedron, which inevitably arises during the transition from the trioctahedral silicate to the dioctahedral one. Substitution with the removal of part of the Li^+ from the interlayer space was also possible, as was assumed in the original chemical formula. This version of substitution, based on the values of the ionic radii, should lead to at least an increase in a and b, while the impact caused to parameter c is less obvious: on the one hand, Li^+ maintains an increased interlayer distance due to its size, while on the other hand, it is present due to the need for charge compensation. Accordingly, the removal of Li^+ could lead either to a decrease in the interlayer distance for steric reasons or to an increase due to electrostatic repulsion forces between adjacent layers. Substitution with Si^{4+} should lead to an increase in cell volume, although the nearly twofold difference in ionic radii limited mixability. Thus, the increase in unit cell volume with increasing Fe^{3+} content seemed justified in terms of the ionic radii of the cations involved in the substitution processes and could indirectly indicate the presence of a more complex Fe^{3+} distribution among crystallographic positions than had been initially assumed in the stoichiometric calculation.

Figure 1(g) shows the results of determining the crystallite sizes separately for the 001 reflection, as well as the values averaged over all directions, obtained as a result of a full-profile analysis in the approximation of anisotropic crystallite shape. The introduction of Fe^{3+} into the system generally contributed to a decrease in the crystallite size of phases with the montmorillonite structure. The change in this trend for the case of hydrothermal treatment at 240 °C and $x < 0.7$ was associated with the release of some of the iron ions into the oxide phase. Compared to the average values, the crystallite sizes along the 001 direction were virtually independent of temperature. An increase in the discrepancy between these two dependences suggests that MMT particles became more anisotropic with increasing treatment temperature and most likely grew in directions perpendicular to 001.

Figure 2 shows nitrogen adsorption/desorption isotherms and pore size distributions obtained from the adsorption branch of the curve. All isotherms can be classified as type IV, with a developed mesoporous structure. A sharp rise at the initial stage indicated the presence of micropores in the samples. Hysteresis loops were of the mixed H2-H3 type, which could be associated with a complex, irregular porous structure. The most likely pore shapes for this type of hysteresis loop were bottle-shaped and slit-shaped. Apparently, slit-shaped pores could be located both in the interlayer space of phyllosilicates and in the interparticle space. The non-uniform pore shape, which led to blockage in narrower areas, could be associated with the non-uniform shape of the particles and their broad size distribution. As expected, the specific surface area and pore volume decreased with increasing hydrothermal treatment temperature, which correlated with the

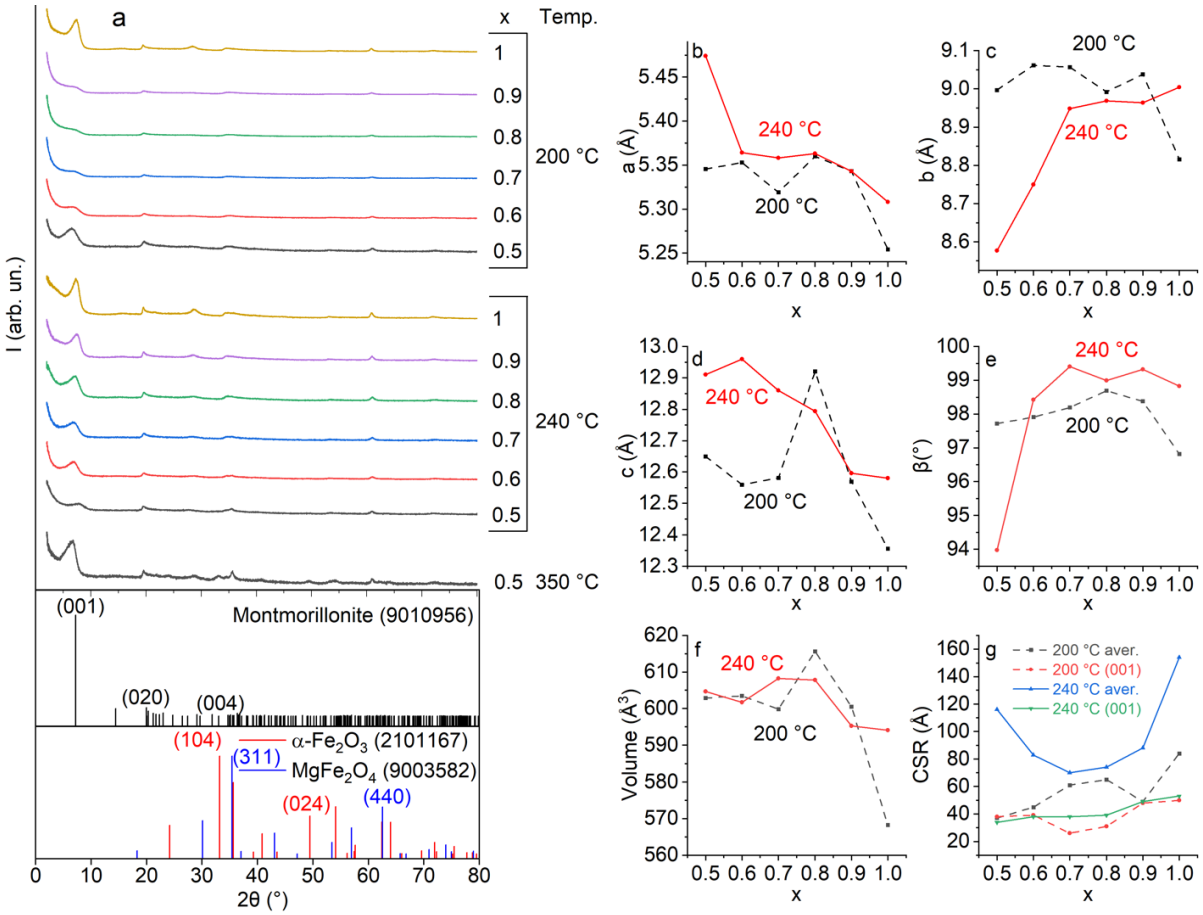

FIG. 1. Results of powder X-ray diffraction analysis. a) PXRD patterns of hydrothermal treatment products together with phase analysis involving COD database. b–f) Calculated unit cell parameters and unit cell volume of MMT phase. g) Crystallite sizes (coherent scattering regions, CSR) of MMT phase

increase in crystallite size as measured by X-ray diffraction (Fig. 1g). The dependence of specific surface area and pore volume on iron content was extreme.

In all cases, the pore size distribution (Fig. 2d–f) showed a maximum in the 1 – 2 nm region, which we believe was due to nitrogen adsorption in the interlayer space of phyllosilicates with a montmorillonite structure. Unfortunately, it was not possible to establish an unambiguous correlation with the interlayer space size according to X-ray diffraction data, which was approximately 50 % of the c parameter, i.e., 0.6 nm (Fig. 1d). The discrepancy between the observed values may be due to both the specific features of the model approximation chosen to describe the adsorption isotherms and the sensitivity of the interlayer distance to the conditions of the adsorption experiment itself (preliminar vacuum and thermal training) [45]. Despite this, the position of the maximum, depending on the hydrothermal treatment temperature, behaved in a manner consistent with the increase in crystallinity, shifting toward smaller sizes due to the compaction of the layer packing (Fig. 2d–f). The distribution in the mesopore region behaved in the opposite direction: with increasing temperature, the center of gravity of the broad maximum shifted from a few to tens of nanometers. This region is formed primarily by interparticle pores, and an increase in particle size typically leads to an increase in the size of the voids between them.

3.2. Element content and iron distribution over phyllosilicate and oxide phases

Table 1 presents the results of EDS analysis of 200 and 240 °C hydrothermal treatment products. In all cases, a deficiency of silicon relative to magnesium and iron cations was observed, which could be caused by both the error of the method itself and the features of the synthesis process. Previously, we noted a systematic deviation of the *Me*:Si ratio from the specified one towards a deficiency of silicon in the case of the formation of impurity oxide phases [46]. A similar situation was observed for the data at high iron contents ($x < 0.7$), especially during hydrothermal treatment at 240 °C. Unfortunately, the lithium content was not available for determination by this method; however, given the observed deficiency of silicon, its underestimated content can also be assumed compared to the calculated chemical formula $Li_{2x}Fe_{2-2x}Mg_{2x}Si_4O_{10}(OH)_2$. The verification experiments that we were able to carry out for x = 0.5 using

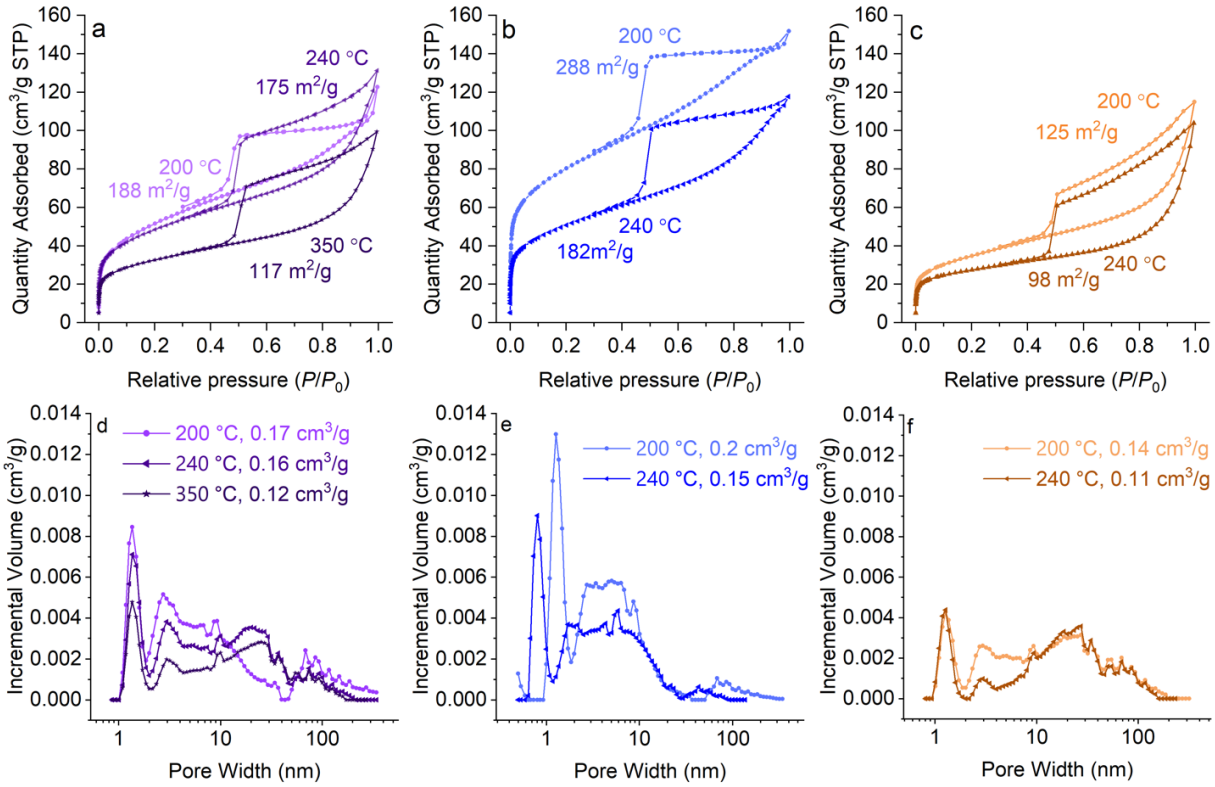

FIG. 2. Results of low-temperature nitrogen adsorption. N_2 adsorbtion/desorbtion isotherms for $x =$ a) 0.5, b) 0.7, and c) 1 together with BET surface area values. Pore size distribution and total pore volume for $x =$ d) 0.5, e) 0.7, and f) 1

atomic emission spectroscopy showed a ratio of Li:Mg = 1:3 – 1:2, which was expectedly underestimated due to the excess of positive charge of the phyllosilicate layer.

It should be noted that the Si/(Mg+Fe) ratio was closer to that of phyllosilicates with sepiolite and talc structures. However, based on the peak positions and intensity ratios, all PXRD patterns (Fig. 1a) corresponded precisely to phases with montmorillonite/saponite structures (including $x = 1$). This circumstance suggests that, to compensate for the lack of silicon, some of the Fe^{3+} cations may be incorporated into the tetrahedral position. According to Mössbauer spectroscopy data (Fig. 3a,b), two main (# 2 and # 3 in Fig. 3b) and one additional "doublet" (# 1) were detected for the products of hydrothermal treatment at 200 °C. Based on the combination of the isomer shift (IS) and quadrupole splitting (QS) values (Table A1), "doublet" # 1 was actually a part of sextet belonging to iron oxides. Based on the share of these minima in the total transmittance, it can be concluded that the content of oxide phase impurity remained negligibly small at $x > 0.6$, and a further abrupt increase in its content was associated with reaching the concentration limit of Fe^{3+} content in the phyllosilicate structure. In the products of phyllosilicate treatment at 200 °C, the presence of oxide was not detected at any x (Fig. 1a), probably due to the lower sensitivity of the method, as well as the X-ray wavelength and Fe absorption effect. The ratio of the two main doublets was on average 80:20 (Fig. 3b), regardless of the iron content. Similar distribution of Fe^{3+} between the octahedral and tetrahedral sites in layered silicates related in structure was noted in [47]. At the same time, the IS and QS values for the smaller doublet in our case were not entirely typical for iron cations in the tetra-position ($^{IV}Fe^{3+}$). If this doublet was erroneously attributed to $^{IV}Fe^{3+}$ instead of, for example, a variation in the octa-position ($^{VI}Fe^{3+}$) due to a change in the type of nearest neighbors, then a correlation between the doublet ratio and the iron content in the system would be expected, which, apparently, was not observed. The larger IS value compared to the data in [47] could be due to the increased unit cell parameters and the ^{IV}Me–O distance [48] in the hydrothermal treatment products compared to natural minerals. In addition, the presence of Li^+ instead of more widespread cations (Na^+, Ca^{2+}, and others) could make a significant contribution to the variation in both IS and QS values [49].

The effect of hydrothermal treatment temperature was considered for the case of the maximum iron content $x = 0.5$ (Fig. 3c). Increasing the treatment temperature to 240 °C resulted in the appearance of sextets in the Mössbauer spectra with parameters (Table A2) typical for spinel of variable composition $Mg_yFe_{2-y}O_4$, as well as α-Fe_2O_3. A further increase in the treatment temperature resulted in a quantitative, rather than qualitative, change in the nature of the iron distribution between the silicate and oxide phases. It is also worth noting the decrease in the line widths of the sextets with increasing hydrothermal treatment temperature, caused by an increase in the crystallinity of the phases.

TABLE 1. Element ratios estimated by the EDS method

Element	x in $Li_{2x}Fe_{2-2x}Mg_{2x}Si_4O_{10}(OH)_2$					
	0.5	0.6	0.7	0.8	0.9	1
calculated						
Fe	1	0.8	0.6	0.4	0.2	0
Mg	1	1.2	1.4	1.6	1.8	2
Si	4	4	4	4	4	4
200 °C hydrothermal treatment						
Fe	1.3	0.8	0.5	0.6	0.3	0.0
Mg	1.3	1.8	1.9	2.0	2.0	2.4
Si	4.0	4.0	4.0	4.0	4.0	4.0
Si/(Fe+Mg)	1.6	1.5	1.6	1.5	1.7	1.6
(Si+0.2Fe)/(0.8Fe+Mg)	1.9	1.7	1.8	1.6	1.8	1.6
240 °C hydrothermal treatment						
Fe	1.4	1.0	0.8	0.5	0.3	0.0
Mg	1.6	1.6	1.9	2.1	2.1	2.5
Si	4.0	4.0	4.0	4.0	4.0	4.0
Si/(Fe+Mg)	1.3	1.6	1.5	1.6	1.7	1.6
(Si+0.2Fe)/(0.8Fe+Mg)	1.6	1.8	1.7	1.7	1.7	1.6

If we take the average ratio of 80:20 for the distribution between $^{VI}Fe^{3+}$ and $^{IV}Fe^{3+}$ and introduce the appropriate correction for the EDS results (Table 1), the resulting ratio will approach that characteristic of phyllosilicates with MMT structure. The possibility of replacing a significant amount of Si^{4+} with Fe^{3+}, despite the large difference in effective ionic radii, was due to the layered crystal structure, which expands the limits of miscibility [50, 51]. In addition, the results of DFT calculations carried out earlier for the case of substitution of Mg^{2+} and Si^{4+} for 1:1 type chrysotile structure [52] revealed close energy equivalence of the substitution schemes exclusively in the octahedral sheet with formation of vacancy ($3Mg^{2+} = 2\,^{VI}Fe^{3+}$ + v) and simultaneous substitution in two sheets ($Mg^{2+} + Si^{4+} = {}^{VI}Fe^{3+} + {}^{IV}Fe^{3+}$).

Additional attempts to investigate the nature of iron distribution in the hydrothermal treatment products were made using diffuse reflectance spectroscopy. Fig. 4 shows recalculated absorption spectra of two spectral ranges obtained using the Kubelka–Munk function. For 200 °C hydrothermal treatment products, two broad absorption maxima appeared in the range of 300 – 400 nm at $x \leq 0.6$, corresponding to the formation of Fe-containing oxide nanoparticles [53]. In the range of 400 – 700 nm, changes in the absorption spectrum also occurred in the form of the appearance of two maxima in the region of 500 – 600 nm, characteristic for iron oxides [54, 55]. The changes in the optical spectra correlated with the results of Mössbauer spectra deconvolution, particularly with the increase in the content of #1 "doublet" (Fig. 3b). Based on the shape of the spectra, it can be concluded that with an increase in the hydrothermal treatment temperature to 240 °C, the formation of impurity phases began even at the minimum iron content in the system ($x = 0.9$). Thus, the synthesized Li–Fe-containing phyllosilicates with a montmorillonite structure exhibited a series of absorption peaks with maxima at 330, 510, and 630 nm.

An assessment of the band gap of the samples using optical spectroscopy showed that, regardless of the hydrothermal treatment temperature, the E_g value decreased almost linearly from 3.7 eV (at $x = 0.8$) to 3.1 eV (at $x = 0.5$). Given the obtained information on the phase composition, the observed value cannot be fully attributed to any one of the phases. At high iron content, E_g tended to the range of values characteristic of Fe_3O_4 [56], while from above it was limited by the capabilities of the spectrometer.

3.3. Temperature shift of silicate crystallization effect

Figure 5(a) shows the TG and DTG curves of 200 °C hydrothermal treatment products with different iron content. At the initial stage of heating, all samples exhibited significant mass loss due to the removal of adsorbed water. The magnitude of the loss correlated with the previously observed extreme dependence of the specific surface area on the

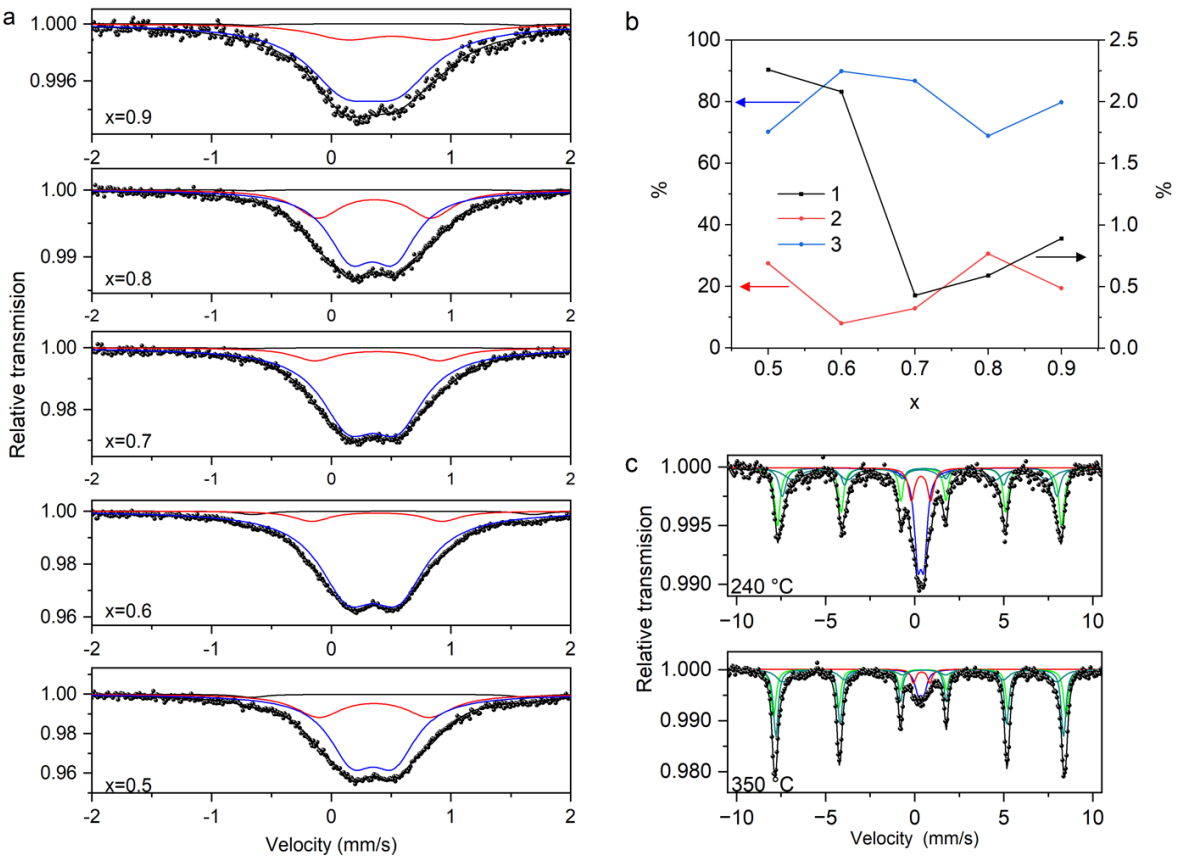

FIG. 3. Results of Mössbauer spectroscopy. a) Mössbauer spectra of 200 °C hydrothermal treatment products. b) Dependence of relative area of three doublets upon iron content. c) Mössbauer spectra of 240 and 350 °C hydrothermal treatment products with $x = 0.5$. Doublets and sextet parameters are shown in Tables A1, A2

iron content (Fig. 2): it was minimal at the edges of the studied x range and maximal at intermediate points. With further heating, the samples lost mass at virtually the same rate up to 450 °C, at which point a low-intensity loss peak was observed in the DTG curves of the samples with $x < 0.9$ (Fig. 5a). As a rule, the temperature range of 450 – 600 °C is characterized by mass losses caused by bulk dehydroxylation of phyllosilicates [57–59]. Compared to 1:1 type layered silicates, the studied 2:1 type silicate has two times less OH groups per formula unit, and therefore the effect was much weaker. Further, for most samples, a sharp peak in mass losses was observed with an intensity proportional to the magnesium content and probably caused by crystallization of (Mg,Fe)SiO_3 pyroxene and SiO_2 cristobalite (Fig. 6).

An interesting feature of the studied samples was the temperature dependence of the last mass loss peak (Fig. 5d,f). Thus, for the case of $x = 0.5$, the shift was about 75 °C with an increase in the hydrothermal treatment temperature from 200 to 240 °C (Fig. 5d). The phase composition of the samples after thermal analysis also varied (Fig. 6): for the sample obtained at 200 °C, the main part consisted of the phases (Mg,Fe)SiO_3, SiO_2, and traces of $Li_2Si_2O_5$, while for the products of hydrothermal treatment at higher temperatures, the main phase was $LiFeSi_2O_6$ with traces of (Mg,Fe)SiO_3 and SiO_2. Except for lithium silicate, all components are products of the decomposition reaction (for $x = 0.5$):

$$LiFeMgSi_4O_{10}(OH)_2 \rightarrow LiFeSi_2O_6 + MgSiO_3 + SiO_2 + H_2O \uparrow .$$

A probable reason for the differences in the observed phase composition after thermal analysis could be the difference in the content of the most mobile component – lithium. Under the conditions of low-temperature hydrothermal treatment (200 °C) and, as a result, small crystallite size (Fig. 1g), Li^+ could be easily washed out of the interlayer space during the process of purification from the solution that served as the hydrothermal environment. An increase in the treatment temperature led to a several-fold increase in the crystallite sizes, and consequently, the linear dimensions of the layers, which complicated the removal of lithium cations. In addition, an increase in temperature contributed to an increase in the entropy factor for the process of Li^+ incorporation directly into the phyllosilicate layer [32, 60].

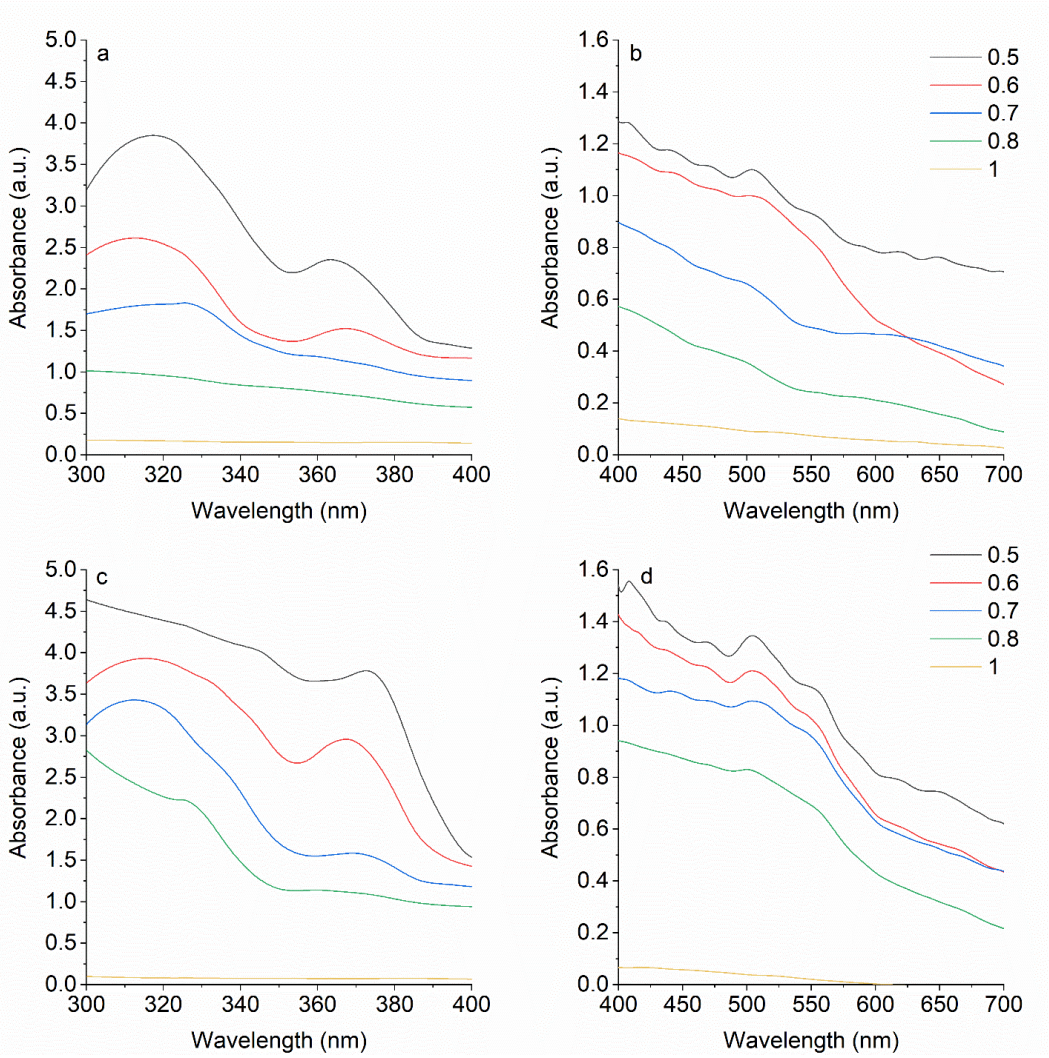

FIG. 4. UV-visible spectra recalculated from diffuse reflectance data for hydrothermal treatment products with $x = 0.5,\ 0.6,\ 0.7,\ 0.8$, and 1 obtained at a,b) 200 °C and c,d) 240 °C

4. Conclusion

The study demonstrated the feasibility of hydrothermal synthesis of Li–Fe phyllosilicates with a montmorillonite-like structure and a minimal amount of impurity phases in the form of Fe_3O_4 and Fe_2O_3-based solid solutions. Using a combination of diffraction and spectroscopic methods, the temperature and concentration thresholds for the formation of oxide phases were established. Thus, the formation of virtually single-phase products should be expected in the temperature range of 200 – 240 °C for x in the calculated chemical formula $Li_{2x}Fe_{2-2x}Mg_{2x}Si_4O_{10}(OH)_2$ being in the range of 0.8 – 1. The specific surface area was shown to depend on the iron content and reach a maximum in the range of $x = 0.7 - 0.8$. It was found that, due to the broader charge compensation capabilities of a multicomponent system, various deviations from the specified stoichiometry are possible within the layer, due to both the substitution of silicon cations by iron cations in the tetrahedral position (approximately 20 % of the total iron content) and the removal of some lithium cations from the interlayer space. Thermal analysis and X-ray diffraction revealed the role of MMT particle size factor and hydrothermal treatment temperature in the retention of lithium cations.

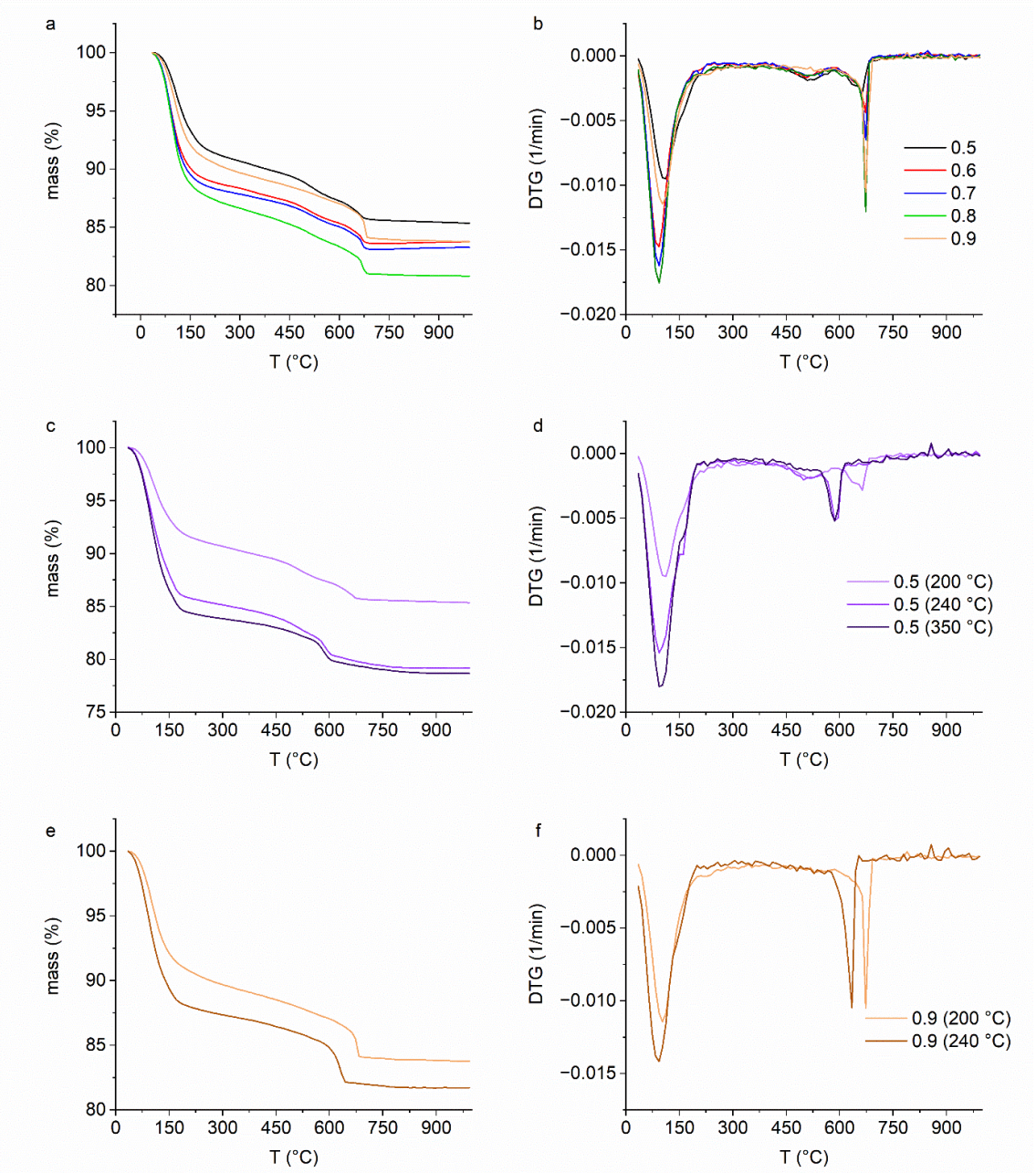

FIG. 5. TG and DTG curves of: a,b) 200 °C hydrothermal treatment products with different x; samples with $x =$ c,d) 0.5 and e,f) 0.9, obtained at various temperatures

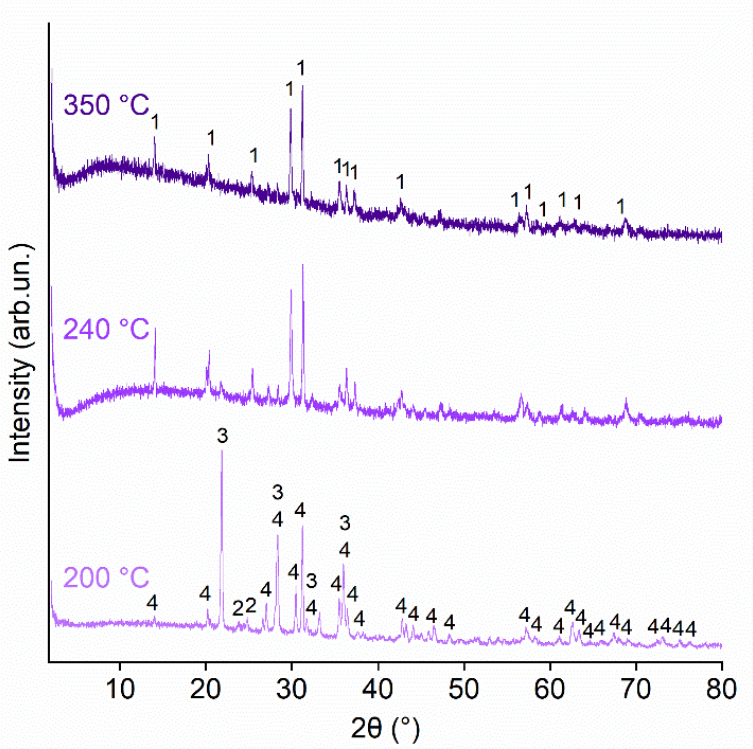

FIG. 6. Post-thermal analysis PXRD patterns of samples with $x = 0.5$ obtained at various hydrothermal treatment temperatures. Phase analysis was carried out using PDF-2 database: "1" – $LiFeSi_2O_6$ (89-225), "2" – $Li_2Si_2O_5$ (40-376), "3" – SiO_2 (75-923), "4" – $MgSiO_3$ (71-786)

Appendix

TABLE A1. Parameters of doublets observed by Mössbauer spectroscopy for 200 °C hydrothermal treatment products

x	Peak #	Width (mm/s)	IS (mm/s)	QS (mm/s)	%
0.5	1	0.278	0.48	2.32	2.2
	2	0.479	0.36	0.92	27.5
	3	0.466	0.35	−0.35	70.3
0.6	1	0.278	0.52	2.35	2.1
	2	0.366	0.38	1.09	8.0
	3	0.575	0.35	−0.43	89.9
0.7	1	0.278	0.48	2.30	0.4
	2	0.441	0.38	1.04	12.8
	3	0.561	0.35	−0.41	86.8
0.8	1	0.278	0.48	2.31	0.6
	2	0.448	0.36	0.94	30.6
	3	0.466	0.34	−0.37	68.8
0.9	1	0.278	0.48	2.30	0.9
	2	0.691	0.51	0.76	19.4
	3	0.736	0.33	−0.45	79.8

TABLE A2. Peak parameters observed by Mössbauer spectroscopy for 240 and 350 °C hydrothermal treatment products with $x = 0.5$

T (°C)	Peak #	Width (mm/s)	IS (mm/s)	QS (mm/s)	Heff (mm/s)	%
240	Doublets					
	2	0.420	0.36	1.08	–	8.8
	3	0.440	0.34	0.34	–	23.7
	Sextets					
	Fe_2O_3	0.363	0.38	0.22	49.5	30.9
		0.340				
		0.315				
	Fe_3O_4 (A)	0.464	0.40	0.25	47.9	16.8
		0.444				
		0.423				
	Fe_3O_4 (B)	1.128	0.33	0.10	44.5	19.8
		0.932				
		0.757				
350	Doublets					
	2	0.308	0.39	0.92	–	3.6
	3	0.443	0.35	0.32	–	7.8
	Sextets					
	Fe_2O_3	0.316	0.38	0.19	51.0	28.6
		0.293				
		0.284				
	Fe_3O_4 (A)	0.314	0.38	0.21	50.1	40.7
		0.298				
		0.282				
	Fe_3O_4 (B)	0.875	0.41	0.23	47.8	19.3
		0.759				
		0.671				

References

[1] Perim E., Machado L.D., Galvao D.S. A brief review on syntheses, structures, and applications of nanoscrolls. *Front. Mater.*, 2014, **1** (2003), P. 1–17.

[2] Krasilin A.A., Khrapova E.K., Maslennikova T.P. Cation Doping Approach for Nanotubular Hydrosilicates Curvature Control and Related Applications. *Crystals*, 2020, **10** (8), 654.

[3] Gatina E.N., Maslennikova T.P. Formation of chrysotile nanotubes with titania in the internal channel. *Nanosystems: Physics, Chemistry, Mathematics*, 2024, **15** (3), P. 380–387.

[4] Kurguzkina M.E., Maslennikova T.P., Gusarov V.V. Formation, Morphology, and Size Parameters of Nanopowders Based on $Mg_3Si_2O_5(OH)_4$–$Ni_3Si_2O_5(OH)_4$ Nanoscrolls. *Inorganic Materials*, 2023, **59** (10), P. 1075–1084.

[5] Drits V.A., Besson G., Muller F. An Improved Model for Structural Transformations of Heat-Treated Aluminous Dioctahedral 2:1 Layer Silicates. *Clays Clay Miner.*, 1995, **43** (6), P. 718–731.

[6] Emmerich K., et al. Clay profiling: The classification of montmorillonites. *Clays Clay Miner.*, 2009, **57** (1), P. 104–114.

[7] García-Romero E., et al. On the structural formula of smectites: a review and new data on the influence of exchangeable cations. *J. Appl. Crystallogr.*, 2021, **54** (1), P. 251–262.

[8] Zango Z.U., et al. Montmorillonite for Adsorption and Catalytic Elimination of Pollutants from Wastewater: A State-of-the-Arts Review. *Sustainability*, 2022, **14** (24), 16441.

[9] França D.B., et al. The versatility of montmorillonite in water remediation using adsorption: Current studies and challenges in drug removal. *J. Environ. Chem. Eng.*, 2022, **10** (2), 107341.

[10] Kryuchkova M., et al. Pharmaceuticals Removal by Adsorption with Montmorillonite Nanoclay. *Int. J. Mol. Sci.*, 2021, **22** (18), 9670.

[11] Golubeva O.Yu., et al. Increased Adsorption of Ciprofloxacin by Systematic Variation of the Composition of Synthetic Montmorilloinites. *ACS Appl. Nano Mater.*, 2025, **8** (16), P. 8489–8498.

[12] Polotskaya G.A., et al. Structure and Transport Properties of Cellulose Acetate/Montmorillonite Composites. *Membranes and Membrane Technologies*, 2022, **4** (6), P. 367–376.

[13] Dumitru M.V., et al. Organically modified montmorillonite as pH versatile carriers for delivery of 5-aminosalicylic acid. *Appl. Clay Sci.*, 2022, **218**, 106415.

[14] Nuruzzaman M., et al. Capability of Organically Modified Montmorillonite Nanoclay as a Carrier for Imidacloprid Delivery. *ACS Agricultural Science & Technology*, 2022, **2** (1), P. 57–68.

[15] Ovchinnikov N.L., et al. The Preparation of Self-Cleaning Wool-Fiber–TiO_2-Pillared Montmorillonite Composites with UV-Protection Properties. *Protection of Metals and Physical Chemistry of Surfaces*, 2023, **59** (3), P. 377–383.

[16] Karthikeyan K., Thirumoorthi A. $BiFeO_3$-Montmorillonite intercalated nano composites – synthesis and its characterization. *Nanosystems: Physics, Chemistry, Mathematics*, 2018, P. 631–640.

[17] Huang W.J., et al. Recent advances in engineering montmorillonite into catalysts and related catalysis. *Catal. Rev. Sci. Eng.*, 2023, **65** (3), P. 929–985.

[18] Wu L., et al. Montmorillonite-based materials for electrochemical energy storage. *Green Chemistry*, 2024, **26** (2), P. 678–704.

[19] Chen C., Ma Y., Wang C. Investigation of electrochemical performance of montmorillonite clay as Li-ion battery electrode. *Sustainable Materials and Technologies*, 2019, **19**, e00086.

[20] Hao L., et al. Interlayer cation effects on optical and dielectric properties of montmorillonite in terahertz frequency band. *Appl. Clay Sci.*, 2025, **274**, 107857.

[21] Qin Y., et al. Effect of Montmorillonite Layer Charge on the Thermal Stability of Bentonite. *Clays Clay Miner.*, 2021, **69** (3), P. 328–338.

[22] Berdinazarov Q., Khakberdiev E., Ashurov N. The effect of layered silicates on the morphological, rheological and mechanical properties of PA and PP blends. *Nanosystems: Physics, Chemistry, Mathematics*, 2024, **15** (3), P. 410–417.

[23] Makarov V.N., Kanygina O.N. Model of destruction of montmorillonite crystal structure in a microwave field. *Nanosystems: Physics, Chemistry, Mathematics*, 2020, **11** (2), P. 153–160.

[24] Zhang Y., et al. Separators Modified with Ultrathin Montmorillonite/Polymer Nanocoatings Achieve Dendrite-Free Lithium Deposition at High Current Densities. *Nano Lett.*, 2024, **24** (29), P. 8834–8842.

[25] Gorospe A.E.G., et al. Ultralong cycle lifespan in lithium metal batteries Unlocked by a lithiophilic montmorillonite separator. *Mater. Lett.*, 2025, **401**, 139240.

[26] Para M.L., et al. Synthesis and characterization of montmorillonite/polyaniline composites and its usage to modify a commercial separator. *Journal of Electroanalytical Chemistry*, 2021, **880**, 114876.

[27] Wang W., Yang Y., Zhang J. Boosting Li^+ Conductivity and Oxidation Stability of Solid Polymer Electrolytes Using a Sustainable Montmorillonite-Based Ion Conductor. *Nano Lett.*, 2025, **25** (10), P. 3867–3874.

[28] Zhou S., et al. Low-cost and high-safety montmorillonite-based solid electrolyte for lithium metal batteries. *Appl. Clay Sci.*, 2024, **251**, 107329.

[29] Wang L., et al. Bifunctional lithium-montmorillonite enabling solid electrolyte with superhigh ionic conductivity for high-performanced lithium metal batteries. *Energy Storage Mater.*, 2023, **63**, 102961.

[30] Yan H., Zhang Z. Effect and mechanism of cation species on the gel properties of montmorillonite. *Colloids and Surfaces A: Physicochemical and Engineering Aspects*, 2021, **611**, 125824.

[31] Wu Z., et al. Thermal Migration Behavior of Na^+, Cu^{2+} and Li^+ in Montmorillonite. *Minerals*, 2022, **12** (4), 477.

[32] Wu Z., et al. The migration and occupation of Li^+ and Na^+ in illite and montmorillonite during the heating process. *Mineral Mag.*, 2024, **88** (5), P. 536–545.

[33] Semenov V.G., Moskvin L.N., Efimov A.A. Analytical potential of Mössbauer spectroscopy. *Russian Chemical Reviews*, 2006, **75** (4), P. 317–327.

[34] Grażulis S., et al. Crystallography Open Database (COD): an open-access collection of crystal structures and platform for world-wide collaboration. *Nucleic Acids Res.*, 2012, **40** (D1), P. D420–D427.

[35] Brunauer S., Emmett P.H., Teller E. Adsorption of Gases in Multimolecular Layers. *JACS*, 1938, **60** (2), P. 309–319.

[36] Sing K.S.W. Reporting physisorption data for gas/solid systems with special reference to the determination of surface area and porosity (Recommendations 1984). *Pure and Applied Chemistry*, 1985, **57** (4), P. 603–619.

[37] Klein J., et al. Limitations of the Tauc Plot Method. *Adv. Funct. Mater.*, 2023, **33** (47).

[38] Gournis D., et al. A neutron diffraction study of alkali cation migration in montmorillonites. *Phys Chem Miner.*, 2008, **35** (1), P. 49–58.

[39] Antao S.M., Hassan I., Parise J.B. Cation ordering in magnesioferrite, $MgFe_2O_4$, to 982 °C using in situ synchrotron X-ray powder diffraction. *American Mineralogist*, 2005, **90** (1), P. 219–228.

[40] Maslen E.N., et al. Synchrotron X-ray study of the electron density in α-Fe_2O_3. *Acta Crystallogr. B*, 1994, **50** (4), P. 435–441.

[41] Korytkova E.N., et al. Hydrothermal synthesis of nanotubular Mg-Fe hydrosilicate. *Russian J. of Inorganic Chemistry*, 2007, **52** (3), P. 338–344.
[42] Krasilin A.A., et al. Formation of variable-composition iron(III) hydrosilicates with the çhrysotile structure. *Russ. J. Gen. Chem.*, 2016, **86** (12), P. 2581–2588.
[43] Bloise A., et al. Synthesis of Fe-doped chrysotile and characterization of the resulting chrysotile fibers. *Crystal Research and Technology*, 2009, **44** (6), P. 590–596.
[44] Shannon R.D., Prewitt C.T. Effective ionic radii in oxides and fluorides. *Acta Crystallogr B.*, 1969, **25** (5), P. 925–946.
[45] Khramchenkov M.G., et al. Microstructural transformations of swelling clay minerals. *Georesursy*, 2023, **25** (1), P. 108–118.
[46] Khrapova E.K., Kozlov D.A., Krasilin A.A. Hydrothermal Synthesis of Hydrosilicate Nanoscrolls $(Mg_{1-x}Co_x)_3Si_2O_5(OH)_4$ in a Na_2SO_3 Solution. *Russian J. of Inorganic Chemistry*, 2022, **67** (6), P. 839–849.
[47] Cuadros J., et al. Controls on tetrahedral Fe(III) abundance in 2:1 phyllosilicates. *American Mineralogist*, 2019, **104** (11), P. 1608–1619.
[48] Annersten H., Olesch M. Distribution of ferrous and ferric iron in clintonite and the Mössbauer characteristics of ferric iron in tetrahedral coordination. *Can. Mineral.*, 1978, **16**, P. 199–203.
[49] Darby Dyar M. A review of Mössbauer data on trioctahedral micas: Evidence for tetrahedral Fe^{3+} and cation ordering. *American Mineralogist*, 1987, **72**, P. 102–112.
[50] Almjasheva O.V., et al. Structural features of ZrO_2-Y_2O_3 and ZrO_2-Gd_2O_3 nanoparticles formed under hydrothermal conditions. *Russ. J. Gen. Chem.*, 2014, **84** (5), P. 804–809.
[51] Almjasheva O.V., Krasilin A.A., Gusarov V.V. Formation mechanism of core-shell nanocrystals obtained via dehydration of coprecipitated hydroxides at hydrothermal conditions. *Nanosystems: Physics, Chemistry, Mathematics*, 2018, **9** (4), P. 568–572.
[52] Krasilin A.A., et al. Young's and shear moduli of Fe^{3+}- doped chrysotile nanoscrolls probed by atomic force microscopy. *Mater. Today Commun.*, 2024, **38**, 108358.
[53] Borghi E., et al. Spectroscopic characterization of Fe-doped synthetic chrysotile by EPR, DRS and magnetic susceptibility measurements. *Phys. Chem. Chem. Phys.*, 2010, **12** (1), P. 227–238.
[54] Kulkarni S.A., et al. Effect of synthesis route on the structural, optical and magnetic properties of Fe_3O_4 nanoparticles. *Ceram. Int.*, 2014, **40** (1), P. 1945–1949.
[55] Mitra S., et al. Synthesis of a α-Fe_2O_3 nanocrystal in its different morphological attributes: growth mechanism, optical and magnetic properties. *Nanotechnology*, 2007, **18** (27), 275608.
[56] Kouotou P.M., et al. Particle size-band gap energy-catalytic properties relationship of PSE-CVD-derived Fe_3O_4 thin films. *J. Taiwan Inst. Chem. Eng.*, 2018, **93**, P. 427–435.
[57] Trittschack R., Grobéty B., Brodard P. Kinetics of the chrysotile and brucite dehydroxylation reaction: a combined non-isothermal/isothermal thermogravimetric analysis and high-temperature X-ray powder diffraction study. *Phys. Chem. Miner.*, 2014, **41** (3), P. 197–214.
[58] Qin M., et al. In-situ observation of nanoscale transformations in dehydrating lizardite. *Sci Rep.*, 2025, **15** (1), 4000.
[59] Khrapova E.K., et al. Thermal behavior of Mg-Ni-phyllosilicate nanoscrolls and performance of the resulting composites in hexene-1 and acetone hydrogenation. *ChemNanoMat.*, 2021, **7** (3), P. 257–269.
[60] Li Q., et al. Revealing atomistic mechanism of lithium diffusion in montmorillonite structure: A molecular simulation study. *Geochim. Cosmochim. Acta*, 2025, **392**, P. 165–174.

Submitted 14 November 2025; accepted 2 December 2025

Information about the authors:

Asiyat A. Iyakhmaeva – Ioffe Institute, 194021 St. Petersburg, Russia; acya.gitinova@gmail.com

Ekaterina K. Khrapova – Ioffe Institute, 194021 St. Petersburg, Russia; ORCID 0000-0003-2674-9653; e.k.khrapova@mail.ioffe.ru

Lev A. Lebedev – Ioffe Institute, 194021 St. Petersburg, Russia; ORCID 0000-0001-9449-9487; L.A.Lebedev@mail.ioffe.ru

Nadezhda V. Glebova – Ioffe Institute, 194021 St. Petersburg, Russia; ORCID 0000-0003-4519-0111; Glebova@mail.ioffe.ru

Valentin G. Semenov – Institute of Chemistry, Saint Petersburg State University, 199034 St. Petersburg, Russia; ORCID 0000-0002-1530-7289; val_sem@mail.ru

Andrey V. Kopylov – RITVERC JSC, St. Petersburg, 194223, Russia; akopylov@ritverc.com

Andrei A. Krasilin – Ioffe Institute, 194021 St. Petersburg, Russia; ORCID 0000-0002-3938-3024; ikrasilin@mail.ioffe.ru

Conflict of interest: the authors declare no conflict of interest.

NANOSYSTEMS:
PHYSICS, CHEMISTRY, MATHEMATICS

Original article

Bugrov A.N., et al. *Nanosystems: Phys. Chem. Math.*, 2025, **16** (6), 850–864.
http://nanojournal.ifmo.ru
DOI 10.17586/2220-8054-2025-16-6-850-864

Synthesis, structure and properties of composite proton-conducting membranes based on a Nafion-type perfluorinated copolymer with $Zr_{1-x}Y_xO_{2-0.5x}$ nanoparticles

Alexander N. Bugrov[1,2,a], Galina N. Gubanova[1,b], Oleg N. Primachenko[1,c], Iosif V. Gofman[1,d], Elena M. Ivan'kova[1,e], Elena N. Popova[1,f], Demid A. Kirilenko[3,g], Victor K. Lavrentyev[1,h], Elena N. Vlasova[1,i], Svetlana V. Kononova[1,j]

[1]NRC "Kurchatov Institute" – PNPI – IMC, St. Petersburg, Russia

[2]St. Petersburg Electrotechnical University "LETI", St. Petersburg, Russia

[3]Ioffe Institute, St. Petersburg, Russia

[a]bugrov.an@mail.ru, [b]gubanovagn@yandex.ru, [c]alex-prima@mail.ru, [d]gofman@imc.macro.ru, [e]ivelen@mail.ru, [f]men682003@mail.ru, [g]demid.kirilenko@mail.ioffe.ru, [h]lavrentev1949@mail.ru, [i]evl021960@gmail.com, [j]svetlanavkononova@gmail.com

Corresponding author: Alexander N. Bugrov, bugrov.an@mail.ru

PACS 61.46.+w, 82.33.Pt, 68.35.Dv

ABSTRACT $Zr_{1-x}Y_xO_{2-0.5x}$ nanoparticles were introduced into the sulfonic acid form of the Nafion-type perfluorinated copolymer prior to membrane formation to improve its water retention, thermal stability, and proton conductivity. Since the conditions under which nanoparticles are formed can significantly influence their size, phase composition, morphology, and surface chemistry, various approaches to filler synthesis were considered in this study. It was found that among the wet-chemical methods used to produce zirconia-based nanoparticles, solvothermal synthesis offers the most promise in terms of increasing the surface proton conductivity of composite membranes. This method ensures small size, large specific surface area, and high hydrophilicity of the nanoparticles. Consequently, their incorporation into a Nafion-type perfluorinated copolymer increases the membrane's moisture retention and improves to its proton-conducting properties. In the case of $Zr_{1-x}Y_xO_{2-0.5x}$ nanoparticles formed under solution combustion conditions, their more hydrophobic surface did not contribute to an increase in the moisture content of the perfluorinated copolymer, but did allow its maximum operating temperature to be increased by 20 °C.

KEYWORDS proton conductivity, impedance spectroscopy, yttria-stabilized zirconia, glycine-nitrate combustion, sol-gel, hydrothermal synthesis, solvothermal method

ACKNOWLEDGEMENTS The authors thank D. A. Gavrilova, M. A. Gavrilova, and N. S. Kormiltsina, students of the St. Petersburg State Institute of Technology (Technical University), for their assistance in determining the conditions for producing nanoparticles. The authors also thank senior researcher G. V. Vaganov and senior laboratory assistant V. D. Vavilova from the NRC "Kurchatov Institute" – PNPI – IMC for measuring the contact angle of the composite membranes and determining their bulk proton conductivity, respectively. X-ray diffraction analysis was performed using equipment from the Engineering Center of the Saint Petersburg State Institute of Technology. TEM studies were performed using equipment of the Federal Joint Research Center "Material science and characterization in advanced technology" supported by the Ministry of Education and Science of the Russian Federation. The research work was carried out within the framework of State Programs of Branch of Petersburg Nuclear Physics Institute named by B. P. Konstantinov of National Research Centre "Kurchatov Institute" – Institute of Macromolecular Compounds (Project 122012000452-9).

FOR CITATION Bugrov A.N., Gubanova G.N., Primachenko O.N., Gofman I.V., Ivan'kova E.M., Popova E.N., Kirilenko D.A., Lavrentyev V.K., Vlasova E.N., Kononova S.V. Synthesis, structure and properties of composite proton-conducting membranes based on a Nafion-type perfluorinated copolymer with $Zr_{1-x}Y_xO_{2-0.5x}$ nanoparticles. *Nanosystems: Phys. Chem. Math.*, 2025, **16** (6), 850–864.

1. Introduction

Proton exchange membrane fuel cells are promising, environmentally friendly electrochemical power sources that are characterized by increased energy density and relatively high power generation efficiency [1]. The most commonly used membranes in fuel cells are Nafion-type membranes due to their mechanical strength, chemical resistance, high selectivity and proton conductivity in the hydrated state [2, 3]. The microstructure of the Nafion membrane is a network of

interconnected clusters of sulfonic acid groups (proton exchange channels) that are formed in a hydrophobic polymer matrix of polytetrafluoroethylene with hydrophilic perfluorinated side chains containing ionic groups [4,5]. Proton migration in membranes of this type depends significantly on the water content [6]. At high temperatures, the Nafion membrane loses moisture, which leads to irreversible mechanical damage and a decrease in proton conductivity. The maximum proton conductivity is achieved when the Nafion membrane is fully hydrated. The use of this membrane in methanol fuel cells is further limited by the permeability of methanol, the incomplete oxidation of which promotes the release of CO, which deactivates the platinum catalyst at the anode. Therefore, in order to maintain high proton conductivity, improve the kinetics of oxidation-reduction reactions at both electrodes, protect the platinum catalyst, and optimize the balance between operating temperature and humidity of the polymer electrolyte membrane in fuel cells [7], approaches have been developed to increase its water retention [8]. One such approach is the physicochemical design of new polymer-inorganic composite membranes capable of effectively binding water within their structure, absorbing moisture, reducing the degree of fuel-oxidizer mixing and electroosmotic resistance in the system, and increasing proton conductivity. At the same time, they must also maintain their mechanical strength, thermal stability and chemical resistance, under conditions of high operating temperatures [9] and low relative humidity [10]. Basically, to retain water in the membrane under high-temperature operating conditions, various types of inorganic fillers were used due to their electrostatic attraction within the double electric layer [11], anti-swelling and hydrophilic properties [12–14]. Moreover, the hydrated water on the surface of such particles can form bridges between clusters of sulfonic acid groups, which can provide additional pathways for proton transfer [17]. The introduction of inorganic fillers, such as silica (SiO_2) [18, 19], titania (TiO_2) [20, 21], ceria (CeO_2) [22], zirconia (ZrO_2) [23, 24] and zeolites [25] allows you to regulate the swelling degree of membranes, change their mechanical properties, as well as the structure of pores and channels, which helps to increase proton conductivity of fuel cells [26–28]. Among the above-mentioned fillers for proton-conducting membranes, nanosized additives based on zirconia have proven to be the most effective. In [10], hybrid polymer-inorganic membranes based on Nafion and four types of oxide nanoparticles (ZrO_2, TiO_2, ZrO_2–TiO_2, ZrO_2–Y_2O_3) were fabricated using the doctor blade method for use as electrolytes in medium-temperature fuel cells with a proton exchange membrane. Pristine, sulfated and phosphated zirconia nanoparticles were used to modify the Nafion membrane to improve water retention, thermal stability, proton conductivity, and reduce methanol permeability [29]. In this study, inorganic nanoparticles were introduced into Nafion using remelting, swelling-impregnation, and ion exchange methods. The proton conductivity of the membrane with 5 wt. % sulfated ZrO_2 exceeded 0.103 S/cm at room temperature and had the highest water absorption rate – 35 %.

It is known that ZrO_2 can be represented by three polymorphic modifications: monoclinic, tetragonal and cubic [30]. Of particular interest among the crystal structures of zirconia are the tetragonal and cubic phases (t, c-ZrO_2) due to their high oxygen-ion conductivity and chemical resistance over a wide range of temperatures and oxygen partial pressures. Therefore, they are a well-known candidate for applications such as the development of fuel cells [31]. To obtain nanoparticles of ZrO_2 high-temperature modifications, stabilizer ions such as calcium (Ca^{2+}), europium (Eu^{3+}), or yttrium (Y^{3+}) are introduced into its structure, which prevent phase transitions upon cooling [32]. The crystal structure, size, shape, and surface chemistry of zirconia nanoparticles are typically determined by the synthesis and thermal treatment methods [33, 34]. Therefore, in this study, t, c-ZrO_2 nanoparticles were obtained using various synthesis techniques, characterized by a combination of physicochemical analysis methods and subsequently used as a modifying additive for Nafion-type proton-conducting membrane.

2. Experimental

2.1. Materials

The following reagents were used for the synthesis of $Zr_{1-x}Y_xO_{2-0.5x}$ nanoparticles: $ZrOCl_2 \times 8H_2O$ (CAS: 13520-92-8, Lenreaktiv, Russia, pure), $ZrO(NO_3)_2 \times 2H_2O$ (CAS: 14985-18-3, Lenreaktiv, Russia, pure), $Zr(OC_4H_9)_4$ (CAS: 1071-76-7, Sigma-Aldrich, 80 % Gew.Lsg.in 1-Butanol), $Y(NO_3)_3 \times 6H_2O$ (CAS: 13494-98-9, Vekton, Russia, chemically pure), $YCl_3 \times 6H_2O$ (CAS: 10025-94-2, Vekton, Russia, pure), ammonia solution (Vekton, CAS: 1336-21-6, 25 % , chemically pure) and C_2H_5OH (CAS: 64-17-5, Ekroskhim, Russia, 99.5 %).

The Nafion-type membrane (LSC-1) based on a precursor copolymer was obtained by aqueous emulsion copolymerization of tetrafluoroethylene with the perfluorinated monomer perfluoro(3,6-dioxa-4-methyl-7-octene)sulfonyl fluoride using the technology described in detail in [35]. A copolymer with equivalent mass values (molecular mass of a polymer chain fragment per sulfonic acid group) of 1030 g-eq/mol SO_3H groups was used as the base chemical structure.

N,N-dimethylformamide (CAS: 68-12-2, Vekton, Russia, extra pure) was used as a solvent in the dispersion preparation of the LSC-1 copolymer in sulfonic acid form.

2.2. Synthesis of $Zr_{1-x}Y_xO_{2-0.5x}$ nanoparticles

2.2.1. Glycine-nitrate combustion. Zirconium (6.58 mmol) and yttrium (0.42 mmol) nitrates were dissolved in 50 ml of water with the addition of 5 ml of concentrated nitric acid, vigorously stirred, and heated in the presence of glycine. The ratio of the glycine mole number to the total metal nitrate mole ones in the reaction mixture was 1.3. After homogenization of the reaction mixture, the solution was placed in a sand bath and heated until ignition occurred. The combustion product,

a gray foam-like substance, was ground in an agate mortar to a powder and annealed in a muffle furnace at 500 °C for 2 hours.

2.2.2. Sol-gel synthesis. 25 ml of 0.02 M $Y(NO_3)_3 \times 6H_2O$ solution was added to 36 ml of 80 % $Zr(OC_4H_9)_4$ zirconium butoxide. The resulting mixture was vigorously stirred at 60 °C for 1 hour. The resulting sol was dried to form a gel and heat-treated at 700 °C for 2 hours. The resulting product was ground in agate mortar to a powder.

2.2.3. Hydrothermal synthesis. $ZrOCl_2 \times 8H_2O$ (6.58 mmol) and $YCl_3 \times 6H_2O$ (0.42 mmol) were dissolved in distilled water and stirred. The corresponding metal hydroxides were then coprecipitated by adding 25 % ammonia solution dropwise to the dissolved reagents with continuous stirring until a white, curdy precipitate formed at pH of 14. The resulting precipitate was then repeatedly washed by decantation until a negative chloride ion reaction was achieved and dried to constant weight at 100 °C. The resulting white powder was poured into an autoclave cell and filled with water. The hydrothermal vessel containing the mixture was then sealed and maintained at 200 °C for 4 hours. The particles formed under hydrothermal conditions were removed from the cell and dried in air at 100 °C.

2.2.4. Solvothermal synthesis. $YCl_3 \times 6H_2O$ (0.5 mmol) dissolved in 15 ml of ethanol was added in small portions to $Zr(OC_4H_9)_4$ (7.7 mmol) with constant stirring. After thorough stirring for 90 minutes, the resulting suspension was placed in an autoclave. The synthesis was carried out for 72 hours at an isothermal holding temperature of 200 °C. The precipitate was then separated from the mother liquor and washed repeatedly with distilled water by centrifugation. The washed precipitate was dried at 100 °C and then heat-treated at 500 °C for 2 hours. The annealed sample was ground to a powder.

2.3. Preparation of composite films

A method for introducing zirconia-based nanoparticles into Nafion-type perfluorinated copolymer dispersions for the subsequent fabrication of composite membranes was developed. Nafion-type (LSC-1) copolymer powders in sulfonic acid form were used as a matrix. To obtain composite membranes, dispersions of ZrO_2-based nanoparticles in N,N-dimethylformamide (DMF) with an LSC-1 concentration of no more than 5 wt. % were prepared, enabling the production of fairly uniform film materials using a casting method. The kinematic viscosity of the dispersions was crucial for the formation of cast composite membranes with a smooth surface. Nanoparticle dispersions in solution were prepared in a glass flask with stirring at 1000 rpm and ultrasonic treatment (3.5 kHz, 50 W) for 30 minutes. The nanoparticle dispersion was then added to a pre-obtained LSC-1 one in DMF and stirred magnetically for 5 min. The ZrO_2-based nanoparticle content in the LSC-1 composite membranes was 0.5 wt. % . Composite membranes were formed on a glass substrate using the casting method with solvent removal under an IR lamp at 80 °C for 4 hours. The composite membrane was then evacuated to remove residual solvent and annealed at 100 °C for 3 hours. Before measuring the proton conductivity of the composite membranes using impedance spectroscopy, they were rinsed with a 15 % nitric acid solution and then with distilled water to neutral pH.

2.4. Research methods

2.4.1. X-ray phase analysis. X-ray phase analysis of $Zr_{1-x}Y_xO_{2-0.5x}$ nanoparticles synthesized by glycine-nitrate combustion and wet-chemical methods was performed using a Rigaku SmartLab 3 X-ray diffractometer (CuK_α, 40 kV, 44 mA) in the 10 – 70° range with a scan rate of 0.5 °/min. Full-profile analysis of X-ray diffraction (XRD) patterns of nanoparticle powders was performed using the PD-Win 4.0 software package (Research and Production Association "Burevestnik", Russia). X-ray phase analysis of the samples was carried out by the Crystallographica Search-Match software package (Oxford Cryosystems, UK) based on the obtained values of interplanar distances, peak widths at half-height, their intensity and position (2θ) using the ICDD PDF-2 database. The average crystallite sizes for nanopowders were estimated based on the broadening of XRD peaks using the Scherrer formula. The MAUD software package (L. Lutterotti, Italy) was used to determine the phase composition and calculate the parameters of a unit cell of nanoparticles [36].

Structural studies of the membranes were performed using a DRON-2.0 automated X-ray diffractometer manufactured by the Leningrad Research and Production Association "Burevestnik". CuK_α radiation was used. Monochromatization was achieved with a Ni filter. The images were taken in transmission mode. The crystallinity degrees of the samples were determined by the ratios of the integral intensities of crystalline reflections and amorphous halo.

2.4.2. Transmission electron microscopy. Transmission electron microscopy (TEM; JEOL JEM-2100F) with an accelerating voltage of 200 kV was used to determine the shape and size of $Zr_{1-x}Y_xO_{2-0.5x}$ nanoparticles. Sample preparation for TEM included the deposition of oxide nanoparticle dispersions onto graphene-coated copper grids and subsequent water removal from them during the drying process [37].

2.4.3. Energy-dispersive X-ray spectroscopy. The elemental composition of synthesized nanoparticles was measured using a Hitachi S-570 (Tokyo, Japan) scanning electron microscope with a Bruker Quantax 200 microanalysis system (Bruker Corporation, USA). Quantitative energy-dispersive X-ray (EDX) spectroscopy was carried out using the method of fundamental parameters. The standard accumulation time of the spectrum was 60 seconds. The composition was determined from the maximum possible area of the test sample.

2.4.4. FTIR spectroscopy. The amount of hydroxyl groups on the surface of the synthesized $Zr_{1-x}Y_xO_{2-0.5x}$ nanoparticles was estimated using FTIR spectroscopy on a Vertex 70 spectrometer (Bruker Optik GmbH, Ettlingen, Germany), which is equipped with an attenuated total reflectance device (Pike Technologies Inc., Madison, WI 53719, USA).

2.4.5. Scanning electron microscopy. The degree of nanoparticle dispersion and the uniformity of their distribution within the polymer matrix were studied by analyzing micrographs of transverse fractures of composite films in liquid nitrogen using a SUPRA 55VP scanning field-emission electron microscope (Carl Zeiss, Germany). Prior to analysis, a conductive platinum coating was applied to the surface of the samples using vacuum deposition.

2.4.6. Determination of the surface wetting angle of composite films. The wetting of the surface of composite films with water was assessed by the sessile drop method using a DSA 30 device (Kruss, Germany).

2.4.7. Thermogravimetric analysis. Thermogravimetric analysis (TGA) of membrane samples was performed using a Netzsch TG 209 F1 (Germany) in a temperature range from ambient to 800 °C at a heating rate of 10 °C/min under an inert gas flow. The test samples weighed between 2 and 3 mg. Processes associated with heat release or absorption during membrane heating were studied using differential scanning calorimetry using a Netzsch DSC 204 F1 (Germany) in a temperature range from room temperature to 280 °C (below the decomposition temperature of sulfo groups) under an argon atmosphere (argon flow rate: 25 ml/min, heating rate: 10 °/min).

2.4.8. Differential scanning calorimetry. Processes associated with heat release or absorption during membrane heating were studied using differential scanning calorimetry using a Netzsch DSC 204 F1 (Germany) in a temperature range from room temperature to 280 °C (below the decomposition temperature of sulfo groups) under an argon atmosphere (argon flow rate: 25 ml/min, heating rate: 10 °/min).

2.4.9. Mechanical testing of films. Mechanical tests of the unfilled and composite films were conducted in uniaxial tension using an AG-100X Plus universal mechanical testing rig (Shimadzu Corp., Japan). The following material properties were determined during testing: elastic modulus (E), plastic yield limit (σ_y), strength (σ_p), and ultimate strain before failure (ε_p).

2.4.10. Impedance spectroscopy. Surface proton conductivity was measured by impedance spectroscopy at equilibrium membrane saturation with water, i.e., at the maximum water content achieved by boiling at 100 °C for 1 hour. A Z-3000X impedance meter (Elins, Russia) with a 4-electrode measuring cell and a frequency range of 10 – 150 kHz was used. Specific electrical conductivity (σ_n) was calculated using the following formula:

$$\sigma_n = L/(R_m \cdot h \cdot b), \tag{1}$$

where L is the distance between the voltage electrodes of the measuring cell (L = 1.77 cm according to the measuring cell specifications), cm; h is the average membrane thickness, cm; b is the average membrane width, cm; R_m is the membrane resistance, Ohm.

The bulk proton conductivity of the membranes was measured in a two-electrode cell using an Elins Z-1500J impedance meter at an initial frequency of 3 kHz and a final ones of 100 kHz. The equilibrium moisture content of the membranes was determined by the weight of the samples, which were dried to constant weight in a vacuum at 80 °C and then subjected to equilibrium saturation in water for 24 hours at 20 °C. Before measurements, the sample was soaked in distilled water for at least 15 minutes, after which it was additionally moistened as measurements were taken. During the measurements, the sample was heated from 25 to 120 °C, with instrument readings taken every 5 °C.

3. Results and discussion

Powders of $Zr_{1-x}Y_xO_{2-0.5x}$ nanoparticles were obtained using solution combustion and wet chemistry methods. According to XRD data, the products formed from zirconium and yttrium nitrate solutions with glycine during combustion synthesis, after their annealing and grinding to a powder state, were a mixture of ZrO_2 nanocrystals of the tetragonal (t) and cubic (c) phases in a ratio of 40:60 (Table 1). A qualitative XRD analysis carried out in the PD-Win 4.0 and Crystallographica Search-Match software packages showed the best correspondence of the synthesized nanocrystalline powder to card No. 49-1642 for c-ZrO_2 from the ICDD PDF-2 database (Fig. 1a). Refinement of the unit cell parameters using the Rietveld method, performed in the MAUD software package, showed that the values of the lattice periods a, b and c for the synthesized ZrO_2 nanocrystals calculated from XRD patterns differ from those given in the literature [38] in the case of thermally stabilized tetragonal phase (Table 1). This fact indicates the incorporation of Y^{3+} ions into the crystal lattice of t-ZrO_2 and the formation of $Zr_{1-x}Y_xO_{2-0.5x}$ solid solutions. A similar conclusion can be made for cubic phase nanocrystallites formed during glycine-nitrate combustion of the reaction mixture, the cell parameters of which were almost identical to those recorded in the literature for stabilized c-ZrO_2 [39]. The average size of the coherent scattering regions (CSRs) for the $Zr_{1-x}Y_xO_{2-0.5x}$ nanoparticles powders obtained by solution combustion, calculated using the Scherrer formula, was 10±2 nm. For tetragonal and cubic ZrO_2 crystallites separated in the MAUD software package, the CSR region sizes were 6 and 31 nm, respectively. According to TEM data, the nanopowder contained mono- and polycrystalline quasi-spherical particles with sizes of 3 – 5 and 8 – 18 nm, respectively (Fig. 2a).

TABLE 1. XRD data for nanoparticles of $Zr_{1-x}Y_xO_{2-0.5x}$ solid solutions obtained by different synthesis methods

Preparation method	$Zr_{1-x}Y_xO_{2-0.5x}$						
	Polymorphic modification	Phase content, vol. %	Unit cell parameters		Microstresses	Average crystallite size, nm	
			lengths	angles		MAUD	PDWin
Literary data [38, 39]	Tetragonal	–	$a = b = 3.612$ $c = 5.212$	$\alpha = \gamma = \beta = 90$	–	–	–
	Cubic	–	$a = b = c =$ 5.129	$\alpha = \gamma = \beta = 90$	–	–	–
Glycine-nitrate combustion	Monoclinic	–	–	–	–	–	–
	Tetragonal	40	$a = b = 3.623 \pm 0.001$ $c = 5.171 \pm 0.002$	$\alpha = \gamma = \beta = 90$	$5.9\times10^{-4}\pm$ 2×10^{-4}	6 ± 1	10 ± 2
	Cubic	60	$a = b = c =$ 5.127 ± 0.001	$\alpha = \gamma = \beta = 90$	$0.0047\pm$ 2×10^{-5}	31 ± 2	
Sol-gel	Monoclinic	–	–	–	–		–
	Tetragonal	76	$a = b = 3.611 \pm 0.001$ $c = 5.171 \pm 0.001$	$\alpha = \gamma = \beta = 90$	$0.002\pm$ 2.8×10^{-5}	57 ± 6	22 ± 4
	Cubic	24	$a = b = c =$ 5.134 ± 0.001	$\alpha = \gamma = \beta = 90$	$0.0073\pm$ 9×10^{-4}	6 ± 2	
Hydrothermal synthesis	Monoclinic	–	–	–	–		–
	Tetragonal	82	$a = b = 3.466 \pm 0.02$ $c = 5.682 \pm 0.056$	$\alpha = \gamma = \beta = 90$	$0.11\pm$ 0.001	–	3 ± 1
	Cubic	18	$a = b = c =$ 5.151 ± 0.003	$\alpha = \gamma = \beta = 90$	$0.018\pm$ 0.0002	–	
Solvothermal synthesis	Monoclinic	–	–	–	–	–	–
	Tetragonal	83	$a = b = 3.415 \pm 0.003$ $c = 5.773 \pm 0.022$	$\alpha = \gamma = \beta = 90$	$0.109\pm$ 0.001	–	3 ± 1
	Cubic	17	$a = b = c =$ 5.131 ± 0.004	$\alpha = \gamma = \beta = 90$	$0.024\pm$ 3.8×10^{-4}	–	

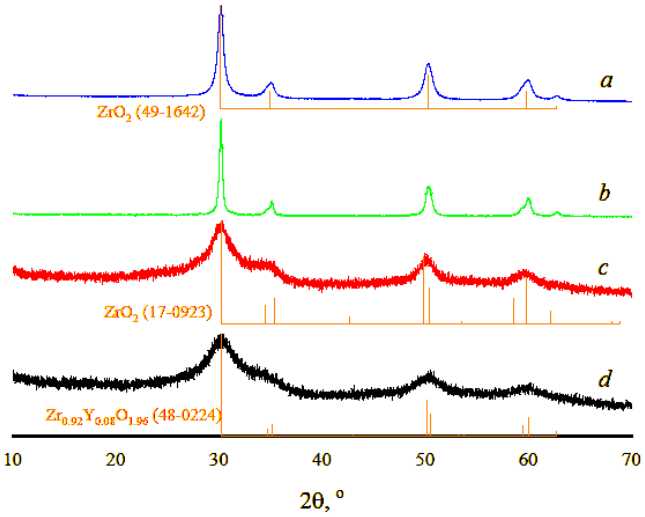

FIG. 1. Comparison with a ICDD PDF-2 database of the XRD patterns of $Zr_{1-x}Y_xO_{2-0.5x}$ nanoparticles obtained by different methods: glycine-nitrate combustion (a), sol-gel (b), hydrothermal (c) and solvothermal syntheses (d)

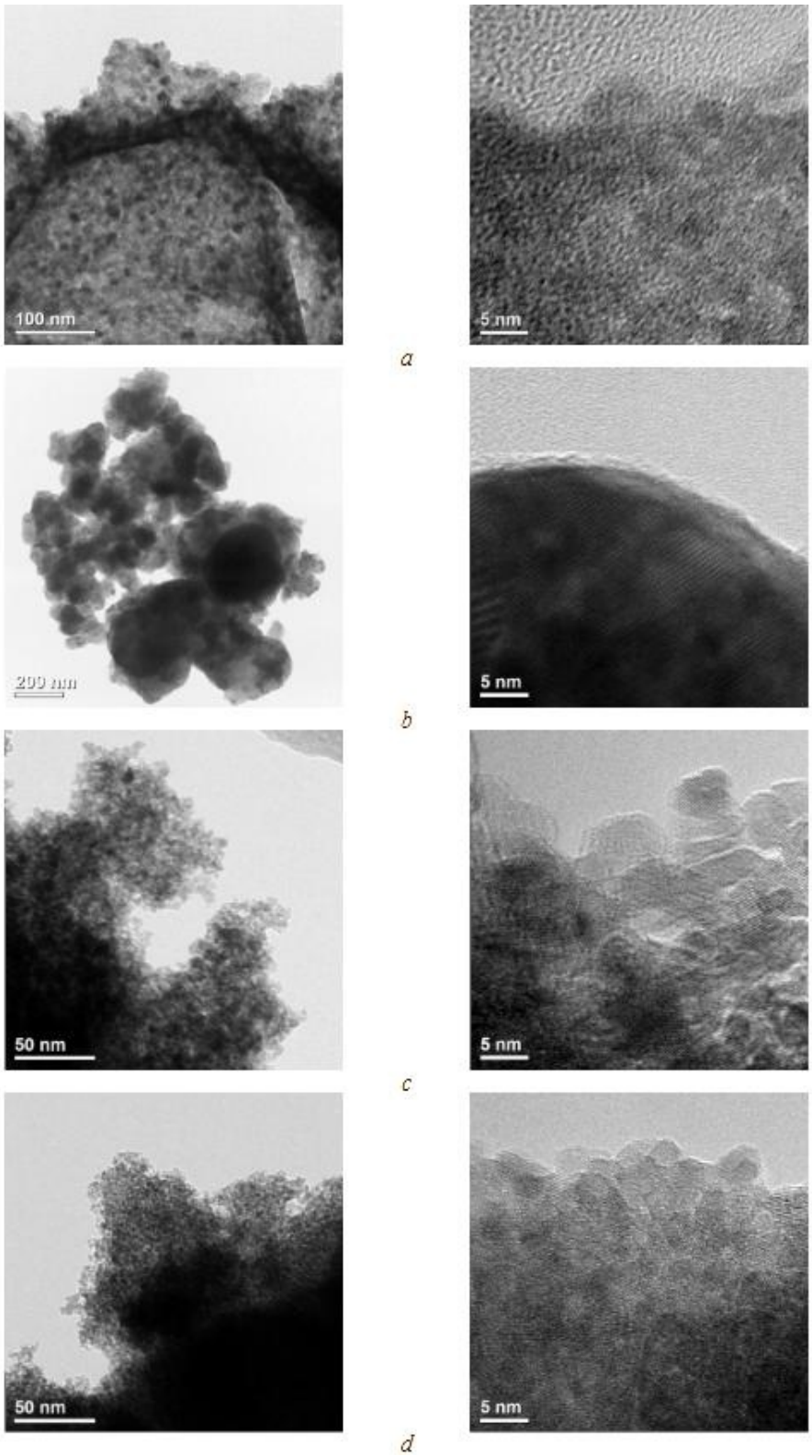

FIG. 2. TEM micrographs of $Zr_{1-x}Y_xO_{2-0.5x}$ nanoparticles obtained by different methods: glycine-nitrate combustion (a), sol-gel (b), hydrothermal (c) and solvothermal syntheses (d)

TABLE 2. Elemental composition of $Zr_{1-x}Y_xO_{2-0.5x}$ nanoparticles obtained by various synthesis methods

Preparation method	at. %	
	Y	Zr
Glycine-nitrate combustion	3.54±0.05	96.46±0.05
Sol-gel	6.9±0.33	93.1±0.33
Hydrothermal synthesis	5.06±0.02	94.94±0.02
Solvothermal synthesis	3.91±0.05	96.09±0.05

Aging of the gel formed by mixing yttrium nitrate and zirconium butoxide solutions, its subsequent annealing at 700 °C for 2 hours, and disintegration yielded t- and c-ZrO_2 nanoparticles in a 76:24 ratio. The average crystallite size, calculated from a full-profile analysis of the nanoparticle X-ray diffraction pattern, was 22±4 nm (Fig. 1b). Qualitative X-ray diffraction analysis of the sample in Crystallographica Search-Match showed the best match for t-ZrO_2 (card No. 48-224). The average crystallite size, calculated using the MAUD program, was 60 nm for $t-ZrO_2$, while for the cubic modification it was an order of magnitude smaller (Table 1). Refinement of the crystal lattice parameters using the Rietveld method revealed that the a and b values correspond to those reported in the literature for undoped t-ZrO_2, while the lattice constant c for the synthesized tetragonal phase nanoparticles was lower [38]. In turn, the calculated unit cell parameters for the cubic phase of $Zr_{1-x}Y_xO_{2-0.5x}$ nanoparticles were higher than those presented in [39] for c-ZrO_2. TEM (Fig. 2b) demonstrated that sol-gel synthesis resulted in the formation of quasi-spherical particles, representing intergrowths of crystallites, with a wide grain size distribution (from 40 to 300 nm).

Qualitative XRD analysis showed that hydrothermal treatment (200 °C, 70 MPa, 4 hours) of a mixture of yttrium and zirconium hydroxides coprecipitated from their chloride solutions using NH_4OH, similar to the previous synthesis method, yielded crystals of t- (82 %) and c-ZrO_2 (18 %) (Fig. 1c). The average crystallite size, calculated from the diffraction maxima of t-/ c-ZrO_2 using the Scherrer formula, was 3±1 nm. It was not possible to determine the separate crystallite sizes of the tetragonal and cubic phases using the MAUD program. The formation of a $Zr_{1-x}Y_xO_{2-0.5x}$ solid solution is indicated by a decrease in the a and b parameters of the unit cell with a significant increase in the lattice constant c, compared to the crystallographic data for t-ZrO_2 given in the literature (Table 1) [38]. For cubic phase crystallites formed under hydrothermal conditions, the lattice parameters were higher than for solid solution samples obtained at temperatures up to 1400 K [39]. Spherical $Zr_{1-x}Y_xO_{2-0.5x}$ nanoparticles with an average diameter of 4±1 nm were observed in the TEM micrographs (Fig. 2c). It should be noted that the diameter of the nanoparticles formed under hydrothermal conditions is comparable with the average size of the CSRs within the error limits, i.e., they are single-crystal.

A similar isothermal holding at 200 °C for 24 hours of a pre-homogenized mixture of zirconium alkoxide and an alcoholic solution of yttrium chloride also promoted the crystallization of nanoparticles of the $Zr_{1-x}Y_xO_{2-0.5x}$ solid solutions (Table 1). The ratio of crystalline phases in the nanoparticle powder obtained by solvothermal synthesis (SS) was practically the same as that obtained during hydrothermal treatment of the $ZrO(OH)_2$–$Y(OH)_3$ precipitate. The average crystallite size was 3±1 nm, which coincided with the particle diameter in the TEM micrographs (Fig. 2d).

EDX spectroscopy results showed that the yttrium content in the resulting $Zr_{1-x}Y_xO_{2-0.5x}$ solid solution nanoparticles was lower than the synthesis target for virtually all methods used, except sol-gel (SG) technology (Table 2). According to the phase diagrams of ZrO_2-Y_2O_3, at yttria concentrations below 3 mol. % , solid solution crystals form, corresponding predominantly to the tetragonal structure of zirconium dioxide [40,41]. This is consistent with the results of our quantitative X-ray phase analysis for all solid solution samples obtained by wet chemistry methods. In the case of glycine-nitrate combustion, due to the high rate of particle formation and the high synthesis temperature, they crystallize predominantly as the cubic polymorph of ZrO_2.

A study using FTIR spectroscopy of the surface chemistry of $Zr_{1-x}Y_xO_{2-0.5x}$ nanoparticles obtained by different methods showed that in the case of hydro- and solvothermal treatment of precursors of both inorganic and organic nature, fillers with a more hydrophilic surface are formed. The integrated intensity of the bands corresponding to the stretching and bending vibrations of OH groups in the range of 3700 – 2690 cm^{-1} and at 1615 cm^{-1} for nanoparticles obtained by the two aforementioned synthesis methods is significantly higher than that in the FTIR spectra of similar systems formed via the sol-gel process or solution combustion (Fig. 3). This circumstance may be useful from the point of view of moisture retention by the surface of $Zr_{1-x}Y_xO_{2-0.5x}$ nanoparticles, which will increase the operating temperature of Nafion-type perfluorinated membranes by introducing a filler.

SEM micrographs of composite film cross-sections were analyzed to control the dispersion degree and distribution homogeneity of $Zr_{1-x}Y_xO_{2-0.5x}$ nanoparticles in the bulk of the Nafion-type polymer matrix. Nanoparticles obtained by hydrothermal synthesis (HS), with a large number of hydroxyl groups on the surface and a small crystallite size, aggregated less and were more uniformly distributed within the perfluorinated polymer (Fig. 4a). Meanwhile, $Zr_{1-x}Y_xO_{2-0.5x}$

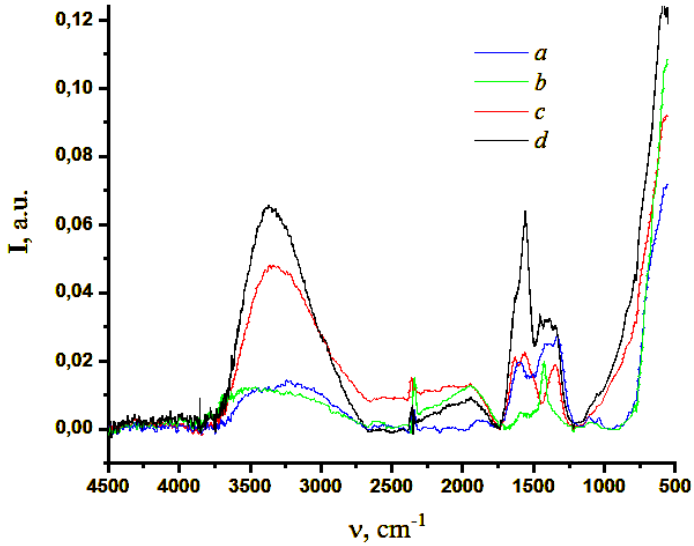

FIG. 3. FTIR spectroscopy of $Zr_{1-x}Y_xO_{2-0.5x}$ nanoparticles obtained by different methods: glycine-nitrate combustion (a), sol-gel (b), hydrothermal (c) and solvothermal (d) syntheses

nanoparticles, formed from zirconium butoxide and yttrium chloride under solvothermal conditions with similar dimensions and a higher surface hydrophilicity, agglomerated intensely within the same polymer and collected in its near-surface layer as large aggregates (Fig. 4b). It should be noted that the majority of the agglomerated particles protruded onto the surface of the composite film. This is probably due to differences in the density of the perfluorinated copolymer and inorganic fillers during the formation of composite membranes. The introduction of nanoparticles obtained using sol-gel technology into the polymer matrix also resulted in strong filler aggregation, but the number of aggregates near the surface was significantly smaller and was hidden beneath the polymer layer (Fig. 4c). The greatest incompatibility between the perfluorinated polymer and $Zr_{1-x}Y_xO_{2-0.5x}$ nanoparticles was observed when the latter were produced using the glycine-nitrate combustion (GNC) method (Fig. 4d). The incorporation of these particles into the polymer was accompanied by the formation of aggregates ranging from a few to tens of microns in size, which settled under their own weight. Therefore, a micrograph of a composite film cleavage shows a gradient in the distribution of aggregates with an increasing concentration toward the substrate on which it was formed, while it is clearly visible that they remain beneath the polymer layer.

Determining the surface contact angle of composite films using the sessile drop method revealed that samples containing $Zr_{1-x}Y_xO_{2-0.5x}$ nanoparticles with a high number of OH groups are more hydrophilic. When a drop was applied to the film surface of a perfluorinated copolymer containing 0.5 wt. % nanoparticles obtained under hydrothermal conditions, its instant swelling was observed (Fig. 5).

Thermogravimetric analysis (TGA) of composite films based on a perfluorinated copolymer incorporating $Zr_{1-x}Y_xO_{2-0.5x}$ nanoparticles with different chemical prehistory revealed three main processes occurring during heating. The first step of mass loss recorded on the TGA curves in the range from room temperature to 180 – 200 °C is associated with the release of water and residual DMF solvent (the boiling point of the solvent is 155.5 °C). A subsequent increase in temperature facilitated the decomposition of sulfo groups in the range from 300 to 420 °C. We believe that the most reasonable parameter for the thermal stability of composite membranes is the temperature corresponding to the maximum mass loss during the destruction of the sulfo-containing fragment (T2 in Table 3), determined based on analysis of the differential thermogravimetric curves. The third stage of intense mass loss began around 400 °C and continued until ∼600 °C, that is, until virtually complete polymer degradation. This final stage was associated with the destruction of the membrane side chains and the subsequent thermal decomposition of the main (T3) skeleton of polytetrafluoroethylene macromolecules [5]. The amount of coke residue for all studied samples after thermal degradation did not exceed 4 % of their initial mass.

The thermal degradation temperatures of sulfonic acid groups for these membranes range from 350 to 382 °C. The maximum value for this temperature is observed for the LSC-1 membrane without nanoparticles. Regardless of the chemical prehistory of the $Zr_{1-x}Y_xO_{2-0.5x}$ nanoparticles, the degradation temperatures of sulfonic acid groups decrease significantly, reaching a minimum value for the filled sample obtained under hydrothermal conditions. The same sample also demonstrated the highest backbone decomposition temperature compared to the unfilled and composite films. It's worth noting that the T2 and T3 temperatures for the composite membranes correlated with the hydroxyl group content on the surface of the $Zr_{1-x}Y_xO_{2-0.5x}$ nanoparticles, as determined using FTIR spectroscopy. It was shown that the

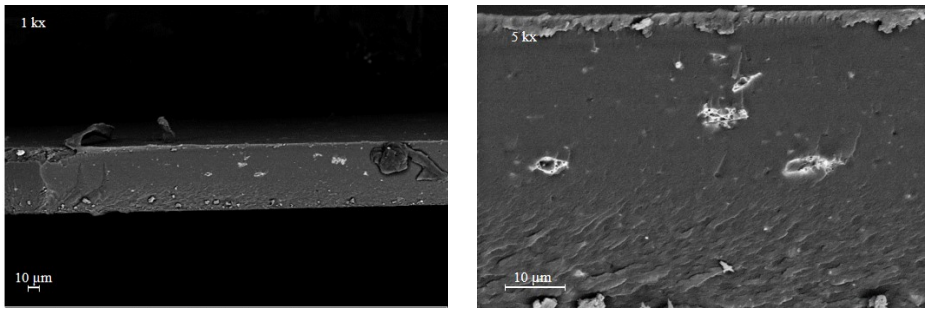

(a)

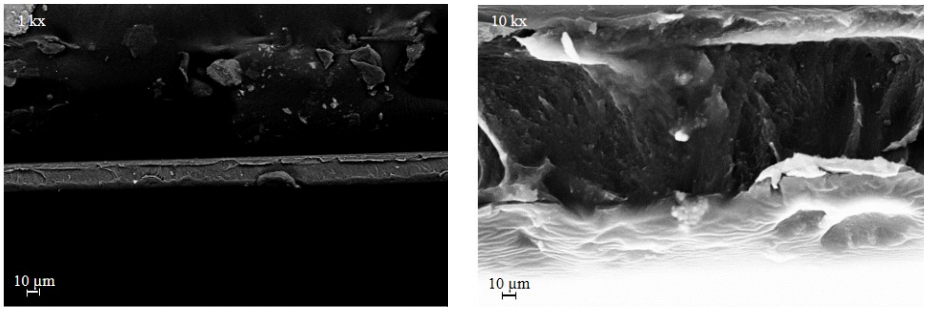

(b)

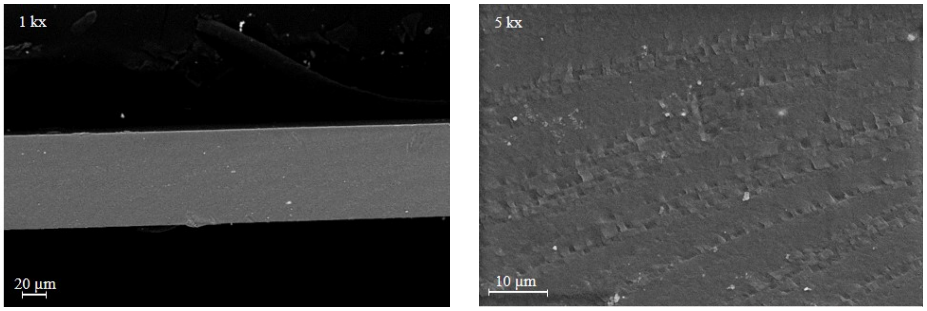

(c)

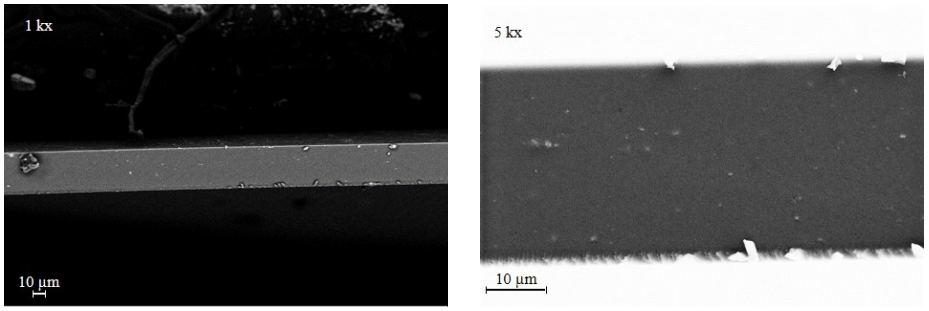

(d)

FIG. 4. SEM cross-section micrographs of the composite films based on perfluorinated polymer and $Zr_{1-x}Y_xO_{2-0.5x}$ nanoparticles obtained by different methods: glycine-nitrate combustion (a), sol-gel (b), hydrothermal (c) and solvothermal (d) syntheses

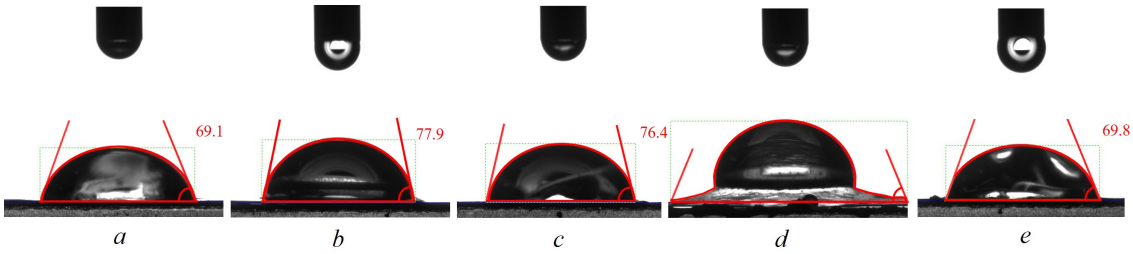

FIG. 5. Image of a droplet when determining the wetting angle of the surface of unfilled (a) and composite films based on a perfluorinated polymer and $Zr_{1-x}Y_xO_{2-0.5x}$ nanoparticles obtained by different methods (glycine-nitrate combustion (b), sol-gel (c), hydrothermal (d) and solvothermal (e) syntheses). Due to instantaneous film swelling of sample d, the value was measured incorrectly

more hydrophobic the surface of the oxide nanoparticles incorporated into the perfluorinated polymer, the higher the degradation temperature of the sulfo-containing fragment and the lower the T3.

TABLE 3. Temperature values of the main stages of mass loss for composite membranes based on perfluorinated copolymer and $Zr_{1-x}Y_xO_{2-0.5x}$ nanoparticles.

Sample	T1	T2	T3
LSC-1	–	382	473
LSC-1 + 0.5 wt. % $Zr_{1-x}Y_xO_{2-0.5x}$ (GNC)	–	373	477
LSC-1 + 0.5 wt. % $Zr_{1-x}Y_xO_{2-0.5x}$ (SG)	–	373	478
LSC-1 + 0.5 wt. % $Zr_{1-x}Y_xO_{2-0.5x}$ (HS)	167	350	518
LSC-1 + 0.5 wt. % $Zr_{1-x}Y_xO_{2-0.5x}$ (SS)	–	369	480

Thermal processes occurring within unfilled and composite membranes during heating were studied using DSC (Fig. 6). For the entire series of samples, two time-extended endothermic effects were observed in the low-temperature region. These effects were caused by the release of adsorbed water from the samples up to 120 °C and the subsequent removal of the amide solvent at temperatures of 120-200 °C. Since the change in the thermal effects of the two aforementioned processes for composite films correlates with the degree of hydrophobicity of the $Zr_{1-x}Y_xO_{2-0.5x}$ nanoparticle surface, it can be confidently concluded that the filler influences the removal of water and DMF from the perfluorinated polymer matrix.

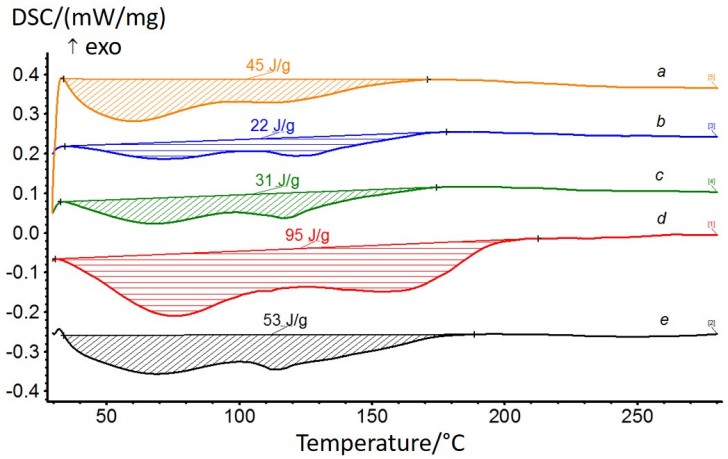

FIG. 6. DSC curves of the first heating of unfilled (a) and composite membranes based on a perfluorinated copolymer and $Zr_{1-x}Y_xO_{2-0.5x}$ nanoparticles obtained under different conditions (glycine-nitrate combustion (b), sol-gel (c), hydrothermal (d) and solvothermal (e) syntheses)

According to XRD data, both the native and composite membranes based on the perfluorinated copolymer have a mesomorphic structure (Fig. 7). Calculation of the crystallinity degree for the unfilled film and samples containing $Zr_{1-x}Y_xO_{2-0.5x}$ nanoparticles with different chemical prehistory yielded virtually identical results. In most cases, the proportion of the crystalline phase was 20 % , with the exception of films with particles obtained using sol-gel technology (25 %) and under hydrothermal conditions (30 %). Therefore, the higher temperature endothermic effect in the DSC curves of composite films is more associated with the removal of solvent from the polymer matrix than with the disordering of chains structured by the filler.

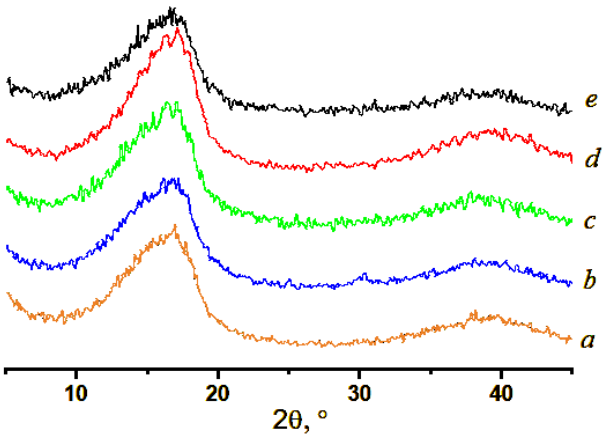

FIG. 7. XRD patterns of unfilled (a) and composite membranes based on perfluorinated polymer and $Zr_{1-x}Y_xO_{2-0.5x}$ nanoparticles obtained by various methods (glycine-nitrate combustion (b), sol-gel (c), hydrothermal (d) and solvothermal (e) syntheses)

The mechanical properties of composite membranes based on the Nafion-type perfluorinated copolymer with $Zr_{1-x}Y_xO_{2-0.5x}$ nanoparticles of varying chemical prehistory were tested using a tensile testing machine in uniaxial tension mode. The characteristics of the tested samples, averaged based on the measurement results, are presented in Table 4, and the type of stress-strain curves themselves are shown in Fig. 8. According to the results of mechanical tests, all films are low-modulus polymeric materials (elastic modulus does not exceed 550 MPa) with deformation at failure in a wide range of values from 30 to 140 % (Table 4). The stress-strain curves of all tested films (Fig. 8) clearly show a transition beyond the plastic limit (a sharp decrease in the slope of the stress-strain curve) at strains of ∼6 – 8 % . The nature of the subsequent deformation process of the tested materials is virtually identical. The curves lack a distinct section of necking through the specimen (as well as a local maximum – the plastic limit). Immediately after strains of 10 – 15 % , a consistent increase in stress begins as the specimens deform, i.e., the so-called strain-hardening region of the material is observed. In all cases, the introduction of ZrO_2-based nanoparticles into the perfluorinated polymer resulted in a decrease in the elastic modulus and plastic limit of the material, along with a significant (2 – 3 times) increase in the ultimate strain before failure (Table 4). In other words, the filler exerts a plasticizing effect on the polymer matrix, apparently by weakening the intermolecular bond system within it.

TABLE 4. Mechanical properties of unfilled and composite films based on a perfluorinated polymer and $Zr_{1-x}Y_xO_{2-0.5x}$ nanoparticles.

Sample	Film thickness, μm	Humidity, %	E, MPa	σ_p, MPa	σ_p, MPa	ε_p, %
LSC-1	58 – 75	54	554±19	16.1±0.7	17.6±0.9	33±4
LSC-1 + 0.5 wt. % $Zr_{1-x}Y_xO_{2-0.5x}$ (GNC)	90	55	466±7	15.7±0.5	19.0±0.8	135±5
LSC-1 + 0.5 wt. % $Zr_{1-x}Y_xO_{2-0.5x}$ (SG)	96-105	54	378±14	14.8±0.5	18.9±0.7	127±9
LSC-1 + 0.5 wt. % $Zr_{1-x}Y_xO_{2-0.5x}$ (HS)	95-105	54	305±16	12.8±0.6	14.4±0.8	70±6
LSC-1 + 0.5 wt. % $Zr_{1-x}Y_xO_{2-0.5x}$ (SS)	98-100	55	325±8	13.1±0.4	15.5±0.4	128±11

$Zr_{1-x}Y_xO_{2-0.5x}$ nanoparticles, synthesized by various methods, were used as a filler for the Nafion-type perfluorinated polymer to enhance its proton conductivity. The surface proton conductivity of unfilled and composite films containing $Zr_{1-x}Y_xO_{2-0.5x}$ nanoparticles was measured at different temperatures using four-probe impedance spectroscopy. It was shown that at room temperature, films containing nanoparticles with the smallest sizes and a more hydrophilic

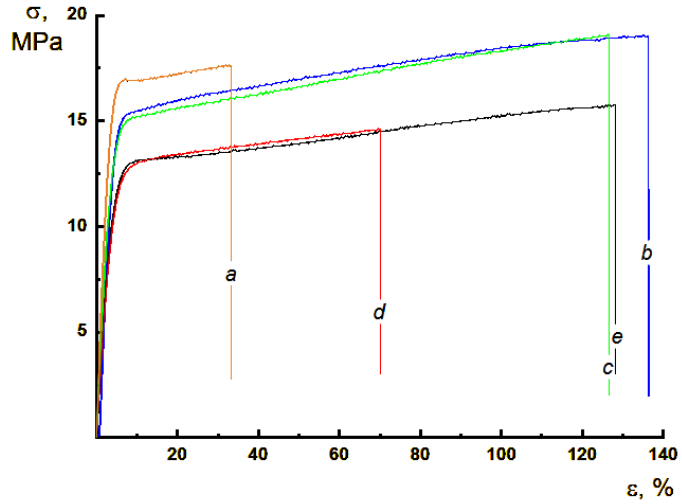

FIG. 8. Strain-strength curves of unfilled and composite films based on perfluorinated polymer and $Zr_{1-x}Y_xO_{2-0.5x}$ nanoparticles obtained by various methods (glycine-nitrate combustion (b), sol-gel (c), hydrothermal (d) and solvothermal (e) syntheses)

surface exhibit the higher proton conductivity, compared to an unfilled membrane (Table 5). In particular, in the case of solvothermal synthesis, the average nanoparticle size was 3 nm, and the surface, due to the process being conducted in a water-alcohol medium, was more hydrophilic than similar particles obtained by other methods. Furthermore, due to the specifics of proton conductivity measurements using the four-probe method, it was important to consider the emergence of nanoparticles on the surface of the perfluorinated polymer and their localization in the near-surface layer, which was only achieved when the filler was produced under solvothermal conditions (Fig. 4d).

Increasing the temperature to 50 °C increased the surface proton conductivity of both the unfilled perfluorinated polymer and its composite membranes with ZrO_2-based nanoparticles. The proton conductivity of the unfilled matrix increased by a factor of 1.5, while that of the composite membranes increased by no more than 1.3. However, the maximum proton conductivity values were still recorded for the LSC-1 + 0.5 wt. % $Zr_{1-x}Y_xO_{2-0.5x}$ (SS) sample, as at room temperature.

TABLE 5. Surface proton-conducting properties of LSC-1 composite membranes with $Zr_{1-x}Y_xO_{2-0.5x}$ nanoparticles obtained by different methods

Sample	Film thickness, μm	Water content, wt. %, 24 hours, 20 °C	Proton conductivity, S/cm RH=100 %	
			23 °C	50 °C
LSC-1	55 – 65	33.0	0.104±0.002	0.152±0.002
LSC-1 + 0.5 wt. % $Zr_{1-x}Y_xO_{2-0.5x}$ (GNC)	80 – 90	32.1	0.122±0.002	0.157±0.009
LSC-1 + 0.5 wt. % $Zr_{1-x}Y_xO_{2-0.5x}$ (SG)	85 – 95	29.3	0.108±0.002	0.145±0.003
LSC-1 + 0.5 wt. % $Zr_{1-x}Y_xO_{2-0.5x}$ (HS)	85 – 95	27.7	0.105±0.007	0.148±0.006
LSC-1 + 0.5 wt. % $Zr_{1-x}Y_xO_{2-0.5x}$ (SS)	85 – 95	33.4	0.134±0.001	0.175±0.001

Measurements of the temperature dependence of the bulk proton conductivity of composite films based on perfluorinated polymer and 0.5 wt. % $Zr_{1-x}Y_xO_{2-0.5x}$ nanoparticles showed that almost all compositions were inferior in this parameter to the unfilled membrane (Fig. 9). At the same time, the range of operating temperatures of the proton-conducting membrane was expanded from 95 to 115 °C due to the introduction of 0.5 wt. % $Zr_{1-x}Y_xO_{2-0.5x}$ (GNC) nanoparticles, which promoted the protection of sulfogroups-containing fragments from premature thermal destruction (Table 3, Fig. 9, dependence b).

Conclusions

Nanoparticles formed in hydrothermal and solvothermal environments are approximately 3 nm in size and contain a large number of hydroxyl groups on the surface, unlike nanoparticles of similar composition synthesized using sol-gel

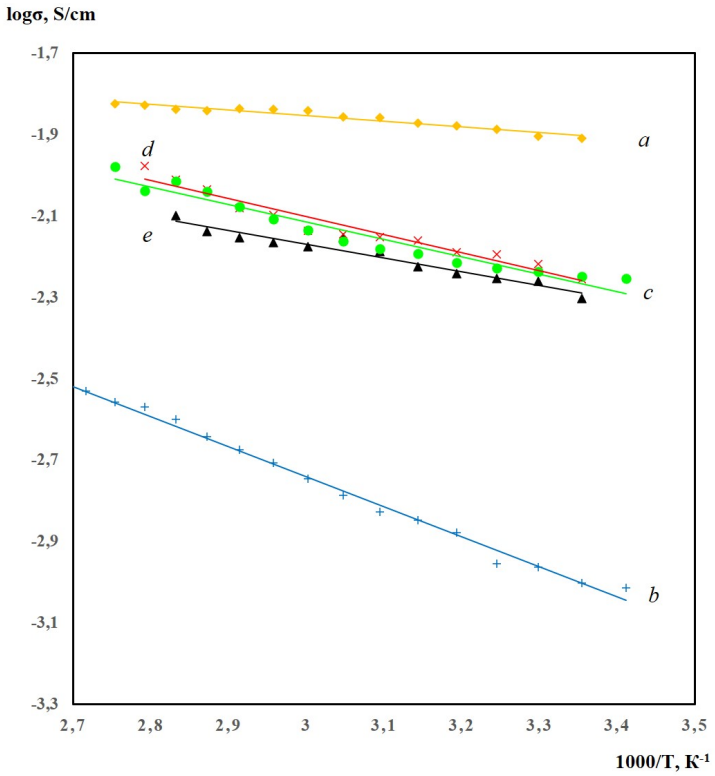

FIG. 9. Temperature dependence of the bulk proton conductivity of unfilled (a) and composite films based on perfluorinated polymer Nafion-type with $Zr_{1-x}Y_xO_{2-0.5x}$ nanoparticles obtained by various methods (glycine-nitrate combustion (b), sol-gel (c), hydrothermal (d) and solvothermal (e) syntheses)

technology or solution combustion. Due to the high synthesis temperatures involved in the latter two methods, particles are larger and have a more hydrophobic surface. Incorporating particles obtained in aqueous and alcohol environments into a perfluorinated copolymer matrix imparted elasticity and increased water retention. This lowered the decomposition temperature of sulfonic acid groups but contributed to an increase in the thermal stability of the main chain. Hydrophilic zirconium dioxide nanoparticles did not aggregate significantly and were uniformly distributed throughout the polymer matrix. Furthermore, surface proton conductivity in membranes containing them was higher than that of composite films with a filler, which had a lower content of hydroxyl groups on the surface. This was particularly noticeable when particles emerged on the surface of the perfluorinated copolymer for LSC-1 + 0.5 wt. % $Zr_{1-x}Y_xO_{2-0.5x}$ (SS). The absolute value of the bulk proton conductivity of all composite membranes was inferior to that of the unfilled perfluorinated copolymer. However, in the case of a sample with nanoparticles synthesized by glycine-nitrate combustion, with a low concentration of OH groups on the surface, it was possible to increase the operating temperature range of such membranes from 95 to 115 °C. It may be promising for the development of membranes for medium-temperature fuel cells.

References

[1] Ketpang K., Son B., Lee D., Shanmugam S. Porous zirconium oxide nanotube modified Nafion composite membrane for polymer electrolyte membrane fuel cells operated under dry conditions. *J. of Membrane Science*, 2015, **488**, P. 154–165.

[2] Mandanipour V., Bemani M., Parsatabar Z. Recent advances in Nafion-based composite membranes for fuel cells: Enhancing performance and durability. *J. Chem. Rev.*, 2026, **8** (1), P. 40–85.

[3] O'Dea J.R., Economou N.J., Buratto S.K. Surface morphology of Nafion at hydrated and dehydrated conditions. *Macromolecules*, 2013, **46** (6), P. 2267–2274.

[4] Zakil F.A., Kamarudin S.K., Basri S. Modified Nafion membranes for direct alcohol fuel cells: An overview. *Renewable and Sustainable Energy Reviews*, 2016, **65**, P. 841–852.

[5] Primachenko O.N., Marinenko E.A., Odinokov A.S., Kononova S.V., Kulvelis Y.V., Lebedev V.T. State of the art and prospects in the development of proton-conducting perfluorinated membranes with short side chains: A review. *Polymers for Advanced Technologies*, 2020, **32** (4), P. 1386–1408.

[6] Okonkwo P.C., Belgacem I.B., Emori W., Uzoma P.C. Nafion degradation mechanisms in proton exchange membrane fuel cell (PEMFC) system: A review. *International J. of Hydrogen Energy*, 2021, **46** (55), P. 27956–27973.

[7] Sigwadi R., Dhlamini M., Mokrani T., Nemavhola F. Wettability and mechanical strength of modified Nafion nanocomposite membrane for fuel cell. *Digest J. of Nanomaterials and Biostructures*, 2017, **12** (4), P. 1137–1148

[8] Karimi M.B., Mohammadi F., Hooshyari K. Recent approaches to improve Nafion performance for fuel cell applications: A review. *International J. of Hydrogen Energy*, 2019, **44** (54), P. 28919–28938.

[9] Kraytsberg A., Ein-Eli Y. Review of advanced materials for proton exchange membrane fuel cells. *Energy and Fuels*, 2014, **28** (12), P. 7303–7330.

[10] Rodriguez J., Rojas N., Sanchez-Molina M., Gonzalez Rodriguez L., Campana R., Rodriguez L. Hybrid membranes based in Nafion-metallic oxides: performance evaluations. *Chemical Engineering Transactions*, 2016, **47**, P. 415–420.

[11] Kim Y., Ketpang K., Jaritphun S., Park J.S., Shanmugam S. A polyoxometalate coupled graphene oxide – Nafion composite membrane for fuel cells operating at low relative humidity. *J. Mater. Chem. A*, 2015, **3**, P. 8148–8155.

[12] Mohanraj V., Kim A.R., Shanmugam R., Yu Y., Yoo D.J. Advanced Nafion nanocomposite membrane embedded with unzipped and functionalized graphite nanofibers for high-temperature hydrogen-air fuel cell system: The impact of filler on power density, chemical durability and hydrogen permeability of membrane. *Composites Part B Engineering*, 2021, **215** (21), 108828.

[13] Liu S., Yu J., Hao Y., Gao F., Zhou M., Zhao L. Impact of SiO_2 modification on the performance of Nafion composite membrane. *Int. J. of Polymer Science*, 2024, **2024** (1), Article ID 6309923, 10 p.

[14] Shao Z.-G., Xu H., Li M., Hsing I-M. Hybrid Nafion–inorganic oxides membrane doped with heteropolyacids for high temperature operation of proton exchange membrane fuel cell. *Solid State Ionics*, 2006, **177** (7), P. 779–785.

[15] Oh K., Kwon O., Son B., Lee D.H., Shanmugam S. Nafion-sulfonated silica composite membrane for proton exchange membrane fuel cells under operating low humidity condition. *J. of Membrane Science*, 2019, **583**, P. 103–109.

[16] Navarra M.A., Abbati C., Scrosati B. Properties and fuel cell performance of a Nafion-based, sulfated zirconia-added, composite membrane. *J. of Power Sources*, 2008, **183** (1), P. 109–113.

[17] Ng W.W., Thiam H.S., Pang Y.L., Chong K.C., Lai S.O. A state-of-art on the development of Nafion-based membrane for performance improvement in direct methanol fuel cells. *Membranes*, 2022, **12** (5), 506.

[18] Ye G., Hayden C.A., Goward G.R. Proton dynamics of Nafion and Nafion/SiO_2 composites by solid state NMR and pulse field gradient NMR. *Macromolecules*, 2007, **40** (5), P. 1529–1537.

[19] Saccà A., Carbone A., Passalacqua E., D'Epifanio A., Licoccia S., Traversa E., Sala E., Traini F., Ornelas R. Nafion–TiO_2 hybrid membranes for medium temperature polymer electrolyte fuel cells (PEFCs). *J. of Power Sources*, 2005, **152**, P. 16–21.

[20] Jian-hua T., Peng-fei G., Zhi-yuan Z., Wen-hui L., Zhong-qiang S. Preparation and performance evaluation of a Nafion-TiO_2 composite membrane for PEMFCs. *International J. of Hydrogen Energy*, 2008, **33** (20), P. 5686–5690.

[21] Yurova P.A., Malakhova V.R., Gerasimova E.V., Stenina I.A., Yaroslavtsev A.B. Nafion/surface modified ceria hybrid membranes for fuel cell application. *Polymers*, 2021, **13** (15), 2513.

[22] Voropaeva D., Merkel A., Yaroslavtsev A. Nafion/ZrO_2 hybrid membranes solvated by organic carbonates. Transport and mechanical properties. *Solid State Ionics*, 2022, **386**, 116055.

[23] Gubanova G.N., Primachenko O.N., Bugrov A.N., Vylegzhanina M.E., Gofman I.V., Lavrentiev V.K., Ivankova E.N., Vlasova E.N., Kononova S.V. Structural and morphological features of perfluorosulfonic acid membranes doped with zirconium dioxide nanoparticles. *J. of Surface Investigation X-ray Synchrotron and Neutron Techniques*, 2024, **17** (S1), P. S391–S403.

[24] Devrim Y., Albostan A. Enhancement of PEM fuel cell performance at higher temperatures and lower humidities by high performance membrane electrode assembly based on Nafion/zeolite membrane. *Int. J. of Hydrogen Energy*, 2015, **40** (44), P. 15328–15335.

[25] Asghar M.R., Zhang W., Su H., Zhang J., Liu H., Xing L., Yan X., Xu Q. A review of proton exchange membranes modified with inorganic nanomaterials for fuel cells. *Energy Adv.*, 2025, **4**, P. 185–223.

[26] Yaroslavtsev A.B., Stenina I.A. Current progress in membranes for fuel cells and reverse electrodialysis. *Mendeleev Commun.*, 2021, **31** (4), P. 423–432.

[27] Saccà A., Carbone A., Gatto I., Pedicini R., Freni A., Patti A., Passalacqua E. Composites Nafion-titania membranes for polymer electrolyte fuel cell (PEFC) applications at low relative humidity levels: Chemical physical properties and electrochemical performance. *Polymer Testing*, 2016, **56** (2), P. 10–18.

[28] Zhu L.-Y., Li Y.-C., Liu J., He J., Wang L.-Y., Lei J.-D. Recent developments in high-performance Nafion membranes for hydrogen fuel cells applications. *Petroleum Science*, 2022, **19**, P. 1371–1381.

[29] Sigwadi R., Mokrani T. Zirconia based/Nafion nanocomposite membranes for fuel cell applications. Proceedings of the 5^{th} International Conference on Nanotechnology: Fundamentals and Applications Prague, Czech Republic, August 11–13, 2014 Paper No. 151.

[30] Almjasheva O.V. Heat-stimulated transformation of zirconium dioxide nanocrystals produced under hydrothermal conditions. *Nanosystems: Physics, Chemistry, Mathematics*, 2015, **6** (5), P. 697–703.

[31] Yamamoto O., Arachi Y., Sakai H., Takeda Y., Imanishi N., Mizutani Y., Kawai M., Nakamura Y. Zirconia based oxide ion conductors for solid oxide fuel cells. *Ionics*, 1998, **4** (5–6), P. 403–408.

[32] Bugrov A.N., Smyslov R.Yu., Zavialova A.Yu., Kopitsa G.P., Khamova T.V., Kirilenko D.A., Kolesnikov I.E., Pankin D.V., Baigildin V.A., Licitra C. Influence of stabilizing ion content on the structure, photoluminescence and biological properties of $Zr_{1-x}Eu_xO_{2-0.5x}$ nanoparticles. *Crystals*, 2020, **10**, 1038.

[33] Bugrov A.N., Almjasheva O.V. Effect of hydrothermal synthesis conditions on the morphology of ZrO_2 nanoparticles. *Nanosystems: Physics, Chemistry, Mathematics*, 2013, **4** (6), P. 810–815.

[34] Bugrov A.N., Smyslov R.Yu., Zavialova A.Yu., Kopitsa G.P. The influence of chemical prehistory on the structure, photoluminescent properties, surface and biological characteristics of $Zr_{0.98}Eu_{0.02}O_{1.99}$ nanophosphors. *Nanosystems: Physics, Chemistry, Mathematics*, 2019, **10** (2), P. 164–175.
[35] Primachenko O.N., Odinokov A.S., Marinenko E.A., Kulvelis Yu.V., Barabanov V.G., Kononova S.V. Influence of sulfonyl fluoride monomers on the mechanism of emulsion copolymerization with the preparation of proton-conducting membrane precursors. *J. of Fluorine Chemistry*, 2021, **244** (4), 109736.
[36] Lutterotti L., Matthies S., Wenk H., Schultz A.S., Richardson J.W. Combined texture and structure analysis of deformed limestone from time-of-flight neutron diffraction spectra. *J. Appl. Phys.*, 1997, **81**, P. 594–600.
[37] Kirilenko D.A., Dideykin A., Aleksenskiy A., Sitnikova A., Konnikov S., Vul' A. One-step synthesis of a suspended ultrathin graphene oxide film: Application in transmission electron microscopy. *Micron*, 2015, **68**, P. 23–26.
[38] Igawa N., Ishii Y. Crystal structure of metastable tetragonal zirconia up to 1473 K. *J. Am. Ceram. Soc.*, 2001, **84** (5), P. 1169–1171.
[39] Martin U., Boysen H., Frey F. Neutron powder investigation of tetragonal and cubic stabilized zirconia, TZP and CSZ, at temperatures up to 1400 K. *Acta Crystallographica Section B*, 1993, **49** (3), P. 403–413.
[40] Tailor S., Singh M., Doub A.V. Synthesis and characterization of yttria-stabilized zirconia (YSZ) nano-clusters for thermal barrier coatings (TBCs) applications. *J. of Cluster Science*, 2016, **27** (4), P. 1097–1107.
[41] Shuklina A.I., Smirnov A.V., Fedorov B.A., Kirillova S.A., Almjasheva O.V. Structure of nanoparticles in the ZrO_2-Y_2O_3 system, as obtained under hydrothermal conditions. *Nanosystems: Physics, Chemistry, Mathematics*, 2020, **11** (6), P. 729–738.

Accepted 8 December 2025

Information about the authors:

Alexander Nikolaevich Bugrov – Branch of Petersburg Nuclear Physics Institute named by B.P. Konstantinov of National Research Centre "Kurchatov Institute" – Institute of Macromolecular Compounds, St. Petersburg, 199004, Russia; Department of Physical Chemistry, Saint Petersburg Electrotechnical University (ETU "LETI"), St. Petersburg, 197022, Russia; ORCID 0000-0003-1052-4919; bugrov.an@mail.ru

Galina Nikolaevna Gubanova – Branch of Petersburg Nuclear Physics Institute named by B.P. Konstantinov of National Research Centre "Kurchatov Institute" – Institute of Macromolecular Compounds, St. Petersburg, 199004, Russia; ORCID 0000-0003-0948-9976; gubanovagn@yandex.ru

Oleg Nikolaevich Primachenko – Branch of Petersburg Nuclear Physics Institute named by B.P. Konstantinov of National Research Centre "Kurchatov Institute" – Institute of Macromolecular Compounds, St. Petersburg, 199004, Russia; ORCID 0000-0003-1637-8537; alex-prima@mail.ru

Iosif Vladimirovich Gofman – Branch of Petersburg Nuclear Physics Institute named by B.P. Konstantinov of National Research Centre "Kurchatov Institute" – Institute of Macromolecular Compounds, St. Petersburg, 199004, Russia; ORCID 0000-0002-1939-2660; gofman@imc.macro.ru

Elena Mikhailovna Ivan'kova – Branch of Petersburg Nuclear Physics Institute named by B.P. Konstantinov of National Research Centre "Kurchatov Institute" – Institute of Macromolecular Compounds, St. Petersburg, 199004, Russia; ORCID 0000-0002-4823-0695; ivelen@mail.ru

Elena Nikolaevna Popova – Branch of Petersburg Nuclear Physics Institute named by B.P. Konstantinov of National Research Centre "Kurchatov Institute" – Institute of Macromolecular Compounds, St. Petersburg, 199004, Russia; ORCID 0000-0001-8470-8994; men682003@mail.ru

Demid Aleksandrovich Kirilenko – Ioffe Institute, St. Petersburg, 194021, Russia; ORCID 0000-0002-1571-209X; demid.kirilenko@mail.ioffe.ru

Victor Konstantinovich Lavrentyev – Branch of Petersburg Nuclear Physics Institute named by B.P. Konstantinov of National Research Centre "Kurchatov Institute" – Institute of Macromolecular Compounds, St. Petersburg, 199004, Russia; ORCID 0000-0002-9930-4666; lavrentev1949@mail.ru

Elena Nikolaevna Vlasova – Branch of Petersburg Nuclear Physics Institute named by B.P. Konstantinov of National Research Centre "Kurchatov Institute" – Institute of Macromolecular Compounds, St. Petersburg, 199004, Russia; ORCID 0000-0002-4644-0445; evl021960@gmail.com

Svetlana Viktorovna Kononova – Branch of Petersburg Nuclear Physics Institute named by B.P. Konstantinov of National Research Centre "Kurchatov Institute" – Institute of Macromolecular Compounds, St. Petersburg, 199004, Russia; ORCID 0000-0001-5468-3909; svetlanavkononova@gmail.com

Conflict of interest: the authors declare no conflict of interest.

NANOSYSTEMS:
PHYSICS, CHEMISTRY, MATHEMATICS

Kashansky V.S., et al. *Nanosystems: Phys. Chem. Math.*, 2025, **16** (6), 865–871.
http://nanojournal.ifmo.ru
DOI 10.17586/2220-8054-2025-16-6-865-871

Original article

Microwave-assisted synthesis of M/TiO_2/C (M=Ni, Cu, Ni–Cu) photocatalysts for CO_2 reduction: structural evolution and photocatalytic properties

Vladislav S. Kashansky[1,2], Alexander V. Sukhov[1,2], Angelina V. Zhurenok[3], Denis D. Mishchenko[4], Olga S. Soficheva[1], Ekaterina A. Kozlova[3], Oleg G. Sinyashin[1], Dmitry G. Yakhvarov[1,2]

[1]Arbuzov Institute of Organic and Physical Chemistry, FRC Kazan Scientific Center RAS, Kazan, Russia

[2]A. M. Butlerov Institute of Chemistry, Kazan Federal University, Kazan, Russia

[3]Boreskov Institute of Catalysis SB RAS, Novosibirsk, Russia

[4]Synchrotron Radiation Facility SKIF, Boreskov Institute of Catalysis, Kol'tsovo, Russia

Corresponding author: Dmitry G. Yakhvarov, yakhvar@iopc.ru

PACS 82.65.+r, 68.43.-h

ABSTRACT This study presents the synthesis of a TiO_2-based composite material with transition metal (Ni, Cu) nanoparticles using microwave radiation. The obtained materials were characterised using X-ray powder diffraction, and the size of the nanoparticles was determined using the Scherrer equation. The photocatalytic activity of the synthesised composites was studied in reaction of CO_2 reduction to CO and CH_4 under the visible light with a wavelength of 400 nm. Microwave treatment of a mixture of TiO_2 with transition metal salts (Ni, Cu) and graphite was founded to decrease a photocatalytic activity in CO_2 reduction reaction, while a mechanical mixture of TiO_2 and graphite, not subjected to microwave treatment, demonstrated increased catalytic activity compared to unmodified TiO_2 Evonik P25. The decrease in catalytic activity of the case of microwave-treated samples is associated with an irreversible phase transition of the photoactive anatase phase into the catalytically inert rutile phase and formation of TiO_{2-x} phases. This process is induced by overheating during microwave synthesis, where graphite (C_g) acts as an effective microwave absorber and a reducing agent for Ti^{4+} cations in TiO_2. The obtained results are interesting for the development of efficient TiO_2-based photocatalysts for CO_2 reduction.

KEYWORDS titanium dioxide, photocatalysis, transition metal nanoparticles, carbon dioxide reduction, X-ray diffraction, green chemistry

ACKNOWLEDGEMENTS This research was funded by the grant of the Ministry of Science and Higher Education of the Russian Federation for large scientific projects of the priority areas of scientific and technological development (Nr. 075-15-2024-646). The photocatalytic activity tests of the obtained materials were carried out under the government contract at Boreskov Institute of Catalysis, Siberian Branch, Russian Academy of Sciences (project FWUR-2024-0033). The XRD studies were performed using the equipment of the Multiaccess Centre "National Centre for Catalyst Research" of the Institute of Catalysis, Siberian Branch, Russian Academy of Sciences.

FOR CITATION Kashansky V.S., Sukhov A.V., Zhurenok A.V., Mishchenko D.D., Soficheva O.S., Kozlova E.A., Sinyashin O.G., Yakhvarov D.G. Microwave-assisted synthesis of M/TiO_2/C (M=Ni, Cu, Ni–Cu) photocatalysts for CO_2 reduction: structural evolution and photocatalytic properties. *Nanosystems: Phys. Chem. Math.*, 2025, **16** (6), 865–871.

1. Introduction

Global climate change caused by greenhouse gas emissions is one of the most serious environmental problems of our time. One of the main greenhouse gases contributing to climate change is carbon dioxide [1]. In view of this, developing of effective methods to convert CO_2 into useful chemical compounds or molecules that are more reactive than carbon dioxide is a pressing issue [2].

The photocatalytic reduction of carbon dioxide using TiO_2 is a promising method for converting CO_2 into valuable chemical compounds and is fully consistent with the fundamental principles of "green" chemistry [3]. The main advantage of this approach is the ability to perform the reaction under the influence of sunlight, which minimizes energy costs and reduces the carbon footprint of the process [4]. During the photocatalytic process on TiO_2, CO_2 can be reduced to various products, including carbon monoxide (CO), methane (CH_4), methanol (CH_3OH), and formic acid (HCOOH), etc. [5]. However, the disadvantage of using unmodified titanium dioxide is its low photoactivity and the predominant formation of CO as a product, which limits its practical application as a photocatalyst [6]. A solution to this problem can be

the modification of TiO_2 with transition metal nanoparticles (TMNPs), such as nickel and copper, including modification with bimetallic particles, that allows not only to increase the efficiency of CO_2 reduction, but also to control the selectivity of the process towards target products, such as methane and C_{2+} products, which are of great practical importance [7–9]. In addition, the modification of titanium dioxide with carbon materials, such as graphene, is promising, allowing the absorption edge of TiO_2 to be shifted to a longer-wavelength region [10].

The aim of this work is to obtain nanocomposite materials based on TiO_2, modified with TMNPs (Ni, Cu) and graphite (C_g), and to investigate their structural and catalytic properties in the process of CO_2 reduction under visible light irradiation. These materials were synthesized via microwave (MW) assisted thermal decomposition of metal acetylacetonate precursors in the presence of graphite under reduced pressure, enabling rapid formation of the nanostructured system.

2. Experimental

2.1. Materials and measurements

Graphite spectral electrodes (graphite purity is 99.999 %) were used as a source of graphite. The rods were crushed using a metal file, and then the resulting powder was additionally ground in a mortar. The commercially available reagents used in the experiments were copper (II) acetylacetonate (Chemkraft, $>$ 99 %), nickel (II) acetylacetonate (Chemkraft, $>$ 99.5 %), titanium dioxide (Evonik P25), methanol (purified by distillation). Deionized distilled water was used for photocatalyst synthesis, ultrapure water was used for kinetic experiments. Ultrapure water was produced by "NuZar Q" water system set.

2.2. Synthesis of modified titanium dioxide

Commercial TiO_2 (Evonik P25) was used as a base for the photocatalyst synthesis. To perform MW treatment, a mixture was prepared from titanium dioxide (0.4 g) and metal salts ($Ni(acac)_2$ and/or $Cu(acac)_2$) in an amount corresponding to 10 wt.% of metal. In the case of synthesis of a bimetallic (Ni–Cu) catalyst, the mass fraction of the metals was maintained in a ratio of 1:1, while their total content was also 10 wt.%. The weighed portions of the salt and TiO_2 were mixed, then 15 – 20 ml of methanol was added until the complete dissolution of the salt. The resulting solution was dispersed in an ultrasonic bath for 1 hour, and after that the solvent was removed by heating in an oil bath. The dried powder was mixed with graphite (0.2 g) and thoroughly ground in an agate mortar until the mixture attained a uniform colour. The resulting mixture was placed in a quartz test tube, which was connected to a vacuum line to create a reduced pressure in the range of 80 – 100 Pa. The tube was placed horizontally, ensuring uniform distribution of the mixture in a thin layer approximately 2 cm long. MW treatment was performed using a Hyundai HYM-M2045 household microwave oven with an output power of 700 W. Irradiation was performed at the power 700 W for 5 minutes. Control samples containing only C_g and TiO_2 were prepared, with (MW-TiO_2/C_g) and without (TiO_2/C_g) MW treatment.

2.3. Photocatalyst characterization

The prepared photocatalysts were analysed by X-ray diffraction (XRD). XRD patterns of the photocatalysts was obtained using a D8 ADVANCE diffractometer equipped with a LYNXEYE linear detector (Bruker AXS GmbH, Karlsruhe, Germany) at room temperature in the 2θ of 15 – 85° with a step of 0.05° with Ni-filtered Cu Kα radiation (λ = 1.5418 Å). The phase composition of the photocatalysts was quantitatively analysed by the Rietveld refinement method using GSAS-II software packages [11]. The coherent scattering region (CSR) of crystallites were estimated from the full width at half maximum of corresponding peaks using the Scherrer formula.

2.4. Photocatalytic experiments

The photocatalytic reduction of CO_2 was carried out in a static glass reactor (170 ml) with a quartz window (16 cm^2). A 30 mg suspension in 500 μL of ultrapure water was pre-sonicated and deposited on a glass substrate (8 cm^2), followed by drying at 50 °C in air. Prior to the reaction, the catalyst was illuminated with a 397 nm LED for 15 min to remove organic contaminants from the catalyst surface, then transferred to the reactor containing 1 mL of ultrapure water. The system was first purged with argon for 20 min to remove oxygen, followed by ultrapure CO_2 (99.995 %) purging for 20 minutes. Then it was illuminated with LED with an intensity maximum at a wavelength of 397 nm. The gas phase composition was determined using a Khromos GC-1000 gas chromatograph equipped with both a flame ionization detector and a thermal conductivity detector. The sample was collected once every 1 hour, the duration of the photocatalytic experiment was 5 hours.

3. Results and discussion

In this research, we propose an original method for modification of TiO_2 by TMNPs (Ni, Cu) based on the reduction of metal salts with graphite under the action of MW radiation. The key advantage of this method is that there is one-stage synthesis of graphene-encapsulated nickel nanoparticles by high-temperature decomposition of nickel acetylacetonate on graphite [12], which can contribute to increasing their catalytic activity in the carbon dioxide reduction reaction. The use

of other metal salts containing chlorides or other anions is not desirable as halogens and some other anions can strongly decrease the catalytic activity when present in the catalytic system. Other advantages include the high synthesis rate, environmental friendliness and simplicity of this approach. The study investigated several sample types: TiO_2/C_g without MW treatment, MW-TiO_2/C_g subjected to MW treatment, 10 % Ni/TiO_2/C_g, 10 % Cu/TiO_2/C_g, and a bimetallic sample of 5 % Cu 5 % Ni/TiO_2/C_g – after MW irradiation.

X-ray diffraction (XRD) analysis confirmed that the sample (TiO_2/C_g) contains anatase and rutile, that is typical for the commercial TiO_2 Evonik P25 sample, and heat treatment leads to the phase transition from anatase to rutile (Fig. 1, Table 1). This is consistent with literature data, that this transition occurs in the range of 400 – 1200 °C [13]. At the same time, with MW treatment, the CSR of both anatase and rutile increases, reaching 200 nm in some cases. Carbon in the photocatalysts is represented by nanosized graphite with a mass fraction of 20 – 40 %. In addition, the presence of a metallic phase corresponding to M^0 (M=Ni, Cu) can be noted in the diffraction patterns.

It has been found that rutile is reduced to mixed-valence oxides (general formula TiO_{2-x} where $0.125 < x < 0.5$) during MW processing (Fig. 1). In the case of MW-TiO_2/C_g sample, Ti_8O_{15}, Ti_6O_{11} phases are formed only. The composition of these phases slightly differs from the stoichiometric one. The presence of metals, especially Cu, promotes a deeper reduction of Ti^{4+} cations in the oxide structure, in particular, with the formation of Ti_2O_3 (Fig. 2). This may be due to the fact that metal ions in oxidation state 2+ are able to reduce the energy required for deformation of the structure and accelerate the transition of anatase to rutile, [14, 15]. The CSR of the resulting TMNPs have been found as 42 nm for 10 % Ni/TiO_2/C_g sample; 90 nm for 10 % Cu/TiO_2/C_g sample; for the mixed sample 5 % Cu 5 % Ni/TiO_2/C_g d_{NiNPs} was equal to 13 nm and d_{CuNPs} was equal 24 nm. The mass fraction of the metals was close to that laid down during the synthesis, taking into account the measurement error.

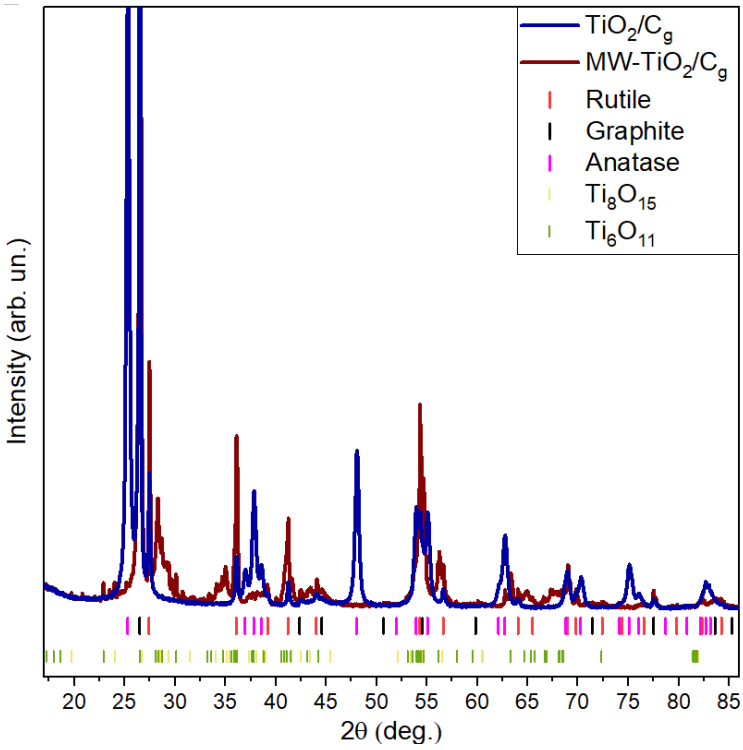

FIG. 1. XRD patterns of TiO_2 before and after MW processing

The obtained samples were investigated in the process of photocatalytic CO_2 reduction. The experiments were conducted in a photocatalytic reactor, where the LED with a maximum of intensity at the wavelength of 397 nm was used as a radiation source (Fig. 3). Based on the data obtained, the rates of the formation of carbon dioxide reduction products were calculated, as well as the total reduction rate ($\omega(CO_2RR)$). The rate of products (CH_4, CO) formation was determined by linear approximation of kinetic curves. The total reduction rate was calculated according to the following formula (1):

$$\omega_{e-}(CO_2RR) = 2 \times \omega(CO) + 8 \times \omega(CH_4), \quad (1)$$

where 2 and 8 are the coefficients for accounting the electronic balance, ω(CO) and $\omega(CH_4)$ – the corresponding rates of the formation of CO and CH_4, respectively.

The photocatalytic activities of the samples in CO_2 reduction are shown in Fig. 4(a,b) and Table 2. For reference, the experiments using commercial TiO_2 Evonik P25 were performed.

TABLE 1. Structural properties of the photocatalysts based on XRD data

Sample	Phase	Mass fraction, %	CSR size, nm
TiO_2/C_g	TiO_2 (anatase)	66(4)*	32(2)
	TiO_2 (rutile)	11(1)	56(5)
	C_g (graphite)	24(5)	68(3)
MW-TiO_2/C_g	TiO_2 (rutile)	22(5)	130(50)
	C_g (graphite)	22(10)	58(5)
	Ti_8O_{15}	37(10)	50(20)
	Ti_6O_{11}	19(5)	50(20)
10 %Cu/TiO_2/C_g MW	TiO_2 (anatase)	17(5)	62(10)
	TiO_2 (rutile)	3(1)	70(20)
	C_g (graphite)	35(10)	62(6)
	Ti_4O_7	20(5)	21(5)
	Ti_3O_5	5(2)	120(50)
	Ti_2O_3	8(2)	110(40)
	Cu	12(3)	90(10)
10 %Ni/TiO_2/C_g MW	TiO_2 (anatase)	16(3)	63(2)
	TiO_2 (rutile)	10(2)	45(10)
	C_g (graphite)	33(10)	76(5)
	Ti_4O_7	23(4)	36(10)
	Ti_3O_5	8(2)	45(3)
	Ni	11(2)	42(5)
5 %Cu 5 %Ni/TiO_2/C_g MW	TiO_2 (anatase)	12(3)	125(50)
	TiO_2 (rutile)	1(0.5)	200(100)
	C_g (graphite)	39(12)	51(5)
	Ti_4O_7	22(6)	18(6)
	Ti_3O_5	6(2)	92(50)
	Ti_2O_3	7(2)	78(30)
	Cu	5(2)	24(10)
	Ni	7(3)	13(5)

*the error in the last significant digit is indicated in brackets

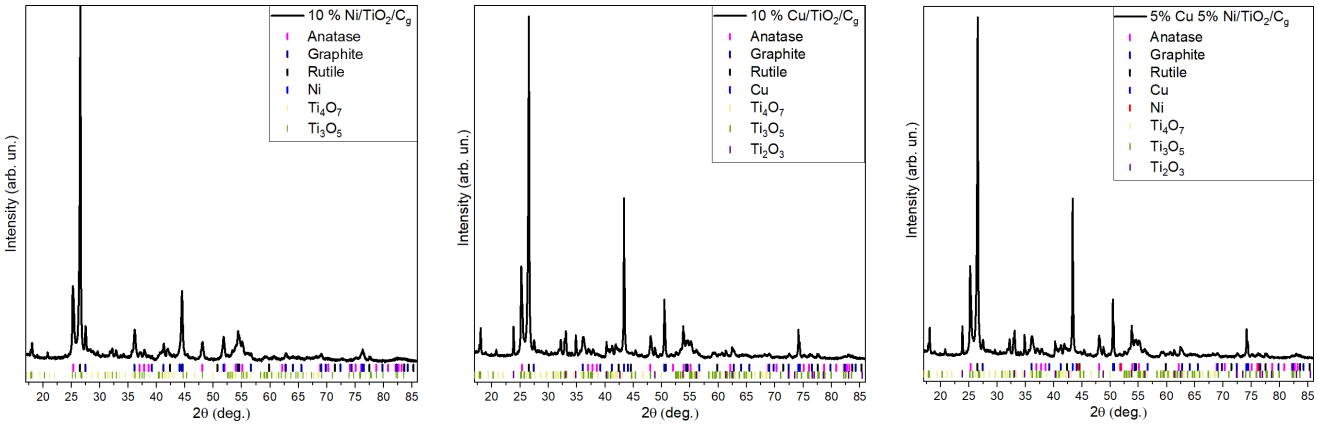

FIG. 2. XRD patterns of TiO_2 modified by TMNPs: 10 % Ni/TiO_2/C_g (a), 10 % Cu/TiO_2/C_g (b), 5 % Cu 5 % Ni/TiO_2/C_g (c)

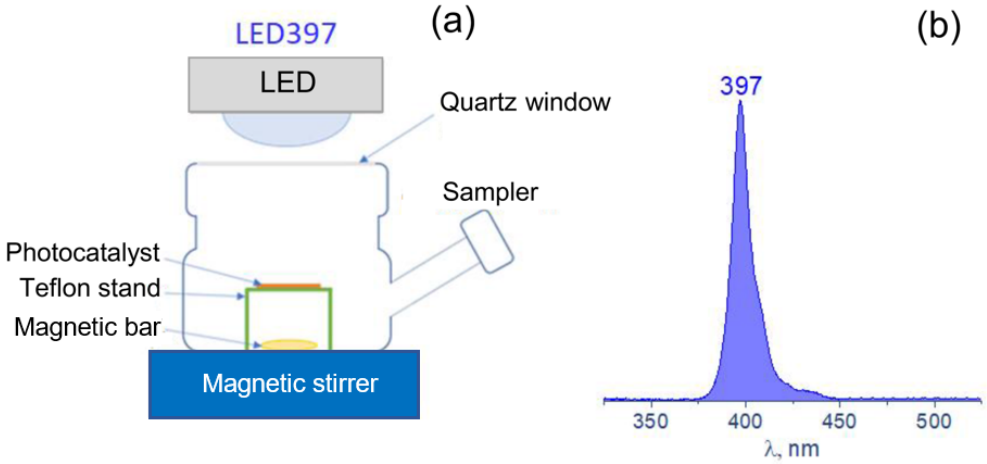

FIG. 3. Photocatalytic reactor used for CO_2 reduction (a) and the spectrum of the LED used (b)

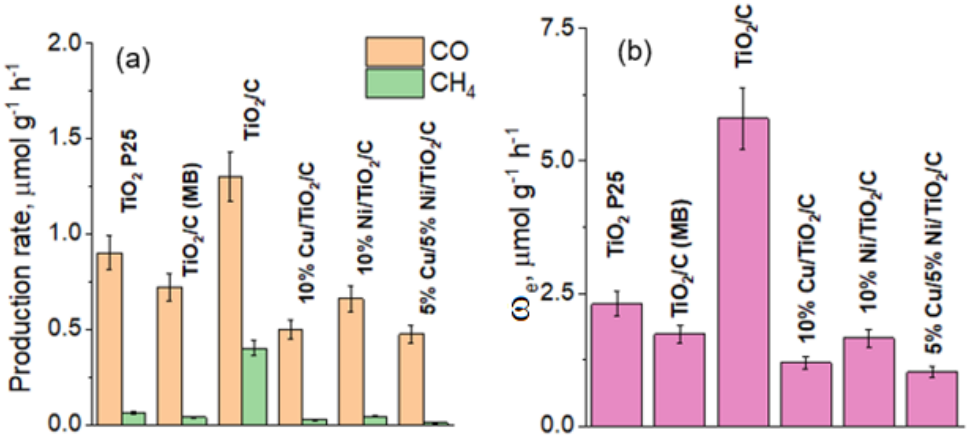

FIG. 4. (a) CO and CH_4 formation rates; (b) total CO_2 redaction rates for TiO_2/C_g and X % M/TiO_2/C_g photocatalysts (M = Ni, Cu, or Ni–Cu). Conditions: M (cat.) $= 30$ mg, t (reaction) $= 5$ hours. Light source: LED with $\lambda = 397$ nm

TABLE 2. Photocatalytic CO_2 reduction activity of the synthesized catalysts

Catalyst	ω(CO), μmol g_{cat}^{-1} h^{-1}	$\omega(CH_4)$, μmol g_{cat}^{-1} h^{-1}	ω_{e-}, μmol g_{cat}^{-1} h^{-1}
MW-TiO_2/C_g	0.72	0.04	1.74
TiO_2/C_g	1.30	0.40	5.80
10 % Cu/TiO_2/C_g	0.50	0.02	1.19
10 % Ni/TiO_2/C_g	0.66	0.04	1.66
5 % Cu/5 % Ni/ TiO_2/C_g	0.47	< 0.01	1.01
TiO_2 Evonik P25	0.90	0.06	2.28

The highest activity was possessed by the photocatalyst TiO_2/C_g, which was not exposed by MW-irradiation (Fig. 4(a,b)). The activity of this sample is more than two times higher than the activity of the commercial TiO_2 Evonik P25, which may be related to the shift in the absorption edges of TiO_2 due to the presence of graphite. It should be noted that the rate of methane formation over this catalyst was higher compared to other samples, suggesting that graphite acts like a metallic cocatalyst (Fig. 2(a)) [16].

For all photocatalysts subjected to MW treatment, a decrease in activity was observed compared to unmodified TiO_2 Evonik P25. This can be attributed to a decrease in the content of catalytically active phase of anatase and the formation of reduced titanium oxide phases with overall formula TiO_{2-x} $(0.125 < x < 0.5)$, which do not show photocatalytic activity. In addition, a significant increase in the CSR of titanium oxides results in decreasing of the photocatalytic activity.

4. Conclusion

As the result of this study, it was found that MW reduction of the investigated metals (Ni, Cu) on TiO_2 surface leads to the formation of a composite material containing Ni and Cu nanoparticles. However, contrary to expectations, such a modification caused a decrease in photocatalytic activity compared to original TiO_2. XRD analysis showed that this decrease is due to two main factors: an irreversible phase transition of photoactive anatase to catalytically inert rutile and partial reduction of TiO_2 during the synthetic process. These processes are initiated by a system local overheating caused by intensive absorption of MW radiation with graphite. The highest catalytic activity was demonstrated by the control sample TiO_2/C_g, which was not subjected to MW, which confirms the negative impact of the modification method on the functional properties of the material. The results obtained are important for the development of TiO_2 modification strategies, indicating the need to use softer synthetic protocols that exclude structural and phase transformations of an oxide matrix. This work makes a significant contribution to the understanding of restrictions related to the use of microwave synthesis for the modification of photocatalysts, and offers new criteria for the development of effective catalytic systems based on TiO_2.

References

[1] Jeffry L., Ong M.Y., Nomanbhay S., Mofijur M., Mubashir M., Show P.L. Greenhouse gases utilization: A review. *Fuel*, 2021, **301**, 121017.

[2] Yoro K.O., Daramola M.O. CO_2 emission sources, greenhouse gases, and the global warming effect. *Advances in carbon capture*. Woodhead Publishing, 2020, P. 3–28.

[3] Zlotin S.G., Egorova K.S., Ananikov V.P., Akulov A.A., Varaksin M.V., Chupakhin O.N., Charushin V.N., Bryliakov K.P., Averin A.D., Beletskaya I.P., Dolengovski E.L., Budnikova Y.H., Sinyashin O.G., Gafurov Z.N., Kantyukov A.O., Yakhvarov D.G., Aksenov A.V., Elinson M.N., Nenajdenko V.G., Zolotukhina A.V. The green chemistry paradigm in modern organic synthesis. *Russ. Chem. Rev.*, 2023, **92** (12), 5104.

[4] Alekseev R.F., Saraev A.A., Kurenkova A.Y., Kozlova E.A. Heterostructures based on g-C_3N_4 for the photocatalytic CO_2 reduction. *Russ. Chem. Rev.*, 2024, **93** (5), 5124.

[5] Kozlova E.A., Lyulyukin M.N., Kozlov D.V., Parmon V.N. Semiconductor photocatalysts and mechanisms of carbon dioxide reduction and nitrogen fixation under UV and visible light. *Russ. Chem. Rev.*, 2021, **90** (12), P. 1520–1543.

[6] Jeon J.P., Kweon D.H., Jang B.J., Ju M.J., Baek J.B. Enhancing the photocatalytic activity of TiO_2 catalysts. *Advanced Sustainable Systems*, 2020, **4** (12), P. 1–19.

[7] Song H., Tan Y.C., Kim B., Ringe S., Oh J. Tunable product selectivity in electrochemical CO_2 reduction on well-mixed Ni–Cu alloys. *ACS Applied Materials and Interfaces*, 2021, **13** (46), P. 55272–55280.

[8] Du Y.R., Li X.Q., Yang X.X., Duan G.Y., Chen Y.M., Xu B.H. Stabilizing high-valence copper(I) sites with Cu–Ni interfaces enhances electroreduction of CO_2 to C^{2+} products. *Small*, 2024, **20** (42), 2402534.

[9] Jun M., Kundu J., Kim D.H., Kim M., Kim D., Lee K., Choi S.I. Strategies to modulate the copper oxidation state toward selective C^{2+} production in the electrochemical CO_2 reduction reaction. *Advanced Materials*, 2024, **36** (21), 2313028.

[10] Qiu J., Zhu H., Chen B., Jing W., Zhou W., Bai Y., Xu L. Scalable development of photocatalysis-mediated aquatic habitat restoration devices based on TiO_2/graphene/$BiVO_4$ and the application in black-odorous river treatment. *J. of Environmental Chemical Engineering*, 2024, **12** (5), 113414.

[11] Toby B.H., Von Dreele R.B. GSAS-II: The genesis of a modern open-source all purpose crystallography software package. *J. of Applied Crystallography*, 2013, **46** (2), P. 544–549.

[12] Pentsak E.O., Gordeev E.G., Ananikov V.P. Noninnocent nature of carbon support in metal/carbon catalysts: Etching/pitting vs nanotube growth under microwave irradiation. *ACS Catalysis*, 2014, **4** (11), P. 3806–3814.
[13] Gouma P.I., Mills M.J. Anatase-to-rutile transformation in titania powders. *J. of the American Ceramic Society*, 2001, **84** (3), P. 619–622.
[14] Shannon R.D., Pask J.A. Kinetics of the anataserutile transformation. *J. of the American Ceramic Society*, 1965, **48** (8), P. 391–398.
[15] Bouzoubaa A., Markovits A., Calatayud M., Minot C. Comparison of the reduction of metal oxide surfaces: TiO_2-anatase, TiO_2-rutile and SnO_2-rutile. *Surface Science*, 2005, **583** (1), P. 107–117.
[16] Zhurenok A.V., Kurenkova A.Y., Zazulya A.E., Vasilchenko D.B., Mishchenko D.D., Lomakina V.A., Gerasimov E.Y., Markovskaya D.V., Kozlova E.A. Heterostructures based on reduced graphene oxide and graphitic carbon nitride for visible light-induced photocatalytic production of H_2. *Russian Chemical Bulletin*, 2025, **74** (3), P. 733–741.

Submitted 2 October 2025; revised 24 October 2025; accepted 26 October 2025

Information about the authors:

Vladislav S. Kashansky – Arbuzov Institute of Organic and Physical Chemistry, FRC Kazan Scientific Center, Russian Academy of Sciences, 420088, Kazan, Russian Federation; A.M. Butlerov Institute of Chemistry, Kazan Federal University, 420008, Kazan, Russian Federation; ORCID 0009-0002-9103-3977; vladkashansky@gmail.com

Alexander V. Sukhov – Arbuzov Institute of Organic and Physical Chemistry, FRC Kazan Scientific Center, Russian Academy of Sciences, 420088, Kazan, Russian Federation; A.M. Butlerov Institute of Chemistry, Kazan Federal University, 420008, Kazan, Russian Federation; ORCID 0000-0001-8481-8544; alex.suhoff@rambler.ru

Angelina V. Zhurenok – Federal State Budgetary Scientific Institution Federal Research Center "G.K. Boreskov Institute of Catalysis of the Siberian Branch of the Russian Academy of Sciences", 630090, Novosibirsk, Russian Federation; ORCID 0000-0003-3908-1963; angelinazhurenok@gmail.com

Denis D. Mishchenko – Synchrotron Radiation Facility SKIF, Boreskov Institute of Catalysis, 630559, Russian Federation; ORCID 0000-0001-8822-5148; q14999@yandex.ru

Olga S. Soficheva – Arbuzov Institute of Organic and Physical Chemistry, FRC Kazan Scientific Center, Russian Academy of Sciences, 420088, Kazan, Russian Federation; ORCID 0000-0003-3107-5251; olga.soficheva@iopc.ru

Ekaterina A. Kozlova – Federal State Budgetary Scientific Institution Federal Research Center "G.K. Boreskov Institute of Catalysis of the Siberian Branch of the Russian Academy of Sciences", 630090, Novosibirsk, Russian Federation; ORCID 0000-0001-8944-7666; kozlova@catalysis.ru

Oleg G. Sinyashin – Arbuzov Institute of Organic and Physical Chemistry, FRC Kazan Scientific Center, Russian Academy of Sciences, 420088, Kazan, Russian Federation; ORCID 0000-0002-2241-9764; oleg@iopc.ru

Dmitry G. Yakhvarov – Arbuzov Institute of Organic and Physical Chemistry, FRC Kazan Scientific Center, Russian Academy of Sciences, 420088, Kazan, Russian Federation; A.M. Butlerov Institute of Chemistry, Kazan Federal University, 420008, Kazan, Russian Federation; ORCID 0000-0002-3906-8841; yakhvar@iopc.ru

Conflict of interest: the authors declare no conflict of interest.

NANOSYSTEMS:
PHYSICS, CHEMISTRY, MATHEMATICS

Kovalevskaya K.S., et al. *Nanosystems: Phys. Chem. Math.*, 2025, **16** (6), 872–886.
http://nanojournal.ifmo.ru
DOI 10.17586/2220-8054-2025-16-6-872-886

Original article

The relationship between the impregnation solution composition and the active component distribution NiMo/ZSM-23 catalysts for the plant lipids hydroprocessing

Ksenia S. Kovalevskaya, Roman G. Kukushkin, Olesya O. Zaikina, Olga A. Bulavchenko, Vadim A. Yakovlev

Boreskov Institute of Catalysis SB RAS, Novosibirsk, Russia

Corresponding author: Roman G. Kukushkin, roman@catalysis.ru

ABSTRACT The nature of the interaction between metals and a catalyst support is a crucial factor in determining the dispersed state of active component phases. In this study, a series of Ni-Mo/ZSM-23 catalysts for the hydroprocessing of plant lipids was prepared by incipient wetness impregnation. The catalysts were prepared by a different sequence of metal deposition and using various complexing agents. The catalysts were investigated by a few physico-chemical methods (TPR, UV-Vis spectroscopy, XRD, TPD-NH_3, Raman spectroscopy, HRTEM). It was found that the charge of the ZSM-23 zeolite surface (positive/negative) and the type of metal ions in the impregnation solution affect the formation of phases on the support surface. The use of ammonia impregnating solutions leads to the formation of phases NiO, α-$NiMoO_4$ and β-$NiMoO_4$. In the case of using aqueous and citrate impregnating solutions, only the formation of NiO and β-$NiMoO_4$ phases is observed.

KEYWORDS nickel, molybdenum, ZSM-23, impregnating solutions, PZC

ACKNOWLEDGEMENTS This work was supported by the Ministry of Science and Higher Education of the Russian Federation within the governmental assignment for Boreskov Institute of Catalysis (project(s) FWUR-2024-0038).

FOR CITATION Kovalevskaya K.S., Kukushkin R.G., Zaikina O.O., Bulavchenko O.A., Yakovlev V.A. The relationship between the impregnation solution composition and the active component distribution NiMo/ZSM-23 catalysts for the plant lipids hydroprocessing. *Nanosystems: Phys. Chem. Math.*, 2025, **16** (6), 872–886.

1. Introduction

Currently, the study of nickel-containing catalysts on zeolites is relevant for the hydroprocessing plant lipids (fatty acids, microalgae lipids, waste cooking oils) to obtain iso-alkanes [1, 2]. This process is carried out to obtain motor fuels similar in their characteristics to diesel and aviation fuels obtained from fossil raw materials [3]. One of the promising supports is the zeolite ZSM-23 [4–6], which, due to its one-dimensional channel system, makes it possible to increase the selectivity of isomerization by suppressing the formation of multibranched alkanes, which can easily be subjected to a side process of hydrocracking. To increase the activity and stability, the catalysts can be modified with transition metals such as Mo [7], W [8], Co [9], Cu [10]. As has been shown in several studies, molybdenum has the greatest effect on the activity of nickel-containing catalysts in the hydroprocessing of plant lipids [7, 11]. Since the nature of metal-support interaction is one of the determining factors in the formation of the dispersed state of the phases of the active component, it is important to know the form the metals in the impregnating solution, as well as charge of the support surface. It is known that surface polarization occurs in an aqueous medium and, depending on the pH of the medium, the support surface can be positively or negatively charged [12]. The pH value at which the surface of the support is not charged is called the point of zero charge (PZC) [13]. In contact with impregnating solutions more acidic than PZC, the surface of the support is positively charged and adsorbs anions. If the impregnating solution is more alkaline than PZC, then the surface of the support is negatively charged and cations are adsorbed [13, 14].

One of the common methods of preparing Ni-Mo catalysts is incipient wetness impregnation, in which the sequence of metal deposition may differ – first Ni, then Mo [15, 16]; first Mo, then Ni [17, 18] and co–precipitation [11, 19–22]. The composition of the impregnation solution may also differ, the most used are aqueous [11, 15–18], citrate [20, 21] and ammonia [19, 22]. All these parameters can affect the distribution of metals on the surface and the degree of their interaction with the support, which in turn will determine the catalytic activity. While the impact of various preparation parameters on traditional hydrodesulfurization (HDS) catalysts has been studied, the influence of these parameters on catalysts designed for the hydroprocessing of plant-based lipids is less well understood. This presents a significant knowledge gap, as the oxygen-rich nature of lipid feedstock and specific reaction pathways, such as deoxygenation, require different demands on catalyst active sites compared to sulfur removal. In particular, the effect of impregnation solution composition on the physicochemical properties and phase evolution of Ni-Mo catalysts optimized for lipid upgrading has not been fully investigated.

The effect of the composition of impregnating solutions on the physico-chemical properties of Ni-Mo catalysts for the hydroprocessing of plant lipids has not been comprehensively discussed in literature. Therefore, the purpose of this work is to study the effect of the composition of impregnating solutions on the formation of phases of the oxide form of active component in Ni-Mo catalysts based on zeolite ZSM-23. This article focuses on the impact of the composition of the impregnation solution on the interaction between the metal and the support, as well as the final distribution of nickel and molybdenum atoms, in order to establish rational design principles for more efficient hydroprocessing catalysts for renewable fuels.

2. Experimental

2.1. Materials

Zeolite ZSM-23 in H^+ form with a SiO_2/Al_2O_3 = 48 was used as a support (Zeolyst International, USA). Nickel (II) nitrate $Ni(NO_3)_2 \cdot 6H_2O$ ($\geq$ 98 %)(Reachim, Russia) and ammonium paramolybdate $(NH_4)_6Mo_7O_{24} \cdot 4H_2O$ ($\geq$ 98 %) (Laverna, Russia) were used as metal precursors. Citric acid $C_6H_8O_7$ (Base No. 1 of Chemical Reagents, Russia) and 25 % ammonia solution (Base No. 1 of Chemical Reagents, Russia) were used as complexing agents. Technical oleic acid (Reachim, Russia) (hereinafter referred to as the FAs mixture) was used as a model raw material, which includes palmitic (5.1 mol. %) (stearic (3.1 mol. %) (oleic (59.2 mol. %) (linoleic (30.4 mol. %) (linolenic acid (1.7 mol. %) (and arachidonic (0.5 mol. %) acids.

2.2. Preparation of catalysts

The catalysts with the following composition – 5 % Ni – 2.5 % Mo/ZSM-23 were prepared by incipient wetness impregnation. One of the samples was prepared by sequentially deposition of metals – first Ni, then Mo. Other samples were prepared by applying an impregnation co-solution in the presence of various complexing agents and with different pH. The NiMo-wat sample was prepared from an aqueous co-solution, the NiMo-cit sample – from a citrate co-solution, NiMo-amm-9 – from an ammonia co-solution with pH = 9, and NiMo-amm-11 – from am ammonia co-solution with pH = 11. After metal deposition, the catalysts were dried at 120 °C for an hour and then calcined at 550 °C for 2 h. Before the catalytic experiments, the samples were reduced *in situ* in a flow of hydrogen (500 ml/min) for an hour at 550 °C at atmospheric pressure. Before physico-chemical studies, the samples were reduced under a hydrogen flow of 500 ml/min for an hour at a temperature of 550 °C at atmospheric pressure, then passivated with ethanol.

2.3. Characterization of the catalysts

The *pH PZC* for zeolite ZSM-23 was determined using the weight titration method [23, 24]. 50 ml of an electrolyte solution (0.01 M NaCl) was added to a 100 ml glass. Then, the zeolite was added to beaker in small portions (0.1 g each) at certain intervals (5 – 10 min) with continuous stirring on a magnetic stirrer, until unchanged pH values of the solution were reached. pH was measured using the Multitest IPL-301 pH meter (Russia). The techniques of temperature-programmed reduction (*TPR*), temperature-programmed desorption of ammonia (*TPD-NH_3*), diffuse reflection spectroscopy in the UV and visible regions (*UV-Vis DRS*), *Raman* and *IR spectroscopy,* X-ray diffraction analysis (*XRD*) were described earlier [25, 26]. The sample microstructure was examined by High-Resolution Transmission Electron Microscopy (HRTEM) using a ThemisZ microscope (Thermo Fisher Scientific, USA) at an accelerating voltage of 200 kV (point-to-point resolution: 0.07 nm).

2.4. Catalytic tests

The catalytic experiments were carried out in a flow reactor. The loading of the catalyst (fraction 0.25 – 0.5 mm) was 1 g. For uniform heat exchange, the catalyst was mixed with quartz (0.63 – 1.0 mm) – 3.8 g. The process was carried out at 300 °C, in a flow of hydrogen and argon (500 and 200 ml/min, respectively). WHSV was 8.4 h^{-1}, the ratio of hydrogen to fatty acids H_2/FAs for standard experiments was 3150 m^3/m^3. The time-on-stream was 10 h. The pressure was 2.5 MPa. The fractional composition of the liquid products of the hydroprocessing was determined by the method of simulated distillation (*Sim-Dist*) [27] The group composition of the liquid products was studied by two-dimensional gas chromatography (*GC×GC*) [27].

3. Results and discussion

3.1. Analysis of impregnating solutions

According to weight titration data, the pH PZC for zeolite ZSM-23 was 4.3. Table 1 shows the pH values of the impregnating solutions. The methods of Raman and IR and UV-vis spectroscopy were used to determine the kind of metal ions in impregnating solutions.

In Fig. 1 and Fig. 2, the IR and Raman spectra of impregnating solutions is shown. In the Raman spectrum of the $Ni(NO_3)_2$ solution, a single band with a maximum of about 1046 cm^{-1} is observed, related to the $n_s(NO_3)$ oscillation of the nitrate ion. In the IR spectrum of this solution, bands of water 1627 cm^{-1} ($\delta(H_2O)$) and nitrate ion 1345 cm^{-1}, 1385 cm^{-1} ($n_s(NO_3)$), 1046 cm^{-1} ($n_s(NO_3)$), 830 cm^{-1} ($\delta_{as}(NO_3)$) are observed [28]. The band of a doubly degenerate

TABLE 1. pH of impregnating solutions

Catalysts	pH of impregnating solutions	
	$Ni(NO_3)_2$	$(NH_4)_6Mo_7O_{24}$
Ni-Mo	5.08	5.24
NiMo-wat	3.92	
NiMo-cit	2.68	
NiMo-amm-9	9.10	
NiMo-amm-11	10.99	

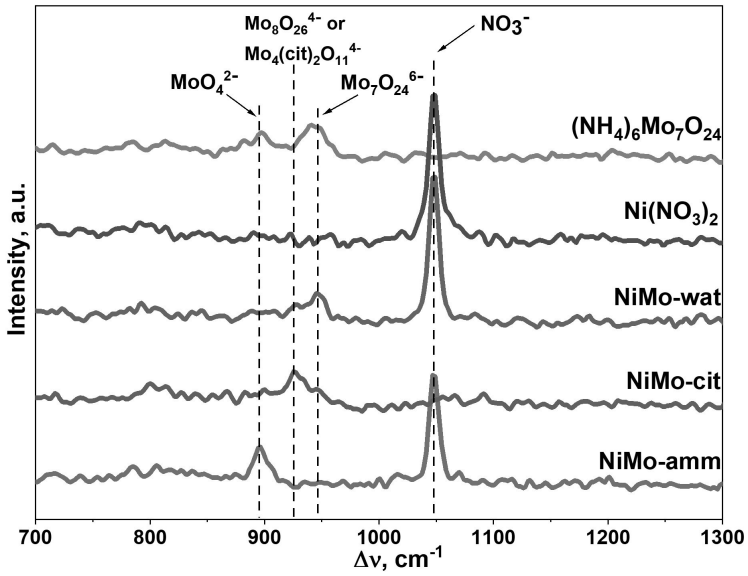

FIG. 1. Raman spectra of impregnating solutions

asymmetric valence oscillation for a free nitrate ion is split into two components (1345 and 1385 cm^{-1}), which indicates the coordination of nitrate ions to nickel cations. Thus, the spectrum corresponds to the compound $Ni(H_2O)_x(NO_3)_y$.

Bands 897 and 944 cm^{-1} are observed in the Raman spectrum of the ammonium paramolybdate solution. Bands 894, 839, 1451 and 1634 cm^{-1} are observed in the IR spectrum of this solution. The appearance of the obtained spectra indicates that both paramolybdate $Mo_7O_{24}{}^{6-}$ (944 cm^{-1} – Raman and 894 cm^{-1} – IR) and monomolybdate $MoO_4{}^{2-}$ (897 cm^{-1} – Raman, 839 cm^{-1} – IR) ions are present in the solution [29]. In addition, ammonium ions (1451 cm^{-1} in IR) and water (1634 cm^{-1} in IR) are present in this solution. A band of paramolybdate 944 cm^{-1} and nitrate 1046 cm^{-1} is observed in the Raman spectrum of NiMo-wat. Bands of paramolybdate 904 and 929 cm^{-1} and nitrate 1382, 1344, 1046 and 830 cm^{-1} and water 1627 cm^{-1} are also observed in the IR spectrum of this solution. The Raman and IR spectra of the NiMo-cit solution correspond to the spectrum of the mixed Ni_xMoCit complex [21]. The spectra of NiMo-amm-9 and NiMo-amm-11 solutions turned out to be similar, therefore, one spectrum is given for an ammonia impregnation solution. The bands $MoO_4{}^{2-}$ 894 cm^{-1} and 1048 cm^{-1} nitrate are observed in the Raman spectrum of the NiMo-amm solution. In the IR spectrum of this solution, in addition to the bands of monomolybdate (827 cm^{-1}) and nitrate (1380, 1346 and 1043 cm^{-1}), a band of NH_3 is observed, probably coordinated to nickel cations (1244 cm^{-1}).

Analyzing the obtained spectra of impregnating solutions and pH PZC for zeolite ZSM-23, a scheme can be proposed for the electrostatic interaction of the surface of zeolite ZSM-23 and metal ions in impregnating solutions (Fig. 3). As mentioned earlier, at pH $<$ PZC, the zeolite surface is positively charged and presumably adsorbs anions on its surface. At pH $>$ PZC, the zeolite surface is negatively charged and preferentially adsorbs cations. According to the IR and Raman spectra, in solutions with a pH below 7, molybdenum mainly presents in the form of polymolybdate anions $[Mo_7O_{24}]^{6-}$ and $[Mo_8O_{26}]^{4-}$. In solutions with a pH greater than 7, molybdenum presents mainly in the form of monomolybdate ion $[MoO_4]^{2-}$. Thus, 3 groups of catalysts can be distinguished in accordance with the charge of the zeolite surface and the state of molybdenum in the impregnation solution during preparation. The first group of catalysts includes samples in which, during preparation, the zeolite surface is positively charged, and molybdenum is in the form of polymolybdate ions. These are NiMo-wat and NiMo-cit catalysts. The second group includes catalysts, in which the zeolite surface is

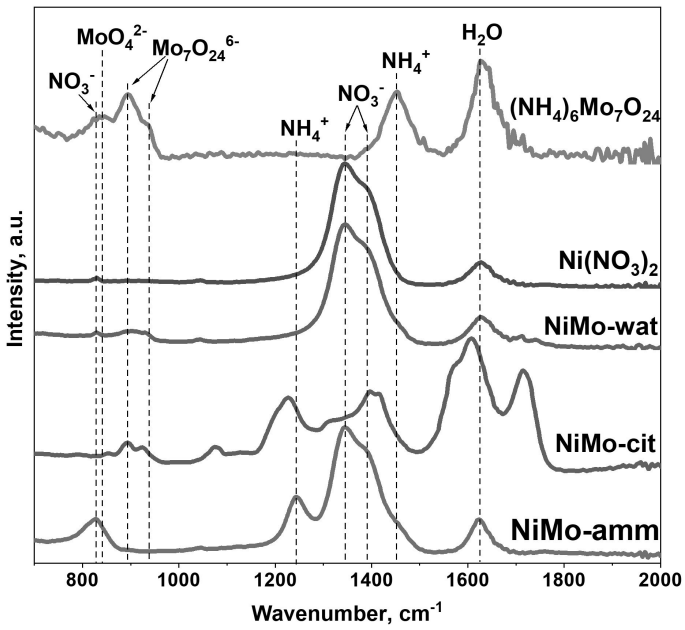

FIG. 2. IR spectra of impregnating solutions

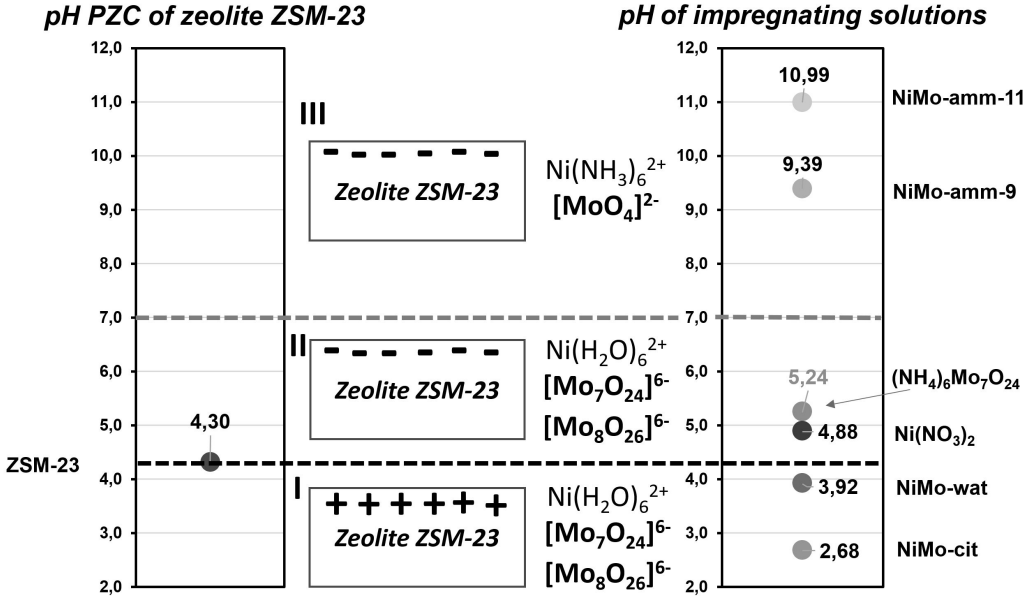

FIG. 3. Scheme of electrostatic interaction of zeolite ZSM-23 and metal ions in impregnating solutions

negatively charged during preparation, and molybdenum is in the form of polymolybdate ions. This is a sample of Ni-Mo. The third group includes catalysts, in which the zeolite surface is negatively charged during preparation, and molybdenum is in the form of monomolybdate ions. These are the NiMo-amm-9 and NiMo-amm-11 samples. It can be expected that the most uniform distribution of nickel and molybdenum will be in the 3rd group of catalysts, since the charge value of metal ions is the same ($[Ni(NH_3)_6]^{2+}$ and $[MoO_4]^{2-}$), which can lead to the formation of a complex with a metal ratio Ni/Mo = 1. In the case of other catalysts, the charge value of the paramolybdate ion is higher ($[Mo_7O_{24}]^{6-}$, $[Mo_8O_{26}]^{4-}$ and $[Ni(H_2O)_6]^{2+}$), therefore, most likely, complexes with a metal ratio of Ni/Mo = 3 will form in the solution.

3.2. UV-vis spectroscopy

To obtain information on the coordination of metal atoms, UV-vis spectra for Ni-Mo/ZSM-23 catalysts in oxide form were recorded. For all catalysts, two main absorption regions can be distinguished – from 10000 to 30000 cm^{-1} (Fig. 4a) and from 30000 to 45000 cm^{-1} (Fig. 4b). In the first absorption region (visible range), due to the manifestation of d-d transitions of Ni^{2+} cations, several main absorption bands can be distinguished. The band at 13800 cm^{-1} corresponds

to Ni^{2+} particles stabilized in an octahedral oxygen environment ($Ni^{2+}O_h$), and the band at 15200 cm^{-1} corresponds to Ni^{2+} particles in a tetrahedral oxygen environment ($Ni^{2+}T_d$). Also, in the spectra of all bimetallic catalysts, there is a wide absorption band at 12220 cm^{-1}, which corresponds to distorted octahedral $Ni^{2+}(O_h)$ particles, which is associated with the formation of a joint Ni-Mo phase in the form of $NiMoO_4$ [30,31]. The intensity of the absorption band may indirectly indicate the size and availability of metal particles. Thus, the lowest absorption in the region of 10000 – 15000 cm^{-1} is observed for the Ni-Mo catalyst, which may indicate the blocking of nickel particles by molybdenum particles [32]. The highest absorption in this region is observed for NiMo-amm-9, which may indicate the most dispersed nickel particles.

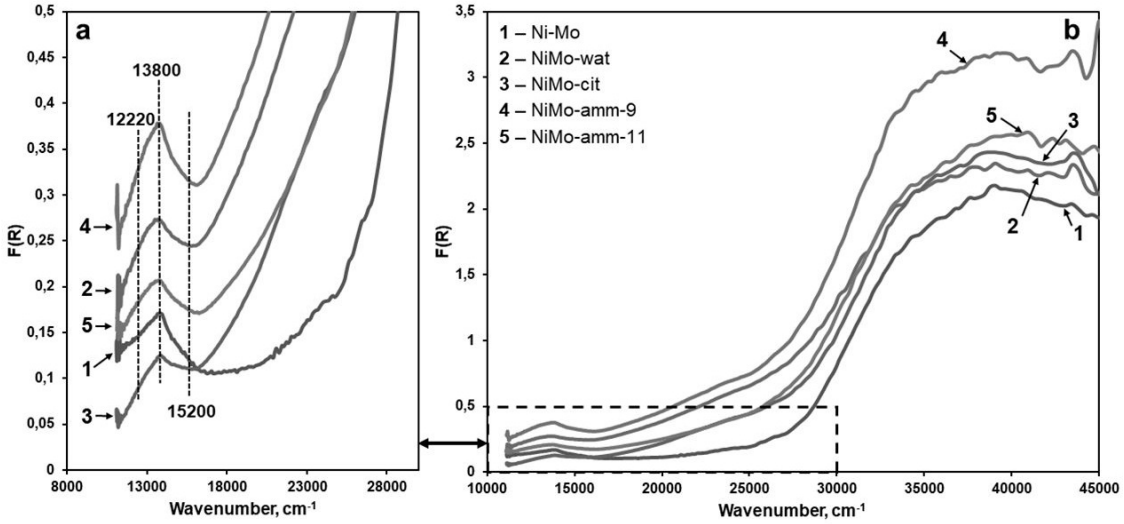

FIG. 4. UV-vis spectra of NiMo/ZSM-23 catalysts in oxide form in the range: (a) from 10000 to 30000 cm^{-1}, (b) from 10000 to 45000 cm^{-1}

The second absorption region (UV range) is usually due to the manifestation of charge transfer bands of ligand-metal cations Ni^{2+} or Mo^{6+} or the general absorption of massive systems such as NiO oxide or MoO_3 [7, 32, 33]. The most intense absorption in this area is observed for the NiMo-amm-9 catalyst. This may be due to the formation of monomolybdates $[MoO_4]^{2-}$ in an ammonia impregnation solution, which, when calcined, form smaller particles compared to particles obtained from polymolybdates $[Mo_7O_{24}]^{6-}$ and $[Mo_8O_{24}]^{4-}$ [31]. It is difficult to identify absorption bands for octahedral and tetrahedral forms of molybdenum Mo^{6+} cations, since these bands are poorly expressed due to the small amount of molybdenum in catalysts.

3.3. Raman spectroscopy

The catalysts in the oxide form were investigated by Raman spectroscopy to determine the types of metal particles in the samples. In the spectra (Fig. 5) of all catalysts, a band at 961 cm^{-1} is observed, which refers to V_s (Mo=O) oscillations of the α-$NiMoO_4$ phase [11, 34, 35]. A small band at 914 cm^{-1} is also found in the spectra of the NiMo-amm-9 and NiMo-amm-11 catalysts, which corresponds to V_a(Mo=O) oscillations of the α-$NiMoO_4$ phase [11, 34]. The appearance of additional bands indicates an increase in the amount of α-$NiMoO_4$ phase in the NiMo-amm-9 and NiMo-amm-11 catalysts. Trace amounts of the β-$NiMoO_4$ phase may also be present in all samples, fluctuations of which should be observed at 900 and 945 cm^{-1} [35,36]. It is worth noting that with an increase in the pH of the ammonia impregnation solution, the intensity of the α-$NiMoO_4$ phase band increases, which may indicate an increase in its amount. No oscillation bands related to the MoO_3 phase were detected.

3.4. Temperature-programmed reduction

For all catalysts on the TPR profiles (Fig. 6), hydrogen absorption in the range from 150 to 350 °C is not observed, which indicates the absence of massive NiO particles [18]. The rest of the TPR profile can be divided into 4 components.

The particles of of nickel oxides weakly bound to the surface of the support [17, 22, 37] are reduced at temperatures of 350 – 450 °C. In the case of NiMo-cit catalyst, the absence of this reduction maximum may be due to the formation of a Ni_xMoCit complex in the impregnation solution, by analogy with $Co_2[Mo_4O_{11}(C_6H_5O_7)_2]$ [38], from which, upon calcination, co-oxides of Ni and Mo or particles of $NiMoO_4$ are formed [7,39]. The next maximum reduction in the region of 450 – 520 °C corresponds to the reduction of interacting NiO and MoO_3 particles. Interaction can be understood as both physical contact between particles [25] and chemical interaction – the formation of the $NiMoO_4$ phase [40]. Further, at a temperature of about 560 °C, Mo^{6+} is reduced to Mo^{4+} [17, 37, 41], which corresponds to the reduction of molybdenum oxide particles that do not encounter nickel-containing particles. At temperatures of 700 – 750 °C, molybdenum is further reduced to a metallic state [7, 18, 41]. It is also worth noting that the amount of hydrogen absorbed differs from catalyst

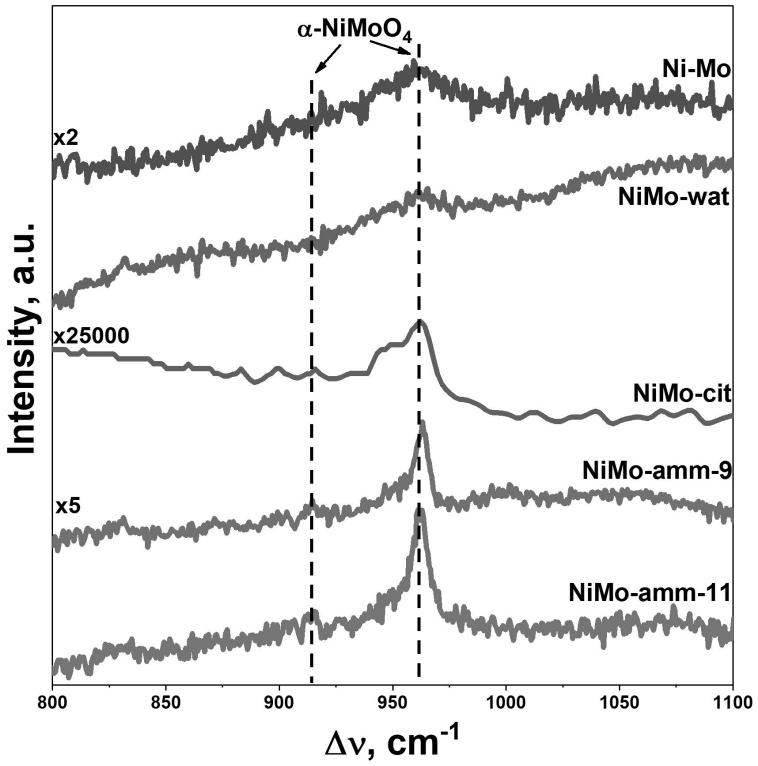

FIG. 5. Raman spectra of NiMo/ZSM-23 catalysts in oxide form

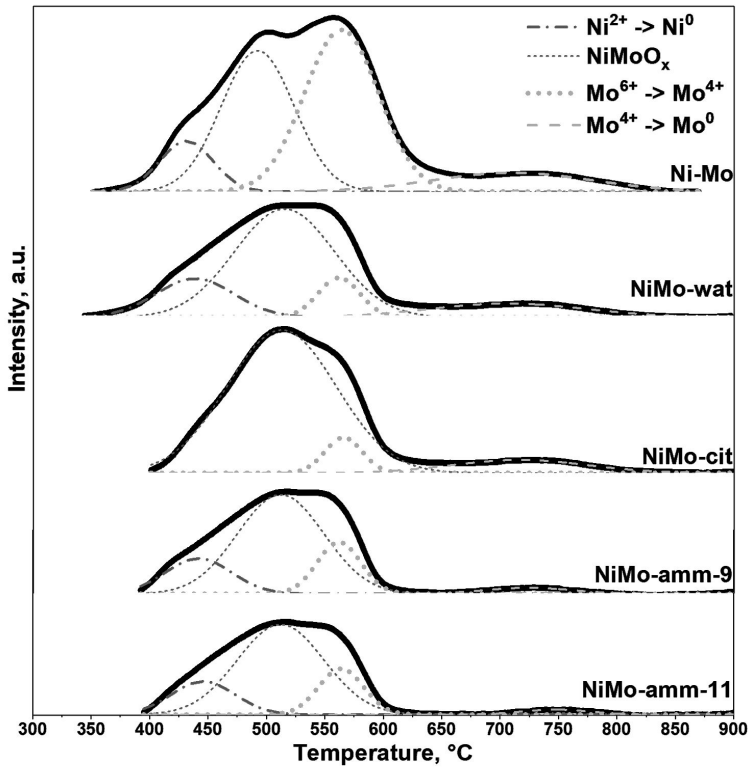

FIG. 6. Decomposed TPR profiles of NiMo/ZSM-23 catalysts in oxide form

to catalyst. The largest amount of absorbed hydrogen is observed for the Ni-Mo sample. In the case of impregnation co-solutions, the smallest amount of absorbed hydrogen is observed for samples NiMo-amm-9 and NiMo-amm-11. This may indicate that in catalysts prepared from ammonia impregnation solutions, there is a stronger interaction of the active component with the surface of the support compared to other samples [42].

3.5. X-ray diffraction analysis

All diffractograms (Fig. 7) show the reflexes of the support – ZSM-23. For all catalysts, a peak at 37.2° can be identified, which refers to 111 NiO (PDF 47-1049). However, for the catalysts prepared by impregnation co-solutions, this peak is weakly expressed. This may indicate the presence of highly dispersed NiO particles, or a smaller number of them than in the Ni-Mo catalyst. Also, for all catalysts, a peak is observed at 26.7°, which corresponds to β-$NiMoO_4$ (PDF 45-142). For the NiMo-amm-9 and NiMo-amm-11 catalysts, a peak at 28.8° can be distinguished, which belongs to α-$NiMoO_4$ (PDF 9-175). Since the diffractograms show relatively weak signals from phases containing nickel and molybdenum, which also overlap with peaks of the support, the intensity ratio of certain phase peaks was used for only qualitative comparison of catalysts. The evaluation method is described in detail in the experimental part. As a comparison, Table 2 shows the ratio of intensities (I) at various points for the zeolite, the remaining samples were analyzed relative to this "control point".

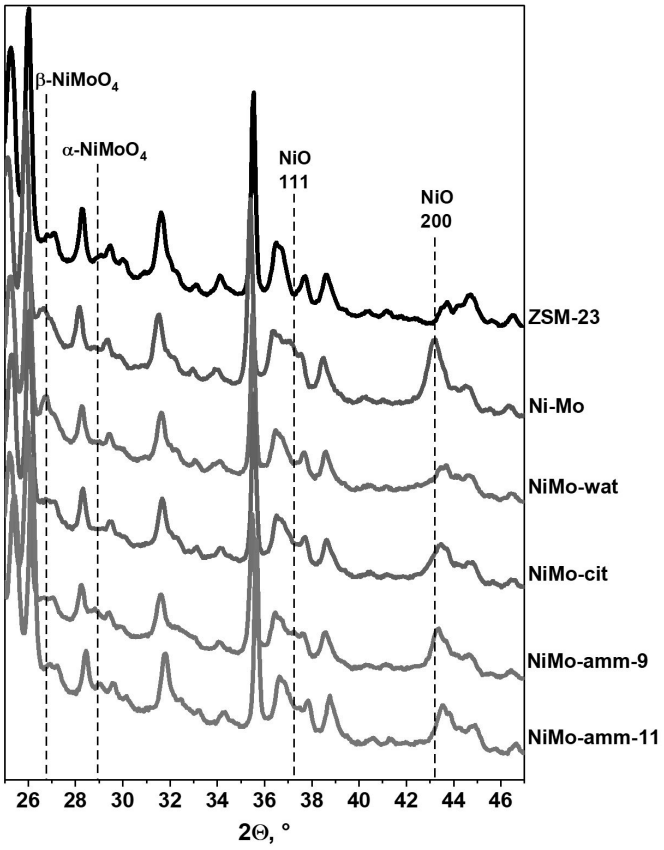

FIG. 7. Diffractograms of NiMo/ZSM-23 catalysts in oxide form

Based on the data given in Table 2, the β-$NiMoO_4$ phase can be identified in all catalysts. The α-$NiMoO_4$ phase presents only in catalysts prepared from ammonia impregnation co-solutions. It is known that pure β-$NiMoO_4$ is a metastable phase that exists at high temperature [43]. However, with an excess of nickel in the catalyst (atomic ratio Mo/(Ni+Mo) < 0.5), the β-$NiMoO_4$ phase can be stable at room temperature [44, 45]. Apparently, nickel-enriched particles forming the β-$NiMoO_4$ phase are present in all catalysts. In the catalysts NiMo-amm-9 and NiMo-amm-11, nickel and molybdenum are distributed more evenly, which allows obtaining the stoichiometric phase α-$NiMoO_4$. The observed phenomenon regarding the formation of phases is consistent with the previously proposed scheme of electrostatic interaction of metals in solution and with the surface of the support.

Figure 8 shows X-ray images of Ni-Mo/ZSM-23 catalysts in reduced form. Narrow peaks of the support (zeolite ZSM-23) are present on all diffractograms. For all catalysts, a peak is observed at 44.1°, which corresponds to (111) Ni (PDF 04-0850). A peak at 51.7° is also observed for the Ni-Mo sample, corresponding to (200) Ni (PDF 04-0850). Reflexes corresponding to the molybdenum-containing phases are not observed.

TABLE 2. Structural characteristics of NiMo/ZSM-23 catalysts in oxide form

Catalyst	I(β-$NiMoO_4$)/ I(ZSM-23)	I(α-$NiMoO_4$)/ I(ZSM-23)	I(NiO)/ I(ZSM-23)	I(β-$NiMoO_4$)/ I(α-$NiMoO_4$)	Phase composition	CSD, Å
ZSM-23	0.48	0.03	0.32	—	ZSM-23	—
5Ni-ZSM-23	0.39	−0.05	1.98	—	NiO ZSM-23	300
Ni-Mo	0.95	−0.05	1.55	—	NiO β-$NiMoO_4$ ZSM-23	160
NiMo-wat	1.32	−0.06	0.62	—	NiO β-$NiMoO_4$ ZSM-23	60
NiMo-cit	0.76	−0.01	0.82	—	NiO β-$NiMoO_4$ ZSM-23	90
NiMo-amm-9	0.64	0.25	0.99	2.6	NiO α-$NiMoO_4$ β-$NiMoO_4$ ZSM-23	170
NiMo-amm-11	0.69	0.21	0.65	3.3	NiO α-$NiMoO_4$ β-$NiMoO_4$ ZSM-23	110

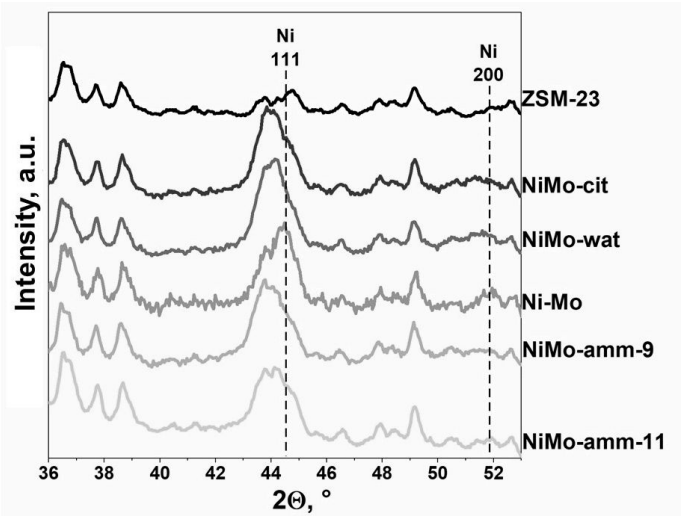

FIG. 8. Diffractograms of NiMo/ZSM-23 catalysts in reduced form

The structural characteristics of the reduced catalysts are presented in Table 3. The lattice parameter for pure nickel is 3.523 Å. For the Ni-Mo sample, this parameter is practically the same, which may indicate the absence of Ni-Mo solid co-solutions. For the remaining samples, the lattice parameter is greater than that of pure nickel, which is associated with the formation of solid co-solutions.

Apparently, this is because nickel and molybdenum, being in the same impregnation solution, can interact to form various complexes, which, when fixed on the surface and further calcination, give solid solutions. It can also be noted that the use of impregnation co-solutions helps to reduce the size of CSD for nickel particles.

3.6. High-resolution transmission electron microscopy

To determine the distribution of metals on the surface of zeolite ZSM-23, catalysts in oxide form were studied by HRTEM. The resulting images and the energy dispersive X-ray (EDX) mapping analysis data of the studied samples are shown in the Fig. 9. The average size of Ni- and Mo-containing particles is represented in Table 4.

The largest size (Table 4) – 14 nm – of metal-containing particles is observed in the Ni-Mo catalyst, which is prepared by successive deposition of Ni and Mo. Smaller particles are observed in the other catalysts prepared from impregnation

TABLE 3. Structural characteristics of NiMo/ZSM-23 catalysts in reduced form

Sample	Phase composition	Lattice parameter, Å	CSD, Å	x in $Ni_{1-x}Mo_x$
Ni-Mo	ZSM-23 Ni	3.528	120	0.01
NiMo-wat	ZSM-23 Ni	3.562	80	0.08
NiMo-cit	ZSM-23 Ni	3.567	100	0.09
NiMo-amm-9	ZSM-23 Ni	3.575	70	0.11
NiMo-amm-11	ZSM-23 Ni	3.571	70	0.10

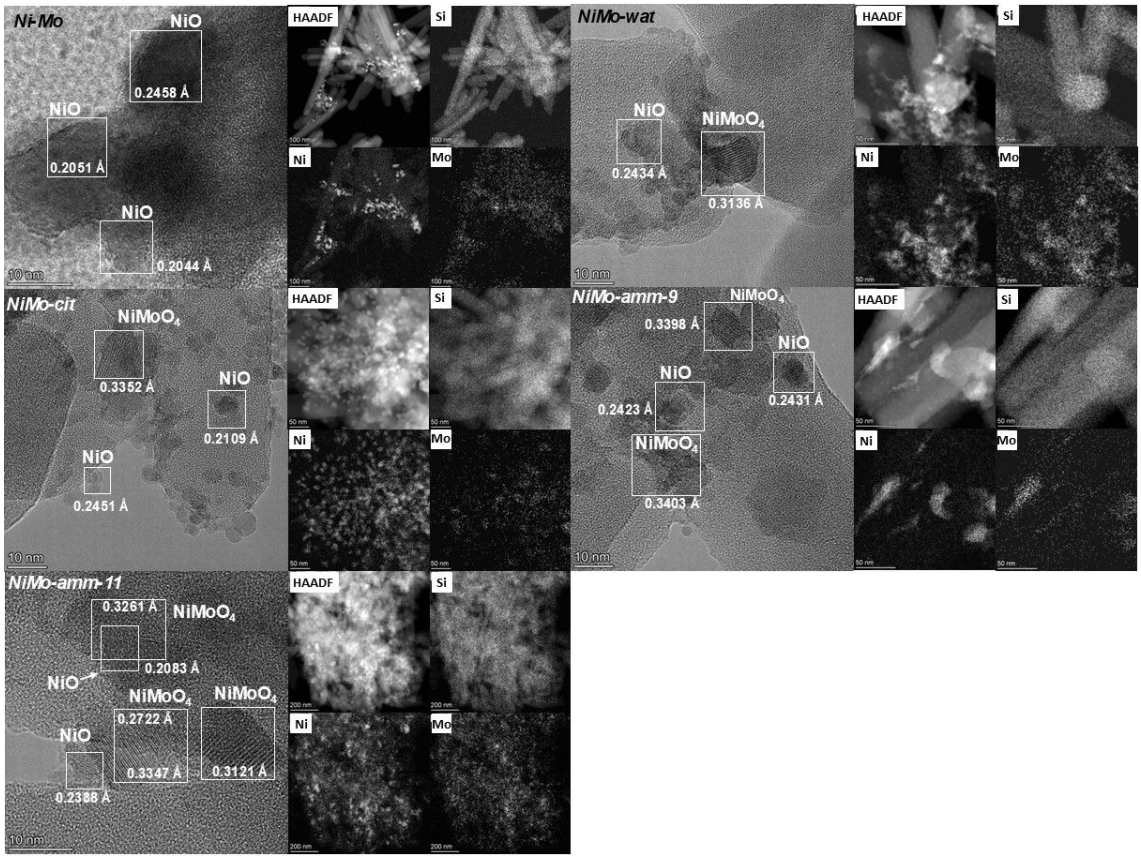

FIG. 9. HRTEM and EDX images for NiMo/ZSM-23 catalysts in oxide form

TABLE 4. Average particle size (HRTEM) for NiMo/ZSM-23 catalysts in oxide form

Catalyst	Average particle size, nm
Ni-Mo	14.1 ± 0.2
NiMo-wat	3.4 ± 0.1
NiMo-cit	3.5 ± 0.1
NiMo-amm-9	3.2 ± 0.1
NiMo-amm-11	3.1 ± 0.1

co-solutions. The determination of the interplane distance showed that in the Ni-Mo catalyst, most of the particles are a phase of nickel oxide. Molybdenum, in the form of a phase of molybdenum oxides, has a dispersed distribution and is localized on the surface of NiO particles and the surface of the support. $NiMoO_4$ particles are also observed for NiMo-wat and NiMo-cit catalysts. For catalysts prepared from ammonia impregnation solutions, $NiMoO_4$ particles are mainly observed in HRTEM images, and to a lesser extent, NiO particles. Thus, the use of impregnation co-solutions contributes to the formation of joint Ni-Mo phases. The use of ammonia impregnating solutions leads to a more uniform particle size distribution and the formation of mainly joint Ni-Mo phases.

According to the EDX mapping data, the distribution of Ni and Mo is quite close for the NiMo-cit and NiMo-wat samples – Ni- and Mo-containing particles with close boundaries and positions could be observed. The main differences were observed for the Ni-Mo sample. On the one hand, Ni-containing particles were found. On the other hand, the distribution of Mo-containing particles was very uniform and close to the distribution of Si, which may mean that Mo is uniformly distributed on the surface of the oxides in contrast to Ni. The distribution of Ni and Mo was close in the case of NiMo-amm-11 and quite uniform for both elements, which is in good agreement with our assumption of more uniform distribution of Ni and Mo in the case of using ammonia impregnating solution.

3.7. Temperature-programmed desorption of ammonia

The number of acid centers (AC) in the reduced catalysts was determined using temperature-programmed desorption of ammonia. The obtained TPD-NH_3 profiles are shown in Fig. 10.

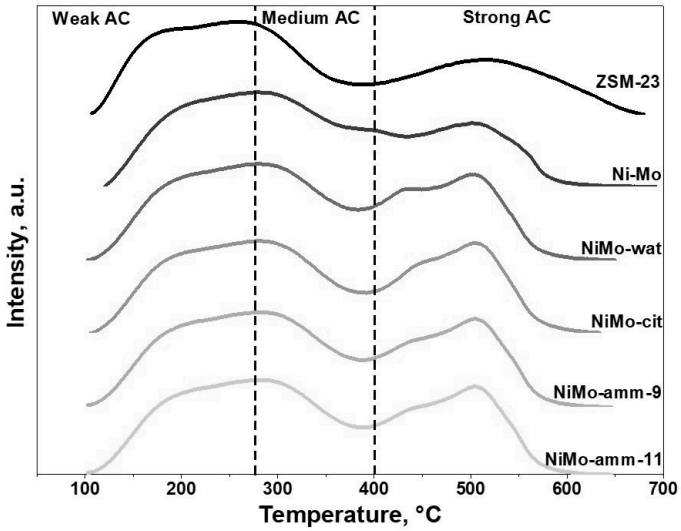

FIG. 10. TPD-NH_3 profiles of zeolite ZSM-23 and reduced catalysts

Table 5 shows the amount of desorbed ammonia from various zeolite centers and reduced catalysts. The acid centers of zeolite can be divided into 3 groups according to strength: weak, from which ammonia is desorbed at temperatures below 275 °C, medium (275 – 400 °C) and strong (over 400 °C) [4, 5, 46–48]. TPD-NH_3 profiles exhibit two clearly distinguishable desorption maxima, which correspond to typical TPD profiles for this zeolite [46–48]. The first maximum is in the temperature range of 100 – 350 °C and corresponds to the desorption of ammonia from weak and medium AC. The high-temperature peak of ammonia desorption, observed in the range of 350 – 550 °C, corresponds to medium and strong AC [46–48].

For all catalysts, compared with zeolite ZSM-23, there is a decrease in the number of weak and strong AC. This takes place because metal particles interact with these types of AC during application, thereby blocking them [49]. An increase in the number of average AC is observed for all samples. Also, transition metal-based catalysts usually have increased low and medium acidity due to the appearance of weak acid centers of transition metals [50, 51]. The increase in the number of average AC may also be due to the presence of MoO_x particles in the catalyst [52, 53].

3.8. Catalytic tests

The component composition of the liquid organic product obtained at the 10^{th} (last) hour of the process is shown in Table 6. The following groups of compounds were found in the organic phase: alkanes, isoalkanes, alkenes, cycloalkanes, aromatic compounds and O-containing compounds – fatty acids, esters of fatty acids, lactones, alcohols. C_6-C_{15} fatty acids are formed as a result of hydrocracking of the initial C_{16}-C_{18} fatty acids. Alcohols are formed as a result of hydrogenation of fatty acids and are an intermediate product of deoxygenation [17]. Esters can be formed from fatty acids (initial and shorter ones) and alcohols, which are obtained in the hydroprocessing from fatty acids [17]. Lactones

TABLE 5. The number of acid centers according to TPD-NH_3

Sample	Desorbed amount of NH_3, mmol/g			
	Weak AC	Medium AC	Strong AC	Σ
ZSM-23	503	164	288	955
Ni-Mo	454	207	183	744
NiMo-wat	488	201	220	910
NiMo-cit	465	182	217	864
NiMo-amm-9	475	191	215	881
NiMo-amm-11	482	196	217	895

are internal cyclic esters and can be formed from fatty acids [54]. C_{15}-C_{18} linear alkanes are formed from the initial C_{16}-C_{18} fatty acids through the deoxygenation stage. C_5-C_{14} linear alkanes are formed as a result of hydrocracking of linear alkanes C_{15}-C_{18}, as well as from fatty acids with a shorter chain length than in the initial mixture. Alkenes are intermediates of hydrocracking and hydroisomerization processes [55]. C_5-C_{18} isoalkanes are formed during the hydroisomerization of the corresponding linear alkanes. Aromatic compounds are products of alkene dehydrocyclization. Cycloalkanes can be products of hydrogenation of aromatic compounds [1, 56].

The content of O-containing compounds in a liquid organic product differs for catalysts prepared by different methods. The lowest content of O-containing compounds is observed when using a Ni-Mo catalyst (9.4 wt. %). In the case of using NiMo-amm-9 and NiMo-amm-11 catalysts, a slight increase in the amount of O-containing compounds is observed – 12.4 and 13.7 wt. %, respectively. The least active catalysts are NiMo-wat and NiMo-cit, for which the amount of O-containing compounds is 32.6 and 49.3 wt. %, respectively. This behavior of catalysts may be related to the varying degrees of interaction of molybdenum particles with the surface of the support. According to the scheme of electrostatic interaction (Fig. 3), during the preparation of NiMo-wat and NiMo-cit catalysts, molybdenum in the form of polymolybdate ions ($[Mo_7O_{24}]^{6-}$ and $[Mo_8O_{26}]^{4-}$) interacts with the positively charged surface of ZSM-23 zeolite, which can lead to a strong metal-support interaction [57, 58]. As a result, the ability to activate O-containing compounds may decrease. It was previously shown that the active phase of the oxide precursors of sulfide hydrotreating catalysts can directly affect the activity of the final catalysts in the hydrotreating process. It was shown that massive sulfided Ni-Mo catalyst is active in the hydroprocessing of sulfide model compounds in the series of works [59, 60]. At the same time, the composition of the sample contained both α-$NiMoO_4$ and β-$NiMoO_4$ phases in the oxide form, but the β-$NiMoO_4$ phase was the main one. Apparently, in our case, the interaction of the molybdate phases with the support can stabilize the α-$NiMoO_4$ phase in some cases (Table 2), which also leads to a change in the selectivity towards oxygen-containing compounds (Table 6).

The target products of the hydroprocessing are isoalkanes. The smallest amount of iso-alkanes is observed when using NiMo-wat and NiMo-cit catalysts. Apparently, this is due to their low activity, which is confirmed by the amount of O-containing compounds in the liquid organic product. The largest amount of isoalkanes is observed in the case of using the NiMo-amm-11 catalyst (35.2 wt. %)(which may be due to its higher acidity than that of the Ni-Mo and NiMo-amm-9 samples (Table 5). On the one hand, previous studies have demonstrated the influence of zeolite-type catalyst support acidity on the yield of isomerized alkanes produced from vegetable oils [61]. On the other hand, it has also been shown that metal incorporation into catalyst supports, such as tungsten, can directly affect their acidity, and consequently, the yield of isomerized alkanes during the hydroprocessing of sunflower oil with using Pt/WO_x-Al_2O_3 catalysts [62].

Thus, from the point of view of the composition of the liquid organic phase, the NiMo-amm-11 catalyst is the most promising. Despite the fact that the amount of O-containing compounds on this catalyst was not minimal (13.7 wt. %) (the content of isoalkanes in the liquid organic product turned out to be maximum (35.2 wt. %).

Figure 11 shows the change in the fractional composition of the liquid organic product obtained at the 10^{th} (last) hour of the process, depending on the catalyst. The largest proportion of the "diesel" fraction is observed in liquid organic products produced on Ni-Mo, NiMo-amm-9 and NiMo-amm-11 catalysts. Liquid organic products produced on NiMo-wat and NiMo-cit catalysts have a high content of "vacuum gasoil" and "vacuum residue". This behavior of the fractional composition is consistent with the data of two-dimensional gas chromatography, where a similar dependence of the amount of O-containing compounds on the catalyst was observed.

TABLE 6. Composition of the liquid organic phase at the 10^{th} (last) hour of the process, according to two-dimensional gas chromatography data

Sample	Ni-Mo	NiMo-wat	NiMo-cit	NiMo-amm-9	NiMo-amm-11
Compound	wt. %				
O-containing compounds:	**9.4**	**32.6**	**49.3**	**12.4**	**13.7**
C_6-C_{15} FAs	0.0	0.0	0.0	0.0	0.3
C_8-C_{35} lactones	2.7	7.6	9.8	3.5	3.3
C_{20}-C_{45} esters of FAs	4.9	20.9	34.1	6.5	5.6
C_9-C_{35} alcohols	0.6	1.1	2.3	0.7	0.2
C_{16}-C_{20} initial FAs	1.2	3.0	3.1	1.7	4.3
Hydrocarbons total:	**90.6**	**67.4**	**50.7**	**87.6**	**86.3**
C_{10}-C_{25} cycloalkanes	3.5	3.8	1.7	3.0	1.1
C_6-C_{20} aromatics	3.4	1.2	1.7	2.4	0.0
C_5-C_{18} alkanes	35.0	19.7	17.0	28.6	26.9
C_5-C_{18} isoalkanes	30.4	17.8	12.2	27.1	35.2
C_5-C_{18} alkenes	18.3	24.9	18.1	26.5	23.1
i/n C_5-C_{18}	**0.9**	**0.9**	**0.7**	**0.9**	**1.3**
C_5-C_8 alkanes	0.6	0.5	0.4	0.6	0.7
C_5-C_8 isoalkanes	0.2	0.1	0.1	0.1	0.2
C_5-C_8 alkenes	0.2	0.2	0.1	0.2	0.8
i/n C_5-C_8	**0.3**	**0.2**	**0.1**	**0.2**	**0.3**
C_9-C_{14} alkanes	1.1	0.6	0.5	1.0	0.9
C_9-C_{14} isoalkanes	0.9	0.4	0.3	0.6	0.6
C_9-C_{14} alkenes	2.1	1.8	1.1	2.3	3.0
i/n C_9-C_{14}	**0.8**	**0.6**	**0.5**	**0.6**	**0.6**
C_{15}-C_{18} alkanes	33.3	18.6	16.1	27.1	25.3
C_{15}-C_{18} isoalkanes	29.3	17.4	11.9	26.4	34.4
C_{15}-C_{18} alkenes	16.0	22.9	16.9	24.0	19.4
i/n C_{15}-C_{18}	**0.9**	**0.9**	**0.7**	**1.0**	**1.4**
Yield of liquid organic product	**83.3**	**87.7**	**90.1**	**85.8**	**85.4**

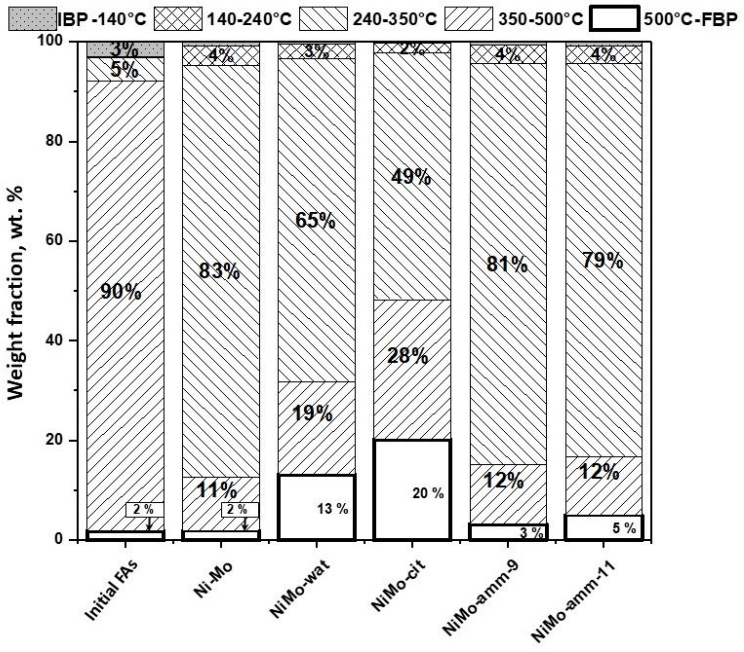

FIG. 11. Fractional composition of the liquid organic phase obtained at the 10^{th} (last) hour of the process, according to SimDist

4. Conclusion

In this work, a series of Ni-Mo catalysts based on zeolite ZSM-23 was synthesized by incipient wetness impregnation using various impregnation solutions. Aqueous, citrate, and ammonia solutions with different pH were used as impregnation solutions. According to IR and Raman spectroscopy data, in impregnating solutions with a pH of less than 7 (aqueous and citrate solutions), nickel is represented as the $Ni(H_2O)_6{}^{2+}$ ion, and molybdenum is present as polymolybdate ions ($[Mo_7O_{24}]^{6-}$ and $[Mo_8O_{26}]^{4-}$). In solutions with a pH of more than 7 (ammonia solutions), nickel is present as the $Ni(NH_3)_6{}^{2+}$ ion, and molybdenum is present as the monomolybdate ion ($[MoO_4]^{2-}$).

Using the XRD and HRTEM methods, the effect of the composition of the impregnation solution on the formation of phases of the metal component was shown. According to the HRTEM data, NiO particles are mainly observed in the catalyst prepared by the method of sequential deposition of metals. According to the XRD data, in addition to the NiO phase, the β-$NiMoO_4$ phase is also observed. The use of aqueous and citrate impregnation solutions leads to the formation of nickel oxide and β-$NiMoO_4$ phases (XRD data). When using ammonia impregnation solutions, the formation of NiO, α-$NiMoO_4$ and β-$NiMoO_4$ phases is observed (XRD data). In addition, according to the HRTEM, the use of ammonia impregnation solutions leads to a decrease in the size of metal-containing particles, as well as to a more uniform distribution of nickel and molybdenum over the surface of the support.

During the hydroprocessing of a mixture of fatty acids (C_{16}-C_{18}) in a flow-type reactor (300 °C, 2.5 MPa, WHSV = 8.4 h^{-1}), the greatest conversion and, consequently, the least amount of O-containing compounds were observed on the Ni-Mo catalyst. The highest yield of the "diesel" fraction was observed using Ni-Mo, NiMo-amm-9 and NiMo-amm-11 catalysts. The highest yield of isoalkanes was observed when using the NiMo-amm-11 catalyst. Thus, from the point of view of fractional and component compositions, as well as the material balance, the NiMo-amm-11 catalyst is the most promising.

References

[1] Yeletsky P.M., Kukushkin R.G., Yakovlev V.A., Chen B.H. Recent Advances in One-Stage Conversion of Lipid-Based Biomass-Derived Oils into Fuel Components — Aromatics and Isomerized Alkanes. *Fuel*, 2020, **278** (1), 118255.

[2] Kordulis C., Bourikas K., Gousi M., Kordouli E., Lycourghiotis A. Development of Nickel Based Catalysts for the Transformation of Natural Triglycerides and Related Compounds into Green Diesel: A Critical Review. *Appl. Catal. B*, 2016, **181**, P. 156–196.

[3] Zhou Y., Remón J., Jiang Z., Matharu A.S., Hu C. Tuning the Selectivity of Natural Oils and Fatty Acids/Esters Deoxygenation to Biofuels and Fatty Alcohols: A Review. *Green Energy and Environment*, 2023, **8** (3), P. 722–743.

[4] Zhang M., Chen Y., Wang L., Zhang Q., Tsang C.W., Liang C. Shape Selectivity in Hydroisomerization of Hexadecane over Pt Supported on 10-Ring Zeolites: ZSM-22, ZSM-23, ZSM-35, and ZSM-48. *Ind. Eng. Chem. Res.*, 2016, **55** (21), P. 6069–6078.

[5] Gao S.B., Zhao Z., Lu X.F., Chi K.B., Duan A.J., Liu Y.F., Meng X.B., Tan M.W., Yu H.Y., Shen Y.G., Li M.C. Hydrocracking Diversity in N-Dodecane Isomerization on Pt/ZSM-22 and Pt/ZSM-23 Catalysts and Their Catalytic Performance for Hydrodewaxing of Lube Base Oil. *Pet. Sci.*, 2020, **17** (6), P. 1752–1763.

[6] Romero D., Rohling R., Meng L., Rigutto M., Hensen E.J.M. Shape Selectivity in Linear Paraffins Hydroconversion in 10-Membered-Ring Pore Zeolites. *J. Catal.*, 2021, **394**, P. 284–298.

[7] Raikwar D., Munagala M., Majumdar S., Shee D. Hydrodeoxygenation of Guaiacol over Mo, W and Ta Modified Supported Nickel Catalysts. *Catal. Today*, 2019, **325**, P. 117–130.

[8] Yang Y., Wang Q., Zhang X., Wang L., Li G. Hydrotreating of C_{18} Fatty Acids to Hydrocarbons on Sulphided NiW/SiO_2-Al_2O_3. *Fuel Processing Technology*, 2013, **116**, P. 165–174.

[9] Zhang Z., Bi G., Zhang H., Zhang A., Li X., Xie J. Highly Active and Selective Hydrodeoxygenation of Oleic Acid to Second Generation Bio-Diesel over SiO_2-Supported $Co_xNi_{1-x}P$ Catalysts. *Fuel*, 2019, **247**, P. 26–35.

[10] Zheng Y., Wang J., Liu C., Lu Y., Lin X., Li W., Zheng Z. Efficient and Stable Ni-Cu Catalysts for Ex Situ Catalytic Pyrolysis Vapor Upgrading of Oleic Acid into Hydrocarbon: Effect of Catalyst Support, Process Parameters and Ni-to-Cu Mixed Ratio. *Renew Energy*, 2020, **154**, P. 797–812.

[11] Cao X., Long F., Zhai Q., Liu P., Xu J., Jiang J. Enhancement of Fatty Acids Hydrodeoxygenation Selectivity to Diesel-Range Alkanes over the Supported Ni-MoO_x Catalyst and Elucidation of the Active Phase. *Renew Energy*, 2020, **162**, P. 2113–2125.

[12] Brunelle J.P. Preparation of Catalysts by Metallic Complex Adsorption on Mineral Oxides. *Pure & Appl. Chem.*, 1978, **50**, P. 1211–1229.

[13] Kyriakopoulos J., Panagiotou G., Petsi T., Bourikas K., Kordulis C., Lycourghiotis A. The Influence of Impregnation Temperature on the PZC of Titania and the Loading of Ni upon Preparation of Ni/TiO_2 Catalysts. *Stud. Surf. Sci. Catal.*, 2010, **175**, P. 643–646.

[14] Hao X., Quach L., Korah J., Spieker W.A., Regalbuto J.R. The Control of Platinum Impregnation by PZC Alteration of Oxides and Carbon. *J. Mol. Catal. A Chem.*, 2004, **219** (1), P. 97–107.

[15] Li K., Wang R., Chen J. Hydrodeoxygenation of Anisole over Silica-Supported Ni_2P, MoP, and NiMoP Catalysts. *Energy and Fuels*, 2011, **25** (3), P. 854–863.

[16] Wang X., Zhao Z., Chen Z., Li J., Duan A., Xu C., Gao D., Cao Z., Zheng P., Fan J. Effect of Synthesis Temperature on Structure-Activity-Relationship over NiMo/γ-Al_2O_3 Catalysts for the Hydrodesulfurization of DBT and 4.6-DMDBT. *Fuel Processing Technology*, 2017, **161**, P. 52–61.

[17] Kordouli E., Sygellou L., Kordulis C., Bourikas K., Lycourghiotis A. Probing the Synergistic Ratio of the NiMo/γ-Al_2O_3 Reduced Catalysts for the Transformation of Natural Triglycerides into Green Diesel. *Appl. Catal. B*, 2017, **209**, P. 12–22.

[18] Qu L., Zhang W., Kooyman P.J., Prins R. MAS NMR, TPR, and TEM Studies of the Interaction of NiMo with Alumina and Silica-Alumina Supports. *J. Catal.*, 2003, **215** (1), P. 7–13.

[19] Liu Z., Han W., Hu D., Sun S., Hu A., Wang Z., Jia Y., Zhao X., Yang Q. Effects of Ni–Al_2O_3 Interaction on NiMo/Al_2O_3 Hydrodesulfurization Catalysts. *J. Catal.*, 2020, **387**, P. 62–72.

[20] Nepomnyashchiy A.A., Buluchevskiy E.A., Lavrenov A.V., Yurpalov V.L., Gulyaeva T.I., Leont'eva N.N., Talzi V.P. Hydrodeoxygenation of Vegetable Oil on NiMoS/WO_3—Al_2O_3 Catalysts. *Russian J. of Applied Chemistry*, 2017, **90** (12), P. 1944–1952.

[21] Salomatina A.A., Nadeina K.A., Klimov O.V., Danilova I.G., Gerasimov E.Y., Prosvirin I.P., Pakharukova V.P., Chesalov Y.A., Noskov A.S. Influence of Ni/Mo Ratio on Structure Formation of Ni-Mo Complex Compounds in NiMo/Al_2O_3 Catalysts for Selective Diene Hydrogenation. *Energy and Fuels*, 2022, **36** (24), P. 15088–15099.

[22] Kordouli E., Pawelec B., Kordulis C., Lycourghiotis A., Fierro J.L.G. Hydrodeoxygenation of Phenol on Bifunctional Ni-Based Catalysts: Effects of Mo Promotion and Support. *Appl. Catal. B*, 2018, **238**, P. 147–160.

[23] Kohler S.D., Ekerdt J.G., Kim D.S., Wachs I.E. Relationship between Structure and Point of Zero Surface Charge for Molybdenum and Tungsten Oxides Supported on Alumina. *Catal. Letters*, 1992, **16**, P. 231–239.

[24] Subramanian S., Noh J.S., Schwarz J.A. Determination of the Point of Zero Charge of Composite Oxides. *J. Catal.*, 1988, **114** (2), P. 433–439.

[25] Shinkevich K.S., Kukushkin R.G., Bulavchenko O.A., Zaikina O.O., Alekseeva M.V., Ruvinskiy P.S., Yakovlev V.A. Influence of the Support on Activity and Stability of Ni and Ni-Mo Catalysts in the Hydroprocessing of Fatty Acids into Motor Fuels Components. *Appl. Catal. A Gen.*, 2022, **644**, 118801.

[26] Kovalevskaya K.S., Kukushkin R.G., Zaikina O.O., Bulavchenko O.A., Larina T.V., Golubev I.S., Yakovlev V.A. NiMo/ZSM-23 Catalysts for Deoxygenation and Isomerization of C_{16}-C_{18} Fatty Acids to Sustainable Diesel and Jet Fuel Components. *Fuel*, 2025, **383**.

[27] Sukhorukov D.A., Kukushkin R.G., Alekseeva (Bykova) M.V., Bulavchenko O.A., Zaikina O.O., Revyakin M.E., Kazakov M.O., Yakovlev V.A. Upgrading of Sewage Sludge-Derived Pyrolysis Oil via Hydrotreatment over NiMo-Based Catalysts. *Fuel*, 2024, **359**, 130383.

[28] Tobias R.S. Infrared and Raman Spectra of Inorganic and Coordination Compounds (Nakamoto, Kazuo). *J. Chem. Educ.*, 1979, **56** (5), A209.

[29] Jeziorowski H., Knözinger H. Raman and Ultraviolet Spectroscopic Characterization of Molybdena on Alumina Catalysts. *J. of Physical Chemistry*, 1979, **83** (9), P. 1166–1173.

[30] Teixeira da Silva V.L.S., Frety R., J M.S. Activation and Regeneration of a NiMo/Al_2O_3 Hydrotreatment Catalyst. *Ind. Eng. Chem. Res.*, 1994, **33**, P. 1692–1699.

[31] Guevara-Lara A., Bacaud R., Vrinat M. Highly Active NiMo/TiO_2—Al_2O_3 Catalysts: Influence of the Preparation and the Activation Conditions on the Catalytic Activity. *Appl. Catal. A Gen.*, 2007, **328** (2), P. 99–108.

[32] Vroulias D., Gkoulemani N., Papadopoulou C., Matralis H. W—Modified Ni/Al_2O_3 Catalysts for the Dry Reforming of Methane: Effect of W Loading. *Catal. Today*, 2020, **355**, P. 704–715.

[33] Priecel P., Kubička D., Čapek L., Bastl Z., Ryšánek P. The Role of Ni Species in the Deoxygenation of Rapeseed Oil over NiMo-Alumina Catalysts. *Appl. Catal. A Gen.*, 2011, **397** (1–2), P. 127–137.

[34] Arun N., Maley J., Chen N., Sammynaiken R., Hu Y., Dalai A.K. NiMo Nitride Supported on Al_2O_3 for Hydrodeoxygenation of Oleic Acid: Novel Characterization and Activity Study. *Catal. Today*, 2017, **291**, P. 153–159.

[35] Fan X., Liu D., Zhao Z., Li J., Liu J. Influence of Ni/Mo Ratio on the Structure-Performance of Ordered Mesoporous Ni–Mo–O Catalysts for Oxidative Dehydrogenation of Propane. *Catal. Today*, 2020, **339**, P. 67–78.

[36] Bankar P.K., Ratha S., More M.A., Late D.J., Rout C.S. Enhanced Field Emission Performance of $NiMoO_4$ Nanosheets by Tuning the Phase. *Appl. Surf. Sci.*, 2017, **418**, P. 270–274.

[37] Al-Dalama K., Stanislaus A. Temperature Programmed Reduction of SiO_2-Al_2O_3 Supported Ni, Mo and NiMo Catalysts Prepared with EDTA. *Thermochim. Acta*, 2011, **520** (1–2), P. 67–74.

[38] Klimov O.V., Pashigreva A.V., Bukhtiyarova G.A., Budukva S.V., Fedotov M.A., Kochubey D.I., Chesalov Y.A., Zaikovskii V.I., Noskov A.S. Bimetallic Co-Mo Complexes: A Starting Material for High Active Hydrodesulfurization Catalysts. *Catal. Today*, 2010, **150** (3–4), P. 196–206.

[39] Brito J.L., Laine J., Pratt K.C. Temperature-Programmed Reduction of Ni-Mo Oxides. *J. Mater. Sci.*, 1989, **24** (2), P. 425–431.

[40] Yang F., Libretto N.J., Komarneni M.R., Zhou W., Miller J.T., Zhu X., Resasco D.E. Enhancement of M-Cresol Hydrodeoxygenation Selectivity on Ni Catalysts by Surface Decoration of MoO_x Species. *ACS Catal.*, 2019, **9** (9), P. 7791–7800.

[41] Yang J., Zuo T., Lu J. Effect of Preparation Methods on the Hydrocracking Performance of NiMo/Al_2O_3 Catalysts. *Chin. J. Chem. Eng.*, 2021, **32**, P. 224–230.

[42] Ameen M., Azizan M.T., Ramli A., Yusup S., Alnarabiji M.S. Catalytic Hydrodeoxygenation of Rubber Seed Oil over Sonochemically Synthesized Ni-Mo/γ-Al_2O_3 Catalyst for Green Diesel Production. *Ultrason. Sonochem.*, 2019, **51**, P. 90–102.
[43] Kaddouri A., Rosso R.D., Mazzocchia C., Fumagalli D. Isotermal Reduction Behavior of Undoped and Ca-, K- Nd P-Doped $NiMoO_4$ Phases Used for Selective Propane Oxydehydrogenation. *J. Therm. Anal. Calorim.*, 2001, **63**, P. 267–277.
[44] Chen M., Wu J.L., Liu Y.M., Cao Y., Guo L., He H.Y., Fan K.N. A Practical Grinding-Assisted Dry Synthesis of Nanocrystalline $NiMoO_4$ Polymorphs for Oxidative Dehydrogenation of Propane. *J. Solid State Chem.*, 2011, **184** (12), P. 3357–3363.
[45] Plyasova L.M., Ivanchenko I.Y., Andrushkevich M.M., Buyanov R.A., Itenberg I.S., Khramova G.A., Karakchiev L.G., Kustova G.N., Stepanov G.A., Tsailingol'd A.L., Pilipenko F.S. Study of the Phase Composition of Nickel-Molybdenum Catalysts. *Kinetics and Catalysis*, 1973, **14** (4), P. 882–886.
[46] Chen Y., Li C., Chen X., Liu Y., Liang C. Synthesis of ZSM-23 Zeolite with Dual Structure Directing Agents for Hydroisomerization of n-Hexadecane. *Microporous and Mesoporous Materials*, 2018, **268**, P. 216–224.
[47] Bai D., Meng J.P., Zou C., Li C., Liang C. H. Manipulation of Hydroisomerization Performance on Pt/ZSM-23 by Introducing Al_2O_3. *Journal of Fuel Chemistry and Technology*, 2023, **51** (2), P. 175–185.
[48] Wang Q., Sim L.B., Xie J., Ye S., Fu J., Wang J., Zhang N., Zheng J., Chen B. Comparative Study of Pt/Zeolites for n-Hexadecane Hydroisomerization: EU-1, ZSM-48, ZSM-23, ZSM-22, and ZSM-12. *Chem. Eng. Sci.*, 2024, **287**, 119785.
[49] Ding S., Li F., Li Z., Yu H., Song C., Xiong D., Lin H. Catalytic Hydrodeoxygenation of Waste Cooking Oil and Stearic Acid over Reduced Nickel-Based Catalysts. *Catal. Commun.*, 2021, **149**, 106235.
[50] Wang Z., Jia X., Yan Z., Fu W., Li Z., Tang T., Zhang L. CrOx Modified Particles Size and Electronic Density of Ni Catalyst on ZSM-23 for Enhanced Hydroisomerization Performance of Long-Chain n-Alkanes. *Fuel*, 2024, **367**, 131476.
[51] Tu C., Chen J., Li W., Wang H., Deng K., Vinokurov V.A., Huang W. Hydrodeoxygenation of Bio-Derived Anisole to Cyclohexane over Bi-Functional IM-5 Zeolite Supported Ni Catalysts. *Sustain. Energy Fuels*, 2019, **3** (12), P. 3462–3472.
[52] Mannei E., Ayari F., Petitto C., Asedegbega-Nieto E., Guerrero-Ruiz A. R., Delahay G., Mhamdi M., Ghorbel A. Light Hydrocarbons Ammoxidation into Acetonitrile over Mo—ZSM-5 Catalysts: Effect of Molybdenum Precursor. *Microporous and Mesoporous Materials*, 2017, **241**, P. 246–257.
[53] Wang J., Chen Y., Liu C., Lu Y., Lin X., Hou D., Luo C., Wang D., Zheng Z., Zheng Y. Highly Stable Mo-Based Bimetallic Catalysts for Selective Deoxygenation of Oleic Acid to Fuel-like Hydrocarbons. *J. Environ. Chem. Eng.*, 2023, **11** (1), 109104.
[54] Bal'zhinimaev B.S., Paukshtis E.A., Suknev A.P., Makolkin N.V. Highly Selective/Enantioselective Pt-ReOx/C Catalyst for Hydrogenation of L-Malic Acid at Mild Conditions. *J. of Energy Chemistry*, 2018, **27** (3), P. 903–912.
[55] Alvarez F., Ribeiro F.R., Perot G., Thomazeau C., Guisnet M. Hydroisomerization and Hydrocracking of Alkanes. 7. Influence of the Balance between Acid and Hydrogenating Functions on the Transformation of n-Decane on PtHY Catalysts. *J. Catal.*, 1996, **162** (2), P. 179–189.
[56] Gosselink R.W., Hollak S.A.W., Chang S.W., Van Haveren J., De Jong K.P., Bitter J.H., Van Es D.S. Reaction Pathways for the Deoxygenation of Vegetable Oils and Related Model Compounds. *Chem. Sus. Chem.*, 2013, **6** (9), P. 1576–1594.
[57] Bourikas K., Kordulis C., Lycourghiotis A. The Role of the Liquid-Solid Interface in the Preparation of Supported Catalysts. *Catal. Rev. Sci. Eng.*, 2006, **48** (4), P. 363–444.
[58] Fedyna M., Żak A., Jaroszewska K., Mokrzycki J., Trawczyński J. Composite of Pt/AlSBA-15+zeolite Catalyst for the Hydroisomerization of n-Hexadecane: The Effect of Platinum Precursor. *Microporous and Mesoporous Materials*, 2020, **305** (May).
[59] Knyazheva O.A., Baklanova O.N., Lavrenov A.V., Buluchevskii E.A., Drozdov V.A., Trenikhin M.V., Leont'eva N.N., Vasilevich A.V., Likholobov V.A. Mechanochemical Synthesis of Nanocrystalline Nickel—Molybdenum Compounds and Their Morphology and Application in Catalysis: III. Catalytic Properties of Massive Ni–Mo Sulfide Catalysts Synthesized Using Mechanochemical Activation. *Kinetics and Catalysis*, 2014, **55** (1), P. 130–138.
[60] Knyazheva O.A., Baklanova O.N., Lavrenov A.V., Buluchevskii E.A., Gulyaeva T.I., Leont'eva N.N., Drozdov V.A., Likholobov V.A., Vasilevich A.V. Mechanochemical Synthesis of β-$NiMoO_4$ as a Precursor of Bulk Highly Dispersed Catalyst for the Hydrocracking of Oil Fractions. *Catalysis in Industry*, 2012, **4** (3), P. 179–185.
[61] Nepomnyashchiy A.A., Saibulina E.R., Buluchevskiy E.A., Gulyaeva T.I., Yurpalov V.L., Mironenko R.M., Potapenko O.V., Lavrenov A.V. Combined Deoxygenation and Isomerization of Sunflower Oil Fat Acid Triglycerides on Pt/Al_2O_3-Zeolite Catalysts. *Catalysis in Industry*, 2024, **16** (2), P. 170–177.
[62] Nepomnyashchiy A.A., Yurpalov V.L., Buluchevskiy E.A., Drozdov V.A., Gulyaeva T.I., Mironenko R.M., Lavrenov A.V. Hydrodeoxygenation of Sunflower Oil on Pt/WO_x-Al_2O_3 Catalyst. *Catalysis in Industry*, 2024, **16** (2), P. 187–195.

Submitted 23 May 2025; revised 21 October 2025; accepted 15 November 2025

Information about the authors:

Ksenia S. Kovalevskaya – Boreskov Institute of Catalysis SB RAS, Akademika Lavrentieva av. 5, 630090, Novosibirsk, Russia; ORCID 0000-0003-3558-4918; shinkevich@catalysis.ru

Roman G. Kukushkin – Boreskov Institute of Catalysis SB RAS, Akademika Lavrentieva av. 5, 630090, Novosibirsk, Russia; ORCID 0000-0001-8124-352X; roman@catalysis.ru

Olesya O. Zaikina – Boreskov Institute of Catalysis SB RAS, Akademika Lavrentieva av. 5, 630090, Novosibirsk, Russia; omironenko@catalysis.ru

Olga A. Bulavchenko – Boreskov Institute of Catalysis SB RAS, Akademika Lavrentieva av. 5, 630090, Novosibirsk, Russia; ORCID 0000-0001-5944-2629; isizy@catalysis.ru

Vadim A. Yakovlev – Boreskov Institute of Catalysis SB RAS, Akademika Lavrentieva av. 5, 630090, Novosibirsk, Russia; ORCID 0000-0001-5015-3521; yakovlev@catalysis.ru

Conflict of interest: the authors declare no conflict of interest.

NANOSYSTEMS:
PHYSICS, CHEMISTRY, MATHEMATICS

Mamanazirov J., et al. *Nanosystems: Phys. Chem. Math.*, 2025, **16** (6), 887–896.
http://nanojournal.ifmo.ru
DOI 10.17586/2220-8054-2025-16-6-887-896

Original article

MXene based electrocatalysts for efficient water splitting

Javlonbek Mamanazirov[1,2,a], Shavkat Mamatkulov[1,7,b], Maxfuza Jumayeva[1,c], Khakimjan Butanov[1,d], Wen He[3,e], Jingxiang Low[4,f], Odilhuja Parpiev[1,g], Olim Ruzimuradov[6,h]

[1]Institute of Materials Science, Uzbekistan Academy of Sciences, Tashkent, Uzbekistan

[2]National Research Institute of Renewable Energy Sources, Ministry of Energy, Tashkent, Uzbekistan

[3]School of Materials Science and Engineering, Anhui University, Hefei, China

[4]School of Physical Science and Technology, Tiangong University, Tianjin, China

[5]Alfraganus University, Tashkent, Uzbekistan

[6]Turin Polytechnic University in Tashkent, Tashkent, Uzbekistan

[7]Institute of Fundamental and Applied Research under TIIAME National Research University, Tashkent, Uzbekistan

[a]j.mamanazirov@imssolar.uz, [b]mi-shavkat@yandex.ru, [c]m.jumayeva1988@gmail.com, [d]kh.butanov@gmail.com, [e]hewen@ahu.edu.cn, [f]jxlow@ustc.edu.cn, [g]o.parpiev@imssolar.uz, [h]o.ruzimuradov@polito.uz

Corresponding author: J. Mamanazirov, j.mamanazirov@imssolar.uz

ABSTRACT In this study, we modified Ni based electrodes with MXene and MXene-based composite catalysts for water splitting. The MXene based catalyst exhibited excellent electrochemical surface area (ECSA) of 1840 cm^2, highlighting its abundant active sites. To further enhance catalytic activity, MXene was modified with graphene oxide (GO) and carbon black (CB), which significantly reduced the overpotential from 300 mV to 196 mV at 10 mA cm^{-2} and improved the reaction kinetics, as evidenced by a low Tafel slope of 96.35 mV dec^{-1}. Moreover, the MXene–GO–CB composite demonstrated outstanding long-term durability, maintaining stable operation for 50 h at 100 mA cm^{-2} with only a 34 mV increase in overpotential at 10 mA cm^{-2}. These results confirm that the synergistic combination of MXene with GO and CB yields a highly active and durable electrocatalyst, offering strong potential for practical water electrolysis applications.

KEYWORDS MXene based composites, HER, OER, electrocatalysts.

ACKNOWLEDGEMENTS The authors gratefully acknowledge the support of the Agency of Innovative Development under the Ministry of Higher Education, Science and Innovation of the Republic of Uzbekistan within the framework of research project No. ALM-20230502808. This support made the successful completion of this work possible.

FOR CITATION Javlonbek Mamanazirov, Shavkat Mamatkulov, Maxfuza Jumayeva, Khakimjan Butanov, Wen He, Jingxiang Low, Odilhuja Parpiev, Olim Ruzimuradov MXene based electrocatalysts for efficient water splitting. *Nanosystems: Phys. Chem. Math.*, 2025, **16** (6), 887–896.

1. Introduction

The transition to sustainable energy sources requires the development of efficient and environmentally friendly technologies for hydrogen production. Water electrolysis, particularly when powered by renewable energy sources, is considered one of the most promising routes for hydrogen generation [1–4]. However, the widespread implementation of this technology is hindered by the necessity of using expensive and scarce metals, such as platinum, ruthenium, iridium, etc. as catalysts for the hydrogen evolution reaction (HER) [5–7]. As a result, intensive efforts are being made to find alternative materials that combine high catalytic activity, stability in harsh environments, and cost-effectiveness. Among such materials, MXenes — two-dimensional transition metal carbides — have attracted significant attention due to their high electrical conductivity, large surface area, and tunable surface chemistry through functional group modification. In particular, $Ti_3C_2T_x$ has demonstrated promising properties as a catalyst for HER [8–19]. Nevertheless, the overtime oxidation of MXenes in aqueous environments limits their long-term stability and catalytic efficiency [20–22]. Various electrode architectures based on combinations of MXenes with other materials have been reported. For instance, in the work by Gao et al. [23] an electrode composed of MXene and carbon nanotubes exhibited high HER activity but limited stability in alkaline media. In another study by Meng et al. [24] the use of MXene combined with metal-organic frameworks resulted in good initial performance, but the material quickly degraded under prolonged operation. These findings highlight the need for more stable composite structures.

To improve the stability of MXene-based catalysts, different strategies have been explored, including the formation of composites with other functional materials [25–27]. The incorporation of graphene oxide (GO) has shown to enhance structural stability and oxidation resistance by forming a protective matrix that slows down the degradation of MXene. Its hydrophilic surface and low work function make it an ideal component for tuning the electronic properties of active sites in composite catalysts, thereby improving their catalytic efficiency. Furthermore, the addition of carbon black (CB) can enhance the catalytic performance by improving electrical conductivity, while GO stabilizes the catalyst structure by preventing nanoparticle aggregation and providing mechanical reinforcement. Its functional groups (–OH, –COOH, –C=O) facilitate strong interactions with materials such as MXene, improving dispersion and structural integrity [28–31]. GO offers corrosion resistance in harsh electrochemical environments, increases hydrophilicity, and promotes ion transport, all contributing to enhanced electrochemical performance [32–34]. In addition, the use of nickel foam as a substrate provides mechanical strength and a three-dimensional porous architecture, which supports efficient mass transport [35–38]. The synergistic combination of MXene, CB, and GO on a nickel foam (NF) substrate can significantly enhance water electrolysis efficiency.

In this work, we developed an advanced MXene based electrocatalyst incorporating carbon black (CB) and graphene oxide (GO) to address the limitations of conventional nickel foam (NF) electrodes. The synthesis involved selectively etching the MAX phase to obtain MXene, followed by its deposition onto NF along with CB and GO to enhance conductivity, catalytic activity, and stability. The resulting MXene electrode demonstrated overpotentials of 300 mV for the hydrogen evolution reaction (HER) at 10 mA/cm^2, with Tafel slopes of 113.57 mV/dec, indicating efficient charge transfer kinetics. Integration of GO and CB into the MXene composite (MXene-GO-CB) achieving significantly lower overpotentials of 196 mV for HER at the same current density and 96.35 mV/dec Tafel slope. Electrochemical impedance spectroscopy (EIS) and electrochemically active surface area (ECSA) analysis confirmed the enhanced performance, with the MXene/NF electrode exhibiting low charge transfer resistance and high surface area (ECSA) values of 1840 cm^2, ensuring efficient reaction kinetics.

2. Experimental section

2.1. Materials

All chemicals and materials used in this study were of analytical grade. Ti_3AlC_2 MAX phase was purchased from Laizhou Kai Kai Ceramic Materials Co. Ltd. (China) with a purity of $>$99 wt% and molecular weight (MW) of 194.6 g/mol. Hydrochloric acid (HCl, 37%) was obtained from Sinopharm Chemical Reagent Co., Ltd. (China) and used as an etchant for the selective removal of the A-site element from the MAX phase. Lithium fluoride (LiF, 99%), with an MW of 25.94 g/mol, was purchased from Shanghai Macklin Biochemical Technology Co., Ltd. for the synthesis of $Ti_3C_2T_x$ MXene. For the fabrication of composite electrodes, carbon black (CB) were obtained from Sigma-Aldrich. Nickel foam (NF) with a high porosity structure was used as a conductive substrate for the deposition of MXene-based materials. Deionized (DI) water was used in all synthesis and washing processes to ensure the removal of residual chemicals and maintain the purity of the synthesized MXene.

2.2. Synthesis of MXene

To synthesize $Ti_3C_2T_x$ MXene, the selectively etching method is used. Initially, 30 mL of HCl was combined with 10 mL of deionized water, followed by the addition of 2 mg LiF to the HCl solution, which was stirred for 1 hour. Subsequently, 2 g of Ti_3AlC_2 powder was gradually added into this solution and allowed to stir at room temperature for 29 hours. The resulting suspension was then washed repeatedly with deionized water, centrifuged, and sonicated multiple times to achieve exfoliation of $Ti_3C_2T_x$ into nanosheets, continuing until the pH of the supernatant reached 6–7. The final supernatant was dispersed in water to yield a solution with a concentration of 1.5 mg mL^{-1}. This MXene solution was then freeze-dried to obtain a fluffy powder form.

2.3. Synthesis of GO

In a typical procedure, 1 g of graphite powder was added to a mixture of sulfuric acid and orthophosphoric acid (9:1, 90 mL:10 mL) under continuous stirring in an ice bath maintained at 0°C for 15 minutes. The mixture was stirred with a magnetic stirrer to ensure uniform dispersion. Subsequently, 6 g of potassium permanganate ($KMnO_4$) was gradually introduced into the solution while maintaining the temperature between 0–5°C, followed by continuous stirring for 2 hours. Afterward, the reaction was stirred at room temperature for 30 minutes and then heated to 35°C by immersing the flask in warm water, with stirring continued for another 30 minutes. The oxidation process was further advanced by heating the mixture in an oil bath at 90°C, where 46 mL of deionized (DI) water was slowly added, followed by stirring for 30 minutes. To terminate the reaction, an additional 180 mL of DI water and 10 mL of 30% hydrogen peroxide (H_2O_2) were added, leading to a color change from dark brown to yellow. The reaction was allowed to cool to room temperature before purification. The obtained suspension was washed with 200 mL of 5% HCl and deionized water several times to remove residual ions and acids. Finally, the GO product was filtered and dried at 60°C for 24 hours to obtain a fine powder.

2.4. Synthesis of MXene/NF electrode

Immersing method is used to prepare MXene/NF electrode for experiments [39]. Initially, the nickel foam (NF) was immersed in 3 M HCl solution for 2 hours to remove impurities and oxides. This was followed by ultrasonic cleaning in acetone, ethanol, and deionized water for 15 minutes each, then drying at 60°C in an oven. The cleaned NF was subsequently immersed in a $Ti_3C_2T_x$ MXene solution (4 mg mL^{-1}) for 1 hour, followed by vacuum drying for 12 hours, yielding the MXene/NF electrode.

2.5. Synthesis of MXene-GO-CB/NF and other composite electrodes

A stock solution of synthesized MXene (1.6 mg mL^{-1}) was prepared, while graphene oxide (GO, 4 mg mL^{-1}) and carbon black (CB, 4 mg mL^{-1}) were dispersed separately in 10 mL deionized water. To fabricate the MXene–GO–CB composite electrode, 25 mL of the MXene solution was mixed with 0.25 mL of GO and 0.25 mL of CB solutions, followed by ultrasonication for 10 min to ensure homogeneous dispersion. Nickel foam (NF) substrates were immersed in the resulting suspension for 1 h and then dried in an oven under continuous argon flow, where the temperature was gradually increased to 170°C and maintained for 24 h. For comparison, MXene–CB and MXene–GO electrodes were prepared using the same procedure but without the addition of GO and CB, respectively.

2.6. Electrochemical analysis

Electrochemical measurements were carried out on a CHI760E electrochemical workstation (China) in 1 M KOH electrolyte under iR-corrected conditions. A three-electrode configuration was employed, in which the synthesized MXene based electrodes served as the working electrodes (WE), a platinum foil was used as the counter electrode (CE), and an Ag/AgCl electrode functioned as the reference electrode (RE). The measured potentials (E_m) were converted to the reversible hydrogen electrode (RHE) scale according to the equation: E vs RHE = E_{SHE} + $E_{Ag/AgCl}$+ 0.059 x pH and pH = 14 for 1 M KOH. The mass loading of the active material on the NF substrate was 0.015 mg cm^{-2} for the MXene–GO–CB/NF electrode. Geometric area of the prepared electrodes are 1.6 cm^2. In order to approximate the empirical data of EIS, Randles electrical circuit was used.

3. Results and discussion

SEM image (Fig. 1) shows a well-formed MAX phase material, displaying the characteristic layered morphology of alternating (M) and (A) element layers, typical of Ti_3AlC_2. The undulating texture with intact stratifications indicates a stable structure, with no signs of delamination, which aligns with the material being a MAX phase rather than an etched MXene. The small particles observed on the surface could be residual synthesis by-products or minor impurities. At 10,000x magnification, the continuity and integrity of the layers suggest good sample quality, with well-preserved lamellar features that support the robustness of MAX phase properties. Fig. 1b shows the morphology of exfoliated $Ti_3C_2T_x$ MXene synthesized by selective etching of MAX with HCl and LiF. The images reveal well-defined, with large surface area, and thin single-layer MXene sheets with a lateral size in the 10 μm range.

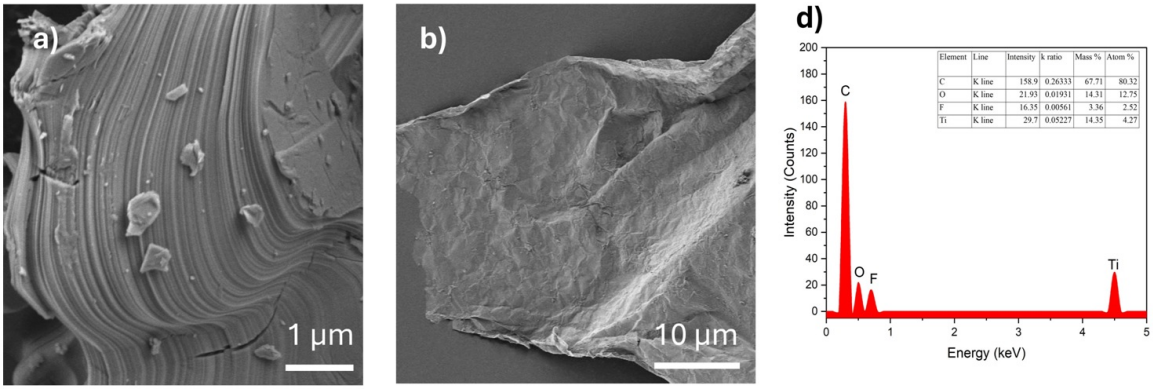

FIG. 1. (a) SEM image of the MAX phase, showing a layered structure. (b) Single-layer MXene sheets. (d) EDX spectrum of MXene, confirming the presence of Ti, C, O, F

The clear exfoliation and separation of individual layers are characteristic of successful delamination, where the thickness of each layer is approximately 1–2 nm, consistent with literature reports for monolayer $Ti_3C_2T_x$ [40]. The wrinkled and crumpled nature of the flakes suggests flexibility and structural integrity at the nanoscale, which are common features of MXene sheets [41]. These characteristics, coupled with the absence of aggregation, confirm the successful synthesis of high-quality, monolayer MXene, a key factor in maximizing surface area and ensuring optimal electrochemical performance in potential applications [42]. The EDS analysis in Fig. 1d and elemental mapping presented in Fig. 2 show that the elements of the material are evenly distributed and the $Ti_3C_2T_x$ MXene was functionalized [43]. By using HCl and LiF,

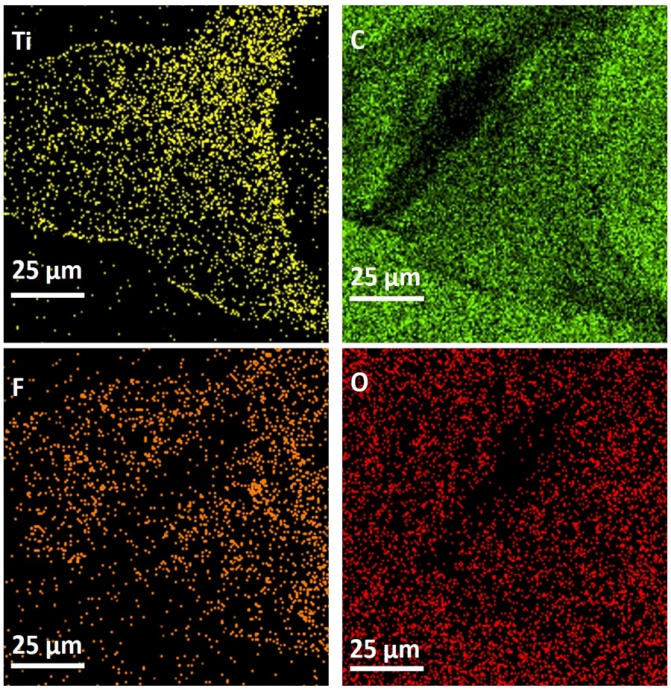

FIG. 2. EDS elemental mapping of $Ti_3C_2T_x$ MXene, showing the distribution of different elements

the aluminium layers were effectively removed from the MAX phase [44]. The high carbon content (80.32 at%) and its predominant presence in the mapping, represented in green, confirm the retention of the carbon layers, essential for the 2D structure and electrical conductivity of MXene [45]. Titanium (4.27 at%) is evenly distributed, as shown in yellow, supporting the structural integrity of the Ti_3C_2 phase. The oxygen (12.75 at%) and fluorine (2.52 at%) content, marked in red and light blue, respectively, indicate the formation of –O and –F surface terminations during the etching process. These functional groups enhance hydrophilicity, provide active sites for electrochemical reactions, and improve charge transfer properties, which are critical for applications such as hydrogen evolution reactions (HER) and energy storage [46]. The surface chemistry, shaped by the presence of these terminations, makes $Ti_3C_2T_x$ MXene a highly promising candidate for use in electrochemical systems, including supercapacitors and water electrolysers, due to its unique combination of electrical conductivity, chemical stability, and surface reactivity.

X-ray photoelectron spectroscopy (XPS) was utilized to determine the surface chemical composition and bonding states of the synthesized MXene. The survey scan (Fig. 3a) confirmes the presence of Titanium (Ti), Carbon (C), Oxygen (O), Fluorine (F), and trace Chlorine (Cl). Analysis of the high-resolution C 1s spectrum (Fig. 3c) revealed a distinct peak component around 282 eV, characteristic of Ti–C bonds within the MXene lattice, alongside peaks for adventitious carbon and carbon-oxygen bonds. The Ti 2p spectrum (Fig. 3b) exhibited broad features consistent with multiple Ti chemical states, including Ti–C, Ti–O, and Ti–F bonds typical for functionalized MXene. Strong signals in the F 1s (centered ∼685–686 eV, Fig. 3d) and O 1s (broad peak ∼530–532 eV, Fig. 3e) spectra confirm the presence of significant –F, –O, and –OH surface terminations, which are expected outcomes of the LiF/HCl etching procedure. These results collectively verify the successful synthesis and surface functionalization of the Ti-based MXene [47]. In Fig. 3f, X-ray diffraction (XRD) pattern of the MAX phase (blue) shows a distinct (002) peak at 9.56° (2θ), corresponding to a d-spacing of 9.3 Å, calculated using Bragg's law [48] with a Cu Kα wavelength of 1.54056Å. This peak reflects the interlayer spacing between Ti_3C_2 layers in the hexagonal crystal structure (P63/mmc) [49]. Additional peaks at 18.8° (004), 39.1° (104), 41.6° (105), 48.5° (107), and minor peaks at 60.6° (2-1-0) and 78.5°C (2-1-8) confirm the presence of characteristic planes, indicating a well-crystallized MAX phase. The absence of extraneous peaks suggests high phase purity, with no significant impurities detected. For the XRD analysis of the MXene (red), the (002) peak observed at 6.1° (2θ) corresponds to a d-spacing of 14.48Å, which is significantly larger than the original MAX phase (002) peak. This increase in interlayer spacing is expected after etching the Al layer [50], as it allows the layers to delaminate, creating a single-layer MXene. The larger d-spacing reflects the successful exfoliation of the MXene layers. The minor peaks at 18.5° (004) and 19.5° (006) suggest the multilayer nature of some residual MXene layers. The thickness of a single MXene layer is around 1–2 nm, which is consistent with typical MXene morphology [51]. The aforementioned characterizations can prove that the successful synthesis of single-layer MXene.

Electrochemical measurements were performed under iR-corrected conditions to evaluate the HER activity of the synthesized electrodes (Fig. 4a). The polarization curves clearly demonstrate that the incorporation of GO and CB into the MXene framework significantly enhances catalytic performance. The MXene–GO–CB composite exhibited the lowest

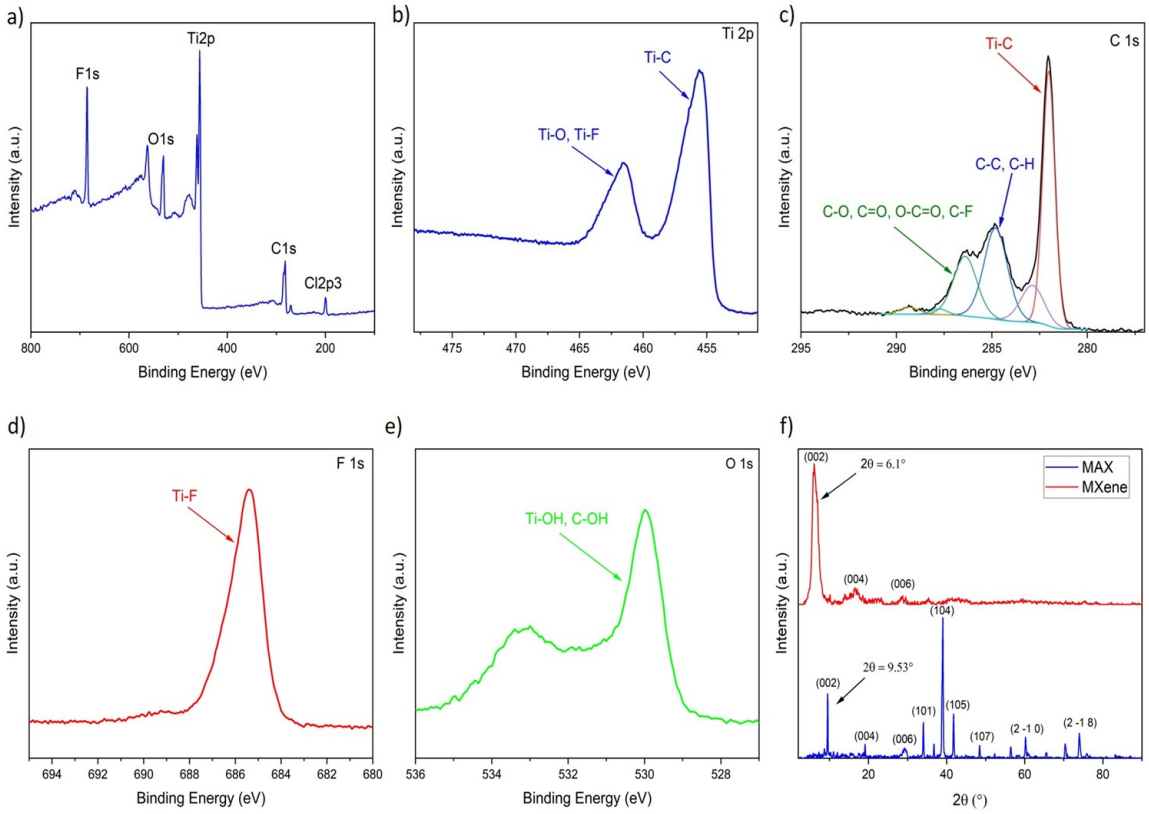

FIG. 3. XPS and XRD characterization of $Ti_3C_2T_x$ MXene synthesized from Ti_3AlC_2 MAX phase. (a) The full XPS survey spectrum. (b) The high-resolution Ti 2p spectrum. (c) The C 1s spectrum. (d) The F 1s peak. (e) The O 1s spectrum. (f) XRD patterns of the MAX phase (blue) and exfoliated MXene (red)

overpotential of 196 mV at 10 mA cm^{-2}, outperforming pristine MXene (300 mV), MXene–GO (248 mV), and MXene–CB (266 mV). This pronounced improvement highlights the synergistic effect of GO and CB in facilitating charge transfer, improving conductivity, and providing additional active sites, thereby accelerating HER kinetics compared to single-component or binary composites. The Tafel slope, which offers insight into the reaction mechanism, was determined by plotting overpotential against the logarithm of current density following the equation [52]:

$$b = \frac{\Delta\eta}{\Delta\left(\log j\right)}$$

where b is the Tafel slope, typically expressed in mV/dec Higher Tafel slope values often indicate a one-electron transfer rate-limiting step, while lower values suggest faster kinetics or differing rate determining steps [53].

The catalytic kinetics of the prepared electrodes were further evaluated by Tafel slope analysis (Fig. 4b). Pristine MXene exhibited a Tafel slope of 113.57 mV dec^{-1}, while the binary composites MXene–GO and MXene–CB showed slopes of 113.95 mV dec^{-1} and 152.8 mV dec^{-1}, respectively. In contrast, the MXene–GO–CB composite achieved the lowest Tafel slope of 96.35 mV dec^{-1}, confirming its faster HER kinetics. These results indicate that the synergistic combination of GO and CB with MXene not only lowers the overpotential but also accelerates the reaction pathway, facilitating more efficient electron transfer and hydrogen evolution compared to individual or binary systems. The observations can be attributed to electron density distribution and interfacial interactions, where MXene's metallic conductivity ensures rapid charge mobility, while GO and CB enhance the exposure of active sites. MXene's surface functional groups (-OH, -F, -O) contribute to its catalytic behavior, influencing intermediate adsorption and reaction pathways. The presence of GO and CB in MXene-GO-CB/NF enhances the catalytic activity by increasing active surface area and promoting mass transport, making it a favorable electrode for reducing overpotential.

The long-term durability of the MXene–GO–CB/NF composite electrocatalyst was evaluated by chronopotentiometry and LSV measurements (Fig. 5). Under a constant current density of 100 mA cm^{-2}, the electrode exhibited rapid stabilization within the first few minutes, followed by a steady operation over 50 h with only a slight potential increase of $\sim$0.07 V, confirming its excellent structural and electrochemical robustness. Furthermore, the LSV curves recorded before and after the stability test showed a minor performance decay, with the overpotential at 10 mA cm^{-2} shifting from 196 to 230 mV. This negligible change (34 mV) highlights the strong durability of the MXene–GO–CB/NF electrode under harsh and continuous HER operating conditions, underscoring its potential for practical water electrolysis applications.

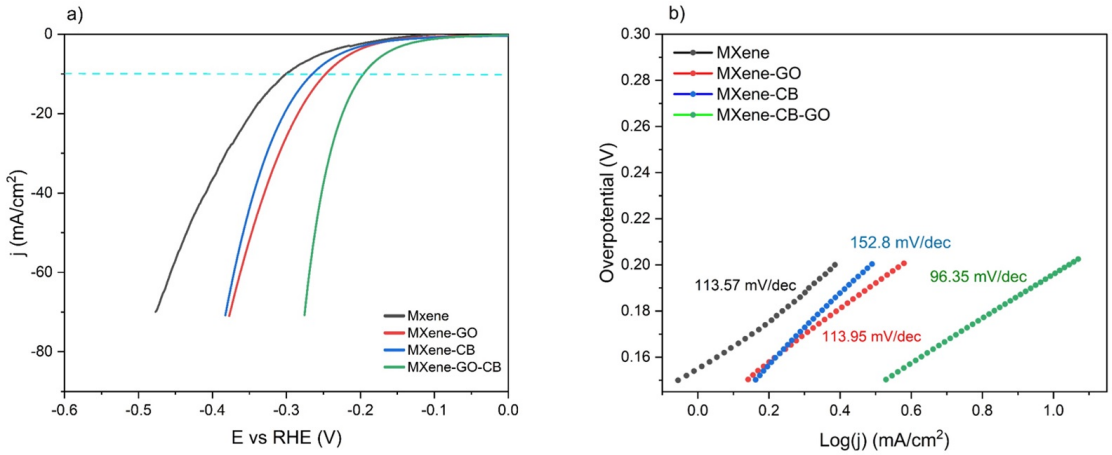

FIG. 4. Electrochemical performance of MXene, MXene-GO, MXene-CB, and MXene-GO-CB composite electrodes in 1 M KOH. (a) Half-cell polarization curves of all electrodes. (b) Corresponding Tafel plots

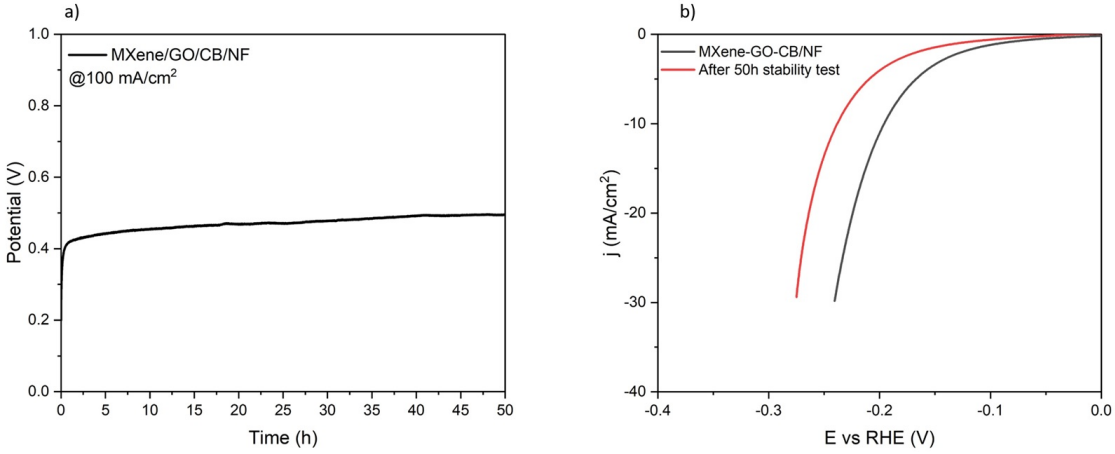

FIG. 5. Stability evaluation of the MXene-GO-CB/NF composite electrocatalyst. (a) Chronopotentiometry measurement at a constant current density of 100 mA cm^{-2} for 50 h. (b) LSV polarization curves recorded before and after the 50 h stability test

Electrochemical impedance spectroscopy (EIS) measurements were conducted at fixed potentials of 1.6 V vs. RHE for OER and −0.3 V vs. RHE for HER. The measurements frequency range is from 0.1 Hz to 100 kHz with a small AC amplitude of 5 mV. The Nyquist plots for both OER and HER were present in Fig. 6, with the real part of the impedance (Z') on the x-axis and the imaginary part (Z'') on the y-axis. The Nyquist plot analysis shows that the MXene/NF electrode exhibits distinct charge transfer resistance (R_{ct}) values for the OER and HER processes, with R_{ct} measured at 1.02 Ω for OER and 0.6 Ω for HER. The relatively low R_{ct} for HER, in particular, indicates more efficient electron transfer, suggesting higher conductivity and catalytic performance under alkaline conditions. These results underscore the MXene/NF electrode's effectiveness as a bifunctional catalyst, capable of facilitating both oxygen and hydrogen evolution reactions with promising efficiency, making it a viable candidate for applications in sustainable hydrogen production and alkaline water electrolysis.

The double-layer capacitance, C_{dl}, is a parameter that represents the capacitance of the electrical double layer formed at the interface between the electrode surface and the electrolyte solution. When a potential is applied to the electrode, ions from the electrolyte are attracted to the surface, creating a double layer of charges with a capacitance that depends on the surface area of the electrode.

Fig. 7a presents cyclic voltammetry (CV) curves for the MXene/Nickel Foam (NF) electrode recorded at various scan rates (1, 2, 3, 4, and 5 mV/s). These curves illustrate the capacitive behavior of the electrode in the non-faradaic region which is from −140 mV to −35 mV, confirming the formation of an electrochemical double layer. The gradual increase in current density with increasing scan rate indicates enhanced charge storage capabilities and surface area exposure. Chosen anodic and cathodic currents were shown in Fig. 7b. To calculate C_{dl}, the linear fitting of $\Delta j/2$ versus scan rate is plotted in Fig. 7c, revealing a double layer capacitance per unit area value of 73.6 mF/cm^2.

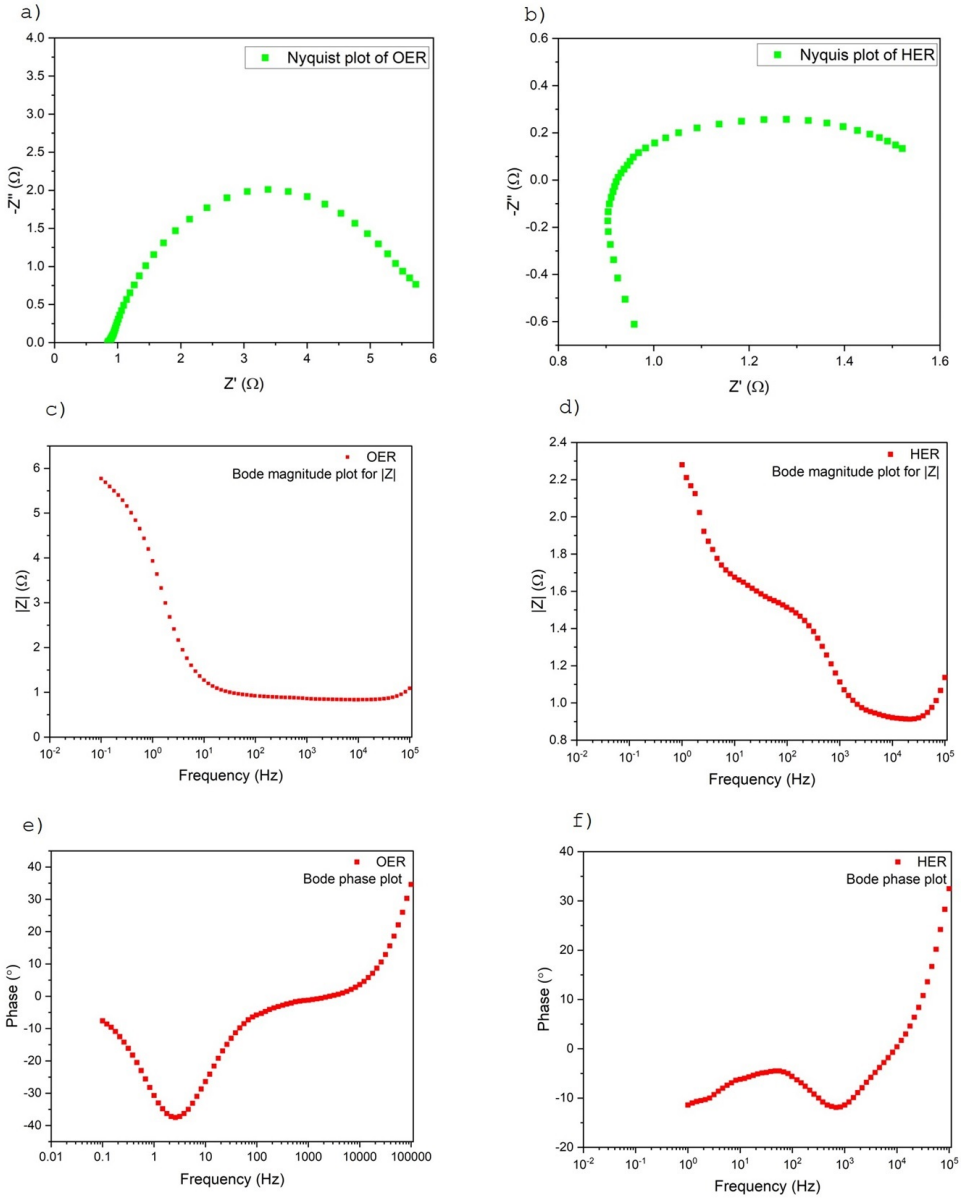

FIG. 6. Electrochemical Impedance Spectroscopy (EIS) analysis of the electrode during the Oxygen Evolution Reaction (OER) and Hydrogen Evolution Reaction (HER). (a, b) Nyquist plots for OER and HER, respectively, showing the real (Z') and imaginary ($-Z''$) components of impedance. (c, d) Bode magnitude plots showing $|Z|$ as a function of frequency for OER and HER, respectively. (e, f) Bode phase plots displaying the phase angle versus frequency for OER and HER, respectively

The specific capacitance, C_s, represents the intrinsic capacitance per unit area of a material in a given electrolyte, and it can vary based on the electrode material and electrolyte conditions. The specific capacitance values (C_s) for a flat standard with 1 cm^2 of the real surface area that is generally in the range of 20 to 60 μF cm^{-2} (40 μF cm^{-2} was taken as the average value) [54]. For our electrode with 1.6 cm^2 surface area, Cs is 64 μFcm^{-2}. These results indicate that the MXene/NF composite provides substantially higher specific capacitance than nickel foam alone, likely due to large electrochemical surface area and elevated capacitance of MXene.

ESCA was calculated by using C_{dl} and C_s [55] using the following equation:

$$\text{ECSA} = \frac{C_{dl}}{C_s}$$

The electrochemical surface area (ECSA) of the MXene/NF composite shows 1840 cm^2. These values are notably higher than those typically observed for conventional electrode materials like pristine nickel foam, which commonly exhibit lower ECSAs due to their relatively limited surface areas and active sites. The enhanced ECSA values observed in the MXene/NF composite are indicative of the substantial increase in active surface area provided by MXenes, which likely contributes to its superior electrocatalytic performance in both OER and HER processes.

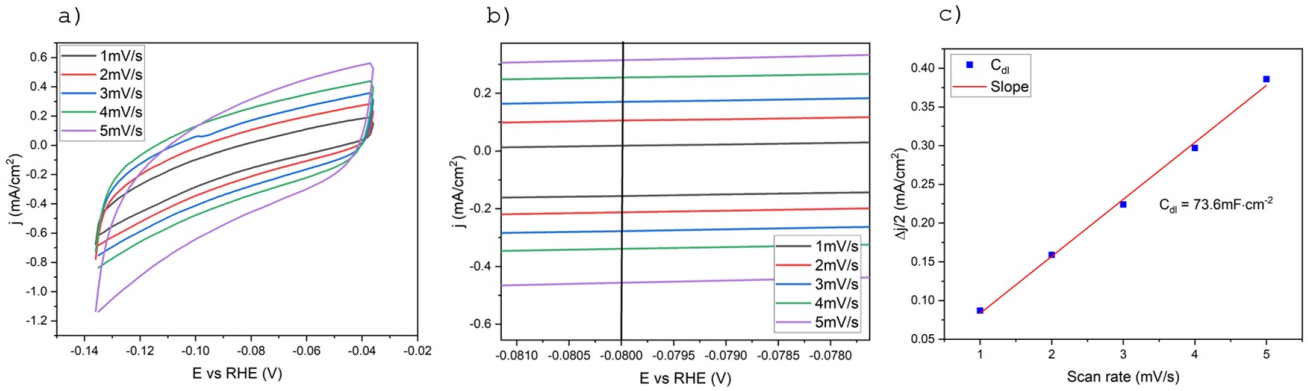

FIG. 7. (a) Cyclic voltammetry curves at various scan rates (1–5 mV s^{-1}) for C_{dl} determination, (b) current density differences (Δj) versus potential at a fixed potential, and (c) linear fitting of Δj/2 versus scan rate for C_{dl} extraction

4. Conclusion

In this study, we successfully synthesized $Ti_3C_2T_x$ MXene and its composite electrodes with graphene oxide (GO) and carbon black (CB) on nickel foam (NF) substrates for efficient water splitting applications. Structural and compositional analyses, including SEM, XRD, and XPS, confirmed the successful etching of the MAX phase, formation of single-layer $Ti_3C_2T_x$ MXene sheets, and the presence of functional surface terminations beneficial for catalytic activity. The incorporation of GO and CB into the MXene framework significantly enhanced electrochemical performance by improving conductivity, stability, and active surface area.

Electrochemical evaluations demonstrated that the MXene–GO–CB composite electrode exhibited a remarkably low overpotential of 196 mV at 10 mA cm^{-2} for the hydrogen evolution reaction (HER), outperforming pristine MXene and binary composites. The reduced Tafel slope (96.35 mV dec^{-1}), low charge-transfer resistance (R_{ct}), and high electrochemical surface area (ECSA = 1840 cm^2) confirmed improved reaction kinetics and abundant active sites. Moreover, the electrode maintained good long-term stability, with only minimal performance degradation after 50 h of continuous operation at 100 mA cm^{-2}, highlighting its robustness under harsh alkaline conditions.

Overall, the synergistic effects of MXene, GO, and CB on NF resulted in a highly efficient, durable, and cost-effective electrocatalyst for hydrogen production. This work provides a promising strategy for the rational design of advanced MXene-based composites for large-scale and sustainable water electrolysis applications. Future studies should focus on optimizing composite architectures, scaling up synthesis techniques, and integrating these materials into practical electrolyzer systems for renewable hydrogen generation.

References

[1] Sampene A.K., Li C., Wiredu J. An outlook at the switch to renewable energy in emerging economies: The beneficial effect of technological innovation and green finance. *Energy Policy*, 2024, **187**, P. 114025.

[2] Ehteshami, S.M.M., Chan S.H. The role of hydrogen and fuel cells to store renewable energy in the future energy network – potentials and challenges. *Energy Policy*, 2014, **73**, P. 103–109.

[3] Anderson D., Leach M. Harvesting and redistributing renewable energy: on the role of gas and electricity grids to overcome intermittency through the generation and storage of hydrogen. *Energy Policy*, 2003, **32**(14), P. 1603–1614.

[4] Luo Z., Hu Y., Xu H., Gao D., Li W. Cost-Economic analysis of hydrogen for China's fuel cell transportation field. *Energies*, 2020, **13**(24), P. 6522.

[5] Olivier P., Bourasseau C., Bouamama Pr.B. Low-temperature electrolysis system modelling: A review. *Renewable and Sustainable Energy Reviews*, 2017, **78**, P. 280–300.

[6] Karthikeyan S.C., Sidra S., Ramakrishnan S., Kim D.H., Sagayaraj P.J., Sekar K., Yoo D.J. Heterostructured NiO/IrO_2 synergistic pair as durable trifunctional electrocatalysts towards water splitting and rechargeable zinc-air batteries: An experimental and theoretical study. *Applied Catalysis B Environment and Energy* 2024, **355**, P. 124196.

[7] Qadeer M.A., Zhang X., Farid M.A., Tanveer M., Yan Y., Du S., Huang Z., Tahir M., Zou J. A review on fundamentals for designing hydrogen evolution electrocatalyst. *Journal of Power Sources*, 2024, **613**, P. 234856.

[8] Tang J., Xu X., Tang T., Zhong Y., Shao Z. Perovskite-Based electrocatalysts for Cost-Effective Ultrahigh-Current-Density water splitting in anion exchange membrane electrolyzer cell. *Small Methods*, 2022, **6**(11).

[9] Amani A.M., Tayebi L., Vafa E., Jahanbin A., Abbasi M., Vaez A., Kamyab H., Chelliapan S. Innovation applications of MXenes in biomedicine. *Materials Today Communications*, 2024, **40**, P. 109929.

[10] Naguib M., Kurtoglu M., Presser V., Lu J., Niu J., Heon M., Hultman L., Gogotsi Y., Barsoum M.W. *Two-Dimensional Nanocrystals Produced by Exfoliation of Ti_3AlC_2*, 2023.

[11] Fu L., Xia W. MAX phases as nanolaminate materials: chemical composition, microstructure, synthesis, properties, and applications. *Advanced Engineering Materials*, 2020, **23**(4).

[12] Haemers J., Gusmão R., Sofer Z. Synthesis protocols of the most common layered carbide and nitride MAX phases. *Small Methods*, 2020, **4**(3).

[13] Sokol M., Natu V., Kota S., Barsoum M.W. On the Chemical Diversity of the MAX Phases. *Trends in Chemistry*, 2019, **1**(2), P. 210–223.

[14] Barsoum M.W., Radovic M. Elastic and mechanical properties of the MAX phases. *Annual Review of Materials Research* 2011, **41**(1), P. 195–227.

[15] Wei Y., Zhang P., Soomro R. A., Zhu Q., Xu B. Advances in the synthesis of 2D MXenes. *Advanced Materials*, 2021, **33**(39).

[16] Kajiyama S., Szabova L., Iinuma H., Sugahara A., Gotoh K., Sodeyama K., Tateyama Y., Okubo M., Yamada A. Enhanced Li-Ion accessibility in MXENE titanium carbide by steric chloride termination. *Advanced Energy Materials*, 2017, **7**(9).

[17] Naguib M., Kurtoglu M., Presser V., Lu J., Niu J., Heon M., Hultman L., Gogotsi Y., Barsoum M.W. Two-Dimensional nanocrystals produced by exfoliation of TI_3ALC_2. *Advanced Materials*, 2011, **23**(37), P. 4248–4253.

[18] Yang S., Zhang P., Wang F., Ricciardulli A.G., Lohe M.R., Blom P.W.M., Feng X. Fluoride-Free synthesis of Two-Dimensional titanium carbide (MXENE) using a binary aqueous system. *Angewandte Chemie International Edition*, 2018, **57**(47), P. 15491–15495.

[19] Ni Q.-Y., He X.-F., Zhou J.-L., Yang Y.-Q., Zeng Z.-F., Mao P.-F., Luo Y.-H., Xu J.-M., Jiang B., Wu Q., Wang B., Qin Y.-Q., Gong L.-X., Tang L.-C., Li S.-N. Mechanical tough and stretchable quaternized cellulose nanofibrils/MXene conductive hydrogel for flexible strain sensor with multi-scale monitoring. *Journal of Material Science and Technology*, 2024, **191**, P. 181–191.

[20] Jiang M., Wang D., Kim Y., Duan C., Talapin D.V., Zhou C. Evolution of Surface Chemistry in Two-Dimensional MXEnES: From mixed to Tunable Uniform Terminations. *Angewandte Chemie*, 2024, **136**(37).

[21] Cao, Fangcheng, et al. Recent Advances in Oxidation Stable Chemistry of 2D MXenes. *Advanced Materials*, 2022, **34**(13), P. 2107554.

[22] Soomro, Razium A., et al. Progression in the Oxidation Stability of MXenes. *Nano-Micro Letters*, 2023, **15**(1), P. 18.

[23] Iqbal, Aamir, et al. Improving Oxidation Stability of 2D MXenes: Synthesis, Storage Media, and Conditions. *Nano Convergence*, 2021, **8**(1), P. 16.

[24] Gao X., Du X., Mathis T.S., et al. Maximizing ion accessibility in MXene-knotted carbon nanotube composite electrodes for high-rate electrochemical energy storage. *Nat Commun*, 2020, **11**, P. 6160.

[25] Meng, Weisong, et al. Alkalized MXene/Carbon Nanotube Composite for Stable Na Metal Anodes. *RSC Advances*, 2024, **14**(17), P. 12030–12037.

[26] Iravani, Siavash, et al. Advancements in MXenes and Mechanochemistry: Exploring New Horizons and Future Applications. *Materials Advances*, 2024, **5**(21), P. 8404–8418.

[27] He Lei, et al. Advances and Challenges in MXene-Based Electrocatalysts: Unlocking the Potential for Sustainable Energy Conversion. *Materials Horizons*, 2024, **11**(18), P. 4239–4255.

[28] Zhang, Qingxiao, et al. Synthesis and Design Strategies of MXene Used as Catalysts. *ChemCatChem*, 2024, **16**(22).

[29] Zhou Tianzhu, et al. Super-Tough MXene-Functionalized Graphene Sheets. *Nature Communications*, 2020, **11**(1), P. 2077.

[30] Li Xiao-Peng, et al. Reshapable MXene/Graphene Oxide/Polyaniline Plastic Hybrids with Patternable Surfaces for Highly Efficient Solar-Driven Water Purification. *Advanced Functional Materials*, 2021, **32**(15).

[31] Gong Kaili, et al. MXene as Emerging Nanofillers for High-Performance Polymer Composites: A Review. *Composites Part B: Engineering*, 2021, **217**, P. 108867.

[32] Iravani Siavash, et al. Synergistic Advancements: Exploring MXene/Graphene Oxide and MXene/Reduced Graphene Oxide Composites for Next-Generation Applications. *FlatChem*, 2024, **48**, P. 100759.

[33] Liu Qi, et al. Improved Anti-Corrosion Behaviour of an Inorganic Passive Film on Hot-Dip Galvanised Steel by Modified Graphene Oxide Incorporation. *Corrosion Science*, 2020, **174**, P. 108846.

[34] Yin Yiming, et al. Distinct Ion Transport Behavior between Graphene Oxide and UV-Irradiated Reduced Graphene Oxide Membranes. *Chemical Engineering Journal*, 2024, **493**, Aug., P. 152304.

[35] Amir Reza Salasel, et al. Role of Graphene Concentration on Electrochemical and Tribological Properties of Graphene-Poly(Methyl Methacrylate) Composite Coatings. *Journal of Composite Materials*, 2023, **57**(24), P. 3877–3896.

[36] Su, Liwei, et al. N-Doped Carbon Nanolayer Modified Nickel Foam: A Novel Substrate for Supercapacitors. *Applied Surface Science*, 2020, **546**, P. 148754–148754.

[37] Zhang Jiaoyuan, et al. Construction of ZnO@Co3O4-Loaded Nickel Foam with Abrasion Resistance and Chemical Stability for Oil/Water Separation. *Surface and Coatings Technology*, 2019, **357**, P. 244–251.

[38] Das, Manisha, et al. Three-Dimensional Nickel and Copper-Based Foam-In-Foam Architecture as an Electrode for Efficient Water Electrolysis. *Catalysis Today*, 2023, **424**(1), P. 113836.

[39] Ao Guang-Hong, et al. Construction of Hierarchical Porous Architecture on Ni Foam for Efficient Oxygen Evolution Reaction Electrode. *Frontiers in Materials*, 2021, **8**.

[40] Yu K., Zhang J., Hu Y., Wang L., Zhang X., Zhao B. Ni Doped Co-MOF-74 Synergized with 2D Ti3C2Tx MXene as an Efficient Electrocatalyst for Overall Water-Splitting. *Catalysts*, 2024, **14**(3), P. 184.

[41] Shi X., Yu Z., Liu Z., Cao N., Zhu L., Liu Y., Zhao K., Shi T., Yin L., Fan Z. Scalable, High-Yield Monolayer MXene Preparation from Multilayer MXene for Many Applications. *Angewandte Chemie*, 2024.

[42] Jiang S., Lu L., Song Y. Recent Advances of Flexible MXene and its Composites for Supercapacitors. *Chemistry – a European Journal* 2024, **30**(24).

[43] Khanal R., Irle S. Effect of surface functional groups on MXene conductivity. *The Journal of Chemical Physics*. 2023, **158**(19).

[44] Zhang Wei, et al. Effect of Carbon Black Concentration on Electrical Conductivity of Epoxy Resin–Carbon Black–Silica Nanocomposites. *Journal of Materials Science*, 2007, **42**(18), P. 7861–7865.

[45] Abdullah N., Ishak N.A.I.M., Tan K.H., Zaed M.A., Saidur R., Pandey A.K. Investigating the impact of various etching agents on Ti_3C_2Tx MXene synthesis for electrochemical energy conversion. *FlatChem*, 2024, **47**, P. 100730.

[46] Verger L., Xu C., Natu V., Cheng H.-M., Ren W., Barsoum M.W. Overview of the synthesis of MXenes and other ultrathin 2D transition metal carbides and nitrides. *Current Opinion in Solid State and Materials Science*, 2019, **23**(3), P. 149–163.

[47] Miao B., Bashir T., Zhang H., Ali T., Raza S., He D., Liu Y., Bai J. Impact of various 2D MXene surface terminating groups in energy conversion. *Renewable and Sustainable Energy Reviews*, 2024, **199**, P. 114506.

[48] Singh, Iqbal, et al. Modification of the Properties of Titanium Carbide MXene by Ag Doping via Ion Implantation for Quantum Dot-Sensitized Solar Cell Applications. *Journal of Electronic Materials*, 2024, **53**(9), P. 5007–5017.

[49] González A. 1.5 X-Ray Crystallography: Data Collection Strategies and Resources. *Comprehensive Biophysics*, 2012, P. 64–91.

[50] Mamanazirov J.I., Ruzimuradov O.N., Mamatkulov Sh.I. THE IMPACT OF 2D MXENE ON ALUMINA BASED INKS FOR DIRECT INK WRITING. *Ceramics International*, 2025, **51**(12PA), P. 15725–15732.

[51] Yun T., Kim H., Iqbal A., Cho Y.S., Lee G.S., Kim M., Kim S.J., Kim D., Gogotsi Y., Kim S.O., Koo C.M. Electromagnetic shielding of monolayer MXENE assemblies. *Advanced Materials*, 2020, **32**(9).

[52] Murthy A.P., Theerthagiri J., Madhavan J. Insights on Tafel constant in the analysis of hydrogen evolution reaction. *The Journal of Physical Chemistry C* 2018, **122**(42), P. 23943–23949.

[53] Thomas J.G.N. Kinetics of electrolytic hydrogen evolution and the adsorption of hydrogen by metals. *Transactions of the Faraday Society*, 1961, **57**, P. 1603.

[54] Sergiienko S.A., Lajaunie L., Rodríguez-Castellón E., et al. Composite MAX phase/MXene/Ni electrodes with a porous 3D structure for hydrogen evolution and energy storage application. *RSC Advances*, 2024, **14**(5), P. 3052–3069.
[55] Granozzi G., Alonso-Vante N. *Electrochemical Surface Science: Basics and applications*, MDPI, 2019.

Submitted 29 July 2025; revised 27 September 2025; accepted 4 December 2025

Information about the authors:

Javlonbek Mamanazirov – Institute of Materials Science, Uzbekistan Academy of Sciences, Chingiz Aytmatov 2B St., Tashkent, 100084, Uzbekistan; National Research Institute of Renewable Energy Sources, Ministry of Energy, Bodomzor Yuli 2B St., Tashkent, 100084, Uzbekistan; ORCID 0009-0004-2222-2461; j.mamanazirov@imssolar.uz

Shavkat Mamatkulov – Institute of Materials Science, Uzbekistan Academy of Sciences, Chingiz Aytmatov 2B St., Tashkent, 100084, Uzbekistan; Institute of Fundamental and Applied Research under TIIAME National Research University, Mirzo Ulug'bek district, Qori Niyaziy street 39, Tashkent, 100000, Uzbekistan; ORCID 0000-0002-9694-4430; mi-shavkat@yandex.ru

Maxfuza Jumayeva – Institute of Materials Science, Uzbekistan Academy of Sciences, Chingiz Aytmatov 2B St., Tashkent, 100084, Uzbekistan; m.jumayeva1988@gmail.com

Khakimjan Butanov – Institute of Materials Science, Uzbekistan Academy of Sciences, Chingiz Aytmatov 2B St., Tashkent, 100084, Uzbekistan; ORCID 0000-0003-1805-9089; kh.butanov@gmail.com

Wen He – School of Materials Science and Engineering, Anhui University, Hefei, 230601, China; ORCID 0000-0002-7673-7274; hewen@ahu.edu.cn

Jingxiang Low – School of Physical Science and Technology, Tiangong University, Tianjin, 300387, P.R. China; ORCID 0000-0002-2486-6357; jxlow@ustc.edu.cn

Odilhuja Parpiev – Institute of Materials Science, Uzbekistan Academy of Sciences, Chingiz Aytmatov 2B St., Tashkent, 100084, Uzbekistan; ORCID 0000-0002-7494-3445; o.parpiev@imssolar.uz

Olim Ruzimuradov – Turin Polytechnic University in Tashkent, Tashkent, 100095, Uzbekistan; ORCID 0000-0002-9186-9080; o.ruzimuradov@new.polito.uz

Conflict of interest: the authors declare no conflict of interest.

NANOSYSTEMS:
PHYSICS, CHEMISTRY, MATHEMATICS

Original article

Luginina A.A., et al. *Nanosystems: Phys. Chem. Math.*, 2025, **16** (6), 897–907.
http://nanojournal.ifmo.ru
DOI 10.17586/2220-8054-2025-16-6-897-907

Formation of NH_4MgF_3 and MgF_2 nanoparticles from magnesium hydroxycarbonate in ammonium hydrofluoride melt

Anna A. Luginina[1,a], Alexander A. Alexandrov[1,2,b], Darya S. Yasyrkina[1,c], Julia A. Ermakova[1,d], Victoria V. Tapero[1,3,e], Sergey V. Kuznetsov[1,f]

[1]Prokhorov General Physics Institute of the Russian Academy of Sciences, Moscow, Russia
[2]Kurnakov Institute of General and Inorganic Chemistry of the Russian Academy of Sciences, Moscow, Russia
[3]Department of Materials Science of Semiconductors and Dielectrics, National University of Science and Technology (MISIS), Moscow, Russia

[a]annaluginina@mail.ru, [b]alexandrov1996@yandex.ru, [c]darya.yasyrkina@gmail.com, [d]julia.r89@mail.ru,[e]kvv.padi@gmail.com, [f]kouznetzovsv@gmail.com

Corresponding author: A. A. Alexandrov, alexandrov1996@yandex.ru

ABSTRACT Ammonium fluorometalates with the perovskite structure NH_4MF_3 (M = 3d metals) are used for cathode materials and NH_4MgF_3 is used for solid electrolytes. There is only fragmentary information in the literature about the production of NH_4MgF_3 powder without available X-ray diffraction data. The conditions enable the synthesis of single-phase NH_4MgF_3 powder are proposed by reaction of magnesium hydroxycarbonate with ammonium hydrofluoride melt at a temperature of 220 °C. It has been established that the process is two-stage: the first reaction is the formation of the $(NH_4)_2MgF_4$ compound and the second reaction is the decomposition of $(NH_4)_2MgF_4$ at a temperature of 220 °C to NH_4MgF_3. Upon decomposition of NH_4MgF_3, anhydrous MgF_2 nanoparticles (28 ± 7 nm) are formed. The proposed method for obtaining single-phase NH_4MgF_3 opens up opportunities for studying its functional properties.

KEYWORDS ammonium fluorometalate, cubic perovskite structure, magnesium fluoride, nanoscale powders, NH_4MgF_3, ammonium hydrofluoride.

ACKNOWLEDGEMENTS The authors are grateful to I. A. Novikov for his help in conducting part the scanning electron microscopy. This research was performed using the equipment of the Shared Equipment Center of the Prokhorov General Physics Institute of the Russian Academy of Sciences and of the JRC PMR IGIC RAS. TEM studies were conducted using the equipment of the Centre for Collective Use "Materials Science and Metallurgy" (National University of Science and Technology "MISIS").

FOR CITATION Luginina A.A., Alexandrov A.A., Yasyrkina D.S., Ermakova J.A., Tapero V.V., Kuznetsov S.V. Formation of NH_4MgF_3 and MgF_2 nanoparticles from magnesium hydroxycarbonate in ammonium hydrofluoride melt. *Nanosystems: Phys. Chem. Math.*, 2025, **16** (6), 897–907.

1. Introduction

Ammonium fluorides (NH_4F and NH_4HF_2) react with many substances to form ammonium fluorometalates [1]. Structure and properties of cubic perovskite ammonium fluorometalates NH_4MF_3 (M = Mg and 3d transition element) have been intensively studied for several decades [2–8]. They crystallize in the cubic perovskite structure (sp. gr. $Pm\,\bar{3}m$, Z = 1) at room temperature, and under cooling, they undergo a structural phase transition into phases with lower symmetry such as tetragonal or orthorhombic crystal systems. NH_4MF_3 (M = Mn, Co, Ni) exhibit magnetic phase transitions at temperatures near or below the structural phase transitions [9–11]. These compounds are model objects for studying phase transitions in crystalline substances and determining the orientation of ammonium ions in the F- framework for various phases [12–19]. The perovskite structure allows for a fairly wide range of variation in the set of ions forming the lattice, thereby achieving the desired combination of material properties. In recent years, the NH_4MgF_3 and NH_4FeF_3 compounds have attracted attention as new solid electrolytes and cathode materials allowing for the direct introduction of lithium ions into the cubic perovskite structure [20, 21].

Unlike most of 3d transition elements, the complexing ability of magnesium is much lower and the formation of the compound NH_4MgF_3 can be explained by the proximity of the ionic radius of Mg^{2+} (0.72 Å) and the ionic radii of Mn^{2+} (0.83 Å), Fe^{2+} (0.78 Å), Co^{2+} (0.745 Å), Ni^{2+} (0.69 Å), and Zn^{2+} (0.74 Å) [22, 23]. NH_4MF_3 compounds were first synthesized by the reaction of MBr_2 with NH_4F in methanol [24, 25], and later obtained by pressing MF_2 with NH_4F upon heating [26]. Palacios et al. synthesized NH_4MF_3 by reacting a homogeneous mixture of solid MF_2 salts with NH_4HF_2 at 152 °C for several hours [4, 5]. Charpin et al. reported the synthesis of NH_4MgF_3 by heating a homogeneous mixture of magnesium carbonate powders with an unspecified excess of ammonium fluoride at 220 °C, followed by

washing off the excess NH_4F with formamide [27]. Ikrami et al. established the stepwise nature of the interaction of a mixture of ammonium fluoride or hydrofluoride powders with active magnesium oxide at a ratio of NH_4F:MgO = 4:1 and NH_4HF_2:MgO = 2:1 with the formation in both cases of intermediate compounds $(NH_4)_2MgF_4$ and NH_4MgF_3, stable in the temperature range of 160–180 °C and 220–230 °C, respectively [28]. However, they did not obtain the pure NH_4MgF_3 compound. The papers present various unit cell parameters of the compound NH_4MgF_3 prepared by "dry" methods (heating homogeneous mixtures of powders): a = 4.056 Å [5] and a = 4.06 Å [27]. Moreover, the diffraction pattern of the NH_4MgF_3 compound is not given in any papers. There is no information about the compound NH_4MgF_3 in the COD, JCPDS, CCDC, PDF-2 databases.

Ammonium hydrofluoride is more reactive than ammonium fluoride [1]. The reactions of interaction of ammonium fluoride or hydrofluoride with MgF_2 proceed according to the equations:

$$MgF_{2(s)} + NH_4HF_{2(s)} \rightarrow NH_4MgF_{3(s)} + HF_{(g)}, \quad (1)$$

$$MgF_{2(s)} + NH_4F_{(s)} \rightarrow NH_4MgF_{3(s)}. \quad (2)$$

The difference between the reactions is that reaction 1 occurs with the release of gaseous HF. An important difference is also that the interaction according to equation 1 occurs in the NH_4HF_2 melt, since its melting point is 126 °C [1]. As a result, the term "solid-phase reaction" which is often applied in the literature to processes involving NH_4HF_2, cannot be applied. In reality, heating processes inevitably occur in molten NH_4HF_2.

In addition to the described methods for synthesizing the NH_4MgF_3 compound, the literature contains no information whatsoever on the interaction of ammonium hydrofluoride with magnesium hydroxycarbonate, which exists in the form of a natural mineral, hydromagnesite, with the chemical formula $Mg_5(CO_3)_4(OH)_2\times4H_2O$.

The study of the conditions for the synthesis of the NH_4MgF_3 compound from magnesium hydroxycarbonate in melt of NH_4HF_2 with its subsequent conversion to magnesium fluoride is promising from the point of view of using the compound NH_4MgF_3 as a self-fluorinating precursor for the production of anhydrous magnesium fluoride.

Magnesium fluoride exhibits high transparency over an extremely wide spectral range, from vacuum ultraviolet to infrared [29–38]. Due to its high transparency and low refractive index, it has found wide application in various optical devices (e.g.: windows, lenses, filters, polarizers, and antireflective coatings for laser devices) [39–44].

The aim of the work is to study the synthesis of the NH_4MgF_3 compound by reacting magnesium hydroxycarbonate with a melt of ammonium hydrofluoride and subsequent thermal decomposition to prepare nanodispersed anhydrous MgF_2.

2. Experimental section

2.1. Materials and methods

The initial reagents such as magnesium hydroxycarbonate $Mg_5(CO_3)_4(OH)_2\times4H_2O$ (PrimeChemicalsGroup, Russia), ammonium fluoride NH_4F and ammonium hydrofluoride NH_4HF_2 (Fluoride Salts Plant, Perm, Russia) were analytical reagent grade. The number of water molecules in magnesium hydroxycarbonate was determined by thermogravimetric method using a MOM Q-1500 D derivatograph.

2.2. Synthesis

A homogeneous mixture of $Mg_5(CO_3)_4(OH)_2\times4H_2O$ and NH_4HF_2 powders was prepared by preliminary grinding of NH_4HF_2 powder in a fluoroplastic mortar with the gradual addition of $Mg_5(CO_3)_4(OH)_2\times4H_2O$ powder and grinding the mixture of powder for 15 min. The prepared homogeneous mixture of powders was transferred into a platinum crucible, covered with a lid and placed in an oven SNOL heated to 220 °C or 165 °C.

The conditions for sample synthesis are given in Table 1. Samples 2 and 3 were prepared in derivatograph upon thermogravimetric analysis (DTA-TG) at a heating rate of 10 °C/min. Sample 7–600 was obtained from Sample 7 by heating it at a rate of 10 °C/min to 600 °C without holding, followed by cooling.

2.3. Characterization

Diffraction patterns (XRD) were obtained on a Bruker D8 Advance powder X-ray diffractometer using CuKα radiation in the angular range from 10 to 140°C 2Θ, a signal acquisition time per point of 0.5–1 s, and sample rotation in the axial plane at a speed of 20 deg/min. Calculations of the unit cell parameters and coherent scattering regions (CSRs) were performed using TOPAS software.

Scanning electron microscopy (SEM) micrographs were obtained on a Tescan Amber scanning electron microscope using an Everhart-Thornley (E–T) detector and a low-energy back-scattered electron (LE-BSE) detector at accelerating voltages of 1–2 kV and a probe current of 300 pA. Particle sizes were determined using ImageJ software. Energy-Dispersive X-ray spectroscopy (EDX) was performed using an Oxford Instruments Ultramax EDS detector with an active area of 100 mm^2 at an accelerating voltage of 20 kV.

Thermogravimetric analysis was performed on a MOM Q-1500 D derivatograph in platinum crucibles in air. The heating and cooling rate was 10°C/min. Infrared spectroscopy was performed on an InfraLUM FT-08 spectrophotometer

TABLE 1. Sample synthesis conditions

Sample	Mg:F ratio	Temperature, °C	Synthesis duration, h
1	1:3	220	5
2 (DTA-TG)	1:3	600	0
3 (DTA-TG)	1:4	600	0
4	1:4	220	5
5	1:4	165	5
6	1:6	220	5
7	1:6	220	10
7–600	1:6	600	0
8	1:6	220	12

in the 4000–400 cm^{-1} range. Transmission electron microscopy (TEM) was performed on a JEM-2100 microscope (JEOL) with preliminary dispersion of the sample in water under ultrasound.

The magnesium content of the samples was determined by complexometric titration using disodium ethylenediamine-N, N, N′, N′-tetraacetic acid (di-Na-EDTA) in the presence of eriochrome black T indicator at pH = 10. The sample was first dissolved by boiling in a mixture of boric and hydrochloric acid solutions. The NH_4^+ content was determined by distillation using the Kjeldahl method, followed by titration with a hydrochloric acid solution in the presence of a mixed indicator (methyl red and methylene blue).

3. Results and discussion

The synthesis of NH_4MgF_3 compound was carried out at 220 °C, based on the results of thermogravimetric analysis, as well as on known literature data on the temperature range of stability of this compound of 220–230 °C [28] and the boiling point with simultaneous decomposition of NH_4HF_2 – 238 °C [45].

Magnesium hydroxycarbonate decomposes in several stages [46], Fig. 1a. The decomposition process begins at 206 °C, with a maximum endothermic effect at 273 °C and the removal of crystallization water with a loss of 18.6%. Then, the removal of chemically bound water occurs with a maximum at 410 °C and a loss of 7.2%. The exothermic effect at 487 °C corresponds to the formation of magnesium carbonate. Magnesium carbonate decomposes at 519 °C, losing 31.4% of its mass. The total mass loss of the sample is 57.2%.

In the DTA curves of the mixture of magnesium hydroxycarbonate powders with ammonium hydrofluoride at a ratio of Mg:F = 1:3 and 1:4, the first endothermic effect with a maximum of 124 °C is associated with the loss of adsorption water and the melting process of NH_4HF_2, Fig. 1b and Fig. 1c, respectively. The second endothermic effect, with a maximum at 213–219 °C, is caused by two processes: the onset of the removal of crystallization water from magnesium hydroxycarbonate and the reaction of interaction of initial reagents, initiated by the released water. The effect on the DTG, with a maximum at 265 °C, is apparently associated with the removal of crystallization water from magnesium hydroxycarbonate. Furthermore, the DTA curves for the mixture of magnesium hydroxycarbonate powders with ammonium hydrofluoride differ slightly for Mg:F ratios of 1:3 and 1:4.

The exothermic effect at 273 °C on the DTA curve with a ratio of Mg:F=1:3 is due to the crystallization of the intermediate compound, Fig. 1b. This intermediate compound in a mixture with MgF_2 was obtained by synthesis at 220 °C (Sample 1) Table 1. It is indexed in the hexagonal crystal system, space group $P6_3/mmc$, Table 2, Fig. 2c. The endothermic effect at 282 °C on the DTA curve is associated with the decomposition of the formed intermediate compound to magnesium fluoride. The exothermic effect at 297 °C is due to the crystallization of MgF_2. On the TG curve, the mass losses in the first (up to 126 °C), second (126 °C–226 °C), and third sections (226 °C–308 °C) are 7.3%, 45.3%, and 13.0%, respectively. The total mass loss was 65.6%, whilst the theoretical loss calculated for the production of MgF_2 is 65.4%.

After DTA-TG, a single-phase MgF_2 (Sample 2) was obtained, Fig. 2e, Table 2. Calculations of mass loss corresponding to the second and third sections on the TG curve, according to equations 3, 4, 5, are presented in Table 3. The phase composition of Sample 1 indicates the possible simultaneous occurrence of reactions at a ratio of Mg:F = 1:3 according to equations 4, 5:

$$Mg_5(CO_3)_4(OH)_2 \times 4H_2O + 7.5NH_4HF_2 \rightarrow 5NH_4MgF_3 + 4CO_2 + 2.5NH_3 + 10H_2O, \quad (3)$$

$$Mg_5(CO_3)_4(OH)_2 \times 4H_2O + 5NH_4HF_2 \rightarrow 5NH_4Mg(OH)F_2 + 4CO_2 + 5H_2O, \quad (4)$$

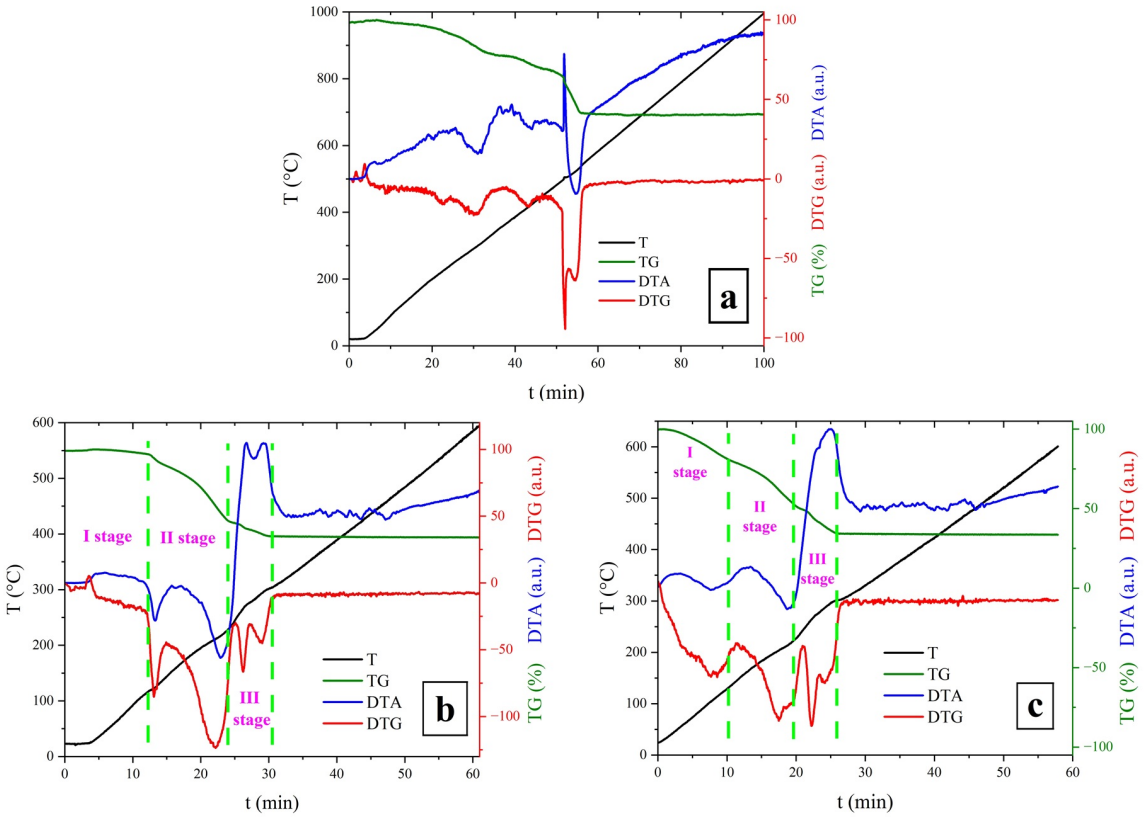

FIG. 1. Thermal analysis: a – magnesium hydroxycarbonate, b – mixtures of magnesium hydroxycarbonate powders with ammonium hydrofluoride at the ratio Mg:F=1:3 (Sample 2), c – same with Mg:F ratio 1:4 (Sample 3)

$$Mg_5(CO_3)_4(OH)_2 \times 4H_2O + 5NH_4HF_2 \rightarrow 5MgF_2 + 4CO_2 + 10H_2O. \quad (5)$$

The presence on the diffractogram of Sample 1, in addition to the reflections of the hexagonal phase (sp. gr. $P6_3/mmc$) and MgF_2, of the reflections of the compound $(NH_4)_2MgF_4$ (card PDF-2 card #00-050-0280) also indicates the possible occurrence of the reaction according to equation 6. Reflexes of the initial magnesium hydroxycarbonate are absent, Fig. 2b, Table 2.

$$Mg_5(CO_3)_4(OH)_2 \times 4H_2O + 10NH_4HF_2 \rightarrow 5(NH_4)_2MgF_4 + 4CO_2 + 10H_2O \quad (6)$$

On the DTG curve of a mixture of magnesium hydroxycarbonate and ammonium hydrofluoride powders with a Mg:F ratio of 1:4, a broad effect is observed at 203 °C with a shoulder at 220 °C, Fig. 1c. On the TG curve, the mass loss in the first (up to 126 °C) and second (126–226 °C) segments are 17.1% and 33.1%, respectively. The theoretical mass loss calculated using equation 6 (38.0%) does not correspond to that determined from the TG curve, which may indicate that reactions 4 and 6 proceed in parallel. The effect at 289 °C on the DTG curve is associated with the decomposition of the intermediate compounds formed into magnesium fluoride. The exothermic effect at 295 °C is due to the crystallization of MgF_2. The total mass loss was 66.3%, whilst the theoretical loss was 64.9%. After DTA-TG, a single-phase MgF_2 (Sample 3) was obtained, Fig. 2f, Table 2.

The XRD analysis confirmed the assumption that reactions (4) and (6) proceed in parallel. At a Mg:F ratio of 1:4, Sample 4 consists of cubic and hexagonal phases indicated on the diffractogram (Fig. 2d, Table 2) without reflections of the initial magnesium hydroxycarbonate. The presence of the cubic phase NH_4MgF_3 and the hexagonal phase confirm the assumption of simultaneous reactions according to equation (4) and (6). Further confirmation that the interaction proceeds according to equation (6) and not equation (3) is provided by the presence of an effect at 220 °C on the DTG curve of a mixture of magnesium hydroxycarbonate and ammonium hydrofluoride powders with a Mg:F ratio of 1:4, Fig. 1c. This effect indicates the decomposition of the $(NH_4)_2MgF_4$ compound formed according to equation 6 into a cubic phase NH_4MgF_3 [28]:

$$(NH_4)_2MgF_4 \rightarrow NH_4MgF_3 + HF + NH_3. \quad (7)$$

The chemical composition of the hexagonal phase of Samples 1 and 4 was not determined, since it was not isolated in pure form and this was not the objective of the study.

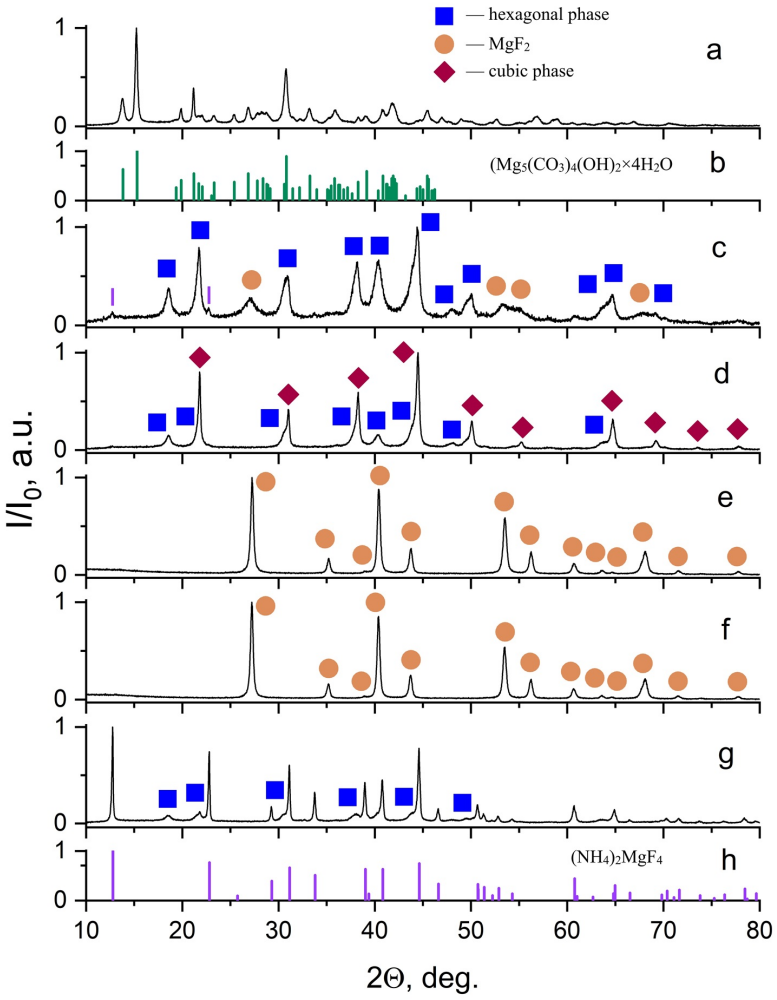

FIG. 2. XRD patterns: a – magnesium hydroxycarbonate, b – $Mg_5(CO_3)_4(OH)_5\times4H_2O$ card PDF-2 #00-025-0513, c – Sample 1, d – Sample 4, e – Sample 2, f – Sample 3, g – Sample 5, h – $(NH_4)_2MgF_4$ card PDF-2 #00-050-0280

The assumption made about the interaction of magnesium hydroxycarbonate with NH_4HF_2 according to equation 6 is further confirmed by the diffractogram of Sample 5, obtained at 165 °C with the ratio Mg:F = 1:4, Fig. 2g. The diffractogram of Sample 5 shows reflections of the $(NH_4)_2MgF_4$ compound and additional reflections indexated in the hexagonal symmetry (sp. gr. *P6₃/mmc*), Table 2. The diffractogram of sample with the ratio Mg:F = 1:5 contains reflections of the cubic phase and additional reflections of hexagonal phase (sp. gr. *P6₃/mmc*), see Supplementary Section (Table S1 and Fig. S1).

The XRD analysis traced the phase composition evolution of the products of the interaction between magnesium hydroxycarbonate and the NH_4HF_2 melt at 220 °C. In case of insufficient excess of ammonium hydrofluoride at the ratio:

1. Mg:F=1:3 results in formation of tetragonal MgF_2 (sp. gr. *P4₂/mnm*) and hexagonal phase (sp. gr. *P6₃/mmc*);

2. Mg:F=1:4 and 1:5 results in formation of cubic NH_4MgF_3 (sp. gr. *Pm* $\bar{3}$*m*) and hexagonal phase (sp. gr. *P6₃/mmc*).

A stepwise nature of the interaction between magnesium hydroxycarbonate and NH_4HF_2 melt has been established through the formation of the compound $(NH_4)_2MgF_4$ and its subsequent decomposition at a temperature of 220 °C to NH_4MgF_3. Thus, the excess amount of NH_4HF_2 required for the synthesis of NH_4MgF_3 compared to the stoichiometric amount according to equation (3) is associated not only with the compensation for the evaporation of NH_4HF_2 during heating, but also with the formation of the compound $(NH_4)_2MgF_4$.

Diffractogram of Sample 6 (Mg:F = 1:6) prepared by 5 h synthesis contains reflections of cubic NH_4MgF_3 and orthorhombic NH_4HF_2, Fig. 3a, Table 2. The increase in synthesis duration up to 10 and 12 h leads to evaporation of NH_4HF_2. There are only reflections of NH_4MgF_3 on Samples 7 and 8 diffractograms, Fig. 3(c,d), Table 2.

The NH_4^+ and Mg^{2+} content in chemical composition of NH_4MgF_3 compound (Sample 7) was determined by quantitative chemical analysis and EDX, Table 4 and 5.

TABLE 2. XRD analysis results of synthesized samples

Sample	Crystal system	Space group	Compound	Unit cell parameters, Å			Coherent scattered regions, nm
				a	b	c	
1	Tetragonal	*P*4$_2$/*mnm*	MgF_2	4.656(3)	–	3.04(1)	4(1)
	Hexagonal	*P*6$_3$/*mmc*	Composition not determined	5.824(3)	–	14.123(8)	15(1)
	Tetragonal*	*I*4/*mmm*	$(NH_4)_2MgF_4$	Traces			
2	Tetragonal	*P*4$_2$/*mnm*	MgF_2	4.624(1)	–	3.051(1)	18(1)
3	Tetragonal	*P*4$_2$/*mnm*	MgF_2	4.625(1)	–	3.051(1)	19(1)
4	Cubic	*Pm* $\bar{3}$*m*	NH_4MgF_3	4.072(1)	–	–	48(3)
	Hexagonal	*P*6$_3$/*mmc*	Composition not determined	5.846(1)	–	14.175(4)	10(1)
	Tetragonal*	*I*4/*mmm*	$(NH_4)_2MgF_4$	Traces			
5	Tetragonal*	*I*4/*mmm*	$(NH_4)_2MgF_4$	4.064(1)	–	13.860(1)	>100
	Hexagonal	*P*6$_3$/*mmc*	Composition not determined	5.848(2)	–	14.086(7)	6(1)
6	Cubic	*Pm* $\bar{3}$*m*	NH_4MgF_3	4.069(1)	–	–	64(3)
	Orthorombic**	*Pbmn*	NH_4HF_2	8.175(1)	8.419(1)	3.685(1)	44(1)
7	Cubic	*Pm*$\bar{3}$*m*	NH_4MgF_3	4.0663(1)	–	–	>100
7–600	Tetragonal	*P*4$_2$/*mnm*	MgF_2	4.623(1)	–	3.052(1)	25(1)
8	Cubic	*Pm*$\bar{3}$*m*	NH_4MgF_3	4.067(1)	–	–	92(4)

*$(NH_4)_2MgF_4$ PDF-2 card #00-050-0280

**NH_4HF_2 PDF-2 card #00-012-0302

TABLE 3. Mass loss according to TG during reagent interaction (Mg:F ratio = 1:3) compared to theoretical losses

Curve segment, Fig. 1b	Temperature range, °C	Mass loss, %			
		Experimental	Theoretical		
			3	4	5
II stage	126–226	45.3	45.1	34.9	65.4
III stage	226–308	13.0	20.6	19.4	-

TABLE 4. Results of quantitative chemical analysis of Samples 7 and 7–600

Sample	Compound	NH_4^+ content, wt. %		Mg^{2+} content, wt. %	
		Experimental	Theoretical	Experimental	Theoretical
7	NH_4MgF_3	18.1±0.5	18.1	24.0±0.7	24.5
7–600	MgF_2	–	–	39.2±0.7	39.0

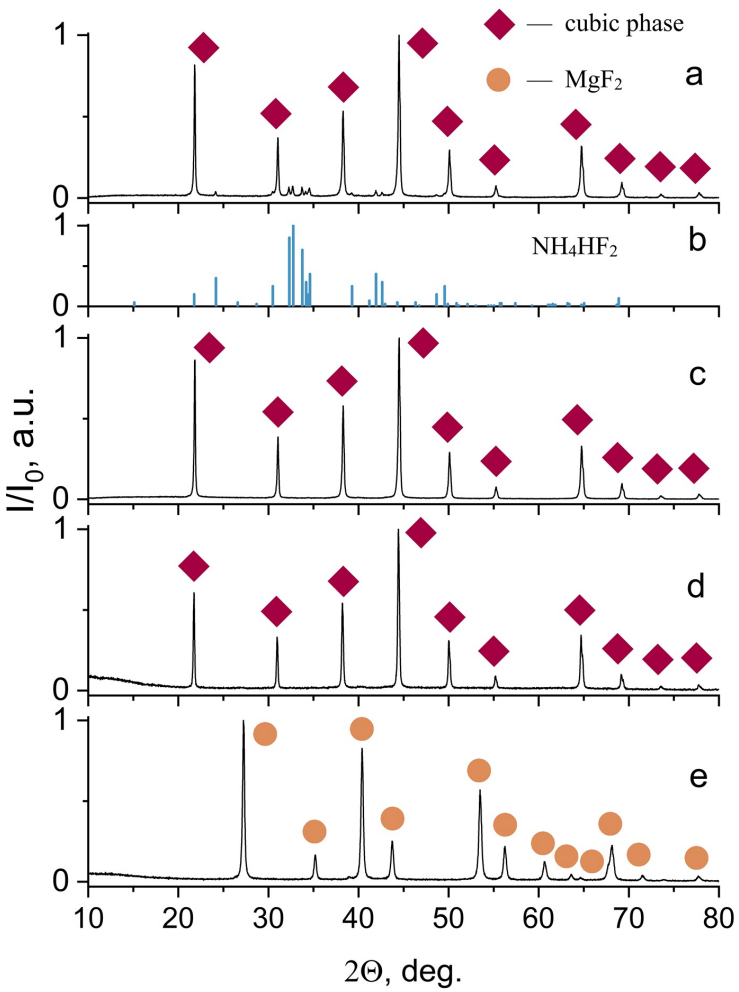

FIG. 3. XRD patterns: a – Sample 6, b – NH_4HF_2 PDF-2 card #00-012-0302, c – Sample 7, d – Sample 8, e – Sample 7–600

TABLE 5. Results of EDX analysis of Samples 7 and 7–600

Sample	Compound	N, at. %		F, at. %		Mg, at. %	
		Experimental	Theoretical	Experimental	Theoretical	Experimental	Theoretical
7	NH_4MgF_3	20±1	20.0	60±1	59.9	20±1	20.2
7–600	MgF_2	–	–	66±1	66.4	34±1	33.6

The formation of NH_4MgF_3 was also confirmed by FTIR-ATR (Fig. 4a). The IR spectrum of Sample 7 shows bands at 1461.2 cm^{-1} and 3220.9 cm^{-1}, corresponding to deformation vibrations (ν_3) and valence vibrations (ν_4) of the NH_4^+ ion [16, 47, 48].

The IR spectrum of Sample 7–600 does not include characteristic H_2O vibrations at ~1640 cm^{-1} and ~3400–3600 cm^{-1}. This observation confirms the absence of moisture traces in obtained MgF_2, Fig. 4b [49].

The DTA–TG data for synthesized sample 7 clearly confirm the XRD analysis results, indicating that the Sample 7 is a pure phase of NH_4MgF_3. The onset of the thermal decomposition according to DTA and TG is 280 °C with maximum at 294 °C and the end at 344 °C, Fig. 5a. Estimated experimental mass loss is 37.32%, which corresponds to theoretical losses 37.37% by following equation:

$$NH_4MgF_3 \rightarrow MgF_2 + HF + NH_3. \quad (8)$$

DTA-TG results in single-phase MgF_2 (Sample 7–600), Fig. 3e, Table 2. Composition of MgF_2 was confirmed by quantitative chemical and EDX analysis, Table 4 and 5.

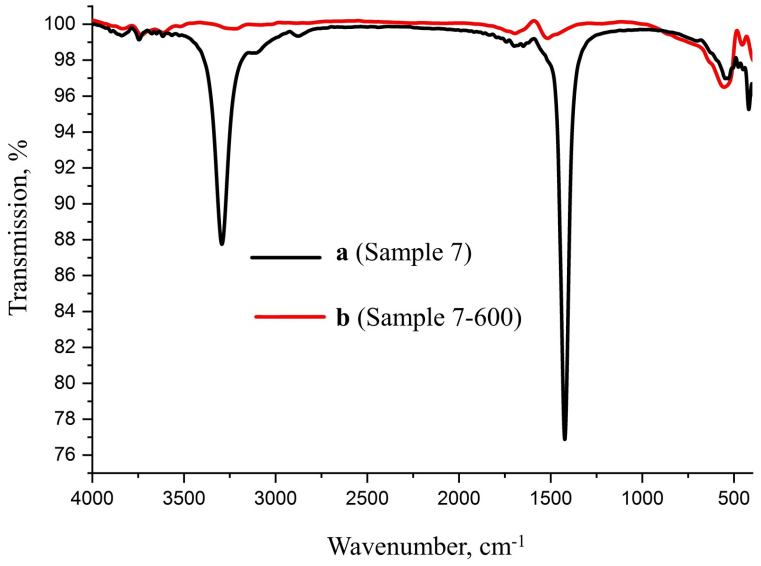

FIG. 4. FTIR-ATR spectra of: a – Sample 7, b – Sample 7–600

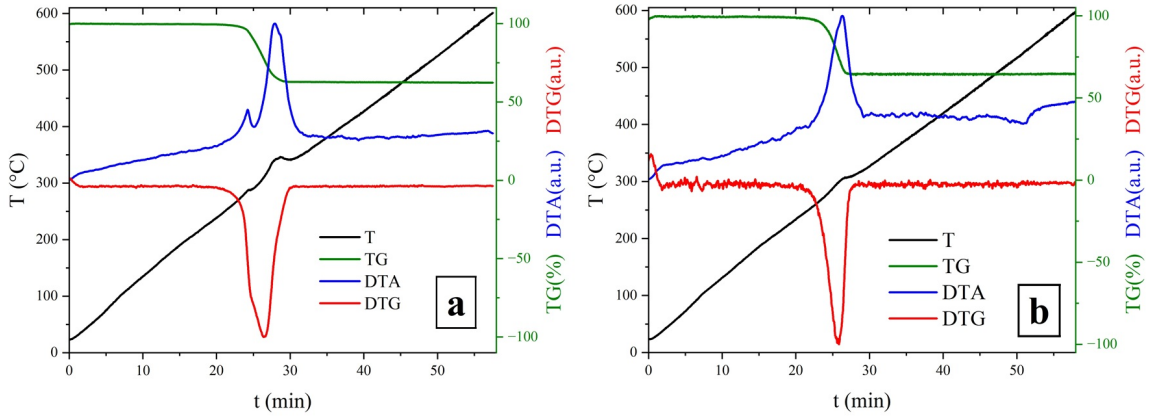

FIG. 5. DTA-TG results: a – Sample 7 and b – Sample 8

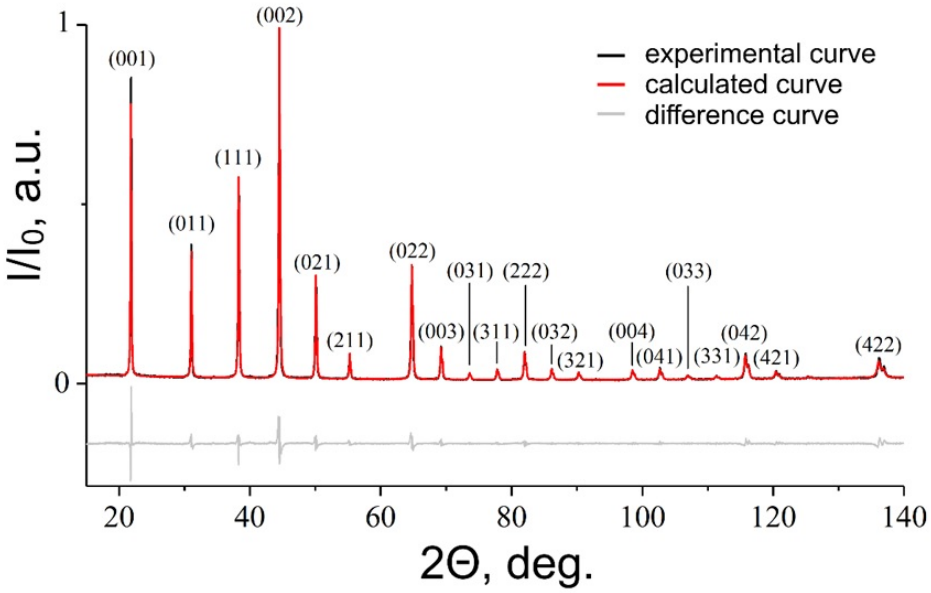

FIG. 6. Results of indexation of XRD pattern of Sample 7

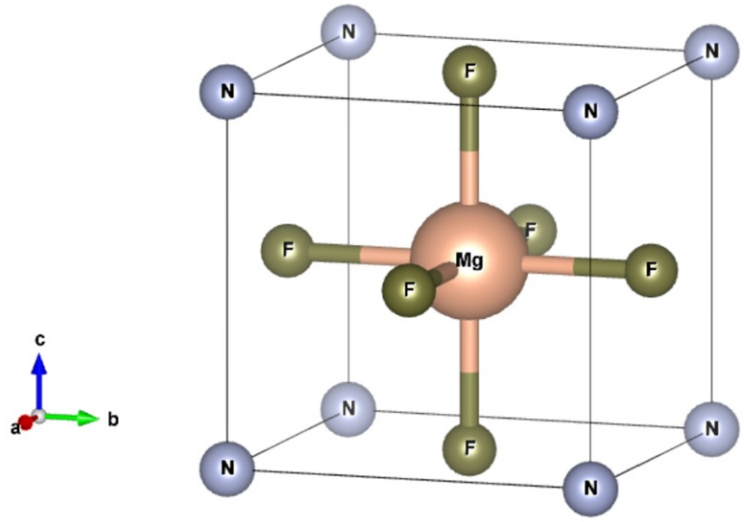

FIG. 7. Visualization of NH_4MgF_3 structure

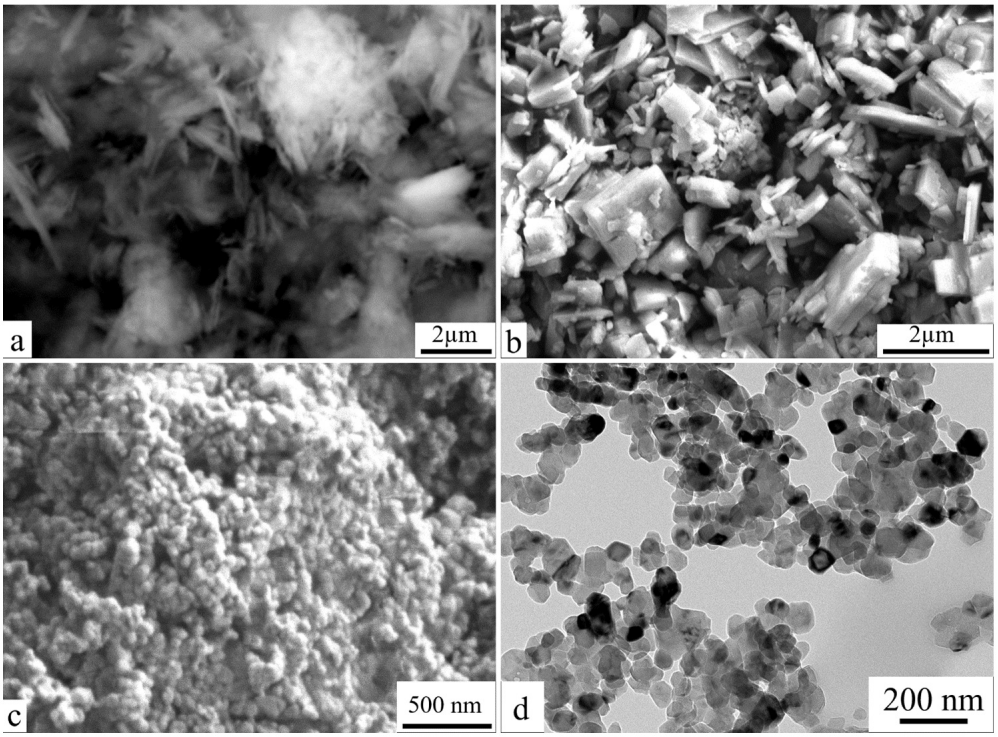

FIG. 8. The SEM/TEM microphotographs: a – magnesium hydroxycarbonate (SEM), b – Sample 7 (SEM), c – Sample 7–600 (SEM) and d – Sample 7–600 (TEM)

During the thermal decomposition of NH_4MgF_3 compound two processes occur simultaneously. Decomposition according to equation (8) the endothermic one and crystallization of the forming MgF_2 the exothermic one. Two exothermic peaks were observed on DTA curve of Sample 7 (Fig. 5a) and one exothermic peak were observed on DTA curve of Sample 8, Fig. 5b. Exothermic processes involving the crystallization of the magnesium fluoride phase are so intense that no endothermic processes were detected against their background.

The crystal structure of NH_4MgF_3 was refined on powder diffraction data in 15–140° 2Θ range using isostructural compound NH_4NiF_3 data [10]. Results of indexation of Sample 7 are presented in Fig. 6 and Supplementary section. The visualization of NH_4MgF_3 structure presented in Fig. 7.

The initial $Mg_5(CO_3)_4(OH)_2 \times 4H_2O$ consisted of flattened, long prismatic particles assembled into aggregates 400–1000 nm long and 30–50 nm thick, whose habitus was determined by the monoclinic structure of hydromagnesite, Fig. 8a. The initial habitus of hydromagnesite particles is not preserved during NH_4MgF_3 synthesis. The SEM image of Sample 7 shows nanoparticles with a 50–70 nm cube shape (Fig. 8b). The fusion of several primary nanoparticles of cubic

morphology with one crystallographic direction into larger particles (120–300 nm) that form micron-sized aggregates was recorded. The discrepancy between the sizes and the calculated values of the average crystal size (Table 2) may indicate the implementation of a non-classical mechanism of crystal formation through the oriented fusion of nanoparticles [50]. The heating of NH_4MgF_3 compound to 600 °C leads to significant changes. NH_4MgF_3 crystallites are destroying with the change of their chemical composition. The formation of rounded MgF_2 nanoparticle aggregates with a size of 71 ± 20 nm is observed, Fig. 8c. These aggregates are formed by nanoparticles with a size of 28 ± 7 nm that have a random orientation, Fig. 8d. The MgF_2 particle sizes determined from TEM micrographs agree reasonably well with the calculated values of the calculated scattering regions, Table. 2.

4. Conclusions

This study showed that NH_4HF_2 excess is required for the synthesis of the NH_4MgF_3. This is related not only to the compensation for NH_4HF_2 evaporation during heating, but also to the formation of a compound $(NH_4)_2MgF_4$. A stepwise nature of the reaction between magnesium hydroxycarbonate and molten ammonium fluoride through the formation of a compound $(NH_4)_2MgF_4$ which decomposes to NH_4MgF_3 at 220 °C has been established. The quantitative course of the reaction of magnesium hydroxycarbonate with molten ammonium hydrofluoride Mg:F=1:6 at 220 °C and 10 h with the formation of NH_4MgF_3 is shown. The fusion of several 50–70 nm primary nanoparticles with cubic morphology with formation of bigger particles with 120–300 nm size is observed.

At a Mg:F ratio lower than 1:6, the formation of multiphase products was observed, including $(NH_4)_2MgF_4$, NH_4MgF_3 and MgF_2 compounds and an impurity phase whose reflections are indicated in the hexagonal crystal system sp. gr. *P*6$_3$*/mmc*. During heat treatment NH_4MgF_3 is decomposing with formation of anhydrous nanocrystals MgF_2 with particle sizes 28 ± 7 nm.

References

[1] Rakov E.G., Mel'nichenko E.I. The properties and reactions of ammonium fluorides. *Russ. Chem. Rev.*, 1984, **53**, P. 851.

[2] Rüdorff W., Lincke G., Babel D. Untersuchungen an ternären Fluoriden. (II). Kobalt(II)- und Kupfer(II)-fluoride. *ZAAC*, 1963, **320**, P. 150–170.

[3] Patil K.S., Secco E.A. Complex fluorides with perovskite structure: thermal analyses, calorimetry, and infrared spectra. *Can. J. Chem.*, 1972, **50**, P. 1529–1530.

[4] Palacios E., Bartolomé J., Navarro R. et al. Heat capacity and N.M.R. study of the NH_4MgF_3 perovskite. *Ferroelectrics*, 1984, **55**, P. 287–290.

[5] Palacios E., Navarro R. Thermal properties of XMF_3: cubic perovskites. I. Heat capacity of NH_4MgF_3 and NH_4CdF_3. *J. Chem. Thermodynamics*, 1986, **18**, P. 1089–1101.

[6] Navarro R., Burriel R., Bartolomé J. et al. Thermal properties of XMF_3 cubic perovskites II. Heat capacity of NH_4ZnF_3 and $KZnF_3$. *J. Chem. Thermodynamics*, 1986, **18**, P. 1135–1146.

[7] Palacios E., Bartolomé J., Burriel R. et al. Proton-lattice relaxation in NH_4MF_3. *J. Phys.: Condens. Matter*, 1989, **1**, P. 1119–1132.

[8] Helmholdt R.B., Wiegers G.A., Bartolome J. Investigation of the structural phase transitions in the ammonium trifluorides of zinc, manganese and cobalt by means of X-ray and neutron diffraction. *J. Phys.: Condens. Matter*, 1980, **13**(27), P. 5081–5088.

[9] Bartolomé J., Navarro R., González D. et al. Magnetic properties of NH_4CoF_3. *Physica B+C*, 1977, **92**, P. 45–51.

[10] Plitzko C., Strecker M., Meyer G. Crystal structure of two modifications of ammonium trifluoro nickelate(II), NH_4NiF_3. *Z. Kristallogr. New Cryst. Struct.*, 1997, **212**, P. 3–4.

[11] Siebeneichler S., Dorn K.V., Smetana V. et al. A soft chemistry approach to the synthesis of single crystalline and highly pure $(NH_4)CoF_3$ for optical and magnetic investigations. *J. Chem. Phys.*, 2020, **153**, P. 104501-8.

[12] Bartolomé J., Navarro R., González D. et al. Librational and reorientational specific heats of NH_4^+ in NH_4ZnF_3 and NH_4CoF_3. *Physica B+C*, 1977, **92**, P. 23–44.

[13] Bartolomé J., Navarro R., González D., et al. Hindered rotational specific heat of NH_4^+ in the cubic perovskite NH_4ZnF_3. *Chem. Phys. Lett.*, 1977, **48**, P. 536–539.

[14] Steenbergen C., de Graaf L.A., Bevaart L. et al. Rotational motions of NH_4^+ groups in NH_4ZnF_3 studied by quasielastic neutron scattering. *J. Chem. Phys.*, 1979, **70**, P. 1450–1455.

[15] Rubin J., Bartolome J., Anne M. et al. The dynamics of NH_4^+ in the NH_4MF_3 perovskites: I. A quasielastic neutron scattering study. *J. Phys.: Condens. Matter*, 1994, **6**, P. 8449–8468.

[16] Plaza I., Rubin J., Laguna M.A. et al. Optical spectroscopy of the NH_4^+ - internal vibrations in the orthorhombic phase of NH_4MF_3 (M is Mn, Zn) perovskites. *Spectrochim. Acta, Part A*, 1996, **52**, P. 57–67.

[17] Smith D. The derivation of the rotational potential function from atom-atom potentials. II. Ammonium-fluorine compound. *J. Chem. Phys.*, 1987, **86**, P. 4055–4065.

[18] Laguna M.A., Sanjuan M.L., Orera V.M. et al. X-ray and Raman study of the low temperature NH_4MnF_3 structure; evidence of librational motion of the NH_4^+ ion. *J. Phys.: Condens. Matter*, 1993, **5**, P. 283–300.

[19] Aleksandrov K.S., Bartolome J., Gorev M.V. et al. Hydrostatic pressure effect on phase transitions in perovskites with ammonium cations. *Phys. Status Solidi B*, 2000, **217**, P. 785–791.

[20] Motohashi K., Matsukawa Y., Nakamura T. et al. Fast fluoride ion conduction of $NH_4(Mg_{1-x}Li_x)F_{3-x}$ and $(NH_4)_2(Mg_{1-x}Li_x)F_{4-x}$ assisted by molecular cations. *Sci Rep.*, 2022, **12**, P. 5955.

[21] Martin A., Santiago E.S., Kemnitz E. et al. Reversible insertion in $AFeF_3$ (A = K^+, NH_4^+) cubic iron fluoride perovskites. *ACS Appl. Mater. Interfaces*, 2019, **11**, P. 33132–33139.

[22] Shannon R.D. Revised effective ionic radii and systematic studies of interatomic distances in halides and chalcogenides. *Acta Cryst.*, 1976, **A32**, P. 751–767.

[23] Cotton F.A., Wilkinson G., Murillo C.A. et al. *Advanced Inorganic Chemistry*. Part 2. 6th ed. John Wiley and Sons, New York, 1999, 1355 p.

[24] Haendler H.M., Johnson F.A., Crocket D.S. The Synthesis of ammonium fluorometallates in methanol. *J. Am. Chem. Soc.*, 1958, **80**, P. 2662.

[25] Crocket D.S., Haendler H.M. Synthesis of fluorometallates in methanol. Some structure relationships. *J. Am. Chem. Soc.*, 1960, **82**, P. 4158–4162.

[26] Crocket D.S., Grossman R.A. The interaction between ammonium fluoride and metal fluorides as compressed powders. *Inorg. Chem.*, 1964, **3**, P. 644–646.
[27] Charpin P., Roux N., Ehretsmann J. Fluorures doubles de magnésium et d'ammonium. *C. R. Acad. Sci. Paris*, 1968, **267**, P. 484–486.
[28] Ikrami D.D., Ol'khovaya L.A., Luginina A.A. et al. Interaction of magnesium oxide with fluoride and ammonium hydrofluoride. *Russ. J. Inorg. Chem.*, 1977, **22**(3), P. 660–663.
[29] Guggenheim H. Growth of highly perfect fluoride single crystals for optical asers. *J. Appl. Phys.*, 1963, **34**, P. 2482–2485.
[30] Cotter T.P., Thomas M.E., Tropf W.J. *Magnesium Fluoride* (MgF_2). Handbook of Optical Constants of Solids, 1997, **2**, P. 899–918.
[31] Dodge M.J. Refractive properties of magnesium fluoride. *Appl. Opt.*, 1984, **23**, P. 1980–1985.
[32] Kitamura Y., Miyazaki N., Mabuchi T. et al. Birefringence simulation of annealed ingot of magnesium fluoride single crystal. *J. Cryst. Growth*, 2009, **311**, P. 3954–3962.
[33] Scott W. Purification, growth of single crystals, and selected properties of MgF_2. *J. Am. Ceram. Soc.*, 1962, **45**, P. 586–587.
[34] Hanson W.F., Arakawa E.T., Williams M.W. Optical properties of MgO and MgF_2 in the extreme ultraviolet region. *J. Appl. Phys.*, 1972, **43**, P. 1661–1665.
[35] Olsen A.L., McBride W.R. Transmittance of single-crystal magnesium fluoride and IRTRAN-1 in the 0.2 to 15-μ range. *J. Opt. Soc. Am.*, 1963, **53**, P. 1003–1005.
[36] Parsons W.E. Kodak Irtran infrared optical materials. *Appl. Opt.*, 1972, **11**, P. 43–48.
[37] Buckner D.A., Hafner H.C., Kreidl N.J. Hot-pressing magnesium fluoride. *J. Am. Ceram. Soc.*, 1962, **45**, P. 435–438.
[38] Chang C.S., Hon M.H., Yang S.J. The optical properties of hot-pressed magnesium fluoride and single-crystal magnesium fluoride in the 0.1 to 9.0 μm range. *J. Mater. Sci.*, 1991, **26**, P. 1627–1630.
[39] Volynec F.K. Optical properties and applications of optical ceramics. *Soviet Journal of Optical Technology*, 1973, **10**, P. 47–58.
[40] Zaidel A.N., Schrader E.D. *Vacuum Spectroscopy and Its Application*. Nauka, Moscow, 1980, 431 p.
[41] Voronkova E.M., Grechushnikov V.M., Distler G.I. et al. *Optical Materials for IR Technology*. Nauka, Moscow, 1965, 335 p.
[42] Zverev V.A., Krivopustova E.V., Tochilina T.V. *Optical materials*. Part 2. Textbook for Designers of Optical Systems and Devices. ITMO, Saint Petersburg, 2013, 248 p.
[43] Kuznetsov S.V., Alexandrov A.A., Fedorov P.P. Optical Fluoride Nanoceramics. *Inorganic Materials*, 2021, **57**(6), P. 555–578.
[44] Sun P., Jiang C., Jiang Y. et al. Structural, infrared optical and mechanical properties of the magnesium fluoride films. *Infrared Phys. Technol.*, 2024, **137**, P. 105184.
[45] Melnichenko E.I. *Fluoride Processing of Rare Earth Ores of the Far East*. DalNauka, Vladivostok, 2002, 268 p.
[46] Kashcheev I.D., Zemlyanoi K.G., Ustyantsev V.M., Voskretsova E.A. Investigation of thermal decomposition of natural and synthetic magnesium compounds. *Novye Ogneupory* (New Refractories), 2015, **10**, P. 28–35. (In Russ.)
[47] Oxton I.A., Knop O. Infrared Spectra of the Ammonium Ion in Crystals. I. Ammonium Hexachloroplatinate(IV) and Hexachlorotellurate(IV). *Can. J. Chem.*, 1975, **53**, P. 2675–2682.
[48] Knop O., Westerhaus W.J. Infrared spectra of the ammonium ion in crystals. Part XIV. Hydrogen bonding and orientation of the ammonium ion in fluorides, with observations on the transition temperatures in cubic cryolite, elpasolite, and perovskite halides. *Can. J. Chem.*, 1985, **63**, P. 3328–3353.
[49] Nakamoto K. *Infrared and Raman Spectra of Inorganic and Coordination Compounds*. John Wiley & Sons, Hoboken, New Jersey, 2009, 419 p.
[50] Ivanov V.K., Fedorov P.P., Baranchikov A.E., et al. Oriented attachment of particles: 100 years of investigations of non-classical crystal growth. *Russ. Chem. Rev.*, 2014, **83**(12), P. 1204–1222.

Submitted 14 November 2025; revised 19 November 2025; accepted 4 December 2025

Information about the authors:

Anna A. Luginina – Prokhorov General Physics Institute of the Russian Academy of Sciences, Vavilova str. 38, Moscow, Russia; ORCID 0000-0002-6564-5729; annaluginina@mail.ru

Alexander A. Alexandrov – Prokhorov General Physics Institute of the Russian Academy of Sciences, Vavilova str. 38, Moscow, Russia; Kurnakov Institute of General and Inorganic Chemistry of the Russian Academy of Sciences Leninskiy Prospekt, 31, Moscow, Russia; ORCID 0000-0001-7874-7284; alexandrov1996@yandex.ru

Darya S. Yasyrkina – Prokhorov General Physics Institute of the Russian Academy of Sciences, Vavilova str. 38, Moscow, Russia; ORCID 0000-0003-3053-4719; darya.yasyrkina@gmail.com

Julia A. Ermakova – Prokhorov General Physics Institute of the Russian Academy of Sciences, Vavilova str. 38, Moscow, Russia; ORCID 0000-0002-9567-079X; julia.r89@mail.ru

Victoria V. Tapero – Prokhorov General Physics Institute of the Russian Academy of Sciences, Vavilova str. 38, Moscow, Russia; Department of Materials Science of Semiconductors and Dielectrics, National University of Science and Technology (MISIS), Leninskiy Prospekt, 4, Moscow, Russia; ORCID 0009-0002-8771-5465; kvv.padi@gmail.com

Sergey V. Kuznetsov – Prokhorov General Physics Institute of the Russian Academy of Sciences, Vavilova str. 38, Moscow, Russia; ORCID 0000-0002-7669-1106; kouznetzovsv@gmail.com

Conflict of interest: the authors declare no conflict of interest.

NANOSYSTEMS:
PHYSICS, CHEMISTRY, MATHEMATICS

Pakholchuk P.P., et al. *Nanosystems: Phys. Chem. Math.*, 2025, **16** (6), 908–914.
http://nanojournal.ifmo.ru
DOI 10.17586/2220-8054-2025-16-6-908-914

Original article

Formation of laser-induced periodic surface structures on an $As_{50}Se_{50}$ film under femtosecond laser irradiation with wavelengths of 400–800 nm

Petr P. Pakholchuk[1,2,a], Dmitrii V. Shuleiko[2,b], Vadim A. Barbashov[1,c], Stanislav V. Zabotnov[2,d], Sergey A. Kozyukhin[3,e], Pavel K. Kashkarov[2,4,f]

[1]Lebedev Physical Institute, Russian Academy of Sciences, Moscow 119991, Russia

[2]Faculty of Physics, Moscow State University, Moscow 119991, Russia

[3]Kurnakov Institute of General and Inorganic Chemistry, Moscow 119071, Russia

[4]National Research Centre "Kurchatov Institute", Moscow 123182, Russia

[a]p.paholchuk@lebedev.ru, [b]shuleyko.dmitriy@physics.msu.ru, [c]barbashovva@lebedev.ru, [d]zabotnov@physics.msu.ru,[e]sergkoz@igic.ras.ru, [f]kashkarov@physics.msu.ru

Corresponding author: P. P. Pakholchuk, p.paholchuk@lebedev.ru

PACS 42.62.-b, 78.20.Fm, 78.67.-n

ABSTRACT Laser-induced periodic surface structures (LIPSS) on chalcogenide glassy semiconductors are of great interest in relation with creating polarization-sensitive optical elements. This study investigates the formation of LIPSS on the surface of $As_{50}Se_{50}$ amorphous film, fabricated by thermal vacuum deposition, under femtosecond laser irradiation in the wavelength range from 400 to 800 nm. The periods of various LIPSS types depend linearly on the laser wavelength. The measured birefringence of so-called low spatial frequency LIPSS, formed by different irradiation wavelengths, are in the 10–85 nm range. The maximum birefringence of 85 nm was obtained for structures irradiated at a 480 nm wavelength. A significant decrease in birefringence was observed at a wavelength of 800 nm, which may be due to the formation of a less pronounced and more disordered surface relief caused by less effective absorption of modifying laser radiation with photon energy lower than optical band gap of $As_{50}Se_{50}$. Decreased optical absorption observed in $As_{50}Se_{50}$ films with LIPSS is caused by increased light scattering on the surface relief.

KEYWORDS laser-induced periodic surface structures, $As_{50}Se_{50}$ amorphous films, laser-induced birefringence, optical retardance.

ACKNOWLEDGEMENTS This work was supported by the Russian Science Foundation (Grant No. 22-19-00035-II, https://rscf.ru/project/22-19-00035/

FOR CITATION Pakholchuk P.P., Shuleiko D.V., Barbashov V.A., Zabotnov S.V., Kozyukhin S.A., Kashkarov P.K. Formation of laser-induced periodic surface structures on an $As_{50}Se_{50}$ film under femtosecond laser irradiation with wavelengths of 400–800 nm. *Nanosystems: Phys. Chem. Math.*, 2025, **16** (6), 908–914.

1. Introduction

Chalcogenide glassy semiconductors (ChGS) of As-Se system are attracting attention due to their unique properties such as transparency in infrared region of the spectrum, high stability and a number of photoinduced phenomena (photodarkening, photobleaching, photocrystallization, etc.) [1–3]. Recently, high attention has been paid to the nonlinear optical properties of ChGS. Measurements of nonlinear refractive index have shown that its value can range from 100 to 1000 times of that in silica glass. A high nonlinear refractive index combined with moderate to low nonlinear absorption makes materials suitable for all-optical signal processing devices, enhancing the performance of telecommunication systems ChGS are very suitable for these kinds of applications, because they are compatible with well-established silica-on-silicon and fiber drawing technologies. Photoinduced phenomena allow the local modification of the material properties by the exposure to suitable radiation which can be utilized in writing waveguide channels, diffraction gratings and so forth [4–6]. The formation of laser-induced surface periodic structures (LIPSS) [7–9] on such materials is of particular interest in this case.

The formation of LIPSS is observed on a wide variety of materials – metals, semiconductors, and dielectrics, both crystalline and amorphous [10] – typically upon irradiation with ultrashort high-power laser pulses. This periodic relief demonstrates a clear relationship with the wavelength and polarization direction of the laser radiation used, and the process of its formation is mainly explained by the excitation of surface electromagnetic waves and their subsequent interference with the incident laser radiation [11, 12]. The main types of such relief include so-called low spatial frequency LIPSS (LSFL), characterized by the ridges orthogonal to the polarization and a period approximately equal to the laser radiation wavelength, and high spatial frequency LIPSS (HSFL) with ridges orientation along the polarization and a period several

times shorter than the wavelength [7, 13]. It has previously been shown that LIPSS formed on As-Se ChGS films can exhibit birefringence [14], which is explained by the form anisotropy of the relief. This allows for laser-structured ChGS films to be considered as a basis for creating optical polarizing elements. The parameters of the LIPSS formed on films are influenced by many factors. These include the film material and thickness, the substrate material, the laser pulses fluence and number, as well as the wavelength. Most studies investigate the dependence of LIPSS generation on various materials upon changing the fluence and number of laser pulses. At the same time, the laser wavelength used affects not only the LIPSS period, but can also significantly affect the depth of the formed relief [15, 16] and, accordingly, the optical anisotropy.

In the present study, our aim was forming LIPSS by exposing an $As_{50}Se_{50}$ amorphous thin film to femtosecond laser pulses of varying wavelengths (400–800 nm) in order to analyze birefringence and optical transmittance of the resulting structured surfaces. We note that during the experiments, the energy and number of laser pulses were also adjusted for different wavelengths to achieve sustainable and uniform LIPSS formation in each case.

2. Materials and methods

The $As_{50}Se_{50}$ bulk glass used in our experiments was obtained under the following conditions: the respective amounts of arsenic and selenium with 5N purity were placed in quartz ampoule evacuated down to $\sim 10^{-3}$ Pa and heated in a rotary furnace. The temperature was maintained constant at the glass melting point while the melt was continuously stirred to ensure better homogenization. After preservation at 900 K for several hours, the melt was cooled by air quenching. The glassy state of the obtained samples was controlled by the characteristic conchoidal fracture in glass. Then the film was produced from the respective bulk glassy sample by thermal evaporation process using a UVN-2M unit, at a temperature of 700–800 K and a residual pressure of less than 5 10^{-4} Pa. A molybdenum boat was used as a resistive evaporator; the distance between the substrate and the evaporator was 15.5 cm, the sample weight was 0.005 g and sublimation duration was 20 sec. The process of material deposition was controlled by visual observation. In order to avoid thickness non-uniformities, the substrate was rotated during the evaporation process. Following the completion of the deposition process, the substrate was left in a vacuum chamber until its complete cooling to room temperature. The fabricated $As_{50}Se_{50}$ film thickness, determined by atomic-force microscopy (AFM) was 840 ± 10 nm.

As a source of femtosecond laser radiation for the film surface structuring, a TETA-20 laser system (Avesta-Project Ltd, Russia; maximum power 10 W, λ = 1030 nm, τ = 250 fs, maximum repetition rate ν = 10 kHz) equipped with a PARUS optical parametric amplifier (Avesta-Project Ltd, Russia) was used, allowing to obtain laser radiation with wavelengths in the range of 400–800 nm. Using this laser system, the film surface was modified with the wavelengths λ = 400, 480, 550, 635 and 800 nm at a pulse duration of $\sim$150 fs. Laser radiation was focused at normal incidence onto the film using a microscope objective with a numerical aperture of NA = 0.03 into a spot with a diameter of 60 μm. A series of 300-μm-long scan lines were formed on the surface using each wavelength. The sample movement relative to the laser beam was implemented by three-axis motorized platform at a speed of 300 μm/s. The employed laser pulse repetition rates were ν = 1, 2, or 10 kHz and pulse energy E varied from 0.1 to 4.5 μJ. The laser pulse energy was measured using a 3A-P thermal power meter (Ophir, Israel), and the variation of the laser pulse energy was ensured by a continuous neutral density filter.

Visualization of the laser-irradiated sample surface for measuring the formed LIPSS periods was carried out using a scanning electron microscope (SEM, Vega 3, Tescan, Czech Republic), the measurement error for the periods was $\sim$5%. After that, to measure optical properties, square 400×400 μm^2 areas were written on the $As_{50}Se_{50}$ film surface, in the irradiation modes corresponding to the formation of LIPSS for each of the selected wavelengths. The optical transmission spectra of the areas with LIPSS were measured at room temperature using an MSFU-K microscope-spectrophotometer (LOMO, Russia); the measurements were carried out with an NA = 0.1 objective. Birefringence within the LIPSS-containing laser-irradiated areas was measured using a Thorlabs LCC7201B polarizing microscope (Thorlabs, USA) at 633 nm wavelength.

3. Results and discussion

Fig. 1 shows SEM images of HSFLs and LSFLs formed under laser irradiation with wavelengths of 400 and 480 nm. For both wavelengths, the formation of HSFLs and LSFLs is observed. The periods of the formed HSFLs were 120 and 180 nm, while those of the LSFLs were 370 and 455 nm, for the laser pulses wavelengths λ = 400 and 480 nm, respectively. Both types of structures were formed in the frequency range of 1–10 kHz, and for each frequency HSFL formation was observed at lower energies compared to LSFL.

With an increase in λ to 550 nm, HSFL with a period of 210 nm and LSFL with a period of 510 nm are formed (Fig. 2a,b). At this wavelength, LIPSS started to form at ν = 2 kHz and higher. At ν = 1 kHz, LIPSS were not observed up to energy of 0.88 μJ, when the film damage began (Fig. 2c). With irradiation at frequency of 2 kHz, HSFL formation was observed at the energy less than 0.38 μJ, and LSFL were observed in the energy range of 0.38–0.66 μJ. When irradiating with highest repetition rate of laser pulses (10 kHz), a hierarchical structure formation was observed, as can be seen in Fig. 2d, with simultaneous LSFL formation within the "grooves"-type LIPSS [10]. The period of the latter was about

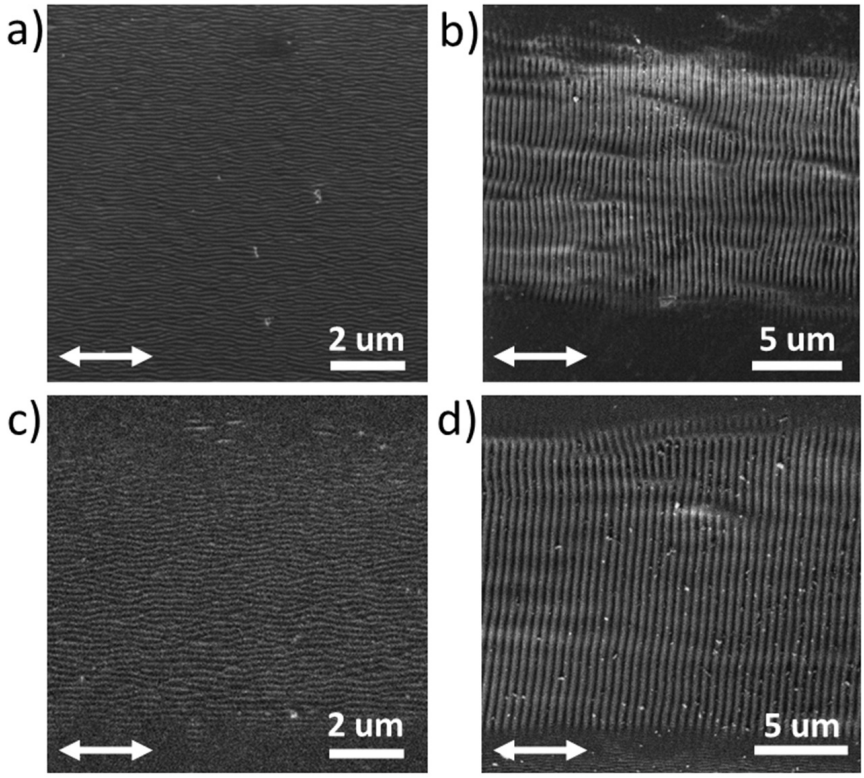

FIG. 1. SEM images of the LIPSS obtained at irradiation with femtosecond laser pulses at λ = 400 nm and (a) ν = 10 kHz, E = 0.14 μJ; (b) λ = 2 kHz, E = 0.6 μJ. LIPSS obtained at λ 480 nm and (c) ν = 10 kHz, E = 0.22 μJ; (d) ν = 2 kHz E = 0.51 μJ. Arrows indicate the laser polarization in each image

1.8 μm, which is higher than the laser wavelength, and the orientation was along the polarization vector of the laser radiation. No LSFL formation was detected at 10 kHz without the "grooves" for this wavelength.

At λ = 635 nm, the period of the surface relief was 230 nm for the HSFL, and 595 nm for the LSFL (Fig. 3a,b); both LIPSS types were formed in the range of ν from 2 to 10 kHz. Similar to the case with λ = 550 nm, at ν = 1 kHz, the LIPSS were not formed up to the laser pulse energy of 2.6 μJ, at which the film damage occurred. In this case, the film melted, forming ring-shaped structures containing fragmented LIPSS near the center of the scan line (Fig. 3d). And a complete film ablation was observed at the threshold laser pulse energy of 2.9 μJ. At a frequency of 2 kHz, LSFL began to form at the energy of 1.8 μJ (Fig. 3c), but their formation ceased with increasing energy. We also note that at ν = 10 kHz, similarly to λ = 550 nm, the formation of grooves was observed, with the period of $\sim$2.5 μm.

For λ = 800 nm, the formation of HSFLs began when using laser pulse energies of 3.1 and 1.8 μJ, at the repetition rates of 1 and 2 kHz, respectively. The period of the formed structures was 300 nm. However, with increasing energy, no LSFLs formation was observed at these repetition rates. Instead, periodic structures similar in appearance to HSFLs were formed in the central region of the scan line, parallel to the polarization of the laser pulses, but with a period of $\sim$720 nm, close to the LSFL period (Fig. 4a). When exceeding the laser pulse energies of 4.6 and 2.5 μJ for 1 and 2 kHz repetition rates respectively, the damage of the film was observed. Using ν = 10 kHz repetition rate, LSFLs were formed at the energy of 1.1 μJ. However, under these conditions, the film damage was observed in a few spots along the irradiated surface, which may be associated with a presence of initial defects in the film there. Contrary, at lower energies, the LIPSS were formed only near these defects. At laser pulse energies above 1.25 μJ and ν = 10 kHz, the film was damaged throughout the entire scanning area.

The dependence of the HSFL and LSFL periods on the laser wavelength is given in Fig. 5. The periods of the both LIPSS types increase linearly with the wavelength. In all cases, the LSFL period observed is slightly shorter than the laser wavelength, while the HSFL period is approximately 2.7 times shorter. The ratio of the LSFL to HSFL periods is about 2.5.

After determining the laser irradiation modes for the LIPSS formation for different wavelengths, 400$\times$400 μm^2 square areas were written to measure the birefringence of these structures. Since, HSFLs have weak birefringence properties due to low modulation of the relief [7], the modes in which LSFL formation occurs were used for each wavelength to obtain a higher birefringence value. Images of irradiated areas obtained by an optical polarizing microscope are shown in Fig. 6. The highest birefringence is observed for λ = 480 nm: corresponding retardance value, calculated as the difference in optical path length for ordinary and extraordinary waves, reaches 85 nm. For the LSFLs formed under irradiation with

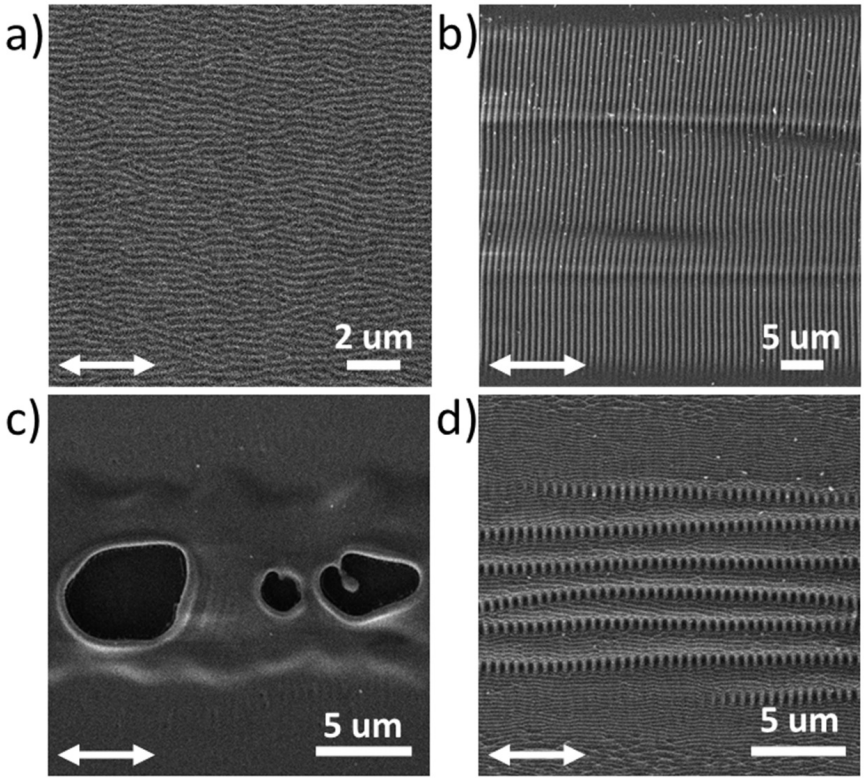

FIG. 2. SEM images of the surfaces irradiated with femtosecond laser pulses at λ = 550 nm and (a) ν = 2 kHz, E = 0.26 μJ; (b) ν = 2 kHz, E = 0.43 μJ; (c) ν = 1 kHz, E = 0.88 μJ; (d) ν = 10 kHz, E = 0.49 μJ. Arrows indicate the laser polarization in each image

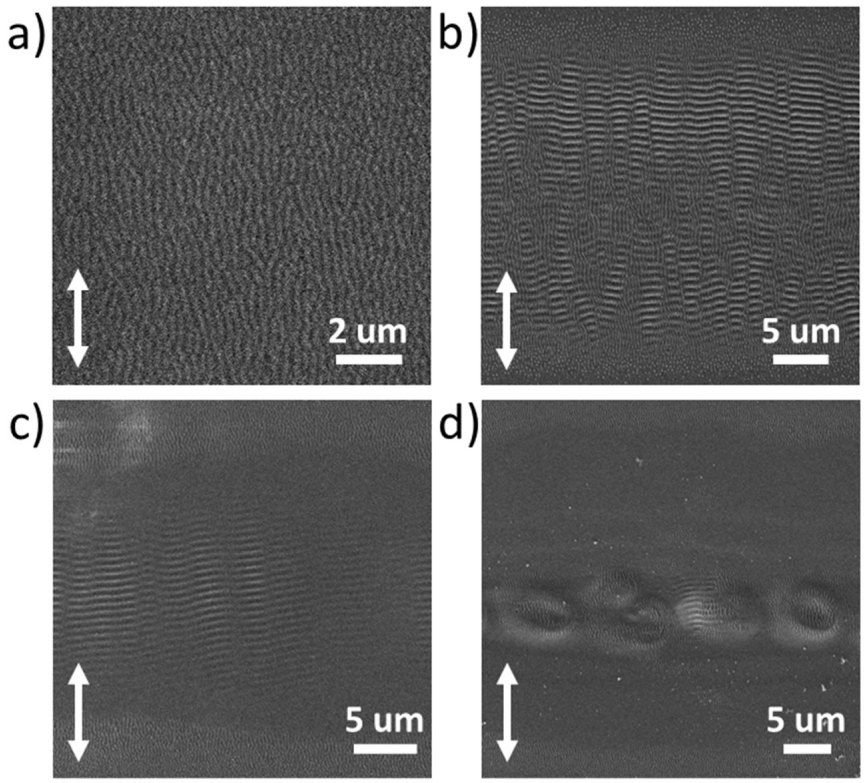

FIG. 3. SEM images of the surfaces irradiated with femtosecond laser pulses at λ = 635 nm and (a) ν = 2 kHz, E = 1.43 μJ; (b) ν = 10 kHz, E = 0.63 μJ; (c) ν = 2 kHz, E = 1.8 μJ; (d) ν = 1 kHz, E = 2.6 μJ. Arrows indicate the laser polarization in each image

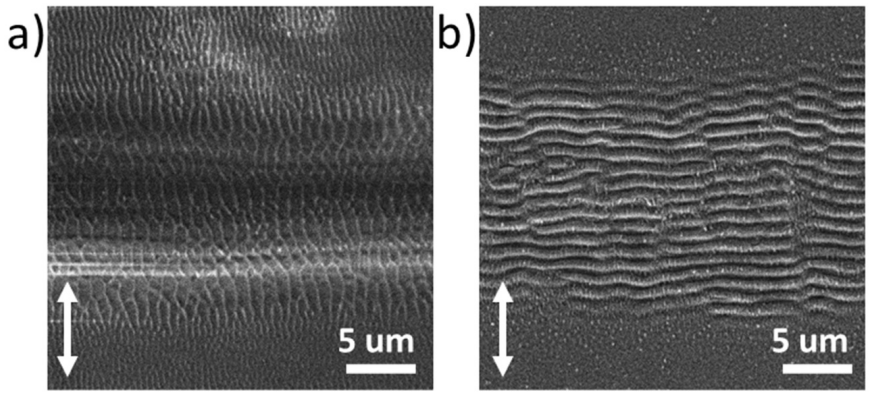

FIG. 4. SEM images of the LIPSS formed at $\lambda = 800$ nm and (a) $\nu = 1$ kHz, E = 4.0 μJ; (b) $\nu = 10$ kHz, E = 1.1 μJ. Arrows indicate the laser polarization in each image

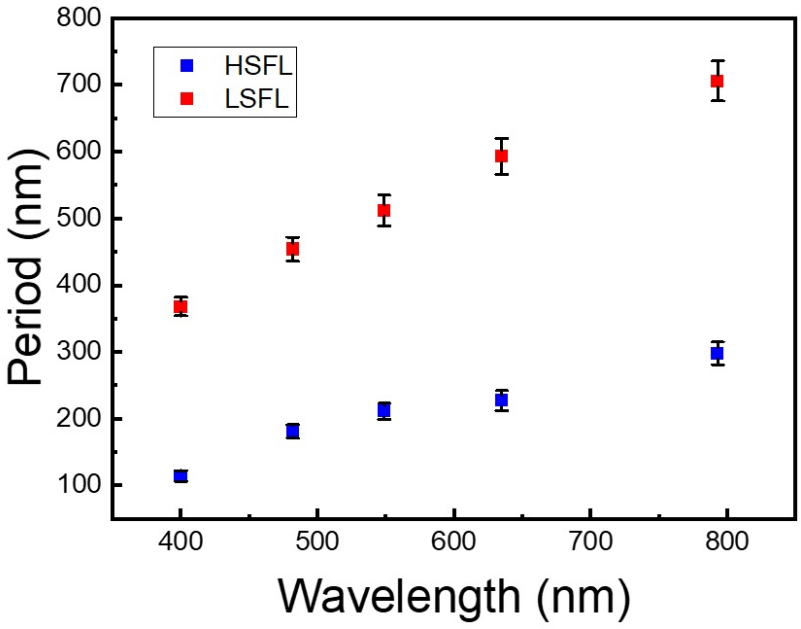

FIG. 5. The dependence of HSFL and LSFL periods on the laser radiation wavelength

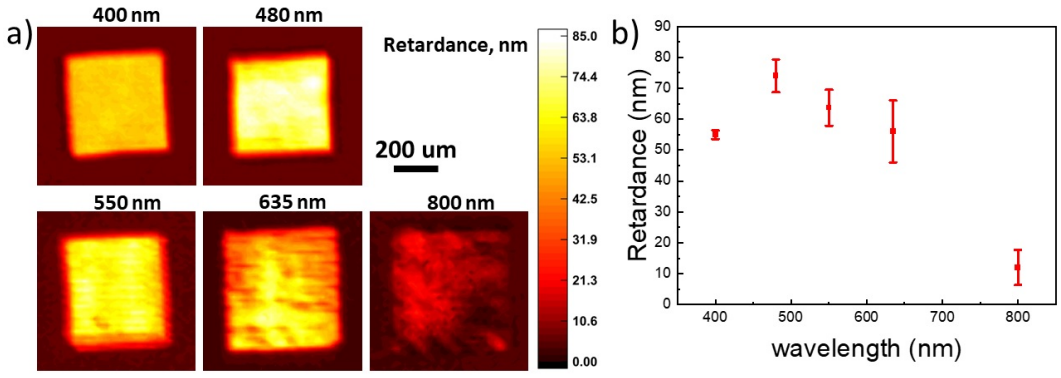

FIG. 6. Optical polarizing microscope images of LIPSS, formed at different wavelengths (a) and the dependence of the retardance on the laser writing wavelength (b)

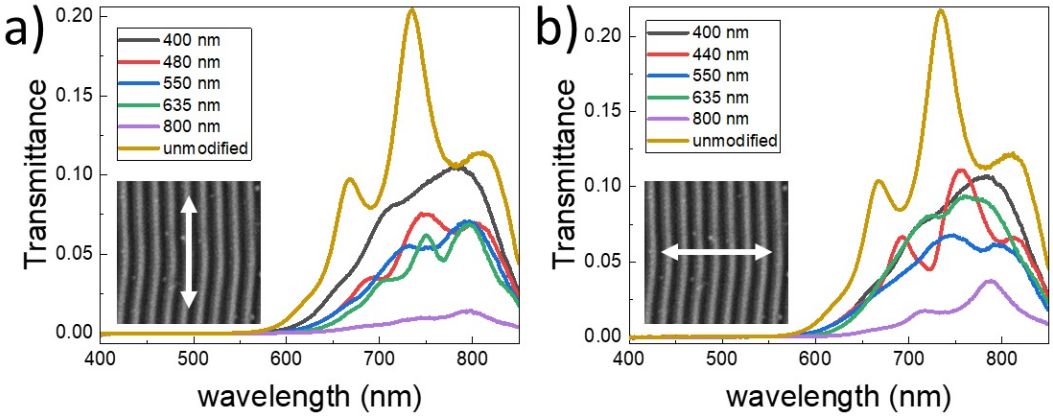

FIG. 7. Optical transmission spectra for the $As_{50}Se_{50}$ films with LIPSS in polarized light. The polarization of the transmitted light is (a) parallel or (b) orthogonal to the LIPSS ridges. The arrows indicate the polarization of the analyzed radiation relative to the LIPPS

λ = 400, 550 and 635 nm, the retardance values lie in the range of 50–75 nm. The minimum retardance value is observed for the LSFL formed at λ = 800 nm and does not exceed 20 nm. Thus, since the retardance value is related to the depth of the formed LIPSS [7, 14], the most prominent surface relief is formed at λ = 480 nm. Note that the photon energy for the laser radiation at λ = 635 nm has a value of ∼1.9 eV, exceeding the optical band gap of $As_{50}Se_{50}$, which is approximately 1.8 eV according to works [17, 18]. This ensures more efficient absorption of modifying laser light at this wavelength and the shorter ones as well, likely causing the formation of a more contrasting surface relief at laser irradiation with $\lambda \leq 635$ nm.

The presence of LIPSS also leads to a decrease in the optical transmission of the $As_{50}Se_{50}$ film. This is presumably due to the increased scattering by surface relief inhomogeneities formed as a result of laser irradiation. Fig. 7 presents the transmission spectra of LIPSS-containing regions on the $As_{50}Se_{50}$ film in polarized light. The spectra correspond to polarization of the transmitted radiation parallel (Fig. 7a) and orthogonal (Fig. 7b) to the ridges of the LIPSS. The structures formed with λ = 800 nm irradiation exhibit the greatest drop in transmission, which, combined with the lowest birefringence value, makes them of little interest for practical application. The smallest drop in transmission is observed for structures written at 400 nm, which may be due to their higher uniformity, compared to all other structures, as evidenced by the smallest variation in the retardance value within the irradiated area, observed in Fig. 6.

4. Conclusion

Examining formation of LIPSS on an $As_{50}Se_{50}$ films under femtosecond laser irradiation in this study allowed determining fabrication regimes for HSFLs and LSFLs at each wavelength used in the experiment from the 400–800 nm range. The LSFL structures formed at higher laser pulse energy compared to the HSFL. With increasing wavelength, a higher laser pulse repetition rate is also required to form LSFLs. Furthermore, specific formation regimes are discovered, for the LIPSS in a form of "grooves", as well as anomalous LSFL structures parallel to the laser polarization but with a period close to the laser wavelength. The dependence of LSFL birefringence on the wavelength of laser radiation used for the surface modification is determined in terms of optical retardance. The highest retardance up to 85 nm was observed for the region irradiated with laser pulses at a wavelength of 480 nm. For the LIPSS formed with $\lambda \leq$635 nm the retardance is at least 50 nm, while at longer wavelengths of the modifying laser radiation it drops to 12 nm. The formed LIPSSs reduce the transmittance of the ChGS film, which is most pronounced for structures written with irradiation at 800 nm.

References

[1] Iovu M.S., Shutov S.D., Popescu M. Relaxation of photodarkening in amorphous As–Se films doped with metals. *J. Non-Cryst. Solids*, 2002, **299**, P. 924–928.

[2] Arsh A., Klebanov M., Lyubin V., Shapiro L., Feigel A., Veinger M., Sfez B. Glassy $mAs_2S_3 \cdot nAs_2Se_3$ photoresist films for interference laser lithography. *Opt. Mater.*, 2004, **26**(3), P. 301–304.

[3] Flaxer E., Klebanov M., Abrahamoff D., Noah S., Lyubin V. Photodarkening of $As_{50}Se_{50}$ glassy films under μs light pulses. *Opt. Mater.*, 2009, **31**(4), P. 688–690.

[4] Savage J.A. Optical properties of chalcogenide glasses. *J. Non-Cryst. Solids*, 1982, **47**(1), P. 101–115.

[5] Petkov K., Ewen P.J.S. Photoinduced changes in the linear and non-linear optical properties of chalcogenide glasses. *J. Non-Cryst. Solids*, 1999, **249**(2), P. 150–159.

[6] Harbold J.M., Ilday F.Ö., Wise F.W., Sanghera J.S., Nguyen V.Q., Shaw L.B., Aggarwal I.D. Highly nonlinear As–S–Se glasses for all-optical switching. *Opt. Lett.*, 2002, **27**(2), P. 119–121.

[7] Shuleiko D., Zabotnov S., Sokolovskaya O., Poliakov M., Volkova L., Kunkel T., Kuzmin E., Danilov P., Kudryashov S., Pepelayev D., Kozyukhin S., Golovan L., Kashkarov P. Hierarchical Surface Structures and Large-Area Nanoscale Gratings in As_2S_3 and As_2Se_3 Films Irradiated with Femtosecond Laser Pulses. *Materials*, 2023, **16**(13), P. 4524.

[8] Yu X., Qi D., Wang H., Zhang Y., Wang L., Zhang Z., Dai Sh., Shen X., Zhang P., Xu Y. In situ and ex-situ physical scenario of the femtosecond laser-induced periodic surface structures. *Optics Express*, 2019, **27**(7), P. 10087–10097.

[9] Zabotnov S., Kolchin A., Shuleiko D., Presnov D., Kaminskaya T., Lazarenko P., Glukhenkaya V., Kunkel T., Kozyukhin S., Kashkarov P. Periodic relief fabrication and reversible phase transitions in amorphous $Ge_2Sb_2Te_5$ thin films upon multi-pulse femtosecond irradiation. *Micro*, 2022, **2**(1), P. 88–99.

[10] Bonse J., Kirner S.V., Krüger J. *Laser-Induced Periodic Surface Structures* (LIPSS). In: Sugioka, K. (eds) Handbook of Laser Micro- and Nano-Engineering. Springer, Cham, 2021, 59 p.

[11] Akhmanov S.A., Emel'yanov V.I., Koroteev N.I., Seminogov V.N. The effect of high-power laser radiation on the surface of semiconductors and metals: nonlinear optical effects and nonlinear optical diagnostics. *Sov. Phys. Usp.*, 1985, **147**(12), P. 675–745.

[12] Bonse J., Rosenfeld A., Krüger J. On the role of surface plasmon polaritons in the formation of laser-induced periodic surface structures upon irradiation of silicon by femtosecond-laser pulses. *Journal of Applied Physics*, 2009, **106**(10), P. 104910.

[13] Bonse J., Krüger J., Höhm S., Rosenfeld A. Femtosecond laser-induced periodic surface structures. *Journal of laser applications*, 2012, **24**(4), P. 042006.

[14] Kuzmin E., Zabotnov S., Shuleiko D., Pepelyaev D., Barbashov V., Efanov V., Kashkarov P. Laser-Induced Structuring of Arsenic Selenide Vitreous Films and Their Optical Properties. *Bulletin of the Russian Academy of Sciences: Physics*, 2024, **88**(3), P. S370–S374.

[15] Kozyukhin S., Lazarenko P., Vorobyov Yu., Baranchikov A., Glukhenkaya V., Smayev M., Sherchenkov A., Sybina Yu., Polohin A., Sigaev V. Laser-induced modification and formation of periodic surface structures (ripples) of amorphous GST225 phase change materials. *Optics and Laser Technology*, 2019, **113**, P. 87–94.

[16] Kozyukhin S., Smayev M., Sigaev V., Vorobyov Y., Zaytseva Y., Sherchenkov A., Lazarenko P. Specific features of formation of laser-induced periodic surface structures on $Ge_2Sb_2Te_5$ Amorphous Thin Films under Illumination by Femtosecond Laser Pulses. *Physica Status Solidi B*, 2020, **257**(11), P. 1900617.

[17] Corrales C., Ramírez-Malo J.B., Márquez E., Jiménez-Garay R. An optical study of the athermal photo-amorphization of $As_{50}Se_{50}$ thin films. *Materials Science and Engineering: B*, 1997, **47**(2), P. 119–126.

[18] Behera M., Naik P., Panda R., Naik R. Optical properties study in $As_{50}Se_{50}$ and $As_{50}Se_{40}Te_{10}$ chalcogenide thin films. Proceeding of "DAE SOLID STATE PHYSICS SYMPOSIUM 2016". Bhubaneswar, 2016, AIP Publishing LLC, 2017, P. 070009.

Submitted 16 November 2025; revised 23 November 2025; accepted 7 December 2025

Information about the authors:

Petr P. Pakholchuk – Lebedev Physical Institute, Russian Academy of Sciences, 53 Leninsky Avenue, Moscow 119991, Russia; Faculty of Physics, Moscow State University, 1/2 Leninskie Gory, Moscow, 119991, Russia; ORCID 0000-0002-2608-7621; p.paholchuk@lebedev.ru

Dmitrii V. Shuleiko – Faculty of Physics, Moscow State University, 1/2 Leninskie Gory, Moscow, 119991, Russia; ORCID 0000-0003-3555-6693; shuleyko.dmitriy@physics.msu.ru

Vadim A. Barbashov – Lebedev Physical Institute, Russian Academy of Sciences, 53 Leninsky Avenue, Moscow, 119991, Russia; ORCID 0000-0001-9615-3869; barbashovva@lebedev.ru

Stanislav V. Zabotnov – Faculty of Physics, Moscow State University, 1/2 Leninskie Gory, Moscow, 119991, Russia; ORCID 0000-0002-2528-4869; zabotnov@physics.msu.ru

Sergey A. Kozyukhin – Kurnakov Institute of General and Inorganic Chemistry, 31 Leninsky Avenue, Moscow, 119071, Russia; ORCID 0000-0002-7405-551X; sergkoz@igic.ras.ru

Pavel K. Kashkarov – Faculty of Physics, Moscow State University, 1/2 Leninskie Gory, Moscow, 119991, Russia; National Research Centre "Kurchatov Institute", 1 Akademika Kurchatova Sq., Moscow, 123182, Russia; ORCID 0000-0001-6889-001X; kashkarov@physics.msu.ru

Conflict of interest: the authors declare no conflict of interest.

NANOSYSTEMS:
PHYSICS, CHEMISTRY, MATHEMATICS

Nasirov P.D., et al. *Nanosystems: Phys. Chem. Math.*, 2025, **16** (6), 915–918.
http://nanojournal.ifmo.ru
DOI 10.17586/2220-8054-2025-16-6-915-918

Original article

Carbon dots with media-independent fluorescence

Pavel D. Nasirov[a], Sagila A. Novikova[b], Elena D. Gribova[c], Pavel P. Gladyshev[d], Irina V. Mukhina[e]

Dubna State University, Dubna, Russia

[a]chembios.lne@gmail.com, [b]sagila@uni-dubna.ru, [c]elena_g67@mail.ru, [d]pglad@yandex.ru, [e]irinamukhina10041989@gmail.com

Corresponding author: Pavel D. Nasirov, chembios.lne@gmail.com

PACS 61.46.Df, 73.21.La, 61.46.+w

ABSTRACT Since their discovery, carbon dots have been of great scientific interest due to their unique properties, including strong fluorescence and biocompatibility, which determine their potential application in biosensorics, bioimaging, drug delivery, and many other fields. This paper presents a new approach for the synthesis of high quantum yield carbon dots with media-independent fluorescence developed in the process of searching for solutions to the problem of carbon dot's application in immunochromatographic analysis.

KEYWORDS carbon dots, nanoparticles, immunoassay

ACKNOWLEDGEMENTS The research was conducted within the state assignment of the Ministry of Science and Higher Education of the Russian Federation (No. 1024011000011-7-1.4.2; 3.5.2 Conjugates of boron-containing quantum dots with biovectors for the diagnosis and boron neutron capture therapy of superficial malignant tumors (FEEM-2024-0011)).

FOR CITATION Nasirov P.D., Novikova S.A., Gribova E.D., Gladyshev P.P., Mukhina I.V. Carbon dots with media-independent fluorescence. *Nanosystems: Phys. Chem. Math.*, 2025, **16** (6), 915–918.

1. Introduction

In immunochemical methods of analysis as labels stand for forming an analytical signal depending on the analyte concentration colloidal gold nanoparticles are typically used [1–4]. Such systems are expensive, have high detection limits and low efficiency. Quantum dots are much more advanced labels allowing one to achieve a high level of sensitivity in immunochemical analysis. However, they are still very expensive and have several disadvantages, such as high cost, biotoxicity, and the need for surface modification preceding their conjugation with biomolecules [4–6]. Carbon dots (CDs) can serve as an alternative to quantum dots. CDs have found wide application in sensorics, microelectronics and other fields. CD-based systems sensitivity can be comparable with systems based on the quantum dots, while the CDs themselves are biocompatible, easy to synthesize and cheap to produce [7–9]. The implementation of CDs as analytical labels in immunoassay is complicated by three main disadvantages in comparison with quantum dots: solvatochromism, excitation-dependent emission shift and aggregation-dependent emission shift [9]. Such phenomena can be useful in the development of sensors based on carbon dots [10–12]. However, they lead to unpredictable behavior of optical properties of nanoparticles when conjugated with biomolecules, which significantly complicates the testing process. In this study, a new approach for the synthesis of CDs designed to fix some of the common problems is presented.

2. Materials and methods

Reagents were used for the work: Citric Acid anhydrous (Reag. USP) for analysis, ACS, 99.5 % PanReac-AppliChem; Tris(hydroxymethyl)aminomethane; 99.7 % Sigma Aldrich; N,N-Dimethylformamide, 99.8 % for synthesis, PanReac-AppliChem; Dimethylsulfoxide, 99.5 % PanReac-AppliChem; Ethanol, 99.9 % LiChrosolv, Supelco; Bidistilled water.

Consumables were used to clean the obtained materials: Omicron Syringe Filter 0.22 μm and 0.45 μm, PES 33 mm, non-sterile; Dialysis Tubing MWCO 0.5 kDa.

Obtaining and study of the physical and chemical properties of the derived samples was carried out with the use of the following equipment: Microwave oven Sineo MDS-10; Spectrofluorometer Solar CM 2203; Spectrophotometer SPEX SCP 715; Fourier transform infrared spectrometer Shimadzu IRAffinity-1S + MIRacle 10.

The calculations of quantum yield of luminescence samples are based on formula (1): [13]

$$\varphi_x = \frac{I_x \cdot \varphi_{st} \cdot \left(1 - T_{st(\lambda_{ex^{st}})}\right) \cdot n_x^2}{I_{st} \cdot \left(1 - T_{x(\lambda_{ex^x})}\right) \cdot n_{st}^2}, \tag{1}$$

where φ_x is the fluorescence quantum yield of the analyzed sample, φ_{st} is the fluorescence quantum yield of a standard fluorescent dye, I_x is the integral fluorescence intensity of the analyzed sample, I_{st} is the integral fluorescence intensity of a standard fluorescent dye, T_x is the transmission coefficient of the analyzed sample at the excitation wavelength, T_{st} is

the transmittance coefficient of a standard fluorescent dye at the excitation wavelength. A 0.5 M quinine sulfate solution in sulfuric acid was employed as a standard, exhibiting a fluorescence maximum at 440 nm and a quantum yield of 54.5 % when excited at 345 nm. The optical properties of the carbon dot sample were studied in a dilute aqueous solution. The fluorescence spectrum ordinates for both the standard and the sample were converted from cps to energy units ($W/m^2 \cdot nm$) to calculate the integral fluorescence intensities.

The synthesis of CDs was performed in a microwave digestion system Sineo MDS-10 with teflon-lined vessels. Suspensions of 3.6 mmol of citric acid and 14.4 mmol of tris-(hydroxymethyl)-aminomethane were dissolved in 5 ml of bidistilled water, then it was placed in a microwave oven for 30 min at a radiation frequency of 2.45 GHz, power 700 W, maximum heating temperature 200 °C. The resulting yellow solution was purified by dialysis (0.5 kDa).

3. Results and discussion

Citric acid (CA) is the most common reagent for the fabrication of CDs by the microwave-assisted methods [14]; however, much better results are demonstrated by CDs obtained by a combination of CA and an amino-containing compound such as urea [15]. In this study tris-(hydroxymethyl)-aminomethane (Tris) was proposed as an additional reagent for the production of citric acid-based CDs similar to publications [16–18]. Tris is a polar compound that has a relatively high dielectric loss tangent and is able to react with citric acid by formation of amide and ester bonds [19]. These properties of Tris are commonly used for surface passivation of carbon dots leading to an increase in their quantum yield.

The optical properties of obtained CD's sample were studied by UV/Vis-spectroscopy and fluorimetry. The results are shown in Fig. 1.

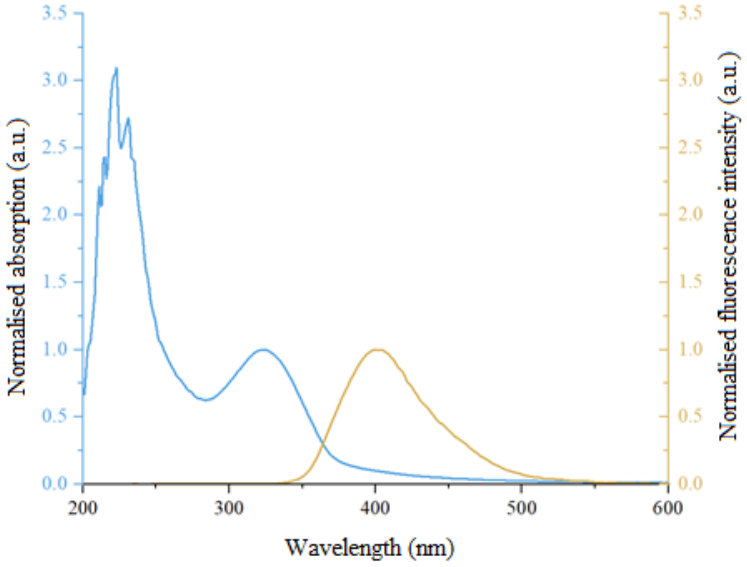

FIG. 1. Absorption and luminescence spectra of CDs derived from citric acid and Tris

The absorption spectrum of CDs derived from citric acid and Tris exhibits two absorption bands with maximums near 225 and 330 nm (Fig. 1). The absorption peak near 225 nm is supposedly due to electronic transitions of organic functional groups in the amorphous part of CDs while the broad band near 330 nm corresponds to absorption of sp^2-hybridised carbon fragments of different nature. The fluorescence peak of these CDs at 405 nm can be characterized as rather wide with negligible asymmetry in the long wave region. For the CDs synthesized in this work, the calculated quantum yield of fluorescence was 70 %, which is a great value for this class of fluorescent materials.

The relatively high content of Tris relative to CA distinguishes this study from the others. The excess of the passivation agent leads to bonding with all carboxyl groups conjugated to the graphitic core.

Interruption of conjugation allows to get rid of some media-dependent properties of CDs such as solvatochromism (Fig. 2a, Fig. 2c) and excitation-dependent emission shift (Fig. 2b) [20].

For the CDs dissolved in different solvents, such as water, ethanol, DMF, and DMSO, the fluorescence maximum remains in the range of 400 – 407 nm. Also, the decrease in the quantum yield in alkaline media does not exceed the measurement error. The negligible decrease in the quantum yield in acid media can appear due to the protonation of nitrogen atoms of amide bonds that are still conjugated to the core [12, 21–23].

The surface chemistry of obtained CD's sample was studied by IR-spectroscopy. The IR spectrum (TIR mode) of the CDs obtained in this work is shown in Fig. 2.

The IR spectrum (TIR mode) of the CDs obtained in this work contains characteristic absorption bands at 1039 cm^{-1} (O–H def.), 1652 cm^{-1} (C=O val. of amide) and wide characteristic band at 3280 cm^{-1} (O–H val.) proving the presence

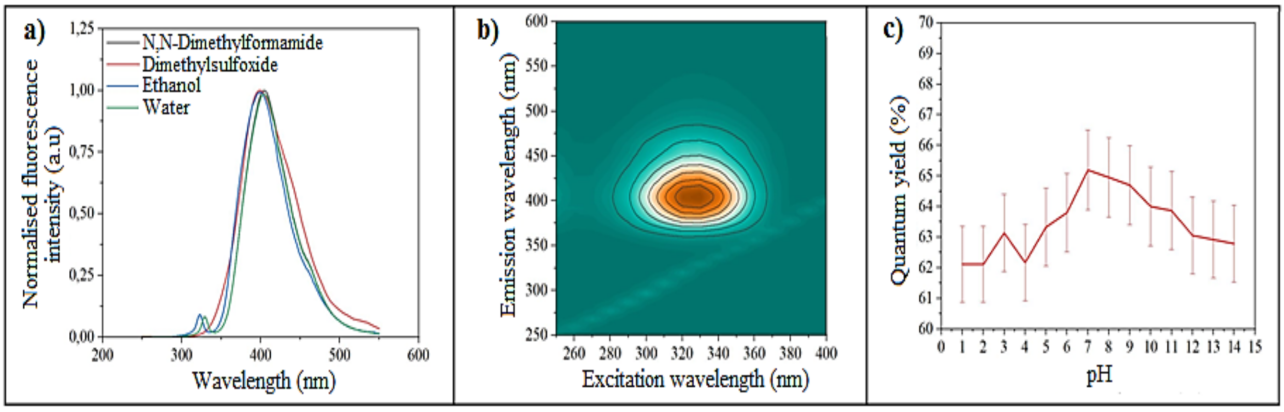

FIG. 2. a) – Fluorescence spectra of CDs derived from CA and Tris in different solvents; b) – Excitation to emission wavelengths diagram of CDs derived from CA and Tris in water; c) – Quantum yield of CDs derived from CA and Tris in aqueous solutions with different pH values

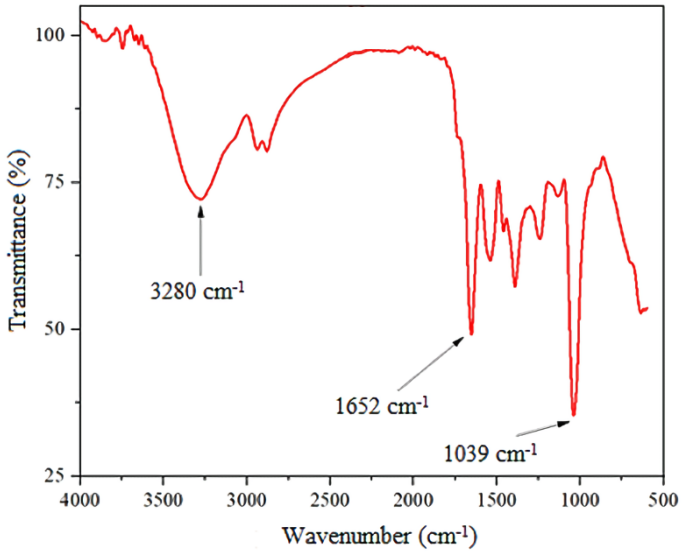

FIG. 3. IR spectrum of CDs derived from CA and Tris

of ester and amide bonds into the CD's surface (Fig. 3.). CDs derived from CA usually possess high quantity of terminal carboxylic groups [20,24]. The complete absence of characteristic bands of free carboxyl groups indicates that the surface passivation was carried out completely.

4. Conclusion

CDs derived from citric acid and Tris are characterized by a rather wide fluorescence peak but with a high quantum yield of 70 %. Fluorescence independent of pH and excitation wavelength highlights them among CDs obtained by other methods. This result was achieved due to the interrupted conjugation of surface carboxyl groups with the core of CDs via Tris excess. All these features make citric acid and Tris-based CDs perspective for use as inexpensive, easy-to-produce, and highly fluorescent analytical labels for immunochemical assay.

References

[1] Martinez-Liu C., et al. Development of a rapid gold nanoparticle-based lateral flow immunoassay for the detection of dengue virus. *Biosensors*, 2022, **12** (7), 495.
[2] Prakashan D., et al. Gold nanoparticle conjugate-based lateral flow immunoassay (LFIA) for rapid detection of RBD antigen of SARS-CoV-2 in clinical samples using a smartphone-based application. *J. of Medical Virology*, 2023, **95** (1), 28416.
[3] Chen Z., et al. Selective surface passivation of gold nanoparticles: A strategy for enhanced sensitivity in lateral flow immunoassay. *Chemical Engineering J.*, 2025, **503**, 158571.
[4] Li J., et al. Quantum Dots for Chemical Metrology. *Analytical Chemistry*, 2025, **97** (13), P. 6891–6910.
[5] Li J., et al. Dual protecting encapsulation synthesis of ultrastable quantum-dot nanobeads for sensitive and accurate detection of cardiac biomarkers. *Sensors and Actuators B: Chemical*, 2021, **344**, 130275.

[6] Schüller M., et al. Investigating conjugated polymer nanoparticle formulations for lateral flow immunoassays. *RSC advances*, 2021, **11** (47), P. 29816–29825.
[7] Zor E., et al. Carbon dots in the detection of pathogenic bacteria and viruses. *Critical Reviews in Analytical Chemistry*, 2024, **54** (2), P. 219–246.
[8] Zhang G., et al. Novel Reporter Based on Aggregation-induced emission Luminogens for Lateral Flow Immunoassay: A Mini Review. *TrAC Trends in Analytical Chemistry*, 2024, 118098.
[9] Devi J.S.A., et al. Luminescent carbon dots versus quantum dots and gold nanoclusters as sensors. *Nanoscale Horizons*, 2024, **9** (10), P. 1683–1702.
[10] Thomas D., et al. Solvatochromic and pH-sensitive fluorescent membrane probes for imaging of live cells. *ACS Chemical Neuroscience*, 2021, **12** (4), P. 719–734.
[11] Alas M.O., Genc R. Solvatochromic surface-passivated carbon dots for fluorometric moisture sensing in organic solvents. *ACS Applied Nano Materials*, 2021, **4** (8), P. 7974–7987.
[12] Singhal P., Vats B.G., Pulhani V. Origin of solvent and excitation dependent emission in newly synthesized amphiphilic carbon dots. *J. of Luminescence*, 2022, **244**, 118742.
[13] Lakowicz J.R. (ed.). *Principles of fluorescence spectroscopy*. Boston, MA, Springer US, 2006.
[14] Ludmerczki R., et al. Carbon dots from citric acid and its intermediates formed by thermal decomposition. *Chemistry–A European J.*, 2019, **25** (51), P. 11963–11974.
[15] Kasprzyk W., et al., Lumenescence phenomena of carbon dots derived from citric acid and urea – a molecular insight. *Nanoscale*, 2018, **10** (29), P. 13889–13894.
[16] Zhou M., et al. Synthesis of highly photoluminescent carbon dots via citric acid and Tris for iron (III) ions sensors and bioimaging. *Talanta*, 2015, **143**, P. 107–113.
[17] Zhang Y., et al. One-step microwave synthesis of N-doped hydroxyl-functionalized carbon dots with ultra-high fluorescence quantum yields. *Nanoscale*, 2016, **8** (33), P. 15281–15287.
[18] Zhang Y.Y., et al. A new hydrothermal refluxing route to strong fluorescent carbon dots and its application as fluorescent imaging agent. *Talanta*, 2013, **117**, P. 196–202.
[19] Saviz M., et al. Dielectric Spectroscopy of Aqueous TRIS Buffer Solutions at Microwave Frequencies. *ICBEM*, 2013.
[20] Kasprzyk W., et al. The role of molecular fluorophores in the photoluminescence of carbon dots derived from citric acid: current state-of-the-art and future perspectives. *Nanoscale*, 2022, **14** (39), P. 14368–14384.
[21] Ma G., et al. Carbon dots-based fluorescent probe for detection of foodborne pathogens and its potential with microfluidics. *Food Chemistry*, 2024, 139385.
[22] Wang L., et al. Recent research progress of fluorescence biosensors based on carbon dots in early diagnosis of diseases. *TrAC Trends in Analytical Chemistry*, 2024, 117962.
[23] Rasheed P.A., et al. Graphene quantum dots for biosensing and bioimaging. *RSC advances*, 2024, **14** (23), P. 16001–16023.
[24] Wang H., et al. Surface modification functionalized carbon dots. *Chemistry – A European J.*, 2023, **29** (65), e202302383.

Submitted 16 October 2024; revised 19 May 2025; accepted 22 November 2025

Information about the authors:

Pavel D. Nasirov – Dubna State University, Universitetskaya, 19, Dubna, 141980, Russia; ORCID 0009-0004-0508-5725; chembios.lne@gmail.com

Sagila A. Novikova – Dubna State University, Universitetskaya, 19, Dubna, 141980, Russia; ORCID 0000-0001-5118-4303; sagila@uni-dubna.ru

Elena D. Gribova – Dubna State University, Universitetskaya, 19, Dubna, 141980, Russia; ORCID 0009-0005-1506-5418; elena_g67@mail.ru

Pavel P. Gladyshev – Dubna State University, Universitetskaya, 19, Dubna, 141980, Russia; ORCID 0000-0002-3764-8412; pglad@yandex.ru

Irina V. Mukhina – Dubna State University, Universitetskaya, 19, Dubna, 141980, Russia; ORCID 0000-0001-8290-3016; irinamukhina10041989@gmail.com

Conflict of interest: the authors declare no conflict of interest.

NANOSYSTEMS:
PHYSICS, CHEMISTRY, MATHEMATICS

Alexeeva O.V., et al. *Nanosystems: Phys. Chem. Math.*, 2025, **16** (6), 919–924.
http://nanojournal.ifmo.ru
DOI 10.17586/2220-8054-2025-16-6-919-924

Original article

Facile synthesis and characterization of FeCoNiPt alloy nanoparticle electrocatalysts with different Pt content

Olga V. Alexeeva[1,a], Olga K. Karyagina[1,b], Sergei S. Kozlov[1,c], Leontiy I. Kuznetsov[1,d], Liudmila L. Larina[1,e], Anna B. Nikolskaya[1,f], Oleg I. Shevaleevskiy[1,d]

[1]N. M. Emanuel Institute of Biochemical Physics RAS, Solar Photovoltaic Laboratory, Moscow, Russia

[a]alexol@yandex.ru, [b]olgakar07@mail.ru, [c]sergeykozlov1@gmail.com, [d]shevale2006@yahoo.com, [e]llarina3333@gmail.com, [f]anickolskaya@mail.ru

Corresponding author: Shevaleevskiy O.I., shevale2006@yahoo.com

ABSTRACT In this work, we present a facile synthesis of FeCoNiPt alloy nanoparticles (NPs) with tunable platinum content (10–30 at.%). The NPs were produced by medium-assisted solid-state reaction using acetylacetonate metal precursors. The structural characterization (TEM, HRTEM, STEM-EDS, and XRD) reveals that the obtained FeCoNiPt NPs exhibit a uniform morphology with an average diameter of 3–7 nm and crystallize in a single-phase face-centered cubic solid solution. Increasing the Pt content leads to lattice expansion and a systematic increase in crystallite size, consistent with the larger atomic radius of Pt. STEM-EDS elemental maps confirm homogeneous incorporation of Fe, Co, Ni, and Pt across individual nanoparticles, demonstrating the successful formation of a multicomponent alloy. This study demonstrates that tuning Pt content in FeCoNiPt multicomponent alloys enables precise modulation of d-band electronic structure. The proposed synthesis approach is simple, cost-effective, and scalable, offering a promising pathway for designing Pt-optimized electrocatalysts.

KEYWORDS nanoparticles, multicomponent alloys, HRTEM, electrodes, electrocatalysis.

ACKNOWLEDGEMENTS The work was carried out within the state assignment of the Ministry of Science and Higher Education of the Russian Federation (theme No. 125020401357-4).

FOR CITATION Alexeeva O.V., Karyagina O.K., Kozlov S.S., Kuznetsov L.I., Larina L.L., Nikolskaya A.B., Shevaleevskiy O.I. Facile synthesis and characterization of FeCoNiPt alloy nanoparticle electrocatalysts with different Pt content. *Nanosystems: Phys. Chem. Math.*, 2025, **16** (6), 919–924.

1. Introduction

The noble metals, including Pt, remain indispensable components of efficient advanced electrocatalysts for hydrogen energy technologies, particularly for the hydrogen and the oxygen evolution reactions [1–7]. However, the high cost and limited availability of Pt significantly restrict its widespread use in large-scale water electrolysis [8–10]. One of the most effective strategies to reduce Pt consumption while maintaining high catalytic efficiency is alloying Pt with Earth-abundant 3d transition metals such as Fe, Co, and Ni. Such alloying lowers the overall precious-metal loading and modifies the electronic structure of Pt, that results in improved catalytic activity through synergistic multimetal interactions [11–14].

Recent studies highlight the exceptional catalytic performance of multicomponent Pt-containing high entropy alloys, including FeCoNiRhPt and FeCoNiTaPt, which exhibit high activity and stability at industrially relevant current densities during water splitting. In line with this, it was shown, that FeCoNiPt alloy exhibits high potential due to its low-cost production possibilities. FeCoNiPt alloy nanoparticles (NPs) can be synthesized using low-temperature chemical routes. It have demonstrated remarkably low HER overpotentials (as low as 11 mV) and mass activities exceeding those of commercial Pt/C by 10–13 times. Thus, one can see high potential of Pt-based multicomponent alloys to be used as efficient and economically feasible electrocatalysts.

A key factor governing the activity of Pt-containing alloys is the electronic structure of the d-band. Alloying induces modifications in several critical parameters, including: the adsorption free energy of hydrogen intermediates, the metal–O–H bond strength governing OER pathways the occupancy and hybridization of d-orbitals, and the position and shape of the d-band centers. Optimizing these d-band characteristics is essential for achieving balanced adsorption energies of HER/OER intermediates, ultimately enhancing catalyst performance.

In this context, FeCoNiPt multicomponent alloy NPs present attractive systems for tuning Pt-centered electronic interactions. The Pt content adjusting makes it possible to regulate the d-band width, orbital overlap, and coordination effects within the alloy lattice. DFT studies predict that a Pt content of approximately 20 % offers an optimal electronic environment, maximizing synergistic interactions while minimizing the amount of Pt used. In this work, FeCoNiPt alloy nanoparticles with controlled Pt contents (10–30 at.%) were synthesized via a simple medium-assisted solid-state reaction [15,16]. Their morphology, crystal structure, elemental distribution, and electrochemical properties were comprehensively

examined. We have shown that the alloy NPs containing ∼20% Pt achieve the most favorable combination of structural uniformity, electronic optimization, and catalytic activity, consistent with the d-band engineering principle. These results provide important insights into the design of multicomponent Pt-based alloys for next-generation electrocatalysts.

2. Experimental

2.1. Synthesis of FeCoNiPt alloy nanoparticles

FeCoNiPt alloy nanoparticles were synthesized using a medium-assisted solid-state reaction, a method previously demonstrated to yield ultrasmall multicomponent alloy nanoparticles with high compositional homogeneity [15]. To synthesize FeCoNiPt alloy NPs, metal acetylacetonate complexes were employed as precursors: iron(III) acetylacetonate ($Fe(acac)_3$), cobalt(III) acetylacetonate ($Co(acac)_3$), nickel(II) acetylacetonate ($Ni(acac)_2$) and platinum(II) acetylacetonate ($Pt(acac)_2$) precursors were used.

To obtain FeCoNiPt nanoparticles with different Pt contents, the total amount of metal precursors was fixed at 1 mmol. Fe, Co, and Ni precursors were introduced in equimolar quantities, while the amount of Pt precursor was varied (0.1, 0.2, and 0.3 mmol), corresponding to targeted Pt contents of approximately 10, 20, and 30 at.%. The precursor mixture was homogenized in an insulating organic medium and subjected to thermal treatment under conditions described previously. After the reaction, the resulting powder was repeatedly washed with organic solvents and purified by centrifugation. The actual elemental compositions of the synthesized nanoparticles were then determined by EDX analysis.

2.2. Materials characterization

The morphology and size distribution of the synthesized NPs were characterized using JEOL 2100F FEG TEM/STEM operated at 200 kV, and JEOL TEM/STEM ARM 200CF equipped with HAADF and annular bright field detectors. High-angle annular dark-field scanning TEM (HAADF-STEM) coupled with energy dispersive X-ray spectroscopy (EDX) was employed for elemental mapping. Selected Area Electron Diffraction patterns were obtained to identify the crystal structure of the NPs. To confirm the structure the d-spacing values were calculated and compared with standard FCC lattice parameters.

3. Results and discussion

3.1. TEM and HRTEM analysis

Transmission electron microscopy confirmed that the FeCoNiPt alloy nanoparticles synthesized using the medium-assisted solid-state reaction exhibit highly uniform morphology and nanoscale dimensions (Fig. 1). The nanoparticles were predominantly spherical and well separated from each other, showing that the synthesis route effectively suppresses agglomeration and enables controlled nucleation and growth. Statistical analysis of particle size shows a narrow distribution centered at 5.31 ± 0.83 nm, that is consistent with the formation of small catalytic grains that may provide enhanced surface reactivity due to their high surface-to-volume ratio that significantly increases the density of exposed active sites.

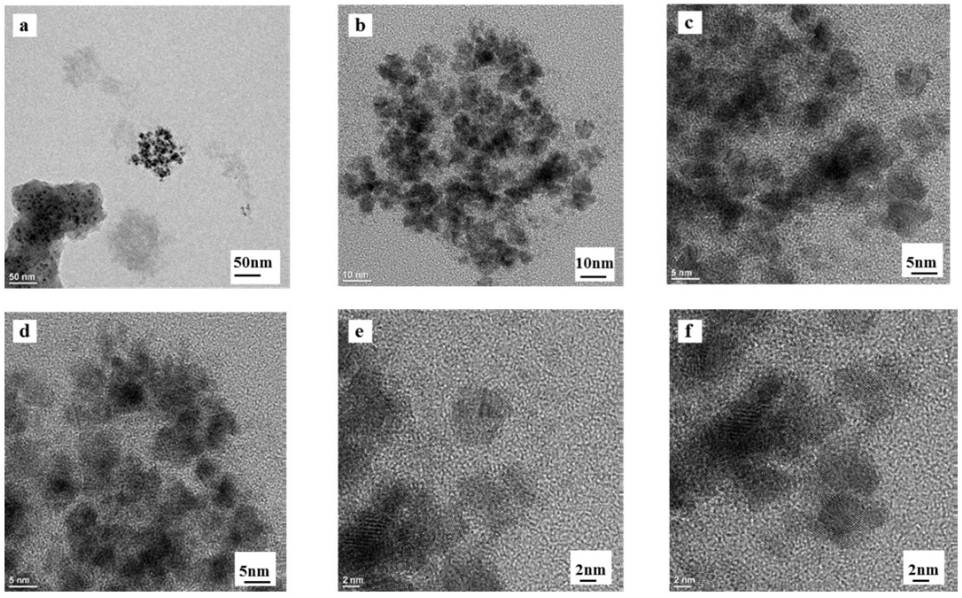

FIG. 1. Transmission electron microscopy (TEM) characterization of FeCoNiPt alloy nanoparticles: high-resolution TEM (HRTEM) images (a, b, c, d) and HRTEM micrographs at higher magnification (e, f).

High-resolution TEM (HRTEM) images show well-dispersed, predominantly spherical FeCoNiPt nanoparticles (Fig, 1: a, b, c, d). Fig. 1 (e, f) presents HRTEM micrographs at higher magnification. It can be seen that high-resolution TEM images display distinct, well-resolved lattice fringes throughout the nanoparticles, confirming their high crystallinity. The presence of continuous and coherent atomic planes suggests that alloying occurs through a homogeneous solid-solution mechanism, with no evidence of core–shell formation, phase separation, or structural defects. The degree of crystalline uniformity is critical for catalytic stability, as grain boundaries and compositional heterogeneities often reduce activity and induce the degradation processes.

3.2. STEM-EDS analysis and quantitative composition of the alloy NPs

High-angle annular dark-field scanning (HAADF) STEM, combined with energy-dispersive X-ray spectroscopy (EDS), was used to evaluate elemental distribution across the nanoparticles. Fig. 2 presents an example of the appropriate data obtained for $Fe_{29.8}Co_{30.2}Ni_{30.6}Pt_{9.4}$ alloy NPs. Z-contrast HAADF images show uniform brightness, implying an even distribution of high- and low-atomic-number elements throughout the sample. As can be seen, elemental mapping confirms that Fe, Co, Ni, and Pt are homogeneously distributed across nanoparticles without detectable segregation and clustering.

The observed compositional uniformity presents a critical characteristic of multicomponent alloys and is essential for achieving synergistic electronic interactions between constituent elements. The formation of a chemically homogeneous alloy ensures that each catalytic site meets similar local bonding environments and enhances the stability of electrocatalytic behavior. Moreover, homogeneous alloying modulates the electronic structure allowing the optimization of adsorption energies for HER and OER processes.

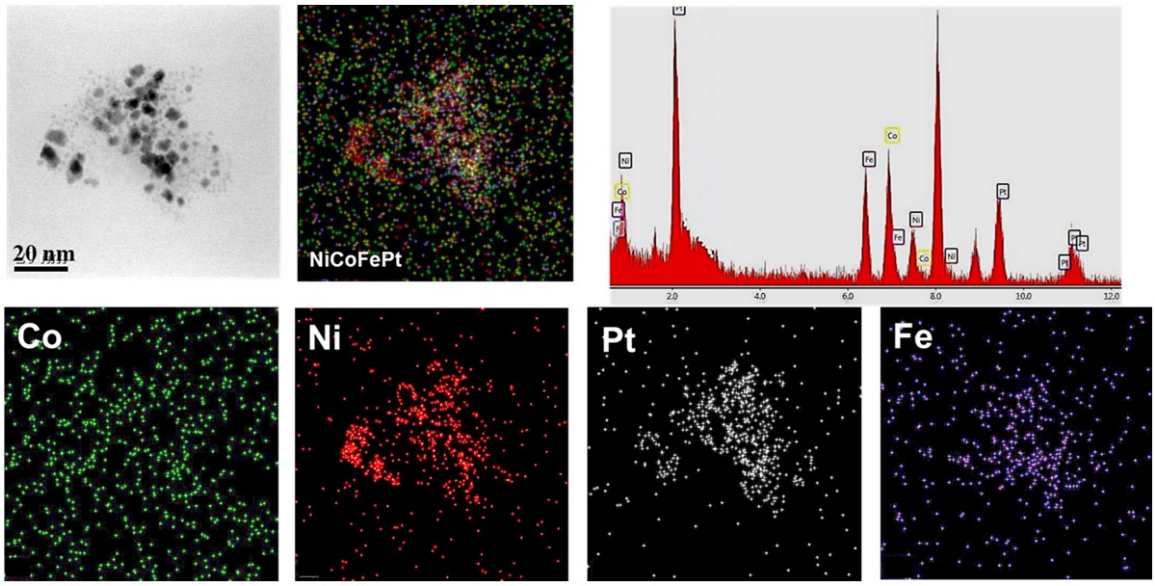

FIG. 2. STEM-EDS elemental mapping of FeCoNiPt alloy nanoparticles. High-angle annular dark-field (HAADF) STEM image of a representative nanoparticles and corresponding elemental maps for Fe, Co, Ni, and Pt.

The combined results of the TEM and STEM-EDS analyses provide strong evidence that the synthesized FeCoNiPt alloy NPs form a single-phase, compositionally homogeneous alloy with ultrasmall particle size. The characteristics obtained are directly relevant for the application in catalysis. Ultrasmall size of NPs ($\sim$5 nm) provides a high density of active surface atoms, homogeneous alloying maximizes synergistic electronic effects among Fe, Co, Ni, and Pt, uniform crystallinity ensures consistent catalytic behavior across particles, while the absence of segregation will prevent the deactivation pathways associated with phase instability. The listed above structural and compositional features will strongly influence the d-band structure of Pt-containing alloys, and enable the possibility of fine-tuning of adsorption strengths for HER and OER intermediates.

The actual elemental compositions of the synthesized alloy NPs determined by EDX analysis and the contents of each element in FeCoNiPt NPs are summarized in Table. The composition of NPs for the initial Pt precursor amount of 10 %, 20 %, and 30 %, was found to be, respectively, $Fe_{29.8}Co_{30.2}Ni_{30.6}Pt_{9.4}$, $Fe_{27.5}Co_{26.7}Ni_{30.6}Pt_{18.7}$, and $Fe_{23.7}Co_{24.3}Ni_{23.8}Pt_{28.2}$. The obtained values correspond closely to the nominal molar ratios used during synthesis, demonstrating reliable incorporation of each precursor into the alloy lattice. Importantly, the agreement between nominal and measured compositions confirms that alloying occurs throughout the nanoparticle volume, not merely at the surface.

TABLE 1. The chemical composition of NPs

Initial Pt precursor amount	Resulted composition of FeCoNiPt NPs (%)			
	Fe	Co	Ni	Pt
10%	29.8	30.2	30.6	9.4
20%	27.5	26.7	27.1	18.7
30%	23.7	24.3	23.8	28.2

The minor deviation in Ni concentration is within typical experimental variation for nanoscale EDS measurements. Critically, the incorporation of all elements in ratios similar to the target stoichiometry confirms that alloying occurs throughout the entire nanoparticle volume, not just at the surface.

3.3. Structural analysis using FFT and SAED

To further elucidate the crystallographic characteristics of the FeCoNiPt nanoparticles, Fast Fourier Transform (FFT) and Selected Area Electron Diffraction (SAED) analyses were carried out. Both techniques provided consistent evidence supporting the formation of a single-phase solid solution with a face-centered cubic (FCC) structure. FFT patterns obtained from several individual nanoparticles exhibit well-defined periodic diffraction spots indicative of ordered atomic arrangements characteristic of the FCC phase (Fig. 3). Inverse FFT (IFFT) reconstruction of selected lattice fringes reveals an interplanar spacing of 0.240 nm, corresponding to the (111) plane of an FCC structure. The average spacing extracted from multiple particles was 0.241 nm, confirming the consistency of the FCC phase throughout the sample. The corresponding lattice parameter, calculated from the (111) spacing, is in good agreement with the expected values for Pt-containing FCC alloys.

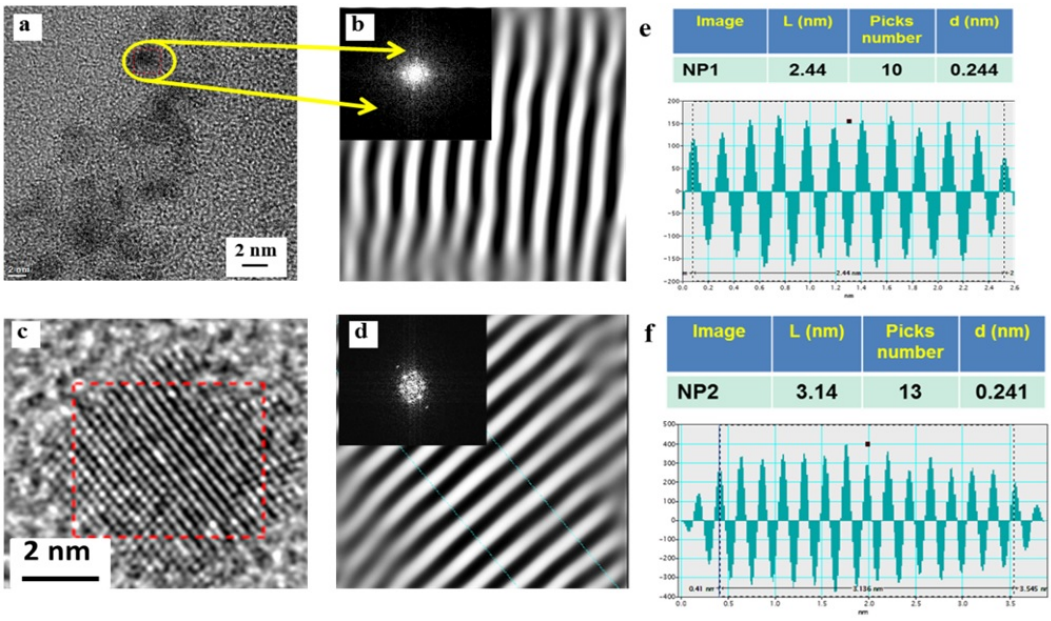

FIG. 3. FFT analysis of representative FeCoNiPt nanoparticles. (a, c) HRTEM images of nanoparticles NP1 and NP2; (b, d) IFFT images showing lattice fringes. In insert: corresponding FFT patterns exhibiting FCC diffraction maxima; (c, e) calculation of the d-spacing values.

The SAED patterns (Fig. 4) display a set of concentric diffraction rings, which can be indexed to the (111), (200), and (200) reflections of an FCC crystal structure. The absence of an additional diffraction rings or discrete spots indicates that the FeCoNiPt nanoparticles crystallize in a single-phase solid solution without detectable secondary phases or elemental segregation. According to SAED measurements the interplanar spacings were found to be: 0.247 nm for (111), 0.219 nm for (200), and 0.162 nm for (220). These values closely match the expected spacings. The excellent agreement between the measured and theoretical values, together with FFT results, confirms that the FeCoNiPt nanoparticles adopt a well-defined FCC phase.

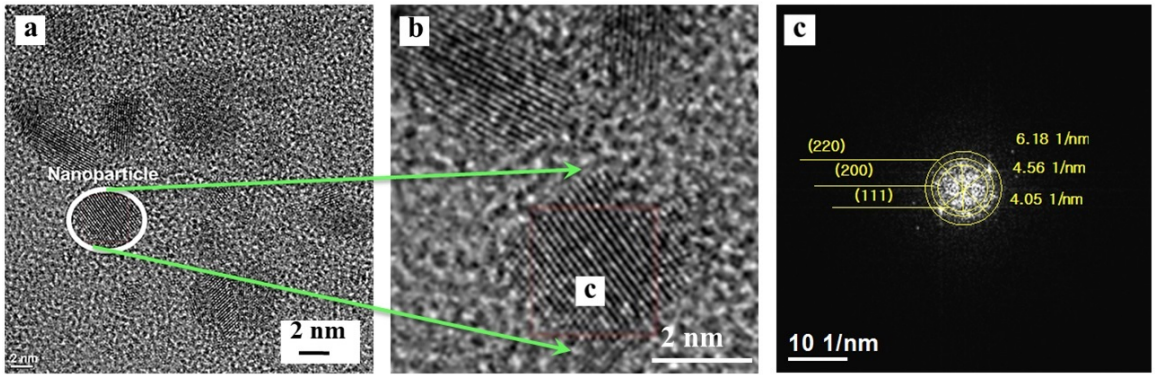

FIG. 4. SAED analysis of FeCoNiPt nanoparticles.(a, b) HRTEM images showing nanoparticle morphology; (c) SAED pattern showing FCC diffraction rings.

3.4. Interpretation of lattice spacing deviations

Minor deviations observed between the experimental and theoretical lattice spacings are expected for multicomponent alloys such as FeCoNiPt. These variations can be attributed to several factors, including atomic-size mismatch between Pt and 3d transition metals; local lattice distortions inherent to multicomponent or high-entropy alloy systems; compositional complexity, including slight differences in the local coordination environment; surface relaxation effects in ultrasmall nanoparticles.

The slightly larger lattice spacing which was observed for the (111) plane (0.247 nm) is consistent with the reported values for other FCC multi-element alloys. In previously reported studies similar d-spacings have been also identified in the range 2.38–2.42 Å for FeNiMnCrCu and 2.35 Å for FeCoNiCrAl. These results demonstrate the stability of FCC structure across a wide compositional range. The agreement between the values obtained in this study and the literature data confirms that the synthesized FeCoNiPt nanoparticles possess a structurally favorable configuration for electrocatalytic activity, which may contribute to their performance in HER and OER.

4. Conclusion

In this work, ultrasmall FeCoNiPt alloy NPs with controlled platinum contents were successfully synthesized using a medium-assisted solid-state reaction. Comprehensive structural and compositional analyses using TEM, HRTEM, FFT, SAED, STEM-EDS, and EDX demonstrate that the obtained NPs form a single-phase, compositionally homogeneous FCC solid solution. The particles exhibit a uniform spherical morphology with a narrow size distribution of $\sim$5 nm, coherent lattice fringes, and an absence of segregation or secondary phases. STEM-EDS mapping confirms the homogeneous incorporation of Fe, Co, Ni, and Pt throughout the nanoparticle volume, verifying the formation of a true multicomponent alloy.

FFT and SAED analyses reveal well-defined FCC diffraction signatures with measured interplanar distances closely matching theoretical predictions. Minor deviations in lattice spacing are attributed to atomic-size mismatch and local lattice distortions typical of multicomponent alloy systems. These features collectively indicate that the alloying process proceeds efficiently, producing structurally stable and electronically interactive FeCoNiPt nanoparticles.

The structural characteristics identified ultrasmall particle size, homogeneous alloying, coherent crystallinity, and lattice strain effects. The listed properties have a direct and beneficial influence on catalytic properties, particularly for electrocatalytic reactions such as the hydrogen evolution reaction (HER) and the oxygen evolution reaction (OER). The observed lattice expansion and uniform multimetal mixing suggest favorable modulation of the electronic structure, including potential tuning of the d-band center, which is a key factor which governs the adsorption energetics on Pt-based alloy surfaces.

Although the present manuscript focuses primarily on synthesis and structural characterization, the demonstrated physico-chemical features strongly suggest that FeCoNiPt alloy NPs are promising candidates for advanced electrocatalytic applications. A detailed investigation of the electrocatalytic performance of FeCoNiPt nanoparticles, particularly towards HER and OER, will be the subject of our next study. The insights obtained here provide a solid foundation for understanding the structure–property relationships that will guide the design of efficient Pt-economized electrocatalysts.

References

[1] Tran D.T., Tran P.K.L., Malhotra D., Nguyen T.H., Duong N.T.A., Kim N.M., Le J.H. Current status of developed electrocatalysts for water splitting technologies: from experimental to industrial perspective. *Nano Convergence*, 2025, **12**, P. 9.

[2] Tahir M., Pan L., Idrees F., Zhang X., Wang L., Zou J.J., Wang Z.L. Electrocatalytic oxygen evolution reaction for energy conversion and storage: A comprehensive review. *Nano Energy*, 2017, **37**, P. 136–157.

[3] Zaman S., Huang L., Douka A.I., Yang H., You B., Xia B.Y. Oxygen reduction electrocatalysts toward practical fuel cells: progress and perspectives. *Angew. Chem. Int. Ed.*, 2021, **60**, P. 17832–17852.
[4] Xiao B., Liu J., Fang J., Zeng J., Liu K., Feng S., Chen J., Lu X.F. Electrospun noble metal-based nanofibers for water electrolysis. *Mater. Chem. Front.*, 2025, **9**, P. 3125–3138.
[5] Wang H., Chen Z.N., Wu D., Cao M., Sun F., Zhang H., You H., Zhuang W., Cao R. Significantly enhanced overall water splitting performance by partial oxidation of Ir through Au modification in core–shell alloy structure. *J. Am. Chem. Soc.*, 2021, **143**, P. 4639–4645.
[6] Reier T., Pawolek Z., Cherevko S., Bruns M., Jones T., Teschner D., Selve S., Bergmann A., Nong H.N., Schlögl R. Molecular insight in structure and activity of highly efficient, Low-Ir Ir–Ni oxide catalysts for electrochemical water splitting (OER). *Am. Chem. Soc.*, 2015, **137**, P. 13031–13040.
[7] Chen H., Guan C., Feng H. Pt-based high-entropy alloy nanoparticles as bifunctional electrocatalysts for hydrogen and oxygen evolution. *ACS Appl. Nano Mater.*, 2022, **5**, P. 9810–9817.
[8] Feng G., Ning F., Song J., Shang H., Zhang K., Ding Z., Gao P., Chu W., Xia D., Sub-2 nm ultrasmall high-entropy alloy nanoparticles for extremely superior electrocatalytic hydrogen evolution. *J. Am. Chem. Soc.*, 2021, **143**, P. 17117–17127.
[9] Guo C., Jiao Y., Zheng Y.. Luo J., Davey K., Qiao S.-Z. Intermediate modulation on noble metal hybridized to 2D metal-organic framework for accelerated water electrocatalysis. *Chem.*, 2019, **5**, P. 2429–2441.
[10] Jin Z., Lv J., Jia H., Liu W., Li H., Chen Z., Lin X., Xie G., Liu X., Sun S. Nanoporous Al–Ni–Co–Ir–Mo high-entropy alloy for record-high water splitting activity in acidic environments. *Small*, 2019, **15**, P. 1904180.
[11] Chuluunbat E., Nguyen A.N., Omelianovych O., Szaniel A., Larina L.L., Choi H.S. Highly electrocatalytic activity of NixFey nanoporous for oxygen evolution reaction in water splitting. *Int. J. Hydrog. Energy*, 2024, **71**, P. 102–109.
[12] Lee G., Nguyen N.A., Nguyen V.T, Larina L.L., Chuluunbat E., Park E., Kim J., Choi, H.S. Keidar M. High entropy alloy electrocatalyst synthesized using plasma ionic liquid reduction. *J. Solid State Chem.*, 2022, **314**, P. 123388.
[13] Nguyen V.T., Lee G.J., Ngo Q.T., Omelianovych O., Nguyen N.A., Trinh V.H., Choi H.S., Mnoyan A., Lee K., Larina L.L., Chen G. Robust carbonencapsulated Ni nanoparticles as high-performance electrocatalysts for the hydrogen evolution reaction in highly acidic media. *Electrochimica Acta*, 2021, **398**, P. 139332.
[14] Ngo Q.T., Omelianovych O., Nguyen V.T., Ahn B.T., Lee K.B., Lee G.J., Larina L.L., Choi H.S. An Economically sustainable NiC catalyst in a solar-to-hydrogen device employing a CIGS submodule. *J. Mater. Chem. A*, 2021, **9**, P. 23828–23840.
[15] Meng C., Wang X., Li Z.,Wu C., Chang L., Liu R., Pei W. Synthesis of FeCoNiCuPt high-entropy alloy nanoparticle electrocatalysts with various Pt contents by a solid-state reaction method. *Materials Advances*, 2024, **5**, P. 719–729.
[16] Chen H., Guan C., Feng H., Pt-based high-entropy alloy nanoparticles as bifunctional electrocatalysts for hydrogen and oxygen evolution. *ACS Appl. Nano Mater.*, 2022, **5**, P. 9810–9817.

Submitted 19 November 2025; revised 29 November 2025; accepted 4 December 2025

Information about the authors:

Olga V. Alexeeva – N. M. Emanuel Institute of Biochemical Physics RAS, Solar Photovoltaic Laboratory, Moscow, Russia; ORCID 0000-0001-8982-3959; alexol@yandex.ru

Olga K. Karyagina – N. M. Emanuel Institute of Biochemical Physics RAS, Solar Photovoltaic Laboratory, Moscow, Russia; ORCID 0000-0002-6702-5195; olgakar07@mail.ru

Sergei S. Kozlov – N. M. Emanuel Institute of Biochemical Physics RAS, Solar Photovoltaic Laboratory, Moscow, Russia; ORCID 0000-0002-8660-5646; sergeykozlov1@gmail.com

Leontiy I. Kuznetsov – N. M. Emanuel Institute of Biochemical Physics RAS, Solar Photovoltaic Laboratory, Moscow, Russia; shevale2006@yahoo.com

Liudmila L. Larina – N. M. Emanuel Institute of Biochemical Physics RAS, Solar Photovoltaic Laboratory, Moscow, Russia; ORCID 0009-0001-5847-6904; llarina3333@gmail.com

Anna B. Nikolskaya – N. M. Emanuel Institute of Biochemical Physics RAS, Solar Photovoltaic Laboratory, Moscow, Russia; ORCID 0000-0002-7430-4133; anickolskaya@mail.ru

Oleg I. Shevaleevskiy – N. M. Emanuel Institute of Biochemical Physics RAS, Solar Photovoltaic Laboratory, Moscow, Russia; ORCID 0000-0002-8593-3023; shevale2006@yahoo.com

Conflict of interest: the authors declare no conflict of interest.

Paper abstracts in Russian / Аннотации статей

Обратный анализ нагруженного уравнения теплопроводности

Умида Балтаева, Правин Агарвал, Бобур Хасанов, Хамробек Хаитбаев, Флоренс Юбер

В данной работе исследуется обратная задача для уравнения теплопроводности, содержащего дробные нагруженные члены и коэффициенты, зависящие от пространственных переменных. Путём сведения исходной задачи к эквивалентной системе нагруженных интегро-дифференциальных уравнений получены достаточные условия существования и единственности решения. Предлагаемый подход основан на принципе сжимающего отображения и использовании дробных интегралов Римана–Лиувилля. Разработанный математический аппарат может быть применён для описания диффузионных процессов в средах с пространственной неоднородностью и эффектами памяти.

Ключевые слова: уравнение теплопроводности, обратная задача, дробное исчисление, идентификация ядра, метод сжимающего отображения

О существовании максимального числа изолированных собственных значений для решёточного оператора Шрёдингера

Лакаев С.Н., Латипова Д.А., Ахмадова М.О. кизи

В данной работе представлен подробный спектральный анализ дискретного оператора Шрёдингера $H_{\gamma\lambda\mu}(K)$, который описывает систему двух одинаковых бозонов на двумерной решётке $\mathbb{Z}^2$. Семейство операторов параметризовано квазиимпульсом $K \in \mathbb{T}^2$ и вещественными константами взаимодействия: γ (для взаимодействия на узле), λ (для взаимодействия с ближайшими соседями) и μ (для взаимодействия со следующими ближайшими соседями). Ключевым результатом нашего исследования является то, что при определённых условиях на параметры взаимодействия (γ, λ, μ) оператор $H_{\gamma\lambda\mu}(K)$ для всех $K \in \mathbb{T}^2$ **всегда имеет ровно семь собственных значений**, лежащих либо ниже нижней границы, либо выше верхней границы его существенного спектра.

Ключевые слова: система двух частиц, дискретный оператор Шрёдингера, существенный спектр, связанные состояния, детерминант Фредгольма.

Математическое моделирование промышленного синтеза аммиака с использованием нелинейных уравнений реакции-диффузии

Жамшид Хасанов, Сохибжан Муминов, Сарвар Искандаров

В данном исследовании предлагается математическая модель синтеза аммиака, основанная на нелинейных уравнениях реакции-диффузии. Модель объединяет вырожденную диффузию газа в реакторе с кинетикой реакции Габера-Боша для исследования эффективности и экологической устойчивости. Проведен теоретический анализ для установления существования и устойчивости глобальных решений для базовой вырожденной параболической системы. Численное моделирование было проверено на основе промышленных данных завода «Навоиазот» в Узбекистане, продемонстрировав 98,2% точность определения профилей концентрации и превосходя модели с постоянной диффузией на 12–15% в областях с низкой концентрацией.

Ключевые слова: нелинейная реакция-диффузия, вырожденная диффузия, синтез аммиака, кинетика Габера-Боша, глобальная устойчивость.

Наноструктурирование тонких титановых пленок на основе субволновых ЛИППС

А.С. Храмов, М.Д. Васильев, Д.А. Синев, Е.А. Шахно

Прецизионное наноструктурирование тонких пленок является важной задачей в производстве современных элементов оптоэлектроники и фотоники. Прямая запись лазерно-индуцированных периодических поверхностных структур (ЛИППС) является перспективным инструментом для прямого субволнового наноструктурирования. Недавние исследования показывают, что динамика формирования ЛИППС существенно изменяется, если пленка является оптически тонкой. В этой работе представлена комплексная аналитическая модель, призванная сократить разрыв между ожидаемой динамикой электромагнитных полей во время формирования ЛИППС и экспериментально получаемыми результатами наноструктурирования. Феноменологическая модель распространения поверхностной электромагнитной волны (ПЭВ) на границе раздела пленка–подложка иллюстрирует механизм формирования ЛИППС с использованием периодического распределения концентрации энергии ПЭВ. Рассчитаны характеристики ПЭВ в зависимости от толщины металлической пленки, а также показана положительная обратная связь между локальной толщиной растущего оксидного слоя и концентрацией энергии ПЭВ. Изменения в механизмах формирования ЛИППС подтверждены экспериментально на пленках титана различной толщины. Эти результаты проясняют внутренние физические механизмы формирования ЛИППС на тонких металлических пленках и расширяют возможности применения ЛИППС для наноструктурирования.

Ключевые слова: лазерно-индуцированные периодические поверхностные структуры, ЛИППС, наноструктурирование, тонкие пленки, прямая лазерная запись

Дефектный монослой нитрида алюминия в качестве электродного материала для суперконденсаторов: исследование методом DFT

Шамсуддин Ахмад, Мд. Махфузул Хаке, Захир Аббас, Мд. Шахзад Хан

В данной работе анализируются квантовые емкостные свойства нанолистов нитрида алюминия (AlNNS) с дефектами, с акцентом на их потенциальное использование в суперконденсаторах. Мы подтвердили структурную стабильность примитивной ячейки с помощью расчетов энергии когезии и анализа фононного спектра. Наши результаты показывают, что монослои, содержащие алюминий (Al), азот (N) или имеющие дефицит Al-N, демонстрируют полупроводниковое состояние p-типа/n-типа или с широкой запрещенной зоной. Расчеты энергии образования дефектов показывают, что AlNNS с дефицитом N является наименее предпочтительным вариантом. Присутствие недокоординированных атомов вблизи дефекта приводит к появлению нового примесного состояния в запрещенной энергетической зоне. Это побудило нас к детальному исследованию их квантовой емкости, на которую сильно влияет плотность состояний вблизи энергии Ферми. Наше исследование показывает, что Al-дефицитные AlNNS достигают максимальной квантовой емкости (CQMax) 690 мкФ/см² в области положительного смещения, что делает их подходящим кандидатом на роль анодного материала в суперконденсаторах. Для сравнения, азот-дефицитные AlNNS достигают CQMax 313 мкФ/см² и максимальной емкости поверхностного заряда (QMax) -91 мкКл/см², что подчеркивает их потенциал в качестве катодного материала. Al-N-дефицитные AlNNS демонстрируют промежуточное поведение с выраженными пиками квантовой емкости в обеих областях смещения, что обеспечивает дополнительную гибкость для потенциальных применений.

Ключевые слова: Теория функционала плотности, зонная структура, нанолисты нитрида алюминия, квантовая емкость, поверхностный заряд.

Влияние наномасштабного конфайнмента водной среды на кривую подвода в сканирующей микроскопии ионной проводимости

Лукашенко С.Ю., Горбенко О.М., Фельштын М.Л., Сапожников И.Д., Пичахчи С.В., Жуков М.В., Голубок А.О.

Исследованы особенности на зависимости ионного тока от расстояния при сближении стеклянной нанопипетки с диаметром апертуры ~100 нм к поверхности твердого диэлектрика в сканирующем микроскопе ионной проводимости. При положительном смещении потенциала электрода, расположенного в нанопипетке, относительно электрода, расположенного в чашке происходит монотонное снижение тока, однако при отрицательном смещении на кривой подвода наблюдается характерный пик. Для объяснения этого необычного поведения предложена модель, учитывающая перекрытие электрических двойных слоев и явление конфайнмента водной среды в наноканалах и нанозазорах. Модель демонстрирует хорошее согласие с экспериментальными данными и обеспечивает основу для количественной оценки поверхностного заряда на границе раздела электролит–твердое тело с наномасштабной пространственной чувствительностью.

Ключевые слова: Наномасштабный конфайнмент воды, нанопора, пик-эффект, уравнения Пуассона–Нернста–Планка, поверхностная плотность заряда.

Метод гетеродинного детектирования многомодовых состояний для квантового распределения ключа на непрерывных переменных с использованием боковых частот

Филипов И.М., Гончаров Р.К., Дашков М.В., Богданова Е.И.,
Зиновьев А.В., Чистяков В.В., Киселев Ф.Д.

Представлен новый метод когерентного детектирования квантовых состояний на боковых частотах (БЧ), применяемый в квантовом распределении ключа на непрерывных переменных (КРК-НП). Предлагаемый подход основан на повторной фазовой модуляции на стороне приемника и пространственном разделении частотных компонент несущей и боковых частот. Выходным сигналом является промежуточная частота, определяемая разностью между частотами модуляции отправителя и получателя. Разработана аналитическая модель выходного сигнала детектора с использованием зависящей от времени модуляции на основе классического метода с функциями Бесселя, и проведен сравнительный анализ с альтернативными методами гетеродинного детектирования. Экспериментальная проверка подтверждает линейную зависимость выходного сигнала от частоты модуляции приемника и индекса модуляции отправителя в режиме малого индекса модуляции. Кроме того, продемонстрирована осуществимость предложенного метода путем детектирования дискретно модулированных сигналов с использованием квадратурной фазовой манипуляции (QPSK).

Ключевые слова: когерентное детектирование, боковые частоты, непрерывные переменные, квантовое распределение ключа.

Многоуровневая физически неклонируемая функция, основанная на наноструктурах из серебра, случайным образом интегрированных в кристаллическую кремниевую пластину

Федорова М.В., Петрова Е.А., Ларин А.О., Сандомирский М.П., Ермина А.А., Павлов С.И., Жарова Ю.А., Пермяков Д.В., Ярошенко В.В., Зуев Д.А.

В этой статье представлена оптическая физически неклонируемая функция (ФНФ), основанная на серебряных (Ag) наноструктурах, случайным образом сформированных на кристаллической кремниевой (Si) пластине путем гальванического смещения и термического отжига. В результате этого процесса образуются наноструктуры со стохастическим пространственным распределением и морфологией, что приводит к непредсказуемым нелинейным оптическим характеристикам. Гибридный интерфейс Ag–Si создает два независимых сигнала: фотолюминесценцию (ФЛ) и генерацию второй гармоники (ГВГ). Пространственные карты ФЛ и ГВГ были бинаризованы и проанализированы с использованием стандартных показателей ФНФ. ГВГ продемонстрировала более высокую энтропию и более сбалансированное распределение битов, что делает ее предпочтительным каналом кодирования, в то время как ФЛ обеспечивает дополнительный уровень верификации. Метод изготовления является масштабируемым, не требует литографии и совместим со стандартными методами изготовления.

Ключевые слова: серебряные наноструктуры; кремний; ГВГ; фотолюминесценция; физическая неклонируемая функция.

УФ-модуляция редокс-свойств нанодисперсного диоксида церия и его конъюгатов с ферментами

Созарукова М.М., Филиппова А.Д., Ратова Д.-М., Михеев И.В., Проскурнина Е.В., Баранчиков А.Е., Иванов В.К.

В настоящей работе исследовано влияние УФ-облучения на редокс-свойства нанодисперсного диоксида церия и его конъюгатов с ферментами – супероксиддисмутазой (СОД) и пероксидазой из корней хрена. По данным хемилюминесцентного анализа, наночастицы CeO_2 обладают СОД-подобной активностью, при этом радикал-перехватывающие свойства конъюгатов CeO_2 с ферментом СОД значительно усиливаются за счет синергетического эффекта. Установлено, что воздействие УФ-облучения снижает СОД-подобную активность наночастиц CeO_2 и их конъюгатов с СОД. В составе конъюгатов нанодисперсный диоксид церия повышает устойчивость СОД к окислительной деструкции, вызванной УФ-облучением, что свидетельствует о фотопротекторных свойствах наночастиц CeO_2. Конъюгаты нанодисперсного CeO_2 с пероксидазой из корней хрена проявляют значительно меньшую прооксидатную активность, но большую фотостабильность по сравнению с индивидуальным ферментом. Влияние УФ-облучения на прооксидантные свойства конъюгатов CeO_2 с пероксидазой из корней хрена носило разнонаправленный характер и зависело от времени взаимодействия диоксида церия с белком. Результаты подтверждают, что конъюгаты наночастиц CeO_2 с ферментами обладают активностью, модулируемой в том числе УФ-излучением, что следует учитывать при разработке современных космецевтических препаратов.

Ключевые слова: нанодисперсный диоксид церия, супероксиддисмутаза, пероксидаза, УФ-облучение, фермент, конъюгат, редокс-регуляция, фотозащита

Термодинамический анализ формирования нанокристаллов в системе TiO_2-H_2O (NaOH, HCl)

Еловиков Д.П., Альмяшева О.В., Гусаров В.В.

В работе проведен термодинамический анализ кристаллизации диоксида титана в модификациях анатаза, брукита и рутила из водно-солевых растворов с учетом влияния pH среды, температуры, концентрации реагентов и удельной поверхностной энергии фаз (σ). Показано, что выбор величины σ для термодинамического анализа кристаллизации анатаза

является определяющим: при σ_A = 0.3 Дж/м² минимальный размер частиц определяется кристаллохимическим критерием (l_{min}~5–7 нм), а при σ_A = 1.3 Дж/м² -термодинамическими критериями (d_{crit} ~ 8 нм, d_{eq} ~ 12 нм). С использованием значений σ, наиболее приближенных к условиям гидратированной поверхности TiO_2 (σ_R = 1.79, σ_B = 1.0, σ_A = 1.13 Дж/м²) определены области возможной кристаллизации каждой модификации. Рутил может кристаллизоваться в относительно широком диапазоне величин pH 0.8-14 (25 °C) и 1.1-10.2 (200 °C), а минимальные размеры частиц рутила в этих условиях определяются термодинамическими критериями – d_{crit} и d_{eq}. Для брукита и анатаза в кислых и щелочных условиях (pH ~1–3 и 9–14) минимальные размеры также, как и для рутила определяются термодинамическими критериями, тогда как в нейтральной области – кристаллохимическим критерием l_{min}. На основе анализа структурных переходов установлено, что анатаз может трансформироваться в рутил или брукит при размерах частиц более ~16 нм. Рассчитанный размер перехода брукит → рутил составляет ~712 нм.

Ключевые слова: нанокристаллы, оксид титана, критический зародыш.

Особенности формирования покрытий фосфата Ce(IV) на поверхности кремнезема при их синтезе методом ионного наслаивания

Чувило Ю., Кукло Л., Толстой В.

В статье представлены условия получения покрытий фосфата Ce(IV) на поверхности кремния и кварца методом ионного наслаивания (ИН). Показано, что при использовании в качестве реагентов растворов $(NH_4)_4Ce(SO_4)_4$ и NaH_2PO_4 на поверхности подложек формируются покрытия состава $Ce(OH)PO_4 \cdot nH_2O$, а при использовании растворов $(NH_4)_4Ce(SO_4)_4$ и Na_3PO_4 – покрытия состава $Na_{0,2}Ce(OH)_{2,4}(PO_4)_{0,6} \cdot nH_2O$. Эти соединения имеют аморфную структуру. Анализ методом СЭМ $Na_{0,2}Ce(OH)_{2,4}(PO_4)_{0,6} \cdot nH_2O$ на поверхности кремния показал, что для образцов, полученных в результате 15 циклов ИН, планарные изотропные покрытия частично сворачиваются в микротрубки с морфологией микросвитков диаметром 3–5 мкм и длиной 30–100 мкм. Состав указанных фосфатов Ce(IV) может быть сравнительно легко допирован в процессе синтеза, например, катионами Fe(II) и вольфрамат-анионами. Установлено, что покрытия $Ce(OH)PO_4 \cdot nH_2O$ характеризуются интенсивной полосой поглощения в УФ-области спектра и могут быть использованы в качестве компонентов различных защитных средств. При этом степень поглощения УФ-излучения в таком покрытии можно контролировать, варьируя условия синтеза, например, количество циклов ИН.

Ключевые слова: фосфаты Ce(IV), покрытия, ионное наслаивание, защита от ультрафиолета, микросвитки.

Влияние окислительно-восстановительного соотношения на структурные и магнитные свойства наноферритов $Zn_{x0.5}Mn_{0.5}Fe_2O_4$ синтезированные методом глицин-нитратного растворного горения

Кирьянов Н.В., Мартинсон К.Д.

Наноструктурированные ферриты $Zn_{0.5}Mn_{0.5}Fe_2O_4$ были синтезированы методом глицин-нитратного растворного горения при соотношении топлива к окислителю *f* в диапазоне от 0,4 до 1,6, для определения влияния окислительно-восстановительного соотношения на структуру и магнитные свойства. Рентгеновская дифракция подтверждает образование однофазной кубической шпинели для всех составов, при этом размер кристаллитов изменяется от ~8 до 108 нм, а минимальные значения как размера кристаллитов, так и

параметра решетки (8,420 Å) получены в условиях дефицита топлива (f = 0,4); микродеформации решетки не превышают 0,5%. Метод СЭМ показал наличие агломератов размером 3–5 мкм, состоящие из частиц размером 30–190 нм, в то время как химический анализ методом ЭДС показал соотношения катионов близкие к теоретическому составу. Магнитные измерения при температуре 300 К демонстрируют типичное магнитомягкое поведение: намагниченность насыщения варьируется от 16,1 до 68,3 эме/г, остаточная намагниченность – от 1,8 до 20,3 эме/г, а коэрцитивная сила – от 34,7 до 85,6 Э. Все эти параметры эффективно регулируются содержанием топлива. Наибольшая намагниченность насыщения достигается вблизи стехиометрического соотношения (f ≈ 0,8–1,0), тогда как избыток топлива приводит к увеличению коэрцитивной силы за счет измельчения микроструктуры и деформации решетки. Установленные корреляции между условиями горения, структурными параметрами и изменениями магнитных свойств показывают, что контролируемое изменение соотношения топлива является эффективным инструментом для адаптации нанопорошков цинк-марганцевого феррита для применения в качестве магнитомягких материалов с низкими потерями.

Ключевые слова: цинк-марганцевый феррит, растворное горение, окислительно-восстановительное соотношение, кристаллическая структура, микроструктура, магнитные свойства, магнитомягкие материалы

Исследование физико-механических свойств и радиационной стойкости магний-индиевого феррита, синтезированного полимер-нитратным способом

Кондратьева О.Н., Смирнова М.Н., Никифорова[1] Г.Е., Япрынцев А.Д., Драник М.С., Кецко В.А.

В статье обсуждаются особенности полимер-нитратного синтеза высокодисперсных частиц магний-индиевого феррита ($MgFeInO_4$), и приводятся результаты экспериментального исследования физико-механических свойств керамики, изготовленной на их основе. По данным порошковой рентгеновской дифракции установлено, что однофазный порошок феррит-шпинели может быть получен только путем высокотемпературной обработки рентгеноаморфного прекурсора, образовавшегося в результате термического разложения смеси поливинилового спирта и нитратов металлов. Керамика, изготовленная с использованием субмикронных частиц $MgFeInO_4$, имеет плотность, близкую к теоретической. Из результатов измерения микротвердости по методу Виккерса установлено, что полученный материал обладает высокой твердостью. По данным спектроскопии диффузного отражения определено значение энергии ширины запрещенной зоны $MgFeInO_4$. С использованием кристаллографических и электрофизических характеристик синтезированного материала спрогнозирована его устойчивость к радиационно-индуцированным структурным изменениям.

Ключевые слова: смешанные ферриты; кубическая кристаллическая решетка; тонкодисперсный порошок; керамика; микротвердость по Виккерсу; энергия ширины запрещенной зоны; радиационная стойкость

Образование Li-Fe-содержащего слоистого силиката типа 2:1 с монтмориллонитоподобной структурой в гидротермальных условиях

Ияхмаева А.А., Храпова Е.К., Лебедев Л. А., Глебова Н. В., Семенов В. Г., Копылов А. В., Красилин А. А.

Проведены гидротермальный синтез и физико-химическая характеризация Li-Fe-содержащего гидросиликата со структурой монтмориллонита (ММТ). На сегодняшний день этот слоистый силикат типа 2:1 привлекает внимание такими свойствами, как высокая ионная подвижность, гидрофильность, электрическое сопротивление и термостойкость. Благодаря этому различные по составу ММТ могут служить перспективными компонентами литий-ионных аккумуляторов. Процесс образования и структурные особенности Li-Fe-содержащего гидросиликата со структурой монтмориллонита исследовались с помощью рентгеновской дифракции, УФ-видимой и мёссбауэровской спектроскопии, а также другими методами. С помощью комплекса методов удалось установить критическое содержание Fe^{3+} и температурный диапазон, необходимые для образования практически однофазных ММТ. Около 20% от общего содержания Fe может занимать тетраэдрическую позицию слоя ММТ. Термическое поведение Li-Fe-ММТ сильно зависит от условий гидротермального синтеза из-за различного количества Li^{+}, присутствующего в межслоевом пространстве, а также в вакансиях октаэдрического подслоя.

Ключевые слова: слоистые силикаты, гидротермальный синтез, изоморфизм, рентгеновская дифракция, мёссбауэровская спектроскопия

Синтез, структура и свойства композитных протонпроводящих мембран на основе перфторированного сополимера типа Нафион с наночастицами $Zr_{1-x}Y_xO_{2-0.5x}$

Бугров А.Н.,, Губанова Г.Н., Примаченко О.Н., Гофман И.В., Иванкова Е.М., Попова Е.Н., Кириленко Д.А., Лаврентьев В.К., Власова Е.Н., Кононова С.В.

Наночастицы $Zr_{1-x}Y_xO_{2-0.5x}$ были введены в сульфокислотную форму перфторированного сополимера Нафион типа перед формированием мембраны для улучшения ее водоудерживающей способности, термической стабильности и протонной проводимости. Поскольку условия формирования наночастиц могут существенно влиять на их размер, фазовый состав, морфологию и химию поверхности, в работе были рассмотрены разные подходы по синтезу наполнителя. Было установлено, что среди мокрохимических методов, которые применялись для получения наночастиц на основе диоксида циркония, наиболее перспективным с точки зрения повышения поверхностной протонной проводимости композитных мембран является сольвотермальный синтез. Данный метод обеспечивает малый размер, большую удельную площадь поверхности и высокую степень гидрофильности наночастиц, вследствие чего их введение в перфторированный сополимер Нафион типа повышает влагоудержание мембраны и способствует улучшению ее протонпроводящих свойств. В случае наночастиц $Zr_{1-x}Y_xO_{2-0.5x}$ сформированных в условиях растворного горения, их более гидрофобная поверхность не способствовала повышению содержания влаги в перфторированном сополимере, но позволила повысить его максимально возможную рабочую температуру на 20°C.

Ключевые слова: протонная проводимость, импедансная спектроскопия, стабилизированный иттрием диоксид циркония, глицин-нитратное горение, золь-гель, гидротермальный синтез, сольвотермальный метод

Синтез фотокатализаторов $M/TiO_2/C$ (M=Ni, Cu, Ni-Cu) для восстановления CO_2 с помощью микроволнового излучения: структурная эволюция и фотокаталитические свойства

Кашанский В.С., Сухов А.В., Журенок А.В., Мищенко Д.Д., Софьичева О.С., Козлова Е.А, Синяшин О.Г., Яхваров Д.Г.

Методом микроволнового синтеза получены композиты на основе TiO_2, модифицированные наночастицами переходных металлов (Ni, Cu). Структура полученных материалов охарактеризована с помощью рентгеновской порошковой дифракции, а размер кристаллитов оценен по уравнению Шеррера. Фотокаталитическая активность синтезированных композитов исследована в реакции восстановления CO_2 до CO и CH_4 при облучении светом с длиной волны 400 нм. Показано, что микроволновая обработка смеси TiO_2 с графитом (C_g) и солями переходных металлов приводит к снижению фотокаталитической активности. В то же время механическая смесь TiO_2 и графита, не подвергавшаяся микроволновому воздействию, проявляет более высокую активность по сравнению с немодифицированным TiO_2 Evonik P25. Снижение активности у обработанных образцов обусловлено необратимым фазовым переходом фотоактивной фазы анатаза в каталитически инертную фазу рутила, а также образованием фаз TiO_{2-x}. Причиной является перегрев в ходе синтеза, при котором C_g выступает в роли эффективного поглотителя микроволнового излучения и восстановителя катионов Ti^{4+} в структуре TiO_2. Полученные результаты важны для разработки эффективных фотокатализаторов на основе TiO_2 для восстановления CO_2.

Ключевые слова: диоксид титана, фотокатализ, наночастицы переходных металлов, восстановление диоксида углерода, рентгеновская дифракция, зелёная химия

Взаимосвязь между составом пропиточного раствора и распределением активных компонентов катализаторов NiMo/ZSM-23 для гидрообработки растительных липидов

Ковалевская К.С., Кукушкин Р.Г., Заикина О.О., Булавченко О.А., Яковлев В.А.

Характер взаимодействия между металлами и носителем катализатора является решающим фактором, определяющим дисперсное состояние фаз активных компонентов. В этом исследовании была получена серия катализаторов NiMo/ZSM-23 путем пропитки по влагоёмкости для гидрообработки растительных липидов. Катализаторы были получены с использованием различной последовательности нанесения металлов и с использованием различных комплексообразователей. Катализаторы были исследованы несколькими физико-химическими методами (ТПВ, УФ-Вид спектроскопия, РФА, ТПД-NH_3, Рамановская спектроскопия, ПЭМ ВР). Было обнаружено, что заряд поверхности цеолита ZSM-23 (положительный/отрицательный) и тип ионов металлов в растворе для пропитки влияют на образование фаз на поверхности носителя. Использование аммиачных пропитывающих растворов приводит к образованию фаз NiO, α-$NiMoO_4$ и β-$NiMoO_4$.В случае использования водных и цитратных пропитывающих растворов наблюдается только образование фаз NiO и β-$NiMoO_4$.

Ключевые слова: никель, молибден, ZSM-23, пропиточные растворы, ТНЗ.

Электрокатализаторы на основе MXene для эффективного расщепления воды

Джавлонбек Маманазиров, Шавкат Маматкулов, Махфуза Джумаева, Хакимжан Бутанов, Вэнь Хэ, Цзинсян Лоу, Одилхуджа Парпиев, Олим Рузимурадов

В этом исследовании мы модифицировали электроды на основе Ni с помощью MXene и композитных катализаторов на основе MXene для расщепления воды. Катализатор на основе MXene продемонстрировал превосходную электрохимическую площадь поверхности (ECSA) 1840 см², что подчеркивает его обилие активных центров. Для дальнейшего повышения каталитической активности MXene был модифицирован оксидом графена (GO) и сажей (CB), что значительно снизило перенапряжение с 300 мВ до 196 мВ при 10 мА $см^{-2}$ и улучшило

кинетику реакции, о чем свидетельствует низкий наклон Тафеля 96,35 мВ dec^{-1}. Более того, композит MXene–GO–CB продемонстрировал выдающуюся долговременную долговечность, сохраняя стабильную работу в течение 50 ч при 100 мА $см^{-2}$ с увеличением перенапряжения всего на 34 мВ при 10 мА $см^{-2}$. Эти результаты подтверждают, что синергетическое сочетание MXene с GO и CB дает высокоактивный и долговечный электрокатализатор, обладающий большим потенциалом для практического применения в электролизе воды.

Ключевые слова: композиты на основе MXene, HER, OER, электрокатализаторы.

Формирование наночастиц NH4MgF3 и MgF2 из гидроксикарбоната магния в расплаве гидрофторида аммония

Лугинина А.А., Александров А.А., Ясыркина Д.С., Ермакова Ю.А.,
Таперо В.В., Кузнецов С.В.

Фторметаллаты аммония со структурой перовскита NH_4MF_3 (M = 3d металлы) используются в качестве катодных материалов, а NH_4MgF_3 — в качестве твердых электролитов. В литературе имеется лишь фрагментарная информация о получении порошка NH_4MgF_3 и отсутствуют данные рентгеновской дифракции. Предложены условия, позволяющие синтезировать однофазный порошок NH_4MgF_3 путем взаимодействия гидроксикарбоната магния с расплавом гидрофторида аммония при температуре 220 C. Было установлено, что процесс является двухэтапным: первая реакция представляет собой образование соединения $(NH_4)_2MgF_4$, а вторая реакция представляет собой разложение $(NH_4)_2MgF_4$ при температуре 220 °C до NH_4MgF_3. При разложении NH_4MgF_3 образуются безводные наночастицы MgF_2 (28 ± 7 нм). Предлагаемый способ получения однофазного NH_4MgF_3 открывает возможности для изучения его функциональных свойств.

Ключевые слова: фторометаллат аммония, структура кубического перовскита, фторид магния, наноразмерные порошки, NH4MgF3, гидрофторид аммония.

Формирование лазерно-индуцированных периодических поверхностных структур на пленке $As_{50}Se_{50}$ при фемтосекундном лазерном облучении с длинами волн 400-800 нм

Пахольчук П.П., Шулейко Д.В., Барбашов В.А., Заботнов С.В., Козюхин С.А., Кашкаров П.К.

Лазерно-индуцированные периодические поверхностные структуры (ЛИППС) на халькогенидных стеклообразных полупроводниках представляют большой интерес для создания поляризационно-чувствительных оптических элементов. В данной работе исследуется формирование ЛИППС на поверхности аморфной пленки $As_{50}Se_{50}$, изготовленной методом термического вакуумного осаждения, при фемтосекундном лазерном облучении в диапазоне длин волн от 400 до 800 нм. Периоды различных типов ЛИППС линейно зависят от длины волны лазера. Измеренное двойное лучепреломление так называемых низкочастотных пространственных ЛИППС, формируемых различными длинами волн излучения, находится в диапазоне 10-85 нм. Максимальное двулучепреломление, равное 85 нм, было получено для структур, облученных при длине волны 480 нм. Значительное снижение двулучепреломления наблюдалось на длине волны 800 нм, что может быть связано с формированием менее выраженного и более неупорядоченного рельефа поверхности, вызванного менее эффективным поглощением модифицирующего лазерного излучения с энергией фотонов ниже ширины оптической запрещенной зоны $As_{50}Se_{50}$. Снижение оптического поглощения, наблюдаемое в пленках $As_{50}Se_{50}$ с ЛИППС, вызвано повышенным рассеянием света на рельефе поверхности.

Ключевые слова: лазерно-индуцированные периодические поверхностные структуры, $As_{50}Se_{50}$ аморфные пленки, лазерно-индуцированное двулучепреломление, оптический ретарданс

Микроволновой синтез углеродных точек с высокой флуоресценцией

Насиров П.Д., Новикова С.А., Грибова Е.Д., Гладышев П.П., Мухина И.В.

С момента своего открытия углеродные точки представляют большой научный интерес благодаря своим уникальным свойствам, включая сильную флуоресценцию и биосовместимость, которые определяют их потенциальное применение в биосенсорике, биовизуализации, доставке лекарств и многих других областях. В данной статье представлены новые подходы к синтезу углеродных точек с высокой люминесцентнцией, разработанные в процессе поиска решения проблемы применения углеродных точек в иммунохроматографическом анализе.

Ключевые слова: углеродные точки, наночастицы, иммуноанализ.

Простой синтез и исследование наночастиц сплава FeCoNiPt с различным содержанием Pt для электрокатализа

Алексеева О.В., Карягина О.К., Козлов С.С., Кузнецов Л.И., Ларина Л.Л., Никольская А.Б., Шевалеевский О.И.

В этой работе представле простой синтез наночастиц (NPs) сплава FeCoNiPt с регулируемым содержанием платины (10–30 ат.%). NPs были получены мотодоа твердофазной реакции, с использованием ацетилацетонатных металлических прекурсоров. Структурные хисследования (TEM, HRTEM, STEM-EDS и XRD) показывают, что полученные NPs FeCoNiPt имеют однородную морфологию со средним диаметром 3–7 нм и кристаллизуются в однофазном гранецентрированном кубическом твердом растворе. Увеличение содержания Pt приводит к увеличению параметра решетки и увеличению размера кристаллитов, что согласуется с большим атомным радиусом Pt. Элементные данные STEM-EDS подтверждают однородное включение Fe, Co, Ni и Pt в отдельные наночастицы, демонстрируя формирование многокомпонентного сплава. Данное исследование показало, что регулирование содержания Pt в многокомпонентных сплавах FeCoNiPt позволяет модулировать электронную структуру d-зоны. Предложенный подход синтеза являяется экономически эффективным и масштабируемыи, открывая перспективный путь для разработки оптимизированных по содержанию Pt электрокатализаторов.

Ключевые слова: наночастицы, многокомпонентные сплавы, ПЭМВ, электроды, электрокатализ.

NANO ФИЗИКА & ХИМИЯ & МАТЕМАТИКА

NANOSYSTEMS:

PHYSICS, CHEMISTRY, MATHEMATICS

INFORMATION FOR AUTHORS

The journal publishes research articles and reviews, and also short scientific papers (letters) which are unpublished and have not been accepted for publication in other magazines. Articles should be submitted in English. All articles are reviewed, then if necessary come back to the author to completion.

The journal is indexed in Web of Science Core Collection (Emerging Sources Citation Index), Chemical Abstract Service of the American Chemical Society, Zentralblatt MATH and in Russian Scientific Citation Index.

Author should submit the following materials:

1. Article file in English, containing article title, the initials and the surname of the authors, Institute (University), postal address, the electronic address, the summary, keywords, MSC or PACS index, article text, the list of references.
2. Files with illustrations, files with tables.
3. The covering letter in English containing the article information (article name, MSC or PACS index, keywords, the summary, the literature) and about all authors (the surname, names, the full name of places of work, the mailing address with the postal code, contact phone number with a city code, the electronic address).
4. The expert judgement on possibility of publication of the article in open press (for authors from Russia).

Authors can submit a paper and the corresponding files to the following addresses: nanojournal.ifmo@gmail.com, popov1955@gmail.com.

Text requirements

Articles should be prepared with using of text editors MS Word or LaTex (preferable). It is necessary to submit source file (LaTex) and a pdf copy. In the name of files the English alphabet is used. The recommended size of short communications (letters) is 4-6 pages, research articles– 6-15 pages, reviews – 30 pages.

Recommendations for text in MS Word:

Formulas should be written using Math Type. Figures and tables with captions should be inserted in the text. Additionally, authors present separate files for all figures and Word files of tables.

Recommendations for text in LaTex:

Please, use standard Latex without macros and additional style files. The list of references should be included in the main LaTex file. Source LaTex file of the paper with the corresponding pdf file and files of figures should be submitted.

References in the article text are given in square brackets. The list of references should be prepared in accordance with the following samples:

[1] Surname N. *Book Title*. Nauka Publishing House, Saint Petersburg, 2000, 281 pp.
[2] Surname N., Surname N. Paper title. *Journal Name*, 2010, **1** (5), P. 17-23.
[3] Surname N., Surname N. Lecture title. In: Abstracts/Proceedings of the Conference, Place and Date, 2000, P. 17-23.
[4] Surname N., Surname N. Paper title, 2000, URL: http://books.ifmo.ru/ntv.
[5] Surname N., Surname N. Patent Name. Patent No. 11111, 2010, Bul. No. 33, 5 pp.
[6] Surname N., Surname N. Thesis Title. Thesis for full doctor degree in math. and physics, Saint Petersburg, 2000, 105 pp.

Requirements to illustrations

Illustrations should be submitted as separate black-and-white files. Formats of files – jpeg, eps, tiff.

НАНОСИСТЕМЫ:

ФИЗИКА, ХИМИЯ, МАТЕМАТИКА

Научный журнал
ISSN 2220-8054
DOI: 10.17586/2220-8054

2025. Том 16. № 6

Свидетельство о регистрации средства массовой информации ПИ № ФС 77–49048
выдано 22.03.2012 г. Федеральной службой по надзору в сфере
связи, информационных технологий и массовых коммуникаций (Роскомнадзор)

Учредитель и издатель:
федеральное государственное автономное образовательное учреждение высшего образования «Национальный исследовательский университет ИТМО»
197101, Российская Федерация, Санкт-Петербург, Кронверкский пр., 49, литер А

Адрес редакции:
191002, Санкт-Петербург г., ул. Ломоносова, д. 9, литер А
телефон: (812) 607-02-54, e-mail: nanojournal@itmo.ru
http://nanojournal.ifmo.ru/

Главный редактор: д.ф.-м.н., проф. Попов Игорь Юрьевич, iypopov@itmo.ru

Подписано в печать 27.12.2025 Дата выхода в свет 31.12.2025

Тираж 100 экз. 1 завод – 16 экз. Заказ № 17. Подписная цена.

Отпечатано: в ООО «Университетские телекоммуникации» Типография на Биржевой
Адрес: 199034, Санкт-Петербург, В.О., Биржевая линия, д. 16
Телефон: +7(812) 915-14-54, e-mail: zakaz@TiBir.ru

Журнал распространяется по подписке.
Подписку можно оформить online по Объединенному каталогу «Пресса России»
(http://www.pressa-rf.ru), подписной индекс 57385